Analysis and control of transitional shear flows using global modes

by

Shervin Bagheri

Akademisk avhandling som med tillstånd av Kungliga Tekniska Högskolan i Stockholm framlägges till offentlig granskning för avläggande av teknologie doktorsexamen fredagen den 12:e februari 2010, kl 10.15 i sal F3 vid Kungliga Tekniska Högskolan, Lindstedsv. 26, Stockholm.

To my grandfather, Mirhashem Hajimiragha.

Analysis and control of transitional shear flows using global modes

Shervin Bagheri
Linné Flow Centre
Department of Mechanics, Royal Institute of Technology (KTH)
SE-100 44 Stockholm, Sweden

Abstract

In this thesis direct numerical simulations are used to investigate two phenomena in shear flows: laminar-turbulent transition over a flat plate and periodic vortex shedding induced by a jet in crossflow. The emphasis is on understanding and controlling the flow dynamics using tools from dynamical systems and control theory. In particular, the global behavior of complex flows is described and low-dimensional models suitable for control design are developed; this is done by decomposing the flow into global modes determined from spectral analysis of various linear operators associated with the Navier–Stokes equations.

Two distinct self-sustained global oscillations, associated with the shedding of vortices, are identified from direct numerical simulations of the jet in crossflow. The investigation is split into a linear stability analysis of the steady flow and a nonlinear analysis of the unsteady flow. The eigenmodes of the Navier–Stokes equations, linearized about an unstable steady solution reveal the presence of elliptic, Kelvin-Helmholtz and von Kármán type instabilities. The unsteady nonlinear dynamics is decomposed into a sequence of Koopman modes, determined from the spectral analysis of the Koopman operator. These modes represent spatial structures with periodic behavior in time. A shear-layer mode and a wall mode are identified, corresponding to high-frequency and low-frequency self-sustained oscillations in the jet in crossflow, respectively.

The knowledge of global modes is also useful for transition control, where the objective is to reduce the growth of small-amplitude disturbances to delay the transition to turbulence. Using a particular basis of global modes, known as balanced modes, low-dimensional models that capture the behavior between actuator and sensor signals in a flat-plate boundary layer are constructed and used to design optimal feedback controllers. It is shown that by using control theory in combination with sensing/actuation in small, localized, regions near the rigid wall, the energy of disturbances may be reduced by an order of magnitude.

Descriptors: Fluid mechanics, flow control, hydrodynamic stability, global modes, jet in crossflow, flat-plate boundary layer, laminar-turbulent transition, Arnoldi method, Koopman modes, balanced truncation, direct numerical simulations.

Preface

This thesis in fluid mechanics consists of two parts. The objective of the first part is to provide an introduction to some aspects of flow physics by analyzing two relevant examples. The analysis is mainly carried out numerically and therefore this part also contains a section on the algorithms and techniques used throughout the thesis. The presentation is at a non-expert level providing the necessary background for part 2. The second part contains 8 papers. The papers are adjusted to comply with the present thesis format for consistency, but their contents have not been altered compared to published or submitted versions, except for minor corrections. Division of work among the authors is given in part 1.

Paper 1. BAGHERI, S., HŒPFFNER, J., SCHMID, P. J. & HENNINGSON, D. S. 2009 Input–output analysis and control design applied to a linear model of spatially developing flows. *Appl. Mech. Rev.* **62** (2), 1–27.

Paper 2. BAGHERI, S., BRANDT, L. & HENNINGSON, D. S. 2009 Input–output analysis, model reduction and control design of the flat-plate boundary layer. *J. Fluid Mech.* **620**, 263–298.

Paper 3. BAGHERI, S., ÅKERVIK, E., BRANDT, L. & HENNINGSON, D. S. 2009 Matrix-free methods for the stability and control of boundary layers. *AIAA J.* **47**, 1057–1068.

Paper 4. SEMERARO, O., BAGHERI, S., BRANDT, L. & HENNINGSON, D. S. 2009 Feedback control of three-dimensional Tollmien–Schlichting wavepackets using reduced-order models. *Internal report.*

Paper 5. BAGHERI, S., SCHLATTER, P., SCHMID, P. J. & HENNINGSON, D. S. 2009 Global stability of a jet in crossflow. *J. Fluid Mech.* **624**, 33–44.

Paper 6. SCHLATTER, P., BAGHERI, S. & HENNINGSON, D. S. 2009 Self-sustained global oscillations in a jet in crossflow. *Theor. Comp. Fluid Mech.* Submitted.

Paper 7. ROWLEY, C. W., MEZIĆ, I., BAGHERI, S., SCHLATTER, P. & HENNINGSON, D. S. 2009 Spectral analysis of nonlinear flows. *J. Fluid Mech.* **641**, 115–127.

Paper 8. BAGHERI, S. & HANIFI, A. 2007 The stabilizing effect of streaks on Tollmien-Schlichting and oblique waves: A parametric study. *Phys. Fluids* **9** (7), 0708103.

Contents

Part 1

Introduction

CHAPTER 1

Introduction

Despite the long history of fluid mechanics we lack a complete understanding of why fluid flows have a tendency to change pattern when perturbed. Two examples of flows that transition from an organized and steady state to an irregular and fluctuating state when perturbed are the laminar-turbulent transition of flows on slender bodies and the alternating shedding of vortices of flows behind bluff bodies. It has been known for over a century that these flow phenomena are governed by the basic conservation laws of mechanics, but the difficulties that arise when one attempts to solve or analyze the system of equations have proved to be a major obstacle. With the advent of numerical simulations remarkable advancements have been made in fluid mechanics in the past two decades. In particular, the analysis and control of flows using tools developed by the mathematical community has emerged as an important discipline in the field.

In this thesis, we are concerned with the laminar-turbulent transition of a flow along a flat plate and the vortex shedding in a jet in a crossflow. In particular, a global viewpoint is adopted where the flow is allowed to move as it wishes in the physical domain without assumptions about or constraints on its dynamics. There are countless examples in both nature and industry pertaining to the study of the flow along a flat plate, since it is the archetype of boundary layer flows. In these flows the layer of fluid in the immediate vicinity of the surface is sheared, resulting in rapid velocity change over a short distance normal to the surface. Examples of boundary-layer flows are the layer of air near the ground or near an aircraft wing, where the observed flow pattern depends on the smoothness of the surface, level of diurnal heat, moisture, turbulence levels far away from the surface and so on. The fundamental issue is a physical and mathematical understanding of the transition of a laminar smooth flow to a turbulent unpredictable one. Compared to a laminar flow, a turbulent flow is more expensive and often undesirable in practical applications. For instance, to sustain a turbulent flow in a pipe, more pressure is required to maintain the same volume of discharge as a laminar flow. Also, turbulent flow around vehicles increases the friction, resulting in higher fuel costs. Understanding the transition process is adjacent to the field of flow control and in particular *transition control*, where the aim is to modify the flow conditions in order to delay the laminar-turbulent transition. The necessary flow conditions can be obtained by changing initial and boundary conditions (e.g. surface roughness),

the flow properties (e.g. velocity, pressure distribution, turbulence level) or the fluid properties (e.g. density, viscosity and temperature).

The classical example of vortex shedding is the von Kármán vortex street that can be observed in the formation of clouds behind mountains and islands or in the flow behind vehicles, buildings and chimneys of factories. It is of great practical significance to identify the source from which alternating pairs of vortices are shed downstream, since they often lead to large structural vibrations, acoustic noise and resonance. Another example of a flow dominated by vortex shedding is the jet in crossflow, which is found when gas or liquid is injected through a small orifice into a crossflow of a similar fluid. The flow is related to a wide range of applications. A few examples are plume dispersal from smoke stacks and volcanos, reduction of environmental pollution (the "jet" represents a stream flowing into a lake) and film cooling applications in jet engine combustors.

This introductory chapter is organized as follows. Section 1.1 describes the laminar-turbulent transition of a flow over a flat plate in a phenomenological way and introduces the key ideas behind transition control. Section 1.2 gives an insight into the physics of the jet in crossflow obtained by direct numerical simulations and paves the way for the analysis in chapter 2. The present chapter concludes with an overview of the main results of the thesis and a brief motivation of the global mode approach undertaken in the subsequent chapters of the thesis.

1.1. Physics of the flow on a flat plate

Viscous flows in straight tubes, pipes, channels and on flat plates are steady for sufficiently small values of the (dimensionless) number UL/ν, where U and L are, respectively, a velocity and a length characteristic of the flow and ν is the kinematic viscosity of the fluid. At higher values, however, the flow shows intermittent oscillations and eventually becomes highly irregular and unsteady. This transition from a laminar flow to a turbulent one at a critical *Reynolds number*, $Re = UL/\nu$ was first investigated in a pipe by Reynolds (1883).

Consider a steady uniform stream of flow with speed U that encounters a flat plate of length L. It is appropriate to define the Reynolds number as $Re_x = Ux/\nu$ where $0 \leq x \leq L$ is the distance on the plate from the leading edge. The critical Reynolds number, Re_x, for the laminar-turbulent transition is notoriously difficult to determine. Transition can occur abruptly, gradually and at completely different locations on the plate depending on the size, spatial structure and temporal behavior of the disturbances that can be found in the laboratory or numerical experiments. For example, the presence (or combination) of acoustic waves, roughness on the plate, vortical structures in the free stream critically affects the transition process. A number of books (Batchelor 1967; Schlichting & Gersten 2000; Schmid & Henningson 2001) treat the different laminar-turbulent transition scenarios in boundary layers. We proceed by
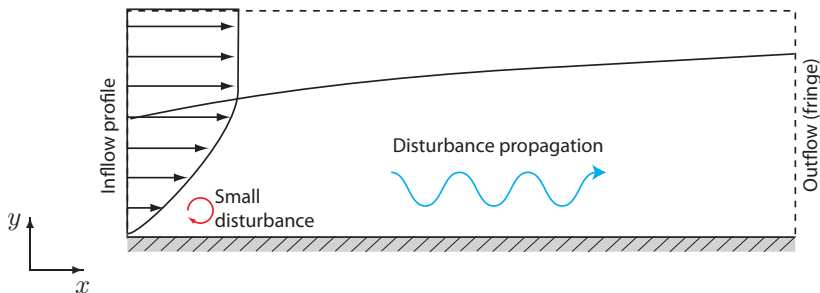
FIGURE 1.1. Sketch of a numerical experiment of the evolution of a wavepacket disturbance in a flat-plate boundary layer. The Reynolds number at the computational inlet is $Re_x \approx 3 \times 10^5$ and the computational outlet it is $Re_x \approx 1 \times 10^6$. The numerical parameters are given in table 4.2 (case 3D-NLIN-BL) in section 4.4 of this thesis.

a simple numerical experiment to characterize the evolution of a small disturbance in the flow on a flat plate in order to highlight the essential physics that is relevant for our purposes. In practice, flow conditions are significantly more complicated than our single-disturbance example but the underlying physics is essentially the same. The simulation is performed using the spectral Simson code described in section 4.4.

A sketch of the setup is given in figure 1.1. Prandtl (1905) introduced the concept of a boundary layer, as a thin (about $2-5$ mm on a 180 cm plate) layer, where the effects of viscosity are important. This layer is the region (marked in figure 1.1 with solid black line) where diffusion of the vorticity generated at the surface is significant. The thickness of the laminar boundary layer δ is related to the viscosity and the downstream distance as $\delta \sim (\nu U/x)^{-1/2}$, which indicates that the layer grows slowly in the downstream direction. Prandtl showed that for the boundary layer, the Navier–Stokes equations (see section 2.1) can be reduced to a simpler form and it was Prandtl's student Blasius (1908) who formulated a nonlinear ODE and solved it, with the velocity profile shown schematically (as the inflow profile) in figure 1.1. Inside the boundary layer and far upstream in the flow domain we place a small localized perturbation. As the disturbance is released, it propagates in the downstream direction and its fate depends on its initial amplitude and on its initial physical shape. The disturbance could for instance be introduced by using a loudspeaker to generate a short pulse, injected through a small hole in the plate. The volume of the loudspeaker would then determine the disturbance amplitude and the structure of the hole in the plate its shape.
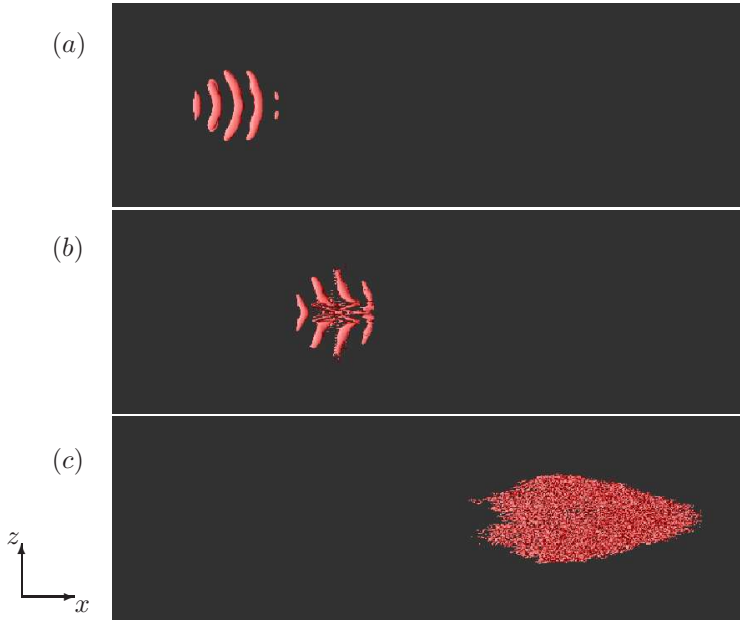
FIGURE 1.2. Snapshots of the disturbance at $t = 300, 600$ and $t = 1000$ are shown in (a), (b) and (c) respectively. Red iso-contour levels depict the λ_2-criterion. The plate is shown in black and viewed from top.

Figure 1.2 shows "snapshots" of the disturbance (top view of the plate) at three different instances in time using iso-contour levels of the λ_2-criterion (Jeong & Hussain 1995). The λ_2 levels are useful to identify vortical structures in the flow. In the initial stage (figure 1.2a), the disturbance is nearly two dimensional in the spanwise direction (z) and it grows in amplitude rapidly. After approximately 300 time units the disturbance has a different structure; now significant three-dimensional components (figure 1.2b) and smaller wavelengths are observed. Finally at $t = 1000$, a localized turbulent spot is developed with a typical arrow-shaped structure. The disturbance is now characterized by a wide range of scales in all spatial directions (figure 1.2c). The turbulent spot eventually leaves the computational domain and the flow returns to the steady boundary layer. We have thus identified three distinct flow regimes; (i) *the laminar region* where a smooth disturbance grows in size; (ii) *the transition region* where there is breakdown of the disturbance into a significantly more complicated structure; (iii) *turbulent region* where a turbulent spot emerges.

Depending on the Reynolds number, the drag due to the skin friction in the laminar region can be as much as an order of magnitude less than that
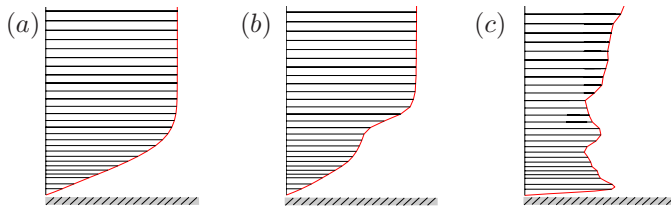
FIGURE 1.3. Velocity profiles of the streamwise component
(u) as a function of the wall-normal distance from the plate (y).
The profiles (a), (b) and (c) correspond to the snapshots (a-c)
in figure 1.2 and are extracted approximately in the center of
the disturbance.

in the turbulent region (Schlichting & Gersten 2000). For an aircraft[1] or a
vehicle the reduced drag means longer range, reduced fuel cost or increased
speed. To illustrate this, for each snapshot in figure 1.2, the streamwise veloc-
ity component u at the location on the plate where the disturbance is present
is shown as a function of the wall-normal coordinate y in figure 1.3. For the
first snapshot, the characteristic laminar boundary-layer profile (figure 1.3a) is
observed, but already after a short period, the disturbance has modified the
profile considerably (figure 1.3b), and an inflection point can be observed. The
third profile (figure 1.3c) extracted from the turbulent spot is very distorted
and the smooth boundary layer has changed its character completely. The tur-
bulent profile changes rapidly over a very short distance normal to the surface
compared to the laminar profile. As a consequence the local shear stress is
considerably higher in the turbulent region.

1.1.1. *Linear amplification*

If the upstream disturbances in the boundary layer are small – determined by
the receptivity (Goldstein & Hultgren 1989) of the boundary layer to external
flow conditions – the initial stage in the transition process is a linear ampli-
fication. In figure 1.4 the time evolution of the disturbance kinetic energy of
the numerical experiment is shown with a black solid line. We observe a rapid
energy growth until the disturbance is propagated out of the computational
domain at $t = 1500$. In the figure, the kinetic energy of a disturbance with an
infinitesimal amplitude – where the nonlinear effects are neglected – is shown
by the dashed line. We observe that the energy of the infinitesimal amplitude
and the finite-amplitude disturbance initially grow with the same rate.

The linearized flow is considerably easier to analyze, since the temporal
part of the disturbance can be decomposed into a number of waves that grow

[1]Friction drag constitutes more than half of the total aircraft drag, with $18\%, 4\%, 3\%$ and
3% for wing, horizontal tail plane, fin and nacelles, respectively. If the flow were laminar on
40% of the surfaces, the total drag would be reduced by 16% (Schrauf 2005).
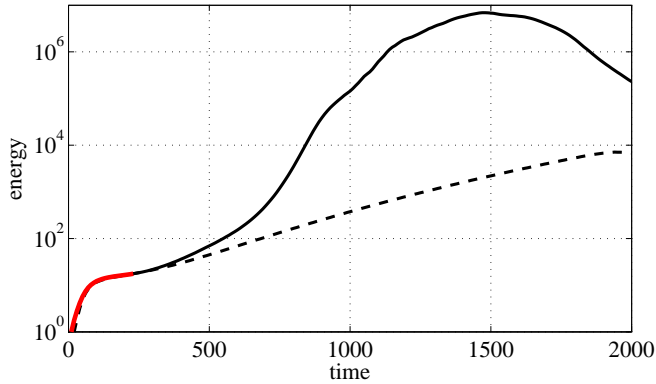
FIGURE 1.4. The evolution of the kinetic energy of a distur-
bance in time corresponding to a nonlinear simulation (solid
black) and linear simulation (dashed black). The initial growth
phase where the linear and nonlinear curves nearly collapse is
marked in red color.

or decay independently of each other as predicted by linear stability theory.
However, for the boundary layer, no single wave grows exponentially in time;
in fact all waves decay for long times, but their superposition may result in
a wavepacket that grows as it propagates downstream. Since late 1980's a
new (linear) mathematical approach to characterize the disturbance behav-
ior has emerged, based on transient growth analysis (Reddy & Henningson
1993), pseudo spectra (Trefethen 1997), categorizing flows as noise amplifiers
or oscillators (Huerre & Monkewitz 1990) and analysis of input-output norms
(Jovanovic & Bamieh 2005).

1.1.2. *Transition control*

The natural question that arises is: If we can suppress the growth of the distur-
bance, can we delay the transition to turbulence? In many cases the answer is
yes; for our numerical example above if we assign an order of magnitude smaller
amplitude to the initial disturbance, it breaks down further downstream and
the development of the turbulence spot is delayed. One major objective of flow
control is thus to damp the amplitude of disturbances at an early stage in the
boundary layer in order to delay transition to turbulence. Since we observe
that the disturbance energy growth is initially a linear process (see also e.g.
Kim & Bewley 2007; Schmid & Henningson 2001), transition control focuses
mainly on the simpler linear system.

If the necessary flow conditions resulting in lower disturbance growth are
achieved in a way that requires energy input, one needs to introduce actuators,
such as loudspeakers, synthetic jets (Smith & Glezer 1998), electro-magnetic ac-
tuators (Pang & Choi 2004), plasma actuators (Grundmann & Tropea 2008) or

various MEMS actuators (Ho & Tai 1998) constructed using micro-machining techniques. Flow control is indeed engineering, where besides the type of actuators, the distribution and location of actuators has to determined. In general, the more physical insight one has into the disturbance behavior, the better design decision one is able to make. If we know *exactly* what type of disturbances are present in the flow, e.g. if perturbations are traveling waves or in the form of elongated streamwise vortices called streaks, using the actuators we can introduce other disturbances that counter-act them. For example a second wave of appropriate amplitude and phase would cancel the traveling wave by interference (Milling 1981) or blowing and suction at the wall (Hammond *et al.* 1998) would cancel out the streaks. If we don't know the exact form of the disturbance, we can monitor the flow using sensors and adjust the actuation accordingly to achieve the control objectives. This type of control is known as feedback control, where in addition to actuators, the design and distribution of sensors have to be taken into account. The sensor measurements could be a few pressure measurements using a small microphone membrane mounted flush to the wall, velocity measurements using hot-wire anemometry near the wall or shear-stress measurements using thermal sensors (wall wires).

1.2. Physics of the jet in a crossflow

The jet in crossflow (JCF) is the interaction of two well-studied canonical flows, the flat-plate boundary layer flow and the flow ejected through an orifice into a quiescent environment, a free jet flow. Since vorticity cannot be created or destroyed in the interior of a flow and is produced only at boundaries (or by initial conditions), the orifice is the only source of vorticity for a free jet and consequently, the dynamics of jets are commonly described by convection, diffusion, stretching and turning of vorticity in an otherwise irrotational flow. In contrast (as discussed previously), in a flat-plate boundary layer, vorticity generated at the wall convects and diffuses in the wall-normal direction, causing growth of the boundary layer. The interaction of the boundary layer and the jet vorticity results in a highly unsteady fully three-dimensional flow and a number of "vortical structures", which refer to flow features that are relatively well organized and appear rotational in nature. These structures can be identified in three different regions of the flow domain as shown schematically in figure 1.5; the jet region, the wake region and the wall region. In particular, four large-scale vortical structures of the JCF have been studied extensively by researchers; (1) the counter-rotating vortex pair (Moussa *et al.* 1977); (2) the horse-shoe vortex and its wall vortices (Kelso & Smits 1995); (3) loop-like or ring-like vortices (Kelso *et al.* 1996; Lim *et al.* 2001) and (4) upright vortices (Kelso *et al.* 1996; Fric & Roshko 1994).

1.2.1. *Steady-unsteady transition*

We will now illustrate how a steady jet in crossflow gradually exhibits unsteady behavior that is sustained for all times when it is perturbed. One major obstacle towards understanding the physical mechanisms of the unsteadiness in
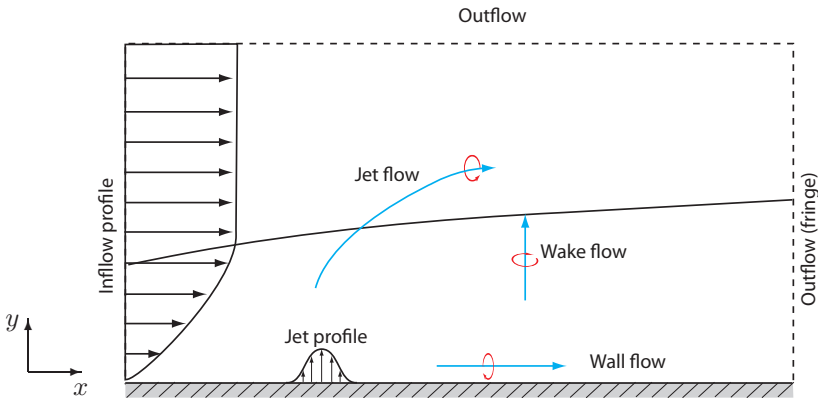
FIGURE 1.5. Sketch of a numerical experiment of the jet in crossflow. The initial fields are the flat-plate boundary layer profile and a parabolic jet profile. The ratio between the jet flow and the crossflow denoted by R, is three. The numerical parameters are given in table 4.2 (case JCF) in section 4.4.

the flow is that the "natural state" of the JCF is unsteady. A steady flow will never be observed in laboratory experiments or in applications. One of the advantages of numerical experiments is that we can artificially force the unsteady flow to become steady, in order to better understand the underlying physics. Figure 1.5 shows a sketch of the numerical setup used to simulate the jet in crossflow. In addition to the laminar boundary-layer profile at the upstream inlet investigated in the previous section, an inhomogeneous parabolic boundary condition is imposed in order to model a laminar pipe flow mounted to the plate.

The steady flow obtained by filtering out all the unsteady structures (Åkervik *et al.* 2006) is "released" and its evolution in time is followed by a numerical simulation. A disturbance is not explicitly introduced, instead background numerical noise acts as flow perturbation. Figure 1.6 shows the λ_2 criterion (red) and the streamwise velocity (gray) of a sequence of snapshots from the numerical experiment. We observe how a well organized smooth flow is gradually transformed into a more complicated irregular flow with significantly smaller vortices. The most dominant feature of the steady flow (label ① in figure 1.6a) – and the largest vortical structure of the JCF – is the *counter-rotating vortex pair* (CVP) that takes the form of two distinct tubes. The direction of rotation is in such a way that fluid is lifted up in between the vortices. This vortex pair develops because the crossflow skirts laterally around the jet and shears the jet fluid along its edges and then folds the face of the jet over itself to form the CVP. The CVP emerge from the center of an cylindrical vortex sheet (or a shear layer) developed when the crossflow and the jet fluid come into contact.
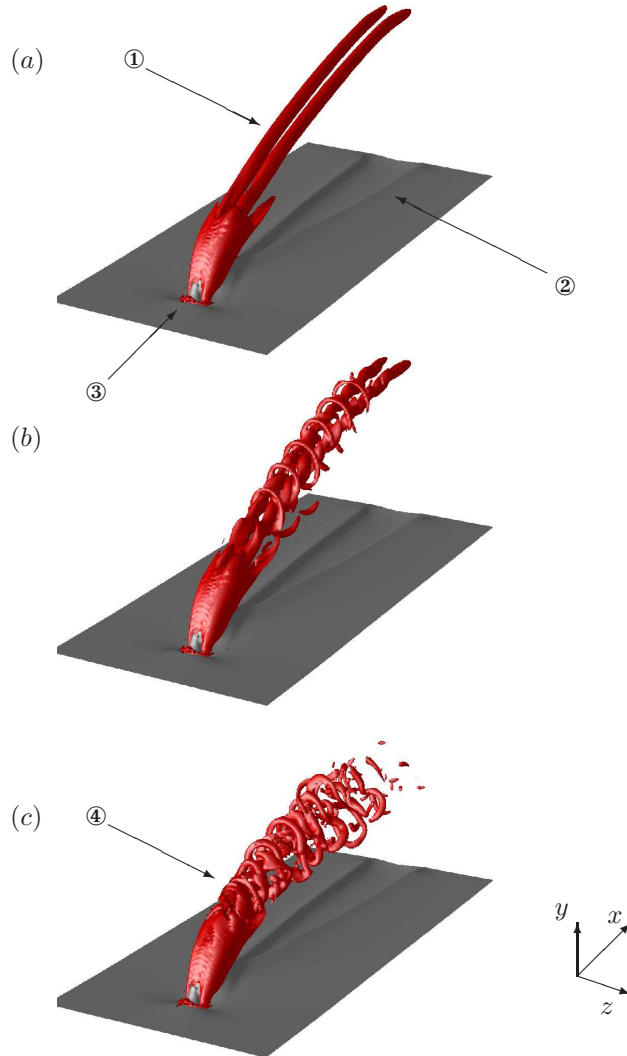
FIGURE 1.6. Three instantaneous snapshots of the steady-unsteady transition at $t = 0, 300$ and $t = 500$ are shown in (a), (b) and (c) respectively. Red contour levels represent the $\lambda_2 = -0.09$ and the gray contour levels represent the stream-wise velocity $u = 0.2$. See text for explanations of labels ①-④.

Close to the wall, when the crossflow encounters the jet, part of the crossflow is deflected in direction of the jet flow and part of it is pushed towards the wall, to form a spanwise oriented vortex, the *horse-shoe vortex* (label ③ in figure 1.6a). This vortex wraps around the base of the jet and forms a streamwise vortex

pair, *the wall vortices* in the wall region, as shown in by the gray contour levels of the streamwise velocity (label ② in figure 1.6).

After a long time ($t = 300$) the disturbances triggered by the background noise have grown sufficiently in amplitude to modify the steady flow. As shown in figure 1.6(b), the disturbance modifies mainly the CVP; a varicose out-of-phase oscillation of the two vortex tubes is observed and "arches" are created, i.e. the vortex loops coil up around the upper side of the CVP and their bases join with the CVP. This type of symmetric structures are associated with the roll-up of the cylindrical vortex sheet. Finally, at $t = 500$, the symmetric vortex loops are distorted into half-ring shaped asymmetric vortices (label ④ in figure 1.6c) which rapidly break down into a series of smaller vortices. This flow is sustained for all times; half-ring shaped vortices are continuously generated from an internal source upstream, they grow as they are convected downstream, and finally they gradually dissipate due to viscosity.

1.2.2. *Self-sustained oscillatory behavior*

It is of interest to determine whether the unsteadiness depends on the external disturbance environment (in our case numerical noise due to discretization errors) or if it is an intrinsic property of the JCF. It is well known (Huerre & Monkewitz 1985) that (co-flowing) shear layers amplify upstream incoming disturbances and the frequencies observed in the flow depend highly on the frequencies present in the external disturbance environment. However, under certain flow conditions a resonance can arise where one observes a few dominant frequencies, independent of the spectral content of the noisy outside environment. A resonance can for example be triggered when one introduces a rigid body at an appropriate downstream location in the flow. The body creates a pressure feedback loop giving rise to oscillations at discrete resonant frequencies[2]. However, such a feedback loop can also be produced by purely hydrodynamic means, where a downstream body is not necessary. Such flows often have a region of significant reversed flow (e.g. backflow). A classical example is the von Kármán vortex street developing behind a circular cylinder at low Reynolds numbers. The unsteadiness usually consists of small patches of vorticity being released periodically from a location, i.e. *vortex shedding*, where the oscillation frequency is insensitive to external low-amplitude forcing. Many examples of hydrodynamic resonances exist, (see e.g. Chomaz *et al.* 1987; Monkewitz *et al.* 1990; Strykowski & Niccum 1992; Barkley *et al.* 2002), and during the last decade a large number of experimental and numerical studies have been devoted to categorization of flows as oscillators or amplifiers (see Huerre & Monkewitz 1990; Huerre 2000).

The simplest approach, that provides only supporting evidence for oscillatory behavior, is to place probes in the flow and study single-point spectral data. The time signal of a probe located in the shear layer of the JCF is shown in figure 1.7(a), where Fourier analysis reveals a dominant frequency of

---

[2]Similar to bounded states in quantum mechanics, resulting in a discrete energy spectrum.
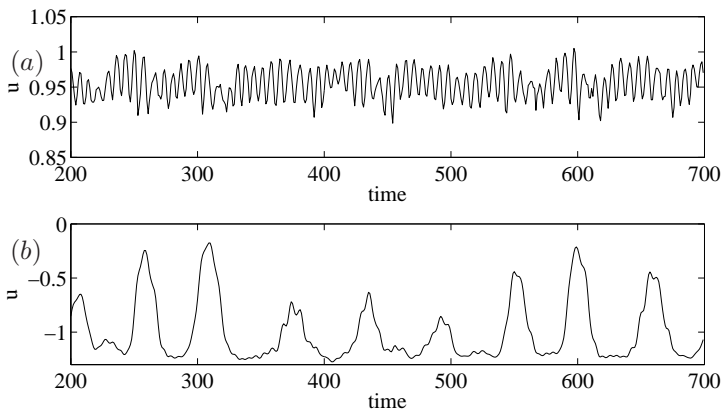
FIGURE 1.7. Time signals of two probes measuring the streamwise velocity u component at a single point in the flow. In (a) the probe is placed in the shear layer and in (b) near the separated region downstream of the jet near the wall.

Strouhal number $St_2 \equiv f_2 D/V_{\text{jet}} = 0.14$. In addition to this high frequency, a distinct low frequency $St_1 = 0.017$ is observed by a probe located in the wall region downstream of the jet orifice (figure 1.7b). Several time signals from other probes have been obtained and all the additional frequency peaks are linear combinations of St_1 and St_2, corresponding to higher harmonics triggered by nonlinear interactions between the two main frequencies.

There is some evidence (Hammond & Redekopp 1998) and numerous studies (Theofilis *et al.* 2000; Alam & Sandham 2000; Barkley *et al.* 2002; Marquillie & Ehrenstein 2002; Theofilis 2005; Giannetti & Luchini 2007; Åkervik *et al.* 2007) that connect self-sustained oscillations in fluid systems with large unsteady separated regions. The flow under investigation here has two regions of reversed flow: a smaller, steady separated region upstream of the jet which coincides with the horse-shoe vortex, and a larger unsteady region of reversed flow directly downstream of the emerging jet near the wall. The animation of the DNS data shows that the separation region downstream of the jet orifice is highly unsteady. In the upper part of this region, patches of negative u are periodically released in the wall-normal direction with the fundamental frequency $St_2 = 0.14$. The separated region also oscillates with the lower fundamental frequency $St_1 = 0.017$, however this time the entire recirculation zone downstream of the jet is periodically moving back and forth in the spanwise direction. In figure 1.8, the movement of the separation region, downstream of the jet, oscillating in two directions with two distinct frequencies is shown.
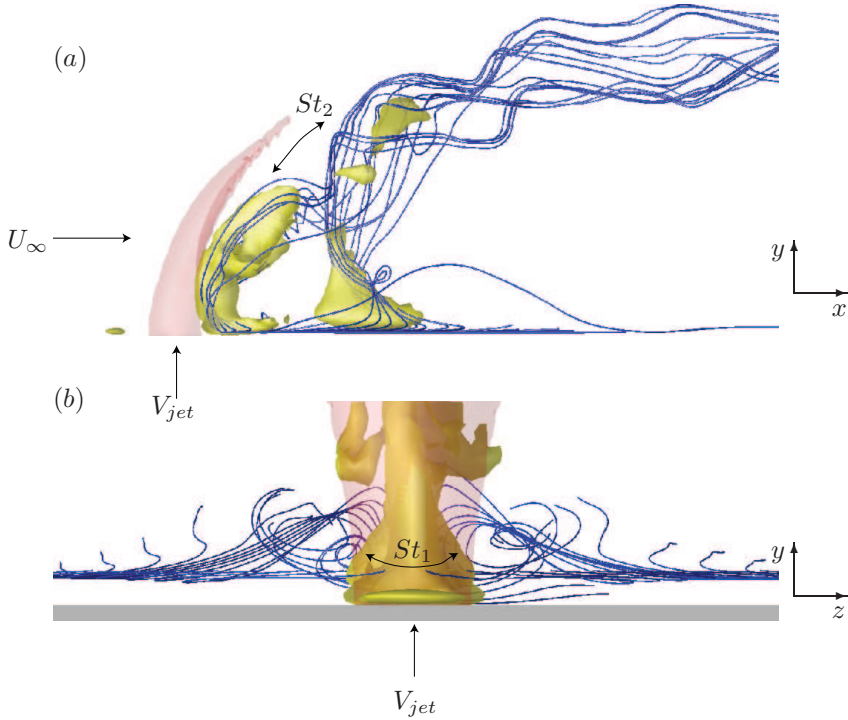
FIGURE 1.8. Yellow iso-contour levels represent zero stream-wise velocity, marking the region of reversed flow, red levels show positive wall-normal velocity, marking the jet fluid. The blue streamlines originate from the crossflow fluid and show how the crossflow is sucked into the jet (a) and how it develops a pair of streamwise wall vortices (b). Top figure is a side view, where the region of reversed flow oscillates back and forth in the wall-normal direction. Bottom figure is a front view, illustrating the movement of the separated region in the spanwise direction.

1.3. Thesis overview

In the previous two sections, using numerical experiments, we have observed the following:

(i) The breakdown of a small-amplitude disturbance in a boundary layer, resulting in a turbulent spot. Our interest lies in damping the growth of disturbances at an early stage in the transition process in order to delay the development of turbulence.

(ii) The nonlinear saturation of a small-amplitude disturbance (background numerical noise), resulting in self-sustained oscillatory behavior of the flow. Our interest lies in understanding the underlying mechanisms of the disturbance growth and identifying the spatial flow structures associated with the oscillations.

The aim of the present thesis is to study these two phenomena using *global modes*.

1.3.1. *Global modes*

The concept of global modes in fluid mechanics has over the last two decades been used in various contexts. In the early nineties it was part of a theoretical framework (Huerre & Monkewitz 1990) for the understanding of self-sustained oscillations. A global mode was defined as a flow structure that oscillates with one single frequency and satisfies certain boundary conditions, similar to bound states in quantum mechanics. More recently (Theofilis 2005; Henningson & Åkervik 2008), global modes have been associated with the eigenmodes of the linearized Navier–Stokes operator for flows that have two or three inhomogeneous spatial directions. The term "global" in this context is used to differentiate from the approach to the classical local hydrodynamic stability analysis applicable to parallel shear flows, for example the eigenmodes of the Orr-Sommerfeld/Squire equations. A third usage of the term "global mode" is to denote any localized vortical structure that is contained in the full global spatial domain. In this sense, global modes are not simply instantaneous snapshots of flow fields containing vortical structures, rather they are extracted from experiments or numerical simulations by some method to isolate certain dynamical features, such as coherent structures either growing with one rate, oscillating with one frequency or containing the largest possible kinetic energy, etc. We adopt the latter definition of a global mode.

In particular, the following global modes are considered:

(i) *Linear global eigenmodes* are small-amplitude perturbations that grow or decay exponentially and pulsate with one frequency. They are useful to determine the linear stability of a steady flow and to describe the underlying physical mechanisms for perturbation growth.

(ii) *Koopman modes* represent spatial flow structures with time-periodic motion. They are useful to characterize oscillatory nonlinear flow dynamics.

(iii) *Balanced modes* are used to construct low-dimensional models of large-scale flow systems in order to design efficient controllers for transition delay. The reduced-order model captures the relation between inputs (disturbances and actuators) and outputs (sensors used for flow measurements).

1.3.2. *Contributions*

To the author's knowledge, this thesis is the first to perform a simulation-based global stability analysis of a fully three-dimensional flow and to present

a technique for describing the behavior of nonlinear flows, by decomposing the flow into Koopman modes.

During the course of the thesis, the following contributions are described: Direct numerical simulation (DNS) of the three-dimensional jet in crossflow at velocity ratio, $R = 3$, and the identification of two distinct self-sustained flow oscillations. Computation of a three-dimensional steady solution and a number of unstable linear global eigenmodes. The use of global modes to discover the presence of elementary instability mechanisms, such as elliptic instability, Kelvin-Helmholtz instability and von Kármán type of instability. Computation of a number of Koopman modes, and their use to identify coherent structures associated with vortex shedding.

The main contributions of this work for transition control are as follows: The use of a suite of tools to analyze and control linear flow systems, for example controllability, observability, balancing, transfer function norms, stochastic framework, design of estimators, optimal and robust controllers. The use of a few localized sensors/actuators and control theory to reduce the energy growth of two- and three-dimensional disturbances in the flat-plate boundary layer by one order magnitude or more. Development and validation of reduced-order models of the flat-plate boundary layer using balanced modes.

1.3.3. *Organization*

In chapter 2, the transition from a steady flow to an unsteady one is analyzed using linear global eigenmodes and Koopman modes. The global mode theory is presented for general fluid systems followed by examples on the jet in crossflow. Chapter 3 gives a treatment of linear systems theory including model reduction and control design. Along the way, the concepts are illustrated on the flat-plate boundary layer flow. Chapter 4 provides a detailed description of the numerical algorithms used to compute global modes, with a few simple examples to demonstrate convergence behavior of the methods. This first part of the thesis finalizes with a short summary and outlook in chapter 5.

Flow analysis using global modes

The jet in crossflow is a complex flow. It involves the interaction of at least four shear layers, namely the boundary layer, the jet shear layer, a separated shear layer and a wake. Due to the strong coupling between the shear layers, one is obliged to study the *global* behavior of the flow, in order to obtain a complete picture of the dynamics. The complete steady-unsteady dynamics of the jet in crossflow can be divided into a number of stages. Figure 2.1 shows the time evolution of the streamwise velocity component at $(x, y, z) = (12, 6, \pm 2)$ extracted from the numerical simulation discussed in section 1.2. The trajectory starting at the steady flow at $t = 0$ (marked with filled black circle in figure 2.1), departs from the steady solution and advances towards an attractor region where the trajectory appears to fluctuate randomly back and forth. In this chapter, we describe the dynamics in the two regions (marked schematically with circles in figure 2.1): the linear dynamics in a small neighborhood (black circle) of the steady solution and the nonlinear dynamics evolving in the attractor region (blue circle).

Global linear stability analysis determines whether exponentially growing perturbations exist in a neighborhood of the steady solution. These perturbations, called linear global eigenmodes, represent spatially coherent structures that grow or decay exponentially and pulsate with one frequency. The fact that the instabilites are global modes does not mean that the elementary mechanisms of the instabilities are not local. In fact, this is often the case, where locally the inviscid Kelvin-Helmholtz instability, inviscid elliptic instability or viscous Tollmien-Schlichting waves are active, but the coupling between them is a truly global phenomenon. If unstable global eigenmodes exist, disturbances will grow until they saturate nonlinearly to a more complicated state. For self-sustained oscillatory flows, the nonlinear flow commonly evolves near a limit cycle or quasi-periodic attractors. The most convincing reports so far are the milestone experiments of Provansal *et al.* (1987) that showed that the vortex shedding behind a circular cylinder at low Reynolds number is due to an amplified global instability that saturates via Hopf bifurcation to a self-sustained limit cycle.

The flow dynamics evolving in the attractor region is difficult to analyze by studying individual trajectories. To understand the global features of the unsteady flow, an easier task is to study its statistical properties, such as time-averages. One approach, explained in this thesis, is the decomposition of the
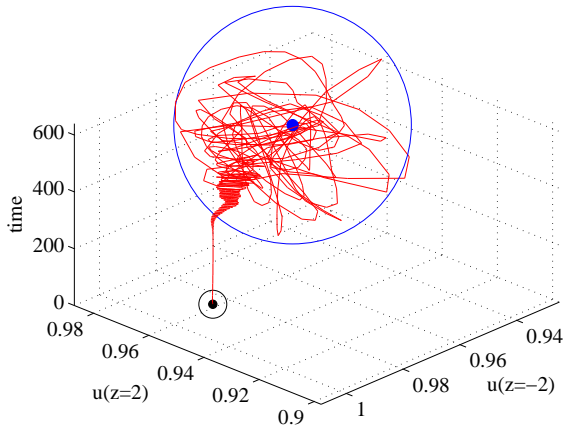
FIGURE 2.1. The streamwise velocity at $(x, y, z) = (12, 6, \pm 2)$ is plotted as function of time. The black circle marks the region where the flow behavior is linear, whereas the blue circle marks the nonlinear flow dynamics. The figure shows the entire linear-transient-nonlinear development.

unsteady nonlinear dynamics into a set of global modes, referred to as the Koopman modes. The modes can be considered as a generalization of the time-averaged mean flow; the first mode is the mean flow, whereas other Koopman modes are harmonic averages, i.e. spatial structures that display periodic behavior in time. In this way we can identify the flow structures that oscillate with precisely the same frequency as the vortex shedding observed in the flow.

This chapter is organized as follows. In section 2.1, we present the governing equations for an incompressible flow. In section 2.2, we define the linear global eigenmodes and discuss their significance for the jet in crossflow. Finally, in the last section of the chapter we introduce the spectral properties of the Koopman operator and the nonlinear analysis of the jet in crossflow.

2.1. Equations of motion

The Navier–Stokes equations governing the rate of change of momentum per unit volume of an incompressible fluid are given by

$$\frac{\partial \mathbf{u}}{\partial t} + (\mathbf{u} \cdot \nabla)\mathbf{u} = -\nabla p + \frac{1}{Re}\nabla^2 \mathbf{u} + \mathbf{F} \tag{2.1a}$$

$$\nabla \cdot \mathbf{u} = 0 \tag{2.1b}$$

where $\mathbf{u}(\mathbf{x}, t) = (u, v, w)^1$ and $p(\mathbf{x}, t)$ are the velocity and pressure in space $\mathbf{x} = (x, y, z) \in \Omega$ and time $t \geq 0$, $\nabla = (\partial_x, \partial_y, \partial_z)$ is the divergence operator and the term $\mathbf{F} = (f_1, f_2, f_3)$ represents a body force. The Reynolds number is defined as

$$Re = \frac{U_\infty \delta_0^*}{\nu}$$

where U_∞ is the constant streamwise free-stream velocity, δ_0^* is the displacement thickness at a particular distance from the leading edge x_0 and ν is the kinematic viscosity. The flow evolves in the spatial domain defined by,

$$\Omega = \{\mathbf{x} \in \mathbb{R}^3 | 0 \leq x \leq L_x, 0 \leq y \leq L_y, -L_z/2 \leq z \leq L_z/2\}.$$

For all flows investigated in this thesis the solutions to (2.1) are periodic in the streamwise x and spanwise z directions with periodicity L_x and L_z respectively. For the flow on a flat plate and the jet in crossflow, periodic boundary conditions in the streamwise direction are artificially enforced by $\mathbf{F}$. In the wall-normal direction y, different boundary conditions are imposed depending on the flow configuration. See section 4.4.2 and table 4.2 for details on the imposed boundary conditions.

We omit entirely any discussion of partial differential equations and the subsequent analysis is presented for finite-dimensional systems – ordinary differential equations – for simplicity. One can either think that the flow is represented on a number of grid points obtained by discretizing the domain Ω, or that the dynamics takes place over some finite-dimensional smooth manifold (see e.g. Temam 1997, p. 10).

Henceforth, let the flow dynamics be described by an n-dimensional nonlinear system

$$\dot{\mathbf{u}} = \mathbf{f}(\mathbf{u}) \tag{2.2}$$

where $\mathbf{u} \in \mathbb{U}$ is the state variable. The state space $\mathbb{U} \subset \mathbb{R}^n$ is endowed with the inner-product denoted by $\langle \cdot, \cdot \rangle_\mathbb{U}$ so that the associated norm $\| \cdot \|_\mathbb{U}^2$ equals twice the kinetic energy of the flow field. The subscript $_\mathbb{U}$ will be omitted unless it is necessary to include.

Associated with the vector-field is the *evolution operator*, $\mathbf{T}(t) : \mathbb{U} \to \mathbb{U}$

$$\mathbf{u}(s + t) = \mathbf{T}(t)\mathbf{u}(s) \tag{2.3}$$

that satisfies (i) $\mathbf{T}(0) = \mathbf{I}$ and (ii) $\mathbf{T}(s + t) = \mathbf{T}(s)\mathbf{T}(t)$. Given a flow field at time s, $\mathbf{T}(t)$ provides the velocity field at a later time $t + s$ by solving (2.2) with $\mathbf{u}(s)$ as initial condition. Our analysis is often based on flow fields sampled at discrete equidistant points in time, where for a fixed $t = \Delta t$, (2.3) is a discrete dynamical system,

$$\mathbf{u}_{k+1} = \mathbf{g}(\mathbf{u}_k), \tag{2.4}$$

---

[1]A note on the basic notation used through out the thesis is appropriate at this point. Square brackets [and] are used to construct matrices and vectors, i.e. $[1\ 2]^T$ is a column vector $\in \mathbb{R}^{2\times 1}$ which is abbreviated as $\mathbb{R}^2$. Curved brackets (and) are used surrounding lists of entries, delineated by commas as an alternative method to construct (column) vectors, $(1, 2) = [1\ 2]^T$.

where $\mathbf{g} = \mathbf{T}(\Delta t)$ and k is an integer index. Note that, in the context of fluid mechanics, $\mathbf{g}$ represents a numerical flow solver, which in its simplest form, sets up a grid in space and time and computes approximate solutions on this grid by marching in time.

2.2. Linear global eigenmodes

We are interested in the behavior of disturbances evolving near the steady-state solution as $t \to \infty$, that is the linear perturbation dynamics after "a short transient period". For highly unsteady flows, finding a steady solution $\mathbf{u}_s$, so that $\mathbf{f}(\mathbf{u}_s) = 0$ is a formidable task when n is large. Usually, one has to resort to iterative (Trefethen & Bau 1997) or filtering (Åkervik *et al.* 2006) techniques. For now, suppose that we have found $\mathbf{u}_s$.

To characterize the flow field near $\mathbf{u}_s$, let

$$\mathbf{u} = \mathbf{u}_s + \mathbf{u}' \qquad (2.5)$$

with $\|\mathbf{u}'\| \ll 1$ as a small perturbation. We substitute (2.5) into (2.2) and expand in Taylor series around $\mathbf{u}_s$ to obtain

$$\dot{\mathbf{u}}' = \nabla \mathbf{f}(\mathbf{u}_s)\mathbf{u}' + \mathcal{O}(\|\mathbf{u}'\|^2),$$

where $\nabla \mathbf{f}(\mathbf{u}_s)$ is the Jacobian $n \times n$ matrix with the elements as first partial derivative $\partial \mathbf{f}_i / \partial \mathbf{u}_j$ at $\mathbf{u}_s$. Denoting the Jacobian matrix by $\mathbf{A}$, omitting the primes and neglecting high-order terms, we obtain the linear system,

$$\dot{\mathbf{u}} = \mathbf{A}\mathbf{u}. \qquad (2.6)$$

The matrix $\mathbf{A}$ can be regarded as the discretized and linearized Navier–Stokes equations, and could also be obtained by substituting (2.5) directly into the PDE (2.1), neglecting nonlinear terms and then discretizing the spatial domain Ω.

The *linear global eigenmodes* are defined as the eigenvectors and eigenvalues of $\mathbf{A}$,

$$\mathbf{A}\boldsymbol{\phi}_j = \lambda_j \boldsymbol{\phi}_j \qquad j = 1, \ldots, n, \qquad (2.7)$$

where $\boldsymbol{\phi}_j \in \mathbb{U}$ are complex valued and

$$\lambda_j = \sigma_j + i\omega_j. \qquad (2.8)$$

The modes form a basis, in which any perturbation $\mathbf{u}$ can be expanded as follows

$$\mathbf{u}(t) = \sum_{j=1}^{n} a_j \boldsymbol{\phi}_j e^{\lambda_j t},$$

where a_j are the scalar expansion coefficients. From the above expression and (2.8), it is clear that if $\sigma_j > 0$ for any j, the corresponding mode $\boldsymbol{\phi}_j$ will be grow in time, regardless of the behavior of other modes, and the steady flow (or "baseflow") is rendered unstable. Conversely if $\sigma_j < 0$ for all j the steady flow is stable, since any perturbation for long times will decay in time. If there exists $\sigma_j = 0$, the stability of $\mathbf{u}_s$ cannot be determined by linearization and one
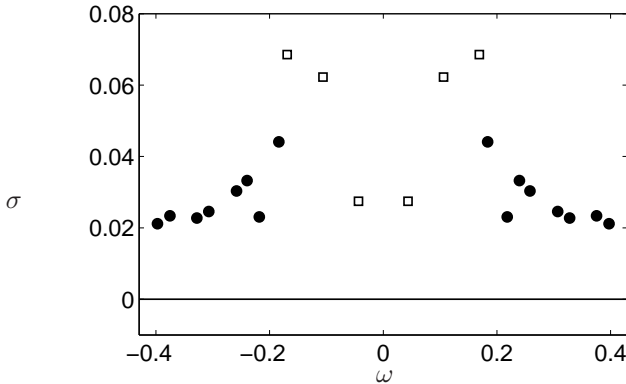
FIGURE 2.2. The linear spectrum of the jet in crossflow at $R = 3$. The eigenvalues marked with open squares correspond to anti-symmetric eigenmodes, whereas black circles correspond to symmetric eigenmodes.

Mode	Local Mechanism	Symmetry	Location
A	Elliptic instability	Anti-symmetric	Jet & wake region
B	Kelvin-Helmholtz instability	Symmetric	Jet region
C	von Kármán instability	Anti-symmetric	Wall region

TABLE 2.1. Properties of three global eigenmodes.

has to resort to other methods (Guckenheimer & Holmes 1983). The frequency at which the eigenmode ϕ_j pulsates is given by ω_j.

2.2.1. *Linear global eigenmodes of the jet in crossflow*

In this section, the linear stability analysis of the steady solution (discussed in section 1.2.1) of the jet in crossflow is presented. The steady solution is obtained using the selective frequency damping (SFD) approach introduced by Åkervik *et al.* (2006). The linear global eigenmodes of JCF are fully three-dimensional ($n \approx 10^7$), and must be computed using iterative algorithms (such as the Arnoldi method) described in section 4.1. From the linear spectrum shown in figure 2.2 it is clear that $\sigma_j > 0$ for all the leading modes, rendering the steady solution strongly unstable for the chosen parameters (velocity ratio, $R = V_{jet}/U_\infty = 3$). The Strouhal number, defined as $St = fD/V_{\text{jet}}$ (D is the jet diameter), of the unstable modes are in the range $[0.04, 0.17]$, and none of the frequencies of the linear modes match the nonlinear shedding frequencies observed in the numerical simulations. Recall from section 1.2.2, that one separation region just downstream of the jet orifice was observed to oscillate in two directions, slowly in the spanwise direction with $St_1 = 0.017$ and rapidly along the jet trajectory with $St_2 = 0.14$. However, the stability analysis merely
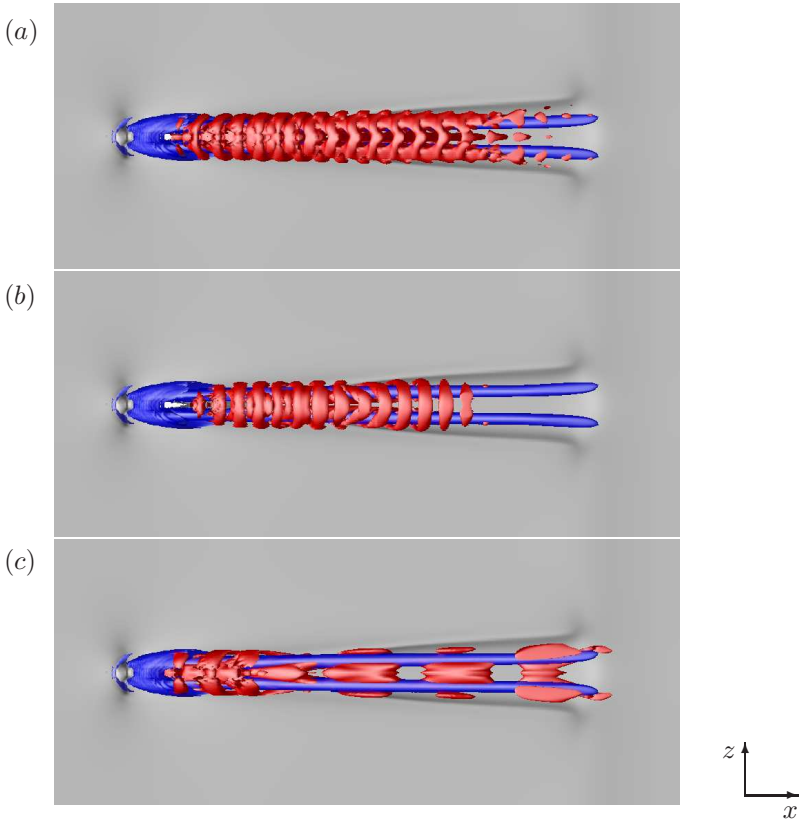
FIGURE 2.3. Linear global eigenmodes A, B and C of the jet in crossflow shown from top view. The red contour levels represent the λ_2 criterion, whereas the baseflow is shown in blue (λ_2) and gray (u). The modes are complex and shown at one phase only.

accounts for the linear dynamics in the neighborhood of the steady solution, where the Strouhal numbers can be considerably different from the saturated dynamics near the attractor (also indicated by figure 2.1). The eigenvalues in figure 2.2 marked by black circles are symmetric, where the symmetry refers to the u and v component with respect to the $z = 0$ axis, i.e.

$$(u(x,y,z), v(x,y,z), w(x,y,z)) =$$
$$(u(x,y,-z), v(x,y,-z), -w(x,y,-z))$$

The modes marked with open squares display opposite symmetry properties.

The global modes provide a remarkable insight into the underlying growth mechanisms present in the flow. We will focus on three global modes, listed

FIGURE 2.4. Streamwise vorticity at $x = 40$ for the steady baseflow (a) and mode A (b). Contour levels are 0.1, 0.2, . . . , $1.0 \cdot \omega_{x,\max}$, red is positive, blue negative. Only a portion of the zy-plane is shown.

in table 2.1, each associated with one global spatial structure and one local physical instability mechanism.

Mode A — elliptic instability

The most unstable mode (ϕ_1), shown in figure 2.3(a) is an anti-symmetric mode. The instability extends spatially in all three regions discussed in section 1.2 (see also Bagheri *et al.* 2009d; Schlatter *et al.* 2009); in the jet region it takes the form of a wavepacket located on and around the CVP; in the wake region it is associated with the upright vortices; and finally the mode has a small amplitude in the wall region. The various vortex systems are thus coupled and in a linear approximation grow with the same rate and oscillate with the same frequency, illustrating the global character of the flow.

   This instability has the strongest direct effect on the CVP; the two vortex tubes of the CVP are modified by a sinuous in-phase wavy oscillation in top view (xz-plane) and an out of phase oscillation in side view (xy-plane). Moreover, the wavelength of the instability is of the same order as the diameter of the vortex cores of the CVP. These observations are the traits of a short-wavelength instability of a vortex pair as observed by the experiments of Leweke & Williamson (1998) and the numerical simulations of Laporte & Corjon (2000). Such an instability is due to a resonance between two waves of one vortex and the straining field induced by the other vortex. In figure 2.4 the streamwise vorticity component in a cross plane (yz-plane) far downstream is shown for the baseflow and the most unstable global mode. The CVP centered around $y = 14$ can clearly be seen in figure 2.4(a). The global mode
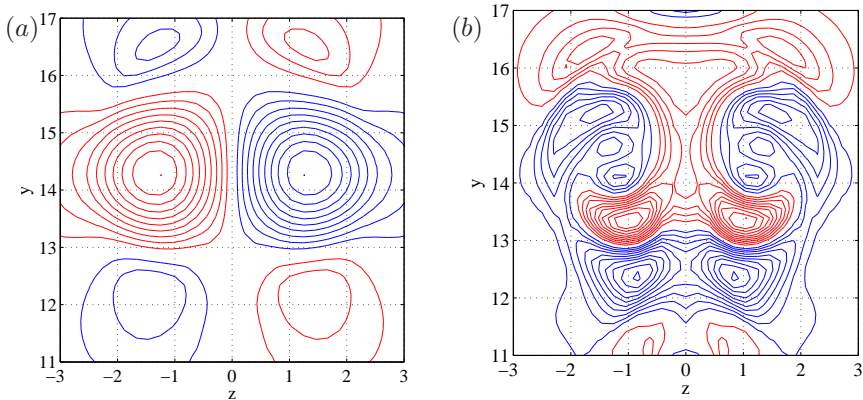
FIGURE 2.5. Spanwise vorticity at $z = 0$ for the steady base-flow (a) and the mode B (b). Contour levels are 0.1, 0.2, ..., $1.0 \cdot \omega_{z,\mathrm{max}}$, red is positive, blue negative. Only a portion of the xy-plane is shown.

(figure 2.4b) shows a characteristic two-lobe structure in each CVP vortex. This is remarkably similar to the vorticity computed analytically for the elliptic instability (Waleffe 1990, figure 2) and the short-wave instability (Leweke & Williamson 1998, figure 10).

Mode B — Kelvin–Helmholtz instability

The most unstable symmetric mode is shown in figure 2.3(b). The global mode consists of a symmetric spanwise oriented row of vortex loops that wrap around the upper part of the CVP. They are gradually stretched, and develop "legs" that align with the direction of CVP tubes. In figure 2.5 the spanwise vorticity of the steady flow and mode B is compared at the center xy-plane ($z = 0$). The baseflow shows a shear layer, which is due to the cylindrical vortex sheet emerging from the jet nozzle and its interaction with the crossflow. The effect of the global instability (figure 2.5b) on the shear layer is a periodic deformation of the shear layer, which results in a redistribution of the vorticity in an alternating manner. Such a perturbation of a shear layer is unstable and is referred to as the Kelvin-Helmholtz instability. More generally, when two streams of different velocities come into contact, a vortex sheet develops which is unstable to infinitesimal periodic perturbations (see Batchelor 1967, p. 511 for an elementary stability analysis of the vortex sheet). Mode B modifies the CVP in a varicose fashion viewed from top (xz-plane). The nonlinear simulation discussed in section 1.2.1 (see figure 1.6b), shows how mode B grows in amplitude and develops the characteristic "arches". This type of symmetric structures has been observed in many experimental studies (see e.g. Kelso et $al.$ 1996; Lim et $al.$ 2001).
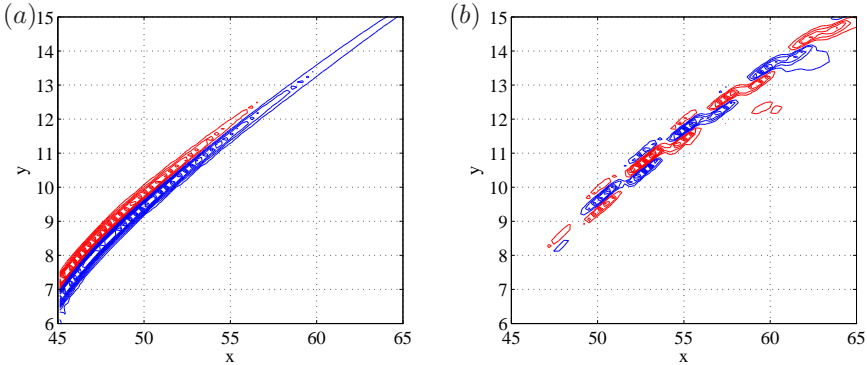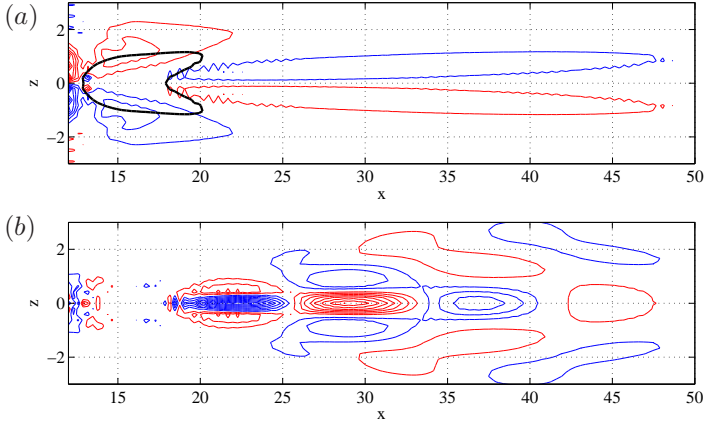
FIGURE 2.6. Wall-normal vorticity at $y = 1$ for the steady baseflow (a) and mode C (b). Contour levels are $0.1, 0.2, \ldots,$ $1.0 \cdot \omega_{y,\mathrm{max}}$, red is positive, blue negative. Inside the region marked by solid black line there is a backflow. The small-scale wiggles are numerical artifacts. Only a portion of the xz-plane is shown

Mode C — von Kármán instability

Mode C shown in figure 2.3(c), is an anti-symmetric mode that oscillates with the frequency $St = 0.043$. Its global structure is mostly concentrated close to the wall, although it has a small amplitude along the CVP. In particular, the structure near the wall is considerably different compared to the other modes. The wall-normal vorticity of mode C and the steady flow is compared in figure 2.6. In figure 2.6(a) the black contour marks the region of reversed flow ($u = 0$) in the wall region downstream of the jet orifice. On each side of the recirculation zone, two lobes of positive and negative wall-normal vorticity are observed. This is strikingly similar to the unstable steady solution computed for the wake behind a circular cylinder (Barkley 2006, figure 1). Moreover, the global mode shown in figure 2.6(b) shows alternating positive and negative wall-normal vorticity, which is almost identical to the first global mode of the cylinder wake (Barkley 2006, figure 3). It thus seems that although, the jet is a "soft" body and there exists a rigid flat wall, the vortex street of von Kármán is present. One can compare the low frequency oscillation of the separation bubble in the spanwise direction with $St_1 = 0.017$, with the Strouhal number of the von Kármán vortex street behind a solid cylinder. For a cylinder wake, the relevant Strouhal number is defined as $St_c = fD/U$ with U being the uniform flow velocity in the far field. Adapting the present definition of the frequency based on the jet velocity gives $St_c = St_1(V_{\mathrm{jet}}/U_\infty)(U_\infty/U)$. Assuming $U/U_\infty \approx 1/3$ due to the reduced streamwise velocity in the proximity of the wall gives $St_c \approx$

$9St_1 = 0.153$, which is close to the cylinder wake frequency in the supercritical range ($Re = 50 - 100$ is approximately $St_c = 0.13 - 0.16$). It should be mentioned that mode A, which is associated with the elliptic instability in the jet region, also contains the von Kármán instability near the wall, although not as dominant and distinct as mode C.

2.2.1.1. *Relation to the separated region*

Global modes do not directly identify the mechanisms that initially generate a disturbance, i.e. rather than the source of the instability, the consequences of the instability are identified. It has therefore been difficult to establish a rigorous connection between unstable linear global eigenmodes and separated regions in the flow, although there is some evidence (Hammond & Redekopp 1998; Pier 2002) and an increasingly number of investigations (Theofilis *et al.* 2000; Alam & Sandham 2000; Barkley *et al.* 2002) that couple them. Instead, local stability concepts based on the notions of absolute and convective instabilities applied to weakly non-parallel flows have been useful in this context. It is shown that spatially developing flows with self-sustained oscillatory behavior have localized regions in the flow that act as oscillators and localized regions in the flow that act as amplifiers (see Huerre & Monkewitz 1990, for a review). Observations and analysis indicate that sufficiently large separated regions act as oscillators and various co-flowing shear layers act as amplifiers. Although not rigorously investigated in this thesis, it is likely that for the jet in crossflow an oscillator – the separated region downstream of the orifice – periodically sheds patches of vorticity, which are convected into the jet, wake and wall regions and amplified due to different *local* mechanisms (such as Kelvin-Helmholtz or short-wave elliptic instability).

2.3. Koopman modes

When global instabilities saturate after a transient phase, a global mode analysis of the fully nonlinear flow has to be undertaken. Another issue is that, while in numerical simulations and analytical studies the full state **u** can be "observed", in experiments this is not the case. Usually the velocity is probed – either at a point using hot-wire measurements or at 2D planes using Particle Image Velocimetry (PIV)– or some bulk quantity associated with the flow is measured (such as mass flux, drag, lift). It turns out (see e.g. Packard *et al.* 1980) that by observations of one or more time signals only, called *observables*, one can characterize the (possibly low-dimensional) behavior of fluid systems (such as chaotic or quasiperiodic attractors, heteroclinic cycles etc.). The important point here is that, monitoring an observable over a very long time interval allows in a statistical sense the reconstruction of the phase space.

An observable is defined as a function $a(\mathbf{u})$ that associates a scalar to each $\mathbf{u} \in \mathbb{U}$. Define the *Koopman*[2] operator $U : L^2(\mathbb{U}) \to L^2(\mathbb{U})$ (Koopman 1931), with respect to $\mathbf{g}$, as the operator that steps forward the observable, i.e.

$$Ua(\mathbf{u}) = a(\mathbf{g}(\mathbf{u})). \tag{2.10}$$

Comparing (2.10) with (2.4), we observe that whereas the finite-dimensional and nonlinear operator $\mathbf{g}$ steps forward the state, the Koopman operator is infinite-dimensional and it steps forward an observable. The operator is linear since for $a, b \in L^2(\mathbb{U})$,

$$\begin{aligned} U(\alpha a(\mathbf{u}) + \beta b(\mathbf{u})) &= \alpha a(\mathbf{g}(\mathbf{u})) + \beta b(\mathbf{g}(\mathbf{u})) \\ &= \alpha U a(\mathbf{u}) + \beta U b(\mathbf{u}). \end{aligned}$$

We can study certain properties of the trajectory of the nonlinear flow $\mathbf{g}$ by the spectral properties of linear operator U. Let therefore, $\varphi_j : \mathbb{U} \to \mathbb{R}$ denote the eigenfunctions and $\lambda_j \in \mathbb{C}$ denote the eigenvalues[3] of the Koopman operator,

$$U\varphi_j(\mathbf{u}) = \lambda_j \varphi_j(\mathbf{u}), \qquad j = 0, 1, 2, \dots$$

It can be shown (e.g. Ding 1998) that as $t \to \infty$, U is a unitary operator and therefore the sequence of its eigenfunctions $\{\varphi_j\}_{j=0}^{\infty}$ forms an orthonormal expansion basis.

We proceed with defining the global modes that are referred to as Koopman modes, by first introducing a vector-valued observable $\mathbf{a}(\mathbf{u}) : \mathbb{U} \to \mathbb{R}^p$. For example, the scalar observable $a(\mathbf{u})$ can be considered as an observation of a velocity component at a single coordinate in Ω (obtained via hot-wire measurements) and $\mathbf{a}(\mathbf{u})$ can be considered as a velocity measurement in a plane in Ω (obtained via PIV). Consider a long time series of the observable $\mathbf{a}$ on the trajectory of the system $\mathbf{g}$ starting at the initial condition $\mathbf{u}_0$,

$$\mathbf{X} = [\mathbf{a}(\mathbf{u}_0) \ \mathbf{a}(\mathbf{u}_1) \ \mathbf{a}(\mathbf{u}_2) \ \dots]. \tag{2.11}$$

Next, assuming that each of the components of $\mathbf{a}(\mathbf{u}_0)$ lies within the span of $\{\varphi_j\}_0^{\infty}$ (see Mezic 2005, for the general case), an orthogonal projection of $\mathbf{a}(\mathbf{u}_0)$

---

[2]The analysis requires some measure theory, but here we make no attempt to be mathematically precise and refer to Lasota & Mackey (1994) for rigorous treatment on the subject. Most importantly, we need to introduce an *invariant measure*, essentially meaning that we can find a measure μ such that the value of a integral,

$$\int_{\mathbb{U}} a(\mathbf{u}) d\mu = \int_{\mathbb{U}} a(\mathbf{g}(\mathbf{u})) d\mu.$$

is invariant. Henceforth we drop μ and use the notation $d\mu = d\mathbf{u}$. Such a measure can always be found (Lasota & Mackey 1994) if $\mathbf{g}$ satisfies certain properties (that $\mathbf{g}$ is a measure-preserving operator). Observables are thus elements in the space

$$L^2(\mathbb{U}) = \{a : \mathbb{U} \to \mathbb{R} | \int_{\mathbb{U}} |a|^2 d\mathbf{u} < \infty\}.$$

[3]Here, we consider only the point spectrum of U, see Mezic (2005) for the continuous spectrum.

onto the space spanned by the Koopman eigenfunctions yields,

$$\mathbf{a}(\mathbf{u}_0) = \sum_{j=0}^{\infty} \phi_j \varphi_j(\mathbf{u}_0)$$

where the vector-valued expansion coefficient $\phi_j \in \mathbb{R}^p$, given by

$$\phi_j = \langle \mathbf{a}(\mathbf{u}_0), \varphi_j(\mathbf{u}_0) \rangle_{L^2(\mathbb{U})} = \int_{\mathbb{U}} \mathbf{a}(\mathbf{u}_0) \varphi_j^*(\mathbf{u}_0) \, d\mathbf{u}_0 \qquad (2.12)$$

is defined as the jth *Koopman mode* under the map $\mathbf{g}$. Note that in numerical simulations, where the entire flow field is observable $\mathbf{a}(\mathbf{u}) = \mathbf{u}$, the Koopman modes are fully global, $\phi_j \in \mathbb{U}$. The Koopman modes and eigenfunctions are determined only for the first sample in (2.11) and the remaining samples on the trajectory can be expressed entirely in terms of these. To see this, note that the kth sample in the series (2.11) is given by,

$$\mathbf{a}(\mathbf{u}_k) = U^k \mathbf{a}(\mathbf{u}_0) = U^k \left(\sum_{j=0}^{\infty} \varphi_j(\mathbf{u}_0) \phi_j \right) = \sum_{j=0}^{\infty} \lambda_j^k \varphi_j(\mathbf{u}_0) \phi_j.$$

We expand the entire sequence (2.11) in Koopman eigenfunctions and write it in matrix form

$$\mathbf{X} = \mathbf{\Phi S}, \qquad (2.13)$$

where the columns of $\mathbf{\Phi}$ contain the Koopman modes and the corresponding Koopman eigenfunctions,

$$\mathbf{\Phi} = [\varphi_0(\mathbf{u}_0)\phi_0 \ \varphi_1(\mathbf{u}_0)\phi_1 \ \varphi_2(\mathbf{u}_0)\phi_2 \ \ldots]$$

and $\mathbf{S}$ is the infinite Vandermonde matrix

$$\mathbf{S} = \begin{bmatrix} 1 & \lambda_0 & \lambda_0^2 & \cdots \\ 1 & \lambda_1 & \lambda_1^2 & \cdots \\ \vdots & \vdots & \vdots & \ddots \end{bmatrix}. \qquad (2.14)$$

Note that the first eigenfunction of U, corresponding to the eigenvalue $\lambda_0 = 1$, is related to the time average of a sequence $\mathbf{X}$,

$$\varphi_0(\mathbf{u}) = \lim_{n \to \infty} \frac{1}{n} \sum_{j=0}^{n-1} a(\mathbf{u}_j). \qquad (2.15)$$

This can be easily seen, since the average φ_0 is constant on the orbit $\mathbf{g}(\mathbf{u})$,

$$\varphi_0(\mathbf{u}) = \varphi_0(\mathbf{g}(\mathbf{u})) = U\varphi_0(\mathbf{u}).$$

The sequence of observables obtained from $\mathbf{g}$ starting with $\mathbf{u}_0$, can thus be decomposed into spatial structures (Koopman modes) whose temporal behavior is given by the associated Koopman eigenvalue, i.e. the phase $\arg(\lambda_j)$ determines its frequency, and the magnitude $|\lambda_j|$ determines the growth rate of mode ϕ_j. The Koopman eigenfunctions φ_j, on the other hand, associate with each Koopman mode ϕ_j an amplitude, which determines the significance of that mode. As explained in Mezic & Banaszuk (2004) and Mezic (2005), by investigating

a large number of trajectories (starting from different $\mathbf{u}_0$), the state space can be partitioned into level sets of constant φ_j, i.e. one can identify regions in $\mathbb{U}$ that oscillate with a single frequency only and the value φ_j determines how significant that frequency is in the flow. For complex flows, after a transient regime, the flow evolves near some attracting set in $\mathbb{U}$, which might show very complicated behavior such as strange attractors or simple behavior, such as periodic orbits. In this limit there exists a countable set of nonzero eigenvalues λ_j that all are on the unit circle, $|\lambda_j| = 1$ for all j. The means that each eigenfunction φ_j is associated with a temporal frequency ω_j (the phase of λ_j) only since the growth rate is zero for all modes.

The Koopman modes can in principle be determined by solving the integral (2.12). However, this is too expensive, since every possible initial condition has to be considered. Alternatively, one can use *harmonic averages* as described by Mezic (2005) or by finding the inverse of the truncated Vandermonde matrix, i.e. $\mathbf{\Phi} = \mathbf{X}_r \mathbf{S}^{-1}$, as shown in section 4.2.

2.3.1. *Other approaches*

It has somewhat "accidentally" been noticed that a linear stability analysis using the time-average mean flow, instead of a truly steady flow, provides modes whose discrete frequencies are in good agreement with the global nonlinear shedding frequency. As a consequence a number of linear stability studies (see e.g. Pier 2002; Barkley 2006; Thiria & Wesfreid 2007, and references therein) have recently been conducted in order to identify coherent structures that can be associated with vortex shedding. Although the averaged mean flow takes into account some of the nonlinear effects implicitly, such analysis is "ad-hoc" and lacks rigorous foundation. In fact, it was shown (Sipp & Lebedev 2007) that such an analysis works only for some specific cases, such as the circular cylinder.

Proper orthogonal decomposition (POD) is a method to extract information from large datasets, either obtained from numerical simulations or experiments. The method was introduced by Lumley (1970) for fluid systems for extracting coherent structures in turbulent flows. The POD modes identify those parts of the phase space which contain the most kinetic energy, typically attractors in phase space (Holmes *et al.* 1996). It is likely that the structures are a result of the vortex shedding. Unfortunately, the POD method averages in time and the correlation in time is completely lost, rendering the task of pinning down one structure to one frequency impossible.

2.3.2. *Koopman modes of the jet in crossflow*

A long sequence of flow-field snapshots are collected from direct numerical simulations (DNS) of the jet in crossflow. The transient time from the unstable fixed point to the attractor is not sampled, i.e. only the asymptotic motion in phase space is considered. The eigenvalues λ_j, eigenfunctions φ_j and the global modes $\boldsymbol{\phi}_j$ associated with the Koopman operator of the sequence are computed
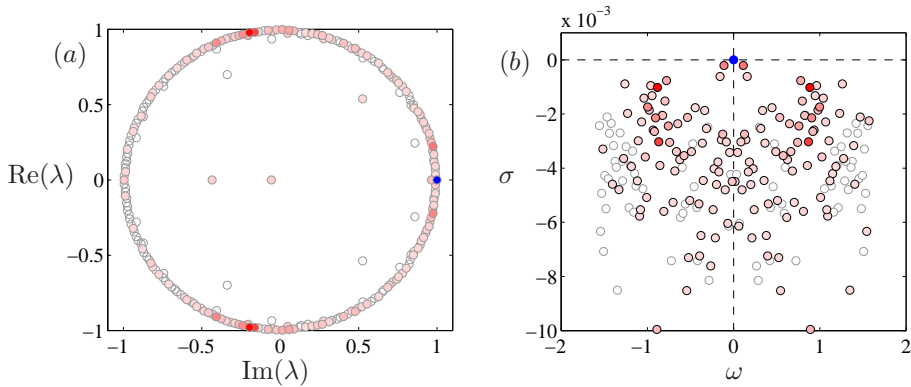
FIGURE 2.7. Time-discrete (a) and time-continuous (b) Koopman spectra of the JCF. The Koopman eigenvalue λ_0 is shown with a blue symbol, while the other eigenvalues vary smoothly in color from red (high magnitudes) to white, depending on the magnitude φ_j of the corresponding Koopman mode.

using the DMD algorithm described in section 4.2. The time-discrete spectrum and the time-continuous spectrum of the Koopman operator are shown in figure 2.7. The two spectra are related to each other via a linear transformation (see section 4.1). From the time-discrete (figure 2.7a) we can observe that nearly all the eigenvalues lie on or very close to the unit circle. Note that as $t \to \infty$ all the eigenvalues will lie exactly on the unit circle since the Koopman operator is unitary. The time-continuous spectrum (figure 2.7b) confirms that all eigenvalues are marginally stable and therefore one cannot expect any flow structures growing or decaying exponentially in the nonlinear flow.

The Koopman mode corresponding to the Koopman eigenvalue λ_0 is the time-averaged flow and is depicted with blue symbol in figure 2.7. The other (unsteady) Koopman eigenvalues vary smoothly in color from red to white, depending on the magnitude (Koopman eigenfunctions) φ_j of the corresponding Koopman mode. The magnitudes of the modes are shown in figure 2.8(a) with the same coloring as the spectrum, where a few (10–14) leading modes are observed to have significantly larger values, as the magnitudes rapidly decay and gradually level out. In figure 2.8(b) each mode is displayed with a vertical line scaled with its magnitude at its corresponding Strouhal number. Only the $\omega_j \geq 0$ are shown, since the eigenvalues come in complex conjugate pairs. Ordering the modes with respect to their magnitude, the first (1–2) and second (3–4) pair of modes oscillate with $St_2 = 0.141$ and $St_4 = 0.136$ respectively, whereas the third pair of modes (5–6) oscillate with $St_6 = 0.017$. All linear combinations of the frequencies excite higher modes, for instance, the nonlinear interaction of the first and third pair results in the fourth pair, i.e. $St_8 = 0.157$ and so on. Therefore, the spectral properties of the Koopman operator for the
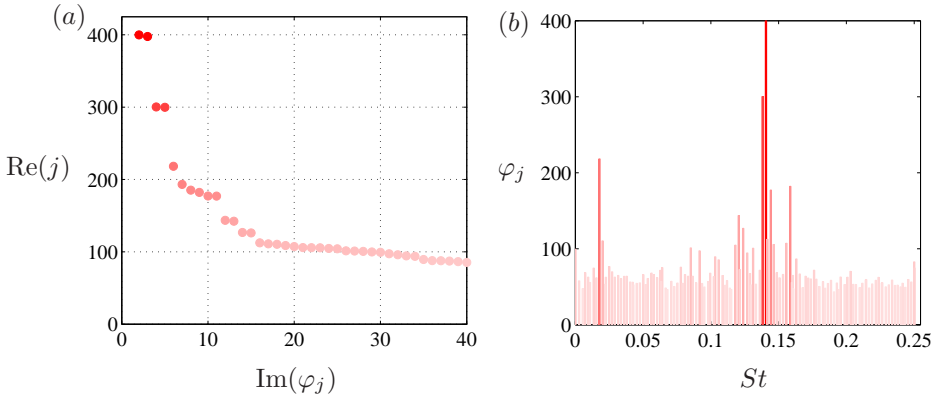
FIGURE 2.8. Left figure: The magnitudes φ_j associated with the Koopman modes $j = 1, \ldots, 40$. Right figure: The magnitudes φ_j are plotted as a function of the Strouhal number St_j.
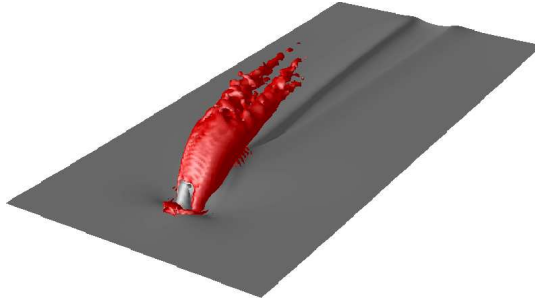
FIGURE 2.9. The zeroth Koopman mode (time-averaged mean flow) is shown with red contour levels depicting the λ_2-criterion and gray contour level show the u component.

jet in crossflow, suggest that the attractor dynamics is dominated by a few discrete distinct frequencies. The associated Koopman modes are considered next, where each global mode identifies a region where the flow oscillates with its corresponding frequency.

The zeroth Koopman mode ϕ_0 (shown in figure 2.9) is the time-averaged mean flow, corresponding to the eigenvalue marked with a blue symbol in the spectrum. A common feature of unsteady flows with separated regions is a large difference between the steady solution and the time-averaged mean flow solution, which is due to a significant transient time from the fixed point to the attractor. The difference between the two flows, usually called mean flow distortion (correction), quantifies how much the saturated disturbances modify the steady flow, i.e. where the mean flow distortion is large there is
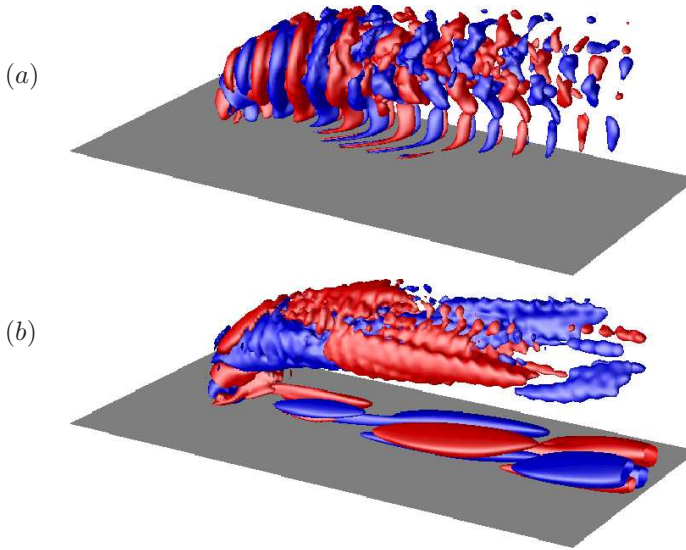
FIGURE 2.10. The positive (red) and negative (blue) stream-wise velocity component of the first (a) and fifth (b) Koopman modes. The flat plate is shown in gray.

significant alteration of the steady solution due to the saturated disturbance. Physically, the mean flow correction is due to the Reynolds stresses generated by the fluctuating field. The most significant change in the flow is due to breakdown of the CVP (possibly attributed to the elliptic instability) resulting in a retardation of the two CVP vortex tubes, whereas the cylindrical vortex sheet, horse-shoe/wall vortices are not modified noticeably. The separated region downstream of the jet orifice is reduced in size (compared to the steady flow), similarly to the observations made by other researchers (Noack *et al.* 2003; Barkley 2006). The mean flow distortion being confined to the CVP and the separated region near the wall indicates that the saturating fluctuations are large in those locations.

The first pair of unsteady Koopman modes ϕ_1–ϕ_2 oscillates with $St_2 = 0.14$ – which is precisely the fundamental shedding frequency observed in the numerical simulations – and is an anti-symmetric nonlinear wavepacket. The mode (shown in figure $2.10a$) identifies the regions in the flow domain where the frequency $St_2 = 0.14$ can be detected. The largest amplitude is along the jet trajectory; the streamwise velocity of opposite sign gives rise to the spanwise-oriented vortex loops that gradually break up into smaller vortex filaments in the downstream direction. Similar to the mean flow, most coherence in the spatial structure is located in region where jet fluid and crossflow come into contact; its shape is similar to the "array of transverse secondary vortex pairs" observed in the late nonlinear stages of the short-wave instability as reported

Mode	DNS	Global	POD	Koopman
Shear layer	0.141	0.169	$0.138, 0.158, 0.121$	0.141
Wall	0.017	0.043	$0.0188, 0.0094, 0.158, 0.121$	0.017

TABLE 2.2. Comparison of the frequencies (St) obtained from DNS probes (shown in figure 1.7); the global eigenmodes of the linearized Navier–Stokes; POD modes 1 and 6, corresponding to mainly shear-layer and wall oscillations, respectively; and Koopman modes.

by Laporte & Corjon (2000) and Leweke & Williamson (1998). This analysis clearly shows that the fundamental shedding frequency of the jet in crossflow is associated with vortex loop structures on the jet, as a result from a saturation of the first global instability mode discussed in the previous section.

The third pair ϕ_5–ϕ_6 oscillates with precisely the low-frequency vortex shedding, $St_1 = 0.017$ observed from numerical simulations. This anti-symmetric mode is shown in figure 2.10(b) and is clearly related to coherent structures in the wall region. The alternating positive and negative streamwise velocity near the wall contributes to the wall-normal vorticity constituting the nonlinear von Kármán vortex street. In fact, the structure of the wall-normal vorticity near the wall is similar to the nonlinear wavepacket reported by Pier (2002) and Barkley (2006) for the cylinder wake flow. We conclude that the low-frequency shedding of the jet in crossflow is indeed associated with the von-Kármán vortex street developing near the wall downstream of the jet, resulting from a saturation of the global instability modes. It can be noted that this mode has a nonzero amplitude in the jet region (along the jet body), which is confirmed by the observation that the whole jet wiggles back and forth in the spanwise direction.

2.3.3. *Concluding remarks*

For complex flows, where several self-sustained oscillations exist and are potentially coupled, one is interested in studying the dynamics of the different oscillations separate from each other. The Koopman modes are able decouple and isolate these dynamics. In table 2.2 the frequencies obtained from the analysis based on the Koopman modes and global eigenmodes of the linearized system for the jet in crossflow are shown. For completeness, the frequencies extracted from the Proper Orthogonal Decomposition (POD) modes are also included in the table. The POD modes of the JCF are described in Schlatter *et al.* (2009). The global eigenmodes capture the dynamics only in a neighborhood of the unstable fixed point, resulting in linear frequencies that are different from the nonlinear shedding frequencies. The Koopman modes, on the other hand, correctly capture to the asymptotic dynamics on the attractor of the nonlinear system. The method is thus able (by construction) to extract global modes that oscillate with precisely the same frequency as the shedding
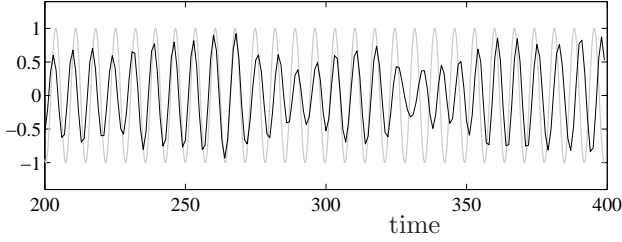
FIGURE 2.11. Comparison of time coefficients: the projection of the flow field onto the most energetic POD mode (black), and the coefficient of the most energetic Koopman mode (gray).

frequencies. Although, POD modes are also associated with the nonlinear system, they capture the most energetic structures, resulting in modes that contain several frequencies. The coefficient of the first POD mode oscillates mainly with frequency $St = 0.138$, which is close to the shear-layer oscillation frequency $St_2 = 0.141$ observed in DNS. However, the signal contains other frequencies as well, resulting from the interaction of the two fundamental oscillations (shear-layer and wall), $St = 0.138 \pm 0.017$, which cause the beating shown in figure 2.11.

CHAPTER 3

Flow control using balanced modes

In wall-bounded shear flows, for a given Reynolds number $Re > Re_c$, a laminar flow is observed if disturbance amplitudes are below a critical value, whereas a fluctuating turbulent flow is gradually developed for higher amplitudes. As discussed in section 1.1, the aim of transition control is to keep the amplitudes of the incoming perturbations small, in order to avoid turbulence. It thus suffices to focus on the dynamics of small amplitude disturbances near the laminar solution governed by the linear system $\dot{\mathbf{u}} = \mathbf{Au}$. For the flat-plate boundary layer, significant amplification of disturbances $\mathbf{u}$ – usually several orders of magnitude – takes place before disturbances eventually propagate out of the flow domain and leave behind the steady unperturbed boundary-layer flow. This transient growth of disturbance energy is due to the nonnormality (Trefethen & Embree 2005) of the stable matrix $\mathbf{A}$.

We return to the flat-plate example introduced in chapter 1, where the emergence of a turbulent spot from a finite-amplitude disturbance was discussed. In figure 3.1 a sketch of flat-plate configuration is shown, where in addition to the disturbances upstream in the boundary layer, one row of sensors and one row of actuators are introduced near the wall. The objective is to use the sensor-actuator system to minimize the disturbance energy in a domain downstream in the boundary layer. This domain is spanned by a number of prudently chosen (objective) functions. In the present configuration, there are 10 inputs (one disturbance, 9 actuators) and 19 outputs (9 sensors, 10 objective functions). Assuming all inputs and outputs have been modelled appropriately, there are a number of important decisions to be made: Given the sensor measurements, how do we determine what action the actuators should take in order to minimize the disturbance energy? Should the action of an actuator depend on all sensors measurements or only the sensor located upstream of it? How can we model sensor noise or penalize the actuation effort? Are there guarantees that the actuators will not introduce more "dangerous" disturbances in flow?

These issues can be addressed in a systematic way by control theory. In particular, the objective of feedback control is to minimize the effects of external influences on the system behavior when not having a complete knowledge of the disturbances that are present. This indirectly means that a more reliable system (closed-loop system) is designed whose amplifying behavior of disturbances is significantly reduced, and as a consequence less likely to transition to turbulence. In figure 3.2(a) the energy evolution (red solid line) of a
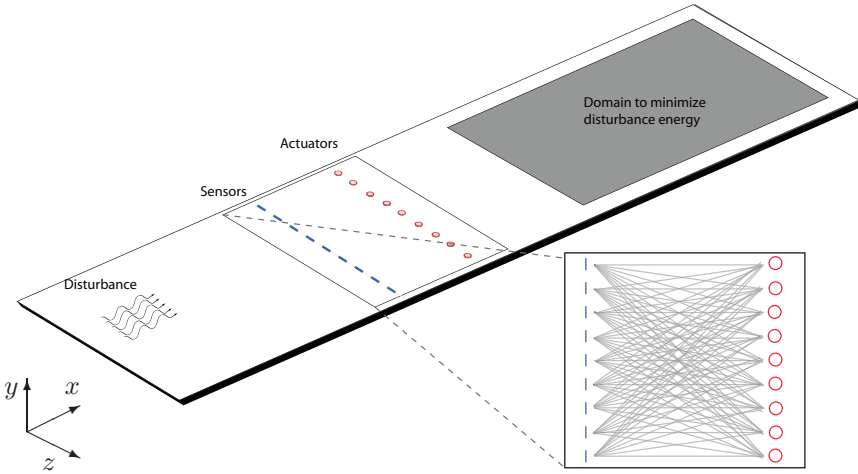
FIGURE 3.1. Sketch of the input-output configuration. The disturbance is located far upstream inside the boundary layer. Approximately half way in the downstream direction, 9 actuators are modelled by a spanwise row of localized volume forcing. Similarly, the sensor measurements used for estimation consist of a spanwise array of 9 localized functions (same as actuators) near the wall placed a small distance upstream of the actuators. The inset figure shows the how the sensors are connected to the actuators. Finally, 10 sensors, located further downstream are used to define the objective functional (3.22). The numerical parameters are given in table 4.2 (case 3D-LIN-BL) in section 4.4.

infinitesimal-amplitude disturbance clearly demonstrates the transient growth phenomena; we observe an exponential growth of three orders of magnitude until the energy peaks at $t = 2000$ and then decays rapidly. In the same figure the disturbance energy of the closed-loop system obtained using feedback control is shown with a blue line. We observe that the peak value of the disturbance energy is considerably smaller (about one order of magnitude) than the original system. Snapshots of disturbances of the two systems at $t = 1750$ are compared in figure 3.2(b-c), where we clearly see that the nearly two-dimensional structure of disturbance of the Navier–Stokes system has been replaced by a smaller scale three-dimensional disturbance in the closed-loop system.

Although feedback systems have been used for several centuries to modify dynamics and a rigorous theory has existed for several decades, it is only very recently that it has been used in flow control applications. The main reason is that control theoretical tools have essentially been unaccessible to all but
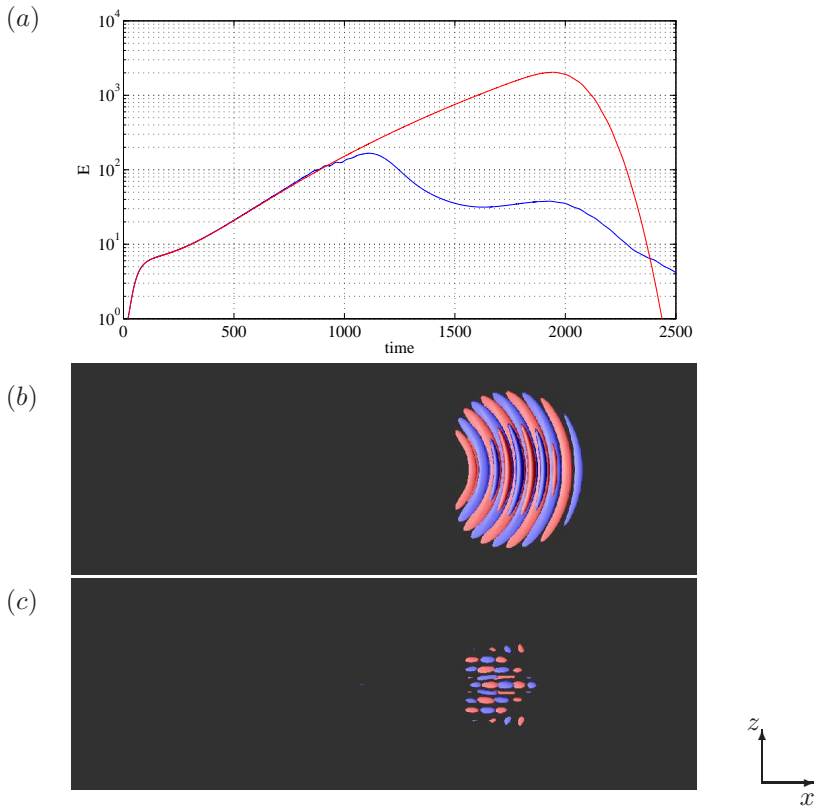
FIGURE 3.2. (*a*) Kinetic energy of a three-dimensional distur-
bance in the flat-plate boundary layer without (red) and with
feedback control (blue). A sketch of the control configuration
is given in figure 3.1. Snapshots of the disturbance field at
$t = 1750$ without (*b*) and with feedback control (*c*).

the very simplest fluid systems, due to the high-dimensional system that arise
from discretization of the Navier–Stokes equations. Model reduction, where
the complex system is approximated with a very low-order system, is therefore
an important step in the control design process.

3.1. Control design: An overview

The main steps of the control design process are outlined in this section.
Throughout the chapter, examples on the simpler two-dimensional flat-plate
configuration are provided. The three-dimensional configuration can be treated
in an analogous manner, although the design requires more care due to the ad-
ditional direction in the spanwise direction.
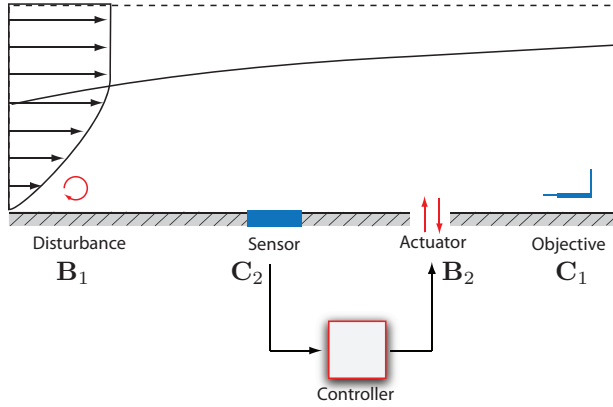
FIGURE 3.3. A sketch of input-output configuration for the control of perturbations in a two-dimensional flat-plate geometry. The domain size and numerical parameters are listed in table 4.2 (case 2D-LIN-BL) in section 4.4.

A sketch of the configuration for the control of two-dimensional perturbations is shown in figure 3.3. The first input $\mathbf{B}_1$, located far upstream, models the initial receptivity phase, where disturbances are induced by free-stream turbulence, acoustic waves or wall roughness. The second input is the actuator, $\mathbf{B}_2$, which provides a way to manipulate the flow. Two sensors, $\mathbf{C}_1$ and $\mathbf{C}_2$, are used to provide measurements of the perturbation. The upstream measurements are used to estimate the amplitude and the phase of the incoming perturbations, while the downstream sensor is used to quantify the modification of the flow due to the action of the actuator. The aim is to minimize the kinetic energy of the disturbance in the region defined by $\mathbf{C}_1$, using the actuator $\mathbf{B}_2$ and sensor $\mathbf{C}_2$. Of course, the overall goal is to reduce the perturbation growth in the entire flow domain in order to delay the initial phase of the transition process. However, this is achieved by placing $\mathbf{C}_1$ far downstream: if we demand the disturbance energy to be small at $\mathbf{C}_1$, the disturbance amplitude has to decrease significantly before it reaches the objective function to accomplish this task. For the three-dimensional disturbance discussed in the beginning of this chapter, $\mathbf{C}_1$ must be chosen with more care to achieve a significant damping of perturbation. The choice of the relative position of the actuator and sensor is based on the knowledge of the behavior of boundary layer instabilities and is described in Bagheri *et al.* (2009*b*).

The key point is that the signal given to the actuator at each instant in time is based only on the measurement signal provided by the sensor $\mathbf{C}_2$. Rather

	System	Complexity	2-norm	∞-norm
Plant	$\mathbf{G}$	10^5	9.7	144.6
Reduced-order model	$\mathbf{G}_r$	60	9.4	144.3
Closed-loop system	$\mathbf{G}_c$	10^5	0.4	6.4

TABLE 3.1. Properties of the three systems considered in the thesis. See text for additional information.

than velocity fields $\mathbf{u} \in \mathbb{U}$, we are interested in characterizing time signals and in particular the relation between input signals and output signals, since this relation underlies most of the basic treatments in the control design. We adopt an operator-viewpoint, where the operators represent "systems" that map input signals to output signals. In particular, three systems will be used throughout this chapter, each of them related to one major step in the control design:

1. The characterization of the input-output behavior of the plant (open-loop system) $\mathbf{G}$, represented by the linearized Navier–Stokes equations including two-dimensional disturbances, actuators, sensors and objective functions. In section 3.2 the input-output behavior between signals is evaluated by computing system norms (2-norm and ∞-norm).

2. Section 3.3 describes a method to construct a low-dimensional model $\mathbf{G}_r$ that essentially shows the same input-output behavior as the plant $\mathbf{G}$.

3. The final step is taken in section 3.4, using $\mathbf{G}_r$, the closed-loop system $\mathbf{G}_c$ is designed such that its norms – thus its amplifying behavior of disturbances – are small compared to the plant $\mathbf{G}$.

The three systems and their properties are listed in table 3.1.

3.2. Linear systems and input-output signals

In order to characterize the input-output behavior of a linear system we first need to define systems and signals. We begin with defining a *linear state-space system* as

$$\dot{\mathbf{u}} = \mathbf{A}\mathbf{u} + \mathbf{B}\mathbf{w} \tag{3.1a}$$

$$\mathbf{y} = \mathbf{C}\mathbf{u} + \mathbf{D}\mathbf{w} \tag{3.1b}$$

where $\mathbf{u} \in \mathbb{U}$ is the state variable, $\mathbf{w} \in \mathbb{R}^m$ is the input and $\mathbf{y} \in \mathbb{R}^p$ is the output of the system. The input space and output space are endowed with the Euclidean norm denoted by $|\cdot|$. The matrices $\mathbf{A} \in \mathbb{R}^{n \times n}$, $\mathbf{B} \in \mathbb{R}^{n \times m}$ and $\mathbf{C} \in \mathbb{R}^{p \times n}$ are constant and the latter two matrices are usually low-rank, i.e. $m, p \ll n$. We assume (3.1) is stable, meaning that all the eigenvalues of $\mathbf{A}$ have negative real part. Since it does not affect the results, assume for now

that both the initial condition $\mathbf{u}_0$ and the feed-through term $\mathbf{D} \in \mathbb{R}^{p \times m}$ are zero.

A *signal* is a (vector-valued) function of the independent variable time only, and is an element of the function space

$$L_s^2(t_1, t_2) = \{\mathbf{z}(t) : \mathbb{R} \to \mathbb{R}^s | \int_{t_1}^{t_2} |\mathbf{z}|^2 \leq \infty\},$$

where $s = m$ for the input space $s = p$ for the output space (subscript will omitted in most cases). Often we will consider signals over the infinite time intervals $L^2(-\infty, \infty)$, $L^2(0, \infty)$ and $L^2(-\infty, 0)$, which physically can be obtained after the transients asymptotically die out (owing to stability). The time-domain space $L^2(-\infty, \infty)$ can be represented by a frequency-domain space $\hat{L}^2(i\mathbb{R})$ by means of a Fourier transform, which preserves the inner-product (Parseval's theorem), i.e. $\|\mathbf{z}\|_{L^2} = \|\hat{\mathbf{z}}\|_{\hat{L}^2}$. Therefore we will not make notational distinction between time-domain signals and their frequency-domain counterparts.

A *system* is a linear mapping between an input signal to an output signal, $\mathbf{G} : L^2 \to L^2$

$$\mathbf{y}(t) = (\mathbf{G}\mathbf{w})(t).$$

We are interested in the asymptotic and causal input-output properties; assuming knowledge of $\mathbf{w}(t)$ in the time interval $(-\infty, t)$, the output at time t is uniquely given by the system $\mathbf{G} : L^2(-\infty, \infty) \to L^2(-\infty, \infty)$

$$\mathbf{y}(t) = (\mathbf{G}\mathbf{w})(t) = \mathbf{C} \int_{-\infty}^{t} e^{\mathbf{A}(t-s)} \mathbf{B}\mathbf{w}(s) \, ds \qquad (3.2)$$

where $\exp(\mathbf{A})$ is the matrix exponential (Trefethen & Embree 2005). Similar to signals, linear time-invariant (LTI) systems can be represented in the frequency domain. A Laplace transform of (3.2) results in a transfer function matrix

$$\mathbf{y}(s) = \hat{\mathbf{G}}(s)\mathbf{w}(s) = (\mathbf{C}(s\mathbf{I} - \mathbf{A})^{-1}\mathbf{B})\mathbf{w}(s) \qquad (3.3)$$

with $s \in \mathbb{C}$. Henceforth the hat on $\hat{\mathbf{G}}$ is omitted since it is related to $\mathbf{G}$ by a linear transformation. Occasionally we write the input-output system in compact form

$$\mathbf{G} = \left(\begin{array}{c|c} \mathbf{A} & \mathbf{B} \\ \hline \mathbf{C} & 0 \end{array} \right). \qquad (3.4)$$

Performance criterions for control design and error bounds for model reduction are given by different system norms. In general, $\|\mathbf{G}\|_2$ is an appropriate measure of performance when the input signal is a stochastic process, whereas $\|\mathbf{G}\|_\infty$ is appropriate when considering largest possible amplification due to an input signal. The latter norm quantifies the amplification of an input signal, which is given by the induced L^2-norm of a system,

$$\|\mathbf{G}\|_\infty = \sup_{\mathbf{w} \neq 0} \frac{\|\mathbf{G}\mathbf{w}\|_{L^2}}{\|\mathbf{w}\|_{L^2}}.$$

It can be shown (see e.g. Green & Limebeer 1995, p. 92) that the induced norm is the infinity norm of its transfer function matrix,

$$\|\mathbf{G}\|_\infty = \sup_\omega |\mathbf{G}(i\omega)|, \tag{3.5}$$

where $|\mathbf{G}|$ denotes the largest singular value of the transfer function matrix. Moreover, this norm is finite for all stable systems. So, $\|\mathbf{G}\|_\infty$ measures how much energy is transfered from the input to the output.

The 2-norm of system $\mathbf{G}$ is the expected root-mean-square (RMS) value of the output when the input is a white noise process with unit variance. If $\mathbf{w}(t)$ is white noise, then

$$\|\mathbf{G}\|_2^2 = E\left(\frac{1}{T}\|\mathbf{Gw}\|_{L^2}^2\right) = E\left(\frac{1}{T}\int_0^T |\mathbf{y}|^2 dt\right) \tag{3.6}$$

where it can be shown (see e.g. Green & Limebeer 1995, p. 94) that as $t \to \infty$

$$\|\mathbf{G}\|_2^2 = \frac{1}{2\pi}\int_{-\infty}^\infty \mathrm{trace}\left(\mathbf{G}(i\omega)\mathbf{G}^T(i\omega)\right)d\omega. \tag{3.7}$$

The 2-norm can be computed either by the average output energy of a large number of realizations to stochastic forcing, or by solving one Lyapunov equation (Green & Limebeer 1995). However, when n is large, as in our case, a more feasible way is to compute the output energy of an impulse response, since white noise is a set of impulses that are uncorrelated in time.

Comparing equation (3.7) with equation (3.5), we note that ∞-norm measures the response to the "worst" frequency, whereas 2-norm measures the response to all frequencies in an average sense.

3.2.1. *Input-output analysis of the flat-plate boundary layer*

Before we consider the full system in figure 3.3, the input-output behavior between the disturbance and objective function is characterized; the "sensor", "controller" and "actuator" are not included in the analysis for now. Consider the stable linear system $\mathbf{G}$ given by; (i) the Navier–Stokes equations linearized about the steady boundary-layer flow ($\mathbf{A} \in \mathbb{R}^{n \times n}$), (ii) a two-dimensional volume forcing inside the boundary layer at an upstream location ($\mathbf{B}_1 \in \mathbb{R}^{n \times 1}$) and (iii) a two-dimensional sensor ($\mathbf{C}_1 \in \mathbb{R}^{1 \times n}$), also represented by function inside the boundary layer, but located further downstream.

We will characterize $\mathbf{G}$ by computing its 2-norm and ∞-norm, since these measures are necessary components when performing model reduction and designing control schemes in the subsequent sections of this chapter. The norms are obtained by computing the energy of the output signal $\mathbf{y}$ when the input $\mathbf{w}$ is a impulse/stochastic (2-norm) signal and harmonic signal (∞-norm).

The 2-norm, defined by equation (3.6), is given by the output energy due to an impulsive input $\mathbf{w}(t) = \delta(t)$. The impulse response given by,

$$\mathbf{y}(t) = \mathbf{C}e^{\mathbf{A}t}\mathbf{B}, \tag{3.8}$$
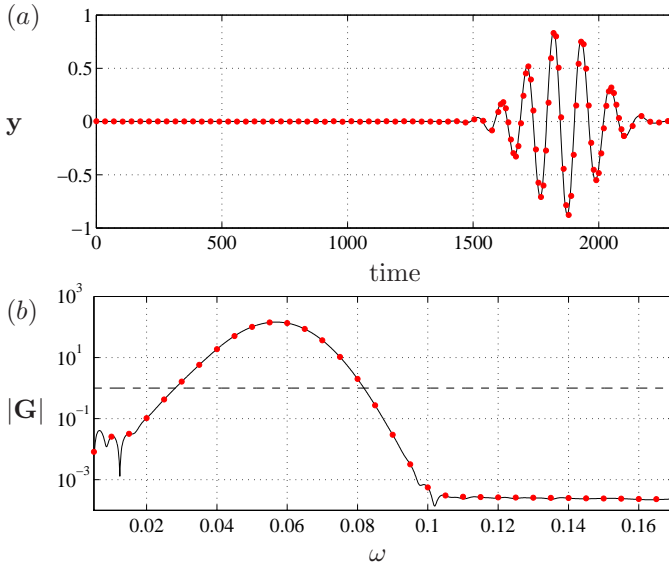
FIGURE 3.4. Impulse (*a*) and frequency response (*b*) of the flat-plate boundary layer. The black lines show responses from DNS computations ($n \approx 10^5$). The red symbols show the responses from the reduced-order model ($r = 60$).

is shown in figure 3.4(*a*) with a black solid line. The impulse triggers a wavepacket that grows in amplitude as is propagates in the downstream direction. The output signal $\mathbf{y}(t)$ is zero for a long time, but as the disturbance passes the sensor location, the wavepacket is registered. The 2-norm of $\mathbf{G}$, which for the present case is $\|\mathbf{G}\|_2 = \|\mathbf{y}\|_{L^2} = 9.7$ quantifies the signal amplification of a unit norm input in an averaged sense.

The ∞-norm, defined by equation (3.5), is computed by finding the harmonic input signal that results in the largest output energy. The response to harmonic forcing $\mathbf{w}(t) = e^{i\omega t}$ is given by

$$\mathbf{y}(t) = |\mathbf{G}(i\omega)|e^{i\omega t + \phi}. \tag{3.9}$$

Due to the linear nature of the system, the input frequency ω will generate an output signal with same frequency but with a phase shift $\phi = \text{Arg}(\mathbf{G})$ and a gain $|\mathbf{G}(i\omega)|$. The gain is shown in figure 3.4(*b*) with a black solid line. A range of frequencies are amplified with the peak at $\omega = 0.055$, whereas the low and high frequencies are damped. The ∞-norm is given by the peak value value of the gain $|\mathbf{G}|$. In table 3.1 the norms of $\mathbf{G}$ are listed. In the next section, we attempt to construct a new system, $\mathbf{G}_r$ with system norms very close to $\mathbf{G}$, but a significantly smaller dimension.

3.3. The model reduction problem

The state space $\mathbb{U}$ contains all possible solenoidal velocity fields that satisfy the boundary conditions. However, for a given structure of $\mathbf{B}$ and $\mathbf{C}$, only certain velocity fields can be triggered by the input and observed by the output. These states are called controllable and observable states respectively. The flow structures that are neither controllable nor observable are redundant for the input-output behavior. The minimum number of states[1] $\hat{n} \leq n$ that can be both observed and controlled for a given $\mathbf{B}$ and $\mathbf{C}$ is defined as the *complexity* of $\mathbf{G}$. Henceforth we will omit the hat on $\hat{n}$. It turns out that when $m, p \ll n$, the complexity of $\mathbf{G}$ can be significantly reduced, while preserving the relation between the inputs and outputs. The reason for this reduction is that a large number of the states are nearly uncontrollable/unobservable and they can be discarded since they have a very weak influence on the input-output behavior. A systematic approach of removing these states is called balanced truncation (Moore 1981).

A *reduced-order system* (ROM) is an "approximation" of $\mathbf{G}$, defined as

$$\mathbf{G}_r = \left(\begin{array}{c|c} \mathbf{A}_r & \mathbf{B}_r \\ \hline \mathbf{C}_r & \mathbf{D}_r \end{array} \right),$$

such that the complexity of $\mathbf{G}_r$ is r where $r \ll n$. We would like to choose $\mathbf{G}_r$ such that

$$\|\mathbf{G} - \mathbf{G}_r\|_\infty \tag{3.10}$$

is small. Requiring a small error in the 2-norm is a substantially more difficult problem.

3.3.1. *SVD of the Hankel operator*

Matrices and linear systems are both linear transformations and have thus a lot in common. It is well known that if one wants to approximate an n-rank matrix $\mathbf{A}$ with a $r < n$ rank matrix $\mathbf{A}_r$, then the smallest possible error is given by

$$\min_{\text{rank}(\mathbf{A}_r) \leq r} \|\mathbf{A} - \mathbf{A}_r\| = \sigma_{r+1}, \tag{3.11}$$

where $\| \cdot \|$ is the induced Euclidean norm and σ_{r+1} is the $r+1$ largest singular value of $\mathbf{A}$. One can also compute singular value decomposition (SVD) of signals which amounts to a POD analysis (Moore 1981). However, a SVD of a linear input-output system $\mathbf{G}$ in order to find a $\mathbf{G}_r$ is not straightforward, since $\mathbf{G}$ is not always a finite rank operator. In fact there is no known solution to the optimal model reduction problem in the infinity norm. A simpler input-output mapping, is the finite-rank *Hankel operator* $\mathbf{\Gamma_G} : L^2(-\infty, 0] \rightarrow L^2[0, \infty)$ of the system $\mathbf{G}$, defined by

$$(\mathbf{\Gamma_G}\mathbf{w})(t) = \int_{-\infty}^0 \mathbf{C}e^{\mathbf{A}(t-s)}\mathbf{B}\mathbf{w}(s) \; ds.$$

---

[1]In the literature, $\hat{n}$ is refereed to as the McMillan degree.
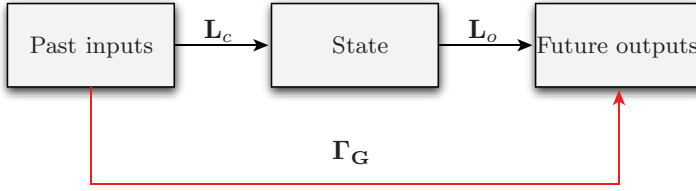
FIGURE 3.5. The controllability operator $\mathbf{L}_c$ relates past inputs to the present state, while the observability mapping $\mathbf{L}_o$ relates the present state to the future outputs. Their combined action is expressed by the Hankel operator $\mathbf{\Gamma_G}$.

The induced norm of $\mathbf{\Gamma_G}$ is equal to the Hankel norm of $\mathbf{G}$, $\|\mathbf{\Gamma_G}\|_\infty = \|\mathbf{G}\|_H$. The Hankel norm quantifies the energy transfered from past inputs to future outputs. In this norm there is a solution to the optimal model reduction problem, called the Hankel norm approximation (Glover 1999). However, we will use the Hankel operator to introduce a non-optimal model reduction problem, referred to as balanced truncation, which has error bounds very close (a factor of 2 larger in ∞-norm) to the Hankel norm approximation, but is considerably easier to compute.

To understand why $\mathbf{\Gamma_G}$ has finite rank, we decompose the input-output operator into two parts

$$\mathbf{\Gamma_G} = \mathbf{L}_o \mathbf{L}_c.$$

The controllability operator $\mathbf{L}_c : L^2(-\infty, 0] \to \mathbb{U}$, maps past input signals to an initial state $\mathbf{u}_0$,

$$\mathbf{L}_c \mathbf{w} = \int_{-\infty}^0 e^{-\mathbf{A}s} \mathbf{B} \mathbf{w}(s) ds. \tag{3.12}$$

The second mapping $\mathbf{L}_o : \mathbb{U} \to L^2[0, \infty)$, called observability operator, is from the initial state to future outputs signals,

$$\mathbf{L}_o \mathbf{u}_0 = \mathbf{C} e^{\mathbf{A}t} \mathbf{u}_0 \qquad t \geq 0. \tag{3.13}$$

As sketched in figure 3.5, the input is mapped via a state at a reference time $t = 0$, given by $\mathbf{u}_0 = \mathbf{L}_c \mathbf{w}$, to the output given by $\mathbf{y} = \mathbf{L}_o \mathbf{u}_0$. Therefore in order to determine the output, it is sufficient to know the state $\mathbf{u}_0$ that results from driving the system with $\mathbf{w}$. The key point is: all inputs that give rise to the same $\mathbf{u}_0$ produce the same output. Any two linearly independent states, $\mathbf{u}_1, \mathbf{u}_2 \in \mathbb{U}$ result in two linearly independent future outputs $\mathbf{y}_1, \mathbf{y}_2 \in \mathbb{R}^p$. Thus, the number of linearly independent outputs, and hence the rank of $\mathbf{\Gamma_G}$, is n.

We can compute the singular value decomposition (SVD) of $\mathbf{\Gamma_G}$,

$$(\mathbf{\Gamma_G} \mathbf{w})(t) = \sum_{j=1}^n \sigma_j \langle \mathbf{s}_j, \mathbf{w} \rangle_{L^2} \mathbf{t}_j, \tag{3.14}$$

where $\mathbf{s}_j \in L^2(-\infty, 0)$ and $\mathbf{t}_j \in L^2(0, \infty)$ are sets of orthonormal signals. The singular values of $\mathbf{\Gamma_G}$, $\sigma_j > 0$ are called *Hankel singular values* (HSV) of $\mathbf{G}$ and are ordered in descending order of magnitude. Of all possible unit-norm (past) input signals, $\mathbf{s}_1$ results in the (future) output signal with the largest norm, given by $\sigma_1^2 \mathbf{t}_1$.

3.3.2. *Reduced-order system*

The mappings, $\mathbf{L}_c$ and $\mathbf{L}_o$, are related to the concepts of controllability and observability. A state is called controllable if it belongs to the range of $\mathbf{L}_c$, that is, if $\mathbf{u} = \mathbf{L}_c \mathbf{w}$ exists for some $\mathbf{w}$. By forming the $n \times n$ positive (semi) definite matrix $\mathbf{P}$,

$$\mathbf{P} \quad = \mathbf{L}_c \mathbf{L}_c^T = \int_0^\infty e^{\mathbf{A}t} \mathbf{B} \mathbf{B}^T e^{\mathbf{A}^T t} dt, \qquad (3.15)$$

called the controllability Gramian, we can rank different states according to how easily they can be influenced by an input. In particular, the most easily influenced, or most controllable, flow structures are the eigenvectors of $\mathbf{P}$ associated to the largest eigenvalues of $\mathbf{P}$.

The linear system $\mathbf{G}$ is observable if $\mathbf{L}_o \mathbf{u}_0 = 0$ occur only if $\mathbf{u}_0 = 0$, i.e. if the knowledge of the output determines the initial state uniquely. Fluid systems are rarely completely observable when using localized sensing. However, among all possible $\mathbf{u}_0$, we can find the initial conditions which produce the largest possible output energy, by forming the $n \times n$ observability Gramian $\mathbf{Q}$,

$$\mathbf{Q} \quad = \mathbf{L}_o^T \mathbf{L}_o = \int_0^\infty e^{\mathbf{A}^T t} \mathbf{C}^T \mathbf{C} e^{\mathbf{A}t} dt. \qquad (3.16)$$

The matrix provides a way to rank states according to their contribution to the output. The most observable states are given by the eigenvectors of the matrix $\mathbf{Q}$ corresponding to its largest eigenvalues. The sketch in figure 3.6, illustrates the concepts of the Gramians. Note that $\mathbf{L}_o^T$ and $\mathbf{L}_c^T$ are the adjoint observability and controllability operators respectively and are derived in Bagheri *et al.* (2009*b*).

It is easy to show (see Green & Limebeer 1995, p. 344) that (3.14) holds if

$$\mathbf{P}\mathbf{Q}\boldsymbol{\phi}_i = \sigma_i^2 \boldsymbol{\phi}_i, \qquad i = 1, \ldots, n. \qquad (3.17)$$

We call the eigenvectors, $\boldsymbol{\phi}_j \in \mathbb{U}$, *balanced modes*. This set is not orthogonal, and we define the set of left eigenvectors of $\mathbf{P}\mathbf{Q}$ as the *adjoint balanced modes* and denoted them by $\boldsymbol{\psi}_j \in \mathbb{U}$. The two sets are bi-orthogonal, i.e. $\langle \boldsymbol{\phi}_i, \boldsymbol{\psi}_j \rangle_{\mathbb{U}} = \delta_{ij}$. The balanced mode $\boldsymbol{\phi}_j$ is a global structure in the flow that is "influenced" by the input $\mathbf{B}$ by an amount given by its HSV σ_j, whereas the corresponding adjoint mode $\boldsymbol{\psi}_j$ is a flow structure that – if used as an initial condition – will result in an output energy $\|\mathbf{y}\|_{L_2}$ given also by σ_j. These global modes that come in pairs have thus ranked the flow fields according to their response behavior (controllability) and output sensitivity (observability).
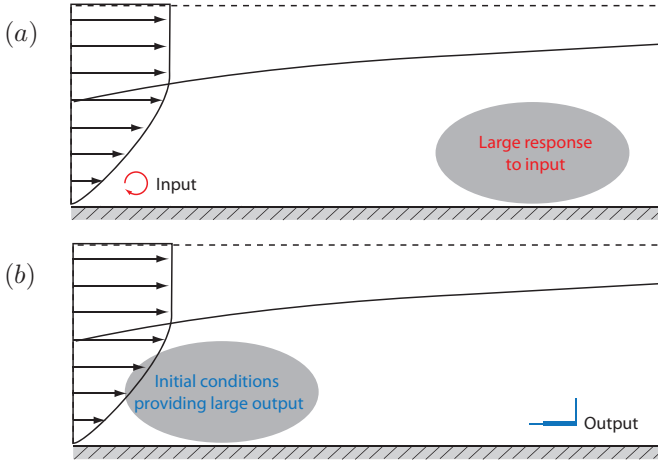
FIGURE 3.6. Sketch of controllability (a) and observability (b) for the flat-plate boundary layer. The response to an input is large downstream (because of strong convection), which results in a large controllability of flow structures in the downstream part of the domain. Similarly, the flow structures that will after a transient time, result in a large sensor output are located far upstream, resulting in strong observability in that region.

Let the columns of the matrices $\mathbf{\Phi}$ and $\mathbf{\Psi}$ contain r balanced modes and r adjoint modes respectively, corresponding to the r largest HSV,

$$\mathbf{\Phi} = [\boldsymbol{\phi}_1 \ \ldots \ \boldsymbol{\phi}_r], \qquad \mathbf{\Psi} = [\boldsymbol{\psi}_1 \ \ldots \ \boldsymbol{\psi}_r].$$

The *reduced order system* $\mathbf{G}_r$ is given by,

$$\mathbf{G}_r = \left(\begin{array}{c|c} \mathbf{\Psi}^T \mathbf{A} \mathbf{\Phi} & \mathbf{\Psi}^T \mathbf{B} \\ \hline \mathbf{C} \mathbf{\Phi} & \mathbf{D} \end{array} \right).$$

To obtain the above system, we have performed an oblique projection of the original high-dimensional state-space system (3.1) onto a subspace $\mathbb{U}_r \subset \mathbb{U}$ spanned by r balanced modes. The projection is along a direction orthogonal to the subspace $\mathbb{U}_r^* \subset \mathbb{U}$ spanned by the adjoint balanced modes (see Ahuja 2009, p. 12). Traditionally, to obtain $\mathbf{G}_r$ one adopts a transformation-truncation approach (Moore 1981) called *balanced truncation*. In this approach – which also explains the term balancing – the system $\mathbf{G}$ is via a linear transformation represented in coordinates, where the controllability and observability Gramians are diagonal and equal to the HSV (the controllable and observable properties are thus "balanced").

The system $\mathbf{G}_r$ is not optimal in any way, although it is derived from SVD of the Hankel operator. Nevertheless, balanced truncation is arguably the most

widely used method for model reduction of linear input-output systems, because of the following two properties: (i) $\mathbf{G}_r$ is guaranteed to be asymptotically stable if $\sigma_j \neq \sigma_{j+1}$ for all j (Pernebo & Silverman 1982); (ii) there exist tight error bounds (Glover 1999),

$$\sigma_{r+1} \leq \|\mathbf{G} - \mathbf{G}_r\|_\infty \leq 2 \sum_{j=r+1}^{n} \sigma_j \qquad (3.18)$$

that can be determined *a priori* to computing $\mathbf{G}_r$. Comparing the error bound to equation (3.11), we see that the Hankel singular values play a similar role in linear systems to singular values of matrices.

3.3.3. *Model reduction of the flat-plate boundary layer*

We return to the single-input single-output flat-plate boundary layer example, where the number of degrees of freedom to describe two-dimensional disturbances is $n \approx 10^5$. In this section, we construct a low-order model $\mathbf{G}_r$ using balanced modes and compare its performance to the Navier–Stokes system.

When the input $\mathbf{B}_1$ is placed upstream and the output $\mathbf{C}_1$ downstream, the controllable velocity fields and the observable fields are spatially separated in the streamwise direction. As shown in schematically in figure 3.6, observability is strong far upstream, whereas controllability is strong at the downstream part of the domain. This is a consequence of the convective nature of the instabilities arising in the Blasius flow where disturbances grow in amplitude as they are convected in the downstream direction. The large difference between observable and controllable states, makes it particularly important to perform balancing in order to construct a reduced-order model that captures the input-output behavior. Figure 3.7(*a-b*) show that the first adjoint ($\boldsymbol{\psi}_1$) and forward balanced mode ($\boldsymbol{\phi}_1$) appear as localized wavepackets, located at each end of the domain. Modes corresponding to higher HSV look similar, but have different spatial wavelengths. It is because of the bi-orthogonal projection, where the adjoint balanced modes account for the output sensitivity and the direct balanced modes for the most controllable structures, that the resulting reduced-order model captures the input-output behavior. It is interesting to point out that for many convectively unstable flows, this spatial separation is also observed between the global eigenmodes of the linearized Navier–Stokes equations and eigenmodes of the adjoint Navier–Stokes equations, where it is associated to the streamwise nonnormality of the system (Chomaz 2005).

In figure 3.4 the impulse and frequency responses of the balanced reduced-order model $\mathbf{G}_r$ ($r = 60$) are compared to full Navier–Stokes system ($n = 10^5$). We observe that the curves essentially collapse for both types of forcing, albeit the remarkable reduction in the number of degrees of freedom. This clearly indicates that capturing the input-output behavior of a linear system when $m, p \ll n$ (in this single-input single-output case $m = p = 1$) requires significantly smaller degrees of freedom, compared to capturing the full spatiotemporal disturbance dynamics. A more quantitative evaluation is provided in figure
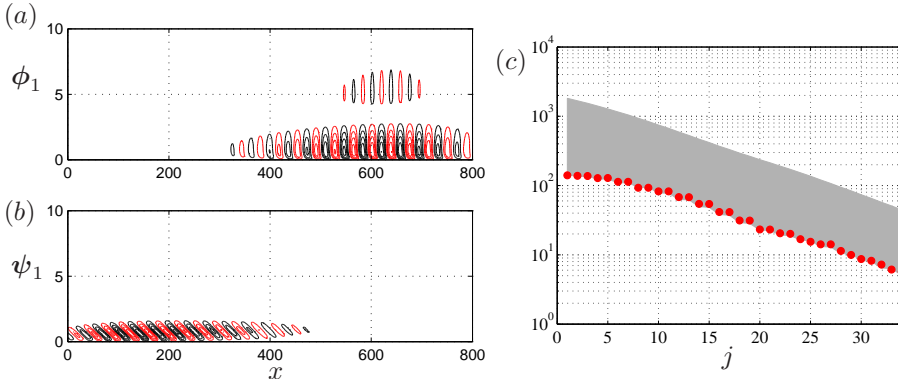
FIGURE 3.7. Left: The streamwise velocity component (positive in red and negative in black) of first balanced mode ϕ_1 and it associated adjoint mode ψ_1. Right: The ∞-norm model reduction error. The upper and lower theoretical bounds (equation 3.18) are depicted with a gray region and the actual model reduction error is shown with red symbols.

3.7(b), where the actual model reduction error $\|\mathbf{G} - \mathbf{G}_r\|_\infty$ is compared to the theoretical error bounds given by HSV (3.18). We observe that the error (red circles) decays rapidly with increasing modes, and is close to the lower theoretical bound. Note that the lower bound in the ∞-norm holds for *any* model reduction procedure applied to a linear system and not only balanced reduced-order model. See also table 3.1 for the norms of $\mathbf{G}_r$ ($r = 60$).

3.4. The control problem

In the previous sections, we have characterized the input-output behavior of the plant (Navier–Stokes system) $\mathbf{G}$ by computing system norms. In the context of flow stability, large system norms are closely linked to transient growth of perturbation energy (see e.g. Bewley & Liu 1998; Bewley 2001, for more on this relation). By minimizing the system norms we can expect smaller transient growth of perturbations and a laminar flow system that is less likely to transition to turbulence.

The control problem can formulated as follows: By applying feedback control to $\mathbf{G}$, find a closed-loop system

$$\mathbf{G}_c = \left(\begin{array}{c|c} \mathbf{A}_c & \mathbf{B}_c \\ \hline \mathbf{C}_c & \mathbf{D}_c \end{array} \right),$$

such that

$$\|\mathbf{G}_c\|_2 < \|\mathbf{G}\|_2 \tag{3.19}$$

and its complexity is of the same order as the plant $\mathbf{G}$. Recall from section 3.2 that the 2-norm of a system is the output energy when the input to the system is a stochastic process. In other words, forcing both systems $\mathbf{G}$ and $\mathbf{G}_c$

with unit-variance white noise, the closed-loop system is required to result in a significantly smaller output signal than the plant. The aim of this section is to design $\mathbf{A}_c, \mathbf{B}_c, \mathbf{C}_c$ and $\mathbf{D}_c$ such that the 2-norm of $\mathbf{G}_c$ is the smallest possible. We present a systematic method to find $\mathbf{G}_c$, known as the linear quadratic Gaussian (LQG) optimal control problem (Anderson & Moore 1990; Lewis & Syrmos 1995; Doyle *et al.* 1989; Dullerud & Paganini 1999). The main disadvantage of LQG is that it does not account for uncertainties of the system $\mathbf{G}$ (Doyle 1978) which is required to guarantee a robust performance and even robust stability of the closed loop system $\mathbf{G}_c$. One can only check the robustness by *ad-hoc* testing the controller for various parameters. The LQG problem can be extended to robust optimal control problem referred to as the H_∞ control, see Zhou *et al.* (2002); Bagheri *et al.* (2009c).

3.4.1. *The plant*

So far in this chapter, the inputs has represented disturbances and the outputs some arbitrary sensor measurements. In order to construct $\mathbf{G}_c$ by formulating a feedback control problem, we need to arrange the inputs and outputs in a specific manner (Doyle *et al.* 1989). Consider the following stable plant (or open–loop system) with three inputs and two outputs,

$$\dot{\mathbf{u}} = \mathbf{A}\mathbf{u} + \mathbf{B}_1 w_1 + \mathbf{B}_2 w_2 \tag{3.20a}$$

$$y_1 = \mathbf{C}_1 \mathbf{u} + l w_2 \tag{3.20b}$$

$$y_2 = \mathbf{C}_2 \mathbf{u} + \alpha g. \tag{3.20c}$$

The system (3.20) in a compact form is given by

$$\mathbf{G} = \left(\begin{array}{c|ccc} \mathbf{A} & \mathbf{B}_1 & 0 & \mathbf{B}_2 \\ \hline \mathbf{C}_1 & 0 & 0 & l \\ \mathbf{C}_2 & 0 & \alpha & 0 \end{array} \right). \tag{3.21}$$

Figure 3.3 shows a sketch corresponding to the above system. The physical shape of the inputs/outputs, described by the constant input and output vectors $\mathbf{B} = [\mathbf{B}_1 \ 0 \ \mathbf{B}_2]$ and $\mathbf{C} = [\mathbf{C}_1 \ \mathbf{C}_2]^T$, were discussed in section 3.1. The corresponding time signals $\mathbf{w}(t) = [w_1 \ g \ w_2]^T$ and $\mathbf{y}(t) = [y_1 \ y_2]^T$ represent the following:

- The disturbance signal w_1 is assumed to be a temporal white noise with unit intensity.
- The control signal w_2 is to be determined in order to minimize the objective function.
- The objective functional is the mean of the output signal y_1,

$$E\left(\|y_1\|_{L^2}^2\right) = E\left(\int_0^\infty (\mathbf{u}^T \mathbf{C}_1^T \mathbf{C}_1 \mathbf{u} + l^2 w_2^T w_2) dt \right). \tag{3.22}$$

  The disturbance energy is minimized in the domain defined by $\mathbf{C}_1$, and at the same time the control effort is penalized with a scalar l.
- The measurement signal y_2 estimates amplification and phase of temporal frequencies in the flow at the location of the sensor $\mathbf{C}_2$. The signal

is forced with an unit variance temporal noise $g(t)$ (large values of the scalar α, indicate high level of noise corruption).

As alluded to above, we will determine the optimal control $w_2(t)$ in (3.20) based on noisy measurements $y_2(t)$ such that the cost functional (3.22) is minimized. The assumptions that external disturbances w_1 and the sensor noise g are white noise may in some applications be unrealistic, however, it is possible to describe a system with colored noise input, in terms of an augmented system with white-noise input (Lewis & Syrmos 1995).

3.4.2. *Linear quadratic Gaussian design*

One can show (Doyle *et al.* 1989) that the system $\mathbf{G}_c$ with smallest 2-norm, satisfies

$$\|\mathbf{G}_c\|_2^2 = \underbrace{\|\mathbf{G}_f\|_2^2}_{\text{Full information}} + \underbrace{\|\mathbf{G}_e\|_2^2}_{\text{Estimation}} .$$

In order to construct $\mathbf{G}_c$ we need to compute two simpler linear systems $\mathbf{G}_f$ and $\mathbf{G}_e$, by solving a full-information control and an estimation problem. It turns out that the two systems $\mathbf{G}_f$ and $\mathbf{G}_e$ can be solved independently from each other. Moreover, if both subsystems are stable and optimal then the closed-loop system is also guaranteed to be stable and optimal.

We briefly state the solution of the two problems and refer to Doyle *et al.* (1989) for details.

Full-information problem

In this first step, assume we can measure the full state at all times. We further assume that the control $w_2(t)$ and the state $\mathbf{u}(t)$ satisfy a linear relation involving some yet unknown matrix $\mathbf{K}$, i.e.

$$w_2(t) = \mathbf{K}\mathbf{u}(t). \tag{3.23}$$

Inserting (3.23) into (3.20) and neglecting the redundant output y_2, we get

$$\mathbf{G}_f = \left(\begin{array}{c|c} \mathbf{A} + \mathbf{B}_2\mathbf{K} & \mathbf{B}_1 \\ \hline \mathbf{C}_1 + l\mathbf{K} & 0 \end{array} \right).$$

It remains to choose $\mathbf{K}$ such that $\mathbf{G}_f$ is stable and the control signal $w_2(t)$ minimizes the system norm $\|\mathbf{G}_f\|_2$. The solution is provided by a optimal control state-feedback problem, (see e.g. Anderson & Moore 1990), where the optimal control signal (3.23) is given by the feedback gain,

$$\mathbf{K} = -\mathbf{B}_2^T\mathbf{X},$$

and $\mathbf{X}$ is a solution of the (algebraic) Riccati equation

$$0 = \mathbf{A}^T\mathbf{X} + \mathbf{X}\mathbf{A} - \mathbf{X}\mathbf{B}_2\mathbf{B}_2^T\mathbf{X} + \mathbf{C}_1^T\mathbf{C}_1.$$

Estimation problem

The second step in constructing $\mathbf{G}_c$ is to estimate the full state $\mathbf{u}(t)$ via the linear system $\mathbf{G}_e$ given only the noisy measurements y_2. Denoting the estimation error by $\mathbf{u}_e = \mathbf{u} - \hat{\mathbf{u}}$, where $\hat{\mathbf{u}}$ is the estimated state and assuming that both w_1 and g are white noise processes, an estimator can be formulated as follows

$$\dot{\mathbf{u}}_e = \mathbf{A}\mathbf{u}_e + \mathbf{B}_1 w_1 + \mathbf{L}(y_2 - \hat{y}_2) \tag{3.24a}$$

$$\hat{y}_2 = \mathbf{C}_2\hat{\mathbf{u}} \tag{3.24b}$$

$$y_2 = \mathbf{C}_2\mathbf{u} + \alpha g. \tag{3.24c}$$

In the above expression, we compare the measurement y_2 from the state and the measurement $\hat{y}_2$ from the estimated state and feed back the mismatch in these two quantities using the estimator gain $\mathbf{L}$.

It can be shown (Kalman 1960) that the estimation gain that minimizes the estimation error $\|\mathbf{u}_e\|_{L^2(0,\infty)}$ and results in a stable estimator is given by

$$\mathbf{L} = -\mathbf{Y}\mathbf{C}_2^T,$$

where $\mathbf{Y}$ is a solution of the Riccati equation,

$$0 = \mathbf{A}\mathbf{Y} + \mathbf{Y}\mathbf{A}^T - \mathbf{Y}\mathbf{C}_2^T\mathbf{C}_2\mathbf{Y} + \mathbf{B}_1\mathbf{B}_1^T.$$

Now, if the state has been successfully estimated, it can be shown that the optimal control signal $w_2(t)$ is given by $w_2(t) = \mathbf{K}\hat{\mathbf{u}}(t)$ where $\mathbf{K}$ is the full information control gain computed previously. By substituting the explicit dependence of the two measurements on the state $\mathbf{u}$ and the estimated state $\hat{\mathbf{u}}$, respectively, into the estimator (3.24) we obtain the second part of the closed-loop system $\mathbf{G}_c$:

$$\mathbf{G}_e = \left(\begin{array}{c|cc} \mathbf{A} + \mathbf{L}\mathbf{C}_2 & \mathbf{B}_1 & \alpha\mathbf{L} \\ \hline \mathbf{K} & 0 & 0 \end{array} \right).$$

Note that the input of $\mathbf{G}_e$ is $[w_1 \ g]^T$ and the output is the control signal w_2.

The closed-loop system

The cost of solving a Riccati equation is $O(n^3)$, which is a computationally intractable task when $n > 10^5$. In the previous section we showed that our reduced model $\mathbf{G}_r$ is able to capture the input-output behavior of the Navier–Stokes system $\mathbf{G}$. During the design of $\mathbf{G}_c$ we can assume that the reduced-model is the plant that we wish to control. Once we have determined $\mathbf{G}_e$ and $\mathbf{G}_f$ for this approximating model, we will apply it to the full Navier–Stokes system. This means that the feedback gains and have the same dimension (r) as the reduced-order model $\mathbf{G}_r$.

The final step is to connect the controller $\mathbf{G}_f$ and the estimator $\mathbf{G}_e$ to the plant $\mathbf{G}$ given by equation (3.21) to obtain the matrices $\mathbf{A}_c, \mathbf{B}_c, \mathbf{C}_c$ and $\mathbf{D}_c$ of
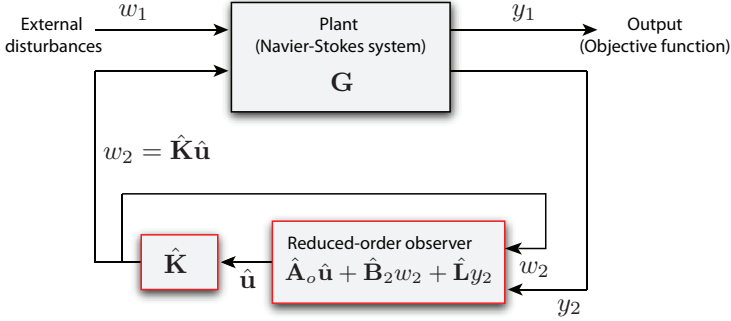
FIGURE 3.8. Sketch of the closed-loop system $\mathbf{G}_c$. The controller (red borders) of order r consists of an observer and feedback gain $\hat{\mathbf{K}}$ that forces the plant $\mathbf{G}$ of size n with the control signal w_2 based on the noisy measurements y_2 so that the effect of w_1 on the output signal y_1 is minimized. The observer is governed by $\hat{\mathbf{A}}_o = \hat{\mathbf{A}} + \hat{\mathbf{L}}\hat{\mathbf{C}}_2$.

closed-loop system $\mathbf{G}_c$. A straightforward derivation gives

$$
\mathbf{G}_c = \left(
\begin{array}{cc|cc}
\mathbf{A} & \mathbf{B}_2\hat{\mathbf{K}} & \mathbf{B}_1 & 0 \\
-\hat{\mathbf{L}}\mathbf{C}_2 & \hat{\mathbf{A}} + \hat{\mathbf{B}}_2\hat{\mathbf{K}} + \hat{\mathbf{L}}\hat{\mathbf{C}}_2 & 0 & -\alpha\hat{\mathbf{L}} \\
\hline
\mathbf{C}_1 & l\hat{\mathbf{K}} & 0 & 0
\end{array}
\right).
$$

The output of the system is y_1 and the inputs are $[w_1 \; g]^T$. The state for the above system is $[\mathbf{u} \; \hat{\mathbf{u}}]^T \in \mathbb{R}^{(n+r)\times 1}$ where $\mathbf{u} \in \mathbb{U}$ is the full state and the $\hat{\mathbf{u}} \in \mathbb{R}^{r\times 1}$ is the reduced estimated state. A sketch of the closed-loop system is shown in figure 3.8. It is important to note that in the above closed-loop system the quantifies marked with hat are of order $r \ll n$. This results in a fast "online" controller running in parallel with the experiments. As shown in figure 3.8, the controller can be decomposed into an observer governed by $(\hat{\mathbf{A}} + \hat{\mathbf{L}}\hat{\mathbf{C}}_2)\hat{\mathbf{u}} + \hat{\mathbf{B}}_2 w_2 + \hat{\mathbf{L}}y_2$ and the feedback gain $\hat{\mathbf{K}}$.

3.4.3. Feedback control of the flat-plate boundary layer

The full input-output system $\mathbf{G}$ for the flat-plate boundary layer is shown in figure 3.3 and was described in section 3.1. Recall that LQG design minimizes the 2-norm of the closed-loop system $\mathbf{G}_c$ when the external disturbances (w_1, g) are white noise process. We therefore force both systems $\mathbf{G}$ and $\mathbf{G}_c$ with unit-variance white noise signal in w_1 and compare the root-mean-square values (averaged in the directions z, y and the time t) of the streamwise velocity component u. Note that the purpose of the measurement noise g is to account for uncertainties in the sensor measurements during the control design. When evaluating the closed-loop performance the system is only forced with w_1. In figure 3.9(a) the performance of a controller is investigated with (control
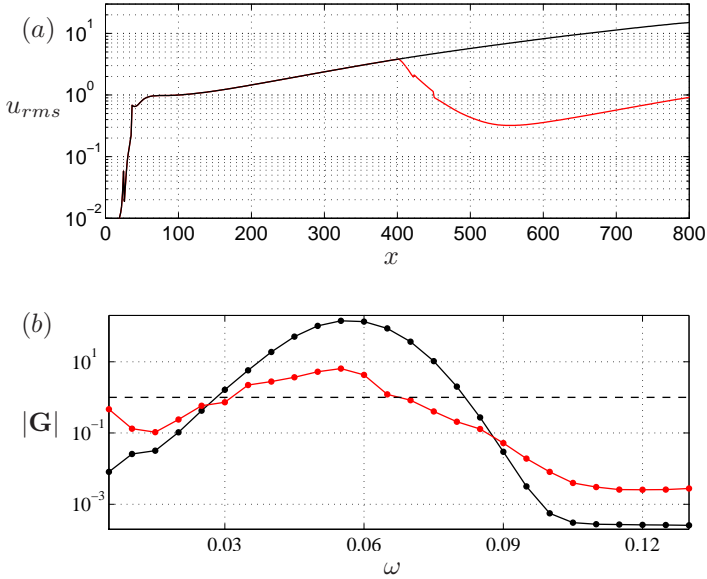
FIGURE 3.9. (a) The streamwise rms-values of the uncontrolled system (blacks), and the closed-loop (red) as a function of the streamwise direction x. (b) Comparison of the frequency response from disturbances to objective function of uncontrolled (black) and the closed-loop system (red).

penalty) $l = 0.1$ and (sensor noise contamination) $\alpha = 0.1$. The rms-value of the disturbance grows exponentially downstream in the uncontrolled case until $x = 800$. The rms-value of the perturbation when the control is active grows only until it reaches the actuator position ($x = 400$), where it immediately begins to decay. At the location of the objective function $\mathbf{C}_1$ ($x = 750$), the amplitude of the perturbation is one order of magnitude smaller than in the uncontrolled case.

There are a number of additional ways to evaluate the control performance. In figure 3.9(b) the frequency response from the disturbance $\mathbf{B}_1$ to the objective function $\mathbf{C}_1$ of the uncontrolled system is compared to that of the closed-loop system. The controller suppresses the most dangerous frequencies close to $\omega = 0.055$ significantly. Note that compared to the uncontrolled model, the highly damped frequencies $\omega > 0.11$ have larger gain in amplitudes. This behavior is often observed in closed-loop systems and is related to the "waterbed" effect, i.e. when certain frequencies are suppressed, the response at other frequencies is amplified. The 2-norm and the ∞-norm of $\mathbf{G}_c$ are compared to those of the plant in table 3.1, which illustrates the significantly smaller of the amplifying behavior of $\mathbf{G}_c$.

We have shown that by using systematic methods from control theory in combination with localized sensing/actuation, it is possible to reduce the growth of small-amplitude disturbances in the boundary layer. As demonstrated in the introduction of this chapter, using this approach, the energy of three-dimensional disturbances are damped by an order of magnitude. Further conclusions are provided in the final chapter of this thesis.

Algorithms for global modes

To accurately describe the flow dynamics in two- or three-dimensional domains, a large number of degrees of freedom is necessary, yielding a high-dimensional dynamical system (2.2). Table (4.1) shows the dimension of the state space $\mathbb{U}$ for the flow cases studies in this thesis. Dynamical-system analysis involving the computation of steady solutions, global eigenmodes and Koopman modes commonly involves solving nonlinear systems or eigenvalue problems of size n. In systems and control theory the most elegant results require the solution of various matrix equations, such as the Riccati or Lyapunov equations. All of these computations scale $O(n^3)$, which means that even with the use of super-computers it is prohibitively expensive to solve such problems for large systems. Therefore, numerical linear algebra and numerical algorithms to find approximate solutions have played a central role in computational fluid mechanics.

The main idea of the methods presented here is to identify a low dimensional subspace $\mathbb{U}_r \subset \mathbb{U}$ with $r \ll n$, on which the large systems can be projected along a certain direction. The problem at hand can then be solved by standard methods in this low-dimensional subspace. The subspace is spanned by r prudently chosen states $\mathbf{u}$

$$\mathbb{U}_r = \mathrm{span}\{\mathbf{u}_1, \dots, \mathbf{u}_r\}.$$

In the simplest case, these states are simply sampled along one or more state trajectories obtained by integrating the governing equations, whereas in other cases a recurrence relation provides the necessary states. In either case, all the methods require flow fields at discrete time and it is therefore convenient to present the algorithms using discrete-time systems. In this so called "time-stepper approach", matrices are never stored explicitly and storage demands in memory of all algorithms are of the same order as r times the storage of a single flow field.

Recall that the time-discrete dynamical system representing the discretized Navier–Stokes equations is given by

$$\mathbf{u}_{k+1} = \mathbf{g}(\mathbf{u}_k), \tag{4.1}$$

and let the linearized equations be given by

$$\mathbf{u}_{k+1} = \mathbf{A}_\mu \mathbf{u}_k \tag{4.2}$$

where

$$\mathbf{A}_\mu \mathbf{u}_k = \exp\left(\mathbf{A}\Delta t(k+1)\right) \mathbf{u}(k\Delta t).$$

	Dimension of Ω	Dimension of $\mathbb{U}$	Storage of $\mathbf{A}$
Ginzburg-Landau	1D	10^2	1 MB
Flat-plate boundary layer	2D	10^5	25 GB
Jet in crossflow	3D	10^7	500 TB

TABLE 4.1. Example of the state-space dimension for some of the flow configurations considered in this thesis.

4.1. Linear global eigenmodes

In section 2.2 we defined the linear global eigenmodes as the eigenvectors ϕ_j and eigenvalues λ_j of the discretized and linearized Navier–Stokes equations $\mathbf{A}$. Solving the enormous eigenvalue problem for the $n \times n$ matrix $\mathbf{A}$ using direct methods (such as the QR algorithm) is not only an unfeasible computational task when $n \geq 10^5$, but also very wasteful since we are interested in a small subset of the spectrum only: in order to determine the stability of the baseflow and to gain insight into the main instability mechanisms it is sufficient to compute a few, say $r \ll n$, of the least stable global modes. Fortunately, it turns out that we can compute r approximate global modes $\tilde{\lambda}_j, \tilde{\phi}_j$ from a small eigenvalue problem of size $r \times r$.

Note that the jth eigenvalue, $\lambda_j = \sigma_j + i\omega_j$, of the time-continuous matrix $\mathbf{A}$ is related to the jth eigenvalue, $\lambda_{\mu,j}$, of the time-discrete matrix $\mathbf{A}_\mu$ as follows:

$$\omega_j = \arg(\lambda_{\mu,j})/\Delta t, \qquad \sigma_j = \ln(|\lambda_{\mu,j}|)/\Delta t. \tag{4.3}$$

The eigenvectors of $\mathbf{A}$ and $\mathbf{A}_\mu$ are the same[1]. Henceforth, the subscript μ on $\mathbf{A}_\mu$ and λ_μ is omitted and we work entirely with discrete-time systems.

Denoting the residual (i.e. the error) introduced by the approximation with $\mathbf{r}_j$, we have

$$\mathbf{A}\tilde{\phi}_j = \tilde{\phi}_j \tilde{\lambda}_j + \mathbf{r}_j \qquad j = 1, \ldots, r. \tag{4.4}$$

One can show that by requiring the residual $\mathbf{r}_j$ to be orthogonal to a r-dimensional subspace $\mathbb{U}_r \subset \mathbb{U}$, we can choose $\tilde{\lambda}_j, \tilde{\phi}_j$ such the error is the smallest possible. Let r of linearly independent vectors given in the matrix,

$$\mathbf{X}_r = [\mathbf{u}_1 \ \mathbf{u}_2 \ \ldots \ \mathbf{u}_r] \in \mathbb{R}^{n \times r}, \tag{4.5}$$

span $\mathbb{U}_r$. We call $\tilde{\lambda}_j$ the *Ritz values* of $\mathbf{X}_r$ associated with the *Ritz vectors* $\tilde{\phi}_j$ if

$$\tilde{\phi}_j \in \mathrm{span}\{\mathbf{X}_r\}, \qquad \mathbf{r}_j \perp \mathrm{span}\{\mathbf{X}_r\}.$$

Since $\tilde{\phi}_j \in \mathrm{span}\{\mathbf{X}_r\}$, we can expand it in terms of the columns of $\mathbf{X}_r$,

$$\tilde{\mathbf{\Phi}} = [\tilde{\phi}_1 \ \tilde{\phi}_2 \ \ldots \tilde{\phi}_r] = \mathbf{X}_r \mathbf{T}, \tag{4.6}$$

---

[1]The eigenvectors are the same if the the sampling period Δt is chosen properly, i.e. so that it reflects the characteristic time scale of the physical structures in the flow. More specifically, to avoid aliasing Δt must be small enough such that two sampling points in one period of the highest frequency mode are obtained (the Nyquist criterion).

Algorithm 1 Arnoldi method

$[\Phi, \Lambda, r] = \text{Arnoldi}(\mathbf{u}_1)$

  Input: unit norm initial vector $\mathbf{u}_1$
  Output: r Ritz vectors Φ
                 r Ritz values Λ
                 residuals $\mathbf{r}$
  Requires: time stepper $\mathbf{A}_\mu$

  1: $\mathbf{X}(:,1) = \mathbf{u}_1$
  2: **for** $j = 1$ to r **do**
  3:    $\mathbf{v} = \mathbf{A}_\mu \mathbf{u}_j$
  4:    **for** $i = 1$ to j **do**
  5:      $\mathbf{M}(i,j) = \text{innerproduct}(\mathbf{A}\mathbf{u}_j, \mathbf{u}_i)$
  6:      $\mathbf{v} = \mathbf{v} - \mathbf{M}(i,j)\mathbf{u}_j$
  7:      $\mathbf{M}(j+1,j) = \text{norm}(\mathbf{v})$
  8:      $\mathbf{u}_{j+1} = \mathbf{v}/\mathbf{M}(j+1,j)$
  9:    **end for**
 10:   $\mathbf{X}(:,j+1) = \mathbf{u}_{j+1}$
 11: **end for**
 12: $[\mathbf{T}, \Lambda] = \text{eig}(\mathbf{M})$
 13: $\Phi = \mathbf{X}\mathbf{T}$
 14: $\mathbf{r} = \text{norm}(\mathbf{A}\Phi - \Phi\Lambda, 1)$

---

where the yet unknown matrix $\mathbf{T} = [T_1 \ \ldots \ T_r] \in \mathbb{R}^{r \times r}$ contains the expansion coefficients. Inserting this expansion into (4.4), multiplying from left with $\mathbf{X}_r^T$ and letting $\tilde{\Lambda} = \text{diag}\{\tilde{\lambda}_1, \tilde{\lambda}_2, \ldots \tilde{\lambda}_r\}$, we get

$$\underbrace{\mathbf{X}_r^T \mathbf{A} \mathbf{X}_r}_{\mathbf{C}_r} \mathbf{T} - \underbrace{\mathbf{X}_r^T \mathbf{X}_r}_{\mathbf{B}_r} \mathbf{T}\tilde{\Lambda} = 0, \tag{4.7}$$

since $\mathbf{X}_r^T \mathbf{r}_j = 0$ for all j. The expansion coefficients $\mathbf{T}$ are thus the eigenvectors and the Ritz values the eigenvalues of the small $r \times r$ matrix $\mathbf{B}_r^{-1}\mathbf{C}_r$,

$$(\mathbf{B}_r^{-1}\mathbf{C}_r)\mathbf{T} = \mathbf{T}\tilde{\Lambda}. \tag{4.8}$$

We have replaced the large eigenvalue problem (2.7) of size n with a smaller one (4.8) of size $r \ll n$. The question is, how fast the Ritz values and vectors converge to exact linear global eigenmodes and with what accuracy? The answer depends on the choice of vectors $\mathbf{u}_j$ in $\mathbf{X}_r$. Note that the matrix $\mathbf{C}_r$ can be interpreted as the orthogonal projection of $\mathbf{A}$ onto the space spanned by the columns of $\mathbf{X}_r$, where the projector is given by $\mathbf{P}_r = \mathbf{X}_r \mathbf{B}_r^{-1} \mathbf{X}_r^T$.

4.1.1. *Arnoldi algorithm*

The best – and computationally the most involved to determine – choice of basis for $\mathbb{U}_r$, resulting in a fast convergence with a satisfactory accuracy is an orthonormal basis. The Arnoldi method (Arnoldi 1951) is an algorithm that

simultaneously computes an orthonormal sequence $\mathbf{B}_r = \mathbf{X}_r^T \mathbf{X}_r = \mathbf{I}$ and an upper Hessenberg matrix $\mathbf{C}_r = \mathbf{X}_r^T \mathbf{A} \mathbf{X}_r$.

The method of Arnoldi computes the $j + 1$ basis vector in $\mathbf{X}_r$ by the recurrence

$$\mathbf{v} \quad = \mathbf{A}\mathbf{u}_j - (h_{1j}\mathbf{u}_1 + h_{2j}\mathbf{u}_2 + \cdots + h_{jj}\mathbf{u}_j) \qquad (4.9a)$$

$$\mathbf{u}_{j+1} \quad = \mathbf{v}/h_{j+1,j} \qquad (4.9b)$$

where $h_{ij} = \langle \mathbf{A}\mathbf{u}_j, \mathbf{u}_i \rangle$ and $h_{j+1,j} = \|\mathbf{v}\|$. This is simply the Gram-Schmidt method of orthogonalizing and normalizing a sequence. If we start with some unit-norm initial vector (usually noise) $\mathbf{u}_1$ and perform the above recurrence $r + 1$ times, we arrive at the following expression,

$$\mathbf{A}\mathbf{X}_r = \mathbf{X}_r\mathbf{M} + h_{r+1,r}\mathbf{u}_{r+1}\mathbf{e}_r^T,$$

where $\mathbf{e}_r^T = [0 \; 0 \; \ldots \; 0 \; 1] \in \mathbb{R}^{1 \times r}$ and $\mathbf{M}$ is a upper Hessenberg matrix

$$\mathbf{M} = \begin{bmatrix} h_{11} & h_{12} & \ldots & h_{1r} \\ h_{21} & h_{22} & \ldots & h_{2r} \\ 0 & h_{32} & \ldots & h_{3r} \\ \vdots & & & \vdots \\ 0 & 0 & \ldots & h_{rr} \end{bmatrix} \in \mathbb{R}^{r \times r}.$$

By construction of the Arnoldi algorithm we have $\mathbf{u}_{r+1} \perp \mathbf{X}_r$, therefore from (4.7) it is easy to see that $\mathbf{M} = \mathbf{B}_r^{-1}\mathbf{C}_r = \mathbf{C}_r$. The Ritz values of $\mathbf{A}$ in $\mathbb{U}_r$ are the eigenvalues $\tilde{\Lambda}$ of the upper Hessenberg matrix $\mathbf{M}$ and the Ritz vectors are given by $\tilde{\Phi} = \mathbf{X}_r\mathbf{T}$ where the columns of $\mathbf{T}$ are the eigenvectors of $\mathbf{M}$ (see algorithm 1).

The residual in equation (4.4) of the jth Ritz pair is thus given by

$$\mathbf{r}_j = (\mathbf{A} - \tilde{\lambda}_j\mathbf{I})\tilde{\phi}_j = h_{r+1,r}T_j(r)\mathbf{u}_{r+1},$$

where $T_j(r)$ is the last component of the jth eigenvector of $\mathbf{M}$. One can stop the algorithm when the desired accuracy – usually $\|\mathbf{r}_j\| \leq 10^{-10}$ – is attained for the Ritz vectors of interest. To avoid a very large r and still obtain low residuals, one can repeat the Arnoldi algorithm with the initial vector $\mathbf{u}_1$ replaced by a Ritz vector or a combination of Ritz vectors (Saad 1980). In the Arnoldi-software package ARPACK (Lehoucq *et al.* 1998) a more efficient method based on polynomial filtering (Sorensen 1992) is applied to obtain an improved initial guess. Moreover, the standard Gram-Schmid (4.9) gives rise to severe cancellation errors, so in practice more advanced techniques such as the modified Gram-Schmid method (Trefethen & Bau 1997) are used.

4.1.2. *Dynamic Mode Decomposition*

The simplest – and most ill-conditioned – choice of basis for $\mathbb{U}_r$ (see Ruhe 1984; Saad 1980) is simply samples (or snapshots) obtained from the timestepper

$$\mathbf{u}_{j+1} = \mathbf{A}\mathbf{u}_j.$$

Algorithm 2 Dynamic Mode Decomposition

$[\Phi, \Lambda, r] = \text{DMD}(\mathbf{X})$

  Input: $r + 1$ sequence of observables $\mathbf{X} = (\mathbf{u}_1, \ldots, \mathbf{u}_{r+1})$
  Output: r empirical Ritz vectors Φ
                r empirical Ritz values Λ
                scalar residual r

  1: $n = \text{size}(X, 1)$
  2: $r = \text{size}(X, 2) - 1$
  3: $\mathbf{u}_{r+1} = \mathbf{X}(:, r+1)$
  4: $\mathbf{X}_r = \mathbf{X}(:, 1 : r)$
  5: $\mathbf{X}_{r+1} = \mathbf{X}(:, 2 : r+1)$
  6: $\mathbf{c} = \mathbf{X}_r \backslash \mathbf{u}_{r+1}$
  7: $\mathbf{M} = \text{companion}(\mathbf{c})$
  8: $[\mathbf{T}, \Lambda] = \text{eig}(\mathbf{M})$
  9: $\Phi = \mathbf{X}_r \mathbf{T}$
10: $r = \text{norm}(\mathbf{X}_{r+1} - \mathbf{X}_r \mathbf{C})$

The basis $\mathbf{X}_r = [\mathbf{u}_1 \ \mathbf{A}\mathbf{u}_1 \ \mathbf{A}\mathbf{u}_2 \ \ldots \ \mathbf{A}\mathbf{u}_{r-1}]$ becomes gradually ill-conditioned, since its columns gradually align with the dominant eigenvectors of $\mathbf{A}$. For some r, the vector at step $r + 1$ becomes nearly linearly dependent of the previous r vectors, i.e.

$$\mathbf{u}_{r+1} = c_1 \mathbf{u}_1 + c_2 \mathbf{u}_2 + \cdots + c_r \mathbf{u}_r + \tilde{\mathbf{u}}_{r+1}, \tag{4.10}$$

where $\tilde{\mathbf{u}}_{r+1}$ is the residual, i.e. the part of $\mathbf{u}_{r+1}$ that is not in the span of $\mathbf{X}_r$. We can write (4.10) in matrix form,

$$\mathbf{A}\mathbf{X}_r = \mathbf{X}_r \mathbf{M} + \tilde{\mathbf{u}}_{r+1} \mathbf{e}_r^T, \tag{4.11}$$

where $\mathbf{e}_r^T = [0 \ 0 \ \ldots \ 0 \ 1] \in \mathbb{R}^{1 \times r}$ and

$$\mathbf{M} = \begin{bmatrix} 0 & 0 & \ldots & 0 & c_1 \\ 1 & 0 & \ldots & 0 & c_2 \\ 0 & 1 & \ldots & 0 & c_3 \\ \vdots & & \ddots & & \vdots \\ 0 & 0 & \ldots & 1 & c_r \end{bmatrix} \in \mathbb{R}^{r \times r} \tag{4.12}$$

is a matrix in companion form. It remains to determine the scalar elements c_j of $\mathbf{M}$. If we choose them such that $\tilde{\mathbf{u}}_{r+1} \perp \mathbf{X}_r$ then from (4.7) it is easy to see that $\mathbf{M} = \mathbf{B}_r^{-1} \mathbf{C}_r$: the Ritz values of $\mathbf{A}$ in $\mathbb{U}_r$ and the Ritz vectors $\tilde{\boldsymbol{\Phi}} = \mathbf{X}_r \mathbf{T}$ are thus attained by diagonalizing the companion matrix $\mathbf{M}$, instead of the upper Hessenberg matrix obtained via the Arnoldi method.

A few remarks are appropriate at this point. There is no normalization step in the algorithm, and hence the modes come with amplitudes, $a_i = |\tilde{\phi}_i|$ that provide a way to rank their contribution to the overall energy in the set $\mathbf{X}_r$. The normalized amplitude a_i / a_1 for mode $\tilde{\phi}_i$ serves as a condition number

for that mode. If $a_i/a_1 \leq \tau$ where τ is some tolerance (usually $\tau = 10^{-15}$), then the corresponding mode is discarded. See the example in section 4.1.3.

The companion matrix may be a highly nonnormal matrix, which results in an ill-conditioned eigenvalue decomposition problem. One can improve the accuracy in several steps as it is done by default in the eigenvalue routines of Lapack (DxGEEV) and Matlab (EIG); first, *balancing* (Parlett & Reinsch 1969) of the matrix by a similarity transformation is performed, followed by a reduction to upper Hessenberg form via a second similarity transformation and finally the eigenvalues are computed using the QR algorithm. Alternatively, as a preconditioning, one can perform a similarity transformation (via a singular value decomposition) of the companion matrix to obtain a full matrix $\tilde{\mathbf{M}}$ (Schmid 2009).

The norm of the residual in equation (4.4) of the jth Ritz pair is given by

$$\mathbf{r}_j = (\mathbf{A} - \tilde{\lambda}_j \mathbf{I})\tilde{\boldsymbol{\phi}}_j = \tilde{\mathbf{u}}_{j+1} T_j(r) \tag{4.13}$$

For a given dimension of $\mathbb{U}_r$, the residuals from this algorithm are significantly higher than the Arnoldi method. The advantage of this algorithm is that it provides Ritz vectors and values of any sequence of data. In contrast to the Arnoldi method, it does not perform $\mathbf{A}\mathbf{u}_j$ at each step and is unaware of $\mathbf{A}$ altogether. As observed by Schmid (2009), the present algorithm which we call *Dynamic mode decomposition* algorithm can thus also be used to extract Ritz vectors and values from experimental data or even from a sequence of snapshots collected from nonlinear simulations. In the next section we show that in the nonlinear case the Ritz vectors approximate the Koopman modes. However, first we compare the DMD and the Arnoldi method for a linear flow.

4.1.3. *Example: Linearized Blasius boundary layer*

The Arnoldi and the DMD algorithm are applied to the Navier–Stokes equations linearized about a steady Blasius boundary layer solution to demonstrate the convergence behavior of the two methods. The resulting matrix $\mathbf{A}$ ($n \approx 10^5$) is stable, i.e. the flow is globally stable but it is locally unstable to two-dimensional Tollmien–Schlichting wavepackets (see e.g. Bagheri *et al.* 2009*a*). Figure 4.1 shows the frequency ω_j and growth rates σ_j associated with the linear global eigenmode $\boldsymbol{\phi}_j$ computed with both the Arnoldi method (red symbols) and the DMD algorithm (black and gray symbols). It is interesting to note that, although the DMD algorithm is numerically less stable than the Arnoldi algorithm, the TS-wave branch in the spectrum matches the Ritz values obtained from the Arnoldi algorithm.

The residuals $\|\mathbf{r}_j\|$ of the Ritz vectors computed using the Arnoldi method are of order 10^{-15}. For the DMD algorithm, the average residual of the Ritz vectors are shown in figure 4.2(*a*) as a function of the number of snapshots included in the matrix $\mathbf{X}_r$. Initially, there is a rapid decay with increasing snapshots, but the average residual levels out at a rather large value. As discussed previously, this is due to the fact that the columns of $\mathbf{X}_r$ become increasingly
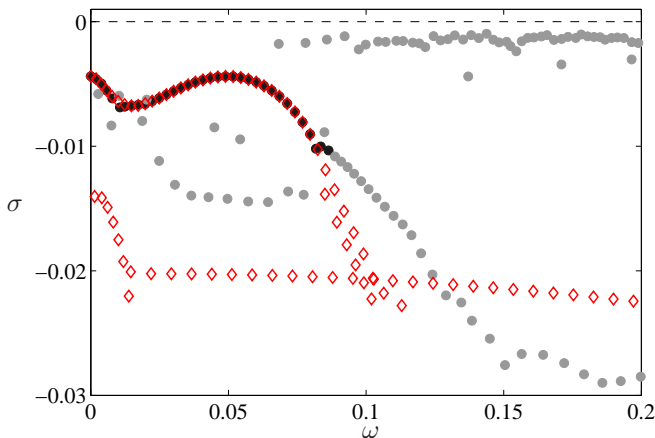
FIGURE 4.1. The two-dimensional global linear spectrum of the flat-plate boundary layer. Ritz values computed using the Arnoldi method (red symbol) and the DMD algorithm (black and gray symbols). DMD Ritz values that correspond to Ritz vectors with smaller magnitude than 10^{-15} are shown in gray. The numerical parameters are given in table 4.2 (case 2D-LIN-BL) in section 4.4 of this thesis.

linearly dependent as they align with the most dominant Ritz vectors. The magnitudes a_j of the Ritz vectors from the DMD method are shown in figure 4.2(b), where – in contrast to the residuals – a decay of several orders of magnitude is observed for first few Ritz vectors. The Ritz values obtained from the DMD algorithm that correspond to Ritz vectors with magnitudes smaller than 10^{-15} are shown in gray symbols in the spectrum (figure 4.1). Thus it seems that the magnitudes (or condition numbers) of the Ritz vectors provide a way to rank the modes according to their significance; modes with very small magnitudes can be regarded as numerical noise and thus discarded.

4.2. Koopman modes

The DMD algorithm described in the previous section yields Ritz vectors and values of a sequence of data without the knowledge of the system that generated the data sequence. It turns out, as first noticed by Rowley *et al.* (2009), that if the nonlinear system $\mathbf{g}(\mathbf{u}_k)$ generated the sequence of data, then the Ritz vectors are approximations of Koopman modes under the map $\mathbf{g}$.

Let r vectors form the columns of the full-rank matrix,

$$\mathbf{X}_r = [\mathbf{a}(\mathbf{u}_0)\ \mathbf{a}(\mathbf{u}_1)\ \mathbf{a}(\mathbf{u}_2)\ \ldots\ \mathbf{a}(\mathbf{u}_{r-1})] \tag{4.14}$$

where $\mathbf{a}(\mathbf{u}_j)$ could be full flow field snapshots $\mathbf{u}_j \in \mathbb{U} \subset \mathbb{R}^n$ obtained from numerical simulations or vector-valued observables $\mathbf{a}(\mathbf{u}_j) \in \mathbb{R}^p$ from experimental

(a)

(b)
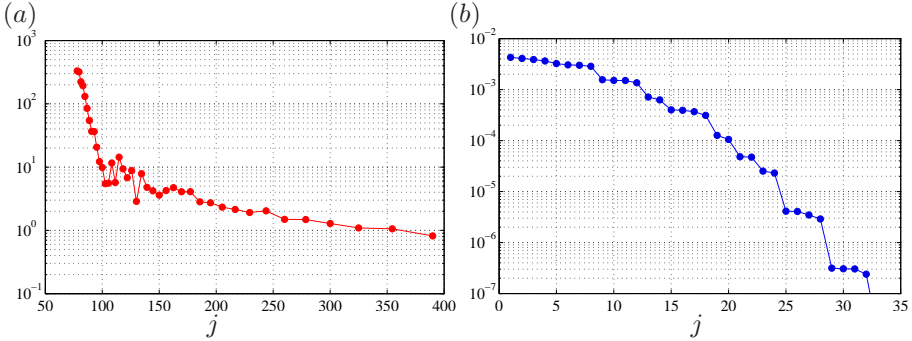
FIGURE 4.2. The average residuals, given by equation (4.13) as function of the number of snapshots included in $\mathbf{X}_r$ are shown in (a). The magnitude a_j of the 32 first Ritz values computed for $r = 390$ is shown in (b).

measurements. By shifting the sequence with one time step, we obtain

$$\mathbf{X}_{r+1} = [\mathbf{a}(\mathbf{u}_1)\ \mathbf{a}(\mathbf{u}_2)\ \mathbf{a}(\mathbf{u}_3)\ \ldots\ \mathbf{a}(\mathbf{u}_r)].$$

For a sufficiently long time series, we can assume that the rth sample $\mathbf{a}(\mathbf{u}_r)$ is nearly linearly dependent on the previous $r - 1$ observables. Denoting the residual by $\tilde{\mathbf{u}}_r$, we have the following relation between the two sequences

$$\mathbf{X}_{r+1} = \mathbf{X}_r\mathbf{M} + \tilde{\mathbf{u}}_r\mathbf{e}_r^T, \qquad (4.15)$$

where $\mathbf{M}$ is a companion matrix. If $\mathbf{X}_r$ is a sequence from a linear mapping $\mathbf{A}$, then $\mathbf{X}_{r+1} = \mathbf{A}\mathbf{X}_r$ and we recover the DMD algorithm for computing Ritz values and vectors for linear systems. If, on the other hand, (4.14) is sequence of the observable $\mathbf{a}$ on the trajectory of the system $\mathbf{g}$ starting at the initial condition $\mathbf{u}_0$, then $\mathbf{X}_{r+1}$ is given by applying the Koopman operator U on each element of this sequence

$$\mathbf{X}_{r+1} = [U\mathbf{a}(\mathbf{u}_0)\ U\mathbf{a}(\mathbf{u}_1)\ U\mathbf{a}(\mathbf{u}_2)\ \ldots\ U\mathbf{a}(\mathbf{u}_{r-1})] = U\mathbf{X}_r.$$

The companion matrix for $\mathbf{X}_r$ is uniquely determined by the direction of the residual $\tilde{\mathbf{u}}_r$. Similar to the previous section, we choose the elements of $\mathbf{M}$ such that $\tilde{\mathbf{u}}_r \perp \mathbf{X}_r$. Now, we can define the *empirical Ritz values* of $\mathbf{X}_r$ as the eigenvalues $\tilde{\Lambda} = \mathrm{diag}\{\tilde{\lambda}_0\ \tilde{\lambda}_1\ \ldots\ \tilde{\lambda}_{r-1}\}$ of $\mathbf{M}$ associated with the *empirical Ritz vectors* $\tilde{\mathbf{\Phi}} = [\tilde{\phi}_0\ \tilde{\phi}_1\ \ldots\ \tilde{\phi}_{r-1}]$ given by

$$\tilde{\mathbf{\Phi}} = \mathbf{X}_r\mathbf{T} \qquad (4.16)$$

where the columns of $\mathbf{T}$ are the eigenvectors of $\mathbf{M}$. If the Ritz values are distinct, the matrix containing the left eigenvectors of the companion matrix

is the Vandermonde matrix

$$\mathbf{T}^{-1} = \begin{bmatrix} 1 & \lambda_0 & \lambda_0^2 & \dots & \lambda_0^{r-1} \\ 1 & \lambda_1 & \lambda_1^2 & \dots & \lambda_1^{r-1} \\ \vdots & \vdots & & \ddots & \vdots \\ 1 & \lambda_{r-1} & \lambda_{r-1}^2 & \dots & \lambda_{r-1}^{r-1} \end{bmatrix} \in \mathbb{R}^{r \times r}. \qquad (4.17)$$

Recall that in section 2.3 the Vandermonde matrix $\mathbf{S}$ given in (2.14) was identified as the expansion coefficients when expanding the sequence of observables (2.13) in terms of the Koopman modes $\mathbf{\Phi}$, i.e. $\mathbf{X} = \mathbf{\Phi S}$. Similarly, we can observe that $\mathbf{T}^{-1}$ contains the expansion coefficients when expanding the finite sequence $\mathbf{X}_r$ in terms of the empirical Ritz vectors, $\mathbf{X}_r = \tilde{\mathbf{\Phi}}\mathbf{T}^{-1}$; each element in $\mathbf{X}_r$ can be written as

$$\mathbf{a}(\mathbf{u}_k) = \sum_{j=0}^{r-1} \tilde{\lambda}_j^k \tilde{\phi}_j \qquad k = 0, \dots, r-1. \qquad (4.18)$$

The empirical Ritz vector $\tilde{\phi}_j$ thus approximates the product of the Koopman mode and the Koopman eigenfunction, $\varphi_j(\mathbf{u}_0)\phi_j$, and the Ritz value $\tilde{\lambda}_j$ approximates the Koopman eigenvalue λ_j. Algorithm 2 applied to a set of data $\mathbf{X}_r$ obtained from nonlinear flow provides the approximate Koopman modes and eigenvalues.

4.2.1. *Example: Periodically forced nonlinear Blasius boundary layer*

When the sequence (4.14) is periodic, i.e. $\mathbf{u}_{r-1} = \mathbf{u}_0$, the companion matrix becomes

$$\mathbf{M} = \begin{bmatrix} 0 & 0 & \dots & 0 & 1 \\ 1 & 0 & \dots & 0 & 0 \\ 0 & 1 & \dots & 0 & 0 \\ \vdots & & \ddots & & \vdots \\ 0 & 0 & \dots & 1 & 0 \end{bmatrix} \in \mathbb{R}^{r \times r}$$

with the empirical Ritz values given by $\lambda_k = e^{i\omega_k}$, with $\omega_k = 2\pi k/r$. In this case the Vandermonde matrix $\mathbf{T}^{-1}$ is the discrete Fourier transform matrix. This means for periodic data the Ritz vectors are Fourier modes, given by the discrete Fourier transform of the sequence.

Consider again the flow on a flat plate, where forcing is continuously applied upstream in the boundary layer with a given temporal frequency $\omega_f = 0.036$ (non-dimensional frequency $F = 120$). The amplitude of the forcing is sufficiently high to introduce a few higher harmonics. A snapshot at $t = 85$ of the streamwise velocity component from the simulation is shown in figure 4.3(a), where we observe how the boundary layer is altered due to the periodic forcing. The snapshots ($r = 100$) separated by $\Delta t = 10$ from the simulation are stacked up in the matrix $\mathbf{X}_r$ and its empirical Ritz values and vectors were computed using the DMD algorithm.
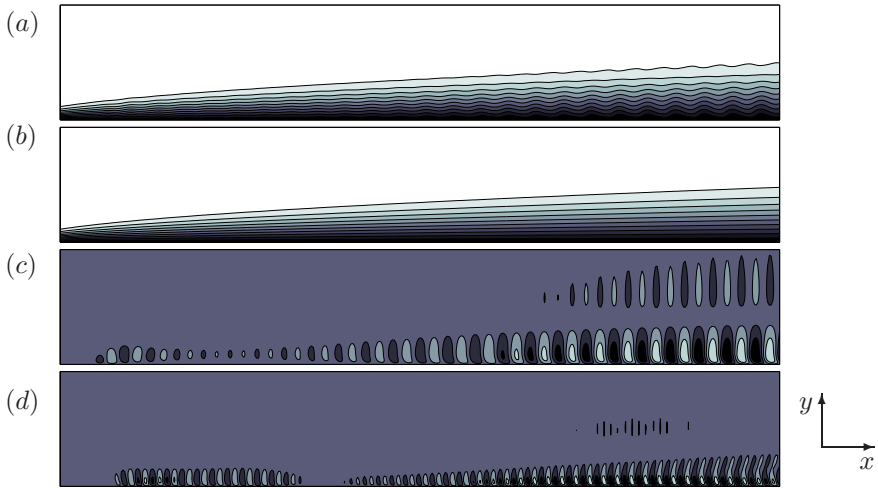
FIGURE 4.3. The streamwise velocity component of a snapshot from the nonlinear simulation at $t = 85$ (a), the zeroth (b), first (c) and third (d) Koopman modes computed using the algorithm explained in section 4.2.

The Koopman modes ϕ_0, ϕ_1 and ϕ_3 are shown in figure 4.3$(b\text{-}d)$. The zeroth Koopman mode corresponds to the mean flow, which in this case is close to the steady Blasius boundary-layer flow. The first Koopman mode corresponds to a TS wave, where the corresponding Koopman eigenvalue λ_j has zero growth rate and a frequency that matches the forcing frequency ω_f precisely. The TS wave (figure 4.3c) decays in amplitude short distance downstream of the forcing location, but begins to grow exponentially at particular streamwise location (branch I) until a location further downstream (branch II). The location of branch I and II for this particular frequency matches the TS neutral curve found in the literature (see e.g. Schmid & Henningson 2001). As we expect from the theory in section 2.3, the first pair of Koopman modes correspond to the flow structure oscillating with the dominant frequency. The second pair of Koopman modes (one mode shown in figure 4.3d) correspond to the subharmonic $2\omega_f$ frequency generated due to nonlinear interactions. This mode is also a TS wave but with a higher frequency. This simple example demonstrates how the DMD algorithm in section 4.2 can be used to decompose a sequence of flow fields into spatial structures with periodic motion.

4.3. Balanced modes

We turn our attention to the linear input-output system (3.1) introduced in chapter 3. In the following, it is convenient to represent the time-continuous system matrix as $\mathbf{A}$ and the discrete-time (i.e. time stepper) matrix as $\mathbf{A}_\mu$ (so far in this chapter the subscript μ has been omitted).

4.3.1. *Laub's method*

In section 3.3.2 it was shown that the balanced modes are the eigenvectors of the product of the controllability Gramian $\mathbf{P}$ (3.15) and observability Gramian $\mathbf{Q}$ (3.16). It can be shown (Green & Limebeer 1995) that $\mathbf{P}$ and $\mathbf{Q}$ associated with the linear system (3.1) satisfy, respectively, the following *Lyapunov equations*

$$\mathbf{AP} + \mathbf{PA}^T + \mathbf{BB}^T = 0$$
$$\mathbf{A}^T\mathbf{Q} + \mathbf{QA} + \mathbf{C}^T\mathbf{C} = 0.$$

For low and moderate dimensional systems $n \le 10^3$, there are efficient direct or iterative methods for solving the Lyapunov equations (Smith 1968; Hammarling 1982) and for computing balanced modes (Laub *et al.* 1987; Safonov & Chiang 1989).

One common way (Laub *et al.* 1987) of computing the balanced modes is as follows. Solve the two Lyapunov equations and compute their Cholesky factors $\mathbf{X} \in \mathbb{R}^{n \times n}$, $\mathbf{Y} \in \mathbb{R}^{n \times n}$ as

$$\mathbf{P} = \mathbf{XX}^T, \qquad \mathbf{Q} = \mathbf{YY}^T$$

and compute the SVD of the $n \times n$ matrix

$$\mathbf{Y}^T\mathbf{X} = \mathbf{U\Sigma V}^T. \tag{4.20}$$

The direct and adjoint balanced modes are then, respectively, given by

$$\mathbf{\Phi} = \mathbf{XV\Sigma}^{-1/2}, \qquad \mathbf{\Psi} = \mathbf{YU\Sigma}^{-1/2} \tag{4.21}$$

such that $\mathbf{\Psi}^T\mathbf{\Phi} = \mathbf{I}$. Note that $\mathbf{X}$ and $\mathbf{Y}$ are the numerical counterparts of the controllability operator $\mathbf{L}_c$ and the observability operator $\mathbf{L}_o$ defined in section 3.3.1. Similarly $\mathbf{Y}^T\mathbf{X}$ is the Hankel matrix, representing the Hankel operator $\mathbf{\Gamma_G}$ and the diagonal matrix $\mathbf{\Sigma}$ contains the Hankel singular values. Unfortunately, the above method is unfeasible for high-dimensional systems as the computational complexity is $O(n^3)$ and storage requirement is $O(n^2)$.

4.3.2. *Low-rank Cholesky factors*

Usually the number of inputs and outputs is much smaller than the state dimension, $m, p \ll n$. Therefore, the Gramians often have very low numerical rank $k \ll n$ and the storage requirements can be reduced to $\mathcal{O}(nk)$ and computational complexity to $\mathcal{O}(k^3)$. Moreover, if the purpose is model reduction, it seems imprudent to solve for all n balanced modes, to construct a reduced-order model of size $r \ll n$.

Consider the low-rank Cholesky factors $\mathbf{X}_r \in \mathbb{R}^{n \times r}$ and $\mathbf{Y}_r \in \mathbb{R}^{n \times r}$,

$$\mathbf{P} = \mathbf{X}_r\mathbf{X}_r^T + \mathbf{R}_P \quad \mathbf{Q} = \mathbf{Y}_r\mathbf{Y}_r^T + \mathbf{R}_Q \tag{4.22}$$

where $\mathbf{R}_P$ and $\mathbf{R}_Q$ are residuals due to replacing the full Cholesky factors with partial ones. The SVD given in (4.20) can now be computed for the small $r \times r$ matrix $\mathbf{Y}_r^T\mathbf{X}_r = \mathbf{U}_r\mathbf{\Sigma}_r\mathbf{V}_r^T$ and subsequently r approximate balanced modes can be obtained from,

$$\mathbf{\Phi}_r = \mathbf{X}_r\mathbf{V}_r\mathbf{\Sigma}_r^{-1/2}, \qquad \mathbf{\Psi}_r = \mathbf{Y}_r\mathbf{U}_r\mathbf{\Sigma}_r^{-1/2}. \tag{4.23}$$

The question is, how close $\boldsymbol{\Phi}_r$ and $\boldsymbol{\Psi}_r$ using low-rank Cholesky factors are to the "true" balanced modes $\boldsymbol{\Phi}$ and $\boldsymbol{\Psi}$ using full-rank factors. Are the two important properties (stability and tight error bounds) of the balanced reduced-model preserved when computed by $\boldsymbol{\Phi}_r$ and $\boldsymbol{\Psi}_r$? Antoulas (2005) derives non-trivial estimates of the residuals given in (4.22). In general, numerical tests (Ilak & Rowley 2008; Ahuja 2009; Bagheri *et al.* 2009*a*,*b*) show that $\boldsymbol{\Phi}_r$ is a good approximation and that $\boldsymbol{\Sigma}_r$ are close to the true HSV. This can be attributed, as mentioned earlier, to the low numerical rank of the Gramians, when $m, p \ll n$. Unfortunately, stability of the reduced-model is no longer guaranteed when using $\mathbf{X}_r$. Note that $\mathbf{A}_r$ is stable if $\mathbf{A}_r^T \mathbf{M} + \mathbf{M}\mathbf{A}_r + \mathbf{N} = 0$ has a solution for any $\mathbf{N} = \mathbf{N}^T > 0$ and $\mathbf{M} = \mathbf{M}^T > 0$. One can derive (see e.g. Antoulas 2005),

$$\mathbf{A}_r \boldsymbol{\Sigma}_r + \boldsymbol{\Sigma}_r \mathbf{A}_r^T + \mathbf{B}_r \mathbf{B}_r^T + \boldsymbol{\Psi}_r^T (\mathbf{A}\mathbf{R}_P + \mathbf{R}_P \mathbf{A}^T)\boldsymbol{\Psi}_r = 0$$

where the additional term due to the residuals in not necessarily positive definite.

We have thus dealt with the high-dimensionality problem if we can find low-rank Cholesky factors. The reduced-order model $\mathbf{G}_r$ can be computed for very large system using algorithm 3. Various methods may be used to find $\mathbf{X}_r$ and $\mathbf{Y}_r$: ADI/Smith methods (Penzl 2000; Gugercin *et al.* 2003), snapshot-based methods (Lall *et al.* 2002; Rowley 2005) and Krylov subspace methods (Jaimoukha & Kasenally 1994). As was observed by Sorensen & Rowley (private communication), there exists a close connection between Smith-type of methods and snapshot-based methods. The former is an iterative process aiming directly at solving the Lyapunov equation and requiring the knowledge of $\mathbf{A}$. The snapshot-based method on the other hand computes low-rank Cholesky factors directly from the definition of the Gramians, where the integrals are approximated by numerical simulations of the linear system.

4.3.3. *Snapshot-based method*

We describe the snapshot-based method (Rowley 2005) for computing the low-rank Cholesky factor $\mathbf{X}_r$ of the controllability Gramian $\mathbf{P}$. To obtain the factor $\mathbf{Y}_r$ of the observability Gramian $\mathbf{Q}$, the method is applied to the dual input-output system, defined by

$$\mathbf{G}^* = \left(\begin{array}{c|c} \mathbf{A}^T & \mathbf{C}^T \\ \hline \mathbf{B}^T & 0 \end{array} \right).$$

Comparing the above dual equations with (3.4) we observe that the output and input matrices have exchanged place; the state is now forced with the adjoint of $\mathbf{C}$ and the output is given by the adjoint of $\mathbf{B}$. Note that $\mathbf{A}^T$ represents the discretized adjoint Navier–Stokes equations (see Bagheri *et al.* 2009*b*, for a thorough derivation of the dual system). This is a dual problem to $\mathbf{G}$ (3.4), in the sense that the controllability Gramian of $\mathbf{G}^*$ is equal to the observability Gramian of $\mathbf{G}$.

Algorithm 3 Balanced reduced model

$[\mathbf{G}_r, e_l, e_u] = \text{balmodes}(\mathbf{X}_r, \mathbf{Y}_r)$

  Input: low-rank Cholesky factor of $\mathbf{P}$ $\mathbf{X}_r$

                low-rank Cholesky factor of $\mathbf{Q}$ $\mathbf{Y}_r$

  Output: linear reduced-order model $\mathbf{G}_r = (\mathbf{A}_r, \mathbf{B}_r, \mathbf{C}_r)$

                lower theoretical error bound e_l

                upper theoretical error bound e_u

1: $[\mathbf{U}, \boldsymbol{\Sigma}, \mathbf{V}] = \text{SVD}(\mathbf{Y}_r^T \mathbf{X}_r)$
2: $\boldsymbol{\Phi} = \mathbf{X}_r \mathbf{V} \boldsymbol{\Sigma}^{-1/2}$
3: $\boldsymbol{\Psi} = \mathbf{Y}_r \mathbf{U} \boldsymbol{\Sigma}^{-1/2}$
4: $\mathbf{A}_r = \boldsymbol{\Psi}^T \mathbf{A} \boldsymbol{\Phi}$
5: $\mathbf{B}_r = \boldsymbol{\Psi}^T \mathbf{B}$
6: $\mathbf{C}_r = \mathbf{C} \boldsymbol{\Phi}$
7: $e_l = \boldsymbol{\Sigma}(r+1, r+1)$
8: $e_u = 2\left(\text{sum}(\boldsymbol{\Sigma}(r+1\text{:end}, r+1\text{:end}))\right)$

Suppose that we have p constant input vectors, $\mathbf{B} = [\mathbf{B}_1 \ \ldots \ \mathbf{B}_p] \in \mathbb{R}^{n \times p}$ associated with the input signals $\mathbf{w}(t) = [w_1(t) \ \ldots \ w_p(t)] \in \mathbb{R}^{p \times 1}$. When $w_j = \delta(t)$ and $\mathbf{u}_0 = 0$, the state at any time is given by,

$$\mathbf{u}_j(t) = e^{\mathbf{A}t} \mathbf{B}_j.$$

The controllability Gramian can thus be written as a sum of impulse responses to p inputs,

$$\mathbf{P} = \int_0^\infty e^{\mathbf{A}t} \mathbf{B} \mathbf{B}^T e^{\mathbf{A}^T t} \, dt = \int_0^\infty \sum_{j=1}^p \mathbf{u}_j(t) \mathbf{u}_j(t)^T \, dt.$$

Define the *empirical controllability Gramian* as the quadrature approximation of $\mathbf{P}$,

$$\tilde{\mathbf{P}}_r = \sum_{j=1}^r \sum_{i=1}^p \mathbf{u}_i(t_j)(\mathbf{u}_i(t_j))^T \delta_j = \mathbf{X}_r \mathbf{X}_r^T,$$

where the Cholesky factor $\mathbf{X}_r \in \mathbb{R}^{n \times pr}$ is given by

$$\mathbf{X}_r = [\mathbf{u}_1(t_1)\sqrt{\delta_1} \ \ldots \ \mathbf{u}_1(t_r)\sqrt{\delta_r} \ \ldots \ \mathbf{u}_p(t_1)\sqrt{\delta_1} \ \ldots \ \mathbf{u}_p(t_m)\sqrt{\delta_r}] \qquad (4.24)$$

and δ_j are the quadrature coefficients (for example resulting from a trapezoidal rule). To compute $\mathbf{X}_r$, one needs to perform p numerical simulations of the linear system. For each simulation r snapshots are collected, which results in memory requirements of the order $O(npr)$ to store the Cholesky factor.

To obtain the factor $\mathbf{Y}_r$ of the observability Gramian $\mathbf{Q}$, the above method is applied to the dual input-output system. Suppose

$$\mathbf{z}_j(t) = e^{\mathbf{A}^T t} \mathbf{C}_j^T \qquad j = 1, \ldots, m$$

is the impulse response of the adjoint system to output vector $\mathbf{C}_j^T$. Then the *empirical observability Gramian* is

$$\tilde{\mathbf{Q}}_r = \sum_{j=1}^{r} \sum_{i=1}^{m} \mathbf{z}_i(t_j)(\mathbf{z}_i(t_j))^T \delta_j = \mathbf{Y}_r \mathbf{Y}_r^T.$$

Similarly, $\mathbf{Y}_r \in \mathbb{R}^{n \times mr}$ is obtained by m numerical simulations of the adjoint system,

$$\mathbf{Y}_r = [\mathbf{z}_1(t_1)\sqrt{\delta_1} \ \ldots \ \mathbf{z}_1(t_m)\sqrt{\delta_m} \ \ldots \ \mathbf{z}_m(t_1)\sqrt{\delta_1} \ \ldots \ \mathbf{z}_m(t_r)\sqrt{\delta_r}]. \quad (4.25)$$

The snapshot method to compute Cholesky factors thus amounts to collecting snapshots from p simulations of the forward linear system and m simulation of the adjoint system. In this way, we trade the storage of very large matrices for numerical simulations.

A few remarks on the method are noteworthy. As shown by Ma *et al.* (2009) a theoretical equivalence between snapshot-based balanced truncation and a system identification technique called eigensystem realization algorithm (ERA) (Juang & Pappa 1985) exists. Unlike the snapshot-based method, ERA does not require the dual system (adjoint simulations) and the oblique projection onto a set of balanced modes is not performed. The method is significantly cheaper than the snapshot method; the main disadvantage is that it does not provide a set of global balanced modes, which can be useful for physical insight into the input-output properties of the linear system.

For more complex three-dimensional configurations, the number of inputs and output may become of the order $p, m \in O(10^2)$ and a large number of snapshots $r \in O(10^3)$ must be collected if there are slowly decaying modes that pulsate with different frequencies. As a consequence the storage requirement for each Cholesky factor is demanding and the SVD to compute the approximate balanced modes might become computationally intractable. Moreover, many inputs and outputs may have the same spatial structure and are located close to each other. This is the situation for actuators and sensors in the three-dimensional set-up sketched in figure 3.1. In such cases, the states triggered by the impulse response of each input/output do not differ significantly from each other. As a consequence the factors $\mathbf{X}_r, \mathbf{Y}_r$ become gradually ill-conditioned for increasing number of snapshots, since the columns are nearly linearly dependent. There is remedy for very large and ill-conditioned Cholesky factors as first addressed by Gugercin *et al.* (2003) for the so called modified Smith's method. However, the "modified" method also applies to the method of snapshot for computing low-rank Cholesky factors.

4.4. Time stepping

The methods presented to compute global modes are all "matrix-free" and based on flow field snapshots. These snapshots are obtained by abstract notion of a time stepper $\mathbf{g}$,

$$\mathbf{u}_{k+1} = \mathbf{g}(\mathbf{u}_k). \quad (4.26)$$

In practice, the implementation of a validated, three-dimensional and efficient time-stepper to solve the time-dependent nonlinear Navier–Stokes equations is a formidable task to undertake. The Navier–Stokes equations given by (2.1) can be solved by splitting the task into a number of subproblems. Examples of subproblems are a scheme for time advancement, method for spatial discretization and how to address the pressure term in the Navier–Stokes equations (since an evolution equation for the pressure is missing in explicit form, the equations are not fully parabolic in time). Moreover, the choice of numerical method for each subproblem depends on the complexity of the geometry, numerical accuracy, efficiency, ability to parallelize etc. For example, even small modifications of a highly efficient parallelized Fortran implementation, where the different subproblems are tightly coupled might turn out to be very time consuming and prone to errors. In other cases, flexible codes for example implemented using object-oriented design, makes the switch between different equations (linear, nonlinear, adjoint) simple and advanced algorithms (for computing global modes, steady solutions) can easily be "wrapped" around the code.

4.4.1. *Overview of Simson code*

Essentially, all the results presented in this thesis are based on an existing simulation code called Simson. The main structure of the code and the simulation parameters are given in the following. For details, the reader is referred to the comprehensive user guide (Chevalier *et al.* 2007).

The approach adopted in the Simson code, is based on pressure-free formulation of the Navier–Stokes equation (2.1). By applying the Laplace and curl operators to the momentum equations given by equation (2.1*a*), the Navier–Stokes equations in primitive variables $\mathbf{u} = (u, v, w)$ can be replaced with a nonlinear advection-diffusion equation, describing quantities related to the wall-normal component of the velocity and vorticity.

The Simson code implements a spectral algorithm, where the solution is approximated by an expansion in Fourier functions in the wall-parallel directions (x, z) and Chebyshev polynomials in the wall-normal direction (y). In the so called pseudo-spectral approach, the nonlinear advection term is computed by forming products in physical space, whereas the linear diffusion term is computed in Fourier space. Therefore, efficient transformations between physical and spectral space are performed at each time-step using FFT routines and aliasing errors from the evaluation of the nonlinear terms are removed by the 3/2-rule. For sufficiently smooth velocity fields, the spectral approach is a significantly more accurate approximation compared to other discretization methods, such as finite difference or finite element. To preserve the spectral accuracy however, mapping of grid-points cannot be applied, and therefore more complex geometries are difficult (and inefficient) to model. The time advancement is a four-step third-order Runge-Kutta method for the nonlinear advection term, and a second-order Crank-Nicolson method the the linear diffusion term.

Case	$Re_{\delta_0^*}$	Box (L_x, L_y, L_z)	Grid (n_x, n_y, n_z)	B.C. $y = 0/y = L_y$
JCF	165	$(75, 20, 30)$	$(256, 201, 144)$	Parabolic/Neumann
2D-LIN-BL	10^3	$(1000, 30, 1)$	$(768, 101, 1)$	No-slip/Dirichlet
3D-LIN-BL	10^3	$(1000, 30, 370)$	$(768, 101, 120)$	No-slip/Dirichlet
3D-NLIN-BL	10^3	$(1000, 30, 250)$	$(768, 101, 256)$	No-slip/Neumann

TABLE 4.2. Parameters of the numerical simulations performed in this thesis. For all simulations the fringe region is 20% of the length of the domain (L_x).

4.4.2. *Boundary conditions*

Fourier expansion in the wall-parallel directions requires periodic boundary conditions in x and z, i.e.

$$\mathbf{u}(0, y, z) = \mathbf{u}(L_x, y, z) \qquad \mathbf{u}(x, y, -L_z/2) = \mathbf{u}(x, y, L_z/2). \qquad (4.27)$$

However, since neither the boundary-layer flow nor the jet in crossflow are periodic in the streamwise direction x, a "fringe" region can be added at the downstream end of the computational box. In this region, the forcing function

$$F(\mathbf{u}) = \lambda_f(x)(\mathbf{v} - \mathbf{u}), \qquad (4.28)$$

is applied. The desired inflow velocity is denoted by $\mathbf{v}$, which for simulations of boundary layer and the jet in crossflow is chosen as the laminar Blasius boundary-layer profile. The fringe function $\lambda_f(x)$ is identically zero inside the physically relevant domain, and raises smoothly to order one inside the fringe region. The length of the region with $\lambda_f > 0$ is about 20% of the complete domain length. The fringe forcing has been thoroughly validated and we refer to Nordström *et al.* (1999) for details on the convergence properties and upstream influence of the method. The computation of the linear global eigenmodes is slightly dependent on the fringe (shape of the forcing and position). As discussed by Åkervik *et al.* (2008) the growth rate of individual damped eigenvalues might depend on the outflow boundary condition. Moreover, there are also additional modes in the global spectrum related to the fringe forcing. However, these changes have been observed in the damped part of the spectrum; due to the nature of the fringe forcing, there is no growing fringe eigenmode to be expected.

For the simulation of disturbances evolving in the boundary layer, homogeneous no-slip condition is prescribed on the flat plate ($y = 0$). Far away from the wall, in the free-stream the perturbation velocity is vanishingly small, where a Dirichlet boundary condition can be imposed. The boundary conditions in the wall-normal direction for the jet in crossflow are as follows. On the flat plate, no-slip conditions for the wall-parallel velocity components u and w are prescribed. The jet discharging into the crossflow is imposed by a wall-normal

velocity

$$v(r, y = 0) = \frac{V_{\text{jet}}}{U_\infty}(1 - r^2)\exp(-(r/0.7)^4) \, ,$$

with r being the distance from the jet center $(x_{\text{jet}}, z_{\text{jet}})$, normalized by half the jet diameter D. This inflow profile corresponds to a (laminar) parabolic velocity profile of the pipe flow, smoothened with a super-Gaussian function to allow for an efficient treatment with the spectral discretization of the simulation code. At top boundary of the computational box $y = L_y$ the following Neumann condition is imposed,

$$\left.\frac{\partial \mathbf{u}}{\partial y}\right|_{y=L_y} = \left.\frac{\partial \mathbf{U}}{\partial y}\right|_{y=L_y} \, , \qquad (4.29)$$

where $\mathbf{U}(x, y)$ is a Blasius solution.

In table 4.2 the parameters of the simulations performed in this thesis are listed.

CHAPTER 5

Conclusions

This chapter contains an overview of the results of this thesis and a few suggestions for future work.

5.1. Analysis of complex flows

For complex flow configurations, assumptions like periodicity in a direction, a separation in space or time between the development of perturbations and the basic flow and other similar simplifications are not obvious to make. In many applications, there are a number of flow mechanisms and dynamic structures developing at different temporal and spatial scales. Moreover, the various structures might be tightly coupled, competing and interacting with each other. To get a complete picture of the dynamical structures that are present and their significance to the overall flow, it is necessary to adopt a global viewpoint.

The work presented in this thesis is among the first to apply a linear and a nonlinear analysis, using tools that have a theoretical foundation, to a fully three dimensional and highly unsteady flow, namely the jet in crossflow. In practice, the analysis is performed by the use of DNS in conjunction with "matrix-free" techniques from numerical linear algebra (e.g. Arnoldi and DMD). The work on the jet in crossflow can be considered as a "proof-of-concept" as it shows that is possible and numerically feasible to perform linear and nonlinear analysis of complex flows without making a number of simplifications on the geometry, the fluid properties or the flow parameters.

In the study performed here, the unsteady dynamics of the jet in crossflow was broken into two parts; the linear stability analysis of the steady flow and the nonlinear attractor analysis of the unsteady flow. The results and physical insights gained can be summarized as follows. Analysis of the computed global eigenmodes and the unstable steady solution of the jet in crossflow at a velocity ratio $R = 3$ have revealed the presence of three types of elementary instabilities: elliptic instability; Kelvin-Helmholtz instability and a von Kármán type of instability. These instabilities have been studied extensively on simple canonical flows, and it is important to identify them in more complex flows, since they provide an understanding of the elementary physical mechanism for perturbation growth. This knowledge is indispensable for the modification of the flow behavior by external means, since the perturbations are responsible for the initial stage of the transition between different flow regimes.

In flows exhibiting vortex shedding, identifying precisely where in the domain the oscillations have a significant effect is useful both for the physical understanding and for applications. For the jet in crossflow, placing probes in single points in the domain gave supporting evidence of two distinct sustained global oscillations: one high-frequency associated with the jet flow and one low-frequency associated with the wall region. However, probe placement is a local analysis, and collecting spectral data of each relevant spatial point in a three-dimensional domain is an impossible task. In this thesis, we have presented a method based on spectral analysis of the Koopman operator – that can be applied to experimental data as well – to extract global flow structures with periodic motion. The analysis identified a shear mode and wall mode corresponding to the high and low oscillations respectively.

The work presented in this thesis provides a number of future research directions. We outline a few examples.

Sensitivity analysis and passive control: Recent theoretical results (Giannetti & Luchini 2007) show that much physical insight can be gained by investigating the sensitivities of various flow properties to different parameters. The methods have their roots in calculus of variations and generally involve adjoint-based analysis and optimization. By solving the adjoint equations we can locate regions where the flow is most sensitive to forcing and we can compute the perturbations that are the most dangerous to the flow.

Oscillator versus amplifier region: Absolute and convective instabilities are local concepts applicable to weakly non-parallel flows and is not straightforward to conduct such an analysis for the jet in crossflow. However, due to the fact that globally unstable flows have a region or pocket of local absolute instability somewhere in the flow (Chomaz *et al.* 1991) and that this pocket is connected to a region of significant backflow (Hammond & Redekopp 1998), it is likely that the separated region acts as an oscillator in the jet in crossflow. A local analysis of the steady solution could reveal regions in the flow that act as oscillators and regions that act as amplifiers.

Bifurcation analysis: We have performed linear global stability analysis of a steady solution of the jet in crossflow at a single velocity ratio. To fully understand the type of bifurcation that the flow undergoes, a more encompassing global stability analysis of the jet in crossflow, where the velocity ratio is varied should be performed. If the critical velocity ratio is found, a weakly nonlinear analysis could be employed by tracing a global instability in time from its inception through its small-amplitude linear stage to saturation in order to evaluate the coefficients of the Landau equation.

Koopman modes of the transient regime: The theory based on the Koopman operator presented in this thesis considered the asymptotic nonlinear dynamics, whereas the linear analysis considered the dynamics in a small neighborhood of the steady solution. In the transition from a steady to unsteady flow, the transient time from the unstable fixed point to the attractor has not been considered. It could be possible to incorporate the spectral theory of the

Koopman operator to account for this regime. An accurate description of the transient regime using global modes is important for reduced-order modeling of globally unstable flows (Noack *et al.* 2003).

5.2. Laminar-turbulent transition delay

Many aspects in flow control have traditionally been based on intuition and physical insight into the specific flow configuration. There are a number of situations where this approach has proven successful. Nevertheless, there is a well established theory and a large number of methods for a more systematic approach to flow control. The advantages are that even small improvements in the control performance in many applications may have important consequences. For instance, the world-wide shipping consumes over 2.1 billion barrels of oil per year and the airline industry consumes more than 1.5 billion barrels per year. Finding the best possible solution, given certain constrains, that results in a few percents increase of performance can save a lot of money and resources. The work in this thesis takes us one step closer to incorporating theoretical tools into the flow control community.

The starting point of modern optimal and robust control design is an input-output formulation. Given the physical distribution of the inputs and outputs, the control design process amounts to the determination of input signals when output signals are given. Therefore, for successful control design it is sufficient to capture only a fraction of the dynamics, namely the relationships between the input and output signals. We have built a model of low dimension that captures the input-output behavior of the flat-plate boundary layer, and used this model for optimal feedback control design. We have shown that by using systematic methods from control theory in combination with localized sensing/actuation, it is possible to reduce the growth of small-amplitude disturbances in the boundary layer. It was demonstrated that the energy of two and three-dimensional disturbances are damped by an order of magnitude.

Although the significance of the order-of-magnitude reduction of perturbation energy for transition control remains to be tested, such a drastic energy reduction is likely to result in a delay of the initial stages of the transition process. If the actuators and sensors represent realistic models of physically implementable devices, it is possible to use the low-dimensional controller designed numerically in laboratory experiments. The fact that we have modeled the inputs and outputs as volume forcing does not mean that they are unrealistic (see Bagheri *et al.* 2009*a*, for a similar analysis, but instead of volume forcing, the actuators are inhomogeneous boundary conditions). It is the effect of an actuator that is important to model, and not the actuator itself. Therefore, the action that the volume forcing has on the flow, could possibly be reproduced for example using plasma actuators. Another issue that needs to be taken into account is control robustness. If the numerically-designed controller is used in laboratory experiments, it is unavoidable that some parameters (such as Reynolds number and pressure gradients) will mismatch. Fortunately, modern

developments in robust control theory take rigorously into account uncertainties that may be present in the design process. The method for optimal control presented in this thesis, can be incorporated into a robust control framework. Another way that numerical investigations can be useful for wind-tunnel experiments, is by providing guidelines for the shape and spatial distribution of actuators and sensors. In this sense, one can set-up experiments after evaluating a large number of numerical simulations, in order to understand how to design and place actuators and sensors.

We have focused on the flat-plate geometry which still poses a computational challenge, however, the flow control techniques presented in this thesis do not rely on physical insight into the specific flow configuration and can in principle be applied to any geometry. A similar analysis on more complex flows, such as flows in ducts, corners, diffusers and on elliptic leading edges are waiting to be undertaken.

Acknowledgements

I would like to thank Dan Henningson for his guidance and generosity during these four years. His enthusiasm and foresight have been important to the outcome of this thesis. I'm very grateful to Philipp Schlatter and Luca Brandt for the countless discussions and great ideas. I have been fortunate to have three advisors, who always leave their door open and are glad to discuss science. Thanks to Ardeshir Hanifi and Jérôme Hœppfner for teaching me the basics of fluid mechanics in the first months of my studies.

I have had the opportunity to visit two great research groups in Paris (LadHyx) and Princeton. During this time, I have learned a lot from Peter Schmid and Clancy Rowley and have been inspired by their work. I have also been fortunate to meet colleagues and make friends from other places in the world, thanks to Carlo Cossu, Jan Pralits, Fulvio Martinelli, Jan Schulze, Youann Duguet and Milos Ilak.

During the course of my studies, I have enjoyed the friendship of my fellow PhD students Antonious Monokrossous, Onofrio Semeraro, Johan Olsson, Qiang Lee, Andreas Vallgren, Andreas Carlson, Stefan Ivanell, Espen Åkervik, Daniel Ahlman, Tobias Strömgren, Outi Tamissoula, Gabrielle Bellani and Bengt Fallenius. It was pleasure to share office with my clever German roommates Lars-Uwe Schrader and David Tempelmann. Thanks to Hanno Essen, Erik Lindborg, Hans Silverhag and the others in the Department for the chatting during the coffee breaks.

Financial support by the Swedish Research Council (VR) and computer time from the Swedish National Infrastructure for Computing (SNIC) is gratefully acknowledged.

Thank you, my parents, Goli & Rahmat, for your love and support. Welcome Arvid and thank you for your warmth during this winter. Sara, without your constant love, neither I nor this thesis would be the same.

Author contributions

Division of work among the authors in the papers contained in part 2 is as follows.

In paper 1, the theory, code development, simulations and writing were done by Shervin Bagheri (SB) with continuous feedback from Jerome Hœpffner (JH). JH wrote the section on stochastic forcing, Peter J. Schmid (PJS) wrote the introduction and both PJS and JH helped with the writing of the entire paper. Dan Henningson (DH) provided feedback on the manuscript.

In paper 2, the theory was formulated by SB with feedback from DH. The code development, simulations and writing were done by SB. Luca Brandt (LB) provided the adjoint simulation code and helped with the writing, while DH provided feedback on the manuscript.

In paper 3, the writing was done by SB and Espen Åkervik (EÅ) with feedback from LB and DH. The calculations were mainly performed by EÅ, who also implemented the inhomogeneous boundary forcing.

In paper 4, the code development and the set-up of flow configurations were done in close collaboration between Onofrio Semeraro (OS) and SB. The numerical simulations were done by OS with continuous feedback from SB. The background and theory in the paper were written by SB. The results were written by OS with the help of SB. LB and DH provided feedback on the manuscript.

In paper 5, SB performed the DNS simulations of the jet in crossflow, developed the stability code and performed the stability and baseflow computations. The jet boundary condition was implemented by SB and Philipp Schlatter (PS). SB wrote the paper with the help of PS and PJS. DH provided feedback on the manuscript.

In paper 6, SB wrote the "Global mode" section and PS the "DNS" section. The computation of the global modes and their analysis were performed by SB. The DNS computations of the asymmetric flow were performed by SB and PS. The comparison between different flows (steady, mean, symmetric and asymmetric) were done by PS. DH provided feedback on the manuscript.

In paper 7, the recognition that the DMD algorithm could be used to compute Koopman modes was done by Clarence W. Rowley (CWR). Igor Mezić (IM) was involved in developing the idea of expansion of observables into a

sequence of Koopman modes. SB implemented the DMD algorithm, computed the Koopman modes and wrote the section related to the jet in crossflow in paper 7. CWR wrote the introduction, the Koopman theory and the algorithm with the help of IM, whereas PS and DH gave feedback on the manuscript.

In paper 8, the streaks were implemented by SB in a code developed by Ardeshir Hanifi (AH). There parametric studies were performed by SB. The paper was written by SB and AH.

Bibliography

AHUJA, S. 2009 Reduction methods for feedback stabilization of fluid flows. PhD thesis, Princeton University, New Jersey.

ÅKERVIK, E., BRANDT, L., HENNINGSON, D. S., HŒPFFNER, J., MARXEN, O. & SCHLATTER, P. 2006 Steady solutions of the Navier-Stokes equations by selective frequency damping. *Phys. Fluids* **18** (068102), 1–4.

ÅKERVIK, E., EHRENSTEIN, U., GALLAIRE, F. & HENNINGSON, D. S. 2008 Global two-dimensional stability measures of the flat plate boundary-layer flow. *Eur. J. Mech. B/Fluids* **27**, 501–513.

ÅKERVIK, E., HŒPFFNER, J., EHRENSTEIN, U. & HENNINGSON, D. S. 2007 Optimal growth, model reduction and control in a separated boundary-layer flow using global eigenmodes. *J. Fluid. Mech.* **579**, 305–314.

ALAM, M. & SANDHAM, N. D. 2000 Direct numerical simulation of laminar separation bubbles with turbulent reattachment. *J. Fluid Mech.* **403**, 223–250.

ANDERSON, B. & MOORE, J. 1990 *Optimal control: Linear Quadratic Methods*. Prentice Hall, New York.

ANTOULAS, C. A. 2005 *Approximation of Large-Scale Dynamical Systems*. SIAM, Philadelphia.

ARNOLDI, W. E. 1951 The principle of minimized iterations in the solution of the matrix eigenvalue problem. *Quart. Appl. Math.* **9**, 17–29.

BAGHERI, S., ÅKERVIK, E., BRANDT, L. & HENNINGSON, D. S. 2009*a* Matrix-free methods for the stability and control of boundary layers. *AIAA J.* **47**, 1057–1068.

BAGHERI, S., BRANDT, L. & HENNINGSON, D. S. 2009*b* Input-output analysis, model reduction and control design of the flat-plate boundary layer. *J. Fluid Mech.* **620**, 263–298.

BAGHERI, S., HŒPFFNER, J., SCHMID, P. J. & HENNINGSON, D. S. 2009*c* Input-output analysis and control design applied to a linear model of spatially developing flows. *Appl. Mech. Rev.* **62** (2).

BAGHERI, S., SCHLATTER, P., SCHMID, P. J. & HENNINGSON, D. S. 2009*d* Global stability of a jet in crossflow. *J. Fluid Mech.* **624**, 33–44.

BARKLEY, D. 2006 Linear analysis of the cylinder wake mean flow. *Europhys. Lett.* **75**, 750–756.

BARKLEY, D., GOMES, M. G. & HENDERSON, R. D. 2002 Three-dimensional instability in flow over a backward-facing step. *J. Fluid Mech.* **473**, 167–190.

BATCHELOR, G. 1967 *An Introduction to Fluid Dynamics*. Cambridge University Press.

BEWLEY, T. R. 2001 Flow control: New challenges for a new renaissance. *Progr. Aerospace. Sci.* **37**, 21–58.

BEWLEY, T. R. & LIU, S. 1998 Optimal and robust control and estimation of linear paths to transition. *J. Fluid Mech.* **365**, 305–349.

BLASIUS, P. 1908 Grenzschichten in flussigkeiten mit kleiner reibung. *Z. Math. Phys.* **56** (1).

CHEVALIER, M., SCHLATTER, P., LUNDBLADH, A. & HENNINGSON, D. S. 2007 A pseudo spectral solver for incompressible boundary layer flows. Trita-Mek 7. KTH Mechanics, Stockholm, Sweden.

CHOMAZ, J. M. 2005 Global instabilities in spatially developing flows: Non-normality and nonlinearity. *Ann. Rev. Fluid Mech.* **37**, 357–392.

CHOMAZ, J. M., HUERRE, P. & REDEKOPP, L. G. 1987 Models of hydrodynamic resonances in separated shear flows. *Symposium on Turbulent Shear Flows, 6th, Toulouse, France*.

CHOMAZ, J. M., HUERRE, P. & REDEKOPP, L. G. 1991 A frequency selection criterion in spatially developing flows. *Stud. Appl. Math.* **84**, 119-114.

DING, J. 1998 The point spectrum of Frobenius-perron and Koopman operators. *Proc. Amer. Math. Soc.* **126** (5), 1355–1361.

DOYLE, J. C. 1978 Guaranteed margins for LQG regulators. *IEEE Trans. Automat. Control* **23**, 756–757.

DOYLE, J. C., GLOVER, K., KHARGONEKAR, P. P. & FRANCIS, B. A. 1989 State-space solutions to standard H_2 and H_∞ control problems. *IEEE Trans. Automat. Control* **34**, 831–847.

DULLERUD, E. G. & PAGANINI, F. 1999 *A course in robust control theory. A convex approach*. Springer Verlag, New York.

FRIC, T. F. & ROSHKO, A. 1994 Vortical structure in the wake of a transverse jet. *J. Fluid Mech.* **279**, 1–47.

GIANNETTI, F. & LUCHINI, P. 2007 Structural sensitivity of the first instability of the cylinder wake. *J. Fluid Mech.* **581**, 167–197.

GLOVER, K. 1999 All optimal Hankel-norm approximations of linear multivariable systems and the l^∞-error bounds. *Int. J. Control* **39**, 1115–1193.

GOLDSTEIN, M. E. & HULTGREN, L. S. 1989 Boundary-layer receptivity to long-wave free-stream disturbances. *Ann. Rev. Fluid Mech.* **21** (1), 137–166.

GREEN, M. & LIMEBEER, J. N. 1995 *Linear Robust Control*. Prentice Hall, New Jersey.

GRUNDMANN, S. & TROPEA, C. 2008 Active cancellation of artificially introduced Tollmien–Schlichting waves using plasma actuators. *Exp. Fluids* **44** (5), 795–806.

GUCKENHEIMER, J. & HOLMES, P. 1983 *Nonlinear Oscillations, Dynamical system and Bifuracations of vector fields*. Springer Verlag, New York.

GUGERCIN, S., SORENSEN, D. & ANTOULAS, A. 2003 A modified low-rank Smith method for large-scale Lypunov eqations. *Num. Algorithms.* **32**, 27–55.

HAMMARLING, S. J. 1982 Numerical solution of the stable, non-negative definite Lyapunov equation. *IMA J. Numer. Anal.* **2**, 303–323.

HAMMOND, D. A. & REDEKOPP, L. G. 1998 Local and global instability properties of separation bubbles. *Eur. J. Mech. B/Fluids* **17** (2), 145 – 164.

HAMMOND, E. P., BEWLEY, T. R. & MOIN, P. 1998 Observed mechanisms for turbulence attenuation and enhancement in opposition-controlled wall-bounded flows. *Phys. Fluids* **10** (9), 2421–2423.

HENNINGSON, D. S. & ÅKERVIK, E. 2008 The use of global modes to understand transition and perform flow control. *Phys. Fluids* **20**, 031302.

HO, C. M. & TAI, Y. 1998 Micro-electro-mechanical systems MEMS and fluid flows. *Ann. Rev. Fluid Mech.* **30**, 579–612.

HOLMES, P., LUMLEY, J. & BERKOOZ, G. 1996 *Turbulence Coherent Structuresm Dynamical Systems and Symmetry*. Cambridge University Press.

HUERRE, P. 2000 Open shear flow instabilities. In *Perspectives in Fluid Dynamics*, pp. 159–229. Cambridge University Press.

HUERRE, P. & MONKEWITZ, P. 1990 Local and global instabilities in spatially developing flows. *Ann. Rev. Fluid Mech.* **22**, 473–537.

HUERRE, P. & MONKEWITZ, P. A. 1985 Absolute and convective instabilities in free shear layers. *J. Fluid Mech.* **159**, 151–168.

ILAK, M. & ROWLEY, C. W. 2008 Modeling of transitional channel flow using balanced proper orthogonal decomposition. *Phys. Fluids* **20**, 034103.

JAIMOUKHA, I. M. & KASENALLY, E. M. 1994 Krylov subspace methods for solving large Lyapunov equations. *SIAM J. Num. Anal.* **31** (1), 227–251.

JEONG, J. & HUSSAIN, F. 1995 On the identification of a vortex. *J. Fluid Mech.* **285**, 69–94.

JOVANOVIC, M. R. & BAMIEH, B. 2005 Componentwise energy amplification in channel flows. *J. Fluid Mech.* **534**, 145–183.

JUANG, J. & PAPPA, R. S. 1985 An eigensystem realization algorithm for modal paramter identification and model reduction. *J. Guid. Con. Dyn.* **3** (25), 620–627.

KALMAN, R. E. 1960 A new approach to linear filtering and prediction problems. *Trans. ASME, Ser. D. J. Basic Eng.* **82**, 24–45.

KELSO, R., LIM, T. & PERRY, A. 1996 An experimental study of round jets in cross-flow. *J. Fluid Mech.* **306**, 111–144.

KELSO, R. M. & SMITS, A. J. 1995 Horseshoe vortex systems resulting from the interaction between a laminar boundary layer and a transverse jet. *Phys. Fluids* **7** (1), 153–158.

KIM, J. & BEWLEY, T. R. 2007 A linear systems approach to flow control. *Ann. Rev. Fluid Mech.* **39**, 383–417.

KOOPMAN, B. 1931 Hamiltonian systems and transformations in Hilbert space. *Proc. Nat. Acad. Sci. USA* **17**, 315–318.

LALL, S., MARSDEN, J. E. & GLAVASKI, S. 2002 A subspace approach to balanced truncation for model reduction of nonlinear control systems. *Int. J. Robust Nonlinear Control* **12**, 519–535.

LAPORTE, F. & CORJON, A. 2000 Direct numerical simulations of the elliptic instability of a vortex pair. *Phys. Fluids* **12** (5), 1016–1031.

LASOTA, A. & MACKEY, C. M. 1994 *Chaos, fractals and noise: Stochastic aspects of dynamics*. Springer Verlag, New York.

LAUB, A., HEATH, M., PAIGE, C. & WARD, R. 1987 Computation of system balancing transformations and other applications of simultaneous diagonalization algorithms. *IEEE Trans. Automat. Control* **32** (2), 115–122.

LE DIZÉS, S., HUERRE, P., CHOMAZ, J. M. & MONKEWITZ, P. A. 1996 Linear global modes in spatially developing media. *Phil. Trans. R. Soc. Lond. A* **354**, 169–212.

LEHOUCQ, R. B., SORENSEN, D. C. & YANG, C. 1998 *ARPACK Users' guide: Solution of Large-Scale Eigenvalue problems with implicitly restarted Arnoldi methods*. SIAM, Philadelphia.

LEWEKE, T. & WILLIAMSON, C. H. K. 1998 Cooperative elliptic instability of a vortex pair. *J. Fluid Mech.* **360**, 85–119.

LEWIS, F. L. & SYRMOS, L. V. 1995 *Optimal Control*. John Wiley & Sons, New York.

LIM, T. T., NEW, T. H. & LUO, S. C. 2001 On the development of large-scale structures of a jet normal to a cross flow. *Phys. Fluids* **13** (3), 770–775.

LUCHINI, P. 2000 Reynolds-number-independent instability of the boundary layer over a flat surface: Optimal perturbations. *J. Fluid. Mech.* **404**, 289–309.

LUMLEY, J. L. 1970 *Stochastic Tools in Turbulence*. Academic Press, New York.

MA, Z., AHUJA, S. & ROWLEY, C. W. 2009 Reduced order models for control of fluids using the Eigensystem Realization Algorithm. *Theoret. Comput. Fluid Dyn.* In press.

MARQUILLIE, M. & EHRENSTEIN, U. 2002 On the onset of nonlinear oscillations in a separating boundary-layer flow. *J. Fluid Mech.* **458**, 407–417.

MEZIC, I. 2005 Spectral properties of dynamical systems, model reduction and decompositions. *Nonlinear Dynamics* **41** (1), 309–325.

MEZIC, I. & BANASZUK, A. 2004 Comparision of systems with complex behavior. *Physica D: Nonlinear Phenomena* **197** (1-2), 101–133.

MILLING, W. 1981 Tollmien–Schlichting wave cancellation. *Phys. Fluids* **24** (5), 979–981.

MONKEWITZ, P. A., BECHERT, D. W., BARSIKOW, B. & LEHMANN, B. 1990 Self-excited oscillations and mixing in a heated round jet. *J. Fluid Mech.* **213**, 611–639.

MOORE, B. 1981 Principal component analysis in linear systems: Controllability, observability, and model reduction. *IEEE Trans. Automat. Control* **26** (1), 17–32.

MOUSSA, Z. M., TRISCHKA, J. W. & ESKINAZI, S. 1977 The near field in the mixing of a round jet with a cross-stream. *J. Fluid Mech.* **80** (01), 49–80.

NOACK, B., AFANASIEV, K., MORZYNSKI, M., TADMOR, G. & THIELE, F. 2003 A hierarchy of low-dimensional models for the transient and post-transient cylinder wake. *J. Fluid Mech.* **497**, 335–363.

NORDSTRÖM, J., NORDIN, N. & HENNINGSON, D. S. 1999 The fringe region technique and the fourier method used in the direct numerical simulation of spatially evolving viscous flows. *SIAM J. Sci. Comput.* **20** (4), 1365–1393.

PACKARD, N. H., CRUTCHFIELD, J. P., FARMER, J. D. & SHAW, R. S. 1980 Geometry from a time series. *Phys. Rev. Lett.* **45** (9), 712–716.

PANG, J. & CHOI, K.-S. 2004 Turbulent drag reduction by lorentz force oscillation. *Phys. Fluids* **16** (5), L35–L38.

PARLETT, B. N. & REINSCH, C. 1969 Balancing a matrix for calculation of eigenvalues and eigenvectors. *Numer. Math* **13** (503), 293–304.

PENZL, T. 2000 A cyclic low-rank Smith method for large sparse Lyapunov equations. *SIAM K. Sci. Comput.* **21**, 1401–1418.

PERNEBO, L. & SILVERMAN, L. 1982 Model reduction via balanced state space representations. *IEEE Trans. Automat. Control* **27**, 382–387.

PIER, B. 2002 On the frequency selection of finite-amplitude vortex shedding in the cylinder wake. *J. Fluid Mech.* **458**, 407–417.

PRANDTL, L. 1905 Über Flussigkeitsbewegung bei sehr kleiner Reibung. *Verhandlungen des dritten internationalen Mathematiker-Kongresses in Heidelberg* .

PROVANSAL, M., MATHIS, C. & BOYER, L. 1987 Bénard-von Kármán instability: Transient and forcing regimes. *J. Fluid. Mech.* **182**, 1–22.

REDDY, S. C. & HENNINGSON, D. S. 1993 Energy growth in viscous channel flows. *J. Fluid Mech.* **252**, 209–238.

REYNOLDS, O. 1883 An experimental investigation of the circumstances which determine whether the motion of water shall be direct or sinuous, and of the law of resistance in parallel channels. *Phil. Trans. R. Soc. Lond.* **174**, 935–982.

ROWLEY, C. W. 2005 Model reduction for fluids using balanced proper orthogonal decomposition. *Int. J. Bifurc. Chaos* **15** (3), 997–1013.

ROWLEY, C. W., MEZIC, I., BAGHERI, S., SCHLATTER, P. & HENNINGSON, D. S. 2009 Spectral analysis of nonlinear flows. *J. Fluid Mech.* **641**, 115–127.

RUHE, A. 1984 Rational Krylov sequence methods for eigenvalue computation. *Lin. Alg. Appl.* **58**, 391 – 405.

SAAD, Y. 1980 Variations on Arnoldi's method for computing eigenelements of large unsymmetric matrices. *Lin. Alg. Appl.* **34**, 269–295.

SAFONOV, M. & CHIANG, R. 1989 A schur method for balanced-truncation model reduction. *IEEE Trans. Automat. Control* **34** (7), 729–733.

SCHLATTER, P., BAGHERI, S. & HENNINGSON, D. S. 2009 Self-sustained global oscillations in the jet in crossflow. Under review.

SCHLICHTING, H. & GERSTEN, K. 2000 *Boundary-Layer Theory*. Springer Verlag, Heidelberg.

SCHMID, P. 2009 Dynamic Mode Decomposition. Submitted.

SCHMID, P. J. & HENNINGSON, D. S. 2001 *Stability and Transition in Shear Flows*. Springer Verlag, New York.

SCHRAUF, G. 2005 Status and perspectives of laminar flow. *Aeronautical J.* **109** (1102), 639–644.

SIPP, D. & LEBEDEV, A. 2007 Global stability of base and mean flows: A general approach and its applications to cylinder and open cavity flows. *J. Fluid Mech.* **593**, 333–358.

SMITH, B. L. & GLEZER, A. 1998 The formation and evolution of synthetic jets. *Phys. Fluids* **10** (9), 2281–2297.

SMITH, R. A. 1968 Matrix equation xa + bx = c. *SIAM J. Appl. Math.* **16** (1), 198–201.

SORENSEN, D. 1992 Implicit application of polynomial filters in a k-step Arnoldi method. *SIAM J. Matrix Anal. Appl* **13**, 357–385.

STRYKOWSKI, P. J. & NICCUM, D. L. 1992 The influence of velocity and density ratio on the dynamics of spatially developing mixing layers. *Phys. Fluids* **4** (4), 770–781.

TEMAM, R. 1997 *Infinite Dimensonal Dynamical Systems in Mechanics and Physics*, 2nd edn. Springer, New York.

THEOFILIS, V. 2005 Advances in global linear instability analysis of nonparallel and three-dimensional flows. *Progr. Aerosp. Sci.* **39**, 249–315.

THEOFILIS, V., HEIN, S. & DALLMANN, U. 2000 On the origins of unsteadiness and three-dimensionality in a laminar separation bubble. *Philos. Trans. R. Soc. Lond. A* **358**, 3229–3246.

THIRIA, B. & WESFREID, J. E. 2007 Stability properties of forced wakes. *J. Fluid Mech.* **579**, 137–161.

TREFETHEN, L. N. 1997 Pseudospectra of linear operators. *SIAM Review* **39** (3), 383–406.

TREFETHEN, L. N. & BAU, D. 1997 *Numerical Linear Algebra*. SIAM, Philadelphia.

TREFETHEN, L. N. & EMBREE, M. 2005 *Spectra and Pseudospectra — The Behavior of Nonnormal Matrices and Operators*. Princeton University Press, New Jersey.

WALEFFE, F. 1990 On the three-dimensional instability of strained vortices. *Phys. Fluids* **2** (1), 76–80.

ZHOU, K., DOYLE, J. C. & GLOVER, K. 2002 *Robust and Optimal Control*. Prentice Hall, New Jersey.

Part 2

Papers

1

Paper 1

Input–output analysis and control design applied to a linear model of spatially developing flows

Shervin Bagheri, Jérôme Hœpffner[1], Peter J. Schmid[2] and Dan S. Henningson

This review presents a framework for the input-output analysis, model reduction and control design for fluid dynamical systems using examples applied to the linear complex Ginzburg-Landau equation. Major advances in hydrodynamics stability, such as global modes in spatially inhomogeneous systems and transient growth of non-normal systems is reviewed. Input-output analysis generalizes hydrodynamic stability analysis by considering a finite-time horizon over which energy amplification, driven by a specific input (disturbances/actuator) and measured at a specific output (sensor), is observed. In the control design the loop is closed between the output and the input through a feedback gain. Model reduction approximates the system with a low-order model, making modern control design computationally tractable for systems of large dimensions. Methods from control theory are reviewed and applied to the Ginzburg-Landau equation in a manner that is readily generalized to fluid mechanics problems, thus giving a fluid mechanics audience an accessible introduction to the subject.

1. Introduction

Whereas stability theory has long occupied a central role in fluid mechanics research, control theory has only recently been applied to fluid systems. Despite its long history, stability theory has undergone remarkable changes over the past decades. The incorporation of short-term instabilities into a traditionally asymptotic stability concept, the equal treatment of stability and response behavior within the same mathematical framework, and use of system-theoretical tools to probe the disturbance behavior of fluid systems have reinvigorated hydrodynamic stability theory and developed it into a modern tool of fluid dynamic research. Especially the formulation of the governing equations in

---

[1]Institut de Recherche sur les Phénomènes Hors Équilibre (IRPHÉ) CNRS-Université d'Aix-Marseille, F-13384 Marseille, France
[2]Laboratoire d'Hydrodynamique (LadHyX), CNRS-École Polytechnique, F-91128 Palaiseau, France

state-space form combined with an input-output viewpoint of the perturbation dynamics has brought the two fields of stability and control theory closer together. Whereas stability theory is concerned with all aspects of the open-loop dynamics of the governing equations, control theory connects the output to the input and focuses on the closed-loop characteristics — including optimal design and performance analysis — of the underlying dynamical system. These two closely related disciplines, and the unifying formulation that connects them, are the subject of this review. Due to the vastness of these two fields, we restrict ourselves to concepts of direct relevance to fluid dynamical systems as well as to a simple model equation. The Ginzburg-Landau equation, a well-known model equation displaying a great variety of phenomena observed in fluid systems, will be used to demonstrate and exemplify concepts and techniques from stability, systems and control theory.

The recognition that short-term instabilities play an important role in fluid dynamical systems can be traced back nearly two decades when scientists searched for disturbances that optimize energy amplification over a finite time span (Farrell 1988; Butler & Farrell 1992; Reddy *et al.* 1993; Reddy & Henningson 1993). These disturbances did not resemble the most unstable eigenvectors of the system which led to the development of a theoretical foundation to describe short-term nonmodal phenomena (Trefethen *et al.* 2005; Farrell & Ioannou 1996; Schmid & Henningson 2001; Schmid 2007). In fact, even if the flow is asymptotically stable, substantial amplification of the input signal (initial condition or external forcing) into an output signal (energy) can occur. By now, the associated theory has matured into an important component for understanding the transition process from laminar to turbulent fluid motion and has been able to explain a variety of observed fluid structures in transitional and turbulent shear flows (Schmid & Henningson 2001). In a further step, an input-output framework has been suggested Jovanovic & Bamieh (2005) which brings the analysis of stability characteristics closer to a system theoretic interpretation, with impulse response, frequency response and transfer functions as the principal tools of investigation.

At the same time, flow control based on control theory has emerged as a new discipline of fluid mechanics (Joshi *et al.* 1997; Bewley & Liu 1998; Lee *et al.* 2001; Högberg *et al.* 2003*a,b*; Hœpffner *et al.* 2005; Chevalier *et al.* 2006, 2007; Åkervik *et al.* 2007; Monokrousos *et al.* 2008). Starting with simple feedback control laws and full-state information control, it has progressed toward more realistic configurations by incorporating the estimation problem and partial-state information control. During the control design process, a strategy is determined that feeds information from the measurements (sensors) back to the input signal (actuators) such that a given control objective is achieved. The accompanying theoretical basis, adapted from control theory (Kwakernaak & Sivan 1972; Anderson & Moore 1990; Lewis & Syrmos 1995; Zhou *et al.* 2002), to determine these strategies has evolved substantially, and flow control has advanced into an independent and active field of fluid dynamics. Comprehensive

Impulse (2,3.1,5.4)
Harmonic (3.1,4,5.4,5.6)
Stochastic (3.2,5.2,5.4)

Flow
Parallel (2,1)
Nonparallel (2.2-5)
Globally unstable (2,5)
Convectively unstable (2-5)
Reduced-order (4)

Flow state (2,3,5)
Kinetic energy (2,3,5)
Sensor (3-5)

Controller
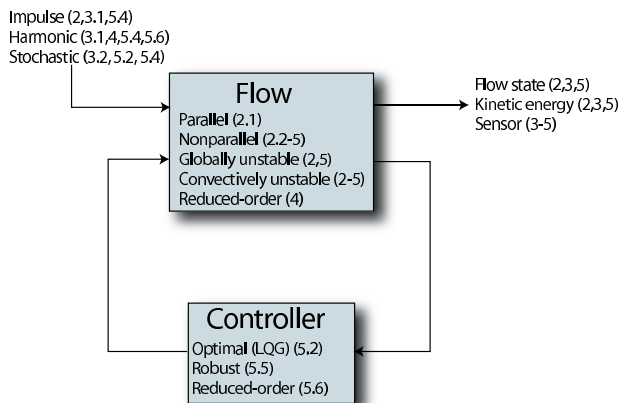Optimal (LQG) (5.2)
Robust (5.5)
Reduced-order (5.6)

FIGURE 1. Overview of the open-loop and closed-loop analysis performed in this review. The response in terms of the flow state, kinetic energy and sensor signal to impulse, harmonic and stochastic inputs of the parallel, non-parallel, convectively unstable and globally unstable Ginzburg-Landau equation is investigated in sections 2 and 3. Model reduction of the system is performed in section 4 followed by optimal (LQG), robust ($\mathcal{H}_\infty$) and reduced-order control design in section 5.

accounts on recent progress in the rapidly expanding field of flow control can be found in Gal-El-Hak (1996); Bewley (2001); Kim (2003) and Kim & Bewley (2007).

The input-output framework provides not only a convenient way of analyzing stability and receptivity characteristics (Hill 1995; Luchini & Bottaro 1998) of fluid systems, it represents the natural starting point for control design. Stability and receptivity analysis as well as control design can thus be accomplished within the same formal setting. This unified analysis shall be exemplified in this review article by investigating the stability and response properties of the Ginzburg-Landau equation and by devising effective control strategies including the evaluation of their efficiency and performance. The Ginzburg-Landau equation has frequently been used as a model for instabilities in fluid systems, see *e.g.* Huerre & Monkewitz (1990) and Chomaz (2005). We will use it here with two different sets of parameters: one set to model globally unstable flows (so-called *oscillators*), and another set to describe convectively unstable flows (so-called *noise amplifiers*). The Ginzburg-Landau equation has also been the subject to several flow control studies (Monkewitz 1989; Park *et al.* 1993; Lauga & Bewley 2003, 2004; Cohen *et al.* 2005).

The review is organized as follows (see also figure 1): we start with a summary of stability results for the Ginzburg-Landau equation in section 2

where results for both asymptotic behavior and transient growth will be presented. In section 3 we investigate the input-output behavior of linear systems in general, and the Ginzburg-Landau equation in particular. The response to impulsive, harmonic and stochastic forcing will be considered, and the concepts of controllability and observability will be introduced. In section 4 we review the projection method of model reduction using global eigenmodes, POD modes and balanced truncation. Section 5 deals with the control design for the Ginzburg-Landau equation. We present a detailed derivation of the LQG (Linear Quadratic Gaussian) control framework, raise the important issue of actuator and sensor placement, and conclude by discussing robust control. Concluding remarks and a summary of the presented material are offered in the last section.

2. Asymptotic and transient behavior

2.1. *Parallel flows — fundamental concepts*

Before applying modern techniques of hydrodynamic stability theory (Schmid & Henningson 2001) to the full Ginzburg-Landau model describing spatially varying flows, we will first introduce and analyze a simpler version of the Ginzburg-Landau equation. By neglecting the spatial dependence of the flow, thus arriving at the parallel (*i.e.* constant-coefficient) Ginzburg-Landau equation, we will apply concepts of linear stability analysis to describe the growth and decay of disturbances in time and/or space.

The parallel Ginzburg-Landau equation on the infinite interval $-\infty < x < \infty$ reads

$$\frac{\partial q}{\partial t} = \mathcal{A}q = \left(-\nu\frac{\partial}{\partial x} + \gamma\frac{\partial^2}{\partial x^2} + \mu\right)q, \tag{1a}$$

$$q(x,t) \rightarrow 0 \quad \text{as} \quad x \rightarrow \pm\infty, \tag{1b}$$

with initial condition $q(x,0) = q_0(x)$ and $\mathcal{A}$ as the Ginzburg-Landau operator. The solutions $q(x,t)$ are complex valued and the inner-product is defined as $\langle f, g\rangle = \int_{-\infty}^{\infty} g^* f \mathrm{d}x$. We occasionally refer to the this norm as the energy norm. The superscript * denotes the complex conjugate. The convective and the dissipative nature of the modeled flow is represented by the complex terms $\nu = U + 2ic_u$ and $\gamma = 1 + ic_d$, respectively. The above equation is of convection-diffusion type with an extra real-valued term $\mu = \mu_0 - c_u^2$ to model the presence of exponential instabilities. The significance of the complex terms c_d and c_u will become clearer when we decompose the system into wave-like solutions.

We first investigate the linear stability of the parallel Ginzburg-Landau equation, *i.e.* the spatio-temporal evolution of the perturbation $q(x,t)$ about the basic state $q_B(x,t) = 0$. As introduced by Briggs (1964), this spatio-temporal evolution of perturbations in fluid flow can be described by three basic types of local behavior: (i) stable, (ii) convectively unstable and (iii)
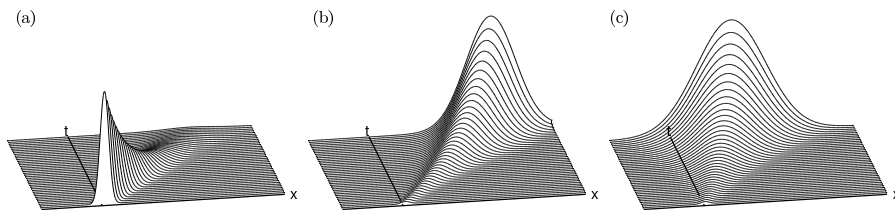
FIGURE 2. Local stability concepts based on the linear response of the parallel Ginzburg-Landau equation to a temporally and spatially localized pulse at $t = 0$ and $x = 0$, displayed in the x-t-plane. (a) stable configuration $\mu_0 \leq 0$: the solution at $t = t_1 > 0$ is damped everywhere; (b) convectively unstable configuration $0 < \mu_0 < \mu_t$: the solution at $t = t_1$ is amplified, but is zero along the ray $x/t = 0$; (c) absolutely unstable configuration $\mu_t \leq \mu_0$: the state is amplified at $t = t_1$ and nonzero along the ray $x/t = 0$.

absolutely unstable. Our model equation, in fact, has by construction the minimum number of required terms to give rise to a successive transition through the three types of instability.

The three types of disturbance behavior can be probed by computing the response to a spatially and temporally localized pulse as this pulse evolves in space and time. Figure 2 demonstrates the three types of responses that may be observed. First, the amplitude may asymptotically decay in time throughout the entire domain (see figure 2a). In this case, the basic flow is deemed linearly stable. Second, a convectively unstable flow is shown in figure 2(b); in this case, the perturbation grows in time, but is convected away from the location at which it was generated, so that the response eventually decays to zero at every spatial location. Finally, for an absolutely unstable flow (see figure 2c) the perturbation is amplified both upstream and downstream of the location it was generated and thus contaminates the entire spatial domain over time.

The response behavior to a δ-function applied at $(x, t) = (0, 0)$ is equivalent to the Green's function or impulse response of the complex Ginzburg-Landau equation. We will return to this concept in a subsequent section of this review. In what follows, we will first exploit the homogeneity in space and time and seek solutions in the wavenumber/frequency (Fourier) space. The dispersion relation linking wavenumber and frequency then fully describes the evolution of wavelike (and by superposition) non-wavelike solutions. Criteria for stability or instability of the solutions, as well as the type of instability, follow easily from the dispersion relation.

We express the solutions $q(x, t)$ as a superposition of normal modes

$$\tilde{q}(k, \omega) \exp(ikx - i\omega t) \tag{2}$$

with wavenumber k, frequency ω, and (complex) amplitude $\tilde{q}$. The imaginary part of k and ω determines the stability of the associated solution, whereas the real part describes the oscillatory behavior in x and t, respectively. Introducing this normal mode decomposition into (1) results in the dispersion relation, $D(k, \omega; \mu_0) = 0$, which takes the form

$$\omega = Uk + c_d k^2 + i(\mu_0 - (k - c_u)^2). \tag{3}$$

Within the temporal framework, an initial periodic perturbation with *real* wavenumber k grows exponentially in time when μ_0 in (3) exceeds $(k - c_u)^2$, *i.e.* when exponential growth exceeds diffusion. In this case, $\omega_i(k) > 0$ and the associated normal mode $\tilde{q}$ exhibits exponential temporal growth. Furthermore, we observe a finite interval $k \in [c_u - \sqrt{\mu_0}, c_u + \sqrt{\mu_0}]$ of unstable spatial wavenumbers. A simple criterion for linear stability of the flow can be deduced by considering the growth rate $\omega_i = \omega_{i,max}$ of the most unstable wave $k = k_{max}$ in this interval. For the dispersion relation (3), we observe that $k_{max} = c_u$ and the corresponding growth rate is $\omega_{i,max} = \mu_0$. Thus, the condition for a local linear instability becomes,

$$\mu_0 \leq 0 \qquad \text{locally stable,} \tag{4a}$$
$$\mu_0 > 0 \qquad \text{locally unstable.} \tag{4b}$$

In figure 3(*a*), the neutral curve, defined by $\omega_{i,max} = 0$, is displayed as a function of μ_0 and k. We see that the range of unstable wavenumbers increases as μ_0 increases.

To further investigate the two types of locally unstable configurations — convectively unstable and absolutely unstable — it is instructive to consider perturbations that consist of a superposition of normal modes near $k = c_u$ which form a travelling wavepacket. From the dispersion relation (3) we conclude that individual wave components of this wavepacket travel at the phase velocity

$$\omega_r / k = U + c_d k, \tag{5}$$

whereas the wavepacket itself, and therefore the perturbation, travels at the group velocity

$$U_{max} = \frac{\partial \omega}{\partial k} = U + 2c_d c_u. \tag{6}$$

In general, the group velocity is complex but carries a physical meaning when it is real, which is always the case for the most unstable wavenumber c_u.

The disturbance behavior in the unstable region depends on the competition between convection and instability. For the Ginzburg-Landau equation we find that the flow is convectively unstable if $U_{max} > 2\sqrt{\mu_0}|\gamma|$, *i.e.*, when the group velocity exceeds the exponential instability of the unstable region (for constant diffusion). This means that, for convection-dominated flows, perturbations grow as they enter the unstable domain but are quickly convected downstream, beyond the unstable region where they decay, and the basic state
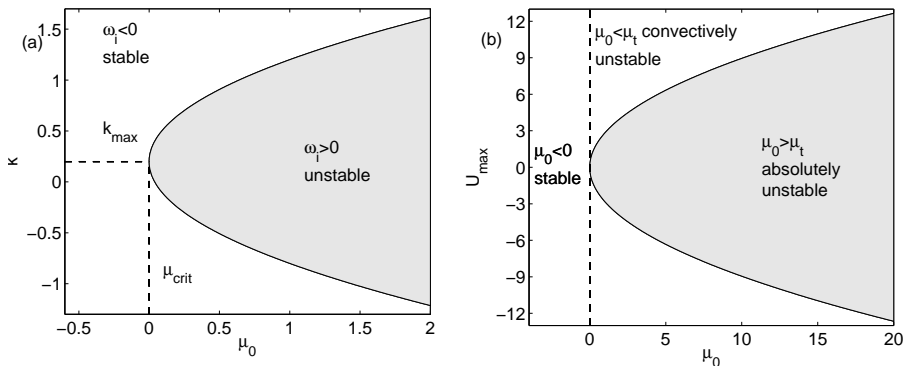
FIGURE 3. (*a*) The neutral stability curve for the parallel Ginzburg-Landau equation (with $c_u = 0.2$) in the (μ_0, k)-plane. (*b*) The neutral absolute stability curve for the parallel Ginzburg-Landau equation (with $\gamma = 1 - i$) in the $(\mu_0, U_{\max})$-plane.

relaxes back to its original state (see figure 2*b*). However, when μ_0 exceeds the critical value of

$$\mu_t = \frac{U_{max}^2}{4|\gamma|^2}, \tag{7}$$

there exists an unstable wavelength with zero group velocity. As the perturbation is amplified in the unstable domain, it will gradually contaminate the entire physical domain and render the flow absolutely unstable. In figure 3(*b*), the neutral curve, defined by $\mu_t = 0$, is displayed as a function μ_0 and U_{max}. The critical value μ_t is obtained by considering a wavepacket with a zero group velocity $\partial\omega/\partial k = 0$ (see Huerre 2000, for an exact derivation). The associated growth rate $\omega_i = \omega_{i,0}$ is the absolute growth rate. Unlike for our case, the absolute frequency ω_0 for realistic flow configurations can seldom be found in analytic form. Instead, one has to resort to Briggs' method (Briggs 1964), see also Huerre (2000) which amounts to locating pinch points in the complex k-plane. In addition to the criterion of zero group velocity, one must ensure that the two spatial branches $k^+(\omega)$ and $k^-(\omega)$ (for real ω) in (3) originate from the upper and lower halves of the complex k-plane.

2.2. *Spatially developing flows — a global approach*

Despite the limitations of a parallel flow assumption, the above results carry over to weakly non-parallel flows as described in Monkewitz (1990); Huerre & Monkewitz (1990); Chomaz *et al.* (1991); Le Dizés *et al.* (1996). Within a Wentzel-Kramers-Brillouin-Jeffreys (WKBJ) approximation, one can draw conclusions about the global stability behavior from investigating the dispersion relation locally. Many realistic flows, however, are strongly non-parallel
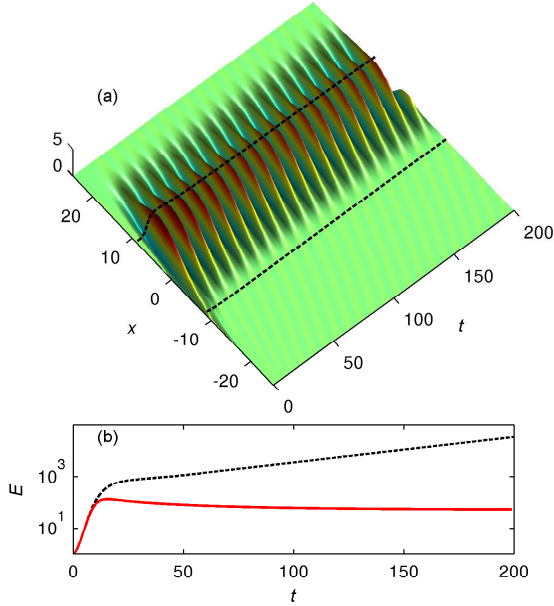
FIGURE 4.   (*a*) The spatio-temporal evolution of a distur-
bance in a globally unstable flow. The disturbance grows ex-
ponentially until the cubic nonlinear term $-|q|^2 q$ (see Chomaz
et al. 1990; Chomaz 2005, for details of the nonlinear Ginzburg-
Landau equation) causes the disturbance to saturate and os-
cillate. (*b*) The energy that corresponds to the evolution in
(*a*) is shown in red, and the linear exponential growth for the
linear Ginzburg-Landau equation is shown in dashed black.

which requires us to resort to a global stability analysis. In this section, we will
adopt this global point of view to investigate the stability properties of a sim-
ple model flow which depends on the flow direction x. We will see that a rich
disturbance behavior is uncovered which has its roots in the non-normality of
the underlying evolution operator (Trefethen 1997; Trefethen & Embree 2005;
Davies 2002). As a first step, one solves a global eigenvalue problem. Assum-
ing completeness, any perturbation can then be decomposed into the global
eigenfunctions of the governing operator. If there exists an unstable global
mode, it is amplified until it saturates due to nonlinearity and may lead to
self-sustained oscillations in the flow (figure 4*a, b*). The short-time, or tran-
sient, behavior can also be captured by global modes (Cossu & Chomaz 1997;
Henningson & Åkervik 2008), if one considers a superposition of them. For a
non-normal stability operator with corresponding non-orthogonal global modes
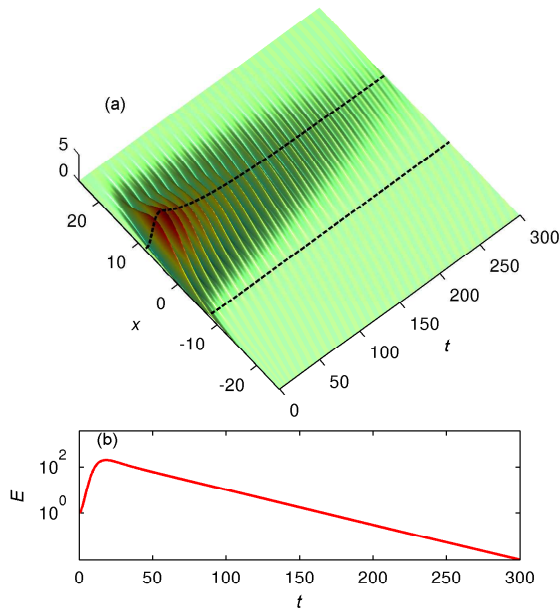
FIGURE 5. (*a*) Linear transient growth of a perturbation in space and time: an optimal initial perturbation grows as it enters the unstable domain at branch I at $x = -8.2$ until it reaches branch II at $x = 8.2$. The two dashed lines depict branch I and II. (*b*) The corresponding optimal energy growth of the convectively unstable flow in (*a*).

a superposition of decaying global modes can result in a large transient amplification of perturbation energy (figure 5*a*, *b*). As demonstrated by Cossu & Chomaz (1997), this transient behavior often corresponds to a local convective instability when using a local approach.

The linear complex Ginzburg-Landau equation serves as a simple model for capturing both the short-time and long-time evolution of small perturbations $q(x, t)$ in spatially developing flows. We will use this model equation to illustrate fundamental concepts of linear global stability analysis. If the parameter μ, responsible for the local instability in equation (1), is now taken as a function of x, the Ginzburg-Landau equation becomes a variable-coefficient partial differential equation modeling non-parallel flows (Hunt & Crighton 1991). The Ginzburg-Landau equation with μ as a linear function in x can be used to mimic flows on the interval $[0, \infty)$ as shown in Chomaz *et al.* (1988). We will adopt the commonly used quadratic function (Hunt & Crighton 1991; Cossu &

Chomaz 1997),

$$\mu(x) = (\mu_0 - c_u^2) + \mu_2 \frac{x^2}{2}, \qquad \mu_2 < 0. \tag{8}$$

The flow is now susceptible to instabilities only when $\mu(x) > 0$, which defines a confined unstable region in the x-direction given by $-\sqrt{-2(\mu_0 - c_u^2)/\mu_2} < x < \sqrt{-2(\mu_0 - c_u^2)/\mu_2}$. The upstream and downstream edge of the unstable domain are referred to as branch I and II, respectively, and are indicated by the two black dashed lines in figures $4(a)$ and $5(a)$. The extent of this region depends on the parameter μ_2 which can be interpreted as the degree of non-parallelism of the flow. The operator $\mathcal{A}$ in (1) is non-normal if the term involving μ_2 and the convection term ν are non-zero. As demonstrated in Cossu & Chomaz (1997) and Chomaz (2005) the smaller μ_2 and/or the larger ν the stronger the non-normality of the operator $\mathcal{A}$. The parameter μ_2 thus plays a dual role: for large values of μ_2 the system is strongly non-parallel but weakly non-normal, while for very small values of μ_2 the system represents weakly non-parallel but strongly non-normal flow. For the latter case, a local analysis may be more appropriate as the resulting global eigensystem is rather ill-conditioned (Chomaz 2005; Trefethen & Embree 2005).

A global mode of the Ginzburg-Landau equation is defined as

$$q(x, t) = \phi(x) \exp(\lambda t) \tag{9}$$

and is a solution to the eigenvalue problem

$$\lambda \phi(x) = \mathcal{A}\phi(x) \qquad \phi(x) \to 0 \quad \text{as} \quad x \to \pm\infty, \tag{10}$$

where $\mathcal{A}$ is the operator defined in (1). The flow is globally unstable when the real part of any eigenvalue λ is positive which results in self-excited linear oscillations in the flow of a frequency given by the imaginary part of λ. For the case $\mu_2 \neq 0$ the eigenvalue problem (10) for the Ginzburg-Landau equation (1) can be solved analytically (Chomaz *et al.* 1987). One obtains

$$\lambda_n = (\mu_0 - c_c^2) - (\nu^2/4\gamma) - (n + 1/2)h, \tag{11a}$$

$$\phi_n(x) = \exp\{(\nu/2\gamma)x - \chi^2 x^2/2\}H_n(\chi x), \tag{11b}$$

with $h = \sqrt{-2\mu_2\gamma}$, $n = 0, 1 \ldots$ and H_n as the nth Hermite polynomial, scaled with $\chi = (-\mu_2/2\gamma)^{1/4}$. Global instability is determined by the sign of the first eigenvalue ($n = 0$) which yields the criterion for global instability as $\mu_0 > \mu_c$ where

$$\mu_c = \mu_t + \frac{|h|}{2}\cos\left(\frac{\text{Arg } \gamma}{2}\right) \tag{12}$$

and μ_t is the threshold value for absolute instability (7). The term Arg denotes the phase angle of γ. We therefore conclude from (12) that the threshold for a global instability is higher than the one for an absolute instability. Formulated in another way, an absolute instability is a necessary condition for a global instability.

The short-time behavior of a disturbance cannot be predicted by studying individual eigenmodes. Instead, a more detailed analysis of the properties of the stability operator $\mathcal{A}$ is necessary. When $\mu_2 \neq 0$ and $\nu \neq 0$ the Ginzburg-Landau operator $\mathcal{A}$ is non-self-adjoint (Davies 2002), *i.e.*, $\langle q_1, \mathcal{A}q_2 \rangle \neq \langle \mathcal{A}q_1, q_2 \rangle$. As a consequence, the global modes are non-orthogonal $\langle \phi_n, \phi_m \rangle \neq \delta_{nm}$, and although they may form a complete basis, they are nearly colinear and their superposition may lead to large transient growth (figure 5a). We will study this issue in more detail by considering an expansion in global modes. To this end, we find the adjoint global modes as

$$\psi_n(x) = \exp\{(-\nu^*/\gamma^*)x\}\phi_n^*(x) \tag{13}$$

which satisfy the adjoint eigenvalue problem

$$\lambda_n^* \psi_n(x) = \mathcal{A}^+ \psi_n(x), \tag{14}$$

where

$$\mathcal{A}^+ = \nu^* \frac{\partial}{\partial x} + \gamma^* \frac{\partial^2}{\partial x^2} + \mu^*(x) \tag{15}$$

with boundary condition $\psi_n(x) \to 0$ as $x \to \pm\infty$. The superscript * denotes the complex conjugate. The adjoint global modes ψ_n are bi-orthogonal to the global modes (11) according to

$$\langle \psi_n, \phi_m \rangle = N_{nm}\delta_{n,m} \tag{16}$$

with N_{nm} as a normalization factor that we choose such that $\|\phi_n\| = \|\psi_n\| = 1$. The adjoint mode (13) distinguishes itself from its direct counterpart (11b) mainly by the sign of the basic flow convection term ν. This manifests itself by a characteristic separation of the direct and adjoint global mode in space. In figure 6(a, b) the two first direct and adjoint global modes of the Ginzburg-Landau equation are shown where the separation in x is seen to increase for higher modes, until the support of the direct and adjoint mode is nearly disjoint. Consequently, $N_{nn} = \langle \phi_n, \psi_n \rangle$ becomes increasingly small, a phenomenon we shall investigate further in what follows.

We continue by stating that a sequence of global modes $\{\phi_n\}_{n=0}^{\infty}$ forms a basis if any solution of the Ginzburg-Landau equation has a norm-convergent expansion

$$q(x, t) = \sum_{n=0}^{\infty} \kappa_n \phi_n(x) \exp(\lambda_n t), \tag{17}$$

where the expansion coefficients κ_n are obtained using the adjoint global modes and the initial condition q_0 according to

$$\kappa_n = \frac{\langle q_0, \psi_n \rangle}{\langle \phi_n, \psi_n \rangle}. \tag{18}$$

The denominator of the above expression, *i.e.* N_{nn}, becomes very small when the direct and adjoint global modes have nearly disjoint spatial support. In this case, the expansion coefficients (18) of q become large. Although the amplitude of all stable global modes decreases monotonically in time, their superposition produces a wavepacket that transiently grows in time as it propagates in space.
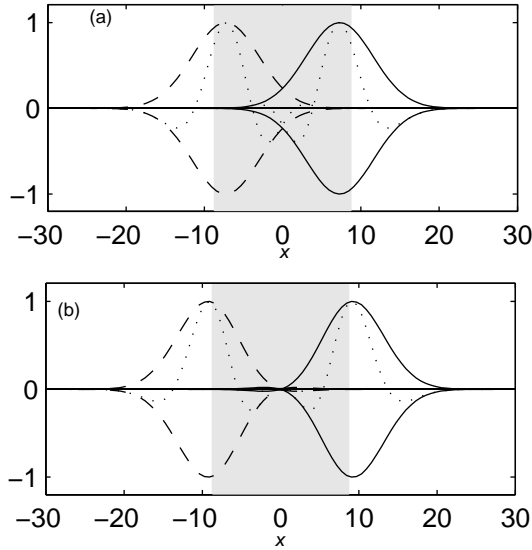
FIGURE 6. The absolute value of the first (*a*) and second (*b*) global (black lines) and adjoint eigenmode (dashed lines) of the Ginzburg-Landau equation. The real part of the modes are in dotted lines. The gray area marks the region of instability

Although it is possible (Ehrenstein & Gallaire 2005; Åkervik *et al.* 2007, 2008; Henningson & Åkervik 2008), in practice the short-time amplification of disturbances is rarely computed using global modes. Instead one computes the norm of the exponential matrix (Trefethen & Bau 1997), $\|e^{\mathcal{A}t}\|$, as we shall demonstrate next.

2.3. *Optimal energy growth and resolvent norms*

For sufficiently large transient amplifications nonlinear effects can no longer be neglected, and, in real flows, more complex instabilities or transition to turbulence are often triggered. For this reason it seems important to investigate the most dangerous initial condition that results in a maximum energy amplification over a specified time interval (Reddy *et al.* 1993; Reddy & Henningson 1993; Farrell 1988; Corbett & Bottaro 2001; Andersson *et al.* 1999; Luchini 2000).

	Subcritical	Supercritical
$\{\mu_0, \mu_2\}$	$\{0.38, -0.01\}$	$\{0.41, -0.01\}$
$\{\nu, \gamma\}$	$\{2 + 0.2i, 1 - i\}$	$\{2 + 0.2i, 1 - i\}$
$\{x_I, x_{II}\}$	$\{\pm 8.2\}$	$\{\pm 8.2\}$
$\{x_w, x_s, x_u, s\}$	$\{-11, 0, -3, 0.4\}$	$\{-11, 9, -9, 0.1\}$
$\{R, W, G, \gamma_0\}$	$\{1, 1., 0.1/1.0, 9\}$	$\{1, 0.1, 9\}$

TABLE 1. Parameters $\{\mu_0, \mu_2\}$, $\{\nu, \gamma\}$ of the Ginzburg-Landau equation given in (1) and (8). The critical values for global and absolute stability are $\mu_c = 0.3977$ and $\mu_t = 0.32$, respectively. External disturbances (B_1), sensor (C_2) and actuator (B_2) are Gaussian functions (see equations 108) with mean given by x_w, x_s and x_u, respectively and a width of $s = 0.4$. Design parameters $\{R, W, G, \gamma_0\}$ for the LQG- and $\mathcal{H}_\infty$-compensators are the control penalty (R), the covariance of the disturbance (W) and sensor noise (G), and a bound on the ∞-norm, (γ_0).

For simplicity, we will formulate and present results using the *discrete* Ginzburg-Landau operator A. See Appendix A for details of the numerical approximation of the operator $\mathcal{A}$. The continuous approach can be found in Trefethen & Embree (2005). The values of the Ginzburg-Landau parameters used in the computations that follows can be found in table 1.

The discrete energy norm given by (107) can, after a Cholesky decomposition of the energy weight matrix $M = F^H F$, be related to the standard Euclidean norm of a disturbance by

$$E(t) = \|q\|_M^2 = \|Fq\|_2^2. \tag{19}$$

We can now define the maximum transient growth of the perturbation energy at time t as

$$
\begin{aligned}
E_{max}(t) &= \max_{\|q_0\| > 0} \frac{\|q(t)\|_M^2}{\|q_0\|_M^2} \\
&= \max_{\|q_0\| > 0} \frac{\|Fe^{At}q_0\|_2^2}{\|Fq_0\|_2^2} = \|Fe^{At}F^{-1}\|_2^2 = \sigma_1^2
\end{aligned} \tag{20}
$$

where σ_1 is determined from a singular value decomposition,

$$Fe^{At}F^{-1} = U\Sigma V^H, \qquad \Sigma = \text{diag}\{\sigma_1, \ldots, \sigma_n\}. \tag{21}$$

The above expression contains an optimization over all possible initial conditions, and the peak value of $\sigma_1^2(t)$ is the maximum energy amplification over time. Optimal initial disturbances can be calculated according to $q_0 = F^{-1}V_1$ where V_1 is the right principal singular vector of the SVD in equation (21). The maximum growth and the corresponding optimal disturbance can also be obtained from power iterations (Andersson *et al.* 1999; Schmid & Henningson 2001).
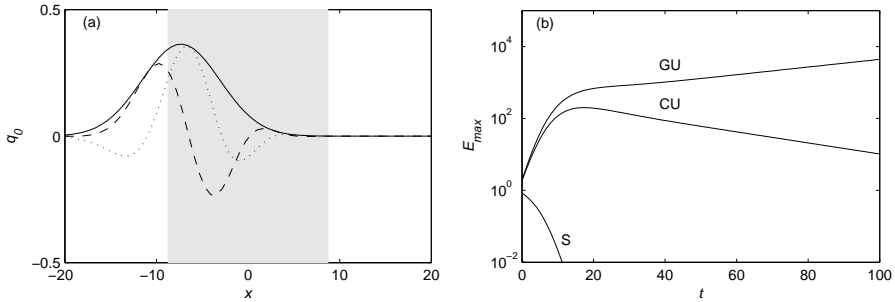
FIGURE 7. (*a*) Shape of an optimal disturbance with the absolute value shown in solid, the real and imaginary part shown in dashed and dotted, respectively. The gray region markes the unstable region, where disturbances grow exponentially. The maximum value of the optimal disturbance is located close to branch I. (*b*) Optimal energy growth, E_{max}, as a function of time. (S) stable configuration $\mu_0 < 0$: the perturbation energy decays exponentially for all time; (CU) convectively unstable configuration $0 < \mu_0 < \mu_c$: the perturbation energy is amplified initially but decays to zero asymptotically; (GU) globally unstable configuration $\mu_c < \mu_0$: the perturbation energy grows exponentially asymptotically. The values of the parameters used in the computations are listed in table 1.

The optimal initial disturbance of the Ginzburg-Landau equation shown in figure 7(*a*) is located at the upstream boundary of the unstable domain. As time evolves it traverses the unstable domain (gray region), where it can exhibit either decay, transient growth or asymptotic exponential growth as illustrated in figure 7(*b*) depending on the value of bifurcation parameter μ_0 (*i.e.* the Reynolds number for Navier–Stokes equations). The optimal energy growth curves shown in figure 7(*b*) corresponds to a stable (S), convectively unstable (CU) and globally unstable (GU) flow configuration. Note that, for both (S) and (CU) configurations, all global modes are stable. However, only for the latter case do we have $\mu_0 > 0$ yielding a locally convectively unstable spatial region. Consequently, a transient energy growth of two orders of magnitude can be observed before asymptotic decay sets in (Cossu & Chomaz 1997).

To conclude this section, we investigate the effect on global modes and on the global spectrum as the operator $\mathcal{A}$ is discretized. The spectrum of $\mathcal{A}$ is displayed in figure 8 by the green symbols using the analytical expression (11). The spectrum of the discretized Ginzburg-Landau operator A is shown by the blue symbols. A characteristic split of the eigenvalue branch is observed which is rather common in finite-precision stability computations of strongly nonnormal flows. The reason for this split is the insufficient resolution to accurately

capture the increasingly oscillatory behavior of the associated eigenfunctions. These observations are closely related to the notion of pseudospectra (Trefethen & Embree 2005).

It is misleading to assume that if $A\phi \approx s\phi$, then s is close the spectrum of A. If s is taken as an approximate eigenvalue in the sense that $\|A\phi - s\phi\|_M < \epsilon\|\phi\|_M$, we can conclude that, for normal systems, ϵ can be as chosen as small as one wishes. For non-normal systems, however, the minimum value of ϵ can become very large. This observation suggests the definition of the pseudospectrum of A as the sets in the complex plane such that

$$\{s \in \mathbb{C} : \|R(s)\|_M = \|(sI - A)^{-1}\|_M > \epsilon^{-1}\}. \tag{22}$$

The pseudospectrum of A (shown in figure 8) is visualized as a contour plot of the norm of the resolvent

$$\|R(s)\|_M = \|FR(s)F^{-1}\|_2 = \sigma_1(s) \tag{23}$$

where $\sigma_1(s)$ is the largest singular value of $FR(s)F^{-1}$. It is then straightforward to conclude that the eigenvalues of the discretized Ginzburg-Landau operator A are in fact ϵ-pseudoeigenvalues for ϵ equal to machine precision and thus align with the 10^{15}-contour of the resolvent norm in figure 8. For an alternative approach to characterize the system sensitivity see Biau & Bottaro (2004).

The resolvent contours moreover give an indication of the existence of non-normal effects, since the amount by which the contours protrude into the unstable half-plane can be used to estimate the maximum transient growth of energy (Trefethen & Embree 2005; Schmid 2007). We will return to this concept and use the resolvent norm from an input-output viewpoint in the next section, where we generalize the resolvent to transfer functions — one of the most central concepts in the design of control strategies.

2.4. *Stability of supercritical and subcritical flows*

Based on the global and local stability concepts introduced in the previous sections we are now in a position to define two fundamentally different scenarios that model the behavior of disturbances in a large number of flows.

The first model is known as the supercritical case, in which any flow disturbance will grow exponentially until it saturates due to nonlinearities, as shown in figure 4(a, b). A global analysis shows at least one unstable eigenmode of $\mathcal{A}$, yielding a globally unstable flow. This type of scenario prevails when the bifurcation parameter μ_0 of the Ginzburg-Landau equation is larger than the threshold μ_c. A local analysis confirms an absolutely unstable region since $\mu_c > \mu_t$ in (12) with μ_t as the threshold for a local absolute instability (given by equation 7). For more details on how the absolutely unstable region acts as a "wavemaker" that sheds waves in the downstream and upstream direction, see Chomaz (2005). Here, we will simply state the fact that linear local stability theory can predict the occurrence of unstable global modes and provide an estimate of the frequency at which these modes oscillate. The Karman vortex street behind a circular cylinder is a generic supercritical flow configuration,
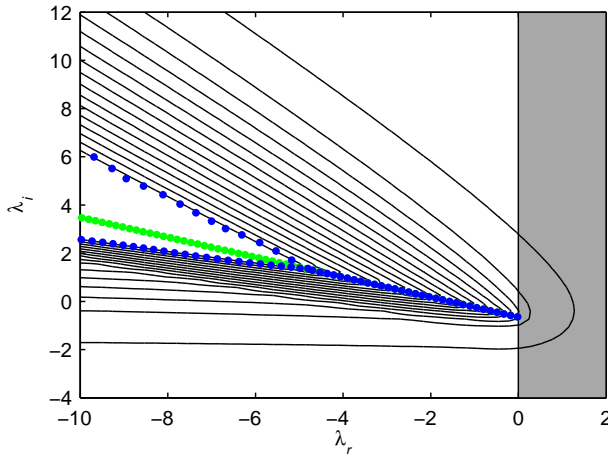
FIGURE 8.   Global spectrum of the subcritical Ginzburg-Landau equation (see table 1), where all the eigenvalues (blue dots) are in the stable half-plane. The unstable domain is in gray and the exact global spectrum is indicated in green. The numerically computed global eigenvalues (blue dots) exhibit a characteristic split, aligning with the resolvent contour that approximately represents machine precision. The resolvent norm contours range from 10^{-1} to 10^{15}.

and a global and local analysis of the cylinder wake can be found in Pier (2002) and Giannetti & Luchini (2007). It was first shown Provansal *et al.* (1987) that the transition in a wake behind a cylinder close to the critical Reynolds number is described by the Landau equation, *i.e.* the nonlinear Ginzburg-Landau equation without diffusion term. Since then, the Ginzburg-Landau equation (often in its nonlinear form) has been used extensively to model cylinder wakes, see Albarède & Monkewitz (1992); Monkewitz *et al.* (1996); Roussopoulos & Monkewitz (1996); Lauga & Bewley (2004); Cohen *et al.* (2005). Other globally unstable flow examples that have been investigated as to their self-sustained oscillatory behavior are, among others, hot jets (Lesshafft *et al.* 2006; Nichols *et al.* 2007) and a separated boundary layer flow over a bump (Marquillie & Ehrenstein 2002).

The second model is known as the subcritical case and describes the behavior of disturbances in convectively unstable flows (figure 5a, b). As a result of the non-normality of $\mathcal{A}$, a global analysis reveals the presence of transient energy growth (figure 5b) which cannot be captured by considering individual eigenmodes of the operator $\mathcal{A}$. Instead, one has to consider a superposition of global modes or the norm of the exponential matrix to accurately describe

this short-term phenomenon. Transient growth is observed for the Ginzburg-Landau equation when $0 < \mu_0 < \mu_c$. A local analysis shows that this corresponds to a region where the flow is convectively unstable. The wavepacket in figure 5(a) travels with a group velocity (U_{max}) composed of a dominant wave (c_u) which is associated with the local dispersion relation (3) analyzed in section 2.1. Prototypical convectively unstable flow configurations contain, among others, the boundary layer on a flat plate (Ehrenstein & Gallaire 2005; Åkervik *et al.* 2008), homogeneous jets and mixing layers (Ho & Huerre 1984).

The Ginzburg-Landau parameters $\{\nu, \mu_0, \mu_2, \gamma\}$ for modeling the linear stability of a subcritical or supercritical flow are listed in table 1. The critical value which delineates the two scenarios is $\mu_c = 0.4$.

3. Input-output behavior

Input-output analysis is a type of analysis of linear systems that is commonplace in systems theory (Kailath 1980). It is concerned with the general response behavior to various excitations of the linear system. In its generality, it goes beyond the concept of classical stability theory commonly practiced in fluid dynamics, as it is not only concerned with issues of stability (*i.e.*, the response to various initial conditions), but also with the short-term dynamics, the response to external (deterministic or stochastic) excitations and the influence of uncertainties in the underlying system (Jovanovic & Bamieh 2005; Schmid 2007). As such, it is thought of as an extension of stability analysis and helps reveal a more complete picture of the behavior of disturbances governed by the linear system.

The temporal response of the Ginzburg-Landau equation to initial conditions (both short-term transient and long-term asymptotic) has been considered in the previous section. In this section, we recast the Ginzburg-Landau model into an input-output framework. The analysis is applied to the convectively unstable case only, since these types of flows are sensitive to forcing and act as noise amplifiers (Huerre 2000). Globally unstable flows behave as *flow oscillators* with a well-defined frequency that is rather insensitive to external forcing.

This framework will build the foundation for the subsequent design of control schemes, since it allows the quantitative description of the open-loop dynamics, *i.e.* the response to, for example, excitation in the free-stream or to blowing/suction at the wall. We will denote the input sources by $u(t)$ and the measured outputs by $y(t)$. In many realistic flow cases, the output $y(t)$ will only be a subset of the state variable $q(t)$. For example, only shear or pressure measurements at the wall (or another specific location) will be available.

The common format for an input-output analysis is given by the state-space formulation

$$\dot{q}(t) \;=\; Aq(t) + Bu(t) \tag{24a}$$
$$y(t) \;=\; Cq(t) \tag{24b}$$
$$q(0) \;=\; q_0 \tag{24c}$$

where A represents the discrete Ginzburg-Landau operator, the matrices B and C govern the type and location of the inputs $u(t)$ and outputs $y(t)$, respectively, and q_0 stands for the initial condition. For the state-space formulation of the linearized incompressible Navier–Stokes equations see Farrell & Ioannou (1993) and Jovanovic & Bamieh (2005).

The continuous equations are discretized in space using a spectral Hermite collocation method described in Appendix A. The inputs $B = \{B_1, \ldots, B_p\}$ and outputs $C = \{C_1, \ldots, C_r\}^H$ have spatial distributions of the form of Gaussian functions given by equation (108). In what follows, we will formulate and present results based on matrices and the *discrete* Ginzburg-Landau operator A.

The corresponding adjoint state-space equations of (24) describing the evolution of adjoint state variable $r(t)$ can be written as (van der Schaft 1991)

$$\dot{r}(t) \;=\; A^+ r(t) + C^+ v(t) \tag{25a}$$
$$z(t) \;=\; B^+ r(t) \tag{25b}$$
$$r(0) \;=\; r_0. \tag{25c}$$

The discrete adjoint matrices are not simply the complex conjugate transpose (in other words, $(A^+, B^+, C^+) \neq (A^H, B^H, C^H)$), unless the inner-product used to derive the adjoint operator (14) has an associated weight M which is unity. For the more general case, $M \neq I$, we have

$$A^+ \;= M^{-1} A^H M, \tag{26a}$$
$$B^+ \;= B^H M, \tag{26b}$$
$$C^+ \;= M^{-1} C^H, \tag{26c}$$

where M is a positive-definite and Hermitian weight-matrix. In this work, M is chosen such that the inner-product produces the energy of the state variable (see Appendix A).

The system of equations (24) has the formal solution

$$y(t) = C e^{At} q_0 + C \int_0^t e^{A(t-\tau)} Bu(\tau) \; d\tau \tag{27}$$

where we identify the first part of the right-hand side with the homogeneous solution and the second part with the particular solution stemming from the forcing term Bu. Having covered the homogeneous solution (for $C = I$) in detail in the previous section, we now turn our attention to the particular solution.
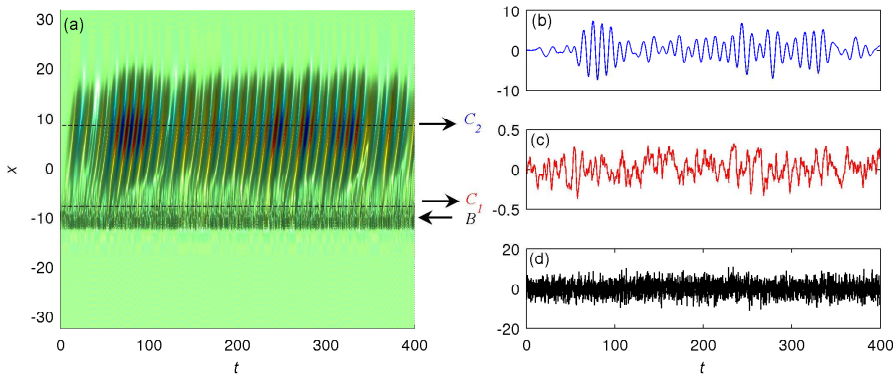
FIGURE 9. Example of the input-output behavior of the Ginzburg-Landau equation with one input and two outputs. In (a) the evolution in space and time of the state when forced by random noise is shown. The region between the dashed lines is convectively unstable. The locations of the forcing B ($x = -11$), the first output C_1 (at branch I) and the second output C_2 (at branch II) are marked by arrows. In (b) and (c) the output signals $y_1 = C_1 q$ and $y_2 = C_2 q$ and in (d) the input signal u are shown. Note that, in (c) the amplitude of the output signal y_1 is less than one, but further downstream in (b), the second output signal y_2 has an amplitude close to 10. This illustrates the amplifying behavior of the system.

Setting $q_0 = 0$ leaves us with the input-output relation

$$y(t) = C \int_0^t e^{A(t-\tau)} Bu(\tau) \; d\tau \qquad (28)$$

from which we will develop tools to capture and characterize aspects of the transfer behavior of an input signal $u(t)$ as it is passes through the linear system given by A.

Before analyzing the above input-output relation in all generality, a first simple numerical experiment shall demonstrate the response behavior of the convectively unstable Ginzburg-Landau equation (see figure 9). As an input signal $u(t)$ we choose white noise — drawn from a normal distribution with zero mean and unit variance — introduced at a location just upstream of the unstable region; the corresponding response $y(t) = Cq(t)$ is extracted at the two boundaries of the unstable domain, *i.e.*, at branch I and II. A first observation confirms the amplification of the signal as it traverses the unstable domain as well as the emergence of a distinct frequency from the noisy input. The system, thus, seems to act as both a noise amplifier (Huerre & Monkewitz 1990) and a filter. These two characteristics will be analyzed in more detail below.
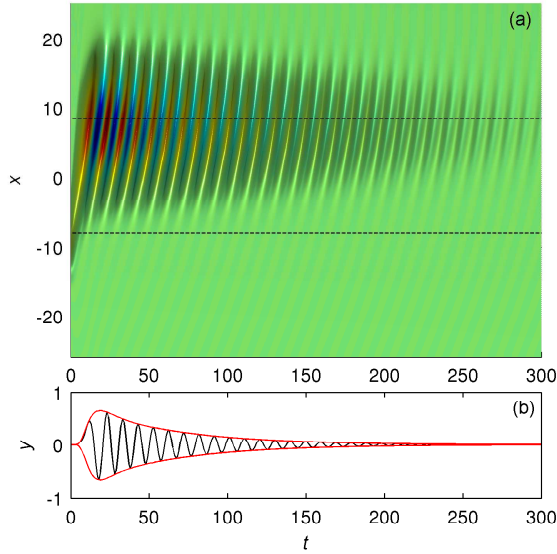
FIGURE 10. Impulse response of the Ginzburg-Landau equation: (*a*) The state response to an impulse introduced at $t = 0$ and $x_w = -11$. (*b*) The impulse response at branch II. The convective character of the instability is evident: a wavepacket grows as it enters the unstable domain, but is gradually convected away from this domain before it begins to decay.

3.1. *Impulsive and harmonic forcing*

The above introductory example has shed some light on the response behavior of the Ginzburg-Landau equations to external forcing. Even though the signal has demonstrated amplification and frequency selection of the linear system, a more general analysis is pursued that parameterizes the input-output behavior more precisely.

For this reason, we will consider two distinct input signals: an impulsive signal applied at a specified location $x_w = -11$ which will trigger what is referred to as the impulse response, and a harmonic signal, again applied at a given location, that yields the frequency response of the linear system.

For the impulse response we thus assume

$$u(t) = \delta(t) \tag{29}$$

which, according to (28), results in

$$y(t) = Ce^{At}B = g(t). \tag{30}$$

The spatial localization of the impulsive input signal is contained in the matrix B (see equation 108a). For $C = I$, the above solution (30) represents the Green's function of the Ginzburg-Landau equation. It forms the fundamental

solution of the linear system since particular solutions to more general external excitations can be constructed by a simple convolution of the input signal with the Green's function. The input-output system (24) is defined as stable if and only if the impulse response (30) decays as time tends to infinity. Consequently, the convectively unstable flow is input-output stable, which is in contrast to the globally unstable flow where an impulse will trigger the growth of an unstable global mode with a well defined frequency. For the convectively unstable case, the state impulse response $q(t) = e^{At}B$ for a pulse introduced at $x_w = -11$ is displayed in figure 10(a); the impulse response (30) is shown in figure 10(b). We observe the rise of a wavepacket with a distinct spatial wavenumber and propagation speed. As expected from the introductory example (figure 5a), the amplitude of the wavepacket grows throughout the unstable domain before it decays as the wavepacket passes branch II. For larger times, only the remnants of the wavepacket near branch II are observed.

The impulsive signal $u(t) = \delta(t)$ contains all temporal frequencies with equal amplitude. It is thus ideally suited to extract and analyze a frequency selection behavior from an unbiased input. On the other hand, we could choose an input signal with only one frequency (rather than all frequencies), *i.e.*

$$u(t) = e^{st} \qquad s \in \mathbb{C}. \tag{31}$$

Inserting the above input into (28), assuming A is globally stable and $t = \infty$ yields

$$y(t) \;=\; \int_0^\infty g(\tau)e^{s(t-\tau)}\,d\tau = \tag{32}$$

$$=\; \underbrace{\int_0^\infty g(\tau)e^{-s\tau}\,d\tau}_{G(s)}\, e^{st} = |G(s)|e^{(st+\phi)}.$$

We can identify the transfer matrix of dimension $r \times p$

$$G(s) = C(sI - A)^{-1}B \qquad s \in \mathbb{C}, \tag{33}$$

as the Laplace transform of the impulse response $g(t)$. Due to the linear nature of the Ginzburg-Landau equation an input e^{st} will generate an output with the same frequency but with a phase shift $\phi = \text{Arg } G(s)$ and an amplitude of $|G(s)|$. Since $G(s)$ is usually a rectangular matrix, the amplitude is defined as

$$|G(s)| = \sigma_1, \tag{34}$$

where $\sigma_1\{\cdot\}$ denotes the largest singular value of $G(s)$. The transfer function $G(s)$ fully describes the input-output behavior of the system, whereas the state-space formulation (24) describes the dynamics of flow.

The transfer function can be regarded as a generalization of the resolvent (22) introduced earlier. In fact, the pseudospectra in figure 8 are contours of $|G(s)|$ for the case $B = I$ which corresponds to a uniform distribution of the input and $C = F$ (where $M = F^H F$) which corresponds to the measurement of the flow energy. As discussed in section 2.4, the contours represent locations
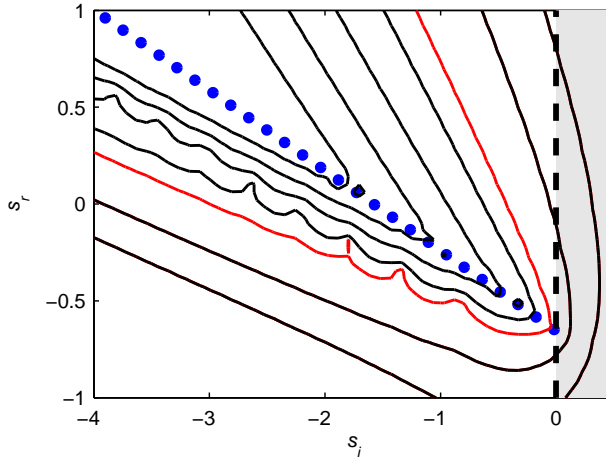
FIGURE 11.	Input-output pseudospectra where the black transfer function contour levels are $\{10^0, 10^1, 10^3, 10^4, 10^5, 10^6\}$. The red contour (with level 208) represents the largest contour value that crosses the imaginary axis. The blue symbols indicate the eigenvalues of A.

in the complex plane where approximate eigenvalues of A can be found for a given error norm ($\epsilon = 1/|G(s)|$). Figure 11 displays pseudospectra of the input-output system with B defined as in (108) and $C = F$. In this case, the contour levels correspond to the response amplitude of the output for a unit amplitude input of the form e^{st}.

As an example, we will concentrate on a purely harmonic forcing and set $s = i\omega$. The response of the linear system to this type of excitation is given by the expression

$$G(i\omega) = C(i\omega I - A)^{-1}B \qquad \omega \in \mathbb{R}, \tag{35}$$

and the largest response to a harmonic input can be defined as the maximum value of $|G(i\omega)|$,

$$\|G\|_\infty = \max_\omega |G(i\omega)|. \tag{36}$$

A remark on the choice of notation seems necessary: in the stability section, we defined the energy norm of the state vector $q(t)$ as $\|q\|_M^2 = q^H M q$, whereas the definition (36) of $\|G\|_\infty$ represents a norm of all stable transfer functions in the complex frequency space.

For normal systems the largest response to harmonic forcing is proportional to the distance of the real part of the largest eigenvalue of A to the imaginary axis, *i.e.*,

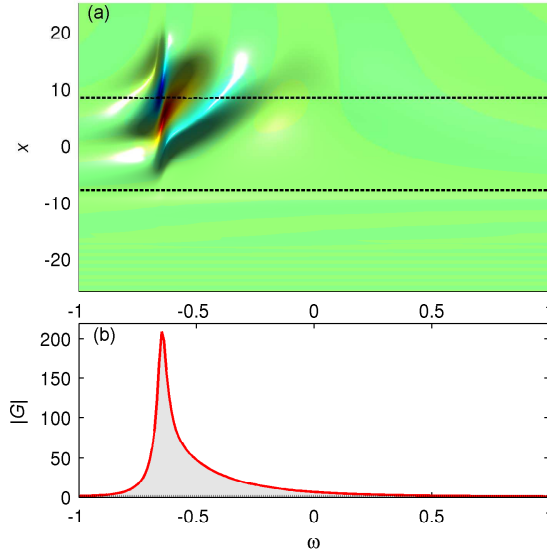$$\|G\|_\infty \sim 1/|\text{Re}(\lambda_1)|. \tag{37}$$

FIGURE 12. (*a*) The state response to harmonic forcing located upstream of branch I (lower of the two dashed lines). The largest response is at branch II (upper dashed line) for $\omega = -0.65$. (*b*) The frequency response, where the output is a Gaussian function (see Appendix A) located at branch II. In the gray area all forcing frequencies are amplified in the unstable domain, all other frequencies are damped illustrating a filtering effect. This response corresponds to the thick dashed line representing the imaginary axis in the pseudospectra plot in figure 11, and the peak value $\|G\|_\infty = 208$ corresponds to the red contour level.

For non-normal systems, however, the response of the system can be substantial even though the forcing frequency is nowhere close to an eigenvalue. The largest response $\|G\|_\infty$, in this case, is proportional to the largest value of the contour $|G(s)|$ that crosses the imaginary axis.

This feature is exemplified on the Ginzburg-Landau equation in figures 11 and 12. The state response (*i.e.*, the special case with $C = I$) to spatially localized, harmonic forcing at $x_w = -11$ is shown in figure 12(*a*). The largest response is obtained for a frequency of $\omega = -0.65$, and the location of the most amplified response in space is — not surprisingly — in the vicinity of branch II. In figure 12(*b*) the frequency response $|G(i\omega)|$ is shown which corresponds to the dashed line in the contour plot of figure 11. The peak of this response $\|G_c\|_\infty = 208$ is associated with the red contour in the pseudospectra plot (figure 11). The response computed from the distance to the nearest eigenvalue (37) has a value of only 56. It is thus confirmed that the frequency response for non-normal

systems is substantially larger than what can be inferred from the distance of the forcing frequency to the nearest eigenvalue.

3.2. *Stochastic forcing*

Under realistic conditions we rarely possess the exact knowledge of the disturbances influencing the flow system, and it is therefore essential to account for a certain amount of uncertainty. In this section we present fundamental techniques to characterize the response behavior within a statistical framework. This framework also gives insight into inherent stability properties of the flow (Hœpffner 2006; Schmid 2007), as for example in the case of channel flow studied by Farrell & Ioannou (1993); Bamieh & Dahleh (2001); Jovanovic & Bamieh (2005) and boundary layer by Hœpffner & Brandt (2008). When a fluid system is externally excited by stochastic disturbances, its response is best characterized by the state statistics, for instance, the *rms* values of the velocity components, the mean energy, or two-point correlations. In the context of aerodynamic flows, stochastic excitation can be attributed, among others, to free-stream turbulence, wall roughness, or incident acoustic waves.

A naive statistical analysis may consist of performing a large number of simulations by choosing sample realizations of the forcing and by subsequent averaging of the resulting flow quantities to obtain the desired statistics. A more direct approach involves the derivation of evolution equations for the statistical properties, such as *e.g.* two-point correlations, of the flow quantities. For linear systems it is possible to solve directly for the two-point correlations of the flow quantities in terms of the two-point correlations of the external excitation. The key equation relating second-order statistics of the excitation to second-order statistics of the state is the Lyapunov equation. In this section we will derive the Lyapunov equation and give examples of how to extract relevant information from its solution.

An introductory example can be seen in figure 13(*a*) where the temporal evolution of the state energy is displayed as a random forcing with zero mean and unit variance applied upstream of branch I. The results of five simulations are shown. Due to the stochastic nature of the forcing each simulation yields different results but, nevertheless, reveals a general trend: no energy is observed at the beginning of each simulation (since the initial condition is identically zero), but considerable energy levels are reached after an initial transient of approximately 100 time units and a quasi-steady regime in which the energy fluctuates about a mean value is established. Because of this observed noise amplification, convective unstable flows are also referred to as noise amplifiers. Furthermore, the dashed line shows the average of 50 simulations, representing the evolution of the mean energy. This curve is compared to the mean energy (red solid line) computed from the algebraic Lyapunov equation; this mean energy level is increasingly better approached as the number of simulations comprising the average is increased.
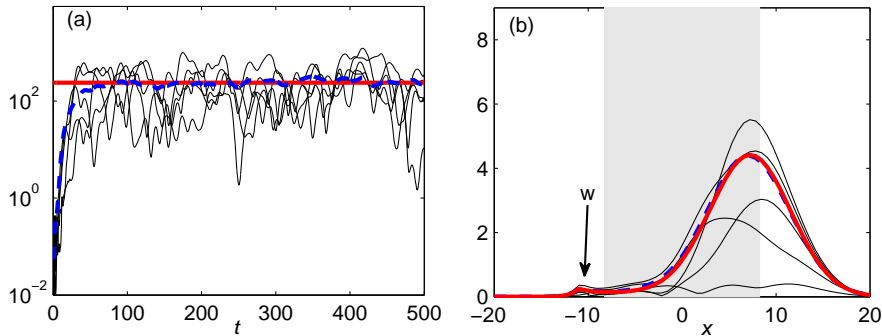
FIGURE 13. The response to stochastic forcing. (*a*) The evolution of the state energy for five different simulations (black lines), the mean state energy given by the solution of the algebraic Lyapunov equation (red solid line) and the energy averaged over 50 simulations (thick dashed line). (*b*) The thick red line shows the rms-value of the Ginzburg-Landau equation when excited by random forcing w at the location marked with an arrow. Five representative snapshots of the response to this forcing are shown by black thin lines; the average over 50 simulations is displayed by a thick blue dashed line.

Although the above experiment already demonstrates the amplification behavior of a convectively unstable linear system driven by stochastic forcing, the relation between the forcing covariance and the resulting state covariance will be established next.

We again consider the linear system given by equation (24), now driven by a stochastic process $u(t)$, *i.e.* a random time-varying input signal. We assume that A is globally stable but convectively unstable. To simplify the analysis, we also assume that the random variable u is normally distributed, *i.e.*, that the probability density function of the stochastic process is Gaussian, completely characterized by its mean and its variance.

To represent the mean and the variance of a random variable, we introduce the expectation operator $\mathcal{E}$. The mean of a scalar random variable ξ is then $m = \mathcal{E}\{\xi\}$, its variance is the quadratic expression $\sigma = \mathcal{E}\{\xi\xi^H\}$. From a statistical point of view, $\mathcal{E}$ can be thought of as an averaging operator (for example the action of an integral in time.)

We can similarly characterize the covariance of two random variables ξ and η as $P_{\xi\eta} = \mathcal{E}\{\xi\eta^H\}$. The covariance of two random variables gives information about the degree of similarity of the two signals. The above definition of the covariance is readily extended to vectors of random variables. The covariance of two random vector variables $f(t)$ and $g(t)$ of dimension n is simply the $n \times n$

matrix,

$$P_{fg}(t) = \mathcal{E}\{f(t)g(t)^H M\}. \tag{38}$$

Using the energy weight matrix M, we recover the kinetic energy of a state by simply taking the trace of the covariance matrix,

$$E(t) = \mathcal{E}\{\text{trace}(q(t)q(t)^H M)\} = \text{trace}(P_{qq}). \tag{39}$$

Furthermore, the diagonal elements of P_{qq} are the variance of the individual elements of $q(t)$. In particular, we define the root-mean-square (rms-value) of the disturbance as

$$q_{rms}(t) = \sqrt{\text{diag}\{P_{qq}\}} \tag{40}$$

From the above equations (39) and (40), it is clear that the covariance of the state contains all the essential statistics that is necessary for evaluating the response to stochastic forcing. We now return to our dynamical system (24) and derive an explicit expression of the state covariance in terms of the forcing covariance. For simplicity, we will assume that the applied forcing is uncorrelated in time, that is, it is a temporal white noise process:

$$\mathcal{E}\{u(t)u(t')^H M\} = WM\delta(t - t') \tag{41}$$

where t and t' are two instances in time, and W denotes the spatial covariance of u. For example, if u is a vector of random variables, $W_{ij} = \mathcal{E}\{u_i u_j{}^H\}$.

To derive an evolution equation for the covariance of the state, we start with the expression describing the time evolution of the state forced by u (*i.e.* equation 28 with $C = I$),

$$q(t) = \int_0^t e^{A(t-t')}Bu(t')\mathrm{d}t'. \tag{42}$$

As before, we have assumed a zero initial condition $q_0 = 0$.

We begin with the definition of the covariance matrix P_{qq} of the state at time t

$$
\begin{aligned}
P &= \mathcal{E}\{q(t)q(t)^H M\} \\
&= \int_0^t \int_0^t e^{A(t-t')} B \underbrace{\mathcal{E}\{u(t')u(t'')^H M\}}_{WM\delta(t'-t'')} B^H e^{A^H(t-t'')}\mathrm{d}t'\mathrm{d}t'' \\
&= \int_0^t e^{A(t-t')} BWB^+ e^{A^+(t-t')}\mathrm{d}t' \tag{43}
\end{aligned}
$$

where we have used the fact that u is uncorrelated in time and omitted the subscript $_{qq}$. We can differentiate this last expression in (43) with respect to time to obtain an evolution equation for P of the form

$$\dot{P} = AP + PA^+ + BWB^+ \qquad P(0) = 0. \tag{44}$$

In this expression $\dot{P}$ denotes the time derivative of the covariance matrix. The above equation is referred to as a differential Lyapunov equation. Given the covariance W of the forcing term u, we obtain the time evolution of the state covariance P. If the system A is asymptotically stable and, furthermore, A, W

and B are time-independent, the stochastically driven system relaxes after an initial transient into a statistical steady state. To obtain this steady state, we set $\dot{P} = 0$ and recover the algebraic Lyapunov equation

$$AP + PA^+ + BWB^+ = 0. \tag{45}$$

This statistical steady state is of interest if we study a system that is exposed to external forcing for a long time horizon, *e.g.*, the flow over a wing under cruise conditions. We like to emphasize that despite the presence of a steady statistical state, the state vector of the system as well as the external forcing are varying in time.

To illustrate the above statistical description of the system dynamics, we revisit the Ginzburg-Landau equation forced at the upstream edge of the convectively unstable region where we apply the external excitation of Gaussian form shown in equation (108a), with $u(t)$ as a scalar white noise process with zero mean and unit variance $W = 1$. The covariance of the state obtained by solving the algebraic Lyapunov equation (Datta 2003) is depicted in figure 15(*a*). The rms-value of this state-covariance is shown with a red line in figure 13(*b*) and the gray area marks the region of convective instability. In addition, we have represented the instantaneous state of five realizations of the forcing as well as the mean of 50 of these realizations, as we did in figure 13(*a*) for the total energy evolution in time. We see that the average of 50 realizations is close to the mean obtained from the Lyapunov equation, but a sample set of 50 realization is not yet enough for a converged statistical result. We will see more examples of this kind in the control section where we will quantify the performance of the controller using mean energy.

We conclude this section by stressing that transient growth mechanisms in hydrodynamic stability theory as well as the spatio-temporal evolution of disturbances can be recast into an input-output framework. For example, in this framework, the output signal $y(t)$ to random, impulsive or harmonic inputs shown in figures 9, 10 and 12, respectively, exhibits an initial growth in time before the signal either decays to zero or stabilizes around a steady state.

3.3. *Controllability and observability*

An important issue in the analysis of linear systems in state-space form concerns the mapping between input signals and the state vector and between the state vector and the output signals. Since for many realistic configurations the matrices B and C are rectangular, reflecting the fact that we force the system only at a few points in space and/or measure the system only at a limited number of sensors, we need to address the topic of controllability and observability (Kailath 1980).

In this section we will characterize the controllability and observability of a system in terms of covariance matrices of the state and the adjoint state, which in this context are called *Gramians*. We will continue to consider one input and one output and assume that A is stable (subcritical Ginzburg-Landau

equation), even though the theory extends to unstable systems as well (Zhou *et al.* 1999).

3.3.1. *Controllability — the POD modes*

The controllability of a system is concerned with finding the flow states most easily influenced by a given input. It can be shown (Lewis & Syrmos 1995; Antoulas 2005) that the minimum amount of input energy $\|u\|_2^2$ to bring the state from zero to the given initial condition q_0 is given by the expression

$$q_0^H P^{-1} q_0 \tag{46}$$

where P is the unique $n \times n$ matrix

$$P = \int_0^\infty e^{A\tau} B B^+ e^{A^+\tau} \, d\tau, \tag{47}$$

referred to as the *controllability Gramian* (for a derivation of this result in terms of an optimal control problem see Lewis & Syrmos 1995). Also note that the adjoint operators with superscript $^+$ are related to the conjugate transpose ^{H} according to (26).

Since for linear systems the state for an impulsive input at any given time is $q(t) = e^{At}B$, we recognize that the controllability Gramian (47) equals an infinite-horizon state covariance (43) with covariance $W = I$. This is not very surprising since one can interpret white noise as a set of impulse inputs that are uncorrelated in time. Furthermore, assuming A is stable, the controllability Gramian can be computed by solving the algebraic Lyapunov equation (45). In figure 15(a) the controllability matrix of the Ginzburg-Landau equation is shown graphically. The state components that respond to an input located just upstream of the unstable region are situated downstream of the unstable domain.

By diagonalizing the matrix P we obtain a measure of controllability for each component of the state vector. The diagonalization of the covariance matrix or, in the linear framework, the controllability Gramian is commonly referred to as the proper orthogonal decomposition (POD) (Lumley 1970) but is also known as empirical eigenfunction (EOF) decomposition, Karhunen-Loève decomposition or principal component analysis (PCA). The eigenvectors and eigenvalues of P are given by

$$P\phi_i = \lambda_i \phi_i, \qquad \lambda_1 \geq \cdots \geq \lambda_n \geq 0. \tag{48}$$

Since P is positive semidefinite, the eigenvalues are real and positive and the eigenvectors are orthogonal. The first two POD modes of the Ginzburg-Landau equation are shown in figure 14. Traditionally, the interpretation of these modes is that they represent decorrelated energy-ranked flow states. For example, the first POD mode ϕ_1 is the most energetic structure in the flow containing $\lambda_1 / \sum_{i=1}^n \lambda_i$ of the total flow energy. From a linear systems point of view, POD modes can be considered as the most controllable structures of the system for a given input. In this case the eigenvalue λ_i is a measure of how much the state
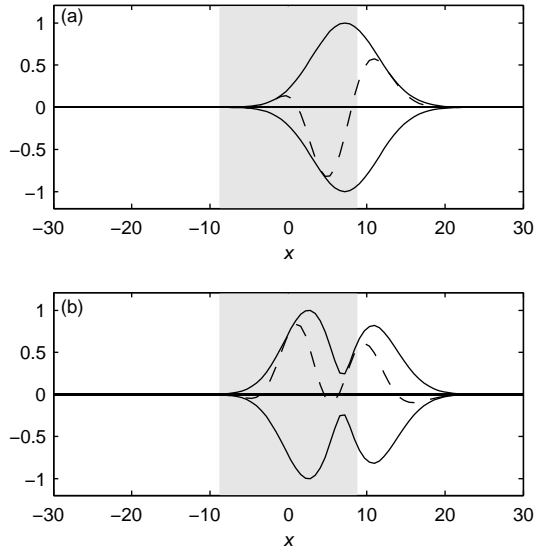
FIGURE 14. The first (*a*) and second (*b*) proper orthogonal decomposition (POD) mode obtained from an eigenvalue decomposition of the controllability Gramian in figure 15(*a*). Note that these modes are orthogonal. The absolute value is shown in solid and real part in dashed. The gray area marks the region of instability.

ϕ_i is influenced by the input. In particular, if P is rank deficient, there exists a zero eigenvalue, $\lambda_i = 0$, which would mean according to equation (46) that the energy required to influence the corresponding state is infinite. If P is not rank-deficient, we say that (A, B) is controllable.

3.3.2. *Observability — the adjoint POD modes*

The POD modes capture the response to input and thus span a controllable subspace of the state space. Equally important in the input-output analysis is to take into account the observable subspace by considering the relation between the outputs and flow states. A similar analysis as in the previous section for POD modes is thus performed, but this time for the adjoint system (25). Comparing the direct state-space equations (24) with their corresponding adjoint state-space equations (25) we observe that the output of the direct equations is related to the input of the adjoint equations.

The observability of a system is concerned with finding the initial conditions q_0 that will produce the largest output energy. For zero input the solution to the state-space equations is

$$y = Ce^{At}q_0. \tag{49}$$

The output energy is then given by

$$\|y\|_2^2 = q_0^H Q q_0 \tag{50}$$

where the *observability Gramian,*

$$Q = \int_0^\infty e^{A^+\tau} C^+ C e^{A\tau} \ d\tau, \tag{51}$$

is a unique matrix of dimension $n \times n$.

If we note that the impulse response of the adjoint state-space equations (25) is given by

$$r(t) = e^{A^+t} C^+ \tag{52}$$

the observability Gramian can be written as the state correlation matrix of the adjoint system

$$Q = \mathcal{E}\{rr^H M\}, \tag{53}$$

and the Gramian can be computed by solving the algebraic Lyapunov equation

$$A^+ Q + QA + C^+ C = 0. \tag{54}$$

In figure 15(*b*) the observability matrix of the Ginzburg-Landau equation is shown. The observable components of the state vector are located upstream of the unstable domain when the output location is at branch II (red dot in figure 15*b*).

By diagonalizing the observability Gramian,

$$Q\psi_i = \lambda_i \psi_i, \qquad \lambda_1 \geq \cdots \geq \lambda_n \geq 0, \tag{55}$$

we obtain an orthogonal set of functions called the adjoint POD modes or the most observable modes. These modes are flow structures that are ranked according to their contribution to the output energy. The corresponding eigenvalues λ_i provide a means to measure how observable the corresponding eigenvectors are. If there exist zero eigenvalues, $\lambda_i = 0$, Q is rank deficient, which means according to equation (50) that the corresponding adjoint POD mode does not contribute to sensor output. If Q has full rank, we say that (C, A) is observable.

It should be evident that in order to build an effective control system, both sufficient controllability and observability has to be established. Only in this case will the actuation have an appreciable effect on the flow system whose response, in turn, will be detectable by the sensors. Without adequate controllability or observability the flow of information from the system's output to the system's input will be compromised, and any control effort will be futile. Within the LQG-based feedback control framework, the controller will always stabilize the system if the unstable global eigenmodes are both controllable and observable. We will show how the controllability and observability of global eigenmodes can be determined in the next section.
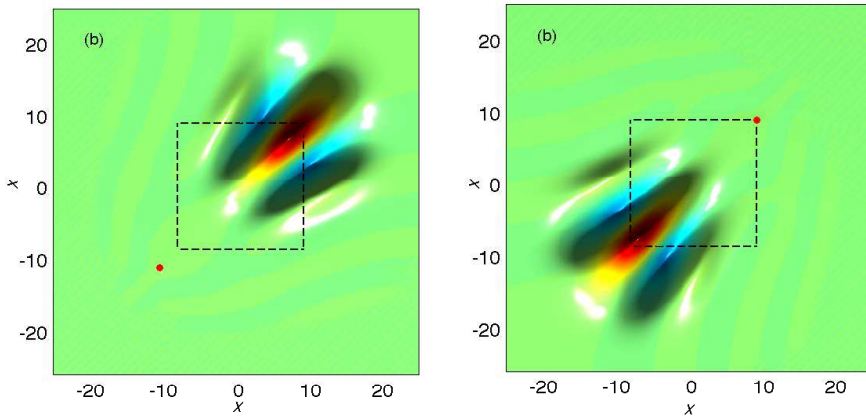
FIGURE 15. (*a*) The state covariance/controllability Gramian *P* of the Ginzburg-Landau equation. The Gramian describing how the state components are influenced by an input corresponds in a stochastic framework to the state covariance for white noise as input. The red circle signifies the forcing location ($x_w = -11$), the dashed box marks the region of instability. The states that are most sensitive to forcing, and thus controllable, are located downstream, at branch II. (*b*) The observability Gramian *Q* of the Ginzburg-Landau equation. The red circle markes the location of the output *C* at branch II. The initial states that contribute most to the output are located upstream, at branch I.

4. Model reduction

Any type of significant flow control applied to the discretized two- or three-dimensional Navier–Stokes equations requires some form of model reduction. Model reduction is concerned with the transformation of a system with a large number of degrees of freedom to an approximately equivalent system of markedly smaller size. The term "approximately equivalent" is often difficult to quantify and usually encompasses a measure of preservation of important system characteristics under the model reduction transformation. In this sense, model reduction becomes problem-dependent: for example, a transformation that preserves the inherent dynamics of the system may be inappropriate in capturing the input-output behavior.

Model reduction techniques for fluid systems typically rely on physical insight into the specific flow situation rather than on a systematic approach detached from the application. For instance, for spatially invariant systems it is possible to decouple the linear state-space equations in Fourier space. Control, estimation and other types of optimization can then be performed

independently for each wavenumber and then transformed back to physical space. This approach has been adopted in Högberg *et al.* (2003*a*,*b*); Hœpffner *et al.* (2005); Chevalier *et al.* (2006, 2007); Monokrousos *et al.* (2008).

The model reduction (or projection) technique (Obintata & Andersson 2001; Antoulas 2005) discussed in this paper involves three steps.

The first step consists of finding an expansion basis $\{\phi_i\}_{i=1}^r$ that spans an appropriate subspace of order r of the state space of order n, with $r \ll n$. We will present and compare three different subspaces using the Ginzburg-Landau equation: the subspace spanned by the least stable global eigenmodes, POD modes and the balanced modes (described in the next section).

In a second step, the state-system given by (24) is projected onto this subspace yielding the reduced-order model

$$\dot{\kappa}(t) = \hat{A}\kappa(t) + \hat{B}u(t) \tag{56a}$$

$$y(t) = \hat{C}\kappa(t) \tag{56b}$$

$$\kappa(0) = \kappa_0. \tag{56c}$$

When the expansion basis is non-orthogonal, we can use a set of adjoint modes $\{\psi_i\}_{i=1}^r$ associated with $\{\phi_i\}_{i=1}^r$, to obtain the entries of κ, $\hat{A}$, $\hat{B}$ and $\hat{C}$,

$$\hat{\kappa}_i = \frac{\langle q, \phi_i \rangle}{\langle \psi_i, \phi_i \rangle} \tag{57a}$$

$$\hat{A}_{i,j} = \frac{\langle \psi_i, A\phi_j \rangle}{\langle \psi_i, \phi_i \rangle} \tag{57b}$$

$$\hat{B}_i = \frac{\langle \psi_i, B \rangle}{\langle \psi_i, \phi_i \rangle} \tag{57c}$$

$$\hat{C}_i = C\phi_i \tag{57d}$$

with $i, j = 1, \ldots, r$. The term $\langle \psi_i, \phi_i \rangle$ is a normalization factor that we choose such that $\|\phi_n\| = \|\psi_n\| = 1$ and is smaller than one if the modes are non-orthogonal, that is $\psi_i \neq \phi_i$. The subscript M in the above inner products is omitted for brevity and we have assumed that B is a column vector and C a row vector, *i.e.* we continue to consider one input and one output.

The third and final step consists of estimating the error of the reduced order model (56). For control purposes it is not necessary for the reduced-order model to capture the entire dynamics described by the general state-space formulation (24), rather it suffices to accurately capture the input-output behavior described by the transfer function $G(s) = C(sI - A)^{-1}B$. It thus seems reasonable to estimate the error of a reduced-order system by comparing the norms of the transfer function (35) of the full system G and the reduced system $G_r = \hat{C}(sI - \hat{A})^{-1}\hat{B}$, *e.g.* $\|G - G_r\|_\infty$ (Obintata & Andersson 2001; Zhou *et al.* 2002; Green & Limebeer 1995). This is equivalent to calculating the difference of the peak values of the frequency response between the two models.
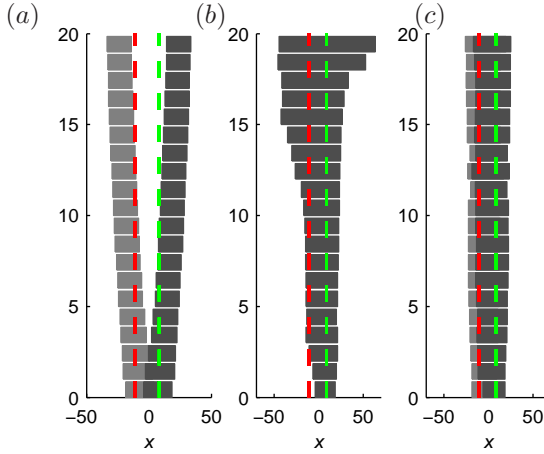
FIGURE 16. The spatial support of the first 20 global (a), POD (b) and balanced modes (c). The spatial support is defined as the region where the amplitude of a particular mode is larger than 2% of its maximum amplitude. The location of the input (just upstream of branch I) and output (at branch II) is marked with red and green dashed lines, respectively. The global modes span only the region around branch II. The first POD modes (b) are located at branch II, even though the higher modes quickly recover the input. The balanced modes (c) cover the region between input and output with only two modes. The areas marked with light gray in (a) and (c) represent the spatial support of the adjoint modes for the global and balanced modes. The spatial separation in x of the direct and adjoint modes, shown in (a) for global modes, is absent in (b) for the balanced modes.

4.1. *Global modes and input/output residuals*

Global modes (figure $6a, b$) preserve the dynamical characteristics of the system matrix A. Model reduction using global modes simply consists of an expansion of the state vector q into the leading global eigenmodes (10), where eigenmodes with substantial decay rates will be neglected. By this process, the resulting new system matrix $\hat{A}$ in (56) will consist of a diagonal matrix of the retained global eigenvalues. The new reduced state vector κ is given by the eigenfunction expansion coefficients, and the expansion coefficients of B (57c) and C (57d) are called the *controllability modal residuals* and the *observability modal residuals,* respectively (see also Bewley & Liu 1998).

It is clear that if $\langle \psi_i, B \rangle$ is zero in (57c), we will not be able to act on the corresponding state component κ_i and therefore on the global mode ϕ_i. Thus, we can use the controllability modal residual as a measure of controllability of
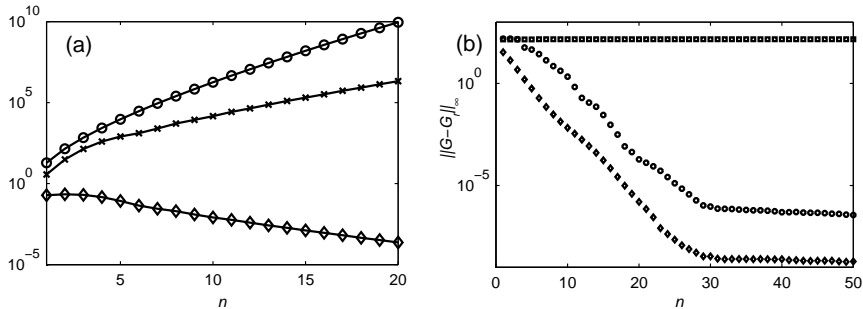
FIGURE 17. (*a*) The controllability modal residuals (crosses) of the first 20 global modes given by equation (57*c*) which is the product of the overlap of the actuator and adjoint mode $\langle \psi_i, B \rangle$ (diamonds) and the sensitivity defined by $(\langle \psi_i, \phi_i \rangle)^{-1}$ (circles). Although, the overlap of the spatial support of the actuator decreases for higher modes, the controllability still increases due to the rapid growth of the receptivity of higher modes to forcing, quantified by the inverse of $\langle \psi_i, \phi_i \rangle$. (*b*) Model reduction error of the POD (circles), balanced (diamonds) and global (squares) modes. For the balanced modes the error always decays by increasing the number of modes, in contrast to the error of POD modes. The error does not decay at all for the first 50 global modes due to the failure to project the input B located upstream of branch I onto the global eigenmodes located close and downstream to branch II.

the global mode by considering the amount of overlap between the support of the input and the support of the corresponding adjoint global mode. If this overlap is zero, the global mode is not controllable (Chomaz 2005; Lauga & Bewley 2004).

A similar derivation based on (57*d*) shows that in order for (C, A) to be observable, the spatial support of the sensor and the support of the global mode must overlap. If $\hat{C}_i = C\phi_i$ is zero, we will not be able to detect the eigenmode ϕ_i using a sensor characterized by C. This eigenmode is thus unobservable.

Owing to the term $\langle \psi_i, \phi_i \rangle$ in the denominator of (57*c*), additional attention has to be paid to the system's sensitivity due to non-normal effects: the forcing response or controllability of ϕ_i is inversely proportional to $\langle \psi_i, \phi_i \rangle$, *i.e.* the separation of global and adjoint modes. This separation is illustrated in figure 16(*a*), where the spatial support — defined as the region where the amplitude of a particular mode is larger than 2% of its maximum amplitude (see also Lauga & Bewley 2003) — of the first 20 global and adjoint modes is shown. We see that the global modes only span a small part of the domain, which is located near and downstream of the unstable domain (green dashed line),

whereas the corresponding adjoint modes are located upstream of the unstable domain (red dashed line); this results in a large sensitivity, $\langle \psi_i, \phi_i \rangle \ll 1$.

In figure 17(a) we display the controllability as the number of global modes is increased, together with the numerator and denominator of expression (57c). Whereas the numerator represents a measure of overlap between the input and the adjoint global modes, the denominator measures the degree of non-normality. The marked rise in controllability as more global modes are added is thus a compound effect of these two components. It illustrates that non-normal systems can be very sensitive to the external perturbation environment and that it is possible to manipulate the flow using very small actuator effort.

An upper limit of the error for reduced-order models based on global modes is given by (Skogestad & Postlethwaite 2005; Antoulas 2005)

$$\|G - G_r\|_\infty \leq \sum_{i=r+1}^{n} \frac{|\hat{C}_i \hat{B}_i|}{|\text{Re}(\lambda_i)|}. \tag{58}$$

From the above expression it is evident that choosing a subspace based on the criterion of dominant eigenvalues may not be appropriate if one wishes to approximate the input-output behavior. The reason is that the error norm (58) depends on the matrices B and C. Although the eigenvalues may exhibit substantial decay, for highly non-normal systems $\hat{B}$ is large yielding a large model reduction error as shown in figure 17(b) using square symbols.

In figure 18 we compare the frequency response of the full model $|G(i\omega)|$ of order $r = 220$ (blue dashed line) to the frequency response of the reduced models $|G_r(i\omega)|$ of order $r = 2, 4$ and 6 (green solid line). As before, the input B (at branch I) is located upstream and the output C (at branch II) downstream. The frequency response of the reduced models shows a large deviation from the true frequency response, even as the number of included modes is increased.

4.2. *POD modes*

For an improved transfer behavior of the reduced model we can base our subspace on the response of the linear system to external forcing. In this case, both the system matrix A and the control matrix B determine the dynamics of the driven system. To reduce a driven model, we will expand the state vector into the POD modes (48) (figure 14). The expansion in POD modes will be truncated at a convenient level that results in a significantly lower-dimensional system matrix but still retains the most energetic structures. These modes are ideal in detecting and extracting coherent fluid structures in a hierarchical manner that is based on their contribution to the overall perturbation energy of the flow. However, for control and input-output behavior low-energy features that are not captured by this expansion may be critically important.

We like to point out that the controllable subspace adequately spans the *response* to inputs but not necessarily the inputs themselves. This is illustrated in figure 16(b), where the spatial support of the first 20 POD modes are shown. The first POD modes capture the largest structures, located at branch II;
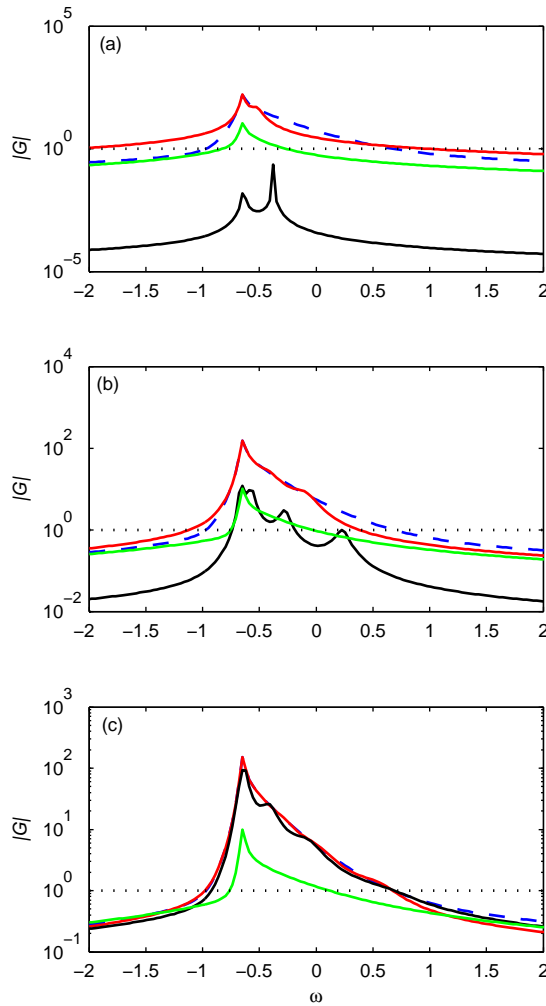
FIGURE 18. Comparison of the frequency response of the full Ginzburg-Landau equation with three reduced-order models. Blue dashed lines represent the full model of order $n = 220$. The performance of reduced-order models based on $r = 2, 4$ and 6 modes are shown in the (a), (b) and (c), respectively. Red lines represent the balanced modes, black lines the POD modes and green lines the global eigenmodes. We observe that the balanced modes capture the peak value of the frequency response which represents the main characteristic of the input-output behavior. The approximation of the frequency response for the open-loop case is unsatisfactory for POD models of order 2 and 4 and for all global-mode models.
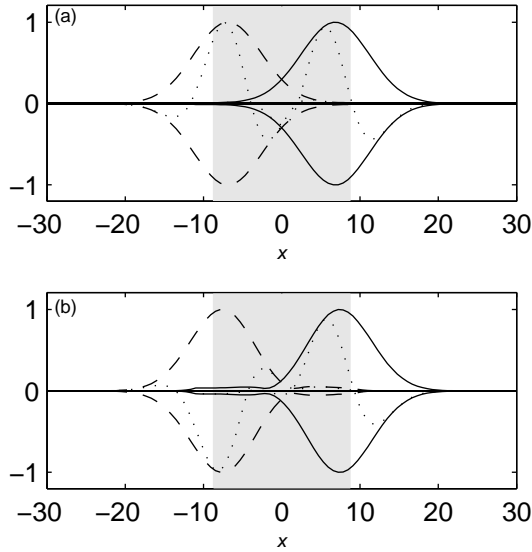
FIGURE 19. The first (*a*) and second (*b*) balanced mode. The modes are non-orthogonal and the adjoint balanced modes are shown in dashed line. The absolute value is shown in solid (direct) and dashed (adjoint), whereas the real part is shown with dotted lines. The gray area marks the region of instability.

however, in contrast to the global modes, the higher modes eventually cover the entire unstable domain including our input location. For this reason the error norm shown with black circles in figure 17(*b*) is not decreasing for the first three POD-modes; only when the fourth mode, which captures some of the input structure, is included in the expansion basis does the error norm begin to decrease. An explicit error estimate does not exist for POD modes; only after computing the frequency response of the two systems can one determine the error (given by the difference of the peak values in the frequency response).

Finally, in figure 18 the frequency response of the POD-based reduced model (black line) $|G_r(i\omega)|$ of order $r = 2, 4$ and 6 is observed to gradually approach the response of the full model.

4.3. *Balanced modes*

The third subspace is based on *balancing* the system and involves the three matrices A, B and C. It is based on the idea of reducing the dimensions of the original system by (i) removing the redundant states for characterizing the input-output behavior — the uncontrollable and unobservable states — and (ii) removing the states that are nearly uncontrollable and unobservable. This

technique of model reduction is referred to as balanced truncation (Moore 1981).

The balanced modes $\{\phi_i\}_{i=1}^r$ are defined as the eigenvectors of the product of the two Gramians,

$$PQ\phi_i = \phi_i \sigma_i^2, \qquad \sigma_1 \geq \cdots \geq \sigma_r \geq 0. \tag{59}$$

The eigenvalues σ_i are called the Hankel singular values (HSV). First two balanced modes are shown in figure 19.

To illustrate what *balancing* refers to, let us consider the projection of the Gramian matrices P and Q on a set of modes, for instance any of the modes introduced in this section. The projected matrices, denoted by $\hat{P}$ and $\hat{Q}$, have the elements

$$\hat{P}_{i,j} = \langle \psi_i, P\psi_j \rangle \tag{60a}$$

$$\hat{Q}_{i,j} = \langle \phi_i, Q\phi_j \rangle \tag{60b}$$

where ψ_i denotes the adjoint mode associated with ϕ_i. Balancing refers to the fact that if $\hat{P}$ and $\hat{Q}$ are obtained from a projection onto balanced modes, they become diagonal and equal to the Hankel singular values, *i.e.*

$$\hat{P} = \hat{Q} = \Sigma = \operatorname{diag}(\sigma_1, \ldots \sigma_r). \tag{61}$$

The balanced modes are flow structures that are ranked according to their contribution to the input-output behavior. These modes are influenced by the input and, in turn influence the output by the same amount, given by the corresponding Hankel singular values σ_i.

A very attractive feature of balanced truncation is the existence of an *a priori* error bound that is of the same order as the lowest bound achievable for any basis,

$$\sigma_{r+1} < \|G - G_r\|_\infty \leq 2 \sum_{j=r+1}^{n} \sigma_j. \tag{62}$$

In contrast to equation (58) the above error norm is independent of the input and output matrices B and C. The error norm for the balanced truncation model in figure 17(*b*) shows a rapid decay. In figure 18 we notice that the performance of balanced reduced-order models (red lines) $|G_r(i\omega)|$ is very good, and only two balanced modes are required to capture the peak response of the full system.

In summary, we would like to recall that each of the three sets of basis vectors (global modes, POD modes, balanced modes) span different subspaces of the state space and are therefore suitable for different applications. The spatial support is shown in figure 16 for the first 20 modes of each of the three sets. The balanced modes (right plot), by construction, cover the region between the input and the output with very few modes and are thus the appropriate set of functions to accurately capture the input-output behavior of our linear system.
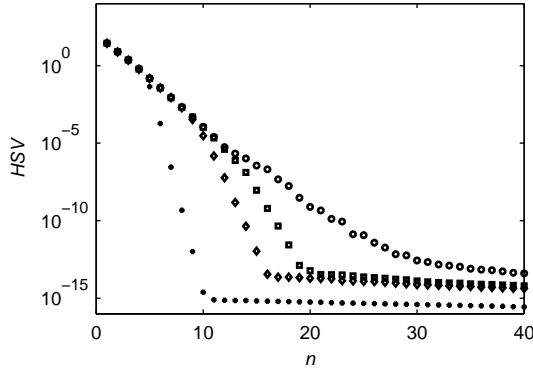
FIGURE 20.   Hankel singular values of the approximate balanced truncation and the exact balanced truncation with open circles. The number of singular values that are correctly captured increases with the number of snapshots (squares: 1000, diamonds: 500 and filled circles: 70 snapshots).

4.4. *The snapshot method*

To compute the POD modes or balanced modes we must first solve Lyapunov equations. This becomes prohibitively expensive as n exceeds approximately 10^5 which usually is the case when discretizing the Navier–stokes equations in two or three dimensions. Recently, numerous iterative methods to solve these equations have appeared (Antoulas 2005; Antoulas *et al.* 2001).

A different approach to approximate the Gramians without solving the Lyapunov equations — the so-called snapshot-based balanced truncation — has recently been introduced (Willcox & Peraire 2002; Rowley 2005). It is based on the snapshot technique first introduced by Sirovich (1987) for computing POD modes. We will demonstrate the method for one input and one output, see Rowley (2005) for additional details.

We begin with collecting r snapshots $q(t_j)$ at discrete times $t_1, \ldots, t_r$, of the response of the system (24) to an impulse $\delta(t)$. These snapshot are gathered as columns in a $n \times r$ matrix X, *i.e.*

$$X = [e^{At_1}B, e^{At_2}B, \ldots, e^{At_r}B]\sqrt{\Delta_r}, \tag{63}$$

where Δ_r stands for the quadrature coefficients of the time integral in equation (47). Instead of solving the Lyapunov equation (45), we can approximate its solution, *i.e.* the controllability Gramian P as

$$P \approx XX^H M. \tag{64}$$

If we observe that $e^{A^+t}C^+$ is the impulse response of the adjoint state-space equation (25), we can construct an approximation of the observability

Gramian Q

$$Q \approx YY^H M \tag{65}$$

by collecting a sequence of snapshots of the adjoint impulse response in the $n \times r$ matrix

$$Y = [e^{A^+ t_1} C^+, e^{A^+ t_2} C^+, \ldots, e^{A^+ t_r} C^+]\sqrt{\Delta_r}. \tag{66}$$

In the method of snapshots, instead of solving the large $n \times n$ eigenvalue problem (59) one can form the singular value decomposition of the $r \times r$ matrix,

$$Y^H MX = U\Sigma V^H. \tag{67}$$

The approximate Hankel singular values (HSV) are given in the diagonal matrix Σ. The normalized balanced modes and the associated adjoint balanced modes are recovered from

$$T = XV\Sigma^{-1/2}, \qquad S = YU\Sigma^{-1/2}. \tag{68}$$

Usually the number of snapshots r is significantly smaller than the number of states n, which makes this method computationally tractable for systems of very large dimensions.

Figure 20 shows the HSVs for the exact balanced truncation (solving two Lyapunov equations) and the approximate HSVs (using the snapshot method). For improved results more snapshots may be taken during periods of large transient energy growth and fewer snapshots as the energy decreases. Snapshot-based balanced truncation has been applied to channel flow (Ilak & Rowley 2008) and to the flow around a pitching airfoil (Ahuja *et al.* 2007).

5. Control

The natural extension to the investigations of the previous sections — the response behavior of a linear system to initial conditions and external excitations — is concerned with attempts to manipulate the inherent dynamics of a system or to control it. A substantial body of literature on flow control has accumulated over the past decade, with topics ranging from laminar flow control (Joslin 1998) to control of turbulence (Moin & Bewley 1994), from opposition control (Choi *et al.* 1994) to suboptimal (Bewley & Moin 1994) and nonlinear control (Bewley *et al.* 2001; Zuccher & Bottaro 2004; Guégan *et al.* 2006). Reviews on the subject of flow control can be found in Gunzburger (1995); Gal-El-Hak (1996, 2000); Bewley (2001); Kim (2003); Kim & Bewley (2007).

The framework laid out in the following sections falls in the category of *linear feedback control* (Kwakernaak & Sivan 1972; Anderson & Moore 1990; Zhou *et al.* 2002; Skelton *et al.* 1998; Skogestad & Postlethwaite 2005). In particular, our objective is to minimize the perturbation energy resulting from asymptotic or transient instabilities of the uncontrolled system during the transition process in order to suppress or delay turbulence (Joshi *et al.* 1997; Bewley & Liu 1998; Högberg *et al.* 2003*a*). Since the disturbance energy growth is initially

a linear process (Schmid & Henningson 2001) it seems prudent to design control schemes for the linearized governing equations. However, linear control has also been applied with considerable success to the full Navier–Stokes equations (Chevalier *et al.* 2007), and attempts have been made to relaminarize a fully developed turbulent flow (Högberg *et al.* 2003*b*).

We will consider two fundamentally different stability scenarios for the evolution of perturbations q governed by the non-parallel Ginzburg-Landau equation: (i) local convective instabilities and (ii) global instabilities. The parameters for the two cases are listed in table 1.

5.1. *The concept of feedback*

The actuation on the flow can be accomplished by various means, such as, for example, the injection of fluid through blowing/suction holes in the wall. Within the region of validity of our underlying physical model, it is possible to compute a control strategy in advance that will retain the flow in a laminar state. This procedure is referred to as open-loop control. However, under the presence of uncertainty over the exact disturbance environment (or the validity of our physical model), open-loop control will fail. Instead, one can monitor the flow through measurements and adjust the actuation accordingly such that predefined objectives are met. A control setup of this type is known as closed-loop control. It uses feedback to establish a connection between the output from the system (*i.e.* the measurement signal) and the input to the system (*i.e.* the control signal). Under realistic conditions, we are faced with a wide range of unknown variations, such as modeling errors or sensor noise, and a feedback-type control system is required to efficiently compensate for these uncertainties.

The main idea of linear feedback control is shown in figure 1. The entire system is described in state-space form as follows

$$\dot{q} = Aq + B_1 w + B_2 u, \tag{69a}$$
$$z = C_1 q + Du, \tag{69b}$$
$$y = C_2 q + g. \tag{69c}$$

This set of equations is commonly referred to as the *plant*. The first equation (69a) describes the dynamics of our linear system captured in the system matrix A as external forces, modeled by $B_1 w$ and $B_2 u$, are applied. We have decomposed the input into two terms with $B_1 w(t)$ describing the effect of external sources of excitations and $B_2 u(t)$ representing the control input. The variable $z(t)$ given by the second equation (69b) represents the objective function as described below. The third equation (69c) describes a connection between the state q and the measurements y, where the additional term g accounts for noise contaminating the measurements. In general, the objective is to find a control signal $u(t)$ such that the influence of the external disturbances w and g on the output z is minimized. The above set of equations (69) has been discretized using a Hermite collocation method as described in Appendix A.

Our objective is to find a control signal $u(t)$ such that the perturbation energy contained in the state variable $q(t)$ is minimized. Furthermore, the energy input expended by the control must be smaller than the amount of energy gained by it. Thus, in addition to focusing on the perturbation energy we also have to penalize our control effort. This results in a objective (or cost) functional of the form

$$\|z\|_2^2 = \|C_1 q\|_2^2 + \|Du\|_2^2 = \int_0^T q^H \underbrace{C_1^H C_1}_{M} q + u^H \underbrace{D^H D}_{R} u \, dt \qquad (70)$$

where M and R are positive semi-definite matrices; we have furthermore assumed that $D^H[C_1 \; D] = [0 \; I]$ in order to get zero cross terms (Zhou *et al.* 2002). It is important to realize that the 2-norm in the above expression is defined both over time and space. Note that if C_1 is chosen as F in equation (19) then the kinetic energy of the disturbance will be minimized. In the above setup we have assumed that the full state q is known, but for realistic flow situations the complete instantaneous velocity field is not available for determining an appropriate feedback. We thus have to *estimate* the full state vector resulting in an approximate state vector $\hat{q}$, reconstructed from the measurements $y(t)$ via an estimation problem. A controller based on an estimated state vector is known as an output feedback controller or a compensator.

5.2. *The LQG framework*

If we assume that the unknown disturbance noise w and the measurement noise g are given by white-noise stochastic processes with zero mean and respective covariances W and G, a compensator can be found that minimizes the cost functional (70). In addition, the closed-loop control is guaranteed to be stable, if the plant is both observable and controllable. In fact, a sufficient condition for a global minimum value of (70) is that the system is stabilizable and detectable. A system is stabilizable (detectable) if all unstable global modes are controllable (observable).

The control will be optimal in minimizing (70) which stems, in one part, from the optimal filtering of noise that has corrupted our signal (Kalman 1960) and, in another part, from the optimal control when the entire state vector is assumed to be available. These two separate problems — the estimation problem and the full-information problem — can then be combined to construct a compensator. This two-step procedural framework matured in the 1960's into what we now refer to as Linear Quadratic Gaussian (LQG) control (Kwakernaak & Sivan 1972; Anderson & Moore 1990). The assumption that $w(t)$ and $g(t)$ are white-noise stochastic processes may be far from reality in some applications; it is, however, possible to describe a plant with colored-noise input in terms of an augmented system with white-noise input (Lewis & Syrmos 1995).

In applications LQG control is particularly successful when the system operator A (in our case the Ginzburg-Landau equation) accurately describes the modeled physical phenomenon. The remaining uncertainties in the overall

model are thus restricted to the inputs represented by stochastic disturbances with known statistical properties. For this reason, the LQG framework is appropriate when we can rely on an accurate plant, while a precise knowledge of external disturbances and the degree of noise contamination of the measurements are not available.

If the external disturbances are stochastic variables, the state will as well be a stochastic process, and the objective function (70) can therefore be written as

$$\|z\|_2^2 = \mathcal{E}\left\{q^H M q + u^H R u\right\}. \tag{71}$$

As alluded to above, we will determine the optimal control $u(t)$ in (69) based on noisy measurements $y(t)$ such that the cost functional (71) is minimized. The first step in constructing such a compensator is to estimate the full state $q(t)$ given only the noisy measurements. After the state has been successfully estimated, we assume, in a second step, that the control $u(t)$ and the estimate of the state $\hat{q}(t)$ satisfy a linear relation involving some yet unknown matrix K, *i.e.*,

$$u(t) = K\hat{q}(t). \tag{72}$$

The goal of this second step is then to find such a matrix K, which is referred to as the control gain.

At the heart of the LQG-framework is the separation principle (Skogestad & Postlethwaite 2005) which states that the controller that minimizes (70) can be computed in two independent steps: (i) we can solve the estimation problem to obtain an approximation $\hat{q}$ of the true state q without any reference to the control problem; (ii) to find the control gain K in (72) we do not need the estimate $\hat{q}$ in (72) but instead can assume the full-information relation $u(t) = Kq(t)$. One of the important consequences of the separation principle is the fact that the final compensator, using (72) based on the control gain K obtained by considering $q(t)$ (not $\hat{q}$), will always yield a closed-loop system that is stable if and only if each of the two separate problems (estimation and full-information control) are themselves stable (see Zhou *et al.* 2002). In addition to stability, the closed-loop system will be optimal. To simplify the expressions in the following analysis we assume that the adjoint system is derived using a standard Euclidean inner-product, *i.e.* the dual or the adjoint of the plant (69) is given simply by its complex conjugate transpose.

5.2.1. *The estimation problem*

Under the assumption that the measurements capture a sufficient amount of the system's dynamics (*i.e.* that we have significant observability), it is possible to estimate or observe the state vector by using a Kalman filter (Kalman 1960). In this section we derive the algebraic Riccati equation for estimation and show examples on the Ginzburg-Landau equation. For additional details see *e.g.* Lewis & Syrmos (1995); Anderson & Moore (1990).

We assume zero initial conditions, since we are interested in the controller performance as an average over long time while the system is excited by external

perturbations. We further assume white-noise stochastic processes for $w(t)$ and $g(t)$ with zero mean. The estimator then takes on the form

$$\dot{\hat{q}} = A\hat{q} + B_2 u - L(y - \hat{y}), \tag{73a}$$
$$\hat{y} = C_2\hat{q}. \tag{73b}$$

In the above expression, we compare the measurement y from the state and the measurement $\hat{y}$ from the estimated state and feed back the mismatch in these two quantities using the estimator gain L. To analyze the performance of the estimation problem, it is instructive to derive the dynamics of the estimation error $\tilde{q} = q - \hat{q}$. Combining (69) and (73) we obtain

$$\dot{\tilde{q}} = A\tilde{q} + B_1 w + L(y - \hat{y}). \tag{74}$$

Substituting the explicit dependence of the two measurements on the state q and estimated state $\hat{q}$, respectively, we obtain

$$\dot{\tilde{q}} = (A + LC_2)\tilde{q} + B_1 w + Lg \tag{75}$$

where the estimation error dynamics is governed by the matrix $A_e = A + LC_2$ and is driven by two source terms, namely the external excitation w and the sensor noise g. We aim at finding an estimator gain L such that A_e is asymptotically stable and is not sensitive to the external perturbations $B_1 w + Lg$. Since (69) is driven by noise, the state $q(t)$ and the output $y(t)$ are consequently random processes whose stochastic properties have to be considered in finding the estimator gain L. The error covariance is given as

$$P(t) = \mathcal{E}\{\tilde{q}\tilde{q}^H\} \tag{76}$$

which represents a measure of uncertainty in the estimate. Smaller values of $P(t)$ indicate a better estimate as the estimation error is more tightly distributed about its mean value of zero. If the estimator (75) is stable, the error $\tilde{q}(t)$ will eventually reach a steady-state with a constant mean and covariance. The steady-state covariance can be readily obtained by solving the Lyapunov equation

$$A_e P + P A_e^H + LGL^H + B_1 W B_1^H = 0 \tag{77}$$

where G and W are the covariance matrices of $g(t)$ and $w(t)$, respectively. The optimal estimation feedback gain L is then chosen to both keep (75) stable and to minimize the mean of the steady-state estimation error. We obtain the mean estimation error from the covariance (76) using the expression (39),

$$J = \mathcal{E}\{\tilde{q}\} = \text{trace}(PM), \tag{78}$$

where the mean is chosen as the kinetic energy. This minimization has to be accomplished under the constraint that P satisfies the above Lyapunov equation (77). We add this constraint to the cost functional J via a Lagrange multiplier Λ and obtain the Lagrangian $\mathcal{M}$

$$\begin{aligned}\mathcal{M} &= \text{trace}(PM) + \\ &\quad + \text{trace}[\Lambda(A_e P + P A_e^H + LGL^H + B_1 W B_1^H)].\end{aligned}$$
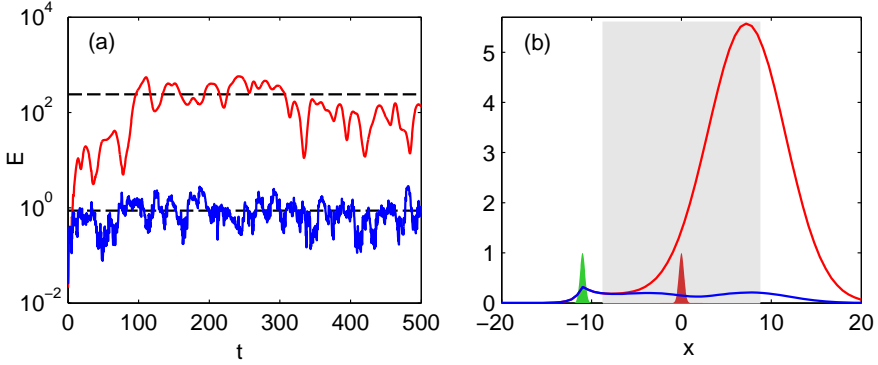
FIGURE 21. (*a*) The mean of the error covariance trace(PM) (lower dashed line) obtained by solving the Riccati-equation (81) is compared to the estimation error (blue line) obtained by marching the estimator in time (73). Also, the mean value of the state (top dashed line/red line) is shown and found to be nearly three orders of magnitude larger than the estimation error. It is evident that both the state and the estimation error reach a steady state. (*b*) The rms-value of the error and the state are shown in blue and red lines, respectively. The red and green Gaussian functions represent the location of the input (stochastic disturbances) and the sensor. The error attains its minimum value just downstream of the sensor location and increases upstream as well as downstream of it.

We thus minimize J subject to the constraint (77) by equivalently finding stationary points of $\mathcal{M}$ without imposed constraints. The necessary conditions for a minimum are given by:

$$\frac{\partial \mathcal{M}}{\partial P} = A_e^H \Lambda + \Lambda^H A_e + M = 0, \tag{79a}$$

$$\frac{\partial \mathcal{M}}{\partial \Lambda} = A_e P + P A_e^H + LGL^H + B_1 W B_1^H = 0, \tag{79b}$$

$$\frac{\partial \mathcal{M}}{\partial L} = 2\Lambda(PC_2^H + LG) = 0. \tag{79c}$$

We can eliminate Λ from equation (79c) to obtain an expression for the estimator gain

$$L = -PC_2^H G^{-1}. \tag{80}$$

Inserting the expression above into the second condition (79b) leads to a quadratic matrix equation for the error covariance P

$$AP + PA^H - PC_2^H G^{-1} C_2 P + B_1 W B_1^H = 0 \tag{81}$$

which is referred to as an algebraic Riccati equation. In Laub (1991); Datta (2003) efficient methods of solving the Riccati equations can be found. We can thus determine the optimal estimation gain L by solving (81) for the error covariance P which, using (80), results in L. No requirements of observability or controllability have to be explicitly imposed on the estimation problem; however, if we place the input describing external disturbances B_1 and the sensor C_2 such that (C_2, A) is observable and (A, B_1) is controllable, then the resulting Riccati equation (81) will have a unique positive definite solution. Moreover, the closed-loop estimator will then be asymptotically stable.

One way to investigate the performance of the estimator, is to compare the energy of the true flow state with the energy of the estimation error. In figure 21(a) the temporal evolution of the state energy (red line) and of the estimation error (blue line) are shown. The energy of the estimation error is nearly three orders of magnitude smaller than the energy of the true state. In the same figure, the mean energy of the estimation error — obtained by solving the Riccati-equation (81) — and the mean energy of the state — obtained by solving the Lyapunov equation (45) — are plotted with dashed lines. We observe that the solutions of the Riccati equation and the Lyapunov equation provide the mean energy in which, respectively, the estimation error and state energy fluctuate about. In figure 21(b), the corresponding rms of the error $\tilde{q}_{rms}$ together with the rms of state q_{rms} are shown.

5.2.2. *Full-information control*

The second step in the design of an LQG-compensator involves the solution of an optimal control state-feedback problem. We show in this section that the optimal solution is, again provided by the solution of a Riccati equation. The reader is directed to Anderson & Moore (1990); Lewis & Syrmos (1995) for more detailed derivations.

We seek a control $u(t)$ as a linear function of the flow state $q(t)$ that minimizes the deterministic cost functional

$$J = \frac{1}{2} \int_0^T q^H M q + u^H R u \; dt, \qquad M, R > 0, \qquad (82)$$

while satisfying the initial value problem

$$\dot{q} = A q + B_2 u, \qquad q(t = 0) = q_0. \qquad (83)$$

We perform the steps analogous to the estimation problem by first defining an augmented Lagrangian $\mathcal{N}$ of the form (Lewis & Syrmos 1995)

$$\mathcal{N} = \frac{1}{2} \int_0^T (q^H M q + u^H R u) + \lambda^T (-\dot{q} + A q + B_2 u) \; dt \qquad (84)$$

where λ is again a Lagrange multiplier which enforces the initial value problem (83). The necessary conditions for a minimum of $\mathcal{N}$ result in the following set

of equations

$$\frac{\partial \mathcal{N}}{\partial \lambda} = -\dot{q} + Aq + B_2 u = 0, \tag{85a}$$

$$\frac{\partial \mathcal{N}}{\partial q} = \dot{\lambda} + Mq + A^H \lambda = 0, \tag{85b}$$

$$\frac{\partial \mathcal{N}}{\partial u} = Ru + B_2^H \lambda = 0. \tag{85c}$$

We proceed by assuming a linear relation between the state $q(t)$ and the Lagrange multiplier $\lambda(t)$

$$\lambda(t) = X(t)q(t), \tag{86}$$

where $X(t)$ is self-adjoint and positive semidefinite. Using this linear relation and the optimality condition (85c) yields the following feedback law:

$$u(t) = \underbrace{-R^{-1}B_2^H X(t)}_{K(t)} q(t). \tag{87}$$

To find $X(t)$ we differentiate (86) and use the state equation (85a) to obtain

$$-\dot{\lambda} = \dot{X}q + X(Aq - B_2^H R^{-1} B_2 Xq). \tag{88}$$

Substituting equation (85b) into this last expression leads to a quadratic matrix equation for $X(t)$ that (assuming controllability of (A, B_2)) asymptotically converges to

$$A^H X + XA - XB_2 R^{-1} B_2^H X + M = 0. \tag{89}$$

As before, we obtain a Riccati equation for the linear mapping X. The solution to this equation provides the optimal steady feedback gain via the relation (87).

Moreover, stabilizability of (A, B_2) and detectability of (A, C_1) imply additional desirable properties: the feedback gain K is guaranteed to stabilize the plant and to yield a global minimum value of (82). We recall that a system is stabilizable (detectable) if all unstable global modes are controllable (observable). In other words, if we place our actuators such that we ensure controllability of the unstable global modes and if we choose M as the kinetic energy weight matrix, then the closed-loop system is guaranteed to be stable. In the limit as $T \to \infty$ the cost functional is given by (Högberg 2001)

$$J = q_0^H X q_0, \tag{90}$$

and any other stabilizing controller will result in a larger value of this objective functional.

5.2.3. *The LQG-compensator*

Combining the estimator and controller we can now control our plant by solely relying on the measurements $y(t)$. To validate the separation principle, we may write the control (72) in terms of the full state q and the estimation error $\tilde{q}$,

$$u = Kq - K\tilde{q}. \tag{91}$$

We can combine the plant (69) and the equation for the estimation error (75) into the augmented system

$$\begin{pmatrix} \dot{q} \\ \dot{\tilde{q}} \end{pmatrix} = \begin{pmatrix} A + B_2 K & -B_2 K \\ 0 & A + LC_2 \end{pmatrix} \begin{pmatrix} q \\ \tilde{q} \end{pmatrix} + \begin{pmatrix} B_1 & 0 \\ B_1 & L \end{pmatrix} \begin{pmatrix} w \\ g \end{pmatrix}. \tag{92}$$

Since this augmented system is block-triangular, the eigenvalues of the augmented closed-loop system consist of the union of the eigenvalues of $A_c = A + B_2 K$ and $A_e = A + LC_2$. Thus, if the full-information controller A_c and the estimator A_e are stable, then the closed-loop system, *i.e.*, the compensator, obtained by combining the plant (69) and estimator (73),

$$\begin{pmatrix} \dot{q} \\ \dot{\hat{q}} \end{pmatrix} = \underbrace{\begin{pmatrix} A & B_2 K \\ -LC_2 & A + B_2 K + LC_2 \end{pmatrix}}_{A} \begin{pmatrix} q \\ \hat{q} \end{pmatrix} + \underbrace{\begin{pmatrix} B_1 & 0 \\ 0 & -L \end{pmatrix}}_{B} \begin{pmatrix} w \\ g \end{pmatrix} \tag{93a}$$

$$z = \underbrace{(C_1 \ DK)}_{C} \begin{pmatrix} q \\ \hat{q} \end{pmatrix} \tag{93b}$$

is also stable. As the separation principle suggests, the compensator consisting of an optimal estimator and an optimal full-state controller is itself optimal. The closed-loop system, given by equation (93), has two inputs, the external disturbances w and the measurements noise g, and one output, the objective function z. This closed-loop system is treated as a new dynamical system whose properties, such as stability, input-output behavior and performance, have to be investigated. Next, we discuss these issues for the two prototypical flow cases.

5.3. *Control of subcritical flow*

For a choice of parameters that results in a convectively unstable plant (table 1), the objective is to apply control schemes that lower transient energy growth or reduce the amplification of external disturbances. We will now construct a LQG-compensator for the Ginzburg-Landau equation to illustrate how a typical convectively unstable flow system may react to control. Similar to the analysis of the uncontrolled system in sections 2 and 3, the response behavior of the closed-loop system — in terms of spatio-temporal evolution of the state, kinetic energy and sensor signal — will be investigated for various inputs: optimal initial disturbance, harmonic forcing and stochastic forcing.

Before control schemes can be designed, one has to decide on the placement of actuators and sensors, the choice of which is reflected in the matrices B_2 and C_2. We assume the spatial distribution of the inputs and the outputs as Gaussian functions of the form given by (108). The width parameter $s = 0.4$ is chosen such that 95% of the spatial extent of the input/output distributions are $\sim 5\%$ of the length of the unstable domain (see figure 22a). In this way, we are restricted — as in any practical implementation of control schemes — to only a limited number of noisy measurements and to actuation in a rather small

region of the full domain. An additional simplification is made by considering only one actuator and one sensor.

Identifying regions of the flow where sensing and actuation are favorable to the feedback control of a convectively unstable system is significantly complicated by the convective nature of the flow. Usually one has to use physical intuition and a trial-and-error approach. Transient growth of energy due to the non-normality of A is associated with the local exponential growth of disturbances between branch I and II. As a consequence — and in contrast to the globally unstable case (see next section), where it suffices to estimate at branch II and control at branch I — the entire unstable domain between branch I and II is of great importance for the flow dynamics.

Appropriate choices for the location of an actuator and a sensor for the subcritical Ginzburg-Landau equation is found to be $x_u = -3$ and $x_s = 0$, respectively. In figure 22(a), the actuator and sensor placement are shown that result in an acceptable closed-loop performance.

5.3.1. *Stochastic disturbance*

Consider a system driven by white noise $B_1 w(t)$ just upstream of branch I. From the noisy measurements $y(t) = C_2 q(t) + g$ between branch I and II an estimated state is obtained. Based on this estimate, the control signal $B_2 u(t)$ is applied upstream to the sensor. The placement of the excitation, sensor and actuator is shown in figure 22(a).

The covariance of the external and measurement noise should be chosen to match as closely as possible the uncertainties that are expected for the chosen design configuration, but it is difficult to make more specific statements. It has however been found (Hœpffner *et al.* 2005; Chevalier *et al.* 2006; Hœpffner & Brandt 2008) that the performance of the estimator can be improved dramatically if the covariances are chosen to reflect physically relevant flow structures rather than generic probability distributions. For our problem, the sensor noise g is chosen to have a variance of $G = 0.1$ which is 10% of the variance of a random input with $W = 1$.

Since (69) is driven by white noise $w(t)$, the state $q(t)$ is consequently a random process and is defined by its stochastic properties, *e.g.* its covariance $P = \mathcal{E}\{qq^H\}$. As we have shown in section 3.2, these properties are linked to the statistical characteristics of the forcing via a Lyapunov equation (45).

In figure 22(a) the rms-values (40) of the state without control (red) and with control (black) are shown. The rms-value of the uncontrolled state grows exponentially as it enters the unstable domain at branch I; this growth prevails until branch II. The rms of the controlled state, however, grows only slightly in the unstable region and is considerably lower than the rms-value of the uncontrolled state at branch II.

In figure 22(b, c) the performance of the compensator is shown more explicitly in form of a temporal simulation of the closed-loop system (93) in time. The control is only engaged for $t \in [250, 750]$. Without control the stochastic
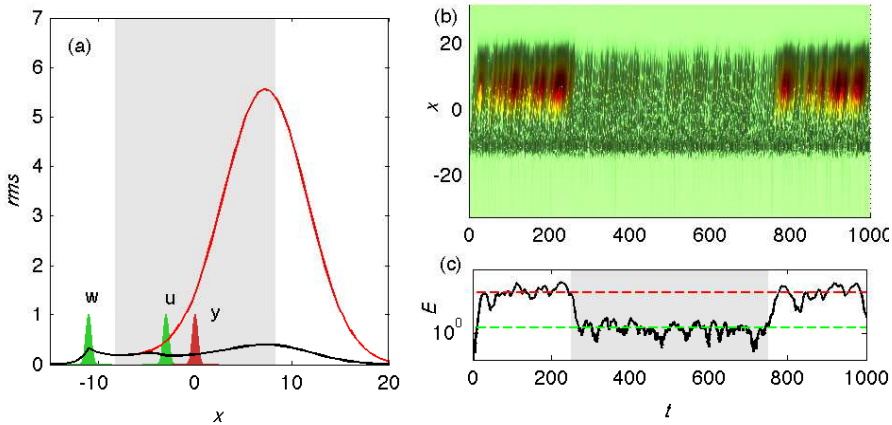
FIGURE 22. The controlled Ginzburg-Landau equation with stochastic excitation: (*a*) white noise w with zero mean and unit variance $W = 1$ forces the system at $x = -11$, just upstream of unstable region with input B_1 as a Gaussian function (green). Measurements $y(t)$ of the state (red Gaussian) contaminated by white noise with zero mean and variance $G = 0.1$ are taken at $x_s = 0$. The actuator u with control penalty $R = 1$ is placed upstream of the sensor at $x_u = -3$. The rms-values of the uncontrolled and LQG-controlled state are given by the solid red and black lines, respectively. The absolute value of the state $|q|$ is shown in an x-t-plane in (*b*), while the lower plot (*c*) displays the kinetic energy $E = \|q\|_M^2$ as a function of time. The control is only engaged for $t \in [250, 750]$. Dashed lines in (*c*) indicate the mean value computed from Lyapunov equation.

disturbances grow exponentially as they enter the unstable region at $x = -8.2$ and decay as they exit the region at $x = 8.2$. When the control is activated the perturbation energy is reduced from $E \approx 10^3$ to $E \approx 1$. When the control is disengaged, the disturbances immediately start to grow again. During and after the time when the control is applied the perturbation energy reaches a steady-state at a level that can be determined from the covariance of the state according to $E = \mathrm{trace}(PM)$, (equation 39). Dashed lines in figure 22(*c*) indicate these levels.

5.3.2. *Harmonic and optimal disturbance*

The aim of feedback control for subcritical flows is to design closed-loop systems with small transfer function norms compared to the stable open-loop system. Maximum transient energy growth of a perturbation and the norm of the system transfer function G are linked for highly non-normal systems (see
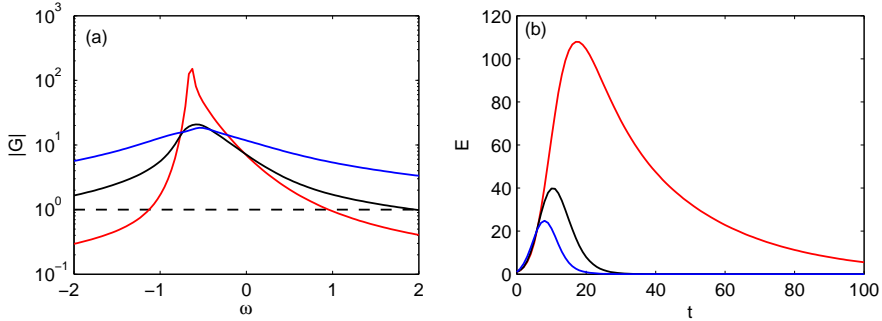
FIGURE 23. (*a*) Comparison of the frequency response of the open-loop (red), LQG-controlled (black) and $\mathcal{H}_\infty$-controlled (blue) Ginzburg-Landau equation. For the open-loop, the ∞-norm corresponding to the peak value of the response is 151, whereas the 2-norm corresponding the to integral of the response is 20.5. The $\mathcal{H}_\infty$ controller minimizes the peak value to 18.4 and reduces the 2-norm to 8.7. The LQG/$\mathcal{H}_2$ controller, on the other hand, minimizes the 2-norm to 6.1 and reduces the peak value to 20.8. (*b*) The energy evolution of an optimal disturbance is shown for the convectively unstable Ginzburg-Landau equation (red line) and the closed-loop system computed with LQG/$\mathcal{H}_2$ (black) and $\mathcal{H}_\infty$ (blue).

section 3.1 for details). To show this link, we will pose the LQG problem as a control problem in the frequency domain with the objective to minimize the 2-norm of the closed-loop transfer function.

The relation between the input and output signals, that is, between disturbance and measurement noise and the objective function, $(w \rightarrow z, g \rightarrow z)$, of the closed-loop system (93) (displayed schematically in figure 1) can be described by the transfer function,

$$G_c(s) = \mathsf{C}(sI - \mathsf{A})^{-1}\mathsf{B} \qquad s \in \mathbb{C}. \tag{94}$$

The relation between the objective function (70) in the time-domain and in the frequency domain can easily be found from Parseval's identity,

$$\int_{-\infty}^{\infty} z^2 \, dt = \frac{1}{2\pi} \int_{-\infty}^{\infty} \mathrm{trace}|G_c(i\omega)|_2^2 d\omega = \|G_c(i\omega)\|_2^2 \tag{95}$$

with $|G_c|_2^2 = G_c^H G_c$. We have thus defined the 2-norm of the transfer function $G_c(s)$ as the integral over the 2-norm of the amplitude of the transfer function along the imaginary axis. The $\mathcal{H}_2$ problem is then to minimize (95). The symbol $\mathcal{H}_2$ stands for the "Hardy space" (Zhou *et al.* 2002) which contains the set of stable transfer functions with bounded 2-norms.
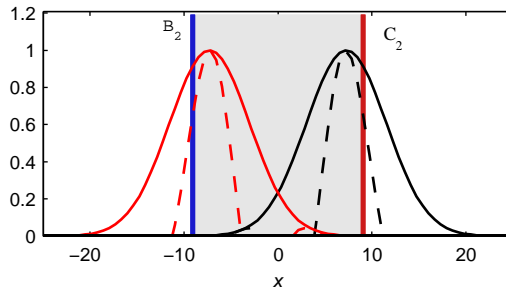
FIGURE 24. Actuator and sensor placement for the supercritical Ginzburg-Landau equation which yields a stabilizable and detectable system. The spatial support of the actuator (blue bar), sensor (red bar), the unstable domain (gray region) as well as the unstable global mode (black lines) together with its corresponding adjoint mode (red lines) are shown.

In figure 23(a) the frequency response ($w \to z, g \to z$) of the open-loop system is shown (red line) for the subcritical Ginzburg-Landau equation; we observe a 2-norm of 20.5. The corresponding LQG/$\mathcal{H}_2$ closed-loop transfer function (94) is displayed (black line) in figure 23, where the 2-norm is now minimized to a value of $\|G_c\|_2 = 6.1$. In figure 23(b) the optimal energy growth (section 2.3) of the uncontrolled and controlled system are compared. The maximum transient energy growth (peak value) is reduced by an order of magnitude.

5.4. *Control of supercritical flow*

For a globally unstable flow (parameters given in table 1), *i.e.*, an unstable plant (69), the influence of uncertainties ($w(t)$ and $g(t)$) on the system dynamics is rather small compared to the asymptotic behavior of the most unstable global mode. This mode will grow exponentially as soon as any disturbance (assuming it is not orthogonal to the unstable mode) enters the unstable region. For this reason disturbance modeling may not play a decisive role for globally unstable flows, in contrast to convectively unstable flows.

The goal of any control effort is to stabilize an otherwise unstable system; this task is particularly straightforward using LQG-based feedback control, since the closed-loop system (93) is guaranteed to be stable as long as the actuator and the sensor are placed such that the system is both stabilizable and detectable.

In other words, the performance of a controller to a globally unstable Ginzburg-Landau equation can only be successful if all unstable global modes are controllable and observable. It was concluded in section 4.1 that a global mode is controllable (observable) if the overlap of the actuator (sensor) and the adjoint mode (global modes) is nonzero. In figure 24, a configuration for
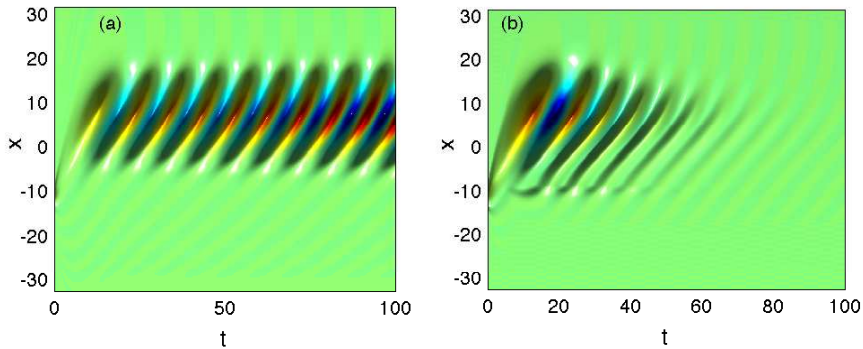
FIGURE 25. The spatio-temporal response to an impulse in time induced at $x = -10$ for the uncontrolled system (a) and LQG-controlled system (b).

the actuator and sensor is shown that yields a plant which is both stabilizable and detectable.

For this set-up a LQG compensator (93) is constructed by solving the Riccati equations (89) and (81). The perturbation energy, the impulse response and the spectrum of the uncontrolled plant (69) and controlled closed-loop system (93) are shown in figures 25 and 26. We observe that the closed-loop system has all eigenvalues in the stable half-plane yielding an asymptotically stable flow.

For a point-wise spatial distribution of actuators $\delta(x - x_u)$ it has been shown in Lauga & Bewley (2003) that the Ginzburg-Landau equation gradually loses stabilizability as the parameter μ_0 is increased. This loss is due to the increasing number of unstable global modes which are located further downstream. Controllability of the unstable global modes is gradually diminished as the support of the actuator and the support of the corresponding unstable adjoint global modes (57c) move apart until controllability is entirely lost. At this point no compensator will be able to stabilize the system using one pointwise actuator.

5.5. *The $\mathcal{H}_\infty$ framework — robust control*

In the previous sections we have tacitly assumed that the system matrices A, B and C are known exactly. In reality, however, this is not the case, since modeling errors (for example, a small mismatch in the Reynolds number between the model and the actual flow) are always present. The presence of these errors raises the important issue of robustness of a specific control design.

Concentrating for simplicity on the dynamic model error, let us consider a model system given by A. The real flow, on the other hand, shall be subject to a small deviation from this model and is described by the dynamic matrix
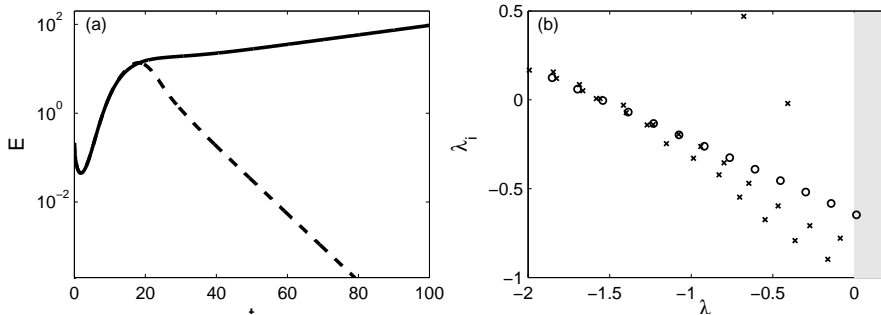
FIGURE 26. Left figure: The perturbation energy of an initial condition which illustrates the asymptotic growth and decay of the global mode of the controlled and uncontrolled systems. Right figure: The spectrum of the uncontrolled (circles) and LQG-controlled (crosses) Ginzburg-Landau equation. The exponential growth of the wavepacket in figure 25(a) is due to one unstable global mode of the open-loop shown by the red circle in the unstable half-plane (gray region). The LQG-based closed-loop is stable with no unstable eigenvalues.

$A + \epsilon\Delta$ with Δ as a unit-norm uncertainty matrix and with ϵ parameterizing the magnitude of the uncertainty. For a given value of ϵ, the controller designed for A has the "robust stability" property if the closed-loop system is stable for all unit-norm uncertainty matrices Δ and, similarly, has the "robust performance" property if the performance of the closed-loop system is satisfactory for all possible unit-norm uncertainty matrices Δ. If information about the specific form of the uncertainties is available, one can restrict the structure of the uncertainty matrix Δ to reflect this information and thus reduce the "uncertainty set". In a similar fashion, the magnitude ϵ of the uncertainty may be estimated or bounded.

Unfortunately, the LQG/$\mathcal{H}_2$-control design does not account explicitly for uncertainties in the system matrices, which is needed to guarantee robust performance or even robust stability. For a given controller, the smallest value of ϵ such that the closed-loop system is unstable is referred to as the *stability margin*. It is known (Doyle 1978) that there are no guaranteed stability margins for LQG/$\mathcal{H}_2$-controllers. However, this does not necessarily mean that the $\mathcal{H}_2$-controller will be unstable for very small values of ϵ; instead, it merely means that the search for robustness is not accounted for.

To incorporate the presence of uncertainties into the control design framework one can adjust the actuation penalty and sensor noise which, in turn, directly affects the strength of the controller and may help push the control design toward robustness. This approach has led to the development of control optimization based on the $\mathcal{H}_\infty$-norm. Instead of minimizing the energy of

the transfer function (*i.e.*, the integral of the frequency response over all frequencies), it concentrates instead on reducing the peak value of the frequency response. These are two very different objectives: for instance, a strong peak in the frequency response localized about one single frequency may not contribute significantly to the energy (integral) of the response. This new $\mathcal{H}_\infty$-objective plays a pivotal role in the search for robustness since closed-loop instabilities can be quantified by the relation between the magnitude of the dynamic uncertainty and the maximum frequency response (Zhou *et al.* 2002).

The steps to compute $\mathcal{H}_\infty$-controllers closely follow the ones for LQG/$\mathcal{H}_2$-design except that a new term is added to the objective functional that will represent the worst possible external forcing. The subsequent optimization scheme will search for a controller that achieves the best performance for the worst perturbation (Bewley & Liu 1998; Bewley 2001). Mathematically, this is equivalent to searching for a saddle point of this new objective functional rather than a minimum. The augmented objective functional reads

$$J = \int_0^T q^H M q + u^H R u - \gamma^2 w^H W w \; dt. \qquad (96)$$

In this expression w represents both external disturbances and measurement noise. We then wish to find the control u which minimizes the control objective (70) in the presence of a disturbance w that maximally disrupts this objective. A new free parameter γ appears that plays the role of ϵ in parameterizing the magnitude of the worst perturbation.

To simplify the following derivation we assume for now that $W = 1$ and $R = 1$. Similar to the LQG-design in 5.2.3, we can also specify the control objective in the frequency domain instead of the time domain (96). In this case we simply aim at restricting the maximum values of the closed-loop transfer function as given by (see *e.g.* Green & Limebeer 1995),

$$\|G_c(i\omega)\|_\infty \le \frac{\|z\|_2}{\|w\|_2} \le \gamma. \qquad (97)$$

The above transfer function norm was defined in (36).

The $\mathcal{H}_\infty$-problem consists of finding a control signal $u(t)$ that minimizes both the perturbation energy and control effort while *maximizing* the effects of the external disturbances w. As the parameter γ approaches infinity the objective functional (and the optimal control) reduces to the one of the LQG-problem. In this review we will merely present the solution of the $\mathcal{H}_\infty$-problem and show how it relates to the LQG-solution. For a more detailed derivation of this link see Zhou *et al.* (2002) or Green & Limebeer (1995).

The solution of the above $\mathcal{H}_\infty$-problem is, similar to the LQG-problem, obtained by solving two Riccati equations which stem from two separate problems: the estimation and the full-information control problem. The full-information control problem leads to the Riccati equation of the form

$$A^H X + X A - X(-\gamma^{-2} B_1 B_1^H + B_2 B_2^H) X + M = 0 \qquad (98)$$

with the control given by

$$u = \underbrace{-B_2^H X}_{K} q. \tag{99}$$

Furthermore, one finds that the worst-case disturbance w is given by

$$w_{worst} = \gamma^{-2} B_1^H X q. \tag{100}$$

The Riccati equation (98), whose solution yields the control feedback gain for $\mathcal{H}_\infty$, is modified such that it takes into account the worst-case disturbance acting on the system. We notice that the term $-\gamma^{-2} B_1 B_1^H$ is absent in the Riccati equation (89) of the LQG-problem. Rather, by modeling and incorporating the structure of the disturbances B_1 when computing the feedback gain K, the components of the state that are expected to be most influenced by external disturbances are forced by the largest feedback, $K\hat{q}$. We would like to point out that the parameter γ is supplied by the user and that the resulting control (99) is only suboptimal rather than optimal. For large values of γ, the full-information solution of the associated LQG-problem and the optimal control signal are recovered.

The estimated state is also computed in the presence of worst-case disturbances $\hat{w}_{worst} = \gamma^{-2} B_1^H X \hat{q}$ and is therefore the result of the following estimation problem

$$\dot{\hat{q}} = A\hat{q} + B_1 \hat{w}_{worst} + B_2 u - L(y - \hat{y}), \tag{101a}$$
$$\hat{y} = C_2 \hat{q}. \tag{101b}$$

Similar to the LQG-estimation problem, the difference between the true measurement y and the estimated measurement $\hat{y}$ is fed back using the estimator gain L. There is, however, no longer any assumption on the disturbances w and g. Instead the additional term $B_1 \hat{w}_{worst}$ provides the estimator with information on the worst-case disturbance. The estimation gain in equation (101) is given by $L = -ZY C_2^H$, where Y is the solution of the following Riccati equation (for a derivation of this result see, *e.g.* Zhou *et al.* 2002)

$$AY + YA^H - Y(-\gamma^{-2} C_1^H C_1 + C_2^H G^{-1} C_2)Y + B_1 B_1^H = 0, \tag{102}$$

and Z is a constant matrix given by

$$Z = (I - \gamma^{-2} YX)^{-1}. \tag{103}$$

Equation (102) can now be compared to the Riccati equation (81) for the LQG-problem. The additional term $-\gamma^{-2} C_1^H C_1$ is present in the above equation which reflects the fact that the computation of the estimation gain L depends on the weights in the cost functional. The components of the estimated state that most contribute to the objective functional are forced stronger by the feedback $L(y - \hat{y})$. In addition we notice that the estimation gain L depends via equation (103) on the solution of the full-state Riccati solution X.

By combining the estimator (101) and the plant (69) it is straightforward to formulate the $\mathcal{H}_\infty$-compensator as a closed-loop system. Even though the required calculations (the solution of two Riccati equations) are reminiscent

of the LQG-approach, in the $\mathcal{H}_\infty$ case we face additional restrictions for the stability of the closed-loop system and a more demanding computational effort for finding an optimal controller.

First, stabilizability and detectability is no longer a sufficient condition to guarantee the stability of the closed-loop system. For the $\mathcal{H}_\infty$-problem to be solvable, the spectral radius ρ of XY has to be smaller than γ^2 (Doyle *et al.* Aug 1989).

Secondly, the solution presented above is merely suboptimal; finding an optimal robust controller involves an iterative process that terminates when a lower bound γ_0 of γ is found which still satisfies $\rho(XY) < \gamma^2$. This optimal γ_0 can typically be found with fewer than 20 iterations using the bisection algorithm.

We use the Ginzburg-Landau equation to exemplify the techniques introduced above. For a more detailed investigation we refer to Lauga & Bewley (2004). In figure 23(*a*) the frequency response (*i.e.*, the mapping $w, g \to z$) of the open-loop system is shown with a red line for the subcritical Ginzburg-Landau equation, displaying a ∞-norm of 151. The corresponding $\mathcal{H}_\infty$ closed-loop design is shown with a blue line where the ∞-norm is now reduced to $\|G_c\|_\infty = 18.4$. Comparing the frequency responses of the controlled systems based on the $\mathcal{H}_2$ and $\mathcal{H}_\infty$, we can confirm that in the former case the 2-norm $\|G_c\|_2$ is minimized while in the latter case $\|G_c\|_\infty$ is minimized. Consequently, the most amplified frequencies are more damped in the $\mathcal{H}_\infty$-case at the expense of the higher frequencies which are amplified compared to the uncontrolled case. The $\mathcal{H}_2$ controller, on the other hand, shows a smaller reduction of the most unstable open-loop frequencies (*i.e.* the peak value in the frequency response). This is not surprising, since the $\mathcal{H}_2$-controller minimizes the energy — the integral of the transfer function along the imaginary axis — whereas the $\mathcal{H}_\infty$-controller minimizes the peak value of the transfer function on the imaginary axis.

The optimal energy growth (see equation 21) in figure 23(*b*) demonstrates that the maximum energy growth is smaller for the $\mathcal{H}_\infty$-design which suggests that reducing the most amplified frequencies, rather than all the frequencies, is a more efficient strategy for damping maximum energy growth. However, to achieve its goal the $\mathcal{H}_\infty$-controller expends more control energy than the corresponding $\mathcal{H}_2$-controller (Lauga & Bewley 2004).

Using the Ginzburg-Landau equation for a set of parameters that yields a globally unstable flow Lauga & Bewley (2004) compared the $\mathcal{H}_\infty$-controller to the $\mathcal{H}_2$-controller for a range of control penalties and various levels of measurement noise. They found that the $\mathcal{H}_\infty$ control design always uses more control energy (for the same control penalty) than the corresponding $\mathcal{H}_2$ control design. A robust controller uses this additional control energy to ensure that the constraint on the maximum value of the transfer function norm $\|G_c\|_\infty$ is satisfied.
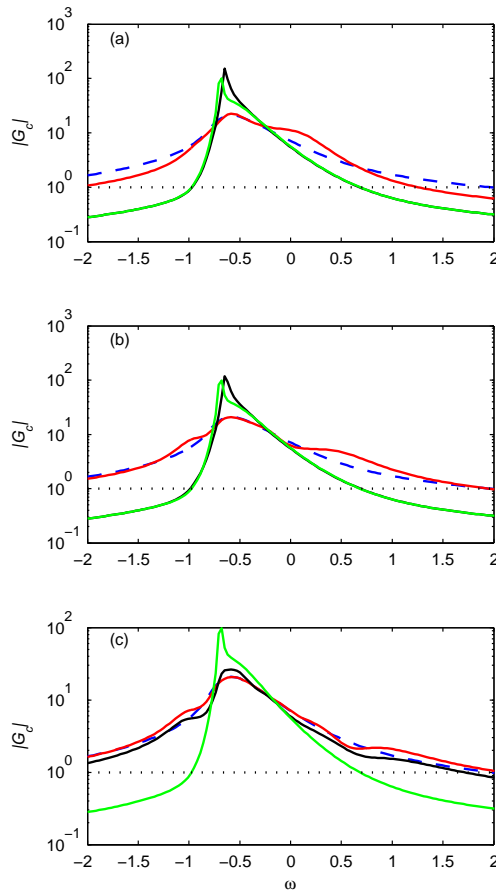
FIGURE 27. The frequency response of the closed feedback-loop based on a LQG-compensator. Blue dashed lines represent the full model of order $n = 220$. The performance of reduced-order models based on $r = 2, 4$ and 6 modes are shown in the (a), (b) and (c), respectively. Red lines represent balanced modes, black lines POD modes and green lines global eigenmodes. We observe that reduced order controller based on balanced modes outperforms the other two models. The poor performance of the reduced-order based on POD and global modes, is directly associated with the unsatisfactory approximation of the open-loop case in figure 18.

5.6. *Reduced-order controllers*

The process of systematic control design as presented above involves the solution of two Riccati equations. The cost of computing a Riccati solution is of

order n^3 where n is the number of components in the discretized state vector. Whereas for the Ginzburg-Landau equation n is still sufficiently low to allow a direct solution of the Riccati equations, for the Navier–Stokes equations the number of state vector components is rather large. The cost of a direct Riccati solution is prohibitively expensive when $n > 10^5$ which is easily reached for two- and three-dimensional flow configurations. As discussed in section 4, this high cost can be avoided by developing a reduced-order model which preserves the essential flow dynamics.

Similar to solving a Lyapunov equation, there exist "matrix-free" methods to solve a Riccati equation. One common approach that significantly reduces the cost of directly solving the Riccati equation — if the number of inputs and outputs is much smaller than the number of states — is known as the Chandrasekhar method (Kailath 1973). In this method the Riccati solution is expressed as the solution to a coupled system of ordinary differential equations which needs to be integrated in time (see Hœpffner *et al.* 2005, for an application).

Even if we manage to obtain the feedback gains from the full system, however, there still remains the issue that the controller is of very high order, which requires a rather fast feedback-system running next to the experiment.

We will return to the issue of model reduction (see section 4) based on the projection of the original high-dimensional system onto a smaller system using a given basis. One of the main advantages of this approach is that the error in the reduced-order model can be quantified in terms of transfer functions as shown in equation (62) and (58).

Once a reduced-order model is devised (using the techniques in section 4) whose transfer function is a sufficiently good approximation of the open-loop transfer function, we can design an $\mathcal{H}_2$- or an $\mathcal{H}_\infty$-controller for this reduced model. This results in a reduced-order controller which, coupled to the full-order open-loop system, will result in the following augmented system

$$\begin{pmatrix} \dot{q} \\ \dot{\hat{q}} \end{pmatrix} = \begin{pmatrix} A & B_2\hat{K} \\ -\hat{L}C & \hat{A} + \hat{B}_2\hat{K} + \hat{L}\hat{C} \end{pmatrix} \begin{pmatrix} q \\ \hat{q} \end{pmatrix} + \begin{pmatrix} B_1 & 0 \\ 0 & -\hat{L} \end{pmatrix} \begin{pmatrix} w \\ g \end{pmatrix}. \tag{104}$$

The expression of the reduced-order controller is equivalent to the full-order given by equation (93), except that the quantities marked with ˆ are of order $r \ll n$. Note that the feedback gain K and estimation gain L have the dimension of the reduced model resulting in a fast online controller.

We can now compare the frequency response of the reduced-order models with and without control. The frequency response of the full model without control was shown by the dashed blue lines in figures 18. The frequency response of reduced-order models using global modes (green), proper orthogonal decomposition (POD) modes (black) and balanced modes (red) were also shown in the figures.

In figures $27(a, b, c)$ we display with dashed blue lines the frequency response $G_c(i\omega)$ of the LQG closed-loop system when solving the full-order

($n = 220$) Riccati equations. Comparing the dashed blue lines in figure 18, where the frequency response of the reduced-model of the open-loop is shown, with the ones of the closed loop in figure 27, we see that the most unstable frequencies are reduced by an order of magnitude. Solving the Riccati equations for the reduced models of order $r = 2, 4$ and 6 for the three sets of modes (global, POD, balanced modes) we observe the same trend for the closed-loop system as we saw for the open-loop system: the reduced-order model based on two balanced modes (red line in figure 27b) is able to obtain a closed-loop performance very similar to the full model, whereas POD modes require a substantially larger basis and global modes fail entirely.

It should be mentioned that model reduction for unstable systems is also possible using global modes (Åkervik *et al.* 2007), POD modes (Gillies 1998) and, more recently, balanced modes (Ahuja & Rowley 2008).

6. Conclusions

A unifying framework for linear fluid dynamical systems has been presented and reviewed that allows the analysis of stability and response characteristics as well as the design of optimal and robust control schemes. An input-output formulation of the governing equations yields a flexible formulation for treating stability problems and for developing control strategies that optimize given objectives while still satisfying prescribed constraints.

The linear Ginzburg-Landau equation on the infinite domain has been used as a model equation to demonstrate the various concepts and tools. It has been modified to capture both subcritical and supercritical disturbance dynamics and thus span the range of fluid behavior observed in various generic shear flow configurations. With a small modification, the equation can also be used to mimic instabilities in other spatially developing flows, for instance flows on semi-infinite domains such as inhomogeneous jets and wakes. We should however keep in mind that Ginzburg-Landau is a great simplification of the dynamics described by linearized Navier–Stokes equations, modelling merely the fundamental behavior of different types of local and global instabilities and the transition between them.

Input-output-based analysis tools, such as the impulse response or the frequency response, have been applied to the model equation. This type of analysis lays the foundation for a thorough understanding of the disturbance behavior and the design of effective control strategies. Concepts such as controllability and observability play an important role for both the input-output behavior and the control design.

The design of effective and efficient control strategies is a challenging task, starting with the placement of actuators and sensors and ending with the judicious choice of a model reduction basis in order to numerically solve the compensator problem. Along the way, compromises between optimality ($\mathcal{H}_2$-control) and robustness ($\mathcal{H}_\infty$-control) have to be made that influence the overall performance of the feedback system.

It is hoped that this review has given a comprehensive and modern introduction to the fields of stability and control theory and has shown the close link between them. It is further hoped that it will spark interest in the fluid dynamics community to continue the exploration of these two exciting disciplines.

The Matlab files to reproduce the results and figures of this review article are available from the FTP server *ftp://ftp.mech.kth.se/pub/review.*

Appendix A. Discretization

The numerical studies in this review article are based on a pseudospectral discretization of the Ginzburg-Landau operator $\mathcal{A}$ using Hermite functions and the corresponding differentiation matrices provided by Weideman & Reddy (2000). To approximate the derivatives in (1), we expand the solution $q(x, t)$ in n Hermite functions

$$q(x, t) = \sum_{j=1}^{n} \alpha_j(t) \exp(-\frac{1}{2}b^2 x^2) H_{j-1}(bx) \qquad (105)$$

where $H_j(bx)$ refers to the jth Hermite polynomial. The differentiation process is exact for solutions of the form

$$f(x) = \exp(-\frac{1}{2}b^2 x^2) p(bx) \qquad (106)$$

where $p(bx)$ is any polynomial of degree $n - 1$ or less. The scaling parameter b can be used to optimize the accuracy of the spectral discretization (Tang 1993). A comparison of the above expression with the analytical form of the global Ginzburg-Landau eigenmodes (11b) shows that they are of the same form except for the exponential term $\exp\{(\nu/2\gamma)x\}$ stemming from the convective part of the Ginzburg-Landau equation. This exponential term is responsible for the non-orthogonality of the eigenmodes of $\mathcal{A}$. The Hermite functions are thus the "orthogonal part" of the global modes. By choosing the Hermite function scaling factor $b = \chi$ we obtain a highly accurate approximation of $\mathcal{A}$, since any solution of the Ginzburg-Landau equation will decay with the same exponential rate as the Hermite functions in the limit as the domain tends to infinity.

The collocation points $x_1, \ldots, x_n$ are given by the roots of $H_n(bx)$. We also notice that the boundary conditions are enforced implicitly and that $-x_1 = x_n = \mathcal{O}(\sqrt{bn})$ in the limit as $n \to \infty$ (Abramowitz & Stegun 1964). The discretization converts the operator $\mathcal{A}$ into a matrix A of size $n \times n$ (with n as

the number of collocation points). Throughout this review article we present results for $n = 220$ yielding a computational domain with $x \in [-85, 85]$.

Discretization transforms flow variable $q(x, t)$ into a column vector $\hat{q}(t)$ of dimension n, and the inner product is defined as

$$
\begin{aligned}
\langle f, g \rangle &= \int_{-\infty}^{\infty} f(x)^* g(x) dx \tag{107} \\
&\approx \sum_{i=1}^{n} \sum_{j=1}^{n} \hat{f}_i^H \hat{g}_j w_{i,j} = \hat{f}^H M \hat{g} = \langle \hat{f}, \hat{g} \rangle_M,
\end{aligned}
$$

where $\hat{f} = [\hat{f}_1 \dots \hat{f}_n]^H$ and $\hat{g} = [\hat{g}_1, \dots, \hat{g}_n]^H$ are column vectors consisting of, respectively, $f(x)$ and $g(x)$ evaluated at the collocation points. The symbol ^{H} denotes the Hermitian (complex conjugate transpose) operation. The positive-definite matrix M contains the weights $w_{i,j}$ of the chosen quadrature rule. For instance, applying the trapezoidal rule to the Hermite collocation points results in a diagonal matrix $M = \frac{1}{2} \text{diag}\{\Delta x_1, \Delta x_2 + \Delta x_1, \dots, \Delta x_{n-1} + \Delta x_{n-2}, \Delta x_{n-1}\}$, with $\Delta x_i = x_{i+1} - x_i$. In this paper, the discrete variables $\hat{f}$ are denoted by f.

The operators B and C, describing the input and output configuration, are represented at their respective collocation points. We assume a spatial distribution of inputs $B = \{B_1, \dots, B_p\}$ and outputs $C = \{C_1 \dots C_r\}^T$ in the form of Gaussian functions

$$
B_i u(t) = \exp\left[-\left(\frac{x - x_{w,i}}{s}\right)^2\right] u(t), \tag{108a}
$$

$$
C_i q(t) = \exp\left[-\left(\frac{x - x_{s,i}}{s}\right)^2\right]^H M q(t), \tag{108b}
$$

where x represents the Hermite collocation points.

References

ABRAMOWITZ, M. & STEGUN, I. E. 1964 *Handbook of mathematical functions : With formulas, graphs, and mathematical tables*. National Bureau of Standards, Washington.

AHUJA, S. & ROWLEY, C. W. 2008 Low-dimensional models for feedback stabilization of unstable steady states. *AIAA Paper 2008-553, 46th AIAA Aerospace Sciences Meeting and Exhibit* .

AHUJA, S., ROWLEY, C. W., KEVREKIDIS, I. G. & WEI, M. 2007 Low-dimensional models for control of leading-edge vortices: Equilibria and linearized models. *AIAA Paper 2007-709, 45th AIAA Aerospace Sciences Meeting and Exhibit* .

ÅKERVIK, E., EHRENSTEIN, U., GALLAIRE, F. & HENNINGSON, D. S. 2008 Global two-dimensional stability measures of the flat plate boundary-layer flow. *Eur. J. Mech. B/Fluids* **27**, 501–513.

ÅKERVIK, E., HŒPFFNER, J., EHRENSTEIN, U. & HENNINGSON, D. S. 2007 Optimal growth, model reduction and control in a separated boundary-layer flow using global eigenmodes. *J. Fluid. Mech.* **579**, 305–314.

ALBARÈDE, P. & MONKEWITZ, P. A. 1992 A model for the formation of oblique shedding and "chevron" patterns in cylinder wakes. *Phys. Fluids A* **4**, 744–756.

ANDERSON, B. & MOORE, J. 1990 *Optimal control: Linear Quadratic Methods*. Prentice Hall, New York.

ANDERSSON, P., BERGGREN, M. & HENNINGSON, D. 1999 Optimal disturbances and bypass transition in boundary layers. *Phys. Fluids* **11**, 134–150.

ANTOULAS, A., SORENSEN, D. & GUGERCIN, S. 2001 A survey of model reduction methods for large-scale systems. *Contemp. Math* **280**, 193–219.

ANTOULAS, C. A. 2005 *Approximation of Large-Scale Dynamical Systems*. SIAM, Philadelphia.

BAMIEH, B. & DAHLEH, M. 2001 Energy amplification in channel flows with stochastic excitation. *Phys. Fluids* **13**, 3258–3269.

BEWLEY, T. & MOIN, P. 1994 Optimal control of turbulent channel flows. In *Active Control of Vibration and Noise* (ed. K.W. Wang, A. H. Von Flotow, R. Shoureshi & T. W. Farabee). ASME DE-Vol. 75.

BEWLEY, T. R. 2001 Flow control: New challenges for a new renaissance. *Progr. Aerospace. Sci.* **37**, 21–58.

BEWLEY, T. R. & LIU, S. 1998 Optimal and robust control and estimation of linear paths to transition. *J. Fluid Mech.* **365**, 305–349.

BEWLEY, T. R., MOIN, P. & TEMAM, R. 2001 DNS-based predictive control of turbulence: An optimal benchmark for feedback algorithms. *J. Fluid Mech.* **447**, 179–225.

BIAU, D. & BOTTARO, A. 2004 Transient growth and minimal defects: Two possible initial paths of transition to turbulence in plane shear flows. *Phys. Fluids* **16**, 3515–3529.

BRIGGS, R. J. 1964 Electron-stream interaction with plasmas. *MIT Press* .

BUTLER, K. & FARRELL, B. F. 1992 Three-dimensional optimal perturbations in viscous shear flow. *Phys. Fluids A* **4**, 1637–1650.

CHEVALIER, M., HŒPFFNER, J., ÅKERVIK, E. & HENNINGSON, D. S. 2007 Linear

feedback control and estimation applied to instabilities in spatially developing boundary layers. *J. Fluid Mech.* **588**, 163–187.

CHEVALIER, M., HŒPFFNER, J., BEWLEY, T. R. & HENNINGSON, D. S. 2006 State estimation in wall-bounded flow systems. Part 2: Turbulent flows. *J. Fluid Mech.* **552**, 167–187.

CHOI, H., MOIN, P. & KIM, J. 1994 Active turbulence control for drag reduction in wall-bounded flows. *J. Fluid Mech.* **262**, 75–110.

CHOMAZ, J., HUERRE, P. & REDEKOPP, L. 1987 Models of hydrodynamic resonances in separated shear flows. *Symposium on Turbulent Shear Flows, 6th, Toulouse, France*.

CHOMAZ, J., HUERRE, P. & REDEKOPP, L. 1988 Bifurcations to local and global modes in spatially developing flows. *Phys. Rev. Lett.* **60**, 25–28.

CHOMAZ, J., HUERRE, P. & REDEKOPP, L. 1990 The effect of nonlinearity and forcing on global modes. In *New Trends in Nonlinear Dynamics and Pattern-Forming Phenomena* (ed. P. Coullet & P. Huerre), pp. 259–274. New York: NATO ASI Ser. B.

CHOMAZ, J., HUERRE, P. & REDEKOPP, L. 1991 A frequency selection criterion in spatially developing flows. *Stud. Appl. Math.* **84**, 119-114.

CHOMAZ, J. M. 2005 Global instabilities in spatially developing flows: Non-normality and nonlinearity. *Ann. Rev. Fluid Mech.* **37**, 357–392.

COHEN, K., SIEGEL, S., MCLAUGHLIN, T., GILLIES, E. & MYATT, J. 2005 Closed-loop approaches to control of a wake flow modeled by the Ginzburg-Landau equation. *Comp. & Fluids* **34**, 927–949.

CORBETT, P. & BOTTARO, A. 2001 Optimal linear growth in swept boundary layers. *J. Fluid. Mech.* **435**, 1–23.

COSSU, C. & CHOMAZ, J. M. 1997 Global measures of local convective instabilities. *Phys. Rev. Lett.* **78**, 4387–4390.

DATTA, B. 2003 *Numerical Methods for Linear Control Systems Design and Analysis*. Elsevier, New York.

DAVIES, E. B. 2002 Non-self-adjoint differential operators. *Bull. London Math. Soc.* **34**, 513-532.

DOYLE, J. 1978 Guaranteed margins for LQG regulators. *IEEE Trans. Automat. Control* **23**, 756–757.

DOYLE, J., GLOVER, K., KHARGONEKAR, P. & FRANCIS, B. Aug 1989 State-space solutions to standard H2 and H∞ control problems. *IEEE Trans. Automat. Control* **34**, 831–847.

EHRENSTEIN, U. & GALLAIRE, F. 2005 On two-dimensional temporal modes in spatially evolving open flows: The flat-plate boundary layer. *J. Fluid Mech.* **536**, 209–218.

FARRELL, B. F. 1988 Optimal excitation of perturbations in viscous shear flow. *Phys. Fluids* **31**, 2093–2102.

FARRELL, B. F. & IOANNOU, P. J. 1993 Stochastic forcing of the linearized navier–stokes equations. *Phys. Fluids* **5**, 2600–2609.

FARRELL, B. F. & IOANNOU, P. J. 1996 Generalized stability theory. Part i. Autonomous operators. *J. Atmos. Sci.* **53**, 2025–2040.

GAL-EL-HAK, M. 1996 Modern developments in flow control. *Appl. Mech. Rev.* **49**, 365–379.

Gal-El-Hak, M. 2000 *Flow Control: Passive, Active And Reactive Flow Management*. Cambridge University Press, London.

Giannetti, F. & Luchini, P. 2007 Structural sensitivity of the first instability of the cylinder wake. *J. Fluid Mech.* **581**, 167–197.

Gillies, E. A. 1998 Low-dimensional control of the circular cylinder wake. *J. Fluid Mech.* **371**, 157–178.

Green, M. & Limebeer, J. N. 1995 *Linear Robust Control*. Prentice Hall, New Jersey.

Guégan, A., Schmid, P. J. & Huerre, P. 2006 Optimal energy growth and optimal control in swept hiemenz flow. *J. Fluid Mech.* **566**, 11–45.

Gunzburger, M. 1995 *Flow Control*. Berlin: Springer.

Henningson, D. & Åkervik, E. 2008 The use of global modes to understand transition and perform flow control. *Phys. Fluids* **20**, 031302.

Hill, D. 1995 Adjoint systems and their role in the receptivity problem for boundary layers. *J. Fluid. Mech.* **292**, 183–204.

Ho, C. M. & Huerre, P. 1984 Perturbed free shear layers. *Ann. Rev. Fluid Mech* **16**, 365–424.

Hœpffner, J. 2006 *Stability and Control of Shear Flows Subject to Stochastic Excitations*. KTH Stockholm, PhD thesis.

Hœpffner, J. & Brandt, L. 2008 Stochastic approach to the receptivity problem applied to bypass transition in boundary layers. *Phys. Fluids* **20**, 024108.

Hœpffner, J., Chevalier, M., Bewley, T. R. & Henningson, D. S. 2005 State estimation in wall-bounded flow systems. Part I: Laminar flows. *J. Fluid Mech.* **534**, 263–294.

Högberg, M. 2001 *Optimal control of boundary-layer transition*. KTH Stockholm, PhD thesis.

Högberg, M., Bewley, T. R. & Henningson, D. S. 2003*a* Linear feedback control and estimation of transition in plane channel flow. *J. Fluid Mech.* **481**, 149–175.

Högberg, M., Bewley, T. R. & Henningson, D. S. 2003*b* Relaminarization of $Re_\tau = 100$ turbulence using gain scheduling and linear state-feedback control flow. *Phys. Fluids* **15**, 3572–3575.

Huerre, P. 2000 Open shear flow instabilities. In *Perspectives in Fluid Dynamics*, pp. 159–229. Cambridge University Press.

Huerre, P. & Monkewitz, P. A. 1990 Local and global instabilities in spatially developing flows. *Ann. Rev. Fluid Mech.* **22**, 471–573.

Hunt, R. E. & Crighton, D. G. 1991 Instability of flows in spatially developing media. *Proc. R. Soc. Lond. A* **435**, 109–128.

Ilak, M. & Rowley, C. W. 2008 Modeling of transitional channel flow using balanced proper orthogonal decomposition. *Phys. Fluids* **20**, 034103.

Joshi, S. S., Speyer, J. L. & Kim, J. 1997 A systems theory approach to the feedback stabilization of infinitesimal and finite-amplitude disturbances in plane poiseuille flow. *J. Fluid Mech.* **332**, 157–184.

Joslin, R. D. 1998 Aircraft laminar flow control. *Ann. Rev. Fluid Mech.* **30**, 1–29.

Jovanovic, M. R. & Bamieh, B. 2005 Componentwise energy amplification in channel flows. *J. Fluid Mech.* **534**, 145–183.

Kailath, T. 1973 Some new algorithms for recursive estimation in constant linear systems. *IEEE Trans. Inf. Theory* **19**, 750–760.

KAILATH, T. 1980 *Linear Systems*. Prentice-Hall.

KALMAN, R. E. 1960 A new approach to linear filtering and prediction problems. *Trans. ASME, Ser. D. J. Basic Eng.* **82**, 24–45.

KIM, J. 2003 Control of turbulent boundary layers. *Phys. Fluids* **15**, 1093–1105.

KIM, J. & BEWLEY, T. R. 2007 A linear systems approach to flow control. *Ann. Rev. Fluid Mech.* **39**, 383–417.

KWAKERNAAK, H. & SIVAN, R. 1972 *Linear Optimal Control Systems*. Wiley Interscience, New York.

LAUB, A. 1991 Invariant subspace methods for the numerical solution of Riccati equations. In *The Riccati equation* (ed. W. Bittaini, Laub), pp. 163–96. Springer. Berlin.

LAUGA, E. & BEWLEY, T. R. 2003 The decay of stabilizability with reynolds number in a linear model of spatially developing flows. *Proc. R. Soc. Lond. A.* **459**, 2077–2095.

LAUGA, E. & BEWLEY, T. R. 2004 Performance of a linear robust control strategy on a nonlinear model of spatially developing flows. *J. Fluid Mech.* **512**, 343–374.

LE DIZÉS, S., HUERRE, P., CHOMAZ, J. M. & MONKEWITZ, P. A. 1996 Linear global modes in spatially developing media. *Phil. Trans. R. Soc. Lond. A* **354**, 169–212.

LEE, K. H., CORTELEZZI, L., KIM, J. & SPEYER, J. 2001 Application of reduced-order controller to turbulent flow for drag reduction. *Phys. Fluids* **13**, 1321–1330.

LESSHAFFT, L., HUERRE, P., SAGAUT, P. & TERRACOL, M. 2006 Nonlinear global modes in hot jets. *J. Fluid Mech.* **554**, 393–409.

LEWIS, F. L. & SYRMOS, L. V. 1995 *Optimal Control*. John Wiley & Sons, New York.

LUCHINI, P. 2000 Reynolds-number-independent instability of the boundary layer over a flat surface: Optimal perturbations. *J. Fluid. Mech.* **404**, 289–309.

LUCHINI, P. & BOTTARO, A. 1998 Gortler vortices: A backward-in-time approach to the receptivity problem. *J. Fluid. Mech.* **363**, 1–23.

LUMLEY, J. L. 1970 *Stochastic Tools in Turbulence*. Academic Press.

MARQUILLIE, M. & EHRENSTEIN, U. 2002 On the onset of nonlinear oscillations in a separating boundary-layer flow. *J. Fluid Mech.* **458**, 407–417.

MOIN, P. & BEWLEY, T. R. 1994 Feedback control of turbulence. *Appl. Mech. Rev.* **47** (6).

MONKEWITZ, P. 1989 Feedback control of global oscillations in fluid systems. *AIAA Paper 89-0991*.

MONKEWITZ, P. 1990 The role of absolute and convective instability in predicting the behavior of fluid systems. *Eur. J. Mech., B/Fluids* **9**, 395–413.

MONKEWITZ, P. A., WILLIAMSON, C. H. K. & MILLER, G. D. 1996 Phase dynamics of Kármán vortices in cylinder wakes. *Phys. Fluids* **8**, 91.

MONOKROUSOS, A., BRANDT, L., SCHLATTER, P. & HENNINGSON, D. S. 2008 DNS and LES of estimation and control of transition in boundary layers subject to free-stream turbulence. *Int. J. Heat Fluid Flow* **29**(3) 841-855.

MOORE, B. 1981 Principal component analysis in linear systems: Controllability, observability, and model reduction. *IEEE Trans. Automat. Control* **26** (1), 17–32.

Nichols, J. W., Schmid, P. J. & Riley, J. J. 2007 Self-sustained oscillations in variable-density round jets. *J. Fluid Mech.* **582**, 341–376.

Obintata, G. & Andersson, B. D. 2001 *Model Reduction for Control System Design*. Springer, New York.

Park, D. S., Ladd, D. M. & W., H. E. 1993 Feedback control of a global mode in spatially developing flows. *Phys. Lett. A.* **182**, 244–248.

Pier, B. 2002 On the frequency selection of finite-amplitude vortex shedding in the cylinder wake. *J. Fluid Mech.* **458**, 407–417.

Provansal, M., Mathis, C. & Boyer, L. 1987 Bénard-von Kármán instability: Transient and forcing regimes. *J. Fluid. Mech.* **182**, 1–22.

Reddy, S. & Henningson, D. 1993 Energy growth in viscous channel flows. *J. Fluid Mech.* **252**, 209–238.

Reddy, S., Schmid, P. & Henningson, D. 1993 Pseudospectra of the orr-sommerfeld operator. *SIAM J. Appl. Math.* **53** (1), 15–47.

Roussopoulos, K. & Monkewitz, P. 1996 Nonlinear modeling of vortex shedding control in cylinder wakes. *Physica D* **97**, 264–273.

Rowley, C. W. 2005 Model reduction for fluids using balanced proper orthogonal decomposition. *Int. J. Bifurc. Chaos* **15** (3), 997–1013.

van der Schaft, A. J. 1991 Duality for linear systems: External and state space characterization of the adjoint problem. In *Analysis of controlled dynamical systems* (ed. B. B. etal), pp. 393–403. Boston: Birkhäuser.

Schmid, P. J. 2007 Nonmodal stability theory. *Ann. Rev. Fluid Mech.* **39**, 129–62.

Schmid, P. J. & Henningson, D. S. 2001 *Stability and Transition in Shear Flows*. Springer Verlag, New York.

Sirovich, L. 1987 Turbulence and the dynamics of coherent structures i-iii. *Quart. Appl. Math.* **45**, 561–590.

Skelton, R., Iwasaki, T. & Grigoriadis, K. 1998 *A Unified Algebraic Approach to Linear Control Design*. Taylor & Francis.

Skogestad, S. & Postlethwaite, I. 2005 *Multivariable Feedback Control, Analysis to Design*, 2nd edn. Wiley.

Tang, T. 1993 The Hermite spectral method for Gaussian-type functions. *J. Sci. Comp.* **14**, 594–606.

Trefethen, L. N. & Bau, D. 1997 *Numerical Linear Algebra.*. SIAM, Philadelphia.

Trefethen, L. N. & Embree, M. 2005 *Spectra and Pseudospectra — The Behavior of Nonnormal Matrices and Operators*. Princeton University Press, New Jersey.

Trefethen, L. N., Trefethen, A., Reddy, S. & Driscoll, T. 2005 Hydrodynamic stability without eigenvalues. *Science* **261**, 578–584.

Trefethen, L. N. 1997 Pseudospectra of linear operators. *SIAM Review* **39** (3), 383–406.

Weideman, J. A. & Reddy, S. C. 2000 A Matlab differentiation matrix suite. *ACM Trans. of Math. Software* **26**, 465–519.

Willcox, K. & Peraire, J. 2002 Balanced model reduction via the proper orthogonal decomposition. *AIAA J.* **40** (11), 2323–2330.

Zhou, K., Doyle, J. & Glover, K. 2002 *Robust and Optimal Control*. Prentice Hall, New Jersey.

Zhou, K., Salomon, G. & Wu, E. 1999 Balanced realization and model reduction for unstable systems. *Int. J. Robust Nonlinear Control* **9**, 183–198.

ZUCCHER, S. LUCHINI, P. & BOTTARO, A. 2004 Algebraic growth in a Blasius boundary layer: Optimal and robust control by mean suction in the nonlinear regime. *J. Fluid. Mech.* **556**, 189–216.

Paper 2

Input–output analysis, model reduction and control of the flat-plate boundary layer

Shervin Bagheri, Luca Brandt and Dan S. Henningson

The dynamics and control of two-dimensional disturbances in the spatially evolving boundary layer on a flat plate are investigated from an input-output viewpoint. A setup of spatially localized inputs (external disturbances and actuators) and outputs (objective functions and sensors) is introduced for the control design of convectively unstable flow configurations. From the linearized Navier–Stokes equations with inputs and outputs, controllable, observable and balanced modes are extracted using the snapshot method. A balanced reduced-order model is constructed and shown to capture the input-output behavior of the linearized Navier–Stokes equations. This model is finally used to design a $\mathcal{H}_2$-feedback controller to suppress the growth of two-dimensional perturbations inside the boundary layer.

1. Introduction

Many powerful linear systems and control theoretical tools have been out of reach for the fluids community due to the complexity of the Navier–Stokes equations. Two elements that have enabled a systematic approach to flow control are the availability of increasingly powerful computer resources and recent advances of matrix-free methods. In this paper, the linearized Navier–Stokes equations including inputs and outputs are analyzed using systematic tools from linear systems and control theory. The techniques do not rely on physical insight into the specific flow configuration and can in principle be applied to any geometry.

We will focus on the flat-plate geometry which still poses a computational challenge. The two-dimensional Blasius boundary layer is non-parallel, *i.e.* spatially evolving and therefore has two inhomogeneous spatial directions. Many tools in both stability analysis and control theory rely on the linearized stability operator, which even for two-dimensional flows becomes very large when it is discretized. As an example, a moderate grid resolution with 200 points in two directions leads to a system matrix with a memory demand of 10 Gigabytes, whereas to store a flow field requires only 3 Megabytes. It is therefore essential to either approximate or develop algorithms where large matrices are avoided and the storage demands are of the order of few flow fields. Matrix-free methods

employ the "timestepper approach" in which given a flow field a Navier–Stokes code is used to provide a field at a later time. The timestepper technique has become increasingly popular in stability analysis, both for computing the largest transient growth (Blackburn *et al.* 2008) and performing asymptotic analysis (Barkley *et al.* 2002). Another example of a matrix-free method is the snapshot method introduced by Sirovich (1987), which allows the proper orthogonal decomposition (POD) of flow fields without solving large eigenvalue problems.

The starting point of modern optimal and robust control design, also denoted as $\mathcal{H}_2$– and $\mathcal{H}_\infty$–control, is an input-output formulation referred to as the standard state-space formulation (Zhou *et al.* 1999). The well-known stochastic approach to optimal control referred to as LQG (Linear Quadratic Gaussian) is an example of a $\mathcal{H}_2$ controller. In this work, we consider three inputs and two outputs; the inputs represent external disturbances, measurement noise and the actuator whereas the outputs represent measurements for estimation and of the objective functional to be minimized. The control problem is to supply the actuator with an optimal signal based on the measurements taken from the first sensor, such that the effect of external disturbances and measurement noise on the disturbance energy is minimized at the location of the second sensor. Given the physical distribution of the inputs and outputs, the control design process amounts to the determination of input signals when output signals are given. Therefore, for successful control design it is sufficient to capture only a fraction of the dynamics, namely the relationships between the input and output signals.

The aim of this study is to build a model of low dimension that captures the input-output behavior of the flat-plate boundary layer, and use this model for optimal feedback control design. With the help of the adjoint Navier–Stokes equations two fundamental dynamical structures are identified; (i) the flow structures that are influenced by the inputs (ii) the flow structures that the outputs are sensitive to. These controllable and observable structures determine the input-output behavior completely for linear systems. It is well known in systems theory that these two set of modes can be balanced, and represented by one set of modes, called the balanced modes. In this way, the flow structures that capture most of the input-output behavior are extracted and used as projection basis for model reduction. The method employed in this work to compute the balanced modes is called snapshot-based balanced truncation (Rowley 2005; Willcox & Peraire 2002). This method has been applied to the channel flow (Ilak & Rowley 2008) and the flow around a pitching airfoil (Ahuja *et al.* 2007). Unlike previous work, we do not combine the snapshot-based balanced truncation with an output projection approach in order to describe the flow dynamics. Our control design and performance evaluation is based on input and output signals rather than on the space-time evolution of the entire flow.

Previous work in flow control involving model reduction and control design has typically relied on physical insight into the specific flow situation rather

than on a systematic approach detached from the application (see Kim & Bewley 2007, for a recent review). For parallel flows, for instance, it is possible to decouple the linear equations in Fourier space. Control, estimation and other types of optimization can then be performed independently for each wavenumber and then transformed back to physical space. This approach has been adopted for channel flow in Högberg *et al.* (2003) and even extended to weakly nonparallel flows by Chevalier *et al.* (2007*a*). Another example is the projection of the linearized Navier–Stokes equations on a set of modes such as global eigenmodes of the stability operator or POD modes. Although, these methods have been applied with considerable success to various flows (Gillies 1998; Åkervik *et al.* 2007) their success is strongly dependent on the dynamics of the specific flow situation. For many open shear flows the global eigenmodes and their associated adjoint modes can become widely separated in the streamwise direction (Chomaz 2005) and gradually move away from the locations of the inputs and outputs (Lauga & Bewley 2003). As a consequence controllability and observability of the global eigenmodes is gradually diminished. If controllability/observability is lost for any unstable eigenmode, no control scheme will be able to stabilize the system. The POD basis also has limitations for describing the input-output behavior. Although it is optimal for capturing the energy of the response to an input, it does not always capture the input itself and takes no consideration of the output. However, examples of successful adaptations of POD modes can be found e.g. in Noack *et al.* (2003); Siegel *et al.* (2008) for the globally unstable flow past a circular cylinder.

The paper is organized as follows: we start with describing the flow domain, the inputs, outputs and the control problem in section 2. In this section the mathematical framework is presented with evolution, controllability and observability operators and their associated adjoint operators. These operators are used to introduce the Gramians and balanced modes in section 3, where we also investigate the input-output behavior of our linear system and discuss the controllable, observable and balanced modes. In section 4 the impulse and harmonic response of the balanced reduced-order model are compared to the full Navier–Stokes equations and the model reduction error is quantified. Section 5 deals with the control design. We briefly introduce the $\mathcal{H}_2$ framework and evaluate the closed-loop performance. Concluding remarks and a summary of the presented material are offered in the last section. Finally, in the appendix we derive the adjoint operators, describe the snapshot method, the solution of the $\mathcal{H}_2$ problem and our timestepper.

2. Problem formulation

2.1. *Governing equations*

We consider the linear spatio-temporal evolution of two-dimensional disturbances in a viscous, incompressible flow over a flat plate. The geometry of the problem and the physical domain, $\Omega = (0, L_x) \times (0, L_y)$, are shown in figure 1. The disturbance behavior is governed by the Navier–Stokes equations
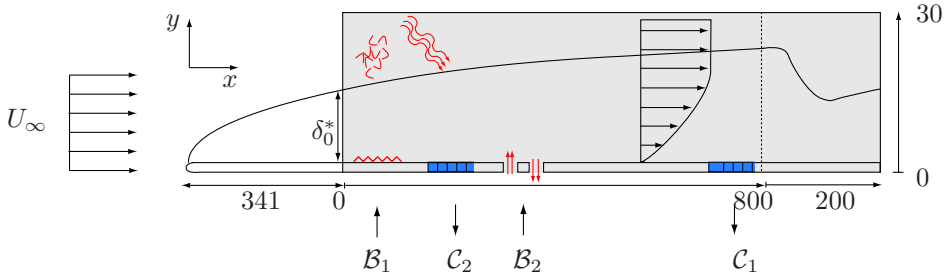
FIGURE 1. Conceptual figure of the input-output configuration used for the control of perturbations in a two-dimensional flat-plate geometry. The computational domain $\Omega = (0, L_x) \times (0, L_y)$, shown by the gray region, extends from $x = 0$ to $x = 1000$ with the fringe region starting at $x = 800$. The first input $\mathcal{B}_1$, located at $(x_w, y_w) = (35, 1)$, models the initial receptivity phase, where disturbances are induced by free-stream turbulence, acoustic waves or wall roughness. The actuator, $\mathcal{B}_2$, provides a mean to manipulate the flow, in this case by a localized volume forcing, and is centered at $(x_u, y_u) = (400, 1)$. Two sensors, $\mathcal{C}_1$ and $\mathcal{C}_2$, are located at $(x_v, y_v) = (300, 1)$ and $(x_z, y_z) = (750, 1)$ respectively. The upstream measurements are used to estimate the incoming perturbations, while the downstream sensor quantifies the effect of the control. Note that in this work all the inputs and outputs are Gaussian functions given by expression (13).

linearized about a spatially evolving zero-pressure-gradient boundary layer,

$$\frac{\partial \mathbf{u}}{\partial t} = -(\mathbf{U} \cdot \nabla)\mathbf{u} - (\mathbf{u} \cdot \nabla)\mathbf{U} - \nabla p + \mathrm{Re}^{-1}\nabla^2 \mathbf{u} + \lambda(x)\mathbf{u}, \qquad (1a)$$

$$0 = \nabla \cdot \mathbf{u}, \qquad (1b)$$

$$\mathbf{u} = \mathbf{u}_0 \qquad \text{at} \quad t = 0. \qquad (1c)$$

The disturbance velocity and pressure field at position $\boldsymbol{x} = (x, y)$ and time t are represented by $\mathbf{u}(\boldsymbol{x}, t) = (u, v)^T$ and $p(\boldsymbol{x}, t)$, respectively. The divergence operator is denoted by $\nabla = (\partial_x, \partial_y)^T$. The Reynolds number is defined as $\mathrm{Re} = U_\infty \delta_0^* / \nu$, where U_∞ is the free-stream velocity and δ_0^* the displacement thickness at the computational inflow $x_0 = 0$. All the simulations were performed at $\mathrm{Re} = 1000$ which corresponds to a distance of $341\delta_0^*$ from the leading edge to the inlet of the computational domain. The base flow $\mathbf{U} = (U, V)^T(x, y)$ is a solution to the steady nonlinear, Navier–Stokes equations.

The term $\lambda(x)$ is used to enforce periodicity of the physical flow in the streamwise direction, so that a spectral Fourier expansion technique can be employed for our numerical solution. This function is nonzero only in a fringe

region at the end of the domain (see figure 1) where it forces the outgoing perturbation amplitude to zero (see Appendix C and Nordström *et al.* 1999, for further details). It is pertinent to comment on the presence of the additional forcing term $\lambda(x)$ in (1). As discussed in (Åkervik *et al.* 2008) the growth rate of individual eigenvalues in the spectrum of the linearized Navier-Stokes equations depend on the outflow boundary conditions. However, the perturbation dynamics remain unaltered for different boundary conditions, including the fringe method.

The solutions to (1) satisfy no-slip condition at the plate and vanish at the upper boundary $L_y = 30\delta_0^*$ which is chosen to be well outside the boundary layer. The boundary conditions hence are

$$\mathbf{u}(0, y) = \mathbf{u}(L_x, y), \tag{2a}$$
$$\mathbf{u}(x, 0) = \mathbf{u}(x, L_y) = 0. \tag{2b}$$

2.2. *Standard state-space formulation & the $\mathcal{H}_2$ problem*

The Navier–Stokes equations may be written in the *standard state-space form* (Zhou *et al.* 2002) useful for applying tools from systems theory and for $\mathcal{H}_2/\mathcal{H}_\infty$ control design.

In the state-space framework, any divergence-free, smooth disturbance field $\mathbf{u}(\boldsymbol{x})$ that satisfies the boundary conditions (2) is an element of the (Hilbert) state-space

$$\mathbb{X} = \{\mathbf{u}(\boldsymbol{x}) \in L^2(\Omega) \mid \nabla \cdot \mathbf{u}(\boldsymbol{x}) = 0, \ \mathbf{u}(0, y) = \mathbf{u}(L_x, y), \ \mathbf{u}(x, 0) = \mathbf{u}(x, L_y) = 0\}, \tag{3}$$

A state is a velocity field $\mathbf{u}(\boldsymbol{x}, t)$ at time t, or equivalently a point on a trajectory in $\mathbb{X}$. Let us introduce a linear bounded solution operator $\mathcal{T}(t) : \mathbb{X} \to \mathbb{X}$ for the state variable $\mathbf{u}$ as

$$\mathbf{u}(\boldsymbol{x}, t + s) = \mathcal{T}(t)\mathbf{u}(\boldsymbol{x}, s). \tag{4}$$

Given a perturbation field at time s, $\mathcal{T}(t)$ provides the velocity field at a later time $t + s$ by solving equations (1) with $\mathbf{u}_0 = \mathbf{u}(\boldsymbol{x}, s)$ and (2). The operator satisfies the properties $\mathcal{T}(t + s) = \mathcal{T}(t)\mathcal{T}(s)$, $\mathcal{T}(0) = I$ and can be considered as a semigroup (see *e.g.* Pazy 1983; Trefethen & Embree 2005) of the form $\exp(\mathcal{A}t)^1$ with the infinitesimal generator,

$$\mathcal{A}\mathbf{u} = \lim_{\delta t \to 0} \frac{\mathcal{T}(\delta t)\mathbf{u} - \mathbf{u}}{\delta t}. \tag{5}$$

The linearized Navier-Stokes equations (1) with boundary conditions (2) can be cast as an initial-value problem in state-space form

$$\dot{\mathbf{u}} = \mathcal{A}\mathbf{u} \tag{6a}$$
$$\mathbf{u} = \mathbf{u}_0 \quad \text{at} \quad t = 0. \tag{6b}$$

---

[1]This is only true if $\mathcal{A}$ is a bounded operator. In general, for a closed operator $\mathcal{A}$ with a dense domain, the relation between $\mathcal{T}$ and $\mathcal{A}$ is $\mathcal{T}(t)\mathbf{u} = \lim_{n \to \infty}(I - t/n\mathcal{A})^{-n}\mathbf{u}$, see *e.g.* Pazy (1983).

Note that the action of $\mathcal{A}$ on $\mathbf{u}$ corresponds to evaluating the right-hand side of the Navier-Stokes equations and enforcing the boundary conditions. The pressure term can be obtained from the velocity field by solving a Poisson equation (Kreiss *et al.* 1993). Alternatively, the state-space form can be obtained by defining a projection operator that projects the equations onto $\mathbb{X}$ (Bewley *et al.* 2000; Chorin & Marsden 1990).

In this work, the action of the operator $\mathcal{A}$ is approximated numerically: $\mathcal{T}(t)\mathbf{u}(\boldsymbol{x}, s)$ is obtained by solving the partial differential equation (1) using a timestepper (Barkley *et al.* 2002) (*i.e.* a Navier–Stokes solver) with $\mathbf{u}(\boldsymbol{x}, s)$ as initial condition. In its simplest form, a timestepper sets up a grid in space and time and computes approximate solutions on this grid by marching in time. This approach is computationally feasible also for very large systems since matrices are not stored. The timestepper used and the corresponding numerical method are described in Appendix C.

We introduce the forcing $\boldsymbol{f}(\boldsymbol{x}, t)$, which is also referred to as the input. The forcing $\boldsymbol{f}$ is decomposed into external disturbances $\mathcal{B}_1\mathsf{w}$ and a control $\mathcal{B}_2\mathsf{u}$, *i.e.*

$$\boldsymbol{f} = \mathcal{B}_1\mathsf{w} + \mathcal{B}_2\mathsf{u}, \tag{7}$$

where the input signals $\mathsf{w}(t), \mathsf{u}(t)$ are functions of time and $\mathcal{B}_1, \mathcal{B}_2$ are bounded linear mappings from $\mathbb{R} \to \mathbb{X}$. The first mapping, $\mathcal{B}_1$, represents the spatial distribution of the sources of external disturbances acting on the flow (see figure 1). In our model, the input forcing $\mathcal{B}_1$ is located at the upstream end of the domain to model the upstream receptivity phase, when disturbances are introduced into the boundary layer by *e.g.* roughness and free-stream perturbations. The actuator used for control is defined by the mapping $\mathcal{B}_2$, which represents a localized volume force, mimicking blowing and suction at the wall. Finally, $\mathsf{u}(t)$ represents the control signal we wish to apply and is based on the sensor measurements.

Information about the disturbance behavior is given by two outputs

$$\mathsf{z} \quad = \mathcal{C}_1\mathbf{u} + l\mathsf{u}, \tag{8}$$
$$\mathsf{v} \quad = \mathcal{C}_2\mathbf{u} + \alpha\mathsf{g}, \tag{9}$$

where the output signals z, v are functions of time and $\mathcal{C}_1, \mathcal{C}_2$ are bounded linear functionals from $\mathbb{X} \to \mathbb{R}$. The sensor defined by $\mathcal{C}_1$ is located far downstream and it is used to evaluate the level of the disturbance amplitude. Therefore it reveals whether the "objective" of our control has been met. In particular, the objective is to find a control signal $\mathsf{u}(t)$ such that the perturbation energy in the flow is minimized downstream at the location defined by $\mathcal{C}_1$. To design an efficient controller, however, the energy input expended in the actuation should be limited; thus, the control effort is penalized with a scalar l. For large values of l the control effort is considered to be expensive, whereas small values indicate cheap control. This results in an objective functional of the form

$$\|\mathsf{z}\| = \|\mathcal{C}_1\mathbf{u}\| + l\|\mathsf{u}\| \tag{10}$$

and explains why the control signal is added to the sensor signal when defining the output signal z. The norms in (10) are associated to the inner products defined in the next section. In the definition of z we have assumed $\langle l u, \mathcal{C}_1 \mathbf{u} \rangle = 0$ so that there is no cross weighting between the flow energy and control input (Zhou *et al.* 1999).

The second output signal $v(t)$ is the measurement signal extracted from the sensor $\mathcal{C}_2$. This signal is the only information delivered to the controller in order to provide a control signal such that the above objective is met. The additional term $g(t)$ accounts for noise contaminating the measurements. This term can be considered as a third forcing, but rather than forcing the Navier–Stokes equations it forces the measurements. Large values of the scalar α indicate high level of noise corruption in the output signal, whereas for low values of α the measurement v reflects information about the flow field with high fidelity.

The choice of the relative position of the sensor $\mathcal{C}_2$ and actuator $\mathcal{B}_2$ used in the control design process and reported in figure 1 is based on the knowledge of the behavior of boundary layer instabilities. For convectively unstable flows, disturbances eventually leave the control domain, therefore there exists only a window of opportunity in time to reduce the growth of these disturbances while they are convected downstream. As a consequence, the sensor placement in the streamwise direction is a trade-off. For a good estimation performance it should be placed downstream so that the disturbance energy has amplified but for a good controller performance, it should be placed upstream to provide the actuator an estimate of the flow dynamics as soon as possible. Similarly, there is a trade-off when choosing the location of the actuator, since its effects on the disturbance behavior is limited to nearby region. It is rather inefficient to place it either far downstream, where the disturbances have already experienced a substantial growth, or far upstream, where the disturbances will again have the opportunity to grow.

A completely different choice of sensor and actuator placement is appropriate in the case of globally unstable flows (see Bagheri *et al.* 2009), when the whole flow beats at a specific frequency. Since the disturbances never leave the laboratory frame, one can place the measurement sensor where the disturbance energy is largest and the actuator where the sensitivity of the disturbances to forcing is the largest. In many open shear flows these locations are, respectively, far downstream where the global eigenmodes of linearized operator are located and far upstream where the adjoint global eigenmodes reveal high flow sensitivity. See for example Åkervik *et al.* (2007) in the case of feedback control applied the flow separation over a long shallow cavity.

The Navier–Stokes equations (1) with input vector $\mathbf{f} = (\mathsf{w}, \mathsf{g}, \mathsf{u})^T$ as an element in the input space $\mathbb{U} = \mathbb{R}^3$ and output vector $\mathbf{y} = (\mathsf{z}, \mathsf{v})^T$ as an element in the output space $\mathbb{Y} = \mathbb{R}^2$ may now be written in the standard state-space

form

$$\dot{\mathbf{u}} = \mathcal{A}\mathbf{u} + \mathcal{B}\mathbf{f} \tag{11a}$$

$$\mathbf{y} = \mathcal{C}\mathbf{u} + \mathcal{D}\mathbf{f} \tag{11b}$$

$$\mathbf{u} = \mathbf{u}_0 \quad \text{at} \quad t = 0 \tag{11c}$$

where $\mathcal{A}$ was defined in (5). Furthermore, we have $\mathcal{C} = (\mathcal{C}_1, \mathcal{C}_2)^T$, $\mathcal{B} = (\mathcal{B}_1, 0, \mathcal{B}_2)$ and

$$\mathcal{D} = \begin{pmatrix} 0 & 0 & l \\ 0 & \alpha & 0 \end{pmatrix}. \tag{12}$$

The system (11) is asymptotically stable, *i.e.* in the global framework all the eigenmodes of the linearized Navier–Stokes system for a spatial boundary layer represent perturbations decaying in time.

Finally, we define the spatial distribution of the sensors and actuators introduced above. In this work, the input and output operators are modeled with the Gaussian function $h(\mathbf{x}, \mathbf{x}_0)$, defined as

$$\boldsymbol{h}(\boldsymbol{x}; \boldsymbol{x}_0) = \begin{pmatrix} \sigma_x \gamma_y \\ -\sigma_y \gamma_x \end{pmatrix} \exp(-\gamma_x^2 - \gamma_y^2) \tag{13}$$

where

$$\gamma_x = \frac{x - x_0}{\sigma_x}, \qquad \gamma_y = \frac{y - y_0}{\sigma_y}. \tag{14}$$

The scalar quantities $\sigma_x = 4$, $\sigma_y = 1/4$, x_0 and y_0 (the latter two are given in the caption of figure 1) determine, respectively, the size and location of the inputs and outputs. They are all of the same size, but located at different streamwise locations, as shown schematically in figure 1. With these definitions we have,

$$\mathcal{B} = (\boldsymbol{h}(\boldsymbol{x}; \boldsymbol{x}_\mathrm{w}), 0, \boldsymbol{h}(\boldsymbol{x}; \boldsymbol{x}_\mathrm{u})) \tag{15}$$

and

$$\mathcal{C}\mathbf{u} = \int_\Omega \begin{pmatrix} \boldsymbol{h}(\boldsymbol{x}; \boldsymbol{x}_\mathrm{z})^T \mathbf{u} \\ \boldsymbol{h}(\boldsymbol{x}; \boldsymbol{x}_\mathrm{v})^T \mathbf{u} \end{pmatrix} \mathrm{d}x \mathrm{d}y. \tag{16}$$

The particular shape of sensor and actuators implies that the inputs amount to localized volume forcing, whereas the flow measurements are obtained by averaging the velocity field over small domains using the Gaussian function as weights.

2.3. *Controllability and observability operators*

When performing model reduction for control design, one wishes to retain the relationship between the inputs and the outputs in the low-order system. Following linear systems theory, the properties of the input-output system (11) can be described by the two operators introduced in this section. In the framework presented below we assume that sufficient regularity exists so that all operators are bounded in the chosen metrics. See figure 2 and table 1 for an overview of the operators.
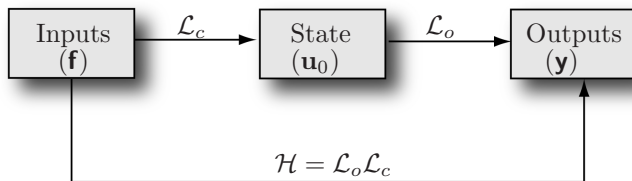
FIGURE 2. The operators used to examine the system input-output behavior. The controllability operator $\mathcal{L}_c$ relates past inputs to the present state, while the observability mapping $\mathcal{L}_o$ relates the present state to the future outputs. Their combined action is expressed by the Hankel operator $\mathcal{H}$.

The operators needed to describe the input-output behavior can be related to the formal solution of the system of equations (11), which is

$$\mathbf{y}(t) = \mathcal{C}\mathcal{T}(t)\mathbf{u}_0 + \mathcal{C}\int_0^t \mathcal{T}(t-\tau)\mathcal{B}\mathbf{f}(\tau)\mathrm{d}\tau + \mathcal{D}\mathbf{f}(t). \tag{17}$$

In the expression above, we identify the first term on the right-hand side with the homogeneous solution and the second term with the particular solution stemming from the forcing $\mathbf{f}$. Note that in our case the forcing term $\mathcal{B}$ is an element in $\mathbb{X}$, *i.e.* divergence-free and satisfies the boundary conditions. For a more general forcing $\boldsymbol{f}$, only the divergence-free part of the forcing $\hat{\boldsymbol{f}}$ will affect the output signal. The difference $\hat{\boldsymbol{f}} - \boldsymbol{f}$ can be written as the gradient of a scalar and thus will only modify the pressure (Bewley *et al.* 2000). The third part of expression (17) relates the input to the output through the matrix $\mathcal{D}$ without any operators involved. Without loss of generality, we will neglect this term for now and consider it again in section 5 for control design.

In systems theory, the quantitative investigation of the input-output properties of a linear system is commonly performed through the mappings sketched in figure 2. We begin by introducing the controllability operator $\mathcal{L}_c : \mathbb{U}((-\infty, 0])$ $\rightarrow \mathbb{X}$,

$$\mathbf{u}_0 = \mathcal{L}_c\mathbf{f}(t) = \int_{-\infty}^0 \mathcal{T}(-\tau)\mathcal{B}\mathbf{f}(\tau)\mathrm{d}\tau. \tag{18}$$

This operator describes the mapping of any input $\mathbf{f}(t)$ with $t \in (-\infty, 0]$ onto the state vector $\mathbf{u}$ at the reference time $t = 0$. The input space $\mathbb{U}((-\infty, 0])$ contains input trajectories in the past time $t \in (-\infty, 0]$. The associated inner-product is given A.1. The action of $\mathcal{L}_c$ can be numerically computed by a timestepper. It amounts to solving the linearized Navier–Stokes equations for the velocity field $\mathbf{u}$ with forcing term $\mathbf{f}(t)$ and zero initial conditions.

The observability operator $\mathcal{L}_o : \mathbb{X} \rightarrow \mathbb{Y}([0, \infty))$ is defined as

$$\mathbf{y}(t) = \mathcal{L}_o(t)\mathbf{u}_0 = \mathcal{C}\mathcal{T}(t)\mathbf{u}_0. \tag{19}$$

Operator	Mapping	Definition	Adjoint operator
Evolution	$\mathbb{X} \to \mathbb{X}$	$\mathcal{T}(t)\mathbf{u}(s) = \mathbf{u}(t+s)$	$\mathcal{T}^*(t)\mathbf{u}(s) = \mathbf{u}(s-t)$
Controllability	$\mathbb{U}((-\infty,0]) \to \mathbb{X}$	$\mathcal{L}_c\mathbf{f}(t) = \int_{-\infty}^{0} \mathcal{T}(-t)\mathcal{B}\mathbf{f}(t)\mathrm{d}t$	$\mathcal{L}_c^*\mathbf{u}_0 = \mathcal{B}^*\mathcal{T}^*(-t)\mathbf{u}_0$
Observability	$\mathbb{X} \to \mathbb{Y}([0,\infty))$	$\mathcal{L}_o(t)\mathbf{u}_0 = \mathcal{C}\mathcal{T}(t)\mathbf{u}_0$	$\mathcal{L}_o^*(t)\mathbf{f} = \int_0^{\infty} \mathcal{T}^*(t)\mathcal{C}^*\mathbf{f}\mathrm{d}t$
Hankel	$\mathbb{U}((-\infty,0]) \to \mathbb{Y}([0,\infty))$	$\mathbf{y} = \mathcal{L}_o(t)\mathcal{L}_c\mathbf{f}$	$\mathbf{f} = \mathcal{L}_c^*(t)\mathcal{L}_o^*\mathbf{y}$

TABLE 1. The linear operators used in this work. See Appendix A for further details and derivations of the adjoint operators.

This operator describes the mapping of any initial velocity field $\mathbf{u}_0$ to the output signal $\mathbf{y}(t)$ with $t \geq 0$. The output space $\mathbb{Y}([0,\infty))$ contains output trajectories in the future time $t \in [0,\infty)$. The action of $\mathcal{L}_o(t)$ can also be numerically computed and it amounts to extracting the output signal while solving the linearized Navier–Stokes equations with the initial condition $\mathbf{u}_0$ at the reference time $t = 0$ and zero forcing.

A direct mapping between input and output can be obtained as the combination of the operators just introduced (see figure 2),

$$\mathbf{y}(t) = \mathcal{L}_o\mathcal{L}_c\mathbf{f}(t) = \int_{-\infty}^{0} \mathcal{C}\mathcal{T}(t-\tau)\mathcal{B}\mathbf{f}(\tau)\mathrm{d}\tau. \tag{20}$$

This expression can be interpreted as a mapping from past inputs to future outputs. It can be shown that equation (20) is the formal solution for a system which is forced by $\mathbf{f}(t)$ in the time interval $t \in (-\infty, 0]$, resulting in the flow field $\mathbf{u}_0$ at $t = 0$. The output is extracted for $t \geq 0$, corresponding to the signal $\mathbf{y}(t)$ produced by the initial condition $\mathbf{u}_0$. Expression (20) is also the starting point for the input-output analysis leading to systematically finding reduced order approximations. The mapping from inputs to outputs given by (20) in terms of $\mathcal{L}_c$ and $\mathcal{L}_o$ is called Hankel operator $\mathcal{H} : \mathbb{U}((-\infty,0]) \to \mathbb{Y}([0,\infty))$, *i.e.*,

$$\mathbf{y}(t) = \mathcal{L}_o(t)\mathcal{L}_c\mathbf{f}(t) = (\mathcal{H}\mathbf{f})(t). \tag{21}$$

We have two different representations of the input-output behavior of the flow system; (i) the state-space representation (11) and (ii) the Hankel operator $\mathcal{H}$ defined in (21). Note that in the latter case it is assumed that inputs and outputs are not active at the same time.

2.4. *Adjoint equations and operators*

Before issues related to controllability, observability and model reduction can be considered the adjoint linear operators corresponding to $(\mathcal{T}, \mathcal{L}_c, \mathcal{L}_o)$ must be introduced. The adjoint variables provide information about how variations in the velocity field affect the system output. We show that the adjoint operators can be associated with the adjoint linearized Navier–Stokes equations in state-space form, where the role of the inputs and outputs is reversed. The operators $(\mathcal{T}^*, \mathcal{L}_c^*, \mathcal{L}_o^*, \mathcal{C}^*, \mathcal{B}^*)$ and adjoint Navier–Stokes equations are derived in Appendix A. The inner products associated with the Hilbert spaces

$\mathbb{X}, \mathbb{U}, \mathbb{Y}, \mathbb{U}((-\infty, 0])$ and $\mathbb{Y}([0, \infty))$ are given in A.1. The adjoint of the linearized Navier–Stokes equations (1) associated with inner product (61a) is

$$-\dot{\boldsymbol{p}} = (\mathbf{U} \cdot \nabla)\boldsymbol{p} - (\nabla \mathbf{U})^T \boldsymbol{p} + \nabla \sigma + \mathrm{Re}^{-1} \nabla^2 + \lambda(\boldsymbol{x})\boldsymbol{p}, \qquad (22a)$$

$$0 = \nabla \cdot \boldsymbol{p}, \qquad (22b)$$

$$\boldsymbol{p} = \boldsymbol{p}_T \qquad \text{at} \quad t = T, \qquad (22c)$$

This system of equations describes the evolution of adjoint flow field $\boldsymbol{p}(\boldsymbol{x}, t) = (u^*, v^*)^T$ backwards in time. The term σ denotes the adjoint pressure field. The boundary conditions for $\boldsymbol{p}$ are given in A.1.

The evolution operator associated with (22) is

$$\boldsymbol{p}(\boldsymbol{x}, s - t) = \mathcal{T}^*(t)\boldsymbol{p}(\boldsymbol{x}, s), \qquad (23)$$

so that given an adjoint field at time s the adjoint evolution operator provides a solution at an earlier time $s - t$. Again, the above operator is approximated numerically using a timestepper solving equations (22). In A.1 it is shown that $\mathcal{T}^*$ is in fact the adjoint of $\mathcal{T}$ under the inner product (61a). Furthermore, the infinitesimal generator $\mathcal{A}^*$ of $\mathcal{T}^*$ is the adjoint of $\mathcal{A}$ given in equation (5) (Pazy 1983).

The adjoint linearized Navier–Stokes equations and its corresponding evolution operator form the basis of the adjoint input-output system dual to (11). This can be obtained in three steps; (i) derive the adjoint input and output operators $\mathcal{B}^*$ and $\mathcal{C}^*$ (ii) use $\mathcal{B}^*$, $\mathcal{C}^*$ and $\mathcal{T}^*$ to derive the adjoint controllability and observability operator $\mathcal{L}_c^*$ and $\mathcal{L}_o^*$ (iii) identify the adjoint state-space with the system which is associated with $\mathcal{L}_c^*$ and $\mathcal{L}_o^*$.

The adjoint of the input and output operators $\mathcal{B}$ and $\mathcal{C}$ associated with the inner products (61b) and (61c) are,

$$\mathcal{C}^* = (\mathcal{C}_1^*, \mathcal{C}_2^*) = (h(\boldsymbol{x}; \boldsymbol{x}_{\mathsf{z}}), h(\boldsymbol{x}; \boldsymbol{x}_{\mathsf{v}})), \qquad (24)$$

and

$$\mathcal{B}^* \boldsymbol{p} = \begin{pmatrix} \mathcal{B}_1^* \boldsymbol{p} \\ 0 \\ \mathcal{B}_2^* \boldsymbol{p} \end{pmatrix} = \int_\Omega \begin{pmatrix} h(\boldsymbol{x}; \boldsymbol{x}_{\mathsf{w}})^T \boldsymbol{p} \\ 0 \\ h(\boldsymbol{x}; \boldsymbol{x}_{\mathsf{u}})^T \boldsymbol{p} \end{pmatrix} \mathrm{d}x \mathrm{d}y, \qquad (25)$$

respectively.

The adjoint controllability and observability operators $\mathcal{L}_c^* : \mathbb{X} \to \mathbb{U}((-\infty, 0])$ and $\mathcal{L}_o^* : \mathbb{Y}([0, \infty)) \to \mathbb{X}$ associated with the inner products (61b) and (61c) (derived in A.2) are given by

$$\mathcal{L}_c^*(-t)\boldsymbol{p}(\boldsymbol{x}, 0) = \mathcal{B}^* \mathcal{T}^*(-t)\boldsymbol{p}(\boldsymbol{x}, 0) \qquad (26a)$$

$$\mathcal{L}_o^* \mathbf{t}(t) = \int_0^\infty \mathcal{T}^*(\tau)\mathcal{C}^* \mathbf{t}(\tau) \, d\tau, \qquad (26b)$$

where $\mathbf{t} \in \mathbb{Y}$ and $\boldsymbol{p} \in \mathbb{X}$. The first mapping, $\mathcal{L}_c^*$, is from the adjoint state at time $t = 0$ onto a signal in $\mathbb{U}$ at time $-t$. The mapping $\mathcal{L}_o^*$ is from an output signal in $\mathbb{Y}$ in $t \in [0, \infty)$ to a state in $\mathbb{X}$ at $t = 0$. In analogy to the case of the forward problem defined by (11), it can be seen that these two mappings

are the observability and controllability operator of the following state-space system,

$$-\dot{\boldsymbol{p}} = \mathcal{A}^*\boldsymbol{p} + \mathcal{C}^*\mathbf{t}, \tag{27a}$$

$$\mathbf{e} = \mathcal{B}^*\boldsymbol{p}. \tag{27b}$$

This system has two inputs contained in the vector $\mathbf{t} = (\mathsf{z}^*, \mathsf{v}^*)$ with $\mathbf{t} \in \mathbb{Y}$ and three outputs contained in the vector $\mathbf{e} = (\mathsf{w}^*, \mathsf{u}^*, \mathsf{g}^*) \in \mathbb{U}$. Comparing the above adjoint equations with (11) we observe that the outputs and inputs have exchanged place. In the dual system (27), the adjoint flow field is forced by the outputs; the adjoint problem will then be used to identify flow fields yielding the largest output response (Dullerud & Paganini 1999).

3. Input–output analysis

In this section, the main input-output characteristics of our problem are analyzed in order to identify the modes to retain in a low-order model. We introduce the concepts of Gramians and balancing using the operators defined in the previous section. For a more detailed presentation of systems theory we refer to Kailath (1980) and Curtain & Zwart (1995). The analysis amounts to computing the eigenmodes of three operators; $\mathcal{L}_c\mathcal{L}_c^*$, $\mathcal{L}_o^*\mathcal{L}_o$ and $\mathcal{L}_c\mathcal{L}_c^*\mathcal{L}_o^*\mathcal{L}_o$. The three sets of modes correspond to flow structures that are the most easily influenced by the input (controllable modes), to the states that produce the largest output energy (observable modes) and to the most relevant states for the input-output behavior (balanced modes). For the sake of clarity, we will show numerical results obtained using only the first input $\mathcal{B}_1$ and the first output $\mathcal{C}_1$ *i.e.* single-input and single-output system (SISO). We will return to the multi-input multi-output (MIMO) state-space system with input vector $\mathbf{f}$ and output vector $\mathbf{y}$ in section 4. The three sets of eigenmodes mentioned above can be computed numerically for systems with many degrees of freedom by using the following two approximations:

(i) *The timestepper:* As mentioned above, solutions of Navier–Stokes system (11) in input-output form are obtained numerically using a forward timestepper, which approximates the action of evolution operator $\mathcal{T}$. An adjoint timestepper is used for computing solutions of the associated adjoint system (27) and the action of the adjoint evolution operator $\mathcal{T}^*$. The numerical code employed is described in Appendix C. In the simulations presented, we have used 768 collocation points in the streamwise direction x and 101 points in the wall-normal direction y, with a computational box of dimensions $L_x = 1000$ and $L_y = 30$ (see figure 1). The discretized system has thus $m \approx 10^5$ degrees of freedom.

(ii) *The snapshot method:* The controllable and observable modes introduced below are computed using the snapshot method introduced by Sirovich (1987). Recently Rowley (2005) extended this method to obtain balanced modes. The snapshot technique is described in Appendix B. For the results presented, the flow structures are computed by collecting 1600 snapshots of the forward simulation using each input as initial condition and 1600 snapshots of

the adjoint simulation using each output as initial condition. The snapshots were taken with equal spacing in the time-interval $[0, 4000]$.

3.1. *Controllable modes*

We begin our input-output analysis by searching for flow states that are most easily triggered by a given input. This issue is related to the concept of controllability, which, in general, quantifies the possibility of steering the flow between two arbitrary states. A state $\mathbf{u}$ is controllable if it belongs to the range of $\mathcal{L}_c$, that is $\mathbf{u} = \mathcal{L}_c \mathbf{f}(t)$ exists for some $\mathbf{f}(t)$[2]. A commonly adopted interpretation of controllability is illustrated by the following optimal control problem: What is the minimum input energy $\|\mathbf{f}\|^2_{\mathbb{U}((-\infty,0])}$ in the time span $t \in (-\infty, 0]$ required to bring the state (if possible) from zero to the given initial condition $\mathbf{u}(\boldsymbol{x}, 0) = \mathbf{u}_0$?

Assuming $\mathbf{u}_0(\boldsymbol{x})$ has an unit norm and that it is controllable, it can be shown[3] that the optimal input is given by

$$\mathbf{f} = \mathcal{L}_c^* \mathcal{P}^{-1} \mathbf{u}_0, \tag{28}$$

where $\mathcal{P}$ is the controllability Gramian defined as

$$\mathcal{P} = \mathcal{L}_c \mathcal{L}_c^* = \int_{-\infty}^0 \mathcal{T}(-t) \mathcal{B} \mathcal{B}^* \mathcal{T}^*(-t) \mathrm{d}t = \int_0^\infty \mathcal{T}(t) \mathcal{B} \mathcal{B}^* \mathcal{T}^*(t) \mathrm{d}t. \tag{29}$$

In the first equality the expressions (18) and (26a) have been used. Using equation (28) the minimum input energy is given by

$$\|\mathbf{f}\|^2_{\mathbb{U}((-\infty,0])} = \int_\Omega \mathbf{u}_0^T \mathcal{P}^{-1} \mathbf{u}_0 \mathrm{d}x \mathrm{d}y. \tag{30}$$

The controllability Gramian $\mathcal{P}$ provides a means to rank different states according to how easily they can be influenced by an input. In particular, the most easily influenced, or most controllable, flow structures are the eigenfunctions of $\mathcal{P}$ associated to the largest eigenvalues of,

$$\mathcal{P} \phi_i^c = \lambda_i^c \phi_i^c. \tag{31}$$

The superscript ^{c} stands for controllable modes. Note that by $\mathcal{P}$ is a self-adjoint and positive semidefinite operator whose eigenvalues are real and positive and the eigenfunctions mutually orthogonal. If $\lambda_i^c \ll 1$, the corresponding eigenfunction ϕ_i^c requires very large energy to be excited by the input since $(\lambda_i^c)^{-1}$ is proportional to $\|\mathbf{f}\|_{\mathbb{U}((-\infty,0])}$. The mode is then referred to as (nearly) uncontrollable.

---

[2] The system (11) is called exactly controllable if all states $\mathbf{u} \in \mathbb{X}$ can be reached for some input. This is rarely the case for elliptic/parabolic PDE's and a less restrictive condition is approximate controllability, where any state $\mathbf{u} \in \mathbb{X}$ can be approximated arbitrary closely by controllable elements (Curtain & Zwart 1995).

[3] For the finite-dimensional case see (Lewis & Syrmos 1995; Dullerud & Paganini 1999). In the general case $\mathcal{P}^{-1}$ is well-defined on any finite-dimensional subspace of $\mathbb{X}$.
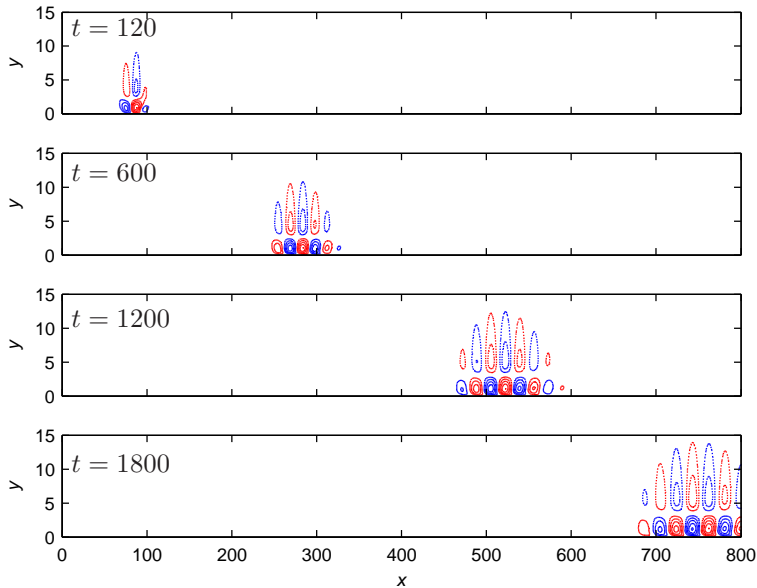
FIGURE 3. Instantaneous snapshots of the streamwise distur-
bance component at $t = 120, 600, 1200$ and 1800 triggered by
an impulse in $\mathcal{B}_1$.

For linear systems the controllability Gramian corresponds to the covari-
ance of the state response to an impulse in time. Therefore, the controllable
modes can be regarded as proper orthogonal decomposition (POD) modes
(Bagheri *et al.* 2009; Ilak & Rowley 2008). Traditionally, the interpretation
of these modes is that they represent decorrelated energy-ranked flow states.
For example, the first POD mode ϕ_1^c is the most energetic structure in the flow
containing $\lambda_1^c / \sum_{i=1}^{\infty} \lambda_i^c \times 100$ percent of the total flow energy. These modes
can be conveniently obtained by collecting r snapshots of the flow at discrete
times $t_1, \ldots, t_r$ and solving a $r \times r$ eigenvalue problem (Sirovich 1987).

The controllable modes can thus be computed from the response of the
flow to an impulse, $\delta(0)$,

$$\mathbf{u}(\boldsymbol{x}, t_j) = \mathcal{T}(t_j)\mathcal{B}_1. \tag{32}$$

The impulse response can be used to build the Gramian and to compute the
most controllable modes as shown in Appendix B. Figure 3 shows the stream-
wise velocity component of the instantaneous velocity field after an impulse
from $\mathcal{B}_1$ at four different times. The generation and convection of a wavepacket
with a dominant spatial wavenumber and a propagation speed of about $0.4U_\infty$
can be observed. The wavepacket grows in amplitude and size in the x-direction
until it reaches the beginning of the fringe region at $x = 800$. As it enters this
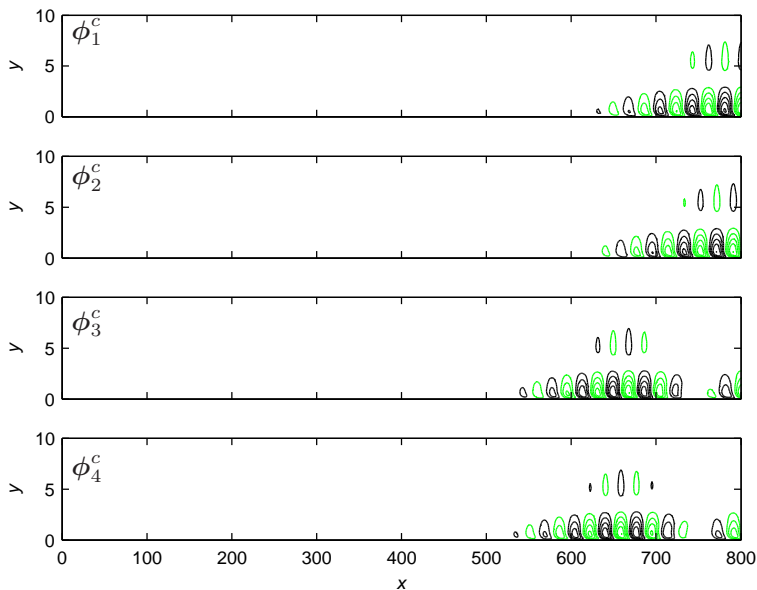region, the disturbance is eventually damped by the fringe forcing reproducing

FIGURE 4. The streamwise component of four most controllable modes ϕ_i^c.

the effect of an outflow. The input-output system (11) is thus asymptotically stable.

The u-component of the four most controllable modes ϕ_i^c with respect to $\mathcal{B}_1$ are shown in figure 4, while the corresponding eigenvalues λ_i^c are displayed in figure 5(a) with square symbols. The first 20 controllable modes contain 99% of the flow energy, meaning that a significant part of the controllable subspace is spanned by 20 modes. Note that the flow structures that are the most easily influenced by the input $\mathcal{B}_1$ are located downstream in the domain, where the energy of the response to forcing is the largest. In other words, low energy is needed at location $\mathcal{B}_1$ to force large structures downstream owing to the amplification provided by the intrinsic flow dynamics. Moreover, the eigenvalues shown in figure 5 come in pairs. The corresponding velocity fields (see the first and the second mode in figure 4) have the same wavepacket structure 90 degrees out of phase. These modes represent traveling structures (see also Rempfer & Fasel 1994).

3.2. *Observable modes*

For a given sensor it is important to determine whether the relevant flow instabilities can be detected, and if so, to which accuracy. The flow fields which can
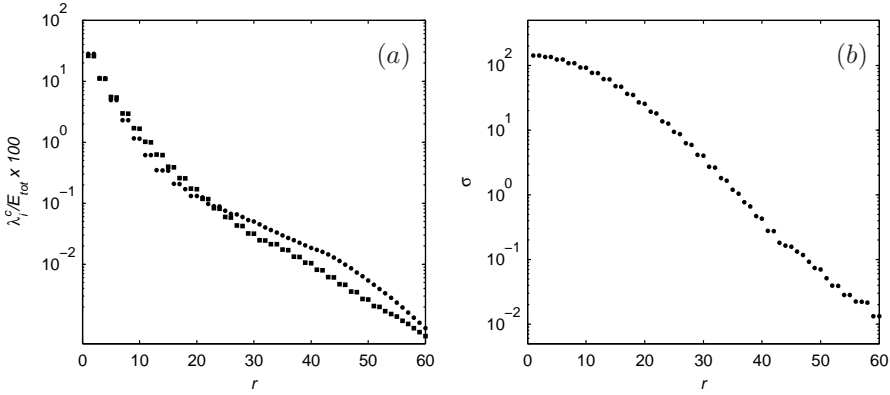
FIGURE 5. (*a*) The normalized eigenvalues λ_i^c (squares) and λ_i^o (circles) associated with controllable modes and observable modes respectively. (*b*) The Hankel singular values σ_i corresponding to the balanced modes.

be most easily detected are called the most observable modes[4]. As in the case of the controllability Gramian, the observability problem can also be cast as an optimization problem. We wish to find the initial conditions producing the largest output energy. The output energy generated by the initial condition $\mathbf{u}_0$, assumed of unit norm, is given by

$$\|\mathbf{y}\|_{\mathbb{Y}([0,\infty))}^2 = \langle \mathcal{L}_o \mathbf{u}_0, \mathcal{L}_o \mathbf{u}_0 \rangle_{\mathbb{Y}([0,\infty))} = \langle \mathbf{u}_0, \mathcal{L}_o^* \mathcal{L}_o \mathbf{u}_0 \rangle_{\mathbb{X}} = \int_\Omega \mathbf{u}_0^T \underbrace{\mathcal{L}_o^* \mathcal{L}_o}_{\mathcal{Q}} \mathbf{u}_0 \mathrm{d}x \mathrm{d}y \tag{33}$$

where $\mathcal{Q}$ is called the observability Gramian. Using equations (19) and (26*b*) we obtain the following expression for $\mathcal{Q}$

$$\mathcal{Q} = \mathcal{L}_o^* \mathcal{L}_o = \int_0^\infty \mathcal{T}^*(t) \mathcal{C}^* \mathcal{C} \mathcal{T}(t) \mathrm{d}t. \tag{34}$$

The observability Gramian provides a means to rank states according to their contribution to the output. The most observable state ϕ_1^o is given by the eigenfunction of the operator $\mathcal{Q}$ corresponding to the largest eigenvalue of,

$$\mathcal{Q}\phi_i^o = \lambda_i^o \phi_i^o. \tag{35}$$

The superscript ^{o} stands for observable modes. Note that $\mathcal{Q}$ is a self-adjoint and positive semidefinite operator so that its eigenvalues are real and positive and its eigenfunctions mutually orthogonal. The most observable mode, ϕ_1^o, contributes $\lambda_1^o / \sum_{j=0}^\infty \lambda_j^o \times 100$ percent to the total sensor energy, the second most observable mode, ϕ_2^o, contributes $\lambda_2^o / \sum_{j=0}^\infty \lambda_j^o \times 100$ percent and so on. In

---

[4]The system (11) is approximately observable if $\mathcal{L}_o \mathbf{u} = 0$ occur only if $\mathbf{u} = 0$, *i.e.* if the knowledge of the output determines the initial state uniquely (Curtain & Zwart 1995).
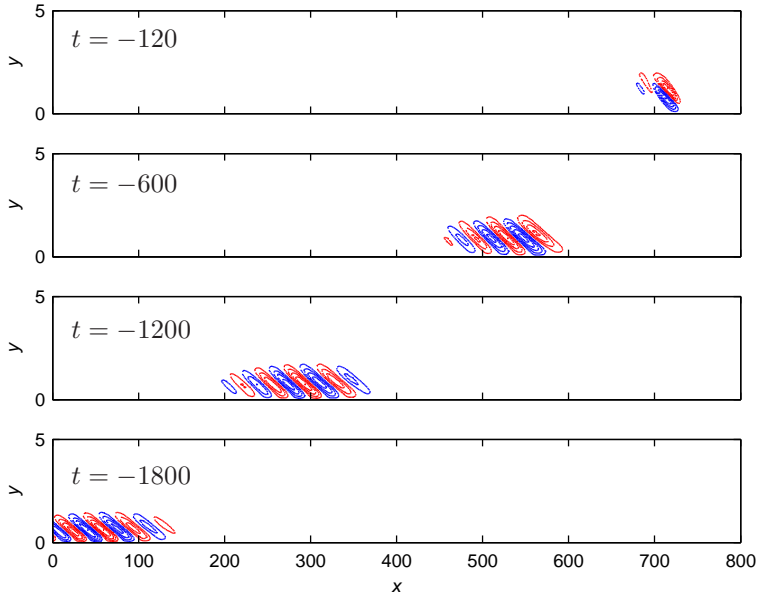
FIGURE 6. Instantaneous snapshots of the streamwise disturbance component at $t = -120, -600, -1200$ and -1800 of the adjoint impulse in $\mathcal{C}_1$.

particular, if $\lambda_i^o \ll 1$, the corresponding mode ϕ_i^o does not make a contribution to sensor output, and is called a (nearly) unobservable mode. Note that the observable modes can regarded as POD modes of the adjoint system.

From the definition of $\mathcal{Q}$ in (34) it follows that the observable modes pertaining a given output can be determined from the impulse response of one adjoint simulation (see Appendix B). The results of this simulation, $\mathcal{T}^*(t)\mathcal{C}^*$, can then be used to build the second order correlation of the flow field, $\mathcal{T}^*(t)\mathcal{C}^*\mathcal{C}\mathcal{T}(t)$, and thus the Gramian. The eigenvalue problem (35) is solved by using the snapshots method as explained above for the case of the controllable modes. Here we present results for the first output $\mathcal{C}_1$ only. Figure 6 shows the instantaneous adjoint field at four different times

$$\boldsymbol{p}(\boldsymbol{x}, -t_j) = \mathcal{T}^*(t_j)\mathcal{C}_1^*, \tag{36}$$

after an impulse from the first output, *i.e.* $\mathcal{C}_1^*\delta(0)$. The triggered wavepacket travels backward in time in the upstream direction with upstream tilted structures. The adjoint solution can be regarded as the sensitivity of the output $\mathcal{C}_1$ with respect to linear perturbations to the underlying base flow. In other words, the flow structures excited by $\mathcal{C}_1^*$ and shown in figure 6, are also the structures to which the sensor $\mathcal{C}_1$ is most sensitive. In this context, the negative time can be interpreted as the delay between the time these structures are present and the instant they can be measured.

The u-component of the four most observable modes ϕ_i^o with respect to $\mathcal{C}_1$ are shown in figure 7, while the associated eigenvalues are reported in figure 5(a) (circles). From the latter figure, we observe that the leading 20 modes are responsible for nearly the entire output energy. The flow structures in figure 7 are initial conditions that contribute with the most energy to the sensor output. These modes are real-valued functions and therefore two of them are needed to describe traveling flow structures, which explains the appearance of pairs of eigenvalues in figure 5(a). The are two further noteworthy remarks:

(i) The spatial support of the observable modes is far upstream, where the sensitivity of the flow is the largest. Hence, the most observable structures are spatially disconnected from the most controllable modes. This spatial separation is also observed between the global eigenmodes of the linearized Navier–Stokes equations and eigenmodes of the adjoint Navier–Stokes, where it is associated to streamwise non-normality of the system (Chomaz 2005).

(ii) The most observable structures are tilted in the upstream direction, "leaning" against the shear layer and are similar to the linear optimal disturbances computed by Åkervik *et al.* (2008). The optimal disturbance is the initial condition maximizing the perturbation energy over the entire domain Ω at a fixed time $t = T$. On the other hand, observable modes maximize the time integral of the perturbation energy in the region defined by the output $\mathcal{C}_1$. Choosing the sensor location in correspondence to the largest flow response leads therefore to the similarity between linear optimals and observable modes. As noticed by Butler & Farrell (1992), the upstream tilting of the optimal initial conditions can be attributed to the wall-normal non-normality of the governing operator; perturbations extract energy from the mean shear by transporting momentum down the the mean velocity gradient (the so-called Orr mechanism).

3.3. *Balanced modes*

So far we have identified modes that either characterize the response to forcing or the sensitivity of an output. In this section we present the balanced modes (Moore 1981), which take into account both the response behavior and the output sensitivity. Similar to the previous section, we wish to excite the largest output energy. However, rather than identifying dangerous initial conditions using the mapping $\mathcal{L}_o$ as in equation (33), we look directly for input signals which produce the largest output energy via the input-output mapping $\mathcal{L}_o\mathcal{L}_c$ given in (21).

The output energy generated by the past input **f**, assumed of unit norm, is given at time t by

$$\|\mathbf{y}\|_{\mathbb{Y}([0,\infty))}^2 = \langle \mathcal{H}\mathbf{f}, \mathcal{H}\mathbf{f}\rangle_{\mathbb{Y}([0,\infty))} = \langle \mathbf{f}, \mathcal{H}^*\mathcal{H}\mathbf{f}\rangle_{\mathbb{U}((-\infty,0])} = \int_{-\infty}^0 \mathbf{f}^T\mathcal{H}^*\mathcal{H}\mathbf{f}\mathrm{d}t. \quad (37)$$
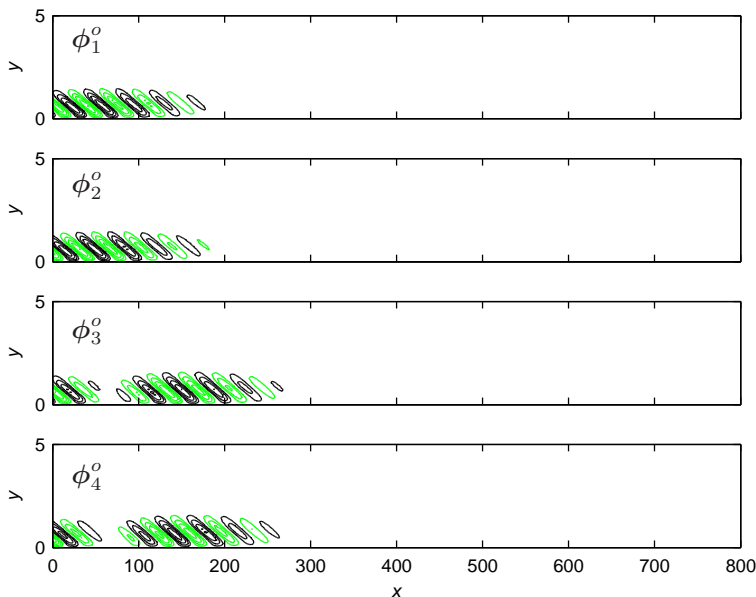
FIGURE 7. The streamwise velocity component of the four most observable modes ϕ_i^o.

If we let the sequence of input vectors $\mathbf{f}_i$ with unit norm represent the (orthonormal) eigenfunctions of $\mathcal{H}^*\mathcal{H}$, *i.e.*

$$\mathcal{H}^*\mathcal{H}\mathbf{f}_i = \sigma_i^2 \mathbf{f}_i \tag{38}$$

then the output energy is given by the square of the so called Hankel singular values (HSV) σ_i. The most dangerous input vector $\mathbf{f}_1$ with $\|\mathbf{f}_1\|_{\mathbb{U}((-\infty,0])} = 1$ thus results in an output signal which has been amplified by σ_1^2. Note that $\sigma_1 \geq \sigma_2 \geq \ldots$, so the eigenmodes of the input-output map are ranked according to how much the input signal is amplified as it is filtered by the linear system and by the output.

Using the controllability operator $\mathcal{L}_c$ we obtain the flow structure associated with the forcing $\mathbf{f}_i$,

$$\phi_i^{oc} = \frac{1}{\sqrt{\sigma_i}} \mathcal{L}_c \mathbf{f}_i. \tag{39}$$

Notice that $\sigma^{-1/2}$ is a convenient normalization factor. The modes are denoted by the superscript ^{oc}, which indicates that these modes are both observable and controllable. The sequence of functions ϕ_i^{oc} are called the balanced modes and as we show next, they diagonalize the observability Gramian. Computing the output energy for $\mathbf{f}_i$ and using (39), we obtain

$$\int_{-\infty}^{0} \mathbf{f}_i^T \mathcal{H}^*\mathcal{H}\mathbf{f}_i \mathrm{d}t \ \ = \sqrt{\sigma_i}\langle \mathbf{f}_i, \mathcal{L}_c^* \mathcal{Q}\phi_i^{oc}\rangle_{\mathbb{U}((-\infty,0])} = \sigma_i \langle \phi_i^{oc}, \mathcal{Q}\phi_i^{oc}\rangle_{\mathbb{X}} = \sigma_i^2, \tag{40}$$
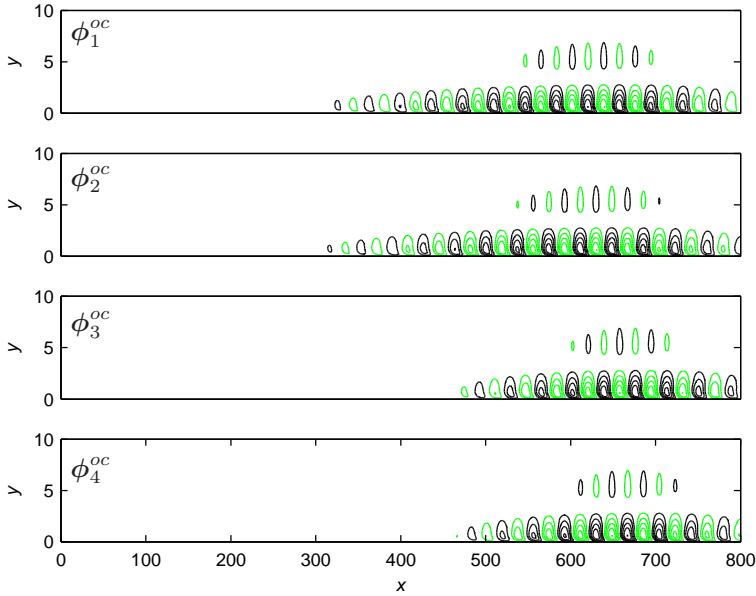
FIGURE 8. The streamwise velocity component of four first balanced modes $\boldsymbol{\phi}_i^{oc}$.

where the definitions $\mathcal{H} = \mathcal{L}_o\mathcal{L}_c$, $\mathcal{H}^* = \mathcal{L}_c^*\mathcal{L}_o^*$ and $\mathcal{Q} = \mathcal{L}_o^*\mathcal{L}_o$ are used. A diagonal observability Gramian implies that these modes can be regarded as orthogonal if this Gramian is used as inner product weight matrix. With respect to inner product defined in $(61a)$ however, these modes are not orthogonal.

A sequence of functions $\boldsymbol{\psi}_i^{oc}$, referred to as the adjoint balanced modes, which is bi-orthogonal to $\boldsymbol{\phi}_i^{oc}$ according to

$$\langle \boldsymbol{\psi}_i^{oc}, \boldsymbol{\phi}_j^{oc}\rangle_\mathbb{X} = \delta_{i,j}, \tag{41}$$

is needed to project our system in the basis given by the balanced modes. The derivation is analogous to $\boldsymbol{\phi}_i^{oc}$ but now we consider instead

$$\mathcal{H}\mathcal{H}^*\mathbf{s}_i = \mathbf{s}_i\sigma_i^2. \tag{42}$$

The adjoint balanced modes are then given by

$$\boldsymbol{\psi}_i^{oc} = \frac{1}{\sqrt{\sigma_i}}\mathcal{L}_o^*\mathbf{s}_i. \tag{43}$$

It is possible to show by the same procedure used in (40) that these modes diagonalize the controllability Gramian,

$$\langle \boldsymbol{\psi}_j^{oc}, \mathcal{P}\boldsymbol{\psi}_i^{oc}\rangle_\mathbb{X} = \sigma_i\delta_{i,j}. \tag{44}$$

Furthermore, the diagonal elements are also equal to the Hankel singular values. The term balancing now becomes clear; using $\boldsymbol{\phi}_i^{oc}$ and $\boldsymbol{\psi}_i^{oc}$ the controllability and observability Gramians become diagonal and equal to the HSV. In other
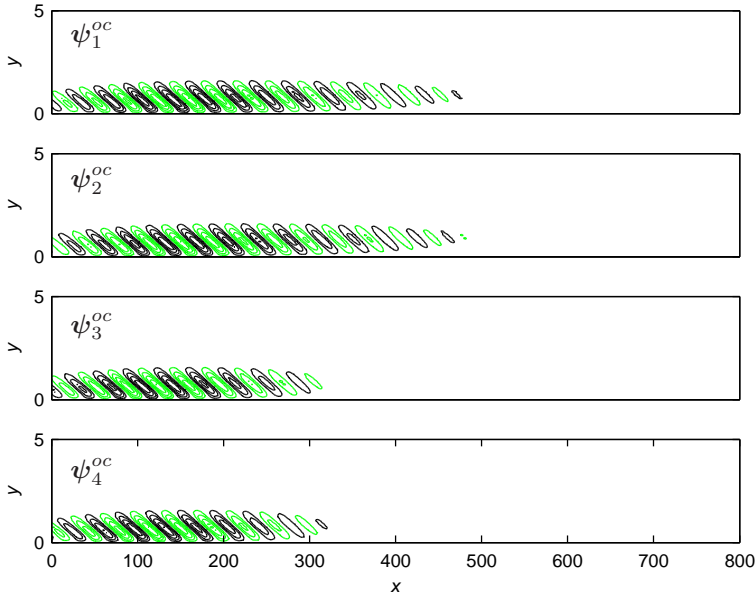
FIGURE 9. The streamwise velocity component of the adjoint balanced modes $\boldsymbol{\psi}_i^{oc}$.

words, the observability and controllability properties are balanced. This is useful for performing model reduction as it allows us to discard modes which are both difficult to measure and difficult to excite by the inputs.

To compute these modes, it is convenient to show that $\boldsymbol{\phi}_i^{oc}$ are the eigenmodes of $\mathcal{P}\mathcal{Q}$; multiplying (38) with $\mathcal{L}_c$ yields

$$\mathcal{L}_c \mathcal{H}^* \mathcal{H} \mathbf{f}_i = \mathcal{P}\mathcal{Q}\boldsymbol{\phi}_i^{oc} = \sigma_i^2 \boldsymbol{\phi}_i^{oc}. \tag{45}$$

The computation of the balanced modes and of their associated adjoints can again be accomplished using a timestepper and the snapshot method described in Appendix B. In this case one combines the sequence of snapshots collected from the solution of the forward problem (11) with a sequence of snapshots collected from the adjoint system (27). In this way we can approximate the eigenvalue problem (45) to obtain the balanced modes (Rowley 2005). The u-component of four first balanced modes $\boldsymbol{\phi}_i^{oc}$ with respect to $\mathcal{B}_1$ and $\mathcal{C}_1$ are shown in figure 8 and the corresponding adjoint modes $\boldsymbol{\psi}_i^{oc}$ in figure 9. The Hankel Singular values σ_i are shown in figure 5(b). As in the case of the observability and controllability eigenvalues λ_i^c and λ_i^o, the singular values come in pairs, indicating that the leading balanced modes are traveling structures. The same observation was made by (Ilak & Rowley 2008) for channel flow.

From figures 8 and 9 we observe that the leading balanced modes appear also as wavepackets but they are somewhat more spatially extended than the

controllable POD modes (figure 4). Similarly, the adjoint balanced modes
have a larger spatial support than the observable modes (figure 7). As noticed
by Ilak & Rowley (2008) and Ahuja *et al.* (2007), we can account for both
controllability and observability through the non-orthogonality of the balanced
modes. In the two previous sections we observed that for an input $\mathcal{B}_1$ located
upstream and an output $\mathcal{C}_1$ located downstream, the associated controllable
and observable modes are spatially located in different parts of the domain.
The controllable subspace and the observable subspace are thus separated in
the streamwise direction. This is a consequence of the convective nature of the
instabilities arising in the Blasius flow where disturbances grow in amplitude
as they are convected in the downstream direction. Essentially, this separation
implies that the distribution of both the input and the output cannot be cap-
tured by an orthogonal projection onto the leading modes of only one subspace.
Conversely, in a bi-orthogonal projection the adjoint balanced modes account
for the output sensitivity and the direct balanced modes for the most energetic
structures.

4. Model reduction

Since the disturbances are represented by an input and the objective consists of
minimizing an output signal, capturing the input-output behavior of the system
— described by the mapping $\mathcal{L}_o\mathcal{L}_c$ — is sufficient for the design of optimal and
robust control schemes. The flow structures that are neither controllable nor
observable are redundant for the input-output behavior. Moreover, the states
that are nearly uncontrollable and nearly unobservable can be discarded since
they have a very weak influence on the input-output behavior. A systematic
approach of approximating the system given by (1) with a finite-dimensional
model, which preserves the main input-output behavior is called balanced trun-
cation (Moore 1981). As we show below, balanced truncation amounts to a
projection of state-space system (11) on the leading balanced modes.

We now return to the multi-input multi-output (MIMO) state-space system
with input vector **f** and output vector **y**. The measurement noise acts on the
output signal and affects the perturbation dynamics only in the closed-loop
system and is hence not included in the analysis.

4.1. *Galerkin projection*

Any flow field can be approximated as a linear combination of the leading r
balanced modes,

$$\mathbf{u}^r(\boldsymbol{x}, t) = \sum_{j=1}^{r} q_j(t)\boldsymbol{\phi}_j^{oc}(\boldsymbol{x}), \tag{46}$$

where $q_j = \langle \mathbf{u}, \boldsymbol{\psi}_j^{oc} \rangle_{\mathbb{X}}$ are the expansion coefficients. Inserting the above expan-
sion into (11) and taking the inner product with the adjoint balanced modes
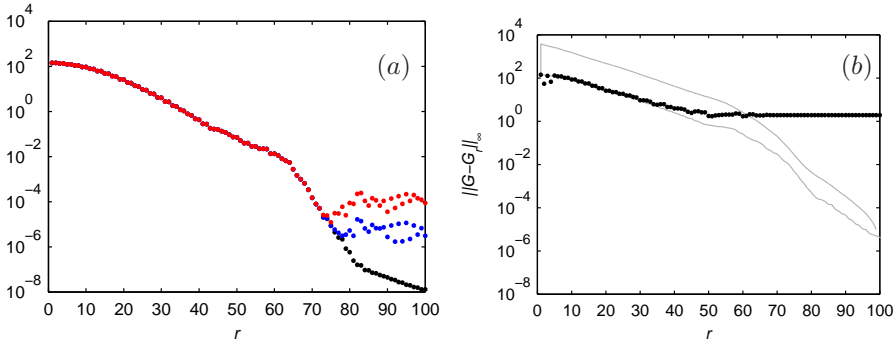
FIGURE 10. (*a*) The Hankel singular values (black symbols) are compared to the diagonal entries of the controllability and observability Gramians associated with the balanced reduced-order system. (*b*) The $\mathcal{H}_\infty$ model reduction error. The upper and lower theoretical bounds are depicted with gray lines and the actual model reduction error is shown with black symbols.

$\boldsymbol{\psi}_i^{oc}$, the following r-dimensional state-space form is obtained,

$$\dot{q} = Aq + B_1\mathsf{w} + B_2\mathsf{u} \tag{47a}$$

$$\mathsf{v} = C_1q + l\mathsf{u} \tag{47b}$$

$$\mathsf{z} = C_2q + \alpha g. \tag{47c}$$

This system is referred to as the reduced-order model (ROM). The column vector q contains q_j and the entries of the matrix A, column vector B_1 and row vector C_1 are

$$A_{i,j} = \langle \boldsymbol{\psi}_i^{oc}, \mathcal{A}\boldsymbol{\phi}_j^{oc} \rangle_{\mathbb{X}} \tag{48a}$$

$$B_{1,j} = \langle \boldsymbol{\psi}_j^{oc}, \mathcal{B}_1 \rangle_{\mathbb{X}} \tag{48b}$$

$$C_{1,j} = \mathcal{C}_1 \boldsymbol{\phi}_j^{oc} \tag{48c}$$

for $i, j = 1, \ldots, r$. The components of the row vectors C_2 and B_2 are obtained in the same manner as for B_1 and C_1. The evolution operator associated with (47) is

$$T(t) = e^{At} = \sum_{j=0}^{\infty} \frac{(At)^j}{j!}. \tag{49}$$

Notice that the balanced modes are computed accounting for all the inputs (except the measurement noise) and outputs and the Galerkin projection (47) is performed only once. The projection of $\mathcal{A}$ on the balanced modes can be approximated by the finite-difference method using the timestepper and expression (5). For the results presented, δt was chosen to be 10^{-4} after a convergence study.

To validate the properties of the snapshot-based balanced truncation, we construct the reduced-model (47) and compute its controllability and observability Gramians. The projected system is internally balanced if and only if its Gramians are diagonal and equal to the HSV. We found that the first 70×70 elements of both Gramians are diagonal. In figure $10(a)$ we compare the leading 100 diagonal elements with the HSV. The first 70 modes are observed to be bi-orthogonal to each other down to numerical accuracy. However, for higher modes as the numerical round-off errors increase, the bi-orthogonality condition is gradually lost and off-diagonal elements are observed in both Gramians. By increasing the numerical resolution and the number of snapshots it is possible to increase the number of balanced modes. However, — as noticed by (Moore 1981) — the ratio σ_1/σ_i serves as a condition number for ϕ_1^{oc}, and therefore the balanced modes corresponding to very small HSV can be ill-conditioned independently of the numerical approximations.

4.1.1. *Performance of reduced-order model*

In this section the input-output behavior of reduced-order model (47) is compared to the full Navier–Stokes system (11). We begin by comparing the impulse response from all inputs to all outputs. In figure (11) three signals $\mathcal{B}_1 \to \mathcal{C}_1$, $\mathcal{B}_1 \to \mathcal{C}_2$ and $\mathcal{B}_2 \to \mathcal{C}_1$ are shown with black lines. The response of $\mathcal{C}_2$ to forcing in $\mathcal{B}_2$ is zero, since disturbances traveling upstream are quickly damped. These impulse responses were obtained by using the timestepper with $\sim 10^5$ degrees of freedom. The impulse responses of the reduced-order model (47) with $r = 50$ given by $\mathbf{y}(t) = Ce^{At}B$ are shown with red dashed lines. We observe that reduced-model registers the same signal as the full model from all inputs to all outputs. The wavepacket triggered by the impulse of $\mathcal{B}_1$ reaches the first sensor $\mathcal{C}_2$ after 600 time units and the second sensor $\mathcal{C}_1$ after 1500 time units. The wavepacket triggered from the actuator reaches the second sensor after 600 time units.

The frequency response of the full system and of the reduced order model are compared next. The frequency response is related to the Laplace transform of the impulse response ($\mathcal{B} \to \mathcal{C}$) (see *e.g.* Skogestad & Postlethwaite 2005), which in our case results in the 2×3 transfer function matrix (TFM),

$$G(s) = \mathcal{C}(s - \mathcal{A})^{-1}\mathcal{B}. \qquad (50)$$

with $s \in \mathbb{C}$. The element $G_{i,j}$ contains the response from $\mathcal{B}_j \to \mathcal{C}_i$. The TFM of size 2×3 of the reduced-model is similarly defined as

$$G_r(s) = C(sI - A)^{-1}B \qquad (51)$$

with I as identity matrix of size r.

Due to the linear nature of the equations, a sinusoidal input signal $e^{i\omega t}$ with constant frequency ω will generate an output with the same frequency but with a phase shift $\text{Arg}\{G(i\omega)\}$ and a different amplitude $|G(i\omega)|$. The frequency response gain is usually measured by the largest singular value of the TFM (Skogestad & Postlethwaite 2005). For the full model we do not have
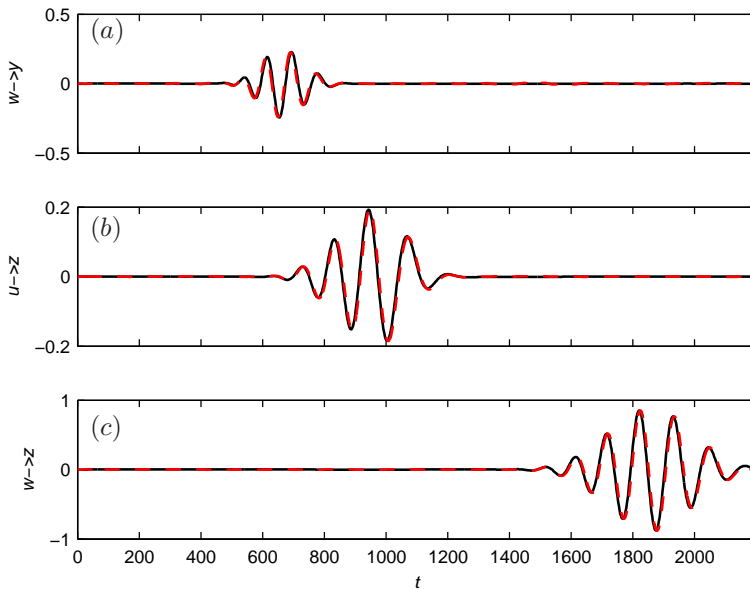
FIGURE 11. The impulse response from $\mathcal{B}_1 \to \mathcal{C}_2$ (*a*), $\mathcal{B}_2 \to \mathcal{C}_1$ (*b*) and $\mathcal{B}_1 \to \mathcal{C}_1$ (*c*). The black solid line represents direct numerical simulations with 10^5 degrees of freedom and the red dashed line the balanced reduced-model with 50 degrees of freedom.

an explicit expression of the TFM. Therefore, we make use of our timestepper and apply a sinusoidal signal with a constant frequency ω in each input and extract the time periodic signal from the outputs once the initial transients have died out. Note that computing the frequency response with the timestepper in this way does not take into account the interaction of input signals, since only one each input is active at a time.

In figure 12 the envelope of the TFM amplitudes — the largest amplification of all the frequency responses from $\mathcal{B}_1 \to \mathcal{C}_1$, $\mathcal{B}_1 \to \mathcal{C}_2$ and $\mathcal{B}_2 \to \mathcal{C}_1$ at each ω — for the full model of order 10^5 is shown with red filled circles. In the same figure the TFM amplitudes of reduced-order models of order $r = 2, 50$ and 100 are shown. We observe that the reduced-order model of order 2 captures the most important aspect of the input-output behavior, which is the response of the most dangerous frequency, *i.e.* the peak response of the full model. The model with 50 modes is able to estimate the gains of all the amplified frequencies, but fails to capture the damped low and high frequencies. Adding 50 additional modes results in a model that preserves the input-output behavior correctly for all frequencies. Note that there are no isolated eigenvalues in the spectrum of the spatially developing Blasius flow (Ehrenstein & Gallaire 2005; Åkervik *et al.* 2008) and therefore the frequency response is rather smooth with
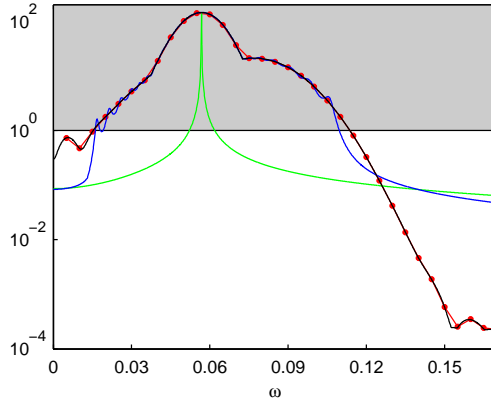
FIGURE 12. The envelope of the MIMO transfer function matrix $G(i\omega)$ from all inputs to all outputs computed using the timestepper is shown with red symbols. The largest response is for $\omega = 0.06$ with a peak value of 144.6. For $\omega \in [0, 0.03]$ the frequency response from the actuator to objective function $(\mathcal{B}_2 \rightarrow \mathcal{C}_1)$ dominates. The frequencies with largest gain are obtained from disturbances to objective function $(\mathcal{B}_1 \rightarrow \mathcal{C}_1)$ in the range $\omega \in [0.03, 0.07]$ and finally for higher frequencies the response from disturbances to measurement sensor $(\mathcal{B}_1 \rightarrow \mathcal{C}_2)$ are amplified the most. The frequencies in the grey domain are amplified. Also shown are the frequency response (the envelope) of the reduced model TFM $G_r(i\omega)$ with rank 2 (green), 50 (blue) and 100 (black).

no peaks. Low-pass filters of this form cannot be represented with only a few degrees of freedom.

Finally, the model reduction error is computed and compared to the theoretical bounds given by the Hankel singular values. An attractive feature of balanced truncation is the existence of error bounds (note that this error bound is obtained *a priori* to Galerkin projection),

$$\sigma_{r+1} < \|G - G_r\|_\infty \leq 2 \sum_{j=r+1}^{n} \sigma_j. \tag{52}$$

The infinity norm of the transfer function equals the peak value of the frequency response gain based on the largest singular value, *i.e.*

$$\|G(s)\|_\infty = \max_\omega \sigma_1(G(i\omega)). \tag{53}$$

Estimating the model reduction error (52) amounts to the calculation of the difference of the peak values of frequency response of the reduced-order and the Navier–Stokes system. For the latter system, we use the peak value of the
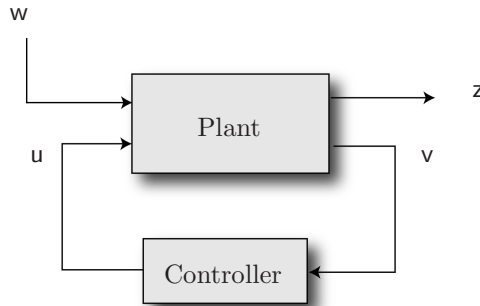
FIGURE 13. The closed-loop system. The plant represent the input-output system given by equation (11) subject to external disturbances w. The controller of order 50 forces the Navier–Stokes equations with the input signal u based on the noisy measurements v so that the effect of w on the output signal z is minimized.

amplitude envelope as shown in figure 12 instead of the largest singular value. The error norm for the balanced truncation model is shown in figure 10(*b*) with black symbols. The error norm is close to the lower bound given by the HSV for the first 50 modes. The peak value for the Navier–Stokes system is 144.60 which is gradually approached by the reduced-order model until it saturates at a peak value of 144.50 due to numerical round-off errors. Note that the error is somewhat lower than the theoretical bounds for the reduced-systems of order 2 and 4. This is because the frequency response of the full system is obtained numerically using our timestepper and that the $\|G\|_\infty$ is based on the maximum of the envelope of the transfer function matrix instead of its largest singular value.

A thorough comparison between reduced order models obtained with POD modes and balanced modes can be found in Ilak & Rowley (2008) for the case of channel flow and in Bagheri *et al.* (2009) for the linear Ginzburg-Landau equation. The latter work also included global eigenmodes of the linearized operator in the comparison.

5. Feedback control

We will now develop a reduced-order feedback controller, which will have the same dimension as the reduced-order model (*e.g.* $r = 50$). The closed-loop behavior and the objective function z will be investigated and compared to the uncontrolled flat-plate boundary layer.

5.1. $\mathcal{H}_2$ — framework

The main idea of linear feedback control is shown in figure 13. As stated in the introduction our objective is to find a control signal $\mathsf{u}(t)$ such that in the

presence of disturbances $\mathsf{w}(t), \mathsf{g}(t)$ the perturbation energy represented by the state variable $\mathbf{u}(\boldsymbol{x}, t)$ is minimized downstream at the location defined by the sensor $\mathcal{C}_1$. This is the $\mathcal{H}_2$ control problem.

In the previous section we showed that our reduced model (47) is able to capture the input-output behavior of the Navier–Stokes system (11). During the control design process we can assume that the reduced-model is the plant that we wish to control. Once we have determined the control law for this approximating model, we will apply it to the full Navier–Stokes system. We refer to (Anderson & Moore 1990; Zhou *et al.* 2002; Bagheri *et al.* 2009) for further details on the $\mathcal{H}_2$ control algorithm, as we will only outline the main steps.

Following the notation introduced for the reduced-model (47), the objective function (10) becomes

$$\|\mathsf{z}\|_{\mathbb{Y}([0,\infty))}^2 = \int_0^\infty q^T C_1^T C_1 q + l^2 \mathsf{u}^T \mathsf{u} \mathrm{d}\tau. \tag{54}$$

The determination of the control signal is based only on the measurements from the sensor $\mathcal{C}_2$. However, for linear systems — due to the separation principle (Zhou *et al.* 2002) — the feedback control law can be determined assuming that the complete velocity field is known. The forcing needed to reproduce the flow only from wall measurements can be computed independently. Hence, the control design of the $\mathcal{H}_2$-control is performed in the following three steps:

(i) Compute the control feedback gain K by solving a Riccati equation (see Appendix D), so that the control signal is of feedback type, *i.e.*

$$\mathsf{u}(t) = Kq(t). \tag{55}$$

This leads to a new system (compared to 47),

$$\dot{q} = (A + B_2 K)q + B_1 \mathsf{w}, \tag{56a}$$
$$\mathsf{z} = C_1 q. \tag{56b}$$

It is expected that the above perturbated operator $A + B_2 K$ has dynamics that results in a smaller amplitude of the output signal z than for the unperturbated operator A in (47).

(ii) Compute the estimation feedback gain L by also solving a Riccati equation (see Appendix D), so that the observer

$$\dot{\hat{q}} = (A + LC_2)\hat{q} + B_2 \mathsf{u} - L\mathsf{v} \tag{57}$$

is asymptotically stable, *i.e.* $\|q - \hat{q}\| \to 0$ as $t \to \infty$. This implies that the estimated state $\hat{q}$ based on the measurements v approaches the true state q exponentially fast.

(iii) The compensator (controller in figure 13) is finally obtained as

$$\dot{\hat{q}} = (A + B_2 K + LC_2)\hat{q} - L\mathsf{v}, \tag{58a}$$
$$\mathsf{u} = K\hat{q}. \tag{58b}$$

Given the measurements signal v from the physical flow, the reduced-order controller provides an optimal control signal u proportional to the estimated flow $\hat{q}$.

To apply feedback control in the numerical simulations, an augmented state-space system with state $(\mathbf{u}, \hat{q})^T$ is considered: its dynamics is given by (11) and (58), inputs (w, g) and with the single output z:

$$\begin{pmatrix} \dot{\mathbf{u}} \\ \dot{\hat{q}} \end{pmatrix} = \begin{pmatrix} \mathcal{A} & \mathcal{B}_2 K \\ -L\mathcal{C}_2 & A + B_2 K + LC_2 \end{pmatrix} \begin{pmatrix} \mathbf{u} \\ \hat{q} \end{pmatrix} + \begin{pmatrix} \mathcal{B}_1 & 0 \\ 0 & -\alpha L \end{pmatrix} \begin{pmatrix} \mathsf{w} \\ \mathsf{g} \end{pmatrix}, \quad (59a)$$

$$\mathsf{z} = \mathcal{C}_1 \mathbf{u}. \quad (59b)$$

This system is referred to as the closed-loop system. Note that the feedback gain K and estimation gain L have the dimension of the reduced model, resulting in a fast online controller.

The spatio-temporal evolution of the perturbations governed by the closed-loop system is obtained by solving the system (59) numerically using the timestepper described in **Appendix C** and the small reduced-system in (58) simultaneously. The latter system is solved using a standard Crank–Nicholson scheme.

5.2. *Performance of closed-loop system*

We will now investigate the performance of the closed-loop system (59). In particular, the output z of the closed-loop — with optimal control signal u — and of the linearized Navier–Stokes equations without control are considered in the case of stochastic and harmonic forcing in w.

Three controllers are investigated: (i) cheap control/low noise contamination with $l = 0.1$ and $\alpha = 0.1$, (ii) expensive control/high noise contamination with $l = 10$ and $\alpha = 10$ and (iii) an intermediate case with $l = 2$ and $\alpha = 0.1$.

Note that the purpose of the measurement noise g is to account for uncertainties in the sensor measurements during the control design. When evaluating the closed-loop performance — solving the controlled Navier–Stokes equations — the system is only forced with w and not with g.

The performance of the control in case (i) is examined first. In figure 14 the input and output signals are shown. The gray region indicates the time when the control is active. As disturbance signal $\mathsf{w}(t)$ we choose white noise; the corresponding response of the sensor $\mathbf{y}(t)$ in figure 14(*b*) confirms the amplification and filtering of the signal as it traverses the unstable domain. The disturbances reach the second sensor (figure 14*d*) after about 1500 time units where they have been amplified by one order of magnitude. The control is activated at time $t = 2500$, the actuator immediately begins to force the system with a control signal (figure 14*c*) based on the output $\mathbf{y}$, and after a delay of another 1500 time units, the stabilizing effect of the control signal on the output z is clear. When the control is deactivated (at $t = 7500$) the disturbances start to grow again.
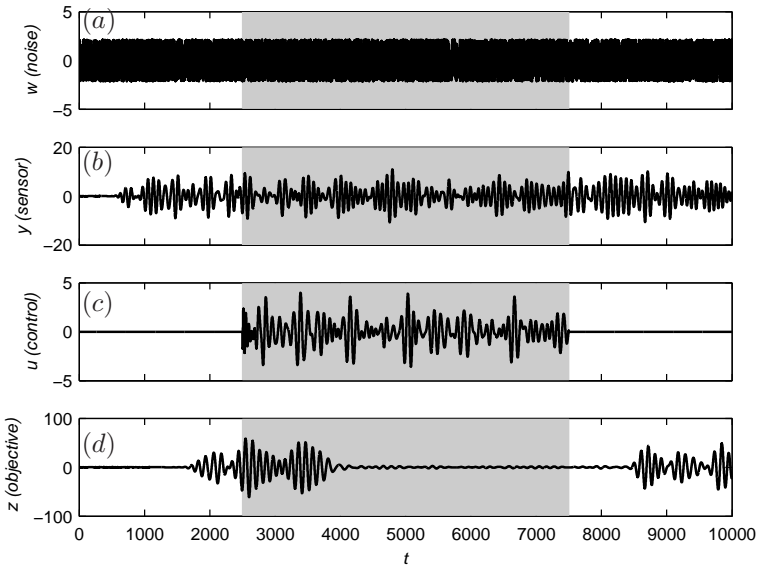
FIGURE 14. Input and output signals of the closed-loop system. The the random forcing w (a), measurements signal v (b), control signal u (c) and the objective function z (d) is shown. The cheap controller is active between $t \in [2500, 7500]$ marked with the gray area.

The wall-normal maximum of the rms-values of the streamwise velocity component in cases with and without control are shown in figure 15. The rms-value grows exponentially downstream in the uncontrolled case until the fringe region at $x = 800$. The rms of the controlled perturbation grows only until it reaches the actuator position where it immediately begins to decay. At the location of the objective function $\mathcal{C}_1$ ($x = 750$), the amplitude of the perturbations is one order of magnitude smaller than in the uncontrolled case for the cheapest controller.

The rms values in the case of the expensive (case ii) and intermediate control (case iii) are shown with dashed and dashed-dotted lines respectively. The expensive control is very conservative as the measurement signals are highly corrupted and the control effort limited; it results only in a small damping of the disturbances. The intermediate controller (case iii) is more cautious in reducing the perturbation energy just downstream of the actuator when compared to the cheap controller. It is interesting to note, however, that at the location where the objective function is measured, the disturbance amplitude has decreased nearly as much as with the cheap controller, although the total perturbation energy is much larger over the entire domain.

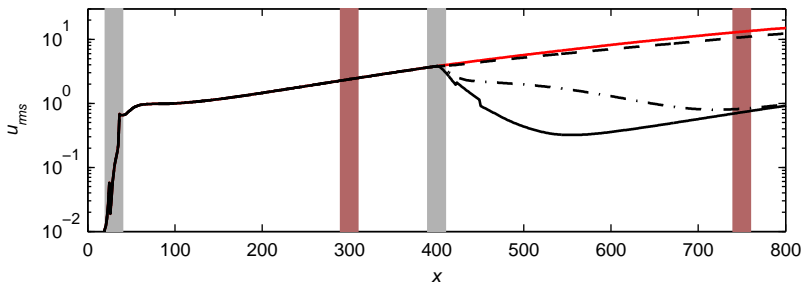FIGURE 15. The rms-values of the uncontrolled system (red line), cheap controller (solid black), intermediate controller (dashed-dotted line) and expensive controller (dashed line). The gray bar represent the size (defined as 99% of the spatial support) and location of the two inputs, whereas the red bars correspond to the two outputs.

In figure 16 the frequency response from $\mathsf{w} \to \mathsf{z}$ of the uncontrolled Navier–Stokes equations (11) (shown in red) is compared to that pertaining the three controllers under consideration. The solid black line corresponds to cheap control, dashed-dotted line to intermediate control and dashed line to expensive control. The two former controllers suppress the most dangerous frequencies close to $\omega = 0.6$ significantly. Note that compared to the uncontrolled model, the highly damped frequencies $\omega > 0.11$ have larger gain in amplitudes. This behavior is often observed in closed-loop physical systems and is related to the "water-bed" effect, *i.e.* when certain frequencies are suppressed, the response at other frequencies is amplified.

6. Conclusions

Model-based feedback control of the instabilities arising in a spatially inhomogeneous boundary layer flow is studied. To build a reduced-order model of the problem, where the application of standard tools from control theory become computationally feasible also for fluid flow systems, the main features of the flow behavior are investigated in an input-output framework. The observable, controllable and balanced modes of the system have been identified. The location and structure of these modes reflect the location of sensors/actuators and the perturbation dynamics, i.e the observable modes are located upstream, where the sensitivity to initial conditions is the largest. The controllable modes, conversely, are located downstream, where the response to the forcing is largest. The analysis presented here can be closely related to stability analysis using global modes and optimal disturbances, except that inputs and outputs are taken into account. The quantity one wishes to optimize for is now defined by a sensor output, while perturbations are introduced by the inputs considered in the model. Furthermore, in view of the control application, the formulation of the control objective function as an output is particularly attractive in this
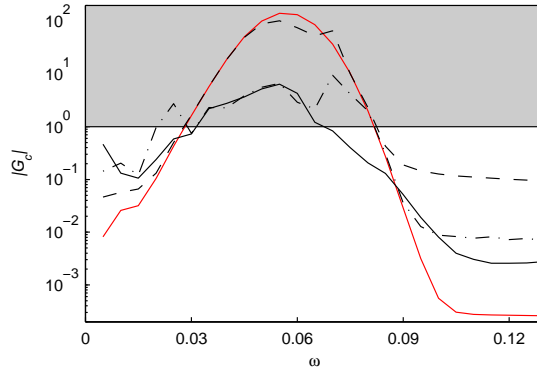
FIGURE 16. Comparison of the frequency response from disturbances to objective function ($\mathcal{B}_1 \rightarrow \mathcal{C}_1$) of open-loop (red) and three closed-loop systems. The cheap, intermediate and expensive controllers are represented by the solid black, dashed-dotted and dashed lines respectively. The infinity norm of the open loop is $\|G\|_\infty$ is 140.7, whereas for the closed-loop systems $\|G_c\|_\infty$ it is 6.4 (cheap), 9.4 (intermediate) and 101.9 (expensive).

input-output setting, since this behavior is well-captured by the reduced-order model.

Model reduction is achieved by projecting the governing equations on the leading balanced modes of the system. We show that the input-output behavior of the flat-plate boundary layer can be captured accurately with a reduced-order model based on these modes. Finally, the model was used to apply feedback control based on measurements from one upstream sensor and an actuator further downstream. The perturbations growth could be reduced efficiently using the $\mathcal{H}_2$ optimal feedback controller.

It is also important to note that the approach followed here requires only the use of a timestepper, a numerical code solving the Navier–Stokes equations, and avoids the use of the large matrices defining the operators governing the input-output behavior. In addition, the present formulation accounts naturally for localized sensors and actuators and therefore, it can be directly applied to different flow configurations. We are currently extending the analysis to three-dimensional disturbances and also incorporating more realistic actuators (blowing/suction) and sensors (wall measurements). These computations are now feasible and will take us a step closer to using the controller in actual experiments.

Appendix A. Derivation of adjoint operators

A.1. *The adjoint operators* $\mathcal{A}^*$, $\mathcal{B}^*$ *and* $\mathcal{C}^*$

For a bounded linear operator between two Hilbert spaces, $\mathcal{L} : \mathbb{X}_1 \to \mathbb{X}_2$, the adjoint operator $\mathcal{L}^*$ satisfies

$$\langle \mathcal{L}\boldsymbol{q}, \boldsymbol{p} \rangle_{\mathbb{X}_2} = \langle \boldsymbol{q}, \mathcal{L}^*\boldsymbol{p} \rangle_{\mathbb{X}_1} \quad \text{for all} \quad \boldsymbol{q} \in \mathbb{X}_1, \boldsymbol{p} \in \mathbb{X}_2. \tag{60}$$

The derivations make use of the following definitions of inner products,

$$
\begin{array}{llll}
\langle \mathbf{u}, \boldsymbol{p} \rangle_{\mathbb{X}} & = & \int_{\Omega} \mathbf{u}(\boldsymbol{x})^T \boldsymbol{p}(\boldsymbol{x}) \, \mathrm{d}x\mathrm{d}y, & \forall \, \mathbf{u}, \boldsymbol{p} \in \mathbb{X}, \\
\langle \mathbf{f}, \mathbf{g} \rangle_{\mathbb{U}} & = & \mathbf{f}^T \mathbf{g}, & \forall \, \mathbf{f}, \mathbf{g} \in \mathbb{U}, \\
\langle \mathbf{z}, \mathbf{y} \rangle_{\mathbb{Y}} & = & \mathbf{z}^T \mathbf{y}, & \forall \, \mathbf{z}, \mathbf{y} \in \mathbb{Y}, \\
\langle \mathbf{f}, \mathbf{g} \rangle_{\mathbb{U}((-\infty,0])} & = & \int_{-\infty}^{0} \mathbf{f}^T \mathbf{g} \mathrm{d}t, & \forall \, \mathbf{f}, \mathbf{g} \in \mathbb{U}((-\infty, 0]), \\
\langle \mathbf{z}, \mathbf{y} \rangle_{\mathbb{Y}([0,\infty))} & = & \int_{0}^{\infty} \mathbf{z}^T \mathbf{y} \mathrm{d}t, & \forall \, \mathbf{z}, \mathbf{y} \in \mathbb{Y}([0, \infty)).
\end{array}
\tag{61}
$$

Note that the kinetic energy of a perturbation $\mathbf{u}$ at time t is measured by $\|\mathbf{u}\|_{\mathbb{X}}^2 = \langle \mathbf{u}, \mathbf{u} \rangle_{\mathbb{X}}$. We begin by deriving the adjoint operator of $\mathcal{B} : \mathbb{U} \to \mathbb{X}$, using the identity

$$\langle \mathcal{B}\mathbf{f}, \mathbf{u} \rangle_{\mathbb{X}} = \langle \mathbf{f}, \mathcal{B}^*\mathbf{u} \rangle_{\mathbb{U}}. \tag{62}$$

The left-hand side is equivalent to

$$\int_{\Omega} (\mathcal{B}\mathbf{f})^T \mathbf{u} \mathrm{d}x\mathrm{d}y = \mathbf{f}^T \int_{\Omega} \mathcal{B}^T \mathbf{u} \mathrm{d}x\mathrm{d}y = \langle \mathbf{f}, \int_{\Omega} \mathcal{B}^T \mathbf{u} \mathrm{d}x\mathrm{d}y \rangle_{\mathbb{U}}; \tag{63}$$

using (62) we identify $\mathcal{B}^* : \mathbb{X} \to \mathbb{U}$

$$\mathcal{B}^*\mathbf{u} = \int_{\Omega} \mathcal{B}^T \mathbf{u} \mathrm{d}x\mathrm{d}y. \tag{64}$$

The adjoint of the output operator $\mathcal{C} : \mathbb{X} \to \mathbb{Y}$ can be derived in an analogous manner by using the identity

$$\langle \mathcal{C}\mathbf{u}, \mathbf{y} \rangle_{\mathbb{Y}} = \langle \mathbf{u}, \mathcal{C}^*\mathbf{y} \rangle_{\mathbb{X}}. \tag{65}$$

The left-hand side can be written

$$(\mathcal{C}\mathbf{u})^T \mathbf{y} = \int_{\Omega} \mathbf{u}^T \hat{\mathcal{C}}^T \mathbf{y} = \langle \mathbf{u}, \hat{\mathcal{C}}^T \mathbf{y} \rangle_{\mathbb{X}} \tag{66}$$

where $\hat{\mathcal{C}}$ is the integrand in (16). We can now identify the adjoint output operator $\mathcal{C}^* : \mathbb{Y} \to \mathbb{X}$ as

$$\mathcal{C}^*\mathbf{y} = \hat{\mathcal{C}}^T \mathbf{y}. \tag{67}$$

The evolution operator $\mathcal{T} : \mathbb{X} \to \mathbb{X}$ was defined in (4). The adjoint of $\mathcal{T}$ satisfies

$$\langle \mathcal{T}\mathbf{u}, \boldsymbol{p} \rangle_{\mathbb{X}} = \langle \mathbf{u}, \mathcal{T}^*\boldsymbol{p} \rangle_{\mathbb{X}}. \tag{68}$$

We begin with taking the inner product of $\boldsymbol{p}$ and σ with the Navier–Stokes equations (1a) and (1b), respectively. By integrating over the time domain and applying integration by parts we obtain

$$
\begin{aligned}
0 \;=\; & \int_0^t \int_\Omega \boldsymbol{p}^T \\
& \left(\frac{\partial \mathbf{u}}{\partial t} - (-(\mathbf{U} \cdot \nabla) - (\nabla \mathbf{U}^T)^T + \mathrm{Re}^{-1}\nabla^2 + \lambda(x))\mathbf{u} - \nabla p] + \sigma(\nabla \cdot \mathbf{u}) \right) \mathrm{d}x\mathrm{d}y\mathrm{d}t \\
\;=\; & \int_0^t \int_\Omega \\
& \left(-\mathbf{u}^T (\frac{\partial \boldsymbol{p}}{\partial t} + ((\mathbf{U} \cdot \nabla) - (\nabla \mathbf{U})^T + \mathrm{Re}^{-1}\nabla^2 + \lambda(x))\boldsymbol{p} + \nabla \sigma) - p(\nabla \cdot \boldsymbol{p}) \right) \mathrm{d}x\mathrm{d}y\mathrm{d}t \\
& + \underbrace{\int_0^t [B.C.]_\Omega \mathrm{d}t}_{2} + \underbrace{\int_\Omega \mathbf{u}(t)^T \boldsymbol{p}(t)\mathrm{d}x\mathrm{d}y - \int_\Omega \mathbf{u}(0)^T \boldsymbol{p}(0)\mathrm{d}x\mathrm{d}y}_{3} \tag{69}
\end{aligned}
$$

By requiring the first two terms to be zero we obtain the adjoint Navier–Stokes equations with boundary conditions. They will be considered after the boundary terms in time denoted by 3 in (69). We thus require that

$$
\int_\Omega \mathbf{u}(t)^T \boldsymbol{p}(t)\mathrm{d}x\mathrm{d}y = \int_\Omega \mathbf{u}(0)^T \boldsymbol{p}(0)\mathrm{d}x\mathrm{d}y. \tag{70}
$$

The left hand side can be rewritten as

$$
\begin{aligned}
\int_\Omega (\mathcal{T}(t)\mathbf{u}(0))^T \boldsymbol{p}(t)\mathrm{d}x\mathrm{d}y &= \langle \mathcal{T}(t)\mathbf{u}(0), \boldsymbol{p}(t)\rangle_{\mathbb{X}} \\
&= \langle \mathbf{u}(0), \mathcal{T}^*(t)\boldsymbol{p}(t)\rangle_{\mathbb{X}} = \int_\Omega \mathbf{u}(0)^T \mathcal{T}^*(t)\boldsymbol{p}(t) \,,
\end{aligned}
$$

where we can identify the action of the adjoint evolution operator $\mathcal{T}^* : \mathbb{X} \to \mathbb{X}$ as

$$
\mathcal{T}^*(t)\boldsymbol{p}(t) = \boldsymbol{p}(0). \tag{71}
$$

Now we proceed with deriving the adjoint equations associated with $\mathcal{T}^*$. The spatial boundary terms given by the second term in (69) are

$$
\begin{aligned}
\int_0^t [B.C.]_\Omega \mathrm{d}t \;=\; & \int_0^t \left[\sigma u + u^* p + U \mathbf{u}^T \boldsymbol{p} - \mathrm{Re}^{-1}\boldsymbol{p}^T \frac{\partial \mathbf{u}}{\partial x} + \mathrm{Re}^{-1}\mathbf{u}^T \frac{\partial \boldsymbol{p}}{\partial x} \right]_0^{L_x} \\
& + \left[\sigma v + v^* p + V \mathbf{u}^T \boldsymbol{p} - \mathrm{Re}^{-1}\boldsymbol{p}^T \frac{\partial \mathbf{u}}{\partial y} + \mathrm{Re}^{-1}\mathbf{u}^T \frac{\partial \boldsymbol{p}}{\partial y} \right]_0^{L_y} \mathrm{d}t = 0.
\end{aligned}
$$

If boundary conditions (2) on $\mathbf{u}$ are used and if we demand the that $\boldsymbol{p} = (u^*, v^*)$, σ^*, and p satisfies

$$
\begin{aligned}
(\sigma, p)(0, y) &= (\sigma, p)(L_x, y), & \text{(72a)} \\
\boldsymbol{p}(0, y) &= \boldsymbol{p}(L_x, y), & \text{(72b)} \\
\boldsymbol{p}(x, 0) &= \boldsymbol{p}(x, L_y) = 0. & \text{(72c)}
\end{aligned}
$$

we observe that the boundary terms vanish.

Finally, the first term in (69) define the adjoint Navier–Stokes equations if we demand that $\boldsymbol{p}$ satisfies equation (22). The equations (22) together with boundary conditions (72*b*) and (72*c*) determine the behavior of adjoint flow field $\boldsymbol{p}$.

A.2. *The adjoint operators* $\mathcal{L}_c^*$ *and* $\mathcal{L}_o^*$

The adjoint of the controllability operator $\mathcal{L}_c : \mathbb{U}((-\infty, 0]) \to \mathbb{X}$ is derived using the identity

$$\langle \mathcal{L}_c \mathbf{f}, \mathbf{u}_0 \rangle_{\mathbb{X}} = \langle \mathbf{f}, \mathcal{L}_c^* \mathbf{u}_0 \rangle_{\mathbb{U}((-\infty, 0])}. \tag{73}$$

We expand the left hand side,

$$\begin{aligned}
\langle \mathcal{L}_c \mathbf{f}, \mathbf{u}_0 \rangle_{\mathbb{X}} &= \int_\Omega \int_{-\infty}^0 (\mathcal{T}(-t)\mathcal{B}\mathbf{f}(t))^T \mathbf{u}_0 \mathrm{d}t \mathrm{d}x \mathrm{d}y \\
&= \int_{-\infty}^0 \mathbf{f}^T(t)(\mathcal{B}^* \mathcal{T}^*(-t))\mathbf{u}_0 \mathrm{d}t \\
&= \langle \mathbf{f}(t), \mathcal{B}^* \mathcal{T}^*(-t)\mathbf{u}_0 \rangle_{\mathbb{U}((-\infty, 0])}.
\end{aligned}$$

In the first equality the definitions of $\mathcal{B}^*$ and $\mathcal{T}^*$ from expressions (64) and (68) were used. We can now identify $\mathcal{L}_c^* : \mathbb{X} \to \mathbb{U}((-\infty, 0])$

$$\mathcal{L}_c^*(-t)\mathbf{u}_0 = \mathcal{B}^* \mathcal{T}^*(-t)\mathbf{u}_0. \tag{74}$$

In a similar fashion the adjoint of the observability operator $\mathcal{L}_o : \mathbb{X} \to \mathbb{Y}([0, \infty))$ is defined by

$$\langle \mathcal{L}_o \mathbf{u}, \mathbf{y} \rangle_{\mathbb{Y}([0,\infty))} = \langle \mathbf{u}, \mathcal{L}_o^* \mathbf{y} \rangle_{\mathbb{X}}. \tag{75}$$

Expanding the left-hand side results in

$$\begin{aligned}
\langle \mathcal{L}_o \mathbf{u}, \mathbf{y} \rangle_{\mathbb{Y}([0,\infty))} &= \int_0^\infty (\mathcal{C}\mathcal{T}(t)\mathbf{u}(t))^T \mathbf{y} \mathrm{d}t \\
&= \int_0^\infty \int_\Omega (\hat{\mathcal{C}}\mathcal{T}(t)\mathbf{u}(t))^T \mathbf{y} \mathrm{d}x \mathrm{d}y \mathrm{d}t \\
&= \int_0^\infty \int_\Omega \mathbf{u}^T (\mathcal{T}^*(t)\mathcal{C}^*\mathbf{y}(t))^T \mathrm{d}x \mathrm{d}y \mathrm{d}t \\
&= \langle \mathbf{u}, \int_0^\infty \mathcal{T}^* \mathcal{C}^* \mathbf{y} \mathrm{d}t \rangle_{\mathbb{X}},
\end{aligned}$$

where $\hat{\mathcal{C}}$ is the integrand in (16). We can identify the adjoint observability operator $\mathcal{L}_o^* : \mathbb{Y}([0, \infty)) \to \mathbb{X}$ as

$$\mathcal{L}_o^* \mathbf{y}(t) = \int_0^\infty \mathcal{T}^*(t)\mathcal{C}^* \mathbf{y}(t) \ \mathrm{d}t. \tag{76}$$

Appendix B. The snapshot method

We will show how to approximate the eigenvalue problems (35),(31) and (45) in order to compute the observable, controllable and balanced modes.

B.1. *Approximate Gramians*

We begin with considering the eigenvalue problem,

$$\mathcal{P}\phi_i^c = \lambda_i^c \phi_i^c, \tag{77}$$

where

$$\mathcal{P}\phi_i^c = \int_0^\infty \mathcal{T}(t)\mathcal{B}\mathcal{B}^*\mathcal{T}^*(t)\phi_i^c \, \mathrm{d}t. \tag{78}$$

The first step is to rewrite the action of the controllability Gramian $\mathcal{P}$ on ϕ_i^c in terms of impulse responses of the state. Recall that the flow field triggered by an impulse $\delta(0)$ applied to the input $\mathcal{B}_1$ is given by $\mathcal{T}\mathcal{B}_1$. Let us define the vector $\bar{\mathbf{u}}$ containing the impulse responses of all inputs (except the measurement noise) as columns, *i.e.*

$$\bar{\mathbf{u}} = \mathcal{T}\mathcal{B} = (\mathcal{T}(t)\mathcal{B}_1(\boldsymbol{x}), \mathcal{T}\mathcal{B}_2(\boldsymbol{x})) = (\mathbf{u}_1(\boldsymbol{x},t), \mathbf{u}_2(\boldsymbol{x},t)). \tag{79}$$

Moreover, from the expression of $\mathcal{B}^*$ and $\mathcal{T}^*$ given by (64) and (68) respectively, we can rewrite the action of $\mathcal{B}^*\mathcal{T}^*$ on ϕ_i^c as

$$\mathcal{B}^*\mathcal{T}^*\phi_i^c = \int_\Omega (\mathcal{T}\mathcal{B})^T \phi_i^c \mathrm{d}x\mathrm{d}y = \int_\Omega \bar{\mathbf{u}}^T \phi_i^c \mathrm{d}x\mathrm{d}y. \tag{80}$$

The controllability Gramian becomes

$$\mathcal{P}\phi_i^c = \left(\int_0^\infty \mathcal{T}(t)\mathcal{B}\mathcal{B}^*\mathcal{T}^*(t)\mathrm{d}t \right) \phi_i^c = \int_0^\infty \bar{\mathbf{u}} \left(\int_\Omega \bar{\mathbf{u}}^T \phi_i^c \mathrm{d}x\mathrm{d}y \right) \mathrm{d}t. \tag{81}$$

The above expression is approximated by discretization in space and time. Suppose that $\boldsymbol{x} = (\boldsymbol{x}_1, \ldots, \boldsymbol{x}_{n/2})$ is a grid in Ω with $n/2$ points. We construct a $n \times 2$ matrix by evaluating $\bar{\mathbf{u}}$ at the grid-points, *i.e.*

$$\hat{u} = \begin{pmatrix} \mathbf{u}_1(\boldsymbol{x}_1,t) & \mathbf{u}_2(\boldsymbol{x}_1,t) \\ \vdots, & \vdots \\ \mathbf{u}_1(\boldsymbol{x}_{n/2},t) & \mathbf{u}_2(\boldsymbol{x}_{n/2},t) \end{pmatrix}. \tag{82}$$

The size of this matrix is $n \times 2$ because there are two velocity components, *e.g.* $\mathbf{u}_1(\boldsymbol{x}_j,t) = (u_1(\boldsymbol{x}_j,t), v_1(\boldsymbol{x}_j,t))^T$. Similarly we define $\hat{\phi}_i$ as the following $n \times 1$ column vector,

$$\hat{\phi}_i = (\phi_i^c(\boldsymbol{x}_1), \ldots, \phi_i^c(\boldsymbol{x}_{n/2}))^T. \tag{83}$$

The integral in Ω in expression (81) can now be approximated by

$$\int_\Omega \bar{\mathbf{u}}^T \phi_i^c \mathrm{d}x\mathrm{d}y \approx \hat{u}^T W \hat{\phi}_i, \tag{84}$$

where the $n \times n$ positive-definite matrix, W, contains the spatial integrations weights $\delta_{\boldsymbol{x}_j}$. The quadrature weights $\delta_{\boldsymbol{x}_j}$ depend on the chosen quadrature rule. For instance in our case, $\delta_{\boldsymbol{x}_j}$ consist of the Chebyshev integral weight functions (Hanifi *et al.* 1996) in the wall-normal direction and a trapezoidal rule in the streamwise direction.

The expression given by (81) becomes

$$\mathcal{P}\phi_i^c \approx \left(\int_0^\infty \hat{u}\hat{u}^T \mathrm{d}t \right) W\hat{\phi}_i \tag{85}$$

where we recognize the term in the parenthesis as the state-covariance matrix. If the flow fields are given as snapshots at discrete times $t_1, \ldots, t_m$, we can further approximate (85) with

$$\left(\int_0^\infty \hat{u}\hat{u}^T \mathrm{d}t \right) W\hat{\phi}_i \approx XX^T W\hat{\phi}_i. \tag{86}$$

The $n \times 2m$ matrix X contains $\hat{u}(t_j)$ in column j multiplied with the square root of the quadrature coefficients δ_{t_j} in time, *i.e.*

$$X = (\hat{u}(t_1)\sqrt{\delta_{t_1}}, \ldots, \hat{u}(t_m)\sqrt{\delta_{t_m}}) \tag{87}$$

where each column of X is referred to as a snapshot.

The eigenvalue problem given by (77) can now be approximated with the following $n \times n$ eigenvalue problem

$$XX^T W\hat{\phi}_i = \lambda_i^c \hat{\phi}_i, \qquad i = 1, \ldots, n. \tag{88}$$

It is prohibitively expensive to diagonalize the matrix $XX^T W$ when $n \geq 10^5$. In the method of snapshots (Sirovich 1987), the modes $\hat{\phi}_i$ can be approximated by diagonalizing the $2m \times 2m$ matrix $X^T WX$ instead. This is efficient when the product of the number of snapshots and the number of inputs is much smaller than the number of spatial grid-points.

In the method of snapshots the modes, $\hat{\phi}_i$ are expanded in snapshots, *i.e.* the columns of matrix X. This can be formulated in matrix form as

$$\phi_i^c = X\mathbf{a}_i \qquad i = 1, \ldots, 2m, \tag{89}$$

with the column vector $\mathbf{a}_i$ containing the expansion coefficients.

The above expansion is inserted to the large eigenvalue problem (88) which results in the $2m \times 2m$ eigenvalue problem

$$X^T WX\mathbf{a}_i = \lambda_i^c \mathbf{a}_i \qquad i = 1, \ldots, 2m. \tag{90}$$

The eigenvalues λ_i^c are the same as the original eigenvalue problem and the controllable modes are recovered from equation (89). The orthonormal set of controllable modes are given by

$$\hat{\phi}_i = \frac{1}{\sqrt{\lambda_i}} X\mathbf{a}_i, \qquad \hat{\phi}_i^T \hat{\phi}_j = \delta_{ij}. \tag{91}$$

There are some important computational issues which should be commented at this point: (i) The Gramian (29) is defined as an infinite integral, which means that in order for the *approximate* Gramian $XX^T W$ to be a sufficiently good approximation, we should take snapshots for a long time. There are no restrictions on how to distribute the snapshots in time and it is prudent to store many snapshots when the flow energy is large. (ii) Due to numerical round–off errors, often not all modes are orthogonal. In our case with

$2m = 3200$, the first 150 modes were orthogonal down to numerical accuracy (i.e $(\phi_i^c)^T \phi_i^c \approx 10^{-15}$), whereas for higher modes the orthogonality condition is gradually lost due to rounding errors. The ratio $\mu_i = \lambda_1/\lambda_i$ can be used as a condition number of the corresponding mode ϕ_i^c. Very large values of μ_c indicate poor orthogonality due to numerical inaccuracy.

The observable modes are computed in a similar manner, but now the snapshots are taken from impulse responses of the adjoint equations for each output, *i.e.* $\bar{\boldsymbol{p}} = (\boldsymbol{p}_1, \boldsymbol{p}_2) = (\mathcal{T}^* \hat{\mathcal{C}}_1^T, \mathcal{T}^* \hat{\mathcal{C}}_2^T)$ with $\hat{\mathcal{C}}$ as the integrand in (16). The approximate observability Gramian is

$$\mathcal{Q}\phi_i^o = \int_0^\infty \mathcal{T}^* \mathcal{C}^* \mathcal{C} \mathcal{T} \phi_i^o \mathrm{d}t = \int_0^\infty \bar{\boldsymbol{p}} \left(\int_\Omega \bar{\boldsymbol{p}}^T \phi_i^o \mathrm{d}x\mathrm{d}y \right) \mathrm{d}t \approx YY^T W \hat{\phi}_i, \quad (92)$$

where Y is the $n \times 2m$ matrix

$$Y = \begin{pmatrix} \boldsymbol{p}_1(\boldsymbol{x}_1, t_1)\sqrt{\delta_{t_1}} & \cdots & \boldsymbol{p}_1(\boldsymbol{x}_1, t_1)\sqrt{\delta_{t_1}} & \cdots & \boldsymbol{p}_2(x_1, t_m)\sqrt{\delta_{t_m}} \\ \vdots & & \vdots & & \vdots \\ \boldsymbol{p}_1(\boldsymbol{x}_{n/2}, t_1)\sqrt{\delta_{t_1}} & \cdots & \boldsymbol{p}_1(\boldsymbol{x}_{n/2}, t_1)\sqrt{\delta_{t_1}} & \cdots & \boldsymbol{p}_2(x_{n/2}, t_m)\sqrt{\delta_{t_m}} \end{pmatrix}. \quad (93)$$

The observable modes are computed in an analogous manner as the controllable modes with Y replacing X in equations (89)–(91).

B.2. *Snapshot-based balanced truncation*

To obtain the balanced modes, we must diagonalize the matrix $\mathcal{PQ}$, which can approximated using the matrices X and Y, *i.e.*

$$\mathcal{PQ}\phi_i^{oc} \approx XX^T WYY^T W \hat{\phi}_i^{oc} = \sigma_i^2 \hat{\phi}_i^{oc}. \quad (94)$$

We expand the balanced modes as linear combinations of the columns of X, with $\mathbf{a}_i = (a_1, \ldots, a_m)^T$ as the expansion coefficients. Inserting this expansion in (94), we get

$$0 = XX^T WYY^T WX\mathbf{a}_i - X\mathbf{a}_i \sigma_i^2 = X(X^T WYY^T WX\mathbf{a}_i - \mathbf{a}_i \sigma_i^2), \quad (95)$$

To solve the above problem we can equivalently diagonalize $X^T WYY^T WX$ or form the singular value decomposition (SVD) of $Y^T WX$. The latter decomposition is preferred since it is numerically more stable, *i.e.*

$$Y^T WX\boldsymbol{b}_i = \sigma_i \mathbf{a}_i, \qquad i = 1, \ldots, 2m. \quad (96)$$

The normalized balanced modes and the associated adjoint balanced modes are recovered from

$$\hat{\phi}_i^{oc} = \frac{1}{\sqrt{\sigma_i}} X\boldsymbol{b}_i, \qquad \hat{\psi}_i^{oc} = \frac{1}{\sqrt{\sigma_i}} Y\mathbf{a}_i, \quad (97)$$

where $(\hat{\psi}_i^{oc})^T \hat{\phi}_j^{oc} = \delta_{ji}$.

The method can be summarized in three steps; (i) compute the impulse response of each input, collect snapshots of the response and construct X (87) (ii) compute the adjoint impulse response of each output, collect snapshots of the response and construct Y (93) (iii) form the matrix $Y^T WX$, compute its

SVD and recover the balanced modes from (97). See Rowley (2005) for further details on the method.

Appendix C. Timestepper

The timestepper used in this work for both the forward and adjoint equations is a spectral code described in detail in Chevalier *et al.* (2007*b*).

If $f(x, y, t)$ is a velocity component then the discrete approximation is the Chebyshev-Fourier series

$$\mathsf{f}(t) = \sum_{l=0}^{n_y} T_l(y) \sum_{m=-n_x/2}^{n_x/2} e^{i\alpha_m x} \hat{u}_{lm} + c.c. \tag{98}$$

where T_l is the lth Chebyshev polynomial, $\alpha_m = 2m\pi/L_x$ and $n_x = 768$ and $n_y = 101$ the number of collocation points in each direction. The coefficients $\hat{u}_{lm}$ are complex functions. The associated collocation grid is defined by $y_l = (L_y/2)(1 - \cos(\pi l/n_y))$ and $x_m = L_x(1/2 + m/n_x)$ with $L_x = 1000$ and $L_y = 30$. The discretized system of equations is projected onto a divergence-free space by transforming to $v - \eta$ formulation and integrated in time using a third-order semi-implicit scheme.

To retain periodic boundary conditions, which is necessary for the Fourier discretization, a fringe region is added at the end of the physical domain where a forcing is applied so that the flow smoothly changes from the outflow velocity of the physical domain to the desired inflow velocity. For the linearized equation the desired inflow condition is zero, so the fringe forcing is of the form $F = \lambda(x)\mathbf{u}$, where

$$\lambda(x) = -\lambda_{max}\left[S\left(\frac{x - x_{start}}{\Delta_{rise}}\right) - S\left(\frac{x - x_{end}}{\Delta_{fall}}\right)\right]. \tag{99}$$

Here $\lambda_{\max}$ is the maximum strength of the damping, $x_{\mathrm{start}} = 800$ to $x_{\mathrm{end}} = 1000$ the spatial extent of the region where the damping function is non-zero and $\Delta_{\mathrm{rise}} = 120$ and $\Delta_{\mathrm{fall}} = 60$ the rise and fall distance of the damping function. The smooth "step" function $S(x)$ rises from zero for negative x to one for $x \geq 1$. We have used the following form for S, which has the advantage of having continuous derivatives of all orders,

$$S(x) = \begin{cases} 0\,, & x \leq 0\,, \\ 1/\left(1 + e^{(1/(x-1)+1/x)}\right)\,, & 0 < x < 1\,, \\ 1\,, & x \geq 1\,. \end{cases} \tag{100}$$

Appendix D. Riccati equations

We briefly outline the full-information control and estimation problems and their solutions. The reader is directed to Anderson & Moore (1990); Lewis & Syrmos (1995); Bagheri *et al.* (2009) for derivations of the solutions.

The first step in the design of an $\mathcal{H}_2$-compensator involves the solution of an optimal control state-feedback problem. The full-information problem is to

find a control $\mathsf{u}(t)$ as a linear function of the flow state $q(t)$ that minimizes the deterministic cost functional

$$J = \frac{1}{2} \int_0^\infty q^T C_1^T C_1 q + l^2 \mathsf{u}^T \mathsf{u} \; dt, \tag{101}$$

while satisfying the initial value problem

$$\dot{q} = Aq + B_2\mathsf{u}, \qquad q(t=0) = q_0. \tag{102}$$

The optimal control signal is given by

$$\mathsf{u}(t) = \underbrace{-\frac{1}{l^2} B_2^T X}_{K} q(t), \tag{103}$$

where X is a solution of the Riccati equation

$$0 = A^T X + XA - \frac{1}{l^2} XB_2 B_2^T X + C_1^T C_1 \tag{104}$$

The solution to this equation provides the optimal steady feedback gain via the relation (103).

The second step in the design of an $\mathcal{H}_2$-compensator involves the minimization of the estimation error $q_e = q - \hat{q}$ given by the estimator

$$\dot{q}_e = Aq_e + B_1 w + L(\mathsf{v} - \hat{\mathsf{v}}), \qquad \hat{q}(t=0) = 0 \tag{105a}$$
$$\hat{\mathsf{v}} = C_1 \hat{q} \tag{105b}$$
$$\mathsf{v} = C_1 q + g, \tag{105c}$$

where w and g are temporal white noise signals. The solution is the feedback gain L that minimizes the objective functional

$$J = \int_0^\infty q_e^T(t) q_e(t) \mathrm{d}t. \tag{106}$$

The functional (106) can be minimized if L is chosen as

$$L = -\frac{1}{\alpha^2} PC_2^T, \tag{107}$$

where P is a solution of the Riccati equation,

$$0 = AP + PA^T - \frac{1}{\alpha^2} PC_2^T C_2 P + B_1 B_1^T. \tag{108}$$

References

AHUJA, S., ROWLEY, C. W., KEVREKIDIS, I. G. & WEI, M. 2007 Low-dimensional models for control of leading-edge vortices: Equilibria and linearized models. *AIAA Paper 2008-553, 46th AIAA Aeros. Sci. Meeting Exhibit*.

ÅKERVIK, E., EHRENSTEIN, U., GALLAIRE, F. & HENNINGSON, D. S. 2008 Global two-dimensional stability measures of the flat plate boundary-layer flow. *Eur. J. Mech. B* **27**, 501–513.

ÅKERVIK, E., HŒPFFNER, J., EHRENSTEIN, U. & HENNINGSON, D. S. 2007 Optimal growth, model reduction and control in a separated boundary-layer flow using global eigenmodes. *J. Fluid. Mech.* **579**, 305–314.

ANDERSON, B. & MOORE, J. 1990 *Optimal control: Linear Quadratic Methods*. Prentice Hall, New York.

BAGHERI, S., HŒPFFNER, J., SCHMID, P. J. & HENNINGSON, D. S. 2009 Input-output analysis and control design applied to a linear model of spatially developing flows. *Appl. Mech. Rev.* **62**(2), 1–27.

BARKLEY, D., GOMES, M. G. & HENDERSON, R. D. 2002 Three-dimensional instability in flow over a backward-facing step. *J. Fluid Mech.* **473**, 167–190.

BEWLEY, T., TEMAM, R. & ZIANE, M. 2000 A general framework for robust control in fluid mechanics. *Physica D: Nonlinear Phenomena* **138**, 360–392.

BLACKBURN, A. M., BARKLEY, D. & SHERWIN, S. 2008 Convective instability and transient growth in flow over a backward-facing step. *J. Fluid Mech.* **603**, 271–304.

BUTLER, K. & FARRELL, B. F. 1992 Three-dimensional optimal perturbations in viscous shear flow. *Phys. Fluids A* **4**, 1637–1650.

CHEVALIER, M., HŒPFFNER, J., ÅKERVIK, E. & HENNINGSON, D. S. 2007a Linear feedback control and estimation applied to instabilities in spatially developing boundary layers. *J. Fluid Mech.* **588**, 163–187.

CHEVALIER, M., SCHLATTER, P., LUNDBLADH, A. & & HENNINGSON, D. S. 2007b A pseudo spectral solver for incompressible boundary layer flows. *Tech Rep, Trita-Mek* **7**, KTH Mechanics, Stockholm.

CHOMAZ, J. M. 2005 Global instabilities in spatially developing flows: Non-normality and nonlinearity. *Ann. Rev. Fluid Mech.* **37**, 357–392.

CHORIN, A. & MARSDEN, J. 1990 *A Mathematical introduction to fluid mechanics*. Springer Verlag, New York.

CURTAIN, R. & ZWART, H. 1995 *An introduction to infinite-dimensional linear systems theory*. Springer Verlag, New York.

DULLERUD, E. & PAGANINI, F. 1999 *A course in robust control theory. A convex approach*. Springer Verlag, New York.

EHRENSTEIN, U. & GALLAIRE, F. 2005 On two-dimensional temporal modes in spatially evolving open flows: The flat-plate boundary layer. *J. Fluid Mech.* **536**, 209–218.

GILLIES, E. A. 1998 Low-dimensional control of the circular cylinder wake. *J. Fluid Mech.* **371**, 157–178.

HANIFI, A., SCHMID, P. J. & HENNINGSON, D. S. 1996 Transient growth in compressible boundary layer flow. *Phys. Fluids* **8** (3), 826–837.

Högberg, M., Bewley, T. R. & Henningson, D. S. 2003 Linear feedback control and estimation of transition in plane channel flow. *J. Fluid Mech.* **481**, 149–175.

Ilak, M. & Rowley, C. W. 2008 Modeling of transitional channel flow using balanced proper orthogonal decomposition. *Phys. Fluids* **20**, 034103.

Kailath, T. 1980 *Linear Systems*. Prentice-Hall, New York.

Kim, J. & Bewley, T. R. 2007 A linear systems approach to flow control. *Ann. Rev. Fluid Mech.* **39**, 383–417.

Kreiss, G., Lundbladh, A. & Henningson, D. S. 1993 Bounds for threshold amplitudes in subcritical shear flows. *J. Fluid Mech.* **1994**, 175–198.

Lauga, E. & Bewley, T. R. 2003 The decay of stabilizability with reynolds number in a linear model of spatially developing flows. *Proc. R. Soc. Lond. A.* **459**, 2077–2095.

Lewis, F. L. & Syrmos, L. V. 1995 *Optimal Control*. John Wiley & Sons, New York.

Moore, B. 1981 Principal component analysis in linear systems: Controllability, observability, and model reduction. *IEEE Trans. Auto. Control* **26** (1), 17–32.

Noack, B., Afanasiev, K., Morzynski, M., Tadmor, G. & Thiele, F. 2003 A hierarchy of low-dimensional models for the transient and post-transient cylinder wake. *J. Fluid Mech.* **497**, 335–363.

Nordström, J., Nordin, N. & Henningson, D. S. 1999 The fringe region technique and the fourier method used in the direct numerical simulation of spatially evolving viscous flows. *SIAM J. Sci. Comput.* **20** (4), 1365–1393.

Pazy, A. 1983 *Semigroup of Linear Operators and Applications to Partial Differential Equations*, 2nd edn. Springer, New York.

Rempfer, D. & Fasel, H. 1994 Evolution of three-dimensional coheren structures in a flat-plate boundary layer. *J. Fluid. Mech.* **260**, 351–375.

Rowley, C. W. 2005 Model reduction for fluids using balanced proper orthogonal decomposition. *Int. J. Bifurc. Chaos* **15** (3), 997–1013.

Siegel, S. G., Seidel, J., Fagley, C., Luchtenburg, D. M., Cohen, K. & McLaughlin, T. 2008 Low dimensional modelling of a transient cylinder wake using double proper orthogonal decomposition. *J. Fluid Mech.* **610**, 1–42.

Sirovich, L. 1987 Turbulence and the dynamics of coherent structures i-iii. *Quart. Appl. Math.* **45**, 561–590.

Skogestad, S. & Postlethwaite, I. 2005 *Multivariable Feedback Control, Analysis to Design*, 2nd edn. Wiley.

Trefethen, L. & Embree, M. 2005 *Spectra and Pseudospectra — The Behavior of Nonnormal Matrices and Operators*. Princeton University Press, New Jersey.

Willcox, K. & Peraire, J. 2002 Balanced model reduction via the proper orthogonal decomposition. *AIAA J.* **40** (11), 2323–2330.

Zhou, K., Doyle, J. & Glover, K. 2002 *Robust and Optimal Control*. Prentice Hall, New Jersey.

Zhou, K., Salomon, G. & Wu, E. 1999 Balanced realization and model reduction for unstable systems. *Int. J. Robust Nonlinear Control* **9**, 183–198.

Paper 3

3

Matrix-free methods for the stability and control of boundary-layer flows

Shervin Bagheri, Espen Åkervik, Luca Brandt and Dan S. Henningson

This paper presents matrix-free methods for the stability analysis and control design of high-dimensional systems arising from the discretized linearized Navier–Stokes equations. The methods are applied to the two-dimensional spatially developing Blasius boundary layer. A critical step in the process of systematically investigating stability properties and designing feedback controllers is solving very large eigenvalue problems by storing only velocity fields at different times instead of large matrices. For stability analysis, where the entire dynamics of perturbations in space and time is of interest, iterative and adjoint-based optimization techniques are employed to compute the global eigenmodes and the optimal initial conditions. The latter are the initial conditions yielding the largest possible energy growth over a finite time interval. The leading global eigenmodes take the shape of Tollmien-Schlichting wavepackets located far downstream in streamwise direction, whereas the leading optimal disturbances are tilted structures located far upstream in the boundary layer. For control design on the other hand, the input-output behavior of the system is of interest and the snapshot method is employed to compute balanced modes that correctly capture this behavior. The inputs represent external disturbances and wall actuation and the outputs represent sensors that extract wall shear stress. A low-dimensional model that captures the input-output behavior is constructed by projection onto balanced modes. The reduced-order model is then used to design a feedback control strategy such that the growth of disturbances is damped as they propagate downstream.

1. Introduction

Control of wall-bounded transitional and turbulent flows has been the subject of several research efforts owing to the high potential benefits. In these fluid-mechanics systems, due to the large flow sensitivity, dramatic effects on global flow parameters may be achieved by minute local perturbations using devices sensing and acting on only small parts of the flow with a small amount of energy. Such control devices can be used to obtain reduction of the skin-friction drag,

for example, implying relevant savings of the operational cost of commercial aircrafts and cargo ships.

In this paper we perform stability analysis and control design for the Blasius flow. The work is motivated by the need to provide efficient numerical tools to analyze complex flows and design efficient control strategies. Although we present results for the Blasius flow the methodology is applicable to any complex flow described by the linearized Navier–Stokes equations. The techniques in this paper share a common methodology: very large eigenvalue problems are solved based only on snapshots of the velocity field at different points in time. No large matrices are stored. Therefore the main tool is a code that integrates the forward and adjoint linearized Navier–Stokes equations in time. This so-called time-stepper technique has become increasingly popular in both stability analysis (Barkley *et al.* 2002; Blackburn *et al.* 2008; Bagheri *et al.* 2009*c*) and for control design (Bagheri *et al.* 2009*a*).

It is now well understood that wall-bounded flows are very sensitive to specific perturbations (Schmid & Henningson 2001). In particular, boundary layer flows support convective instabilities and behave as noise amplifiers (Huerre & Monkewitz 1990). Convectively unstable shear flows are stable from a global point of view (Huerre & Monkewitz 1990; Chomaz 2005); wavepackets generated locally, grow in amplitude as they travel downstream and finally decay or leave the observation window. This behavior can be captured by a non-modal analysis, see e.g. Schmid (2007). It is therefore meaningful to analyze the spatial structure of the initial conditions and forcing yielding largest possible energy growth over a finite time interval. This optimization problem can be solved efficiently for complex flows by solving the direct and adjoint Navier–Stokes equation for the linear evolution of perturbation about a steady state, as shown here (see also Barkley *et al.* 2002, 2008).

Two aspects in flow control have been identified as crucial in order to apply feedback control in more complex flows and to move towards an implementation in wind-tunnel tests. They are i) model reduction to significantly decrease the cost of both constructing the controller and running it online, thus allowing the fast computation of the control signal directly from the sensor output; ii) the need to naturally consider localized sensors and actuators. Both these aspects are addressed in Bagheri *et al.* (2009*a*). In this paper, the results of Bagheri *et al.* (2009*a*) are extended by introducing wall actuation and wall shear stress measurements instead of idealized volume forcing actuation and velocity measurements inside the flow. The incorporation of actuators and sensors at the physical boundaries in our design, takes us one step closer to use the controller in actual experiments.

Recently, several groups have suggested and pursued the combination of computational fluid dynamics and control theory, thus going past early attempts of flow control based on physical intuition or on a trial-and-error basis (see the review in Kim & Bewley 2007). The reader is also referred to Bagheri *et al.* (2009*b*) for a thorough review of the many tools used in flow control.

In early work from our group (Högberg & Henningson 2002; Högberg *et al.* 2003*a*,*b*), a linear model-based feedback control approach, that minimizes an objective function which measures the perturbation energy, is formulated where the Orr-Sommerfeld and Squire equations model the flow dynamics. The latter equations describe the linear evolution of perturbations evolving in a parallel base flow. The control problem is combined with a state estimator: The so called Kalman and extended Kalman filter have been implemented in order to reconstruct the flow in an optimal manner by only considering continuous wall measurements. These studies have also shown the importance of physically relevant stochastic models for the estimation problem (Hœpffner *et al.* 2005; Chevalier *et al.* 2006), in which stochastic noise needs to describe accurately the unmodeled dynamics, such as uncertainties and nonlinearities. Based on these models the estimator is shown to work for both infinitesimal as well as finite amplitude perturbations in direct numerical simulations of transitional flows (Chevalier *et al.* 2007*a*; Monokrousos *et al.* 2008). These studies however assumed a parallel base flow and distributed sensing and actuation at the wall.

Model reduction becomes essential in order to apply modern control theoretical tools to fluid flow systems. For linear control, the aim is to build a model of low dimension that captures the input-output behavior of the Navier–Stokes system and use this model for optimal feedback control design. Balanced truncation (Moore 1981) is a method for model reduction that takes into account both the flow structures most easily influenced by the input and the flow structures to which the outputs are most sensitive. The method provides a set of bi-orthogonal modes, called the balanced modes, that serve as a projection basis for model reduction. The method employed to compute the balanced modes is the snapshot-based balanced truncation introduced by Rowley (2005). This method has been recently applied to the channel flow (Ilak & Rowley 2008), the flow around a pitching airfoil (Ahuja *et al.* 2007) and the Blasius flow (Bagheri *et al.* 2009*a*).

The paper is organized as follows: The modal and nonmodal stability analysis is presented in section 2. We start with describing the flow setup and formulating two eigenvalue problems. We continue with showing how the eigenvalue problems can be solved iteratively and finally present results for the Blasius flow. Section 3 deals with the control design. We introduce inputs, outputs and write the system in the state-space formulation. A brief summary of the LQG framework is provided before model reduction based on balanced modes is introduced. The snapshot method used for model reduction is explained and results on the performance of the reduced-order and controller are shown. Section 4 provides concluding remarks.
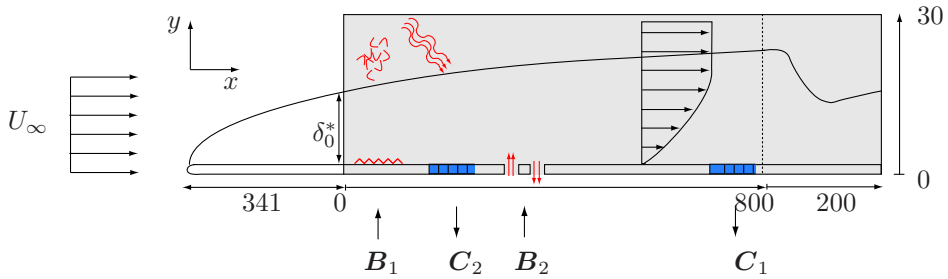
FIGURE 1. The configuration used for the control of perturbations in a two-dimensional flat-plate geometry. The computational domain $\Omega = (0, L_x) \times (0, L_y)$, shown by the gray region, extends from $x = 0$ to $x = 1000$ with the fringe region starting at $x = 800$. The first input $\boldsymbol{B}_1$, located at $(x_w, y_w) = (35, 1)$, models the initial receptivity phase, where disturbances are induced by free-stream turbulence, acoustic waves or wall roughness. The actuator, $\boldsymbol{B}_2$, provides a mechanism to manipulate the flow, in this case by a wall blowing and suction centered at $x_u = 400$. Two sensors $\boldsymbol{C}_1$ and $\boldsymbol{C}_2$, measuring the skin friction near the wall, are located at $x_y = 300$ and $x_z = 750$ respectively. The upstream measurements are used to estimate the incoming perturbations, while the downstream sensor quantifies the effect of the control.

2. Stability analysis

2.1. *Flow configuration and the initial value problem*

We consider the two-dimensional incompressible flow over a flat plate with constant free-stream velocity U_∞ as shown in figure 1. Starting from the leading edge a viscous boundary layer evolves downstream. The evolution of the streamwise velocity u, the wall-normal velocity v and the pressure p in time t and space (x_1, x_2) is governed by the incompressible non-linear Navier–Stokes equation (White 1991). Our analysis deals with the evolution of infinitesimal perturbations on this laminar boundary layer solution and is limited to the computational domain shown by the gray area in figure 1: The inflow boundary is set to the downstream position corresponding to a Reynolds number $Re_{\delta_0^*} = U_\infty \delta_0^*/\nu = 1000$, where δ_0^* is the local displacement thickness of the boundary layer and ν is the kinematic viscosity. Throughout the paper all variables are non-dimensionalized by U_∞ and δ_0^*. The length and height of the domain are $L_x = 1000$ and $L_y = 30$ in the streamwise direction x_1 and wall-normal direction x_2, respectively.

The steady state, about which a linearization is performed, is obtained by marching the nonlinear governing equations in time. The discretized and linearized Navier–Stokes equations with boundary conditions can be cast as an

initial-value problem

$$\begin{aligned} \dot{\mathbf{u}}(t) &= \boldsymbol{A}\mathbf{u}(t) \\ \mathbf{u}(0) &= \mathbf{u}_0 \end{aligned}$$

with $\mathbf{u} = (u, v)^T$. However, for two or three-dimensional base flows the system matrix $\boldsymbol{A}$ will have very large dimension, i.e. the number of grid points times the number of velocity components $n = 2N_x N_y$. Our analysis will therefore be based on the solution of the linearized Navier–Stokes equations that can be represented by the matrix exponential (also referred to as the evolution operator)

$$\mathbf{u}(t) = \boldsymbol{T}(t)\mathbf{u}(0) = e^{\boldsymbol{A}t}\mathbf{u}_0.$$

The matrix exponential, $\boldsymbol{T}(t)$ is the key to both stability analysis and control design, all of which will be discussed in the subsequent sections. However, this discrete operator also poses the greatest computational challenge due its dimension. For example, the storage of the one dimensional Orr-Sommerfeld matrix for the evolution of disturbances in parallel flows requires approximately 1MB of memory, the system matrix for the present spatially inhomogeneous flow with the numerical scheme introduced above requires approximately 200GB, while the memory usage for a full three-dimensional system would be of the order of 200TB.

However, the action of $\boldsymbol{T}(t)$ on any flow field simply amounts to integrating the Navier–Stokes equations in time. In what follows the reader should equate $\boldsymbol{T}(t)\mathbf{u}(s)$ with a DNS simulation starting with an initial condition $\mathbf{u}(s)$ and providing $\mathbf{u}(t + s)$ at a later time. In this so called "time-stepper approach", system matrices are never stored and storage demands in memory are of the same order as a small number of flow fields. Numerically, the equations are solved with the pseudo-spectral Direct Numerical Simulation (DNS) code described in Chevalier *et al.* (2007*b*), where the spatial operators are approximated by Fourier expansion in the streamwise direction with $N_x = 768$ equally distributed points and Chebyshev expansion in the wall-normal direction on $N_y = 101$ Gauss-Lobatto collocation points. A fringe region enforces periodicity in the streamwise direction (Nordström *et al.* 1999).

2.2. *Modal stability*

The first step in the understanding of the fluid problem at hand is examining the hydrodynamic stability of the flow, i.e. the behavior of infinitesimal disturbances to a base flow. In particular, modal stability deals with the response behavior of the baseflow to disturbances as time tends to infinity and is determined by the eigenvalues of $\boldsymbol{A}$:

$$\boldsymbol{A} = \boldsymbol{U}\boldsymbol{\Lambda}\boldsymbol{U}^{-1} \tag{1}$$

where the columns of the matrix $\boldsymbol{U}$ contain the global modes, the columns of $\boldsymbol{U}^{-1}$ the adjoint global modes, (i.e. $\boldsymbol{U}^{-1}\boldsymbol{U} = I$) and the diagonal matrix $\boldsymbol{\Lambda}$ contains the eigenvalues λ_j of $\boldsymbol{A}$. As mentioned previously, in many cases, only

instantenouos velocity fields at different times are available, not matrices. To use the time-stepper technique explained later in section 2.4, it is convenient to rewrite the eigenvalue problem (1) in terms of the evolution operator:

$$\boldsymbol{T}(t) = \boldsymbol{U}\boldsymbol{\Sigma}\boldsymbol{U}^{-1} \tag{2}$$

with $\boldsymbol{\Sigma} = \exp(\boldsymbol{\Lambda}t)$. Note that the evolution operator for a fixed t has the same eigenfunctions as $\boldsymbol{A}$. The temporal growth rate and the frequency of the eigenmodes are given by

$$\mathrm{Re}(\lambda_j) = \ln(|\sigma_j|)/t, \qquad \mathrm{Im}(\lambda_j) = \mathrm{Arg}(\sigma_j)/t,$$

respectively, with $\boldsymbol{\Sigma} = \mathrm{diag}(\sigma_1, \ldots, \sigma_n)$. If $\mathrm{Real}(\lambda_j) > 0$ (or $|\sigma_1| > 1$), the flow is linearly globally unstable.

2.3. *Nonmodal stability*

The amount of information obtained from equation (2) is limited to the asymptotic flow response and does not reveal the short-time behavior of disturbances inherent to many flow systems. Relevant transient growth (Schmid & Henningson 2001) of perturbations is indeed observed for many fluid dynamical systems due to the nonnormality of the operator $\boldsymbol{A}$ (an operator which does not commute with its adjoint) and nonmodal analysis is concerned with finding instabilities that are amplified in a finite time interval. Furthermore, a competition between nonmodal and modal growth is observed in many systems, for example for three-dimensional perturbations in the Blaisus boundary layer (Levin & Henningson 2003). For such flows, different transition scenarios can be observed depending on the external ambient noise. Therefore, to examine the largest possible disturbance growth due to all possible unit-norm initial conditions $\mathbf{u}_0$, we will consider the energy associated to the disturbance at any time t:

$$\|\mathbf{u}(t)\|^2 = (\boldsymbol{T}(t)\mathbf{u}_0, \boldsymbol{T}(t)\mathbf{u}_0) = (\mathbf{u}_0, \boldsymbol{T}^*(t)\boldsymbol{T}(t)\mathbf{u}_0). \tag{3}$$

In the preceding expression, the perturbation kinetic energy is the relevant norm and the adjoint evolution operator $\boldsymbol{T}^*(t)$ is introduced. Applying this operator corresponds to the integration of an adjoint state from time t to time 0. One can show (Bagheri *et al.* 2009*a*) that an initial-value problem for the adjoint linearized Navier–Stokes equations governed by $\boldsymbol{A}^*$ but with negative time derivative can be associated to the adjoint evolution operator $\boldsymbol{T}^*$. For a derivation of the adjoint operators in general, we refer to Giles & Pierce (2000), and for this particular setup, to Bagheri *et al.* (2009*a*).

Initial conditions experiencing the largest nonmodal growth at time t correspond to the leading eigenvalues of the operator $\boldsymbol{T}^*(t)\boldsymbol{T}(t)$, i.e.

$$\boldsymbol{T}^*(t)\boldsymbol{T}(t) = \boldsymbol{U}\boldsymbol{\Sigma}\boldsymbol{U}^*. \tag{4}$$

In this paper the eigenmodes of all matrices are denoted by $\boldsymbol{U}$, and it is clear from the context which matrix they are associated. The first unit-norm eigenvector $\mathbf{u}_1$ is the optimal initial condition, resulting in the largest energy growth at time t. If its corresponding eigenvalue is larger than one, $\sigma_1 > 1$, the system
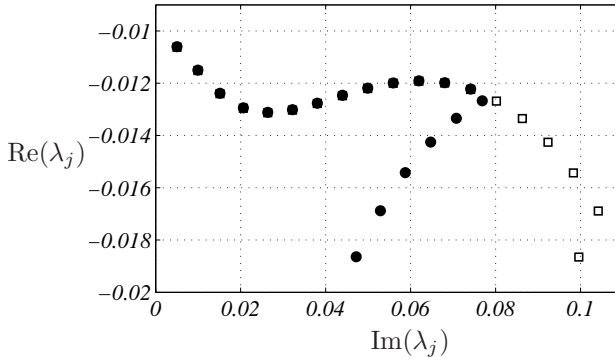
FIGURE 2. Spectrum of of the 2D Blasius flow computed using the timestepping technique with $\Delta t = 30$ (squares) and $\Delta t = 40$ (circles). The high-frequency eigenvalues of the latter computation are mapped/aliased into the low-frequency domain.

can support nonmodal growth. The corresponding flow state at time t can be found by the evaluation of $\boldsymbol{T}(t)\mathbf{u}_1$. To obtain a full map of the potential for transient growth the computations are repeated for different times t.

2.4. *Iterative time-stepping technique*

The eigenvalue problems defined in equations (2) and (4) provide information about the modal and nonmodal flow behavior of the system, respectively. The dimension of the matrices in equations (2) and (4) is too large to be solved by direct methods, such as the standard QR method (Trefethen & Bau 1997). Therefore, one has to resort to iterative methods, such as the Arnoldi (Lehoucq *et al.* 1998), which is based on the projection of the large matrix onto a lower-dimensional subspace $m \ll n$. This results in a significantly smaller system that can be solved with direct methods. In addition, as mentioned previously, in many cases only instantenouos velocity fields at different times are available. A particular subspace is the Krylov $\mathcal{K}$ spanned by snapshots taken from flow fields separated by a constant time interval Δt,

$$\mathcal{K} = \mathrm{span}\{\mathbf{u}_0, \boldsymbol{F}(\Delta t)\mathbf{u}_0, \boldsymbol{F}(2\Delta t)\mathbf{u}_0, \ldots, \boldsymbol{F}((m-1)\Delta t)\mathbf{u}_0\}$$

with $\boldsymbol{F}(t) = \boldsymbol{T}(t)$ (modal stability) or $\boldsymbol{F}(t) = \boldsymbol{T}^*(t)\boldsymbol{T}(t)$ (nonmodal stability) and $\mathbf{u}_0$ is the initial guess that should contain nonzero components of the eigenmodes (it is usually chosen as random noise).

For modal stability analysis, every basis vector of the Krylov subspace is created by a numerical simulation of Δt. The actual time step of these simulations depends on the CFL-condition and is much smaller than the sampling period Δt. The global spectrum using both the matrix method (i.e. storing matrix $\boldsymbol{A}$) and the time-stepper method is compared in figure 3(*a*) and discussed further in the next section. See Bagheri *et al.* (2009*c*) for the application of

this technique on a fully three-dimensional flow, where the size of the problem (A would be approximately a $10^7 \times 10^7$ matrix) prohibits matrix methods. Note that the eigenmodes of T are the same as those of the system matrix A only if Δt is chosen properly, i.e. so that it reflects the characteristic time scale of the physical structures in the flow. More specifically, the choice Δt is a balance between the time scale given by the Nyquist criterion and a sufficient temporal separation of the Krylov vectors to ensure convergence of the iterative method. Frequencies larger than the Nyquist frequency, (i.e. $\omega > \omega_c = \pi/\Delta t$) are spuriously moved into to range $\omega < \omega_c$. To avoid aliasing Δt must therefore be small enough to include two sampling points in one period of the highest frequency mode. In figure 2 the aliasing phenomenon is illustrated. The time stepper with $\Delta t = 30$ (squares) has Nyquist frequency $\omega_c = 0.1$ and therefore captures all frequencies in the range $[0, 0.1]$ correctly. The time-stepper with $\Delta t = 40$ (circles) has $\omega_c = 0.07$ and all frequencies higher than 0.07 are therefore mapped into $[0, 0.07]$.

For nonmodal stability, every basis vector of the Krylov subspace is constructed by first a numerical simulation of Δt yielding the flow field at $t = \Delta t$ which is then used as an initial condition for numerical simulation of the adjoint system backwards in time for Δt.

The Krylov subspace $\mathcal{K}$ is orthonormalized with an m-step Arnoldi factorization yielding the unitary basis V on the which F can be projected on

$$F(\Delta t) \approx V R V^*.$$

This leads to a small $m \times m$ eigenvalue problem of the upper Hessenberg matrix R,

$$RS = \Sigma S$$

which can be computed by standard methods such as the QR algorithm. A number of the so-called Ritz values $\Sigma = \mathrm{diag}(\sigma_1, \ldots, \sigma_m)$ typically converges rapidly to the eigenvalues of the large system F. The eigenmodes corresponding to the m converged eigenvalues with the largest magnitude are recovered by $U = V S$.

Note that one at beforehand does not know how large the Krylov subspace (i.e. m) has to be in order to converge to the desired number of eigenvalues. An implicitly restarted Arnoldi algorithm (Sorensen 1992) implemented in the software package ARPACK (Lehoucq *et al.* 1998) can be used to restart the Arnoldi procedure with a new improved initial guess, $\mathbf{u}_0$, repeatedly until convergence. In this way the Krylov subspace can be very small although the number of flow field snapshots separated by Δt required for convergence can be very large. As an example, the number of snapshots required for convergence of the 22 eigenmodes in Bagheri *et al.* (2009*c*) was 1800, however, thanks to IRAM, the Krylov subspace was only of the order $m \approx 60$.
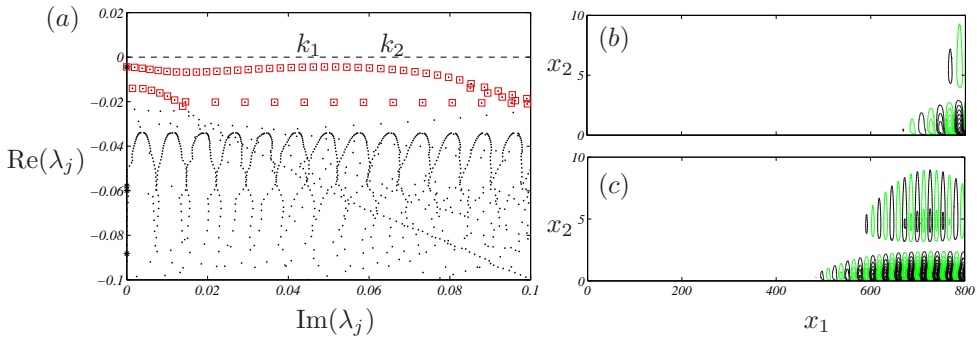
FIGURE 3. (*a*) Eigenvalues of A as computed by the shift and invert Arnoldi method (shown as black circles) and eigenvalues computed by time-stepping using the evolution operator $T(t)$ (shown as red squares). The slightly damped eigenvalues, corresponding to Tollmien-Schlichting (TS) modes, and the free-stream propagating modes are found by both methods. (*b*) Streamwise velocity component of the least stable TS eigenvectors, marked k_1 in (*a*). (*c*) Streamwise velocity component of a high frequency but more damped TS mode, marked k_2 in (*a*).

2.5. *Results*

Results on modal and nonmodal stability of two-dimensional perturbations of the Blasius boundary layer are presented in this section. As mentioned previously, the flow under investigation here is locally unstable but globally stable. Locally unstable perturbations, the Tollmien-Schlichting waves, grow while travelling downstream eventually leaving our control domain. From a global point of view, the flow is then stable, because disturbances have to be continuously fed upstream to avoid that the flow returns to its undisturbed state at each streamwise position. However, a significant transient growth of the disturbance energy in the domain is associated to the propagation of the wavepacket (Ehrenstein & Gallaire 2005; Åkervik *et al.* 2008). This is also referred to as streamwise nonnormality (Cossu & Chomaz 1997; Chomaz 2005).

2.5.1. *Modal stability*

For two-dimensional perturbations of the Blasius boundary layer flow, the memory requirements are still small enough to enable the storage of the system matrix A in memory; the leading eigenmodes from the matrix eigenvalue problem (1) can thus be obtained by means of the shift and invert Arnoldi procedure. Figure 3(*a*) shows the eigenvalues obtained by the shift and invert matrix method as black circles. In the spectrum, one can identify several branches which all can be related to corresponding modes in the spectrum of a parallel Blasius boundary layer, as found by solving the Orr-Sommerfeld equations,

though modified by non-parallelism and boundary conditions (Åkervik *et al.* 2008). The upper branch can be identified as pure Tollmien-Schlichting (TS) waves. These modes are characterized by slightly damped eigenvalues, with the corresponding eigenvectors obtaining their maximum values inside the boundary layer while decaying exponentially in the free stream. More stable modes can be associated to the continuous spectrum: that is modes oscillating in the freestream and decaying inside the boundary layer.

Figures $3(b, c)$ show two examples of TS eigenvectors associated with eigenvalues marked k_1 and k_2 in figure $3(a)$. As a consequence of the convective nature of the instabilities arising in the Blasius flow, where disturbances grow in amplitude as they are convected in the downstream direction, the global eigenmodes are located far downstream, where the flow energy is the largest. The wall-normal structure of these modes is very similar to those obtained by local temporal analysis in the framework of the Orr–Sommerfeld equation. The amplitude of the waves is exponentially increasing downstream: this, together with the temporal decay rate given by the eigenvalue, accounts for the spatial behavior of the mode. The matrix-free method based on the time stepper introduced in section 2.4 successfully locates the least damped eigenvalues by solving the eigenvalue problem (2). The eigenvalues are shown as squares in figure $3(a)$, and are in perfect agreement with the results obtained by the matrix method.

Note that all the eigenvalues are damped, indicating that we will never observe the evolution of single eigenmodes in the flow, but rather we should focus our attention on the nonmodal behavior: in other words the transient growth scenario. It is possible to project the system (3) on a set of eigenmodes obtained from equation (2), thereby approximating the flow dynamics by a low-dimensional model living in the space spanned by a finite number of eigendirections (Schmid & Henningson 2001). For globally unstable flows, only one or few eigenmodes may be sufficient to capture the physical mechanism of the instability (see e.g. the shallow rounded cavity flow in Åkervik *et al.* 2007, where an oscillating cycle could be captured by the sum of two unstable eigenmodes). However for a boundary-layer flow such as that studied here, it is shown in Åkervik *et al.* (2008) that $\mathcal{O}(10^3)$ eigenmodes are needed to capture the full instability mechanism. With the present discretization and boundary conditions, moreover, the sum of the 1500 eigenmodes obtained from the Arnoldi method is not able to correctly describe the Orr mechanism (Orr 1907; Schmid & Henningson 2001; Åkervik *et al.* 2008) as obtained by the optimization via the time stepper defined in equation (4). This is most likely due to the presence of eigenmodes related to the fringe region among the least damped eigenmodes. This points to the limitations of using eigenvalues as a general tool to study stability of complex systems characterized by strong nonnormality.
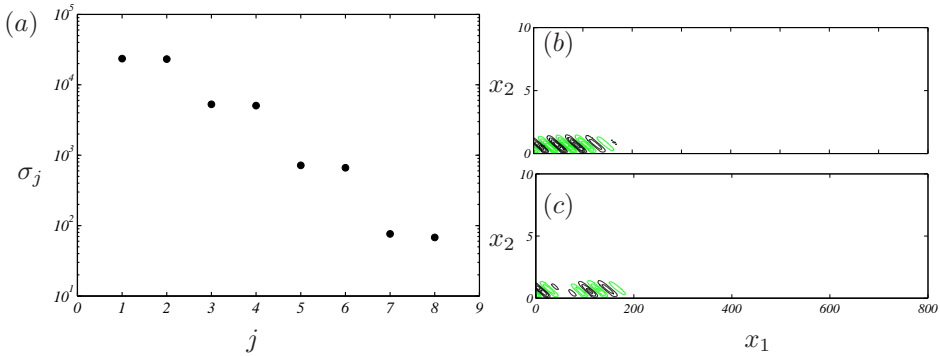
FIGURE 4. (*a*) Eigenvalues of $\boldsymbol{T}^*\boldsymbol{T}$ computed using the forward and adjoint time stepper with $t = 1800$. (*b*) Streamwise velocity component of the optimal disturbance corresponding the largest eigenvalue in (*a*). (*c*) Streamwise velocity component of a suboptimal, corresponding to the third largest eigenvalue in (*a*).

2.5.2. *Nonmodal stability*

Figure 4 shows the spectrum and two eigenfunctions of the eigenvalue problem (4) computed using the time stepper with $t = 1800$. Since $\boldsymbol{T}^*\boldsymbol{T}$ is a self-adjoint positive-definite operator, its eigenvalues are real and positive. Moreover, the eigenvalues shown in figure 4(*a*) come in pairs with similar magnitudes. The corresponding velocity fields have the same wavepacket structure 90 degrees out of phase, representing traveling structures. The most unstable modes (i.e. the optimal disturbance and a suboptimal mode) are shown in figures 4(*b*) and (*c*). They both have a spatial support far upstream, where the sensitivity of the flow is the largest. The modes are tilted in the upstream direction, leaning against the shear layer. As noticed by Butler & Farrell (1992), the upstream tilting of the optimal initial conditions can be attributed to the wall-normal nonnormality of the governing operator; perturbations extract energy from the mean shear by transporting momentum down the mean velocity gradient (the so-called Orr mechanism). Also note the separation of the spatial support of the optimal disturbance modes shown in figure 4(*b*, *c*) (far upstream) and global eigenmodes shown in figure 3(*b*, *c*) (far downstream). This separation is associated to streamwise nonnormality of the system (Chomaz 2005). Finally, note that there is nearly one order of magnitude between the energy of first pair and second pair of eigenvalues shown in figure 4(*a*). As a consequence, one can expect a selection of disturbances in a randomly forced flow that resembles the flow response obtained when using the optimal disturbance as initial condition.
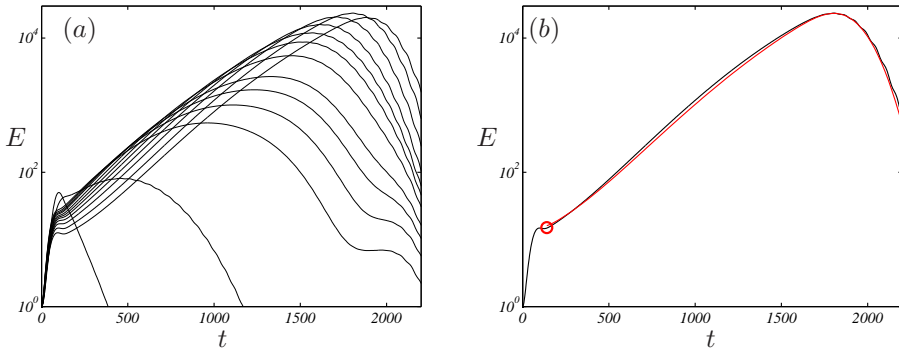
FIGURE 5. (*a*) Energy growth when optimizing for different times. The maximum is achieved for time $t_m = 1800$ for which the maximum energy is $E = 2.35 \cdot 10^4$. (*b*) Solid black line repeats the energy evolution leading to the maximum growth at $t_m = 1800$, whereas red line shows the energy evolution obtained when projecting the system onto a small number of eigenvectors related to the TS branch in figure 3(*a*). The latter clearly does not account for the initial gain due to the Orr mechanism, but by rescaling and shifting in time the two curves collapse, showing that the long time evolution is governed by propagating TS waves.

The energy evolution when solving for the largest eigenvalues of equation (4) at times $t = \{100, 200, \ldots, 2000\}$ is reported in figure 5(*a*). When optimizing for short times the optimal initial condition consists of upstream-tilted structures that exploit the Orr mechanism only (Åkervik *et al.* 2008) to extract energy from the flow. Increasing the optimization time, the upstream-tilted structures move upstream, towards the start of our computational domain, weighting the possibility of growth due to the local Orr mechanism with the energy gain associated to the amplification and propagation of TS waves. The maximum energy growth in this box is obtained for final time $t = 1800$. The corresponding optimal initial condition is shown in the top frame in figure 6. In figure 5(*b*) we compare the energy evolution due to this optimal initial condition with the energy evolution obtained when projecting equation (4) onto the space spanned by a small number of modes; all modes included in the TS branch in figure 3. The evolution in the reduced system clearly does not capture the initial energy gain due to the Orr mechanism; however, by rescaling the energy curve and shifting it in time to account for the initial gain due to the Orr mechanism, the subsequent evolution (amplification and propagation of the TS waves) is almost perfectly matching that of the full system.

The detailed evolution of the streamwise velocity due to the optimal initial condition at time $t = 1800$ is shown in figure 6. At the initial time the structures are leaning backwards against the shear. During the initial phase of
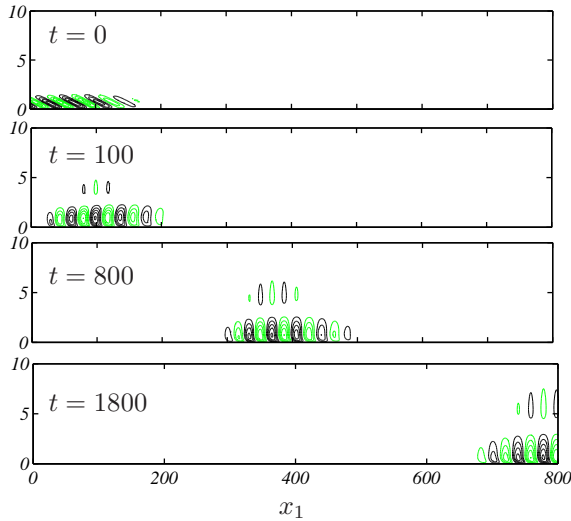
FIGURE 6. Time evolution for streamwise velocity with the combined Orr and TS mechanism, when initiated with the optimal initial condition from $t = 1800$. Note that the maximum amplitude is growing from frame to frame following the energy evolution given in figure 5(b).

the development, the disturbance is raised up, gaining energy through the Orr mechanism and forming a wavepacket consisting of TS-waves. The wavepacket then propagates downstream, grows in size and finally leaves the computational domain; the energy evolution for this flow is reported in figure 5(b).

3. Control design

3.1. *Introducing inputs and outputs*

The next step after the analysis of the internal dynamics of our linear system is to manipulate it or to control it. In particular, our objective is to minimize the perturbation energy resulting from the growth of instabilities during the transition process in order to suppress or delay turbulence. To this end, we introduce the inputs $\boldsymbol{B}_1, \boldsymbol{B}_2$ and the outputs $\boldsymbol{C}_1, \boldsymbol{C}_2$,

$$\dot{\mathbf{u}}(t) = \boldsymbol{A}\mathbf{u}(t) + \boldsymbol{B}_1 w(t) + \boldsymbol{B}_2 \phi(t), \tag{5}$$

$$z(t) = \boldsymbol{C}_1 \mathbf{u}(t) + l\phi(t), \tag{6}$$

$$y(t) = \boldsymbol{C}_2 \mathbf{u}(t) + \alpha g(t). \tag{7}$$

The linearized Navier–Stokes equations represented by $\boldsymbol{A}$ are now forced with external disturbances represented by the term $\boldsymbol{B}_1 w(t)$. These external disturbances may enter the boundary layer upstream through some receptivity

mechanism such as freestream turbulence or acoustic waves interacting with roughness as shown schematically in figure 1.

In practice, the entire spatiotemporal evolution of disturbances is not available and it is therefore necessary to monitor the disturbance behavior through measurements. To accomplish this task, two sensors, C_1 and C_2 are introduced that measure the shear stress near the wall. The partial information of the incoming perturbations provided from the first sensor measurements (C_2 in figure 1) is used to reconstruct the actual flow dynamics by using a Kalman filter. Based on this flow estimation we can alter the behavior of disturbances by injecting fluid through blowing/suction holes in the wall. This type of actuation corresponds to imposing an inhomogeneous boundary condition $\mathbf{u}_w$ at the wall (see equation 19 in Appendix B). In order to pose the system in the standard state-space formulation commonly used in systems and control theory, the boundary term is lifted (Curtain & Zwart 1995) into a volume forcing $\boldsymbol{B}_2\phi(t)$. In Appendix B the lifting technique is demonstrated. The sensor output signal $y(t)$ is forced with noise $g(t)$ to model the uncertainty that may exists in the measurements under realistic conditions. The noise $g(t)$ can be considered as a third forcing, but rather than forcing the Navier–Stokes equations it forces the measurements. Large values of the scalar α indicate high level of noise corruption in the output signal, whereas for low values of α the measurement $y(t)$ reflects information about the flow field with high fidelity.

Measurements provided by the second sensor C_1 located far downstream (see figure 1) is used to determine whether our controller have been successful in reducing the shear stress near the wall. It thus plays the role of an objective function[1], i.e.

$$\|z\|^2 = \int_0^\infty \left(\mathbf{u}^* \boldsymbol{C}_1^* \boldsymbol{C}_1 \mathbf{u} + l^2 \phi^2 \right) \, \mathrm{d}t. \tag{8}$$

For large values of the scalar l the control effort is considered to be expensive, whereas small values indicate cheap control.

The system with all inputs and outputs can be written in a compact state-space form,

$$\boldsymbol{G} := \left(\begin{array}{c|c} \boldsymbol{A} & \boldsymbol{B} \\ \hline \boldsymbol{C} & \boldsymbol{D} \end{array} \right). \tag{9}$$

Here,

$$\boldsymbol{B} = (\boldsymbol{B}_1, 0, \boldsymbol{B}_2) \in \mathbb{R}^{n \times 3}$$

contains the three input operators,

$$\boldsymbol{C} = (\boldsymbol{C}_1, \boldsymbol{C}_2)^T \in \mathbb{R}^{2 \times n}$$

two output operators. The corresponding input time signals are

$$\boldsymbol{f}(t) = (w(t), g(t), \phi(t))^T \in \mathbb{R}^{3 \times 1}$$

---

[1]We assume that the cross weighting between the state and control signal is zero (Zhou *et al.* 1999).

and output time signals are

$$\boldsymbol{y}(t) = (y(t), z(t))^T \in \mathbb{R}^{2 \times 1}.$$

In addition, the feed-through term $\boldsymbol{D} \in \mathbb{R}^{2 \times 3}$ is included to model the effects of measurements noise $g(t)$ and to penalize the actuation effort,

$$\boldsymbol{D} = \begin{pmatrix} 0 & 0 & l \\ 0 & \alpha & 0 \end{pmatrix}.$$

Hereafter, the number of inputs and outputs will be denoted by p and r respectively. The inputs and outputs used in the present study are given in Appendix A. The solution to the input-output system (9) can formally be written as,

$$\boldsymbol{y}(t) = \boldsymbol{G}\boldsymbol{f}(t) = \boldsymbol{C} \int_0^t \boldsymbol{T}(t-\tau)\boldsymbol{B}\boldsymbol{f}(\tau) \, \mathrm{d}\tau + \boldsymbol{D}\boldsymbol{f}(t). \tag{10}$$

3.2. *The LQG/$\mathcal{H}_2$ problem*

The LQG/$\mathcal{H}_2$ framework provides a controller that minimizes the cost functional (8). This approach is appropriate if the system matrix $\boldsymbol{A}$ accurately describes the flow dynamics, whereas a precise knowledge of external disturbances and the degree of noise contamination of the measurements are not available. We refer to (Anderson & Moore 1990; Zhou *et al.* 2002; Bagheri *et al.* 2009*b*) for further details on the $\mathcal{H}_2$ control algorithm, as we will only outline the main steps here. The method can be extended (the so called $\mathcal{H}_\infty$ method) in order to guarantee certain robustness properties. The control problem from an input-output viewpoint, or the $\mathcal{H}_2$ problem, can be formulated as follows:

Find an optimal control signal $\phi(t)$ based on the measurements $y(t)$ such that in the presence of external disturbances $w(t)$ and measurement noise $g(t)$ the output $z(t)$ is minimized.

The determination of the control signal $\phi(t)$ is based only on the measurements $y(t)$ from the sensor $\boldsymbol{C}_2$. However, for linear systems, due to the separation principle (Zhou *et al.* 2002), the feedback control law can be determined by assuming that the complete velocity field is known. The forcing needed to reproduce the flow only from wall measurements can be computed independently. Hence, the design of the $\mathcal{H}_2$-controller is performed by solving two quadratic matrix equations called Riccati equations (Zhou *et al.* 1999) that are independent of each other. Solving the first Riccati equation we obtain the feedback type of control signal $\phi(t) = \boldsymbol{K}\mathbf{u}(t)$. The second Riccati equation provides the estimation feedback gain $\boldsymbol{L}$ so that the estimator

$$\dot{\hat{\mathbf{u}}}(t) = (\boldsymbol{A} + \boldsymbol{L}\boldsymbol{C}_2)\hat{\mathbf{u}}(t) - \boldsymbol{L}y(t)$$

can provide an estimate of the state $\hat{\mathbf{u}}$ from the wall stress measurements contained in $y(t)$. Finally, the controller is obtained by the combination of these

two as (written in compact form)

$$\boldsymbol{G}_c := \left(\begin{array}{c|c} \boldsymbol{A} + \boldsymbol{B}_2\boldsymbol{K} + \boldsymbol{L}\boldsymbol{C}_2 & -\boldsymbol{L} \\ \hline \boldsymbol{K} & 0 \end{array} \right). \tag{11}$$

This controller runs online next to the experiments. Based on wall shear stress measurements $y(t)$ extracted by the first sensor, it provides an optimal control signal $\phi(t)$, i.e. $\phi(t) = \boldsymbol{G}_c y(t)$.

Any adequately accurate spatial discretization of the Navier–Stokes equations linearized about two- or three-dimensional base flows results in a system with at least $n \geq 10^5$ degrees of freedom. Because of the high-dimensional state-space, we cannot, in general, solve the Riccati equations. Moreover, it would be very expensive to run the controller online, since it has the same dimension as the full system. For this reason there is a desire to have a low-order controller (11) for the high-order Navier–Stokes system (also called the plant hereafter). The available methods can broadly be divided into two categories;

i) controller reduction Anderson & Liu (1989), in which a high-order controller $\boldsymbol{G}_c$ is first found and then a procedure used to simplify it;

ii) model reduction, in which a low-order approximation of the plant $\boldsymbol{G}$ is first constructed and then a controller is designed.

In this paper, we will focus on the latter approach, because solving Riccati equations is not straightforward for $n \geq 10^5$.

3.3. *The model reduction problem and balanced truncation*

The main feature of the flow behavior which is relevant to preserve in the reduced-order model is the input-output (I/O) behavior of the system, that is the relation between disturbances, wall actuation and the sensor outputs. Rather than investigating the entire dynamics of flow fields at different times, the I/O behavior considers the time signals, $\boldsymbol{f}(t)$ and $\boldsymbol{y}(t)$. Fortunately, the I/O behavior has significantly simpler dynamics compared to stability analysis, in which the entire flow dynamics is under investigation.

The model reduction problem for the preservation of input-output dynamics can be posed as following: Find the state-space system of order $m \ll n$,

$$\boldsymbol{G}_m := \left(\begin{array}{c|c} \boldsymbol{Y}^*\boldsymbol{A}\boldsymbol{X} & \boldsymbol{Y}^*\boldsymbol{B} \\ \hline \boldsymbol{C}\boldsymbol{X} & \boldsymbol{D} \end{array} \right) = \left(\begin{array}{c|c} \boldsymbol{A}_m & \boldsymbol{B}_m \\ \hline \boldsymbol{C}_m & \boldsymbol{D} \end{array} \right) \tag{12}$$

so that for any input $\boldsymbol{f}(t)$, the difference between the output of the original $\boldsymbol{y}(t) = \boldsymbol{G}\boldsymbol{f}(t)$ and of the reduced system $\hat{\boldsymbol{y}}(t) = \boldsymbol{G}_m\boldsymbol{f}(t)$ is small, i.e.

$$\sup_{\boldsymbol{f}} \frac{\|\boldsymbol{y} - \hat{\boldsymbol{y}}\|}{\|\boldsymbol{f}\|} = \|\boldsymbol{G} - \boldsymbol{G}_m\|_\infty. \tag{13}$$

One way to compute the reduced-order model (12) with a nearly minimal model reduction error (13) is called balanced truncation (Moore 1981). To obtain the balanced reduced-order model (12) $\boldsymbol{G}_m$ we project Navier–Stokes equations including inputs and outputs ($\boldsymbol{G}$) onto the so-called balanced modes
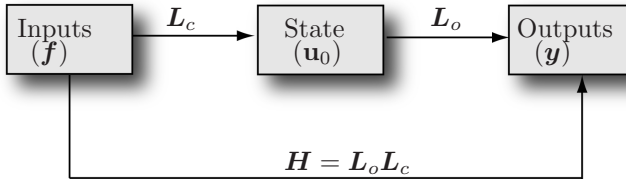
FIGURE 7. The operators used to examine the system input-output behavior. The controllability operator $\boldsymbol{L}_c$ relates past inputs to the present state, while the observability mapping $\boldsymbol{L}_o$ relates the present state to the future outputs. Their combined action is expressed by the Hankel operator $\boldsymbol{H}$.

$\boldsymbol{X} \in \mathbb{R}^{n \times m}$. The modes are bi-orthogonal to adjoint balanced modes $\boldsymbol{Y} \in \mathbb{R}^{n \times m}$ (i.e. $\boldsymbol{Y}^* \boldsymbol{X} = I$).

The method to compute these modes can be introduced in many different ways. Traditionally, the balanced modes are defined as the eigenvectors of the product of the controllability and observability Gramian, defined as

$$\boldsymbol{P} = \int_0^\infty \boldsymbol{T}(\tau)\boldsymbol{B}\boldsymbol{B}^*\boldsymbol{T}^*(\tau)\,\mathrm{d}\tau, \qquad \boldsymbol{Q} = \int_0^\infty \boldsymbol{T}^*(\tau)\boldsymbol{C}^*\boldsymbol{C}\boldsymbol{T}(\tau)\,\mathrm{d}\tau. \qquad (14)$$

The Gramians can be obtained by solving the Lyapunov equations,

$$\boldsymbol{A}\boldsymbol{P} + \boldsymbol{P}\boldsymbol{A}^* + \boldsymbol{B}\boldsymbol{B}^* = 0, \quad \boldsymbol{A}^*\boldsymbol{Q} + \boldsymbol{Q}\boldsymbol{A} + \boldsymbol{C}^*\boldsymbol{C} = 0.$$

In this section we will outline the method in manner that is reminiscent of the optimization problems that arise in the stability analysis. The presentation follows closely Bagheri *et al.* (2009*a*), where also definitions of appropriate Hilbert spaces and adjoint operators are provided. Whereas, in stability analysis we were concerned with the properties of the evolution operator $\boldsymbol{T}(t)$, here our focus will lie on the so-called Hankel operator (Glover 1999) that maps input signals to output signals. In particular, it is defined as the mapping from past inputs $\boldsymbol{f}(t) : t \in (-\infty, 0]$ to future outputs $\boldsymbol{y}(t) : t \in [0, \infty)$,

$$\boldsymbol{y}(t) = (\boldsymbol{H}\boldsymbol{f})(t) = \boldsymbol{C} \int_{-\infty}^0 \boldsymbol{T}(t-\tau)\boldsymbol{B}\boldsymbol{f}(\tau)\,\mathrm{d}\tau.$$

In order to determine $\boldsymbol{H}\boldsymbol{f}$, we decompose it into two parts, $\boldsymbol{H} = \boldsymbol{L}_o\boldsymbol{L}_c$ (shown schematically in figure 7).

First we need to know the state at a reference time (say $\mathbf{u}_0$) that results from driving the system with the input $\boldsymbol{f}(t)$;

$$\mathbf{u}_0 = \int_{-\infty}^0 \boldsymbol{T}(-\tau)\boldsymbol{B}\boldsymbol{f}(\tau)\,\mathrm{d}\tau = \boldsymbol{L}_c\boldsymbol{f}(t).$$

The range of $\boldsymbol{L}_c$, i.e. the restriction of the state-space to all possible initial states that we are able to reach with $\boldsymbol{f}(t)$, is called the controllable subspace.

Second, we define the observability operator $\boldsymbol{L}_o$ as,

$$\boldsymbol{y}(t) = \boldsymbol{C}\boldsymbol{T}(t)\mathbf{u}_0 = \boldsymbol{L}_o\mathbf{u}_0, \quad t \geq 0,$$

which generates future outputs from the reference state. If $\boldsymbol{L}_o\mathbf{u}_0 = 0$ for an initial condition $\mathbf{u}_0$, then $\mathbf{u}_0$ is unobservable, because it cannot be detected by the sensors. Moreover, it is easy to verify that the Gramians are given by $\boldsymbol{P} = \boldsymbol{L}_c\boldsymbol{L}_c^*$ and $\boldsymbol{Q} = \boldsymbol{L}_o^*\boldsymbol{L}_o$ (see Bagheri *et al.* 2009*a*, for derivation of the adjoint operators $\boldsymbol{L}_c^*$ and $\boldsymbol{L}_o^*$).

Note that all inputs that give rise to the same $\mathbf{u}_0$ produce the same future output. Therefore any two linearly independent reference states $\mathbf{u}_0$ result in linearly independent future outputs. Thus the rank of the Hankel operator (i.e. the number of linearly independent outputs) is finite and equals to the minimal number of states required to realize the input-output behavior of the system. One might think that it is more natural to consider the input-output mapping $\boldsymbol{G}$ given by equation (10), but this operator is generally not of finite rank, which makes further analysis difficult (Glover 1999).

The amplification of the output signal at time t is given by

$$\|\boldsymbol{y}(t)\|^2 = (\boldsymbol{H}\boldsymbol{f}(t), \boldsymbol{H}\boldsymbol{f}(t)) = (\boldsymbol{f}(t), \boldsymbol{H}^*\boldsymbol{H}\boldsymbol{f}(t)).$$

In particular, the unit-norm input signals that result in the largest output response are the eigenmodes of $\boldsymbol{H}^*\boldsymbol{H}$, or the right singular vectors of $\boldsymbol{H}$, i.e.

$$\boldsymbol{H} = \boldsymbol{U}\boldsymbol{\Sigma}\boldsymbol{V}^*, \tag{15}$$

with the square root of the eigenvalues, $\sigma_1 > \sigma_2 > \ldots$ are called the Hankel singular values (HSV). If $\sigma_1 > 1$, then the unit-norm input signal (the first column of $\boldsymbol{V}$), active in the past $t \in (-\infty, 0]$ will generate an amplified output signal in the future $t \in [0, \infty)$.

Using the mappings $\boldsymbol{L}_c$ and $\boldsymbol{L}_o$ we can now obtain the bi-orthogonal balanced modes,

$$\boldsymbol{X} = \boldsymbol{L}_c\boldsymbol{V}\boldsymbol{\Sigma}^{-1/2}, \qquad \boldsymbol{Y} = \boldsymbol{L}_o^*\boldsymbol{U}\boldsymbol{\Sigma}^{-1/2}. \tag{16}$$

Note that balanced modes contained in $\boldsymbol{X} = \{\mathbf{u}_1, \ldots, \mathbf{u}_m\}$ are flow fields obtained by mapping the most dangerous inputs signals $\boldsymbol{V}$, i.e. left singular vectors of $\boldsymbol{H}$ onto the state-space using $\boldsymbol{L}_c$ (see Bagheri *et al.* 2009*a*, for further details).

The balanced reduced-order model (ROM) is guaranteed to be asymptotically stable (Pernebo & Silverman 1982) if $\sigma_i \neq \sigma_{i+1}$. Moreover, upper and lower bounds (Glover 1999) of the model reduction error for reduced-order model of order m are given by the HSV as

$$\sigma_{m+1} \leq \|\boldsymbol{G} - \boldsymbol{G}_m\|_\infty \leq 2 \sum_{j=m+1}^{n} \sigma_j. \tag{17}$$
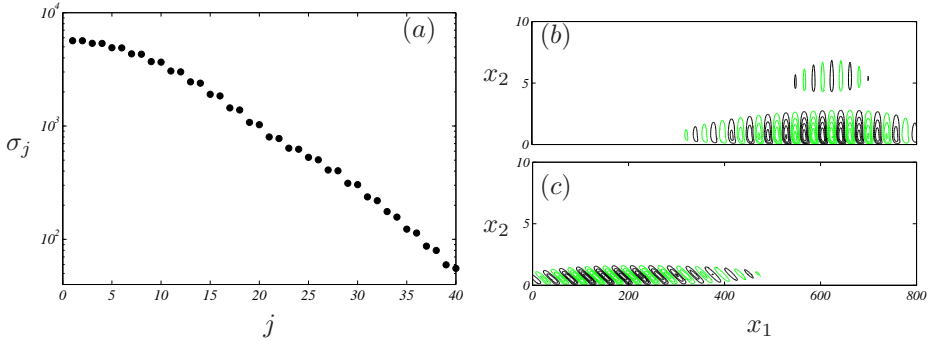
FIGURE 8. (*a*) Singular values of Hankel operator. The streamwise velocity component of first direct mode is shown in (*b*) and its associated adjoint mode in (*c*).

3.4. *Snapshot-based balanced truncation*

Standard balanced truncation is computed by solving two Lyapunov equations, which is not numerically feasible if $n > 10^5$, as the computational complexity is $\mathcal{O}(n^3)$ and storage requirement is $\mathcal{O}(n^2)$. Usually the number of inputs and outputs are much smaller than the state dimension (i.e. $m, p \ll n$). Therefore, the input and output operators $\boldsymbol{L}_o, \boldsymbol{L}_c$ have low numerical rank. In this section a brief summary of the snapshot method (Sirovich 1987) for solving the singular value decomposition (SVD) problem (15) is presented. The method for the computation of the balanced modes based on snapshots was introduced by Rowley (2005), in which it is also described in more detail.

The integrals in (14) can be approximated by quadratures,

$$\boldsymbol{P} \quad = \quad \boldsymbol{L}_c \boldsymbol{L}_c^* \approx \sum_{j=1}^{k} \boldsymbol{T}(t_j) \boldsymbol{B} \boldsymbol{B}^* \boldsymbol{T}^*(t_j) \delta_j = \tilde{\boldsymbol{L}}_c \tilde{\boldsymbol{L}}_c^*$$

and similarly for the observability Gramian we have

$$\boldsymbol{Q} \quad = \quad \boldsymbol{L}_o^* \boldsymbol{L}_o \approx \sum_{j=1}^{k} \boldsymbol{T}^*(t_j) \boldsymbol{C}^* \boldsymbol{C} \boldsymbol{T}(t_j) \delta_j = \tilde{\boldsymbol{L}}_o \tilde{\boldsymbol{L}}_o^*$$

where δ_j are the quadrature weights. The Gramians are thus approximated with low-rank Cholesky factors; $\tilde{\boldsymbol{L}}_o \in \mathbb{R}^{n \times kr}$ and $\tilde{\boldsymbol{L}}_c \in \mathbb{R}^{n \times kp}$ respectively, given by

$$\tilde{\boldsymbol{L}}_c \quad = \quad \left(\boldsymbol{T}(t_1) \boldsymbol{B} \sqrt{\delta_1}, \dots, \boldsymbol{T}(t_k) \boldsymbol{B} \sqrt{\delta_k} \right)$$
$$\tilde{\boldsymbol{L}}_o \quad = \quad \left(\boldsymbol{T}^*(t_1) \boldsymbol{C}^* \sqrt{\delta_1}, \dots, \boldsymbol{T}^*(t_k) \boldsymbol{C}^* \sqrt{\delta_k} \right).$$

For our case, with $p = 3$ and $r = 2$, the columns

$$\boldsymbol{T}(t_i) \boldsymbol{B} = (\boldsymbol{T}(t_i) \boldsymbol{B}_1, 0, \boldsymbol{T}(t_i) \boldsymbol{B}_2)$$

contain snapshots of the state at time t_i, resulting from impulse responses of $\boldsymbol{B}_1$ and $\boldsymbol{B}_2$. In a similar manner,

$$\boldsymbol{T}^*(t_i)\boldsymbol{C}^* = (\boldsymbol{T}^*(t_i)\boldsymbol{C}_1^*, \boldsymbol{T}^*(t_i)\boldsymbol{C}_2^*)^T,$$

contain snapshots of the adjoint state at time t_i resulting from impulse responses of each output. Note that for every additional input (output), the Cholesky factor $\tilde{\boldsymbol{L}}_c$ ($\tilde{\boldsymbol{L}}_o$), increases with k columns.

Similar to the Krylov subspace presented earlier to compute global eigenmodes and optimal disturbances, the Cholesky factors are constructed from simulations of the forward and adjoint systems. The method is therefore matrix-free and based on the employment of a time stepper. The SVD problem (15) can then be approximated as

$$\tilde{\boldsymbol{L}}_o^* \tilde{\boldsymbol{L}}_c = \tilde{\boldsymbol{U}} \tilde{\boldsymbol{\Sigma}} \tilde{\boldsymbol{V}}^*$$

with $\tilde{\boldsymbol{\Sigma}}$ containing the approximate HSV. The SVD is of the size $kr \times kp$ and is small when the number of snapshots m times the number inputs p or outputs r is significantly smaller than the number of states n. If either the number of inputs or the number of outputs is large the output projection method of Rowley (2005) can be employed. The approximate bi-orthogonal balanced modes and the reduced order model are then computed from the expressions (16) and (12). Note that the reduced-order model, $\tilde{\boldsymbol{G}}_m$, computed using the low-rank Cholesky factors is not guaranteed to be stable.

3.5. *Results*

3.5.1. *Performance of reduced-order model*

Figure 8 shows the spectrum (HSV) and two eigenfunctions (balanced modes) computed by the snapshot method. The first balanced mode and its associated adjoint mode are shown in figures 8(b, c). The singular values come in pairs (Ilak & Rowley 2008; Ahuja *et al.* 2007; Bagheri *et al.* 2009a) and therefore the second and fourth balanced mode look like the first and third mode respectively, but shifted in the streamwise direction. We observe that the leading balanced mode (figure 8b) appears as a wavepacket located at the downstream end of the domain, whereas the adjoint balanced mode (figure 8c) is an upstream tilted structure located at the upstream end of the domain. The adjoint modes are similar to the linear optimal disturbances shown in figure 6(a) and the balanced modes are similar to global eigenmodes shown in figure 3(b). The adjoint balanced modes thus account for the output sensitivity and the direct balanced modes for the most energetic structures.

The projection of the full Navier–Stokes equations on the balanced modes results in the reduced-order model $\boldsymbol{G}_m$ given by equation (12). The model reduction error (17) is shown in figure 9(a) together with the theoretical bounds given by the Hankel singular values. The infinity norm of the transfer function equals the peak value of the frequency response. Estimating the model reduction error amounts to the calculation of the difference of the peak values of
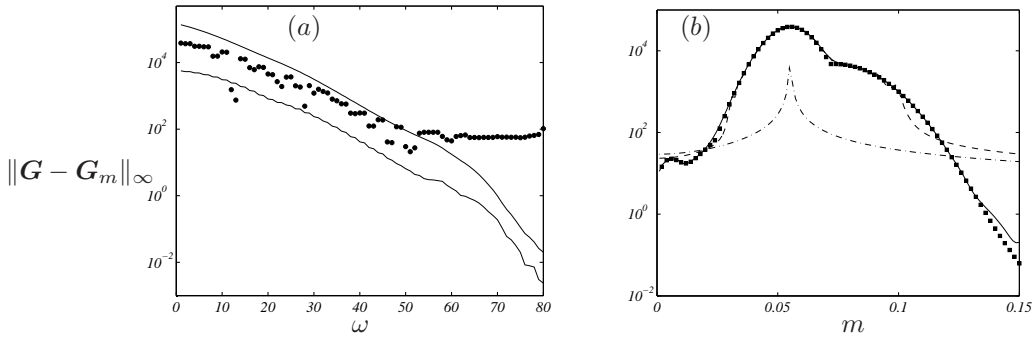
FIGURE 9. (a) The error at capturing the peak frequency is shown with circle. The upper and lower theoretical bounds are depicted with black lines. (b) The largest singular values σ of the transfer function $|G(i\omega)|$ from all input to all outputs computed using the time-stepper is shown with squares. The largest response is for $\omega = 0.051$ with a peak value of 4×10^4. The frequency response of the reduced model with rank 2 (dash-dotted), 40 (dashed) and 70 (solid).

the reduced-order and the Navier–Stokes system. We observe the error norm remains approximately withing the bounds given by the Hankel singular values for the first 50 modes. Higher modes become increasingly ill-conditioned and, as a consequence, the numerical round-off errors increase, the bi-orthogonality condition is gradually lost and the reduced system is no longer balanced. However, the singular values shown in figure 8(a) decrease rapidly, indicating that the I/O behavior of the chosen setup can be captured by a low-dimensional model.

To investigate this further, the amplitudes of the transfer functions with $s = i\omega$, i.e. the frequency response, are displayed in figure 9(b) for reduced-order models of order $m = 2, 40$ and 70 and for the full DNS model of order 10^5. All frequencies in the interval $[0, 0.13]$ are amplified and the most dangerous frequency, i.e. the peak response, is approximately $\omega = 0.051$. From figure 9(b) we observe that the reduced-order model of order 2 captures the most important aspect of the input-output behavior, which is the response of the most dangerous frequency. The model with 40 modes is able to estimate the gains of all the amplified frequencies, but fails to capture the damped low and high frequencies. Adding 30 additional modes results in a model that preserves the input-output behavior correctly for nearly all frequencies.

Finally, the impulse responses from all inputs to all outputs of the reduced-order model (12) are compared to the full Navier–Stokes system (9). In figure (10) three signals $B_1 \rightarrow C_1$, $B_1 \rightarrow C_2$ and $B_2 \rightarrow C_1$ are shown with black lines. The response of C_2 to forcing in B_2 is zero, since disturbances traveling
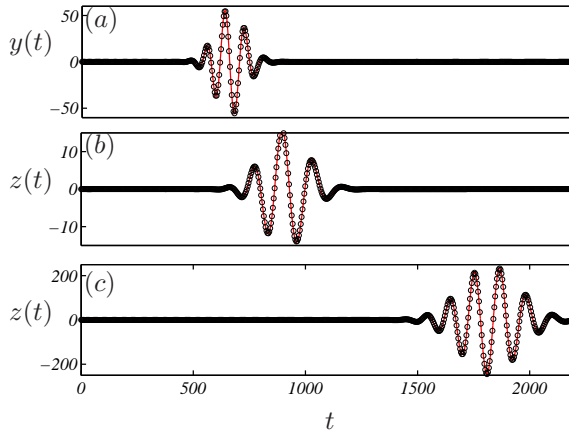
FIGURE 10. The impulse response from $\boldsymbol{B}_1 \to \boldsymbol{C}_2$ (a), $\boldsymbol{B}_2 \to \boldsymbol{C}_1$ (b) and $\boldsymbol{B}_1 \to \boldsymbol{C}_1$ (c). The black solid line represents direct numerical simulations with 10^5 degrees of freedom and the red dashed line the balanced reduced-model with 70 degrees of freedom.

upstream are quickly damped. These impulse responses were obtained by using the time-stepper with $\sim 10^5$ degrees of freedom. The impulse responses of the reduced-order model (12) with $m = 70$ given by $\boldsymbol{y}(t) = \boldsymbol{C}_m e^{\boldsymbol{A}_m t} \boldsymbol{B}_m$ are shown with red lines. We observe that reduced-model registers the same signal as the full model from all inputs to all outputs. The wavepacket triggered by the impulse of $\boldsymbol{B}_1$ reaches the first sensor $\boldsymbol{C}_2$ after 500 time units and the second sensor $\boldsymbol{C}_1$ after 1500 time units. The wavepacket triggered from the actuator $\boldsymbol{B}_2$ reaches the second sensor after 600 time units.

3.5.2. *Performance of controller*

In this section a reduced-order feedback controller, with the same dimension as the reduced-order model ($m = 70$) of the previous section, is developed. The closed-loop behavior of the system and the objective function will be investigated and compared to the uncontrolled case for the flat-plate boundary layer flow. In particular, the output z of the closed-loop (i.e. the controller 11 $\boldsymbol{G}_c$ connected to the full Navier–Stokes model 5 $\boldsymbol{G}$) is compared to the linearized Navier–Stokes equations without control when the system is forced with stochastic excitation or initiated with an optimal disturbance.

Three controllers are investigated; (i) inexpensive control and low noise contamination with control penalty $l = 1$ and noise parameter $\alpha = 10^2$, (ii) expensive control and high noise contamination with $l = 10^2$ and $\alpha = 10^7$ and (iii) an intermediate case with $l = 10$ and $\alpha = 10^5$.

The performance of the inexpensive controller in case (i) for the control of the optimal initial condition discussed in section 2 is examined first. This is
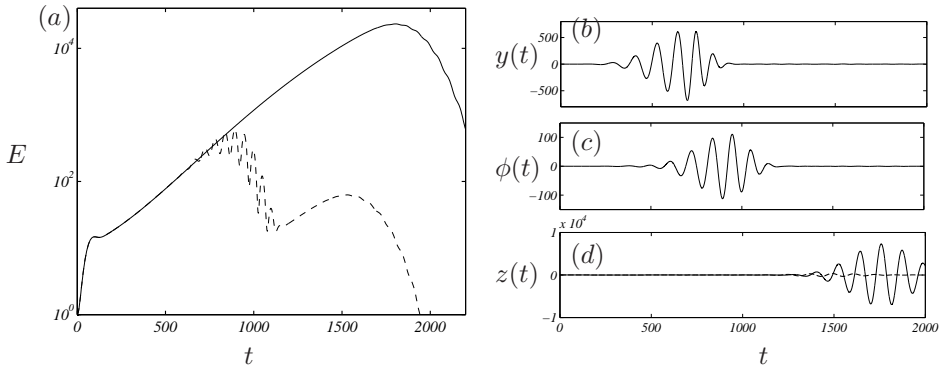
FIGURE 11. Control of the wavepacket due to the worst case initial condition. (*a*) Solid black line shows uncontrolled energy evolution (as in figure 5*b*) and dashed black line shows the energy for the cheap controller. (*b*) Output signal as measured by the sensor C_2 driving the controller. (*c*) Control signal fed into the wall actuator. (*d*) Signals from the sensor C_1 measuring the objective function. Solid black line shows uncontrolled case whereas dashed black line shows the controlled case.

interesting, because the controller is not designed specifically for this configuration and it only has a limited window in time to counteract the disturbances that are propagating through the domain in the form of a localized wavepacket. In figure 11(*a*) the full domain kinetic energy as a function of time is shown as a solid black line for the uncontrolled evolution and as a dashed line for the controlled case. The effect of the controller is evident. The measurement signal detected by the sensor C_2 is shown in figure 11(*b*) revealing that the sensor picks up the front of the wavepacket arriving at $t \approx 350$. A time lag of ≈ 300 consistent with the speed of the propagating wavepacket ($0.3U\infty$) is observed until the controller starts acting on the information (see figure 11*c*). The downstream measurement (i.e. the objective function to be minimized) is shown in figure 11(*d*) as a black solid line for the uncontrolled case and as a dashed black line for the controlled case. It can be seen that also this measure shows a satisfactory performance of the controller.

The three different controllers are tested on a flow case which is forced by the upstream disturbance input B_1 with a random time signal. The wall-normal maximum of the rms-values of the streamwise velocity component in cases with and without control are shown in figure 12. The rms-value grows exponentially downstream in the uncontrolled case until the fringe region at $x_1 = 800$. The rms of the controlled perturbation grows only until it reaches the actuator position where it immediately begins to decay. At the location of the objective function C_1 ($x_1 = 750$), the amplitude of the perturbations is
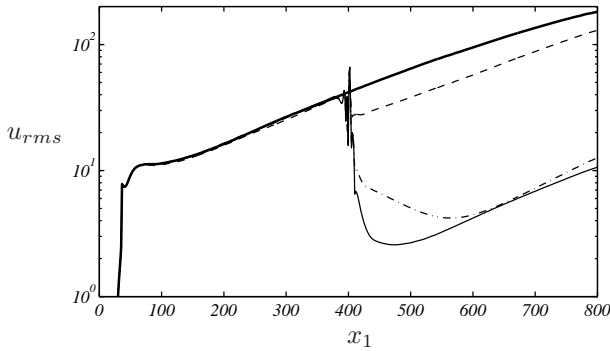
FIGURE 12. The rms-values of the uncontrolled system (thick solid line), cheap controller (solid black), intermediate controller (dashed-dotted line) and expensive controller (dashed line).

one order of magnitude smaller than in the uncontrolled case for the cheapest controller.

The rms values in the case of the expensive (case ii) and intermediate control (case iii) are shown with dashed and dashed-dotted lines respectively. The expensive control is very conservative as the measurement signals are highly corrupted and the control effort limited; it results only in a small damping of the disturbances. The intermediate controller (case iii) is more cautious in reducing the perturbation energy just downstream of the actuator when compared to the cheap controller. It is interesting to note, however, that at the location where the objective function is measured, the disturbance amplitude has decreased nearly as much as with the cheap controller, although the total perturbation energy is larger over the entire domain.

4. Conclusions

Two prerequisites for successful control design are stability analysis and model reduction. The former provides a sound understanding of the instabilities, sensitivities and growth mechanisms in the flow, whereas the latter provides a simple and small model that is able to capture the essential dynamics. This preparatory work for control design amounts to solving various large eigenvalue problems as listed in table 1. The short-time and asymptotic behavior of disturbances can be completely characterized by the solution of two large eigenvalue problems involving the evolution operator of the linearized Navier–Stokes equations $\boldsymbol{T}$. The global spectrum of $\boldsymbol{T}$, determines the asymptotic growth/decay, dominant temporal frequencies and the dominant spatial location of instabilities. The global spectrum of $\boldsymbol{T}^*\boldsymbol{T}$, determines the short-time growth/decay of disturbances and the spatial structure of the most dangerous disturbances.

Modes	EVP	Method
Global modes	$\boldsymbol{T} = \boldsymbol{U\Sigma U}^{-1}$	Arnoldi
Optimal disturbances	$\boldsymbol{T}^*\boldsymbol{T} = \boldsymbol{U\Sigma U}^*$	Arnoldi
Balanced modes	$\boldsymbol{PQ} = \boldsymbol{U\Sigma U}^{-1}$	Snapshot

TABLE 1. An overview of the eigenvalue problems (EVP) discussed in this paper.

This knowledge is indispensable for actuator and sensor placements. Sensors are placed where the flow energy is large, whereas actuators are placed where the flow sensitivity is large in order to minimize the input effort. Because, the relation between a few inputs and outputs has much simpler dynamics than the instability a reduced-order model can be constructed by solving a third eigenvalue problem involving the inputs, outputs and the evolution operator. This results in the balanced modes. The computation of the three sets, global eigenmodes, optimal disturbances and balanced modes is performed only with a time stepper and without storing large matrices. When the entire flow dynamics is of interest the high dimensions of the state require iterative techniques. When the I/O behavior is of interest, on the other hand, computational tractability depends on the number of inputs and outputs. Therefore the snapshot method can be employed in the case of few inputs and outputs.

The results of this paper also enhance our previous work Bagheri *et al.* (2009*a*) by incorporating actuation and sensing at the wall. The next step towards applying the controller in experiments, is to design a similar control strategy for three-dimensional disturbances in the Blasius flow. Rows of localized actuators and sensors at the wall in the spanwise direction and more realistic disturbance environments, such as free-stream turbulence will be modeled.

Appendix A. Inputs and outputs

The expression of inputs $\boldsymbol{B}_1, \mathbf{u}_w$ and outputs $\boldsymbol{C}_1$ and $\boldsymbol{C}_2$ are given in this section. For clarity, we denote the streamwise coordinate with x and the wall-normal component with y. The input $\boldsymbol{B}_1$ is modelled by Gaussian type of volume forcing

$$\begin{bmatrix} \sigma_{w,x}\gamma_{w,y} \\ -\sigma_{w,y}\gamma_{w,x} \end{bmatrix} \exp(-\gamma_{w,x}^2 - \gamma_{w,y}^2), \qquad \gamma_{w,x} = \frac{x - x_w}{\sigma_{w,x}}, \qquad \gamma_{w,y} = \frac{y - y_w}{\sigma_{w,y}},$$

with $(\sigma_{w,x} = 4, \sigma_{w,y} = 0.25)$ determining the width and height of the function of the function centered around $(x_w = 35, y_w = 1)$. The actuator is in this case

a localized zero mass-flux actuation on the wall-normal velocity, $\mathbf{u}_w = (0, v_w)^T$ at the lower wall given by

$$v_w(x) = \left(1 - \left(\frac{x - x_u}{\sigma_{u,x}}\right)^2\right) \exp\left(-\frac{(x - x_u)^2}{2\sigma_{u,x}^2}\right),$$

with the width $\sigma_{u,x} = 2.5$ and centered at $x_u = 400$. Finally, both measurements extract approximately the wall normal derivative of the streamwise velocity component (wall shear stress) in limited regions at the wall

$$\int_\Omega \begin{pmatrix} \gamma_{s,x}\gamma_{s,y}\mathcal{D}_y & 0 \end{pmatrix} \begin{pmatrix} u \\ v \end{pmatrix} \, d\Omega, \tag{18}$$

where

$$\gamma_{s,x} = \exp\left(-\frac{(x - x_s)^2}{\sigma_{s,x}^2}\right), \quad \gamma_{s,y} = \frac{1}{\sigma_{s,y}} \exp\left(-\frac{y^2}{\sigma_{s,y}^2}\right),$$

with $x_e = 300$ for the output $\mathbf{C}_2$ and $x_e = 750$ for $\mathbf{C}_1$. The width of the regions are determined by $\sigma_{s,x} = 5$ for both sensors. The operator $\mathcal{D}_y$ denotes the y-derivative. The y-dependent weighting relies on a width parameter $\sigma_{s,y} = 0.05$. Note that in the limit $\sigma_{s,y} \to 0$ the function approaches the delta function so that (18) defines the exact wall wall shear stress at the wall. The reason for using an approximation to the wall shear stress is the need for an adjoint sensor $\mathbf{C}^*$ (see Section 3.3), which is derived with the respect to the signal to state inner product (Bagheri *et al.* 2009*a*)

$$(r, \mathbf{C}\mathbf{u})_s = (\mathbf{C}^* r, \mathbf{u})_\Omega.$$

These inner products are defined as

$$(r, s)_s = s^T r \quad \text{and}, \quad (\mathbf{p}, \mathbf{q})_\Omega = \int_\Omega \mathbf{p}^T \mathbf{q} \, d\Omega$$

for the scalars s and k, and the states $\mathbf{q}$ and $\mathbf{p}$. The adjoint sensor obtained from this definition is in other words

$$(r, \mathbf{C}\mathbf{u})_s = \int_\Omega r^T \begin{pmatrix} \gamma_{s,x}\gamma_{s,y}\mathcal{D}_y & 0 \end{pmatrix} \mathbf{u} \, d\Omega =$$

$$= \int_\Omega r^T \begin{pmatrix} 2y\gamma_{s,x}\gamma_{s,y}/\sigma_{s,y}^2 & 0 \end{pmatrix} \mathbf{u} \, d\Omega = (\mathbf{C}^* r, \mathbf{u})_{\hat{\Omega}},$$

where we have used integration by parts and the boundary conditions in y. This leads to the recognition of the adjoint sensor in the definition of the observability Gramian (14) as

$$\mathbf{C}^* = \begin{pmatrix} 2y\gamma_{s,x}\gamma_{s,y}/\sigma_{s,y}^2 \\ 0 \end{pmatrix}.$$

Appendix B. The lifting procedure

In the same manner as Högberg *et al.* (2003*a*), the solution **u** is split into a homogeneous part $\mathbf{u}_h$ and a particular part $\mathbf{u}_p$, so that $\mathbf{u} = \mathbf{u}_h + \mathbf{u}_p$. The particular solution fulfils the boundary conditions

$$\dot{\mathbf{u}}_p = \boldsymbol{A}\mathbf{u}_p, \qquad \mathbf{u}_p(t) = (0, v_w)^T \varphi(t), \quad \text{at} \quad x_2 = 0 \tag{19}$$

and the homogeneous part satisfies homogeneous boundary conditions. In principle, we can seek any solution $\mathbf{u}_p$ of the above system, but one suitable choice is to use the steady state $\boldsymbol{A}\mathbf{u}_p = 0$. This is obtained by marching the DNS in time subject to steady ($\varphi = 1$) wall blowing v_w until a stationary state $\dot{\mathbf{u}}_p = 0$ is obtained. In the following we denote this solution $\boldsymbol{Z}$. The inhomogeneous boundary condition is satisfied by this solution, enabling us to write the particular solution for all times as $\mathbf{u}_p = \boldsymbol{Z}\varphi(t)$, implying that the total field is given by $\mathbf{u} = \mathbf{u}_h + \boldsymbol{Z}\varphi(t)$. Again expressing the equation for **u** in terms of the homogeneous and particular solution we get

$$\dot{\mathbf{u}}_h = \boldsymbol{A}\mathbf{u}_h + \boldsymbol{A}\boldsymbol{Z}\varphi - \boldsymbol{Z}\dot{\varphi} = \boldsymbol{A}\mathbf{u}_h + \boldsymbol{B}_2\dot{\varphi}.$$

Here we have used that $\boldsymbol{A}\boldsymbol{Z} = 0$. Further we have defined the input operator $\boldsymbol{B}_2 = -\boldsymbol{Z}$ for the homogeneous system. The evolution of state and φ can be written as an augmented system for $\hat{\mathbf{u}} = (\mathbf{u}_h, \varphi)^T$ as

$$\dot{\hat{\mathbf{u}}} = \hat{\boldsymbol{A}}\hat{\mathbf{u}} + \hat{\boldsymbol{B}}_2\phi \tag{20}$$

with,

$$\hat{\boldsymbol{A}} = \begin{pmatrix} \boldsymbol{A} & 0 \\ 0 & 0 \end{pmatrix}, \ \hat{\boldsymbol{B}}_2 = \begin{pmatrix} \boldsymbol{B}_2 \\ 1 \end{pmatrix}, \ \phi = \dot{\varphi}.$$

Note that in the lifted system (20) the control signal is given by time derivative of the boundary control signal, $\phi = \dot{\varphi}$. Similarly the input operator $\boldsymbol{B}_1$ is extended to $\hat{\boldsymbol{B}}_1 = (\boldsymbol{B}_1, 0)^T$ and the outputs are augmented to $\hat{\boldsymbol{C}}_1 = (\boldsymbol{C}_1, \boldsymbol{C}_1\boldsymbol{Z})$ and $\hat{\boldsymbol{C}}_2 = (\boldsymbol{C}_2, \boldsymbol{C}_2\boldsymbol{Z})$.

References

Ahuja, S., Rowley, C. W., Kevrekidis, I. G. & Wei, M. 2007 Low-dimensional models for control of leading-edge vortices: Equilibria and linearized models. *AIAA Paper 2008-553, 46th AIAA Aeros. Sci. Meeting Exhibit.*

Åkervik, E., Ehrenstein, U., Gallaire, F. & Henningson, D. S. 2008 Global two-dimensional stability measures of the flat plate boundary-layer flow. *Eur. J. Mech. B* **27**, 501–513.

Åkervik, E., Hœpffner, J., Ehrenstein, U. & Henningson, D. S. 2007 Optimal growth, model reduction and control in a separated boundary-layer flow using global eigenmodes. *J. Fluid. Mech.* **579**, 305–314.

Anderson, B. & Liu, Y. 1989 Controller reduction: Concepts and approaches. *IEEE Trans. Auto. Control* **34**, 802–812.

Anderson, B. & Moore, J. 1990 *Optimal control: Linear Quadratic Methods*. Prentice Hall, New York.

Bagheri, S., Brandt, L. & Henningson, D. S. 2009a Input–output analysis, model reduction and control design of the flat-plate boundary layer. *J. Fluid Mech.* **620**, 263–298.

Bagheri, S., Hœpffner, J., Schmid, P. & Henningson, D. 2009b Input-output analysis and control design applied to a linear model of spatially developing flows. *Appl. Mech. Rev.* **62** (2), 1–27.

Bagheri, S., Schlatter, P., Schmid, P. & Henningson, D. S. 2009c Global stability of a jet in crossflow. *J. Fluid Mech.* **624**, 33–44.

Barkley, D., Blackburn, H. & Sherwin, S. J. 2008 Direct optimal growth analysis for timesteppers. *Int. J. Numer. Meth. Fluids* **57**, 1435–1458.

Barkley, D., Gomes, M. G. & Henderson, R. D. 2002 Three-dimensional instability in flow over a backward-facing step. *J. Fluid Mech.* **473**, 167–190.

Blackburn, A. M., Barkley, D. & Sherwin, S. 2008 Convective instability and transient growth in flow over a backward-facing step. *J. Fluid Mech.* **603**, 271–304.

Butler, K. & Farrell, B. F. 1992 Three-dimensional optimal perturbations in viscous shear flow. *Phys. Fluids A* **4**, 1637–1650.

Chevalier, M., Hœpffner, J., Åkervik, E. & Henningson, D. S. 2007a Linear feedback control and estimation applied to instabilities in spatially developing boundary layers. *J. Fluid Mech.* **588**, 163–187.

Chevalier, M., Hœpffner, J., Bewley, T. R. & Henningson, D. S. 2006 State estimation in wall-bounded flow systems. Part 2: Turbulent flows. *J. Fluid Mech.* **552**, 167–187.

Chevalier, M., Schlatter, P., Lundbladh, A. & D.S., H. 2007b A pseudo spectral solver for incompressible boundary layer flows. *Tech Rep, Trita-Mek* **7**, KTH Mechanics, Stockholm.

Chomaz, J. M. 2005 Global instabilities in spatially developing flows: Non-normality and nonlinearity. *Ann. Rev. Fluid Mech.* **37**, 357–392.

Cossu, C. & Chomaz, J. M. 1997 Global measures of local convective instabilities. *Phys. Rev. Lett.* **78**, 4387–4390.

CURTAIN, R. & ZWART, H. 1995 *An introduction to infinite-dimensional linear systems theory*. Springer Verlag, New York.

EHRENSTEIN, U. & GALLAIRE, F. 2005 On two-dimensional temporal modes in spatially evolving open flows: The flat-plate boundary layer. *J. Fluid Mech.* **536**, 209–218.

GILES, M. B. & PIERCE, N. A. 2000 An introduction to the adjoint approach design. *Flow, Turb. Comb.* **65**, 393–415.

GLOVER, K. 1999 All optimal Hankel-norm approximations of linear multivariable systems and the l^∞-error bounds. *Int. J. Control* **39**, 1115–1193.

HŒPFFNER, J., CHEVALIER, M., BEWLEY, T. R. & HENNINGSON, D. S. 2005 State estimation in wall-bounded flow systems. Part I: Laminar flows. *J. Fluid Mech.* **534**, 263–294.

HÖGBERG, M., BEWLEY, T. R. & HENNINGSON, D. S. 2003*a* Linear feedback control and estimation of transition in plane channel flow. *J. Fluid Mech.* **481**, 149–175.

HÖGBERG, M., BEWLEY, T. R. & HENNINGSON, D. S. 2003*b* Relaminarization of $Re_\tau = 100$ turbulence using gain scheduling and linear state-feedback control flow. *Phys. Fluids* **15**, 3572–3575.

HÖGBERG, M. & HENNINGSON, D. S. 2002 Linear optimal control applied to instabilities in spatially developing boundary layers. *J. Fluid Mech.* **470**, 151–179.

HUERRE, P. & MONKEWITZ, P. 1990 Local and global instabilities in spatially developing flows. *Ann. Rev. Fluid Mech.* **22**, 473–537.

ILAK, M. & ROWLEY, C. W. 2008 Modeling of transitional channel flow using balanced proper orthogonal decomposition. *Phys. Fluids* **20**, 034103.

KIM, J. & BEWLEY, T. R. 2007 A linear systems approach to flow control. *Ann. Rev. Fluid Mech.* **39**, 383–417.

LEHOUCQ, R., SORENSEN, D. & YANG, C. 1998 *ARPACK Users' guide: Solution of Large-Scale Eigenvalue problems with implicitly restarted Arnoldi methods*. SIAM, Philadelphia.

LEVIN, O. & HENNINGSON, D. S. 2003 Exponential vs algebraic growth and transition prediction in boundary-layer flow. *Flow, Turb. Comb.* **70**, 183–210.

MONOKROUSOS, A., BRANDT, L., SCHLATTER, P. & HENNINGSON, D. S. 2008 DNS and LES of estimation and control of transition in boundary layers subject to free-stream turbulence. *Int. J. Heat Fluid Flow* **29** (3), 841–855.

MOORE, B. 1981 Principal component analysis in linear systems: Controllability, observability, and model reduction. *IEEE Trans. Auto. Control* **26** (1), 17–32.

NORDSTRÖM, J., NORDIN, N. & HENNINGSON, D. 1999 The fringe region technique and the fourier method used in the direct numerical simulation of spatially evolving viscous flows. *SIAM J. Sci. Comput.* **20** (4), 1365–1393.

ORR, W. M. F. 1907 The stability or instability of the steady motions of a perfect liquid and of a viscous liquid. Part I: A perfect liquid. Part II: A viscous liquid. *Proc. R. Irish Acad. A* **27**, 9–138.

PERNEBO, L. & SILVERMAN, L. 1982 Model reduction via balanced state space representations. *IEEE Trans. Auto. Control* **27**, 382–387.

ROWLEY, C. W. 2005 Model reduction for fluids using balanced proper orthogonal decomposition. *Int. J. Bifurc. Chaos* **15** (3), 997–1013.

SCHMID, P. J. 2007 Nonmodal stability theory. *Ann. Rev. Fluid Mech.* **39**, 129–62.

SCHMID, P. J. & HENNINGSON, D. S. 2001 *Stability and Transition in Shear Flows*. Springer Verlag, New York.

SIROVICH, L. 1987 Turbulence and the dynamics of coherent structures i-iii. *Quart. Appl. Math.* **45**, 561–590.

SORENSEN, D. 1992 Implicit application of polynomial filters in a k-step Arnoldi method. *SIAM J. Matrix Anal. Appl.* **13**, 357–385.

TREFETHEN, L. & BAU, D. 1997 *Numerical Linear Algebra.*. SIAM, Philadelphia.

WHITE, F. M. 1991 *Viscous Fluid Flow*, 2 edn. McGraw–Hill.

ZHOU, K., DOYLE, J. & GLOVER, K. 2002 *Robust and Optimal Control*. Prentice Hall, New Jersey.

ZHOU, K., SALOMON, G. & WU, E. 1999 Balanced realization and model reduction for unstable systems. *Int. J. Robust Nonlinear Control* **9**, 183–198.

Paper 4

4

Feedback control of three-dimensional Tollmien–Schlichting wavepackets using reduced-order models

Onofrio Semeraro, Shervin Bagheri, Luca Brandt and Dan S. Henningson

Using low-dimensional feedback control, the energy growth of three-dimensional Tollmien-Schlichting wavepackets in a transitional boundary-layer flow is reduced by an order of magnitude. In the homogeneous spanwise direction of the flat plate, an array of localized sensors, followed by an array of actuators further downstream are distributed near the rigid wall. The objective is to use the actuators-sensors system to minimize the perturbation energy in a spatial domain in the boundary layer. This domain is spanned by a number of proper orthogonal decomposition (POD) modes. Using approximate balanced truncation method, it is shown that reduced-order models are able to capture the dynamics between the inputs (disturbance and actuators) and the outputs (sensors and POD modes). Control theoretical issues such as controllability, observability, centralized versus de-centralized control design are addressed. Moreover, the dependence of the control performance on the number of actuators and sensors is investigated.

1. Introduction

In recent years, one branch in flow control has progressed toward more systematic configurations by incorporating systems and control theoretical tools, such as controllability, observability, centralized versus de-centralized control, robustness and optimality. So far, most flow control studies using control theory have been based on simple models (Lauga & Bewley 2003, 2004; Cohen *et al.* 2005; Bagheri *et al.* 2009*c*), direct numerical simulations (DNS) of canonical flows (Joshi *et al.* 1997; Bewley & Liu 1998; Högberg & Henningson 2002; Högberg *et al.* 2003) or of a more theoretical nature (Bewley *et al.* 2000). On the other hand, the majority of experimental flow control studies have used control laws based on intuition and physical insight. The efforts have mainly been devoted to the development of devices, such as synthetic jets (Smith & Glezer 1998), electro-magnetic actuators (Pang & Choi 2004), plasma actuators (Grundmann & Tropea 2008) or various MEMS actuators (Ho & Tai 1998) constructed using micro-machining techniques. Both the numerical/theoretical

approach using control theory and the experimental approach based on open-loop techniques (i.e. no sensing) or simple feedback control laws, have been successful for skin-friction reduction (see e.g. Choi *et al.* 1994; Jacobson & Reynolds 1998), flow mixing enhancement and separation control. Nevertheless, the two fields are gradually merging and the long-term aim of this research project is to develop reliable controllers numerically that are possible to use in laboratory experiments. Another way that numerical investigations can be useful for wind-tunnel experiments, is by providing guidelines for the shape and spatial distribution of actuators and sensors. In this sense, one can set-up experiments after evaluating a large number of numerical simulations, in order to understand how to design and place actuators and sensors. The numerical study presented here, takes us one step closer to incorporating theoretical tools into the practical (experimental) flow control community. The present study is based on a fully three-dimensional configuration that resembles actual experimental setups, with a set of localized actuators and sensors distributed near the wall. We show that an order-of-magnitude reduction of perturbation energy can be obtained using actuation and sensing, locally, in a very limited region in the boundary layer (in contrast to distributed control). Such a drastic energy reduction is likely to result in a delay of the initial stages of the laminar-turbulent transition process. We have focused on the flat-plate geometry which still poses a computational challenge, however, the flow control techniques presented in this paper can in principle be applied to any geometry. The approach is based on approximating the complex high-dimensional system that arise from discretization of the Navier-Stokes equations with a low-order system that preserves the dynamics between the actuators and sensors. Model reduction based on balancing techniques (Moore 1981; Rowley 2005), is therefore an important step in the control design process. A similar analysis on more complex flows, such as flows in ducts, corners, diffusers and on elliptic leading edges are waiting to be undertaken.

This paper is organized as follows. In section 2, the control problem is formulated with a description of the disturbance, actuators, sensors and objective functions. Section 3 provides a brief introduction to the balanced truncation method for model reduction, followed by a characterization of the leading balanced modes and the validation of the reduced-order model of the Navier–Stokes system. Section 4 contains the main results of the paper, where the performance of 7 different configurations of sensors-actuators are evaluated. The steps taken to design a reduced-order optimal controller are also outlined. The paper finalizes with conclusions in section 5.

2. Configuration

2.1. *Governing equations and flow parameters*

Using numerical simulations, the dynamics and control of small-amplitude perturbations in a viscous, incompressible flow over a flat plate are considered. The three-dimensional input-output configuration, shown in figure 1, is

an extension of the two-dimensional case studied in Bagheri *et al.* (2009*a,b*). The disturbance velocity field is governed by the Navier–Stokes equations linearized around a spatially evolving zero-pressure-gradient boundary layer flow $\mathbf{U}(\mathbf{x}, t) = (U(x, y), V(x, y), 0)^T$:

$$\frac{\partial \mathbf{u}}{\partial t} = -\left(\mathbf{U} \cdot \nabla\right)\mathbf{u} - \left(\mathbf{u} \cdot \nabla\right)\mathbf{U} - \nabla\pi + Re^{-1}\nabla^2\mathbf{u} + \lambda_f(x)\mathbf{u} \tag{1a}$$

$$0 = \nabla \cdot \mathbf{u} \tag{1b}$$

$$\mathbf{u} = \mathbf{u}_0 \qquad at \quad t = 0. \tag{1c}$$

The disturbance velocity field and the pressure field are $\mathbf{u}(\mathbf{x}, t) = (u, v, w)^T$ and $\pi(\mathbf{x}, t)$, respectively. The flow evolves in the spatial domain Ω defined by,

$$\Omega = \{\mathbf{x} \in \mathbb{R}^3 | x \in [0, L_x], y \in [0, L_y], z \in [-L_z/2, L_z/2]\},$$

where the streamwise, the spanwise and the wall-normal directions are denoted by x,z and y, respectively. The Reynolds number is defined as $Re = U_\infty \delta_0^*/\nu$, where δ_0^* is the displacement thickness at the inflow position, U_∞ is the uniform freestream velocity and ν is the kinematic viscosity.

The following boundary conditions are imposed in Ω,

$$\mathbf{u}(0, y, -L_z/2) = \mathbf{u}(x, y, L_z/2) \tag{2a}$$

$$\mathbf{u}(0, y, z) = \mathbf{u}(L_x, y, z) \tag{2b}$$

$$\mathbf{u}(x, 0, z) = \mathbf{u}(x, L_y, z) = 0. \tag{2c}$$

A no-slip condition is imposed on the flat plate ($y = 0$). Far away from the wall ($y = L_y$), in the freestream, the perturbation velocity is nearly zero, where a homogeneous Dirichlet boundary condition is enforced. Periodicity of the solution is assumed in the spanwise direction, whereas in the streamwise direction, an outflow boundary condition is imposed within the Fourier approximation by the term $\lambda_f(x)\mathbf{u}$ in equation (1a). This forcing is identically zero inside the physically relevant domain ($x \in [0, 800]$) and raises to order one inside the fringe region, starting at x=800, where it forces the perturbations to zero (Nordström *et al.* 1999).

The results presented in this paper are computed with a pseudo-spectral code (Chevalier *et al.* 2007). The computational domain Ω has the dimensions $(L_x, L_y, L_z) = (1000, 30, 120\pi)$ and a resolution of $768 \times 101 \times 120$ in respective direction. The spatial discretization requires thus $n \approx 10^7$ degrees of freedom. All the simulations were performed at $Re = 1000$, corresponding to $Re_x \approx 3 \times 10^5$ at the computational inlet.

The discretized and linearized Navier–Stokes equations (1) with the boundary conditions (2) can be written as an initial-value problem

$$\dot{\mathbf{u}}(t) = \mathbf{A}\mathbf{u}(t) \qquad \mathbf{u}(0) = \mathbf{u}_0, \tag{3}$$

where $\mathbf{u} \in \mathbb{U} \subset \mathbb{R}^n$ is the state variable in the state space $\mathbb{U}$ endowed with the inner product $\langle \cdot, \cdot \rangle_\Omega$. In the following, the subscript Ω is omitted. For the flat-plate boundary layer, the flow is globally stable (Åkervik *et al.* 2008) – but

convectively unstable – resulting in a stable matrix $\mathbf{A}$, i.e. all the eigenvalues of $\mathbf{A}$ have negative real part.

The action of $\mathbf{A} \in \mathbb{R}^{n \times n}$ on $\mathbf{u}$ corresponds to evaluating the right-hand side of the linearized Navier–Stokes equations and enforcing the boundary conditions. Associated with this operator is the evolution operator $\mathbf{T}$, that can be defined as

$$\mathbf{u}(t) = \mathbf{T}(t)\mathbf{u}(0) = \exp(\mathbf{A}t)\mathbf{u}_0. \tag{4}$$

Given an initial flow field $\mathbf{u}_0$, $\mathbf{T}$ provides the velocity field at a later time t; the action of the operator amounts to integrating the governing equations forward in time. In a similar way, the adjoint evolution operator $\mathbf{T}^*$ provides solution of the adjoint linearized Navier–Stokes equations at different instances in time. Applying this operator corresponds to integrating the adjoint state backward in time. The adjoint equations are given in Appendix B; a detailed derivation of the operators for the corresponding two-dimensional case is provided in Bagheri *et al.* (2009*b*).

2.2. *Input-output system*

The input-output configuration is schematically depicted in figure 1. The aim of the present study is to reduce the energy growth of perturbations in the boundary layer using a small number of localized actuators/sensors distributed near the wall. If the amplitude of the disturbances located upstream in the boundary layer is small, the initial phase of the laminar-turbulent transition process is a linear amplification (Schmid & Henningson 2001; Kim & Bewley 2007). We can, therefore, apply linear feedback control schemes to delay the transition process. More specifically, based on the measurement signals extracted from the sensors, a control law provides the actuators with control signals such that the perturbation energy in the downstream part of the domain is minimized.

To design feedback control schemes, it is convenient to introduce inputs and output and arrange them in a specific manner (Doyle *et al.* 1989). Formally, the linear state-space system is defined as

$$\dot{\mathbf{u}}(t) = \mathbf{A}\mathbf{u}(t) + \mathbf{B}_1 \mathsf{w}(t) + \mathbf{B}_2 \mathsf{u}(t) \tag{5a}$$
$$\mathsf{z}(t) = \mathbf{C}_1 \mathbf{u}(t) + l\mathsf{u}(t) \tag{5b}$$
$$\mathsf{v}(t) = \mathbf{C}_2 \mathbf{u}(t) + \alpha \mathsf{g}(t). \tag{5c}$$

The first input $\mathbf{B}_1 \in \mathbb{R}^n$, located far upstream, models the perturbation, whereas the second input $\mathbf{B}_2 \in \mathbb{R}^{n \times m}$ represents m actuators. The time dependence of the inputs is given by the signals $\mathsf{w} \in \mathbb{R}$ and $\mathsf{u} \in \mathbb{R}^m$ respectively. The measurement signals, contained in the vectors $\mathsf{v} \in \mathbb{R}^p$ and $\mathsf{z} \in \mathbb{R}^k$, provide information about the perturbation and are extracted by the sensors $\mathbf{C}_2 \in \mathbb{R}^{p \times n}$ and $\mathbf{C}_1 \in \mathbb{R}^{k \times n}$, respectively. In the following, the $m + 1$ inputs and $p + k$ outputs are explained in detail.
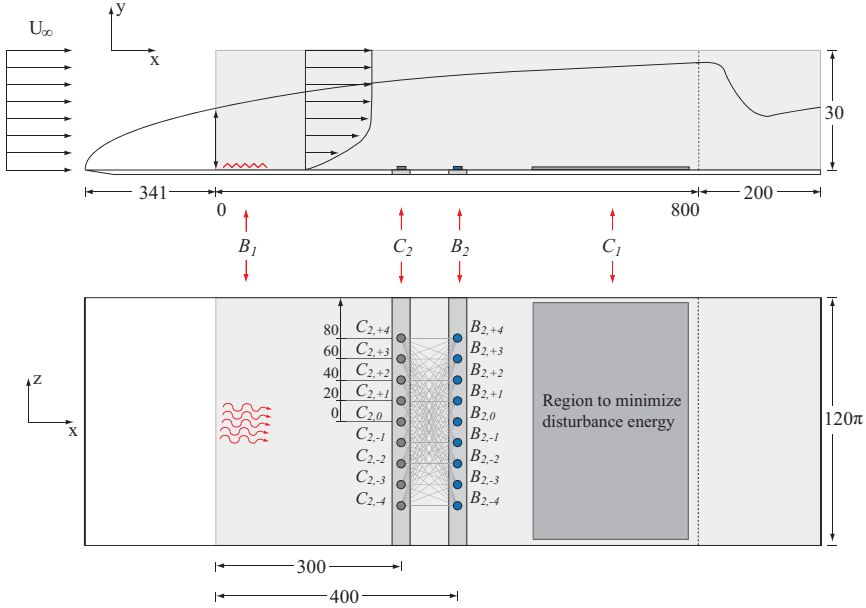
FIGURE 1.   A scheme of the input-output configuration. The computational domain Ω extends from $x = 0$ to $x = 1000$ and from $z = -60\pi$ to $z = 60\pi$. The fringe region starts at $x = 800$. The first input $\mathbf{B}_1$ is located at $(30, 1, 0)$ and represents an optimal initial condition that triggers a TS wavepacket. The control action is provided by the second input, $\mathbf{B}_2$, constituted by a row of actuators located at $x = 400$. The output $\mathbf{C}_2$ at $x = 300$ contains an array of sensors used for flow estimation. A centralized controller is designed, where all the sensors are connected to all the actuators. Finally, the effects of the controller are quantified by the output $\mathbf{C}_1$ located far downstream. This region is spanned by 10 POD modes.

2.2.1. $\mathbf{B}_1$ – *Optimal disturbance*

The upstream disturbance $\mathbf{B}_1$ is a localized initial condition that provides the maximum energy growth for a final time $t = 1820$ (this is roughly the time when the largest possible amplification is obtained). As shown by Monokrousos *et al.* (2009), the initial condition triggers a three-dimensional wavepacket of Tollmien-Schlichting waves. The streamwise component of $\mathbf{B}_1$ is tilted in the upstream direction, leaning against the shear layer. The evolving disturbance extracts energy due to the so-called Orr-mechanism (see e.g. Butler & Farrell
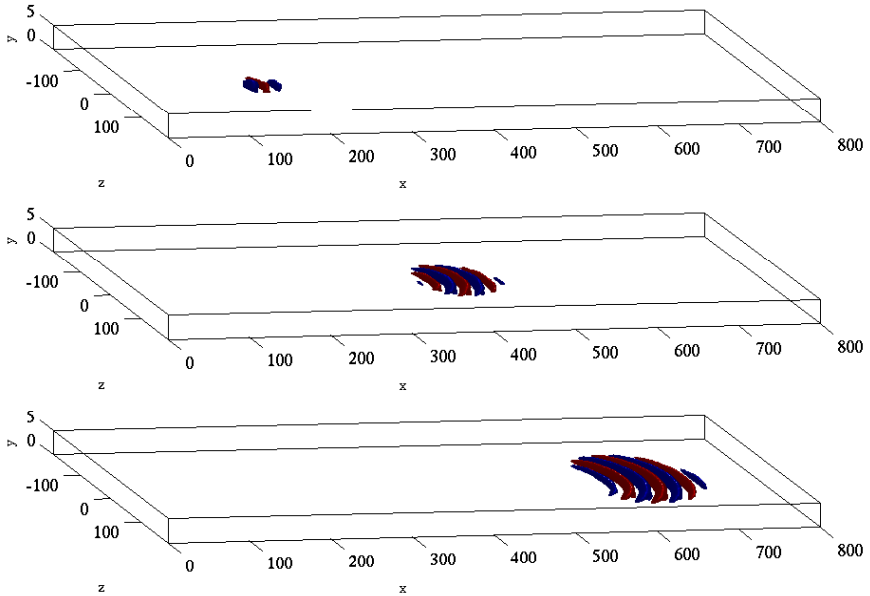
FIGURE 2. Impulse response to an optimal initial disturbance in $\mathbf{B}_1$ at $t = 400, 1008, 1600$. The disturbances is represented by the iso-surfaces of the streamwise component, where the red and blue colours represent positive and negative velocities, respectively.

1992; Åkervik *et al.* 2008) from the mean flow while the structure is rotated until it is aligned with the shear. Figure 2 shows "snapshots" of the u-component of the disturbance velocity at three instances in time. As the disturbance propagates downstream, the wavepacket grows in size and spreads in the spanwise direction. The evolution of the disturbance energy, defined as,

$$E = \langle \mathbf{u}, \mathbf{u} \rangle \tag{6}$$

is shown in figure 8 (solid line). We observe an exponential growth of the energy and an amplification $E(t_{max})/E(0) = 2 \times 10^3$.

2.2.2. $\mathbf{B}_2$ and $\mathbf{C}_2$ – *Actuators and sensors*

Each of the m actuators in $\mathbf{B}_2$ is represented by a localized volume forcing that is able to modify the flow in a region close to the wall. The actuators are placed in a row in the spanwise direction (see figure 1), approximately half way in the downstream direction. Also the p sensors represented by $\mathbf{C}_2$ are composed by a row of localized elements, but located a short distance upstream

Case	actuators m	sensors p	control penalty l	energy reduction E/E_{nc}	system norm $\|\mathbf{G}\|_2^2$
0	-	-	-	1.00	324.25
A	9	9	100	0.070	1.42
B	9	9	250	0.064	13.23
C	9	9	500	0.12	55.27
D	3	3	100	0.55	6.91
E	5	5	100	0.13	2.25
F	7	7	100	0.071	1.28
G	9	5	100	0.068	1.56

TABLE 1. Case A-G correspond to 7 closed-loop systems, whereas case '0' is an uncontrolled configuration. The number of actuators $\mathbf{B}_2$ (m), the number of sensors $\mathbf{C}_2$ (p) and the control penalty (l) varies for the different configurations. The measurement noise is $\alpha = 0.01$ for all set-ups. The peak perturbation energy of the controlled cases as a fraction of the uncontrolled peak disturbance energy together with the 2-norm of the input-output systems are also displayed.

of the actuators. All elements in $\mathbf{B}_2$ and $\mathbf{C}_2$ are analytically expressed by a Gaussian function given in **Appendix A**. The performance of the feedback control schemes is highly dependent on number of elements used, their shape and size and the spanwise spacing between the elements. In table 1, 7 different configurations (labeled A to G) that are considered in this paper, are listed. In all cases, each element is placed equidistantly in the spanwise direction, with $\Delta_z = 20$. The relative position of the arrays in the streamwise direction is fixed and it is based on the knowledge of the boundary-layer.

The measurement signal $\mathsf{v}(t)$ is the spatial integral of the velocity field $\mathbf{u}$ weighted with a Gaussian function (see equation 24). To model measurement noise corrupting the sensors signals, the output equation (5b) is forced with unit-variance white noise $\mathsf{g}(t)$. A large value of the scalar α introduces high level of noise corruption on the measurement $\mathsf{v}(t)$, whereas a small value indicates a high fidelity of the information extracted by the sensors $\mathbf{C}_2$.

2.2.3. $\mathbf{C}_1$ – *Objective function*

The overall goal is to reduce the perturbation growth in order to delay the initial phase of the laminar-turbulent transition process. However, it is not always necessary to minimize the kinetic energy in the entire flow domain; for example outside the boundary layer, in the freestream, there perturbation amplitude is very small. Moreover, a consequence of the convective nature of the instabilities arising in the Blasius flow (where disturbances grow in amplitude as they are convected in the downstream direction) is that the disturbance
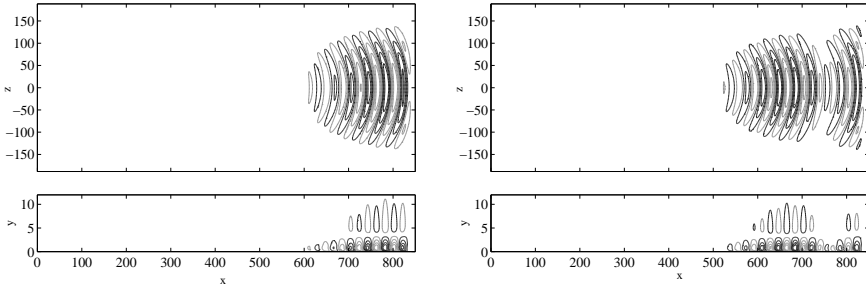
FIGURE 3.　The streamwise velocity component of the first ($\mathbf{C}_{1,1}$) and third ($\mathbf{C}_{1,3}$), POD mode is shown in left and right frame respectively.

energy is significantly larger in the downstream end of the domain than the upstream part. The control objective can therefore be localized to a spatial region downstream as sketched in figure 1.

In particular, the aim is to determine a control signal $\mathsf{u}(t)$, from processing of the noisy measurements $\mathsf{v}(t)$, so that the perturbation energy of the flow is minimized in the downstream region defined by $\mathbf{C}_1$. Moreover, the energy expended by the actuator has to be limited in order to design an efficient controller. Hence, the criterion to be minimized is expressed by the objective functional

$$\|\mathsf{z}\|^2_{L^2(0,T)} = \int_0^T \|\mathbf{C}_1\mathsf{u}\|^2_\Omega + l^2|\mathsf{u}|^2\mathrm{d}t. \tag{7}$$

The scalar parameter l allows to penalize the controller effort; small values of l limit the energy demand of the actuation and indicate a cheap controller.

The subspace of the domain where the controller minimizes the energy is spanned by a basis $\{\mathbf{C}_{1,1}, \dots, \mathbf{C}_{1,k}\}$, which in the present case is a sequence of proper orthogonal decomposition (POD) modes (see e.g. Holmes *et al.* 1996), obtained from the impulse response of the initial disturbance. This approach is similar to the so-called "output projection" technique used by Rowley (2005) and Ilak & Rowley (2008). The POD basis is empirical, i.e. it accurately represents the data used for generating it. An alternative choice for $\mathbf{C}_1$ is used in Semeraro *et al.* (2010), where a set of Fourier modes localized in the streamwise and wall-normal directions were employed to define the basis.

The POD modes are the most energetic structures triggered by the inputs in the flow field; the corresponding eigenvalues $\{\gamma_1 \geq \gamma_2 \geq \cdots \geq \gamma_k\}$ represent a fraction of the total flow energy, computed as $\gamma_i / \sum \gamma_k$. The POD modes come in pairs (see e.g Rempfer & Fasel 1994), because two real-valued functions are required to describe a traveling flow structure; each pair exhibits the same structure, only shifted in the streamwise direction. The first $k = 10$ POD modes capture 93% of the total flow energy and are used as a basis for $\mathbf{C}_1$. In

figure 3, one POD mode of the first two pairs is shown: the structure is mostly located downstream, indicating where the energy response to the forcing is the largest. The different streamwise modulation of the modes is necessary to reproduce the structure of a wave-packet.

3. Model Reduction

As mentioned in the introduction, model reduction provides a way to access control theoretical tools despite the difficulties that arise from discretization of the Navier–Stokes equations. In this section, the Navier–Stokes system is approximated with a low-dimensional system, using an approximation of the balanced truncation method (Moore 1981). Using this approach, the reduced-order model is able to capture the relation between the input and output signals.

3.1. *Projection-based model reduction*

A reduced-order model of the input-output system (5) can be obtained via a projection onto a low-dimensional subspace, spanned by r basis functions, $\mathbf{\Phi} = (\boldsymbol{\phi}_1, \boldsymbol{\phi}_2, \ldots, \boldsymbol{\phi}_r) \in \mathbb{R}^{n \times r}$. The disturbance field $\mathbf{u}$ can be approximated by

$$\tilde{\mathbf{u}} = \sum_{j=1}^{r} q_j \boldsymbol{\phi}_j = \mathbf{\Phi} \mathbf{q} \tag{8}$$

where $\mathbf{q} = (q_1, q_2, \ldots, q_r)^T \in \mathbb{R}^r$ are the scalar expansion coefficients. The coefficients can be computed from

$$q_j = \langle \mathbf{u}, \boldsymbol{\psi}_j \rangle, \quad \text{or} \quad \mathbf{q} = \mathbf{\Psi}^* \mathbf{u}$$

where $\mathbf{\Psi} = (\boldsymbol{\psi}_1, \boldsymbol{\psi}_2, \ldots, \boldsymbol{\psi}_r) \in \mathbb{R}^{n \times r}$ are set of functions (called the adjoint modes) that are bi-orthogonal to expansion basis $\mathbf{\Phi}$, i.e. $\mathbf{\Psi}^* \mathbf{\Phi} = \mathbf{I}$, where $\mathbf{I} \in \mathbb{R}^{r \times r}$ is the identity matrix. The superscript $*$ represents the inner-product $\langle \cdot, \cdot \rangle_\Omega$ between the components of the vectors.

The approximation (8) can be inserted in the input-output system (5) and taking the inner-product with the adjoint modes results in the reduced-order model:

$$\dot{\mathbf{q}}(t) = \mathbf{A}_r \mathbf{q}(t) + \mathbf{B}_{r,1} \mathbf{w}(t) + \mathbf{B}_{r,2} \mathbf{u}(t) \tag{9a}$$
$$\mathbf{z}(t) = \mathbf{C}_{r,1} \mathbf{q}(t) + l\mathbf{u}(t) \tag{9b}$$
$$\mathbf{v}(t) = \mathbf{C}_{r,2} \mathbf{q}(t) + \alpha \mathbf{g}(t). \tag{9c}$$

where $\mathbf{A}_r = \mathbf{\Psi}^* \mathbf{A} \mathbf{\Phi}$, $\mathbf{B}_{r,1} = \mathbf{\Psi}^* \mathbf{B}_1$, $\mathbf{B}_{r,2} = \mathbf{\Psi}^* \mathbf{B}_2$, $\mathbf{C}_{r,1} = \mathbf{C}_1 \mathbf{\Phi}$ and $\mathbf{C}_{r,2} = \mathbf{C}_2 \mathbf{\Phi}$.

3.2. *Balanced modes*

A projection basis that is suitable for capturing the input-output behavior of a linear system is a sequence of balanced modes. The modes are defined as eigenvectors of the product of the observability $\mathbf{Q}$ and controllability Gramian $\mathbf{P}$,

$$(\mathbf{PQ})\mathbf{\Phi} = \mathbf{\Phi}\Sigma^2, \tag{10}$$

where the eigenvalues are contained in the diagonal matrix $\Sigma^2 = \text{diag}\{\sigma_1^2, \ldots, \sigma_r^2\}$. The scalars $\sigma_1 \geq \sigma_2 \geq \ldots \sigma_r$ are called the Hankel singular values (HSV). The set of functions in $\mathbf{\Phi}$ is not mutually orthogonal, and we define the set of left eigenvectors of $\mathbf{PQ}$ as the *adjoint balanced modes* and denoted them by $\mathbf{\Psi}$. The Gramians are defined as

$$\mathbf{P} = \int_0^\infty \mathbf{T}(\tau)\mathbf{BB}^*\mathbf{T}^*(\tau)\mathrm{d}\tau \tag{11a}$$

$$\mathbf{Q} = \int_0^\infty \mathbf{T}^*(\tau)\mathbf{C}^*\mathbf{CT}(\tau)\mathrm{d}\tau. \tag{11b}$$

Each linear input-output system can be associated with a controllability and a observability Gramian. They are useful to characterize how the state vectors are influenced by the inputs and how they can be reconstructed from the measurements, respectively.

The Gramians are positive semidefinite and therefore have positive and real eigenvalues. The eigenvalue decomposition of $\mathbf{P}$ provides a way to rank the flow states according to how much they are influenced by the input. In particular, it can be shown (Bagheri *et al.* 2009*c*) that the eigenvectors associated with the leading eigenvalues of $\mathbf{P}$ are flow structures that are the most influenced by the inputs. These modes are called the controllable modes and can for linear systems be regarded as POD modes (Ilak & Rowley 2008). The observability Gramian $\mathbf{Q}$ allows us to rank the states according to their contribution to the output energy. The eigenvectors related to the dominant directions of $\mathbf{Q}$ correspond to the most *observable* states of the system. Note that both the controllability and observability Gramians can be interpreted as solution of optimization problems.

Using the balanced modes and the related adjoint set, it can be shown that

$$\langle \boldsymbol{\phi}_i, \mathbf{Q}\boldsymbol{\phi}_j \rangle = \langle \boldsymbol{\psi}_i, \mathbf{P}\boldsymbol{\psi}_j \rangle = \sigma_i \delta_{i,j}, \qquad i, j = 1, \ldots, r \tag{12}$$

where $\delta_{i,j}$ is the Kronecker delta. Therefore, using $\boldsymbol{\psi}_i$ and $\boldsymbol{\phi}_i$, the controllability and observability Gramians become diagonal and equal to the HSV; hence the controllability and observability properties are balanced. The balanced mode $\boldsymbol{\phi}_j$ is a global structure in the flow that is "influenced" by the input $\mathbf{B}$ by an amount given by its HSV σ_j, whereas the corresponding adjoint mode $\boldsymbol{\psi}_j$ is a flow structure that – if used as an initial condition – will result in an output energy given also by σ_j. These global modes have thus ranked the flow fields according to their response behavior (controllability) and output sensitivity (observability).

The reduced-order system (9) obtained by projection onto balanced modes is arguably the most widely used method for model reduction of linear input-output systems for two reasons: (i) the reduced-order system is guaranteed to be asymptotically stable if $\sigma_j \neq \sigma_{j+1}$ for all j and (ii) there exist tight error bounds

$$\sigma_{r+1} \leq \|\mathbf{G} - \mathbf{G}_r\|_\infty \leq 2 \sum_{j=r+1}^n \sigma_j, \tag{13}$$
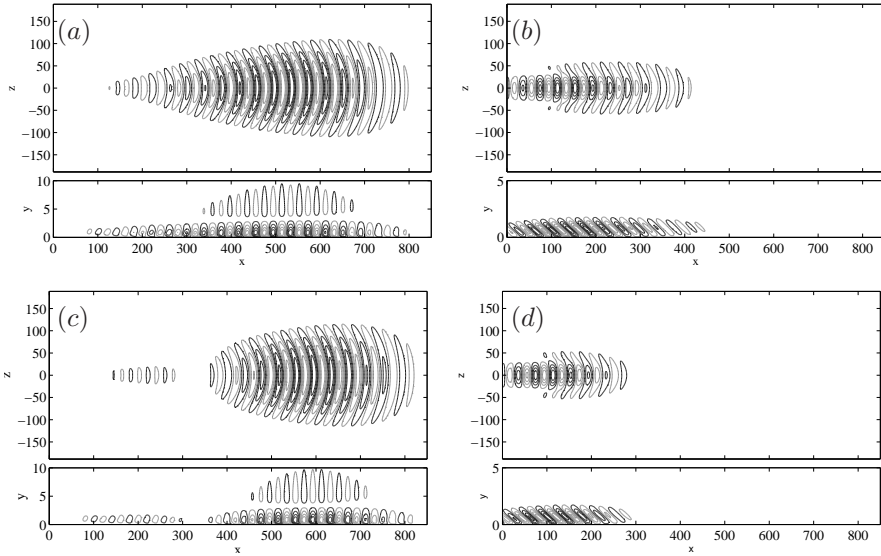
FIGURE 4. Left column: Streamwise component of the leading balanced mode ϕ_1 (a) and the third balanced order mode ϕ_3 (c). Right column: corresponding adjoint modes ψ_1 (b) and ψ_3 (d). Positive velocity is represented in black, while negative one is in gray.

where $\mathbf{G}$ and $\mathbf{G}_r$ are the input-output impulse response of (5) and (9), respectively. It can be shown (Green & Limebeer 1995) that $\mathbf{P}$ and $\mathbf{Q}$ satisfy Lyapunov equations. Unfortunately, solving Lyapunov equations is unfeasible for high-dimensional systems as the computational complexity is $O(n^3)$ and storage requirement is $O(n^2)$.

3.3. *Characterization of the leading balanced modes*

The computation of the balanced modes when $n \geq 10^5$ can be performed using the *snapshot method* introduced by Rowley (2005), where empirical Gramians are computed from numerical simulations of the forward and adjoint systems. The main steps are outlined in the Appendix C. In what follows, for the sake of clarity, we discuss the balanced modes obtained by considering only the first input $\mathbf{B}_1 \in \mathbb{R}^n$ and the output $\mathbf{C}_1 \in \mathbb{R}^{k \times n}$. Since, $k = 10$, to construct the basis, 10 adjoint simulations were necessary. The snapshots from the simulations were collected with constant time spacing, $\Delta t = 16$, in a time-interval $[0, 3000]$ for the forward simulation and in $[0, -2600]$ for the adjoint simulations.

The computed Hankel singular values σ_j are shown in figure 5 (open circles). Similarly to the POD modes discussed previously, the HSV come in
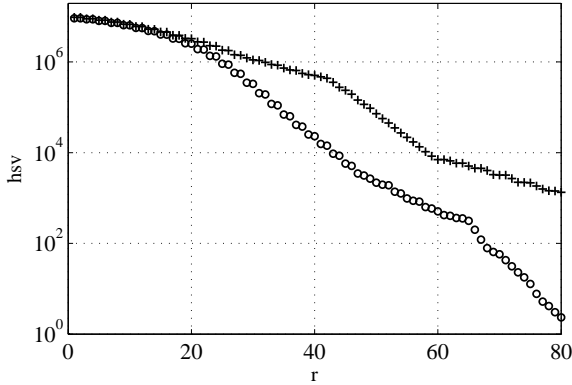
FIGURE 5. The Hankel singular values for the complete model (crosses) and the HSV generated from the first input $\mathbf{B}_1$ and the output $\mathbf{C}_1$ (open circles).

pairs, such that the corresponding modes exhibit the same structure, only shifted along the streamwise direction. The iso-contours of the streamwise components of the first and the third balanced modes (ϕ_1, ϕ_3) and their related adjoint modes (ψ_1, ψ_3) are shown in figure 4; the structure is shown in both the xy-plane and the xz-plane. The leading balanced modes are characterized by a nearly 2-dimensional TS-wavepacket structure, located mostly in the downstream region. These modes are related to the most controllable flow structures, and capture the response behavior of the system to the input $\mathbf{B}_1$; low energy is needed at location $\mathbf{B}_1$ to excite large structures downstream. Higher order modes preserve these main characteristics, although with different spatial wavelengths.

The associated adjoint balanced modes are mostly located far upstream and represent flow structures to which the output $\mathbf{C}_1$ is more sensitive. The spatial separation between these structures and the most controllable structures identified by the direct balanced modes is similar to the spatial separation observed between the direct and adjoint modes of the linearized Navier–Stokes equations, $\mathbf{A}$. This is a sign of the streamwise non-normality of $\mathbf{A}$. Moreover, in figure 4(b–d), the streamwise component in the xy-plane is shown. The spatial distribution results in a tilted structure leaning against the shear, similarly to the optimal initial condition discussed previously.

3.4. *Reduced-order model of the full input-output system*

Figure 5 shows the HSV related to the balanced modes used to compute the reduced-order model using all the inputs $(m + 1)$ and all the outputs $(p + k)$ (crosses), pertaining to Case A in table 1. It is interesting to note that the associated HSV decay slower than the HSV computed using only $\mathbf{B}_1$ and $\mathbf{C}_1$ (open circles). The leading singular values of the two systems are equal, indicating
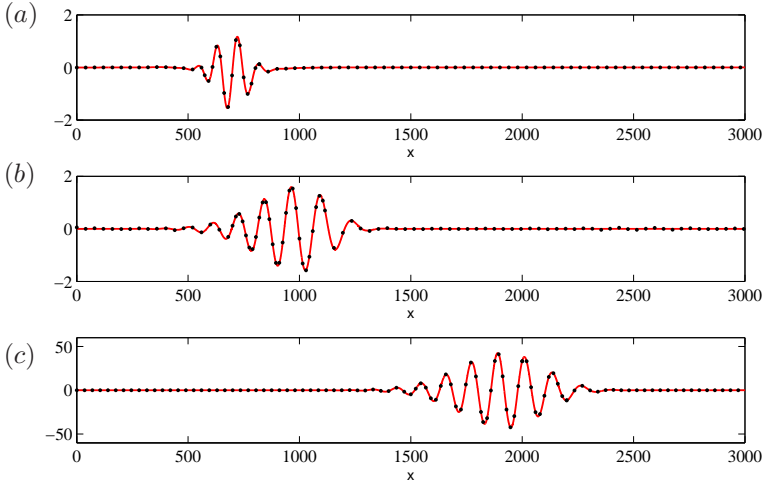
FIGURE 6. Impulse response of the system from the input $\mathbf{B}_1$ to the output $\mathbf{C}_{2,0}$, (b), from $\mathbf{B}_{2,0}$ to $\mathbf{C}_{1,1}$, (c) and from $\mathbf{B}_1$ to $\mathbf{C}_{1,1}$, (d). The red line shows the DNS results, while the dotted, gray line is related to the impulse response of a reduced model of order 60.

that the entire input-output dynamics of the system is strongly influenced by the energy triggered by the input $\mathbf{B}_1$ and the observability characteristics of the function chosen as output $\mathbf{C}_1$.

To validate the snapshots-based balanced truncation method, the balancing property of the reduced model is considered by evaluating equation (12). The diagonal elements of the Gramians associated with the reduced-order model and the HSV were found to be the same for the first 80 modes. Due to numerical discretization errors, higher order modes gradually loose bi-orthogonality, causing the presence of off-diagonal elements in the Gramians.

To validate the reduced-order model, we compare impulse responses obtained of the Navier–Stokes system (5) to impulse responses obtained from the low-order model (9). For configuration A, there are in total 10 input signals and 19 output signals, resulting in 190 impulse responses. We compare the following three signals:

$$\mathbf{B}_1 \to \mathbf{C}_{2,0}, \qquad \mathbf{B}_{2,0} \to \mathbf{C}_{1,1}, \qquad \mathbf{B}_1 \to \mathbf{C}_{1,1}. \qquad (14)$$

The second subscript of $\mathbf{B}_2$ and $\mathbf{C}_2$ indicates the element according to figure 1. The first signal (figure 6a) is triggered by the upstream disturbance $\mathbf{B}_1$ and detected by the sensor located at $z = 0$ ($\mathbf{C}_{2,0}$). The second and third signals (figure 6b, c) are registered by the first POD mode ($\mathbf{C}_{1,1}$), triggered by the center ($z = 0$) actuator $\mathbf{B}_2$ and the disturbance ($\mathbf{B}_1$), respectively. In all the

figures, the impulse responses of a reduced model of order $r = 60$ are shown with a dotted gray line, while the solid red line provides the DNS results. We observe that the low-order model ($r = 60$) is able to preserve the input-output behaviour of the full Navier–Stokes system ($n \approx 10^7$), albeit the significant model order reduction. The agreement between all the impulse responses of the two systems are as good as the three signals shown here.

4. Feedback control

In section 2.2 it was explained how the energy of a small-amplitude three-dimensional disturbance grows three orders of magnitude as it convected in the downstream direction. The aim of this section, is to use the validated and balanced reduced-order model to reduce the growth of the disturbance. Although, the steps taken to design a closed-loop are the same as for two-dimensional case studied by Bagheri *et al.* (2009*b*), due to the additional direction in the spanwise direction, the control problem is significantly more complex. In total, the linear system (case A in table 1) consists of 10 inputs and 19 outputs and its complexity n is of order 10 million. Since the reduced-order model shows essentially the same input-output behavior (but with complexity of 60), during the control design it replaces the Navier–Stokes system. Once the feedback controller is constructed, it can be applied on-line, in parallel to the DNS-simulations.

4.1. *Main steps of LQG design*

By using control theory, we can determine what action the actuators should take to minimize the disturbance energy in a region defined by $\mathbf{C}_1$ and if the action of an actuator should depend on all sensors measurements or only the sensor located upstream of it. In particular, the controller can be designed using the linear quadratic Gaussian (LQG) approach. Assume that the external disturbance signal $\mathsf{w}(t)$ and the measurement noise $\mathsf{g}(t)$ in (9) are unit-variance white noise processes. Then based on the noisy measurements $\mathsf{v}(t)$ extracted from the sensors $\mathbf{C}_2$, the controller provides a control signal $\mathsf{u}(t)$ for the actuators $\mathbf{B}_2$, such that the mean of the output energy of z is minimized, i.e.

$$\mathcal{E}\left\{\|\mathsf{z}\|^2_{L^2(0,\infty)}\right\} = \mathcal{E}\left\{\int_0^\infty \mathbf{q}^T\mathbf{C}^T_{1,r}\mathbf{C}_{1,r}\mathbf{q} + l^2|\mathsf{u}|^2\mathrm{d}t\right\}. \tag{15}$$

The first step in constructing a controller is to estimate the full state $\mathbf{u}$ given only the noisy measurements $\mathsf{v}(t)$. After the state has been successfully estimated, we assume, in a second step, that the control $\mathsf{u}(t)$ and the estimated reduced state $\hat{\mathbf{q}}(t) \in \mathbb{R}^r$ satisfy a linear relation involving some yet unknown matrix $\mathbf{K} \in \mathbb{R}^{m \times r}$, i.e.

$$\mathsf{u}(t) = \mathbf{K}\hat{\mathbf{q}}(t). \tag{16}$$

The goal of this second step is then to find such a matrix $\mathbf{K}$, which is referred to as the control gain. One attractive feature of LQG design is that the two steps (estimation and full-information problem) can be performed independently of

each other. Moreover, if both problems are optimal and stable the resulting closed-loop system, composed of the two problems is also optimal and stable. The main disadvantage of LQG is that it does not account for uncertainties of the underlying system $(\mathbf{A}, \mathbf{B}, \mathbf{C})$ (see Doyle 1978). One can only check the robustness by *ad-hoc* testing the controller for various parameters.

For derivation of the LQG solution, please refer to e.g. Anderson & Moore (1990); Lewis & Syrmos (1995); Bagheri *et al.* (2009c) for a "classical" optimal control framework or Doyle *et al.* (1989); Dullerud & Paganini (1999) for a more "modern" robust control framework. Here, we just state the solution of the two separate problems.

To estimate the full state $\mathbf{u}(t)$ given only the noisy measurements $\mathsf{v}(t)$, an estimator can be formulated

$$\dot{\hat{\mathbf{q}}}(t) = \mathbf{A}_r \hat{\mathbf{q}}(t) + \mathbf{B}_{2,r} \mathsf{u}(t) + \mathbf{L}(\mathsf{v}(t) - \hat{\mathsf{v}}(t)) \tag{17}$$

that governs the reduced estimated state $\hat{\mathbf{q}}$. In the above expression, we compare the measurement from the velocity field $\mathsf{v} = \mathbf{C}_2 \mathbf{u}$ and the measurement from the estimated state $\hat{\mathsf{v}} = \mathbf{C}_{2,r} \hat{\mathbf{q}}$ and feed back the mismatch in these two quantities using the estimator gain $\mathbf{L} \in \mathbb{R}^{r \times p}$. It can be shown (Kalman 1960) that the estimation gain that minimizes the estimation error $\|\mathbf{q} - \hat{\mathbf{q}}\|$, where $\mathbf{q}$ is reduced state given by (9) and results in a stable estimator is given by

$$\mathbf{L} = -\mathbf{Y} \mathbf{C}_{2,r}^T,$$

where $\mathbf{Y} \in \mathbb{R}^{r \times r}$ is a solution to an algebraic Riccati equation (see e.g. Laub 1991).

In the second step, assume the full state is given by $\mathbf{q}$ at all times and that $\mathsf{u}(t) = \mathbf{K}\mathbf{q}(t)$ (instead of 16). Inserting the feedback relation into (5) and neglecting the redundant output v, we get

$$\dot{\mathbf{q}}(t) = (\mathbf{A}_r + \mathbf{B}_{2,r}\mathbf{K})\mathbf{q}(t) + \mathbf{B}_{1,r}\mathsf{w}(t) \tag{18a}$$
$$\mathsf{z}(t) = \mathbf{C}_{1,r}\mathbf{q}(t) + l\mathsf{u}(t) \tag{18b}$$

It remains to choose $\mathbf{K} \in \mathbb{R}^{m \times r}$ such that the system is stable and the control signal $\mathsf{u}(t)$ minimizes output energy, $\|\mathsf{z}\|^2$. The solution is provided by a optimal control state-feedback problem, (see e.g. Anderson & Moore 1990), where the optimal control signal is given by

$$\mathbf{K} = -\mathbf{B}_{2,r}^T \mathbf{X},$$

and $\mathbf{X} \in \mathbb{R}^{r \times r}$ is a solution of an Riccati equation.

Finally, combining the estimator (17) and the full-information controller (18), we obtain the reduced-order controller (also called compensator or observer) of size r:

$$\dot{\hat{\mathbf{q}}}(t) = (\mathbf{A}_r + \mathbf{B}_{2,r}\mathbf{K} + \mathbf{L}\mathbf{C}_{2,r})\hat{\mathbf{q}}(t) - \mathbf{L}\mathsf{v}(t) \tag{19}$$
$$\mathsf{u}(t) = \mathbf{K}\hat{\mathbf{q}}(t) \tag{20}$$

At each instant in time, given only the measurements $\mathsf{v}(t)$, the compensator provides the control signal $\mathsf{u}(t)$ at that time. The controller thus connects measurements from sensors to the actuator, that in combination with the Navier–Stokes system (5) results in a feedback closed-loop system, denoted by $\mathbf{G}_c$ hereafter.

When the external disturbances are white noise processes, the 2-norm of the closed-loop system is a convenient measure of the input-output behavior. The 2-norm of the closed-loop system $\mathbf{G}_c$ can be defined (Green & Limebeer 1995) as

$$\|\mathbf{G}_c\|_2^2 = \int_0^\infty |\mathsf{z}|^2 \mathrm{d}t = \|\mathsf{z}\|^2 \qquad (21)$$

So, the 2-norm of $\mathbf{G}_c$ equals the control objective (7) defined earlier and can be calculated from the signals extracted by the output $\mathbf{C}_1$.

4.2. *Centralized vs. decentralized approach*

The spatial localization of the actuators and the sensors requires a proper multivariable approach for the controller design. A simple approach is a *decentralized control*, where each actuator is connected only with the upstream sensor; in such a controller, each loop can be regarded as a single-input single-output (SISO) system and an equal number of actuators and sensors is required. If the decentralized controller is stable in each SISO loop and the inputs and the outputs are decoupled or only weakly coupled, then the closed loop is also stable; the analysis of the *relative gain array* (RGA) matrix provides a quantitative, *a priori* measurement of the degree of coupling and cross coupling of the input-output system (see e.g. Glad & Ljung 2001). In our case, both the RGA analysis of the reduced system and numerical tests resulted in an unstable closed-loop system, when using a decentralized approach. A physical explanation is that the perturbation triggered in the boundary layer by the localized initial condition $\mathbf{B}_1$ (shown in figure 2) gradually spreads in the spanwise direction while propagating. This results in a dynamic coupling in the spanwise direction. In this work, we design a *centralized controller* for all cases (A-G), i.e. all the actuators are connected with all the sensors used for estimation. Using the LQG approach, a centralized controller is guaranteed to result in a stable closed-loop system. However, in a practical implementation of the controller in wind-tunnel experiments, this approach is more prone to errors compared to a decentralized approach due to the complicated interconnection.

4.3. *Performance of closed-loop systems (case A–G)*

In this section, the performances of the closed-loop system for the different sensor-actuator configurations listed table 1 are investigated. In the reference case A, a *full* set-up is considered, where the row of actuators and the row of estimators are constituted by 9 localized Gaussian elements, equally spaced in the spanwise direction. Using this setup, three cases are considered with different control penalty l: case A can be considered an inexpensive controller,

with $l = 100$ (since the controller effort is relatively cheap); case B is an intermediate case, with $l = 250$, whereas case C is an expensive case, with $l = 500$. In configurations D-G, a reduced number of actuators and/or sensors is used, in order to investigate the dependence of the closed-loop performance on m and p.

The following measures of disturbance amplification are compared between the closed-loop system and the uncontrolled Navier–Stokes system: (i) impulse response (time signals), (ii) the system 2-norms and (iii) the perturbation energy in the full spatial domain Ω.

Whereas time-signals provide a physical and direct measure of the control performance, it is necessary to compute the system 2-norm to obtain a total measure of the input-output behavior. In particular, low system norms indicate smaller amplifying behavior of the linear system. In the context of flow stability, system norms are closely linked to transient growth of perturbation energy (see e.g. Bewley 2001; Bagheri *et al.* 2009c, for more on this relation). However, for three-dimensional disturbances, the minimization of the 2-norm may not necessarily correspond to an actual reduction of the disturbance energy (defined in 6). In table 1, both the 2-norm and the ratio between the energy peak and the initial disturbance energy is tabulated for each case. We observe a significant reduction of both measures. In the following these results are investigated further.

4.3.1. *Input-output analysis*

In figure 7, a few sensor measurements and actuator signals $u(t)$ for an impulse in $w(t)$ pertaining to case A are shown. In figure 1 the location of actuators and sensors are shown schematically.

Figure 7(a) shows measurement signals used for estimation of the disturbance associated with the sensors $\mathbf{C}_{2,0}$ and $\mathbf{C}_{2,2}$ for an impulse in $\mathbf{B}_1$. The measurement detected by $\mathbf{C}_{2,0}$ (solid line) reveals the a wavepacket structure of the evolving disturbance. The traveling disturbance reaches the sensor location at $t \approx 500$, in agreement with the estimated velocity of the wavepacket in a boundary layer ($\approx 0.47 U_\infty$). The element $\mathbf{C}_{2,2}$ (dashed line) shows an analogous behaviour, although a delay due to the spanwise spreading of the wavepacket is observed; moreover the signal is characterized by a smaller amplitude.

Figure 7(b) shows the control signals feeding the actuators $\mathbf{B}_{2,0}$ and $\mathbf{B}_{2,2}$; they are, respectively depicted with a solid line and a dashed line. In both the cases a time lag of 200 time units from the estimation signals is observed. The shift observed between the two signals is related to the the three-dimensional structure of the incoming perturbation. As mentioned previously, the actuator signals are computed using all the 9 sensor measurements extracted.

In figure 7(c), the output signal extracted from $\mathbf{C}_{1,1}$ (first POD mode) is compared between the controlled case (solid line) and the uncontrolled case (dashed-dotted line). It is clear that the amplitude of the closed-loop output
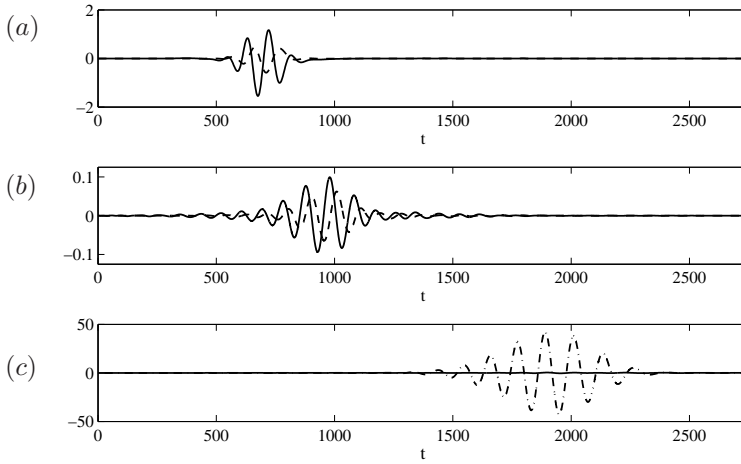
FIGURE 7. Input and output signals of the closed-loop system excited by an impulsive forcing. (*a*) Output signals extracted from $\mathbf{C}_{2,0}$, located in $(x, z) = (300, 0)$ (solid line), and $\mathbf{C}_{2,2}$, placed in $(x, z) = (300, +40)$ (dashed line). (*b*) The controller signals fed in $\mathbf{B}_{2,0}$ and $\mathbf{B}_{2,2}$ are, respectively indicated with a solid line and a dashed line. (*c*) Measurements extracted by the first sensor $\mathbf{C}_{1,1}$ for case A (solid) and uncontrolled (dashed-dotted line).

signal is significantly reduced. Computing the system 2-norm, the performance can be evaluated by taking into account all the $k = 10$ signals extracted by $\mathbf{C}_1$. As shown in table 1, for case A $\|\mathbf{G}_c\|_2^2 = 1.42$; this is a reduction of about 99% of the 2-norm of uncontrolled case ($\|\mathbf{G}\|_2^2 = 324$). As the controller effort is reduced, we observe higher values of $\|\mathbf{G}_c\|_2^2$ (case B, $\|\mathbf{G}_c\|_2^2 = 12.23$ and case C, $\|\mathbf{G}_c\|_2^2 = 55.27$).

4.3.2. *Perturbation energy and disturbance evolution*

Figure 8 shows the kinetic energy (in the full domain Ω) as a function of time for the uncontrolled case (solid line) and the controlled case A (dashed-dotted line). The energy peak for the uncontrolled case is reached at $t = 1820$, with an energy amplification $E(t_{max})/E(0) = 2 \times 10^3$, whereas the controlled case shows one order of magnitude smaller peak value at $t \approx 1100$. By demanding the disturbance energy to be small at $\mathbf{C}_1$, the disturbance amplitude has to decrease significantly before it reaches the objective function to accomplish this task. Therefore, minimization of disturbance energy in the region defined by $\mathbf{C}_1$, results in an actual reduction of the energy in the entire domain.
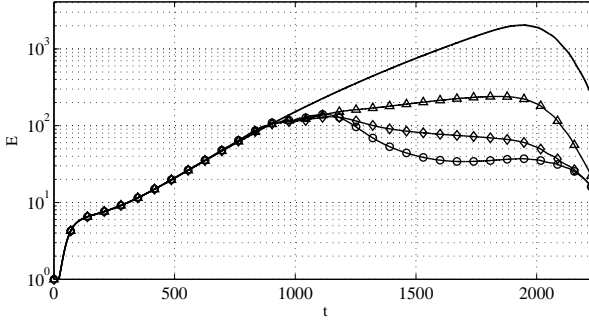
FIGURE 8. Disturbance energy as function of time. The solid line represents the energy growth of the disturbance $\mathbf{B}_1$. Also shown are the closed-loop configurations for three different control penalties: a cheap case $(- \circ -)$, an intermediate case $(- \diamond -)$ and an expensive case $(-\triangle-)$.

The streamwise velocity component of the disturbance field at $t = 1000$, 1200, 1750 for case A (left column) and the uncontrolled case (right column) are shown in figure 9. The iso-contours display the flow field in the xz-plane at $y = 2$. At $t = 1000$, the perturbation is convected pass the location $x = 400$ where the array of actuators are placed; the original structure is distorted into a more complicated three-dimensional pattern, where traces of localized actuators are recognizable. At $t = 1250$, the perturbation appears to be mostly concentrated in the center ($z \approx 0$) of the domain, whereas the spanwise extension of the structures is significantly reduced. The original nearly two-dimensional structure breaks down into a fully three-dimensional structure. Finally, at $t = 1750$, a significant damping of the amplitude results in contour levels that are barely visible for case A, while the perturbation for the uncontrolled case attains its maximum energy. It is interesting to note that similar results were obtained by Sturzebecher & Nitsche (2003). These authors performed an experiment based on an adaptive controller designed to attenuate the TS instabilities; also in this case, the disruption of the original two-dimensional structure resulted in a reduction of the disturbance level.

Figure 8 shows the performance of the *full* set-up controller for different choices of the penalty l (cases A, B and C). It is interesting to point out that for an intermediate value ($l = 250$, case B) the perturbation is characterized by a peak energy value close to the corresponding configuration with a cheap controller effort, although the norm $\|\mathbf{G}_c\|_2^2$ is higher. Case C (expensive controller) is the only configuration where the perturbation energy does not decay monotonically downstream of the actuators.
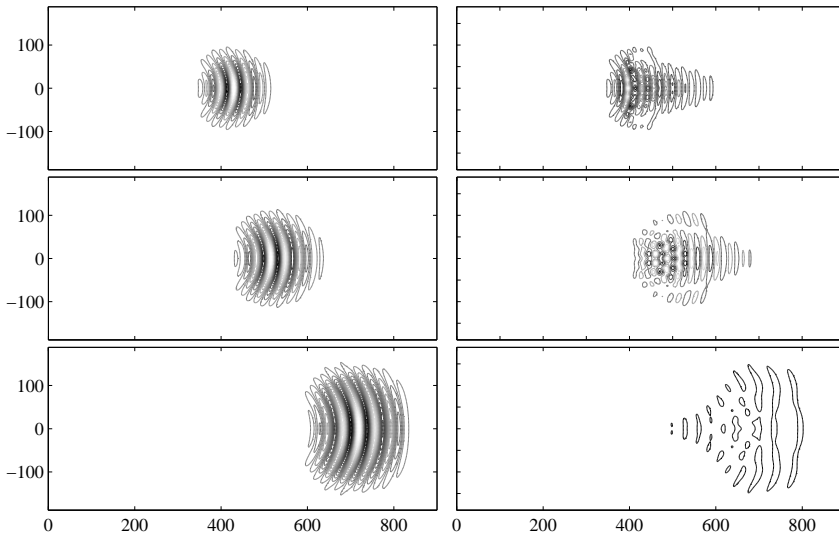
FIGURE 9. Impulse response to an optimal disturbance at $t = 1000, 1250, 1750$ without control (left column) and with control (right column). The iso-contours of the streamwise component are shown in the xz-plane at $y = 2$.

4.3.3. *Influence of the number of sensors and actuators*

The norm $\|\mathbf{G}_c\|_2^2$ and the energy amplification for cases D-F are reported in table 1. It can be concluded that controllers with a lower number of actuators than case A ($m = 9$) are still able to reduce the norm $\|\mathbf{G}_c\|_2^2$ significantly, whereas the perturbation energy amplification shows a somewhat less efficient growth reduction.

Figure 10(a) shows the energy behaviour for cases D-F in addition to the reference case A and the uncontrolled case. A gradual improvement of the performances is observed when the number of actuators is increased. In particular, case D ($m = 3, p = 3$) shows an initial overshoot of the energy in the interval $t \in [1000, 1200]$, when the controller begins to act. Also, the spatial evolution of the perturbation is similar to the uncontrolled case. However, increasing the number of actuators, the row of actuators is able to cover a wider region in the spanwise direction and a considerable reduction of the energy growth is observed.

Figure 10(b) shows the influence of the number of sensors (case E and G). The energy curve for case A ($m = 9$), obtained with nine estimators, is hardly distinguishable from the curve obtained with the controller designed for case G, based only on five estimators. On the other hand, as previously discussed,
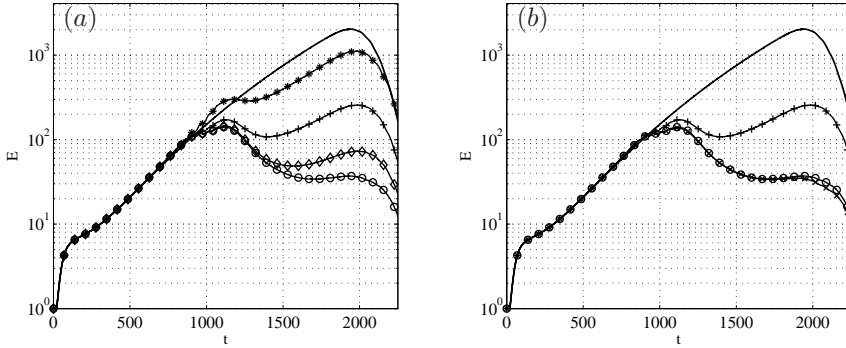
FIGURE 10. Kinetic energy as function of time. In (a) and (b), the solid line shows the energy of $\mathbf{B}_1$. In (a) case D ($-\star-$), E ($-+-$), F ($-\diamond-$) and A ($-\circ-$) are characterized by 3, 5, 7 and 9 actuators respectively. In (b) the curves correspond to case E ($-+-$), G ($-\times-$) and A ($-\circ-$) with 5, 5 and 9 sensors, respectively.

a lower number of actuators (case E) decreases significantly the performances of the controller.

5. Conclusions

We have built a model of low dimension ($r = 60$) that captures the input-output behavior of the flat-plate boundary layer, and used this model for optimal feedback control design. We have shown that by using systematic methods from control theory in combination with localized sensing/actuation, it is possible to reduce the growth of small-amplitude disturbances in the boundary layer. In particular, using 9 sensors for estimation and 9 actuators, it was demonstrated that the energy of three-dimensional Tollmien-Schlichting wavepacket is damped by an order of magnitude. The control performance was investigated when reducing the number of sensors and actuators in the configuration. It was found that, a lower number of actuators (case E) decreases significantly the performances of the controller, whereas a reduced number of sensors has a smaller impact on the performance. The results suggest that for an effective implementation of feedback control of a three-dimensional wavepacket in a boundary layer, the actuation step may be more crucial than the sensing and estimation of the incoming disturbances.

Although the significance of the order-of-magnitude reduction of perturbation energy for transition control remains to be tested, such a drastic energy reduction is likely to result in a delay of the initial stages of the transition process. If the actuators and sensors represent realistic models of physically implementable devices, it is possible to use the low-dimensional controller designed numerically in laboratory experiments. The fact that we have modeled

the inputs and outputs as volume forcing does not mean that they are un-realistic. It is the effect of an actuator that is important to model, and not the actuator itself. Therefore, the action that the volume forcing has on the flow, could possibly be reproduced for example using plasma actuators. An-other issue that needs to be taken into account is control robustness. If the numerically-designed controller is used in laboratory experiments, it is unavoid-able that some parameters (such as Reynolds number and pressure gradients) will mismatch. Fortunately, modern developments in robust control theory take rigorously into account uncertainties that may be present in the design process. The method for optimal control presented in this paper, can be incorporated into a robust control framework.

Appendix A. Analytical expressions of actuators and sensors

Each element of the arrays $\mathbf{B}_2$ and $\mathbf{C}_2$ is a localized Gaussian function

$$\mathbf{h}\left(\mathbf{x}, \mathbf{x}_0\right) = \begin{pmatrix} \sigma_x \hat{y} \\ -\sigma_y \hat{x} \\ 0 \end{pmatrix} \exp\left(-\hat{x}^2 - \hat{y}^2 - \hat{z}^2\right), \qquad (22)$$

where

$$\hat{x} = \frac{x - x_0}{\sigma_x} \qquad \hat{y} = \frac{y}{\sigma_y} \qquad \hat{z} = \frac{z - z_0}{\sigma_z}.$$

The scalar quantities $\sigma_x = 5$, $\sigma_y = 1.5$, $\sigma_z = 6$ define the size and the shape of the Gaussian spatial distribution and are equal for all the elements, while the position is fixed accordingly to the values (x_0, z_0). From this definition, we obtain

$$\mathbf{B}_2 = \left[\mathbf{h}\left(\mathbf{x}, \mathbf{x}_{\mathsf{u},1}\right), \mathbf{h}\left(\mathbf{x}, \mathbf{x}_{\mathsf{u},2}\right), \ldots, \mathbf{h}\left(\mathbf{x}, \mathbf{x}_{\mathsf{u},m}\right)\right], \qquad (23)$$

and

$$\mathbf{C}_2 \mathbf{u} = \int_\Omega \begin{pmatrix} \mathbf{h}\left(\mathbf{x}, \mathbf{x}_{\mathsf{v},1}\right) \mathbf{u} \\ \ldots \\ \mathbf{h}\left(\mathbf{x}, \mathbf{x}_{\mathsf{v},p}\right) \mathbf{u} \end{pmatrix} \mathrm{d}x \mathrm{d}y \mathrm{d}z, \qquad (24)$$

where m and p indicate the number of actuators and sensors, respectively. Each element of $\mathbf{B}_2$ and $\mathbf{C}_2$ is denoted with a second subscript. The actuators mimic a manipulation on the flow close to the wall, whereas the measurements are extracted by averaging the velocity field using the Gaussian function as weights.

Appendix B. Adjoint Navier–Stokes equations

A detailed derivation of the adjoint equations is given by Bagheri *et al.* (2009*b*) where the corresponding adjoint inputs and outputs are also defined. Here, the equations are given for completeness. The adjoint velocity field and the adjoint pressure field are denoted by $\mathbf{p}(\mathbf{x}, t) = (u^*, v^*, w^*)$ and $\sigma(\mathbf{x}, t)$, respectively. Considering the boundary conditions (2) used for $\mathbf{u}$ and requiring that $\mathbf{p} = (u^*, v^*, w^*)$, σ and p satisfy

$$(\sigma, \pi)(0, y, -L_z/2) = (\sigma, \pi)(L_x, y, L_z/2) \tag{25a}$$

$$\mathbf{p}(0, y, -L_z/2) = \mathbf{p}(L_x, y, L_z/2) \tag{25b}$$

$$\mathbf{p}(x, 0, z) = \mathbf{p}(x, L_y, z) = 0, \tag{25c}$$

the adjoint of the linearized Navier–Stokes equations 5 associated with the inner product $\langle \cdot, \cdot \rangle_\Omega$ is given by

$$-\frac{\partial \mathbf{p}}{\partial t} = (\mathbf{U} \cdot \nabla)\mathbf{p} - (\nabla \mathbf{U})^T \mathbf{p} + \nabla \sigma + Re^{-1} \nabla^2 \mathbf{p} + \lambda_f(x)\mathbf{p} \tag{26a}$$

$$0 = \nabla \cdot \mathbf{p} \tag{26b}$$

$$\mathbf{p} = \mathbf{p}_T \quad at \quad t = T. \tag{26c}$$

Together with the boundary conditions, the latter set of equation governs the behaviour of the adjoint flow field $\mathbf{p}$.

Appendix C. Snapshot-based balanced truncation

The exact balanced truncation amounts to solving two Lyapunov problem for the computation of the controllability $\mathbf{P}$ and observability $\mathbf{Q}$ Gramians. Since the computational cost is $\mathcal{O}(n^3)$ and the storage requirement $\mathcal{O}(n^2)$, the standard balanced truncation method (Laub *et al.* 1987) is computationally unfeasible when $n \geq 10^5$. The snapshot-based method (Rowley 2005) approximates true Gramians with quadratures

$$\mathbf{P} \approx \sum_{j=1}^{k} \mathbf{T}(t_j)\mathbf{B}\mathbf{B}^*\mathbf{T}^*(t_j)\delta_j = \mathbf{L}_c \mathbf{L}_c^*, \tag{27}$$

where δ_j are the quadrature weights. The low-rank Cholesky factor $\mathbf{L}_c \in \mathbb{R}^{n \times km}$ is

$$\mathbf{L}_c = [\mathbf{B}, \ \mathbf{T}(t_1)\mathbf{B}\sqrt{\delta_1}, \ \ldots, \mathbf{T}(t_k)\mathbf{B}\sqrt{\delta_k}], \tag{28}$$

where $\mathbf{B} = [\mathbf{B}_1, \ \mathbf{B}_2 \ \ldots, \mathbf{B}_m]$; hence, each element of the Cholesky factor $\mathbf{L}_c$ contains snapshots of the flow field computed by the impulse response to each input $\mathbf{B}_i$ at a given time t_j. In this section, m and p denote the total number of inputs (actuators and disturbances) and total number of sensors, respectively.

Similarly, the Cholesky factor $\mathbf{L}_o$ can be obtained from the approximation of the observability Gramian

$$\mathbf{Q} \approx \sum_{j=1}^{k} \mathbf{T}^*(t_j)\mathbf{C}^*\mathbf{C}\mathbf{T}(t_j)\delta_j = \mathbf{L}_o^*\mathbf{L}_o, \tag{29}$$

where $\mathbf{L}_o$ is given by

$$\mathbf{L}_o = [\mathbf{C}^*, \ \mathbf{T}^*(t_1)\mathbf{C}^*\sqrt{\delta_1}, \ \ldots, \mathbf{T}^*(t_k)\mathbf{C}^*\sqrt{\delta_k}]. \tag{30}$$

The snapshots are computed marching backward in time with the adjoint Navier–Stokes equations (26). Each element contains the flow fields obtained from the impulse response to each output $\mathbf{C}^* = [\mathbf{C}_1^*, \ \mathbf{C}_2^*, \ \ldots, \mathbf{C}_p^*]$ at a given time t_j.

Using the low-rank Cholesky factors, the approximate direct and adjoint balanced modes can be computed as follows. As a first step, the singular values decomposition (SVD) of $\mathbf{L}_o^*\mathbf{L}_c$ is formed,

$$\mathbf{L}_o^*\mathbf{L}_c = \mathbf{U}\mathbf{\Sigma}\mathbf{V}^*. \tag{31}$$

The size of $\mathbf{L}_o^*\mathbf{L}_c$ is $kp \times km$. The method is cheaper than the standard method (using full Cholesky factors of size $n \times n$) as long as the number of degree of freedom n is smaller than the number of collect snapshot k times the number of inputs (m) and output (p). The diagonal matrix $\mathbf{\Sigma}$ contains the approximated HSV. The direct and adjoint balanced modes are then given by

$$\mathbf{\Phi}_r = \mathbf{L}_c\mathbf{V}\mathbf{\Sigma}^{-1/2} \qquad \mathbf{\Psi}_r = \mathbf{L}_o^*\mathbf{U}\mathbf{\Sigma}^{-1/2}. \tag{32}$$

The question is, how close $\mathbf{\Phi}_r$ and $\mathbf{\Psi}_r$ using low-rank Cholesky factors are to the "true" balanced modes $\mathbf{\Phi}$ and $\mathbf{\Psi}$ using full-rank factors. In general, numerical tests (Ilak & Rowley 2008; Ahuja 2009; Bagheri *et al.* 2009*a,b*) show that $\mathbf{\Phi}_r$ is a good approximation and that Σ_r are close to the true HSV. This can be attributed, to the low numerical rank of the Gramians, when $m, p \ll n$.

References

AHUJA, S. 2009 Reduction methods for feedback stabilization of fluid flows. PhD thesis, Princeton University, New Jersey.

ÅKERVIK, E., EHRENSTEIN, U., GALLAIRE, F. & HENNINGSON, D. S. 2008 Global two-dimensional stability measures of the flat plate boundary-layer flow. *Eur. J. Mech. B/Fluids* **27**, 501–513.

ANDERSON, B. & MOORE, J. 1990 *Optimal control: Linear Quadratic Methods*. Prentice Hall, New York.

BAGHERI, S., ÅKERVIK, E., BRANDT, L. & HENNINGSON, D. S. 2009*a* Matrix-free methods for the stability and control of boundary layers. *AIAA J.* **47**, 1057–1068.

BAGHERI, S., BRANDT, L. & HENNINGSON, D. S. 2009*b* Input-output analysis, model reduction and control design of the flat-plate boundary layer. *J. Fluid Mech.* **620**, 263–298.

BAGHERI, S., HŒPFFNER, J., SCHMID, P. J. & HENNINGSON, D. S. 2009*c* Input-output analysis and control design applied to a linear model of spatially developing flows. *Appl. Mech. Rev.* **62** (2).

BEWLEY, T., TEMAM, R. & ZIANE, M. 2000 A general framework for robust control in fluid mechanics. *Physica D: Nonlinear Phenomena* **138**, 360–392.

BEWLEY, T. R. 2001 Flow control: New challenges for a new renaissance. *Progr. Aerospace. Sci.* **37**, 21–58.

BEWLEY, T. R. & LIU, S. 1998 Optimal and robust control and estimation of linear paths to transition. *J. Fluid Mech.* **365**, 305–349.

BUTLER, K. & FARRELL, B. F. 1992 Three-dimensional optimal perturbations in viscous shear flow. *Phys. Fluids A* **4**, 1637–1650.

CHEVALIER, M., SCHLATTER, P., LUNDBLADH, A. & HENNINGSON, D. S. 2007 A pseudo spectral solver for incompressible boundary layer flows. Trita-Mek 7. KTH Mechanics, Stockholm, Sweden.

CHOI, H., MOIN, P. & KIM, J. 1994 Active turbulence control for drag reduction in wall-bounded flows. *J. Fluid Mech.* **262**, 75–110.

COHEN, K., SIEGEL, S., MCLAUGHLIN, T., GILLIES, E. & MYATT, J. 2005 Closed-loop approaches to control of a wake flow modeled by the ginzburg-landau equation. *Comp. & Fluids* **34**, 927–949.

DOYLE, J. C. 1978 Guaranteed margins for LQG regulators. *IEEE Trans. Automat. Control* **23**, 756–757.

DOYLE, J. C., GLOVER, K., KHARGONEKAR, P. P. & FRANCIS, B. A. 1989 State-space solutions to standard H_2 and H_∞ control problems. *IEEE Trans. Automat. Control* **34**, 831–847.

DULLERUD, E. G. & PAGANINI, F. 1999 *A course in robust control theory. A convex approach*. Springer Verlag, New York.

GLAD, T. & LJUNG, L. 2001 *Control Theory - Multivariable and Nonlinear Methods*. Taylor and Francis, London, U.K.

GREEN, M. & LIMEBEER, J. N. 1995 *Linear Robust Control*. Prentice Hall, New Jersey.

GRUNDMANN, S. & TROPEA, C. 2008 Active cancellation of artificially introduced Tollmien–Schlichting waves using plasma actuators. *Exp. Fluids* **44** (5), 795–806.

Ho, C. M. & Tai, Y. 1998 Micro-electro-mechanical systems MEMS and fluid flows. *Ann. Rev. Fluid Mech.* **30**, 579–612.

Högberg, M., Bewley, T. R. & Henningson, D. S. 2003 Linear feedback control and estimation of transition in plane channel flow. *J. Fluid Mech.* **481**, 149–175.

Högberg, M. & Henningson, D. S. 2002 Linear optimal control applied to instabilities in spatially developing boundary layers. *J. Fluid Mech.* **470**, 151–179.

Holmes, P., Lumley, J. & Berkooz, G. 1996 *Turbulence Coherent Structures, Dynamical Systems and Symmetry*. Cambridge University Press.

Ilak, M. & Rowley, C. W. 2008 Modeling of transitional channel flow using balanced proper orthogonal decomposition. *Phys. Fluids* **20**, 034103.

Jacobson, S. A. & Reynolds, W. C. 1998 Active control of streamwise vortices and streaks in boundary layers. *J. Fluid Mech.* **360**, 179–211.

Joshi, S. S., Speyer, J. L. & Kim, J. 1997 A systems theory approach to the feedback stabilization of infinitesimal and finite-amplitude disturbances in plane poiseuille flow. *J. Fluid Mech.* **332**, 157–184.

Kalman, R. E. 1960 A new approach to linear filtering and prediction problems. *Trans. ASME, Ser. D. J. Basic Eng.* **82**, 24–45.

Kim, J. & Bewley, T. R. 2007 A linear systems approach to flow control. *Ann. Rev. Fluid Mech.* **39**, 383–417.

Laub, A. 1991 Invariant subspace methods for the numerical solution of riccati equations. In *The Riccati equation* (ed. W. Bittaini, Laub), pp. 163–96. Springer, Berlin.

Laub, A., Heath, M., Paige, C. & Ward, R. 1987 Computation of system balancing transformations and other applications of simultaneous diagonalization algorithms. *IEEE Trans. Automat. Control* **32** (2), 115–122.

Lauga, E. & Bewley, T. R. 2003 The decay of stabilizability with reynolds number in a linear model of spatially developing flows. *Proc. R. Soc. Lond. A.* **459**, 2077–2095.

Lauga, E. & Bewley, T. R. 2004 Performance of a linear robust control strategy on a nonlinear model of spatially developing flows. *J. Fluid Mech.* **512**, 343–374.

Lewis, F. L. & Syrmos, L. V. 1995 *Optimal Control*. John Wiley & Sons, New York.

Monokrousos, A., Åkervik, E., Brandt, L. & Henningson, D. S. 2009 Global optimal three-dimensional disturbances in the blasius boundary-layer flow using time-steppers. To appear.

Moore, B. 1981 Principal component analysis in linear systems: Controllability, observability, and model reduction. *IEEE Trans. Automat. Control* **26** (1), 17–32.

Nordström, J., Nordin, N. & Henningson, D. S. 1999 The fringe region technique and the fourier method used in the direct numerical simulation of spatially evolving viscous flows. *SIAM J. Sci. Comput.* **20** (4), 1365–1393.

Pang, J. & Choi, K.-S. 2004 Turbulent drag reduction by lorentz force oscillation. *Phys. Fluids* **16** (5), L35–L38.

Rempfer, D. & Fasel, H. 1994 Evolution of three-dimensional coheren structures in a flat-plate boundary layer. *J. Fluid. Mech.* **260**, 351–375.

Rowley, C. W. 2005 Model reduction for fluids using balanced proper orthogonal decomposition. *Int. J. Bifurc. Chaos* **15** (3), 997–1013.

SCHMID, P. J. & HENNINGSON, D. S. 2001 *Stability and Transition in Shear Flows*. Springer Verlag, New York.

SEMERARO, O., BAGHERI, S., BRANDT, L. & HENNINGSON, D. S. 2010 Linear control of 3d disturbances on a flat-plate. In *Seventh IUTAM Symposium on Laminar-Turbulent Transition* (eds. P. Schlatter & D. S. Henningson), , vol. 18. Springer.

SMITH, B. L. & GLEZER, A. 1998 The formation and evolution of synthetic jets. *Phys. Fluids* **10** (9), 2281–2297.

STURZEBECHER, D. & NITSCHE, W. 2003 Active cancellation of tollmien–schlichting waves instabilities on a wing using multi-channel sensor actuator systems. *Int. J. Heat Fluid Flow* **24**, 572–583.

Paper 5

5

Global stability of a jet in crossflow

Shervin Bagheri, Philipp Schlatter, Peter J. Schmid[1] and Dan S. Henningson

A linear stability analysis shows that the jet in crossflow is characterized by self-sustained global oscillations for a jet-to-crossflow velocity ratio of 3. A fully three-dimensional unstable steady-state solution and its associated global eigenmodes are computed by direct numerical simulations and iterative eigenvalue routines. The steady flow, obtained by means of selective frequency damping, consists mainly of a (steady) counter-rotating vortex pair (CVP) in the far field and horseshoe-shaped vortices close to the wall. High-frequency unstable global eigenmodes associated with shear layer instabilities on the CVP and low-frequency modes associated with shedding vortices in the wake of the jet are identified. Furthermore, different spanwise symmetries of the global modes are discussed. This work constitutes the first simulation-based global stability analysis of a fully three-dimensional base flow.

1. Introduction

The generic flow configuration of a jet in crossflow is ubiquitous in a great variety of industrial applications, ranging from the control of boundary layer separation to pollutant dispersal from chimneys, from film cooling of turbine blades to the injection of fuel into combustion chambers and furnaces. The flow structures, mixing properties and general dynamics of jets in crossflow have therefore been the subject of numerous experimental and computational studies. In general four main coherent structures (see e.g. Fric & Roshko 1994; Kelso *et al.* 1996; Muppidi & Mahesh 2007, and references therein) characterize the jet in crossflow: (i) the counter-rotating vortex pair, which originates in the near field of the jet, essentially follows the jet trajectory, and dominates the flow field far downstream; (ii) the shear layer vortices which are located at the upstream side of the jet and take the form of ring-like or loop-like filaments; (iii) horseshoe vortices forming in the flat-plate boundary layer upstream of the jet exit, and corresponding wall vortices downstream of the exit close to the wall; and (iv) "wake vortices/upright vortices" which are vertically-oriented shedding vortices in the wake of the jet. The accurate description of these

[1]Laboratoire d'Hydrodynamique (LadHyX), CNRS-École Polytechnique,
F-91128 Palaiseau, France

relevant features is a prerequisite for a sound understanding of the perturbation dynamics of jets in crossflow and a first step in an attempt to manipulate it.

Recent advances in computational methods have enabled global stability analyses of flows with nearly arbitrary complexity and have furnished the possibility to assess fully two- and three-dimensional base flows as to their stability and response behavior to general three-dimensional perturbations. Specifically, the combination of new efficient methods for computing steady-state solutions, such as the selective frequency damping (Åkervik *et al.* 2006), and for treating very large eigenvalue problems, such as the Arnoldi method implemented in the software package ARPACK (Lehoucq *et al.* 1998), based on only minimal modifications of existing numerical simulation codes (see e.g. Barkley *et al.* 2002) has provided the necessary tools for an encompassing study of the disturbance behavior in complex flows.

Previous stability investigations of the jet in crossflow (Alves *et al.* 2007, 2008) have been based on various inviscid base flows adapted from the vortex–sheet model of Coelho & Hunt (1989); they found that growth rates increase as the jet inflow ratio $R \equiv V_{\text{jet}}/U_\infty$ decreases. Recently, Megerian *et al.* (2007) found experimentally that for a low jet inflow ratio $R < 3.5$ external excitations have a small impact on the flow response, in contrast to the significant effect of forcing for larger values of R. This indicates a transition from a globally unstable flow where intrinsic self-sustained global oscillations are present to a convectively unstable flow that exhibits a noise-amplifying behavior (Huerre 2000). In this paper we analyze the global stability of a jet in crossflow for $R = 3$ based on a steady exact solution to the Navier-Stokes equations. Except for preliminary stability studies of a time-averaged mean flow (Schmid 2007), the present analysis constitutes, to the authors' knowledge, the first simulation-based global stability analysis of the viscous jet in crossflow, and, more generally, of a fully three-dimensional base flow.

2. Flow configuration and numerical method

The stability of a jet in crossflow is analyzed via fully-resolved direct numerical simulations based on the incompressible Navier–Stokes equations. The computational domain consists of a rectangular box containing the crossflow boundary layer subject to a zero pressure gradient starting at a finite Reynolds number $Re_{\delta_0^*}$ downstream of the leading edge. All flow quantities are non-dimensionalized using the (constant) free-stream velocity U_∞, the viscosity ν and the displacement thickness δ_0^* at the inlet of the crossflow into the computational box yielding the definition of the Reynolds number as $Re_{\delta_0^*} \equiv U_\infty \delta_0^*/\nu$. The two parameters of the jet are the diameter D and the inflow ratio $R \equiv V_{\text{jet}}/U_\infty$, where V_{jet} is the centerline jet velocity. The flow parameters of the present study, $Re_{\delta_0^*} = 165$, $\delta_0^*/D = 1/3$ and $R = 3$, are in the same parameter range as for example Kelso *et al.* (1996).

The jet is introduced via non-homogeneous boundary conditions of the wall-normal velocity component at the wall ($y = 0$) at a distance downstream of

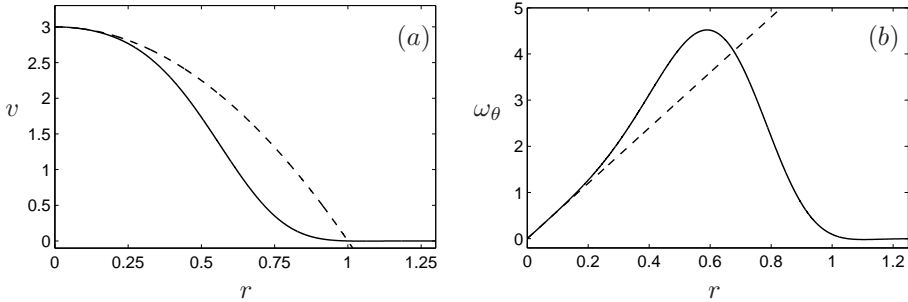FIGURE 1. The wall-normal velocity v (a) and azimuthal vorticity $\omega_\theta = -\partial_r v$ (b) of the imposed jet profile in the present study given by equation (1) is shown with solid black lines and the standard Poiseuille parabolic profile is shown with dashed lines. Note that the streamwise u and spanwise w velocities are assumed to be zero everywhere at $y = 0$.

the inlet. This is in slight contrast to realistic configurations where the jet emanates from a nozzle, and interactions between the crossflow and the flow near the nozzle edge have been observed (Kelso *et al.* 1996). The direct numerical simulations of the jet in section 3 demonstrate that even with the jet modeled as an inhomogeneous boundary condition the main flow characteristics, such as the counter-rotating vortex pair, shear layer vortices and horse-shoe vortices are faithfully reproduced. Moreover, the instabilities explored in the present study are most likely due to the interaction of the crossflow and the shear layer further away from the wall (Megerian *et al.* 2007). The jet profile, mimicking the (laminar) parabolic velocity profile of pipe Poiseuille flow, is imposed as

$$v(r) = R(1 - r^2) \exp\left(-(r/0.7)^4\right), \tag{1}$$

with r denoting the distance from the jet center $(x_{\text{jet}}, z_{\text{jet}})$, normalized by half the jet diameter D. Due to the "super"–Gaussian function, the profile has continuous derivatives for all r without a large modification of the parabolic shape near the jet centerline. The velocity and vorticity of the profile defined by (1) are compared to the parabolic profile $(R(1 - r^2))$ in figure 1.

The simulation code uses a Fourier-Chebyshev spectral method to solve the three-dimensional time-dependent incompressible Navier–Stokes equations over a flat plate, with details given in Chevalier *et al.* (2007). At the downstream edge of the domain a fringe region is added that forces the flow back to the inlet profile and thus allows the treatment of the streamwise direction by Fourier methods; periodic boundary conditions are imposed in the spanwise direction, whereas in the wall-normal direction no-slip (at $y = 0$) and Neumann (at $y = L_y$) conditions are enforced. The computations in this study have been performed with a resolution of $256 \times 201 \times 144$ grid points in a computational
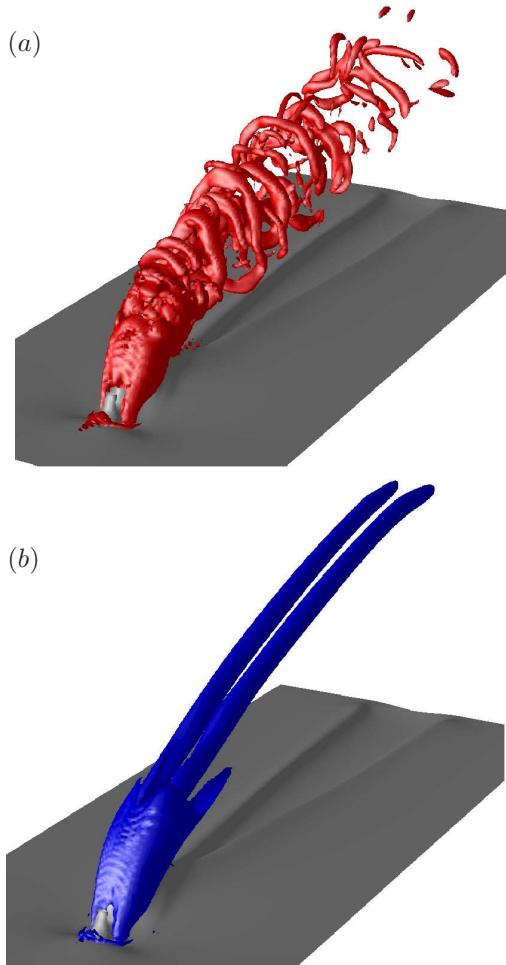
FIGURE 2.   (a-b): The red and blue isocontours correspond to vortical structures visualized by the λ_2-criterion (Jeong & Hussain 1995) at a level $\lambda_2 = -0.09$. The gray contours depicts the streamwise velocity component $u = 0.3$ near the flat plate. (*a*) Snapshot of the unsteady velocity field in a fully-developed state at $t = 151$. (*b*) Converged steady base velocity field.

box $(L_x, L_y, L_z) = (75, 20, 30)$ on a Linux cluster employing between 48 and 72 cores.

3. Observations from direct numerical simulations

The present simulation of a jet in crossflow starts with a laminar Blasius profile above a flat plate. At time $t \geq 0$, the inhomogeneous boundary condition is imposed to introduce the jet into the computational domain; after approximately 50 time units, a statistically stationary state can be observed. A snapshot at $t = 151$ of the flow development is shown in figure 2(a), where isocontours of the λ_2-criterion (Jeong & Hussain 1995) and the streamwise velocity u are displayed. Although both the boundary layer of the crossflow as well as the incoming flow pertaining to the jet are laminar, their interaction results in a highly unsteady flow field. At the upstream edge of the jet body, where the shear layer is strongest, a flow instability develops which leads to the breakdown of the laminar flow into a sequence of small-scale, half-ring shaped vortices. As these structures convect downstream their orientation gradually aligns with the free stream after which they dissipate due to viscous effects. Careful inspection of the velocity fields of the unsteady direct simulations further reveals well-known flow features as reported in e.g. Fric & Roshko (1994) and Kelso *et al.* (1996): Horseshoe-shaped vortices, located inside the crossflow boundary layer, can be detected which wrap around the nozzle and eventually transport fluid from the outer boundary layer region closer to the wall, resulting in a high-speed region around the plane $z = 0$ which widens in the downstream direction (see the gray contours of the u-velocity component depicted in figure 2a). In addition, the core of the jet is composed of two large-scale counter-rotating vortices on which shear-layer instabilities develop. However, wake vortices connecting the crossflow boundary layer and the jet body, reminiscent of a vortex street behind bluff bodies, are not visible in the present simulation. As stated by Fric & Roshko (1994) these vortices appear preferably at higher inflow ratios R and Reynolds numbers Re. For lower R and Re like in our simulation, the spanwise symmetry of the flow field is sustained at all times.

To extract and quantify the observed oscillatory behavior of the flow we place two probes into the computational domain: one probe is located within the jet shear layer slightly upstream of the jet body, approximately three jet diameters from the wall; the other probe is positioned downstream of the jet orifice close to the wall. After a transient period, the time signals of the streamwise velocity u from these probes clearly show two distinct frequencies λ_i: in the jet shear layer a period $T_1 = 2\pi/\lambda_i \approx 5.7$ can be estimated (red line in figure 3a), whereas in the wake of the jet a much longer period of $T_2 \approx 60$ is present (red line in figure 3c). The associated Strouhal numbers, defined as $St = D/(TV_{jet})$, are $St = 0.17$ and $St = 0.016$, respectively. It is interesting to note that the velocity signal recorded by the second probe is negative, i.e., $u \approx -1.1$, which indicates that downstream of the jet exit a region of reversed flow exists. The signal from that region shows oscillations at a rather low frequency. This separation region appears to only oscillate in a spanwise-symmetric manner since the symmetry of the flow field near the jet exit is not broken, given our parameter settings. The frequency measured in the jet shear
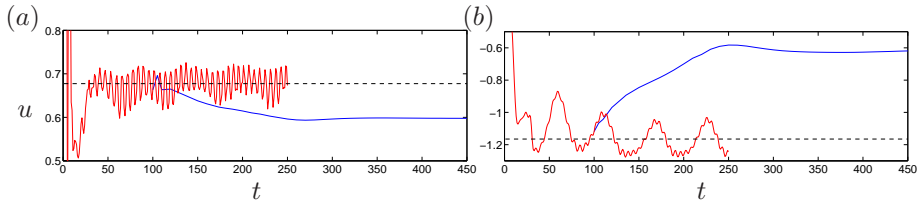
(a)

(b)

FIGURE 3. (a) and (b) show time signals corresponding to the (streamwise) u-component of two probes in the flow field (see text). The red line represents the unsteady flow, whereas the blue line corresponds to the simulation stabilized by SFD which is active for $t > 100$. The dashed lines indicate the time-averaged values of the DNS simulation.

layer corresponds to the incipient vortical structures caused by the presence of the incoming jet. However, even in the shear layer the lower frequency present in the wake downstream of the nozzle is clearly felt, manifesting itself as a slow modulation of the probe signals. This indicates that the entire jet is oscillating with that long period T_2.

4. Global stability analysis

Using the direct numerical simulation code described in section 2 a global stability analysis can be performed in two steps: we first compute a steady solution to the nonlinear Navier–Stokes equations using the selective frequency damping (SFD) method, after which we determine the eigenmodes of Navier-Stokes equations linearized about this base flow using the Arnoldi algorithm from the parallel ARPACK library.

4.1. *The three-dimensional base flow*

When a flow under consideration is either globally unstable or strongly convectively unstable, the computation of a steady-state solution of the Navier–Stokes equations poses a challenging task. Newton iteration methods are often applied, but a different approach that accomplishes the task with less programming effort is favored here. This technique, known as selected frequency damping (Åkervik *et al.* 2006), adds a forcing term

$$-\chi(\mathbf{u} - \hat{\mathbf{u}}),$$

to the right-hand side of the Navier–Stokes equations governing the evolution of the flow $\mathbf{u} = (u, v, w)$. This results in the convergence toward a temporally low-pass-filtered state $\hat{\mathbf{u}}$ of the nonlinear equations using the differential form of an exponential (causal) filter (Pruett *et al.* 2003)

$$\partial_t \hat{\mathbf{u}} = (\mathbf{u} - \hat{\mathbf{u}})/\Delta.$$

The filter coefficients have to be chosen to sufficiently damp the lowest unstable frequencies; information about these frequencies can straightforwardly be
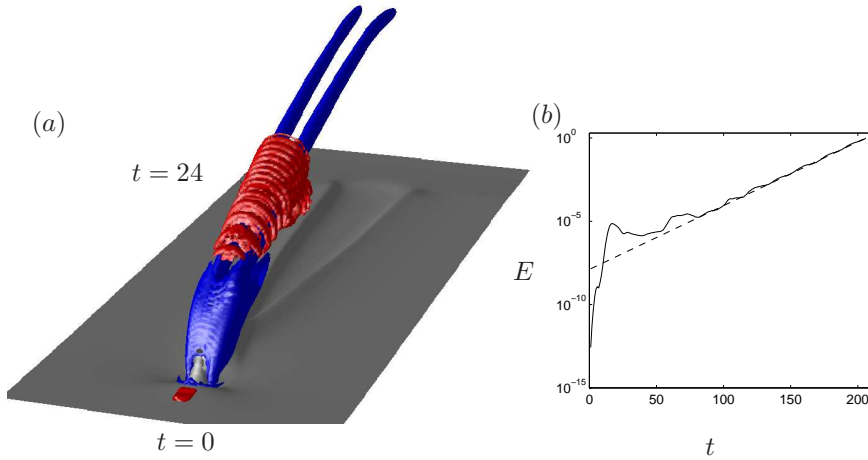
(a)

$t = 24$

$t = 0$

(b)

E

FIGURE 4. In (a) the two structures depicted with red λ_2-isocontours represent, respectively, a symmetric initial perturbation upstream of the jet at $t = 0$ and the perturbation at later time, $t = 24$. The gray and blue isocontours indicate components of the steady base flow as described in the caption of figure 2. In (b) the time evolution of the perturbation energy (solid line) is compared to the growth rate (dashed line) of the most unstable symmetric global mode, marked with S_3 in figures 5(a) and (c).

extracted from the simulations, see figures 3(a) and (b). The same figure also shows the effect of the filtering, turned on at $t = 100$ for $\chi = 1$ and $\Delta = 2$. Moreover, we could observe that after 220 time units, $\|\partial_t \mathbf{u}\|$ decays at an exponential rate, and at $t = 450$ the norm is three orders of magnitude smaller than the unsteady flow, yielding a sufficiently converged steady solution of the nonlinear Navier–Stokes equations and thus our three-dimensional base flow (denoted $\mathbf{U}$ hereafter).

The base flow is shown in figure 2(b) with blue (λ_2) and gray (u velocity) contour levels. The (CVP) is evident as two distinct tubes of negative λ_2-isocontours, deflected along the jet trajectory and slowly decaying in the streamwise direction. Physically, the appearance of the CVP can be explained by the accumulation of the azimuthal vorticity related to the injected jet fluid, which is redirected in the direction of the jet trajectory due to the interaction with the crossflow (Fric & Roshko 1994). Additionally, the steady state features the horseshoe-shaped vortex forming around the jet nozzle. Due to this vortex, a small region of separated flow appears just upstream of the jet nozzle. Moreover, a larger region with negative streamwise velocity is detected at the downstream edge of the nozzle causing entrainment of fluid from the crossflow into the jet.

By construction (Åkervik *et al.* 2006), the converged solution obtained by SFD satisfies the steady nonlinear Navier–Stokes equations. Alternatively, a linear stability analysis can be performed of the time-averaged mean flow. However, this flow is not an equilibrium of the Navier–Stokes equations and, therefore, not a suitable choice for a base flow when the aim is to determine its stability. The time-averaged mean flow may, however, for certain flow configurations, be appropriate as a base flow for predicting the dominant shedding frequencies (Barkley 2006; Sipp & Lebedev 2007). The difference between steady and time-averaged solutions is exemplified in figures 3(*a*) and (*b*), in which the time signals of the probes pertaining to the time-averaged solution (black dashed lines) are clearly different from those obtained using the steady solution (solid blue lines).

A first numerical experiment probing the global stability or instability of the steady flow consists of an initial Gaussian pulse released at $t = 0$ inside the boundary layer just upstream of the jet exit (indicated with red λ_2-contour levels in figure 4*a*). The linear response of the base flow after 24 time units, also shown in figure 4(*a*), is characterized by the formation of a wavepacket which significantly grows in amplitude as it travels along the curved base flow. Quantitative information about the growth rate (figure 4*b*) and local wavenumber of this wavepacket can easily be extracted from the simulation data, but a more general stability analysis is performed next using a "time-stepper" approach which extracts the global modes from direct numerical simulations.

4.2. *Stability analysis using the Arnoldi method and a time-stepper approach*

The stability of **U** is determined by the three-dimensional global modes,

$$\phi_j(x, y, z) \exp(\lambda_j t), \quad j = 1, \ldots, m$$

of the linearized Navier-Stokes operator, denoted here by the matrix **A**. Both the eigenmodes ϕ_j and the eigenvalues λ_j are in general complex valued. The temporal growth rate is given by the imaginary part $\lambda_{j,i}$ and the frequency by the real part $\lambda_{j,r}$.

The size of our problem (**A** would be approximately a $10^7 \times 10^7$ matrix) prohibits matrix methods and suggests the use of iterative techniques combined with our numerical simulations. In general, the iterative technique is based on the orthogonal projection of the large matrix onto a lower-dimensional subspace, which will result in a significantly smaller system that can be solved using direct methods. A particularly useful subspace is the Krylov subspace $\mathcal{K}$ spanned by snapshots taken from flow fields **u** separated by a constant time interval Δt,

$$
\begin{aligned}
\mathcal{K} &= \text{span}\left\{ \mathbf{u}(\boldsymbol{x}, 0), \mathbf{u}(\boldsymbol{x}, \Delta t), \mathbf{u}(\boldsymbol{x}, 2\Delta t), \ldots, \mathbf{u}(\boldsymbol{x}, (m-1)\Delta t) \right\}, &\text{(2a)}\\
&= \text{span}\left\{ \mathbf{u}(\boldsymbol{x}, 0), \mathbf{B}\mathbf{u}(\boldsymbol{x}, 0), \mathbf{B}^2\mathbf{u}(\boldsymbol{x}, 0), \ldots, \mathbf{B}^{m-1}\mathbf{u}(\boldsymbol{x}, 0) \right\} &\text{(2b)}
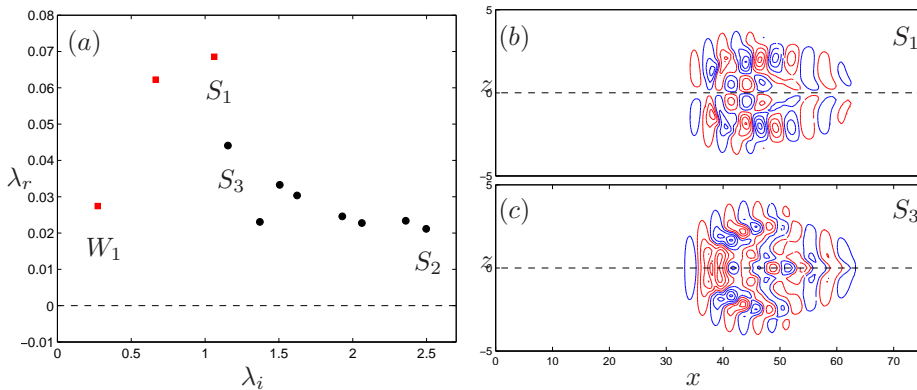\end{aligned}
$$

FIGURE 5. (*a*) The spectrum of the jet in crossflow, where λ_r is the growth rate and λ_i the frequency. High-frequency eigenvalues marked with black circles have symmetric eigenmodes, whereas the red squares have anti-symmetric ones. The shear layer modes marked with S_1 and S_2 are shown in figures 6 and 7, respectively. The wake mode marked with W_1 is shown in figure 8 and the most unstable symmetric mode marked with S_3, triggered by the response of the base flow to a symmetric initial condition, is shown in figure 4. (*b*)-(*c*) Contour levels at a $xz-$plane with $y = 17$ of the u velocity (blue is negative, red is positive) of S_1 (*b*) and S_3 (*c*).

where $\mathbf{B} = \exp(\mathbf{A}\Delta t)$ and $\mathbf{u}(\boldsymbol{x}, 0)$ is an initial guess that should contain nonzero components of the sought-after global modes. The matrix exponential $\mathbf{B}$ is simply an evolution operator; its action is a numerical simulation of the linearized Navier-Stokes equations for time[2] Δt. Note that the eigenmodes of $\mathbf{B}$ are the same as those of the system matrix $\mathbf{A}$ if Δt is chosen properly, i.e. so that it reflects the characteristic time scale of the physical structures in the flow. More specifically, the choice Δt is a balance between the time scale given by the Nyquist criterion[3] and a sufficient temporal separation of the Krylov vectors to ensure convergence of the iterative method.

The Krylov subspace is orthonormalized (standard L_2 vector norm) via a m-step Arnoldi factorization, yielding an unitary basis $\mathbf{V}$ onto which the matrix exponential is projected according to $\mathbf{B} \approx \mathbf{V}\mathbf{H}\mathbf{V}^{\mathbf{T}}$ leading to a small $m \times m$ eigenvalue problem of the form $\mathbf{H}\mathbf{S} = \boldsymbol{\Sigma}\mathbf{S}$. The eigenmodes with the

---

[2]The actual time-step $\delta t \approx 10^{-3}$ of these simulations depends on the CFL-condition and is much smaller than the sampling period Δt.

[3]To avoid aliasing Δt must be small enough such that two sampling points in one period of the highest frequency mode are obtained. See Bagheri *et al.* (2009) for further numerical details.

largest growth rates are recovered according to $\mathbf{\Phi} = (\boldsymbol{\phi}_1, \ldots, \boldsymbol{\phi}_m) = \mathbf{VS}$, and the eigenvalues λ_j are given by $\lambda_j = \ln(\sigma_j)/\Delta t$ with $\mathbf{\Sigma} = \mathrm{diag}(\sigma_1, \ldots, \sigma_m)$.

The computation of the significantly lower-dimensional matrix $\mathbf{H}$ from direct numerical simulations is accomplished by the implicitly restarted Arnoldi method (IRAM) implemented in the software package ARPACK. The number of flow field snapshots separated by $\Delta t = 0.25$ required for convergence of the 22 eigenmodes with the largest growth rates was 1800. However, thanks to IRAM, the Krylov subspace is only of the order $m \approx 60$ and the Arnoldi procedure is restarted with a new improved initial guess, $\mathbf{u}(\boldsymbol{x}, 0)$, repeatedly until convergence. The first initial guess was random noise. See e.g. Lehoucq *et al.* (1998) for details on IRAM.

The residual was $\|\mathbf{B}\boldsymbol{\phi}_j - \sigma_j \boldsymbol{\phi}_j\| < 10^{-6}$ for all eigenmodes, although the residuals of most of the eigenmodes are orders of magnitude smaller than this[4].

4.3. *Global spectrum and global modes*

In figure 5(a) the global spectrum containing the 11 most unstable eigenvalues is shown. The global eigenmodes corresponding to eigenvalues marked with circles are symmetric with respect to the $z-$axis, whereas the modes associated with eigenvalues marked with squares are anti-symmetric. Note that the symmetry refers to the u and v velocity components, w shows the opposite symmetry. It should be mentioned that no symmetry condition was imposed in the direct numerical simulations. The streamwise velocity of two modes (S_1 and S_3) with opposite symmetries are shown figure 5(b) and (c). A symmetric disturbance in the flow (as shown in figure 4a) will trigger the growth of a global mode with the same symmetry only. This is exemplified in figure 4(b), where the solid line shows the time-evolution of the energy $E = \int \mathbf{u}^T \mathbf{u} d\boldsymbol{x}$ of a symmetric initial perturbation and the dashed line shows the energy of most unstable symmetric global mode with the growth rate, $\lambda_r = 0.044$ marked with S_3 in the spectrum (figure 5a). This serves as a further validation that the spectrum provides the correct growth rates.

In figure 6, red λ_2-isocontours pertaining to the most unstable (antisymmetric) mode, oscillating with a period of $T = 5.9$ time units, are shown together with the base flow (blue and gray isocontours) as described earlier in figure 2(b). The mode takes the shape of a wavepacket located on the counter-rotating vortex pair with a distinct spatial wavelength and can therefore be associated with instabilities rising on the shear layer. The amplitude near the wall of this mode is more than one order of magnitude smaller than on the CVP. It is known that the jet width extends more toward the leeward side. It

---

[4]Within the time-stepping framework, the linear stability analysis is robust with respect to the spatial resolution if it is, as in our case, based on fully resolved direct numerical simulations. A convergence test was performed in the following way: The direct numerical simulation with $\approx 50\%$ fewer gridpoints of the linear response of the base flow to an initial condition resulted in a growth rate that was only $\approx 2\%$ different from the growth rate predicted by the original resolution, albeit the significant reduction in resolution.
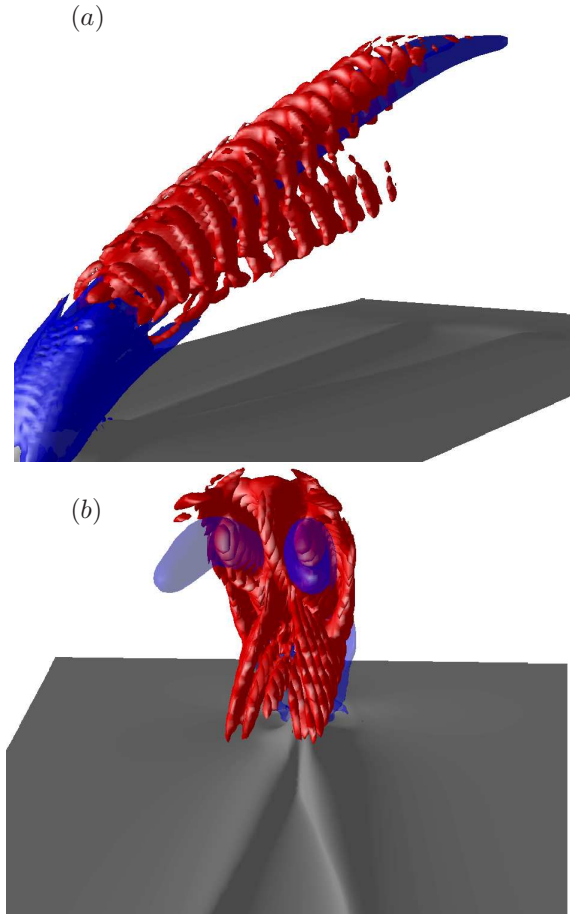
(a)

(b)

FIGURE 6. The most unstable mode $((\lambda_r, \lambda_i) = (0.068, 1.06))$ seen from two different angles, marked with S_1 in figure 5 is shown with red λ_2-isocontours. The base flow is shown in blue (λ_2) and gray (u-velocity).

is interesting to note that the the global mode in figure 6 also contains vortical structures in this region.

Next, a symmetric high-frequency mode is shown in figure 7. The mode is a localized wavepacket wrapped around the counter-rotating vortex pair without any vortical structures close to the wall. The other symmetric modes have a similar structure but with larger wavelengths and lower frequencies. In particular the nonlinear shedding of the shear layer vortices with $T = 5.7$ is closely matched by the linear frequency of the most unstable symmetric mode (S_3) $T = 5.4$. It is interesting to note that the most unstable shear-layer mode has an opposite symmetry to the all the high-frequency shear-layer modes.
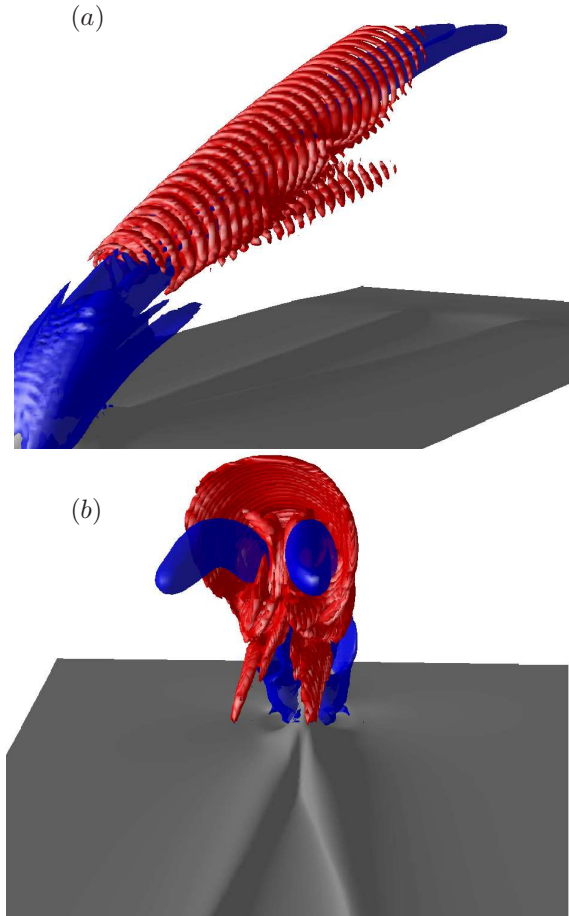
(a)

(b)

FIGURE 7. The mode with the highest frequency $((\lambda_r, \lambda_i) = (0.021, 2.49))$ viewed from two different angles, marked with S_2 in figure 5, is shown with red λ_2-isocontours and base flow in blue (λ_2) and gray (u-velocity).

Whereas the latter modes are wrapped around the CVP, the former is directly located on the CVP, as can be seen by comparing figures 6(b) and 7(b).

The vortical structures near the wall become more pronounced with decreasing temporal frequencies. The spanwise velocity component near the wall (green and black contours) of the anti-symmetric mode with the lowest frequency λ_i is shown in figure 8. Of all the modes, this global mode has the most pronounced spatial structure at the wall in the wake of the jet. It is thus assumed that this mode, which oscillates at a period of $T = 23$ time units, is related to the low frequency self-sustained oscillations observed in our DNS simulation (see figure 3b). However, this unstable wake mode has a smaller
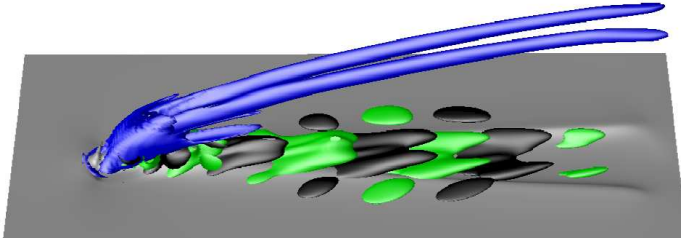
Figure 8. Isocontours of the spanwise velocity component pertaining to the low-frequency mode $((\lambda_r, \lambda_i) = (0.027, 0.27))$, marked W_1 in the spectrum (figure 5) are shown in green (negative w) and black (positive w). Note that here only the structures near the wall are shown, which are approximately one order of magnitude smaller in amplitude than the structures on the CVP. The base flow is again in blue (λ_2) and gray (u-velocity).

growth rate than the shear layer mode, indicating the dominance of the shear layer instabilities in the present base flow.

From the numerical simulation, we could detect that close to the wall, approximately $2 - 3$ jet diameters from the nozzle along the jet trajectory, shear layer vortices were shed periodically into the downstream direction. The largest amplitude of the global eigenmodes, on the other hand, is concentrated further downstream on the jet trajectory of the base flow. This spatial separation of the linear global modes (downstream) and the shedding region (upstream) has been observed for various globally unstable flows (Chomaz 2005) and can be explained by the presence of a "wavemaker". From a local viewpoint this indicates that a pocket of absolute instability feeds regions of convective instability located further downstream. From a global viewpoint, which is more suitable due to the non-parallel nature of the base flow, this region is related to location where the spatial overlap of the global mode with its associated adjoint mode is significant. A localized feedback force of the perturbation velocity in this region results in the largest drift of the eigenvalue (Giannetti & Luchini 2007). Moreover, using the adjoint eigenmodes, a sensitivity analysis can be employed to predict regions where variations of the unstable eigenvalues to base flow modifications are large (Marquet *et al.* 2008). Further analysis is in progress to identify these dynamically important regions.

In general, linear (and weakly nonlinear) stability theory is able to predict shedding frequencies in the unstable regime close to the critical velocity ratio. A large deviation between the linear and nonlinear saturated frequencies can to some extent be related to a large difference between the time-averaged mean flow and the steady solution, i.e. the mean flow distortion (see recent

work by Barkley 2006; Sipp & Lebedev 2007). By comparing the signals in figures 3(a) and (b) pertaining to the mean (dashed) and steady flow (blue), it can be observed that the mean flow distortion near the wall is at least six times larger than on the shear layer. Similar to observations of the wake behind a cylinder (Barkley 2006), the steady separation region (downstream of the jet exit) is altered due to the saturated global modes yielding a significantly larger separation bubble and mean flow distortion. The jet shear layer on the other hand is only slightly modified by the saturated modes.

5. Conclusions

Observations of two self-sustained synchronized oscillations of a jet in crossflow at $R = 3$ by direct numerical simulations places this flow configuration into the category of globally unstable flows. This observation has been confirmed by a global stability analysis based on a three-dimensional steady base state obtained after suppressing global instabilities by selective frequency damping (SFD). The most unstable global modes with high frequencies are compact and represent localized wavepackets on the CVP. These modes are associated with the loop-shaped vortical structures on the jet shear layer. The global modes with lower frequencies, on the other hand, also have a significant amplitude in the wake of the jet close to the wall and can be associated with less pronounced vortical structures arising downstream of the jet in the boundary layer.

The existence of global eigenmodes justifies the global stability approach as an appropriate tool to describe the inherent and dominant dynamics of the jet in crossflow. With the same tool even less pronounced instabilities, *e.g.* associated with the "hanging vortices" formed in the skewed mixing layers on the lateral edges of the jet (Yuan *et al.* 1999) might be detected and extracted from the direct numerical simulations as global modes with growth rates much less than the dominant one presented in this paper. A more encompassing global stability analysis of the jet in crossflow, including a parameter study, is in progress; the presented results, however, form a first and important step in quantifying the stability characteristics of a jet in crossflow and, in general, of fully three-dimensional base flows.

References

ÅKERVIK, E., BRANDT, L., HENNINGSON, D. S., HŒPFFNER, J., MARXEN, O. & SCHLATTER, P. 2006 Steady solutions of the Navier-Stokes equations by selective frequency damping. *Phys. Fluids* **18** (068102), 1–4.

ALVES, L., KELLY, R. & KARAGOZIAN, A. 2007 Local stability analysis of an inviscid transverse jet. *J. Fluid Mech.* **581**, 401–418.

ALVES, L., KELLY, R. & KARAGOZIAN, A. 2008 Transverse-jet shear-layer instabilities. part 2. linear analysis for large jet-to-crossflow velocity ratio. *J. Fluid Mech.* **602**, 383–401.

BAGHERI, S., ÅKERVIK, E., BRANDT, L. & HENNINGSON, D. S. 2009 Matrix-free methods for the stability and control of boundary layers. *AIAA J.* **47** (5), 1057–1068.

BARKLEY, D. 2006 Linear analysis of the cylinder wake mean flow. *Europhys. Lett.* **75**, 750–756.

BARKLEY, D., GOMES, M. G. & HENDERSON, R. D. 2002 Three-dimensional instability in flow over a backward-facing step. *J. Fluid Mech.* **473**, 167–190.

CHEVALIER, M., SCHLATTER, P., LUNDBLADH, A. & HENNINGSON, D. S. 2007 SIM-SON - A Pseudo-Spectral Solver for Incompressible Boundary Layer Flows. *Tech. Rep.* TRITA-MEK 2007:07, ISBN 978-91-7178-838-2. KTH Mechanics, Stockholm, Sweden.

CHOMAZ, J. M. 2005 Global instabilities in spatially developing flows: Non-normality and nonlinearity. *Ann. Rev. Fluid Mech.* **37**, 357–392.

COELHO, S. & HUNT, J. 1989 The dynamics of the near field of strong jets in crossflows. *J. Fluid Mech.* **200**, 95–120.

FRIC, T. F. & ROSHKO, A. 1994 Vortical structure in the wake of a transverse jet. *J. Fluid Mech.* **279**, 1–47.

GIANNETTI, F. & LUCHINI, P. 2007 Structural sensitivity of the first instability of the cylinder wake. *J. Fluid Mech.* **581**, 167–197.

HUERRE, P. 2000 Open shear flow instabilities. In *Perspectives in Fluid Dynamics*, pp. 159–229. Cambridge University Press.

JEONG, J. & HUSSAIN, F. 1995 On the identification of a vortex. *J. Fluid Mech.* **285**, 69–94.

KELSO, R., LIM, T. & PERRY, A. 1996 An experimental study of round jets in cross-flow. *J. Fluid Mech.* **306**, 111–144.

LEHOUCQ, R., SORENSEN, D. & YANG, C. 1998 *ARPACK Users' guide: Solution of Large-Scale Eigenvalue problems with implicitly restarted Arnoldi methods.* SIAM, Philadelphia.

MARQUET, O., SIPP, D. & JACQUIN, L. 2008 Sensitivity analysis and passive control of cylinder flow. *J. Fluid Mech.* **615**, 221–252.

MEGERIAN, S., DAVITIAN, L., ALVES, L. & KARAGOZIAN, A. 2007 Transverse-jet shear-layer instabilities. Part 1. Experimental studies. *J. Fluid Mech.* **593**, 93–129.

MUPPIDI, S. & MAHESH, K. 2007 Direct numerical simulation of round turbulent jets in crossflow. *J. Fluid Mech.* **574**, 59–84.

PRUETT, C. D., GATSKI, T. B., GROSCH, C. E. & THACKER, W. D. 2003 The

temporally filtered Navier-Stokes equations: Properties of the residual stress. *Phys. Fluids* **15** (8), 2127–2140.

SCHMID, P. J. 2007 Nonmodal stability theory. *Ann. Rev. Fluid Mech.* **39**, 129–162.

SIPP, D. & LEBEDEV, A. 2007 Global stability of base and mean flows: a general approach and its applications to cylinder and open cavity flows. *J. Fluid Mech.* **593**, 333–358.

YUAN, L. L., STREET, R. L. & FERZIGER, J. H. 1999 Large-eddy simulation of a round jet in crossflow. *J. Fluid Mech.* **379**, 71–104.

Paper 6

6

Self-sustained global oscillations
in a jet in crossflow

Philipp Schlatter, Shervin Bagheri and Dan S. Henningson

A jet in crossflow with an inflow ratio of 3, based on the maximum velocity of the parabolic jet profile, is studied numerically. The jet is modeled as an inhomogeneous boundary condition at the crossflow wall. We find two fundamental frequencies, pertaining to self-sustained oscillations in the flow, using full nonlinear direct numerical simulation (DNS) as well as a modal decomposition into global linear eigenmodes and proper orthogonal decomposition (POD) modes; a high frequency which is characteristic for the shear-layer vortices and the upright vortices in the jet wake, and a low frequency which is dominant in the region downstream of the jet orifice. Both frequencies can be related to a region of reversed flow downstream of the jet orifice. This region is observed to oscillate predominantly in the wall-normal direction with the high frequency and in the spanwise direction with the low frequency. Moreover, the steady-state solution of the governing the Navier–Stokes equations clearly shows the horseshoe vortices and the corresponding wall vortices further downstream, and the emergence of a distinct counter-rotating vortex pair high in the free stream. It is thus found that neither the inclusion of the jet pipe nor unsteadiness is necessary to generate the characteristic counter-rotating vortex pair.

1. Introduction

A large number of studies have been devoted to the flow case of a jet in crossflow, mainly due to its technical relevance in, for example film cooling, fuel injection, but also dispersion of pollutants from e.g. smokestacks or in assessing V/STOL airplanes. The flow structures, mixing properties and complex dynamics have therefore been studied extensively by means of experiments and – more recently – by computer simulations. In general four main coherent structures (see e.g. Fric & Roshko 1994; Kelso *et al.* 1996; Smith & Mungal 1998; Yuan *et al.* 1999; Cortelezzi & Karagozian 2001; Muppidi & Mahesh 2006; Megerian *et al.* 2007, and references therein) characterize the jet in crossflow; (i) the counter-rotating vortex pair which is thought to originate in the near field and remains the most dominant structure of the flow field far downstream; (ii) the shear-layer vortices which initially take the form of ring-like or loop-like shapes and cause the jet to disintegrate into smaller vortices, (iii) the horseshoe

vortices formed upstream of the jet nozzle, and their extension downstream of the nozzle, usually termed wall vortices, and (iv) the upright vortices populating the jet wake between the jet trajectory and the flat plate. Depending on the exact parameter settings (boundary-layer thickness, jet radius and inflow profile, jet speed, turbulence levels in crossflow and pipe, etc.) the specific characteristics and relative importance of the above main structures might vary considerably (see e.g. Fric & Roshko 1994).

Traditionally, studies of the jet in crossflow have been concerned with the location and scaling of the centerline trajectory, the mean and fluctuating velocity properties and the mixing properties at various jet-to-crossflow ratios R. Despite the large number of studies there are still a number of open questions related to more fundamental issues; the dominant mechanism for the generation of e.g. the counter-rotating vortex pair (Kelso *et al.* 1996; Cortelezzi & Karagozian 2001; Muppidi & Mahesh 2006), or the upright vortices and their relation to the observed low-frequency wiggling of the whole jet configuration that are of interest (Fric & Roshko 1994). Moreover, there is a lack of consensus of the origin of the shear-layer vortices. Numerous studies argue that the main instability mechanism is of Kelvin-Helmholtz (KH) type due to the shearing between the jet and the main stream (see e.g. Kelso *et al.* 1996), whereas other studies (Blanchard *et al.* 1999) indicate that the elliptic instability of the steady longitudinal counter-rotating vortex pair must be taken into account when describing the instability mechanisms of the jet. As we discuss in this paper, both of these physical mechanisms could be present at the same time and the resulting combined *global* instability dynamics should be considered.

Supporting evidence that the jet in crossflow is able to self-sustain global oscillations was provided by Megerian *et al.* (2007) by analyzing single-point spectral data. They found the spectrum peaks rather insensitive to periodic forcing when $R < 3$. The same self-sustained oscillatory behavior have been observed in other experiments (Blanchard *et al.* 1999), and also in the study by Kelso *et al.* (1996) where the frequency of the shear layer instability could not be affected via forcing close to the jet nozzle. However, to ascertain that a flow exhibits self-sustained oscillatory behavior via a bifurcation, a global instability in time from its inception through its small-amplitude linear stage to saturation has to be traced in order to evaluate the coefficients of the Landau equation. Such a study remains to be undertaken for the jet in crossflow. A related, but certainly easier and more feasible task is a linear global stability analysis of a steady solution at a single velocity ratio; in case of a global instability, the steady solution will give rise to a coherent array of vortex structures which oscillate with the frequency of the global modes. However, the nonlinear saturation of the unstable modes and the ultimate nonlinear shedding frequencies cannot be determined by the linear analysis. Note that for highly unsteady flows, such an analysis can only be performed numerically, since the flow never visits unstable equilibria; one observes only the nonlinear dynamics on attractors, resulting from the global instability.

Recently, Bagheri *et al.* (2009*b*) performed the first linear global stability analysis of a steady solution of the jet in crossflow at $R = 3$ using a numerical simulations in conjunction with iterative techniques. They found a number of unstable linear global modes; high frequency modes were predominantly located on the jet trajectory and low-frequency modes near the wall region downstream of the jet nozzle. The global analysis suggests the jet in crossflow may self-sustaining global oscillations. Indeed, time series of probes of DNS calculations showed two fundamental frequencies; one high frequency oscillations associated to unsteady jet shear-layer vortices and one with low frequency associated with oscillating wall structures.

The present study aims at further characterizing the self-sustained oscillatory behavior of the jet in crossflow at $R = 3$. In particular, the following goals are set:

(i) A new nonlinear DNS data set with long time history has been computed where asymmetric flow structures have been initially triggered (in the previous DNS by Bagheri *et al.* 2009*b*, the spanwise symmetry was sustained for all times). The symmetric and anti-symmetric data are compared in order to identify if asymmetry is a necessary ingredient for vortex shedding.

(ii) The various steady flow structures of the jet in crossflow, i.e. the two distinct nearly longitudinal vortex tubes (counter-rotating vortex pair, CVP), the shear layer and separated regions of the steady solution, are discussed and compared the time-averaged mean flow.

(iii) The relation of the unstable global modes to Kelvin-Helmholtz instability, elliptic type of instabilities and the unsteady separated region are discussed qualitatively.

(iv) The fundamental frequencies of the flow are associated to the most energetic global structures in the flow obtained via proper orthogonal decomposition (POD).

The study of a jet in crossflow is challenging for experimental as well as numerical work. The flow is always fully three-dimensional and spatially developing. Moreover, proper inflow conditions need to be specified for both the crossflow boundary layer and the jet exit, and the various shedding frequencies in the flow call for long observation times. Numerically, the jet in crossflow has been initially studied via large-eddy simulation (LES) by Yuan *et al.* (1999), where the authors could find reasonable agreement with experiments performed with similar parameters, and a first classification of the flow structures could be performed. A series of well-resolved direct numerical simulations (DNS) of a round jet in crossflow has been performed recently by Muppidi & Mahesh (2005, 2007) using a turbulent inflow. In particular, new scaling laws for the jet trajectories were proposed, and extensive budgets of turbulent quantities could be provided. Using an alternative simulation approach based on vortex elements, Cortelezzi & Karagozian (2001) studied the development of the counter-rotating vortex pair and the near field of the jet in detail.

In the present study, we employ a fully spectral numerical method, which limits the geometrical flexibility of the simulation setup. In particular, we chose to enforce the jet as a steady Dirichlet boundary condition on the crossflow wall, as opposed to e.g. Yuan *et al.* (1999) or Muppidi & Mahesh (2005, 2007) (see also the discussion in section 2 further below). However, the aim here is to contribute to a more fundamental understanding of the jet dynamics rather than providing additional data points for e.g. the trajectory development at certain parameters. Nevertheless, the complexity of the flow demands for a large number of degrees of freedom for any fully-resolved numerical simulation. Therefore, in addition to traditional (linear and nonlinear) DNS, we apply a timestepper technique, for the computation of the steady solution and the global modes methods, i.e. at no point a full matrix of the evolution operator is explicitly built as its size would be inpractical.

The paper is organized as follows. Section 2 introduces the numerical setup together with the simulation method employed for the present study and the specific parameter settings. A characterization of the steady and unsteady flow features are given in section 3. The steady and oscillatory behavior of separated regions in the flow are studied in section 4. In section 5 a global modal analysis of the flow is presented, both in terms of (linear) global eigenmodes and (nonlinear) modes from proper orthogonal decomposition (POD). Conclusions and an outlook are given in section 6.

2. Numerical methods and parameters

2.1. *Simulation set-up*

The simulation code (Chevalier *et al.* 2007) employed for the direct numerical simulations presented here uses spectral methods to solve the three-dimensional, time-dependent, incompressible Navier–Stokes equations over a flat plate. The streamwise, wall-normal and spanwise directions are denoted by x, y and z, respectively, and the corresponding velocity vector is $\boldsymbol{u} = (u, v, w)^T$,

$$\frac{\partial \boldsymbol{u}}{\partial t} + (\boldsymbol{u} \cdot \nabla)\boldsymbol{u} = -\nabla p + \frac{1}{Re_{\delta_0^*}}\nabla^2\boldsymbol{u} + F(\boldsymbol{u}) , \tag{1a}$$

$$\nabla \cdot \boldsymbol{u} = 0 , \tag{1b}$$

with the pressure p. The volume forcing $F(\boldsymbol{u})$ pertaining to the fringe region is described further below. The algorithm is based on Fourier discretization in the streamwise and spanwise directions, and the wall-normal direction is expanded in Chebyshev polynomials. For efficiency reasons, the nonlinear convection terms are evaluated pseudo-spectrally in physical space using fast Fourier transforms; the corresponding aliasing errors from the evaluation of the nonlinear terms are removed by the 3/2-rule in the wall-parallel x/z plane. In the wall-normal direction, it has been chosen to increase resolution rather than to use polynomial dealiasing. The time is advanced using a standard four-step low-storage third-order Runge–Kutta method for the nonlinear forcing terms, and a second-order Crank–Nicolson method is employed for the linear terms.

The code is fully parallelized for efficient use on both shared and distributed-memory systems.

To correctly account for the downstream growth of the boundary layer of the crossflow, a spatial technique is necessary. This requirement is combined with the periodic boundary conditions in the streamwise direction by adding a fringe region, similar to that described by Bertolotti *et al.* (1992), see also Nordström *et al.* (1999). In this region, located at the downstream end of the computational box, the flow is forced to a desired solution **v** through the forcing (Chevalier *et al.* 2007),

$$F(\boldsymbol{u}) = \lambda_f(x)(\mathbf{v} - \boldsymbol{u}) \ . \tag{2}$$

The desired in- and outflow velocity vector **v** may depend on the three spatial coordinates and time. It is smoothly changed from the laminar boundary-layer profile at the beginning of the fringe region to the prescribed inflow velocity vector. In the present case, this is chosen as the laminar Blasius boundary-layer profile, but may also contain desired inflow disturbances. The fringe function $\lambda_f(x)$ is identically zero inside the physically relevant domain, and raises smoothly to order one inside the fringe region. The length of the region with $\lambda_f > 0$ is about 20% of the complete domain length. Note that due to the spatially developing boundary layer there is weak positive transpiration throughout the physical domain, and negative wall-normal velocity in the fringe region to fulfil global mass conservation. In the spanwise direction, periodic boundary conditions are used, in accordance with the Fourier discretization in that direction.

The computational domain is a rectangular box containing the boundary layer of the crossflow. Due to the spectral discretization method employed, it is not directly possible to adapt the computational grid in such a way to include a discretized model of the jet nozzle in the flat plate. The jet discharging into the crossflow boundary layer is therefore modeled by imposing inhomogeneous boundary conditions of the wall-normal v velocity component on the flat plate, leaving the no-slip conditions on u and w intact. This simplified model does not allow for any interaction of the crossflow with the nozzle. The results of e.g. Yuan *et al.* (1999); Muppidi & Mahesh (2005) highlight the importance of including the nozzle to allow for e.g. separation within the pipe. It was also shown by Kelso *et al.* (1996) that the saddle point in the front part of the jet is moving up and down, a motion with might be reduced or even inhibited by the neglect of the pipe. In addition, the fixed boundary condition at $y = 0$ does not allow for any adjustment of the jet profile at that vertical position to the incoming crossflow (in particular a downstream deflection of the profile). On the other hand, as will be shown below, the present simulation captures all the different flow phenomena and vortex systems observed in other simulations and experiments. However, the relative significance of these systems to the overall dynamics might be slightly changed due to the chosen inflow condition. We believe that the underlying main physical mechanisms responsible for the

generation and development of the vortex systems are correctly captured in our model.

On the flat plate, homogeneous boundary conditions for the wall-parallel velocity components u and w are prescribed, corresponding to the no-slip boundary condition. The main parameters of the jet are the position of the center of the jet orifice $(x_{\text{jet}}, z_{\text{jet}})$, the jet diameter D and the inflow ratio

$$R = \frac{v_{\text{jet}}}{U_\infty} \tag{3}$$

of the centerline velocity v_{jet} and the crossflow velocity U_∞. The jet discharging into the crossflow is imposed by a wall-normal velocity

$$v(r, y = 0) = R(1 - r^2) \exp(-(r/0.7)^4) \,, \tag{4}$$

with r being the distance from the jet center $(x_{\text{jet}}, z_{\text{jet}})$, normalized by half the jet diameter D,

$$r = (2/D)\sqrt{(x - x_{\text{jet}})^2 + (z - z_{\text{jet}})^2} \,. \tag{5}$$

This inflow profile corresponds to a (laminar) parabolic velocity profile of the pipe flow, smoothened with a super-Gaussian function to allow for an efficient treatment with the spectral discretization of the simulation code. This smoothing slightly increases the radial gradient of the profile, leading to a more pointy appearance than a true parabolic profile. This might be interpreted as the applied profile having a slightly smaller diameter than the one used in the normalization. Note also that the wall-normal velocity component v corresponds to the inflow ratio R in the jet center, and is less than $10^{-5}R$ for $D/2 > 1.276$. For the boundary condition given in equation (4) the relation between the maximum and the bulk velocity in the center of the jet is approximately 3.

Although physically the boundary layer is assumed to extend to an infinite distance from the wall, the discretization requires a finite domain. Therefore, an artificial boundary condition is applied in the free-stream at wall-normal position L_y via a Neumann condition

$$\left.\frac{\partial \boldsymbol{u}}{\partial y}\right|_{y=L_y} = \left.\frac{\partial \mathbf{v}}{\partial y}\right|_{y=L_y} \,. \tag{6}$$

Far away from the wall, the wall-normal derivative of the base flow $\mathbf{v}$ is vanishingly small, which together with incompressibility approaches $u(x, y = L_y) \approx U_\infty$.

2.2. *Data base and parameters*

The parameters used for the present simulation cases are described next. The computational domain has a total streamwise length $L_x = 75$, width $L_z = 30$ and height $L_y = 20$ in units of the displacement thickness of the crossflow boundary layer at the domain inlet δ_0^*. The Reynolds number is set to $Re_{\delta_0^*} \equiv \delta_0^* U_\infty/\nu = 165$, with U_∞ being the free-stream velocity of the crossflow. The jet is characterized by the same viscosity as the crossflow, and its inflow ratio (based on the centre velocity) is specified as $R = 3$ according to equation (3).

The jet center is located $L_x \delta_0^*/8$ downstream of the inflow plane. To further define the problem setup, the diameter of the jet D is related to the boundary layer thickness as $D/\delta_0^* = 3$. These parameters are in the same range as e.g. the ones considered by Kelso *et al.* (1996). Compared to Yuan *et al.* (1999) the present Reynolds number $Re_D = U_\infty D/\nu = 500$ and the inflow ratio R are lower. However, we employ resolved spectral DNS as a tool, and do not rely on a subgrid-scale model. All computations were performed with a resolution of $(N_x, N_y, N_z) = (256, 201, 144)$ collocation points in physical space. The adequacy of the resolution has been checked by considering Fourier spectra and requiring a sufficient decay of the energy for small scales. Due to the dense distribution of the Chebyshev collocation points close to the wall and the strong wall-normal velocity component, the time step had to be chosen rather small $\delta t \approx 3 \cdot 10^{-4}$.

The present data base consists of two long DNS runs, each initiated from laminar crossflow fluid (Blasius boundary layer), with the jet smoothly starting to emerge from the wall at $t = 0$. In a first case (denoted DNS-SYM), the simulation at time $t = 0$ does not contain any disturbances apart from the laminar, two-dimensional crossflow boundary layer and the jet boundary condition. The spanwise symmetry of the inflow condition about the plane $z = 0$ is therefore maintained in the whole domain for all $t > 0$, even after the jet breaks up into smaller vortices. In a second run (case DNS-ASYM), an asymmetric disturbance is superimposed upstream of the jet nozzle at $t = 0$, quickly triggering non-symmetric breakup of the jet. In this case, the downstream part of the jet is always asymmetric, although the initial disturbance has convected out of the domain. Both of these simulations were run up to $t = 700$, corresponding to about 14 flow-through times of the crossflow fluid. The jet reaches a statistically stationary state after about $t = 100$, corresponding roughly to two flow-through times. All the analysis in the following will be based on snapshots of the flow obtained for times $150 \leq t \leq 700$. Two instantaneous snapshots of the flow for the two cases DNS-SYM and DNS-ASYM are shown in figure 1. In this figure, the vortical motion in the jet is visualized by the negative λ_2 vortex-identification criterion (Jeong & Hussain 1995), highlighting the complex, unsteady flow patterns characteristic for the jet in crossflow. The different spanwise symmetry of the flow for the cases DNS-SYM and DNS-ASYM is apparent in the outflow plane, which is color-coded according to the spanwise velocity component.

2.3. *Steady flow and mean flow*

In a first step, the time-invariant flow structures are studied. The steady part of the flow is important to be characterized in some detail in order to get a better understanding of the time-dependent oscillations and distortions developing around the steady flow. Two different possibilities to obtain such a time-invariant flow field have been considered. First, a straight-forward time-average is performed for the period $150 \leq t \leq 700$ by a weighted sum of all the snapshots
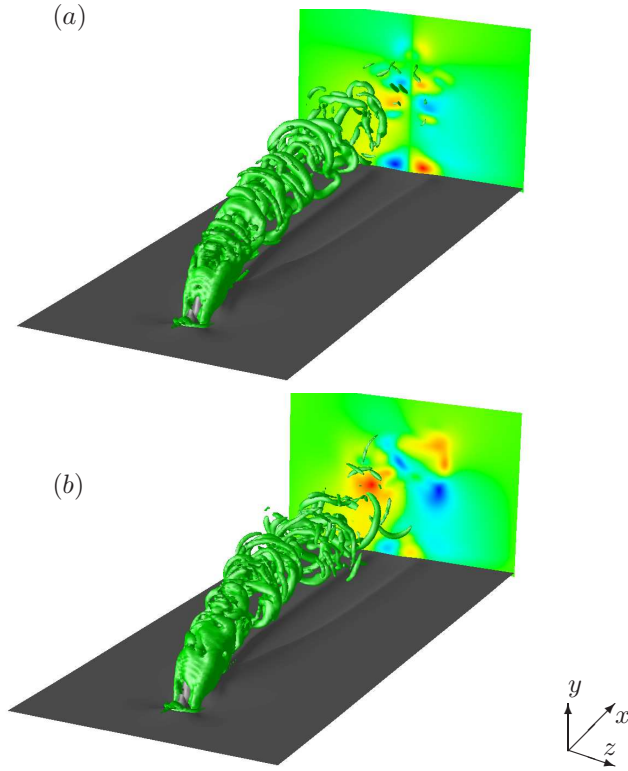
FIGURE 1. Instantaneous snapshots of cases (*a*) DNS-SYM and (*b*) DNS-ASYM at $t = 700$. The vortical structures are visualized by means of iso-contours of constant $\lambda_2 = -0.09$ (green); the gray contour depicts the streamwise velocity component $u = 0.2$ near the flat plate. The symmetry properties of the flow in the outflow plane are highlighted by color shading according to the spanwise velocity component.

recorded with spacing $\Delta t = 1$. This mean flow, however, is in general not a pointwise solution to the governing steady Navier–Stokes equations, but rather to the Reynolds-averaged Navier–Stokes equations, including Reynolds-stress contributions $\langle u_i u_j \rangle$. The mean flow provides the most accurate description of the flow in an averaged sense, i.e. what would be observed experimentally in the mean. It is interesting to note that both cases DNS-SYM and DNS-ASYM lead to essentially the same mean flow, although their instantaneous representation is different (see figure 1).

On the other hand, a true steady solution fulfilling the steady Navier–Stokes equations without additional Reynolds-stress terms can be obtained using the selective frequency damping (SFD) approach as described by Åkervik *et al.* (2006) and applied to the present jet configuration by Bagheri *et al.*

(2009*b*); numerical details and SFD parameters are discussed there. In principle, the SFD adds an explicit forcing term to the governing equations, penalizing any high-frequency disturbances by means of a temporal differential filter. As opposed to the mean flow, this steady flow state represents a true equilibrium solution, which is unstable for the present parameters (Bagheri *et al.* 2009*b*) due to global instability. This flow will therefore never be observed in a real situation. The validity of the steady-state solution has been tested numerically by starting a simulation from the steady state without active SFD forcing. The flow eventually became unstable and developed unsteadily, however, the accuracy of the steady state is such that for about a time span of $\Delta t = 200$ no significant change in the solution is detectable. Thereafter, the instabilities would exponentially grow and eventually lead to similar flow fields as cases DNS-SYM and DNS-ASYM, depending on the symmetry properties.

3. Flow features

In this section, the flow phenomena associated with the jet in crossflow are examined in more detail based on the present DNS. In particular, the ubiquitous features described in the literature are briefly reviewed and related to observations in the present data.

3.1. *Steady features*

We begin by comparing the various vortex systems observed in a purely steady solution with those appearing in the mean flow. Figure 2 compares a three-dimensional visualization of the mean and steady flow. The steady structures observed for both flows are; (i) the ubiquitous counter-rotating vortex pair (CVP) rising up into the free-stream; (ii) a vortex sheet wrapping around the CVP a few jet diameters in the wall-normal direction; (iii) the wall-vortex system (WVS), consisting of the horse-shoe vortex bending around the upstream part of the jet nozzle, and the wall vortices extending for a long distance downstream of the nozzle. The latter vortices are streamwise-oriented, counter-rotating vortices, which can be considered the extension of the horse-shoe vortices downstream of the jet nozzle. These features have been described in many publications for the mean flow, see e.g. Fric & Roshko (1994); Kelso *et al.* (1996); Smith & Mungal (1998); Yuan *et al.* (1999), and they are present in both the steady-state solution and the mean flow in very similar form. The most significant differences are located further away from the wall, indicating that the mean flow distortion due to fluctuations is small in the near-wall region. Most obvious is the clearly stronger, longer and higher-reaching CVP in the steady flow, indicated by the label ① in figure 2. This can be explained by the missing breakup of the vorticity, which leads to a lower momentum loss for the jet fluid, thereby allowing the jet to longer retain its wall-normal velocity. Since the mean flow is a solution to the RANS equations, it exhibits increased momentum diffusion due to the Reynolds stresses.
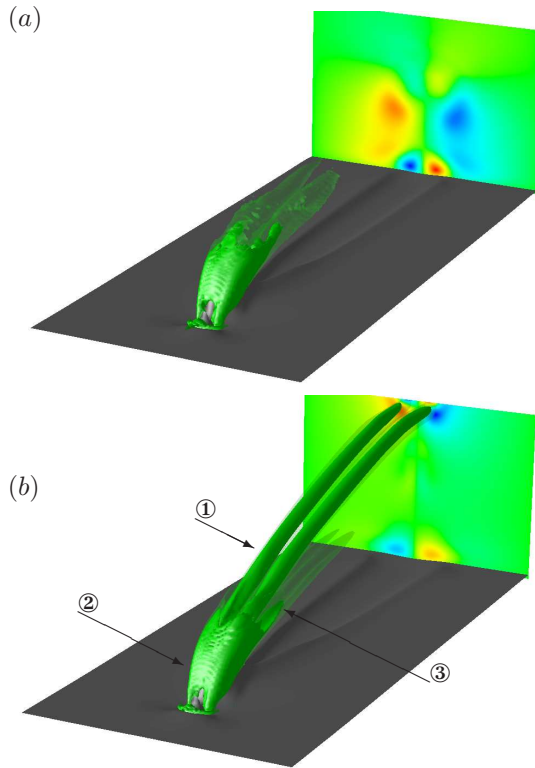
FIGURE 2. (*a*) Mean flow and (*b*) steady flow obtained by
SFD visualized by iso-contours of $\lambda_2 = -0.09$ (solid green),
$\lambda_2 = -0.01$ (opaque green) and $u = 0.2$ (grey) close to the wall.
The vertical plane towards the end of the domain is color-coded
according to the spanwise velocity component. The numbered
labels are discussed in the text.

A closer inspection of the region close to the jet nozzle (figure 2) shows
that up to approximately two jet diameters from the wall, a continuous vortex
sheet is present on the windward side of the jet (label ②). Referring back to
figure 1, this vortex sheet is also clearly visible; Lim *et al.* (2001) termed this
layer as cylindrical shear layer. At this wall-normal position, the leeward side
of the jet already shows the deformation of the jet cross section into the kidney
shape characteristic of the growing CVP (Muppidi & Mahesh 2006). An area
of negative streamwise velocity is located in the same region, indicating that
the roll-up of the sides is sucking in fluid from the downstream part of the
crossflow. Above approximately three jet diameters, a two-layer structure of
the growing CVP becomes apparent. The outer vortex shell is detaching from
the main CVP direction, forming two distinct vortex cores pointing in the
downstream direction and forming a second set of CVP, denoted *lower CVP*,

label ③. The inner vortices continue to extend to higher wall-normal distances; now as distinct counter-rotating vortices forming the dominant far-field CVP labelled ①. Note that the direction of rotation is the the same on each side of the axis of symmetry for the CVP and lower CVP, i.e. directed in such a way that fluid is lifted up in between the vortices. Although the distinction between the two CVP is clearest in the steady solution, they can also be identified in the mean flow, figure 2(a), indicating that the respective dynamics is also present in the time-dependent flow.

The present results show that for the development of a counter-rotating vortex pair, the pipe below the jet nozzle is not necessary. This is in agreement with the studies by Cortelezzi & Karagozian (2001) and Muppidi & Mahesh (2006) which – with different numerical methods and degrees of complexity – obtain a CVP in their simulations without modeling the inflow pipe. In addition, the steady state clearly shows that for the development of a CVP only a steady flow is necessary. To what extent the periodic roll-up of the shear layer might further contribute to the circulation in the CVP (Kelso *et al.* 1996) can of course not be answered by considering the steady solution, however it seems certain that this roll-up is not the origin of the CVP.

3.2. *Unsteady features*

In addition to the steady features, a number of unsteady motions are characteristic of the jet in crossflow. Most dominant are the shear-layer vortices, appearing predominantly on the upstream side of the jet trajectory for the given inflow ratio (Kelso *et al.* 1996; Lim *et al.* 2001). These half-ring shaped vortices grow, and quickly break down into a series of smaller vortices, which continue to convect downstream and eventually dissipate due to viscosity. The origin and evolution of these vortices has been described and documented by many sources, e.g. Fric & Roshko (1994); Kelso *et al.* (1996); Blanchard *et al.* (1999); Lim *et al.* (2001); Muppidi & Mahesh (2007). These vortices can be seen in the visualizations in figure 1 for both the symmetric (DNS-SYM) and asymmetric case (DNS-ASYM). The time signal recorded by a probe located in the shear layer is shown in figure 3(a) for case DNS-ASYM together with its power spectrum. The peak frequency beats with a Strouhal number $St \equiv fD/V_{\text{jet}} = 0.14$ (figure 3c). This frequency will be denoted St_2 in the following. For case DNS-SYM, which is restricted to symmetric motion about the plane with $z = 0$, a slightly higher Strouhal number, $St = 0.17$ (Bagheri *et al.* 2009b) is found. It is interesting to note that this slight difference in frequency for the symmetric and asymmetric shear-layer motion is also captured in the linear global stability analysis (see Bagheri *et al.* 2009b, and section 5 below), which yields $St = 0.19$ and $St = 0.17$ for the symmetric and asymmetric global modes (denoted S_1 and S_3 in Bagheri *et al.* 2009b).

From visualisations it is also apparent that the symmetric case leads to more regular flow patterns after the vortex breakdown; the arising vortex structures clearly resemble those documented by Cortelezzi & Karagozian (2001).
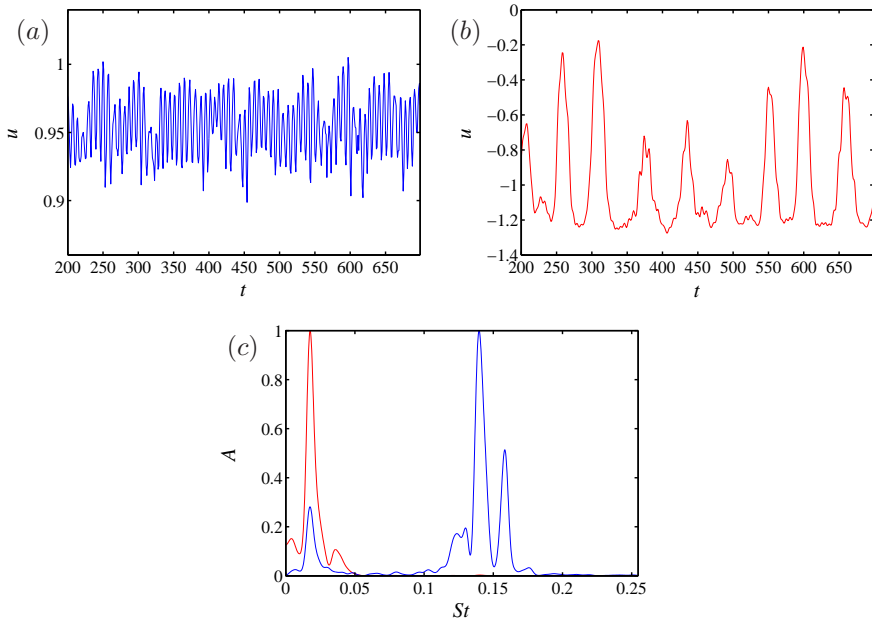
FIGURE 3. (a),(b) Time signals and (c) power spectrum of two probes in the flow. The red line corresponds to a probe located in the separated region downstream of the jet, $(x, y, z) = (10.7, 1, 0)$, the blue line corresponds to a probe in the shear layer, $(x, y, z) = (12, 6, 2)$.

In the asymmetric case, the basic mechanism of vortex generation in the shear layer is still present, however, the arising flow structures are not as clear as in the symmetric case. In addition, the visual density of the visualized vortices is much higher, indicating a more unstable flow configuration in the unconstrained case.

Another characteristic unsteady feature of the jet in crossflow are the upright vortices (Fric & Roshko 1994; Kelso *et al.* 1996) appearing in the wake of the jet, connecting the main jet trajectory and the wall vortex system, i.e. the wall vortices. The upright vortices are roughly aligned with the wall-normal direction, periodically shed away from the upstream part of the jet. Several explanations of their origin have been proposed in the literature (see e.g. Kelso *et al.* 1996), including the classical von Kármán-type vortex street. From the present DNS data, the upright vortices were identified using isocontours of the wall-normal vorticity ω_2, see figure 4 for case DNS-ASYM. In the wake, the upright vortices appear regularly with alternating sign of the vorticity. Probes located in the jet wake record exactly the same frequency peak as in the shear layer, i.e. $St_2 = 0.14$. It thus seems that in the present flow for each shear-layer
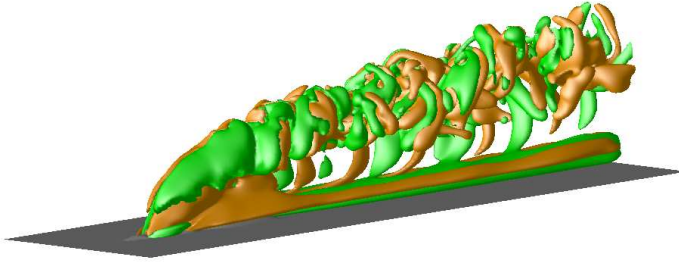
FIGURE 4. Isocontours of the wall-normal vorticity for case DNS-ASYM ($\omega_2 = \pm 0.1$), orange isocontours correspond to positive and green to negative values.

vortex a corresponding upright vortex is created and released. Inspection of an animation clearly confirms this observation, i.e. that the upright vortices are connected to the higher frequency St_2. This physical insight will be further supported below by the global mode analysis.

In addition to this high frequency St_2, there is a clear lower frequency present, both in the shear-layer signal as a secondary peak, but being most dominant in a probe located in the recirculation zone downstream of the jet orifice, see figures $3(b, c)$. This frequency is measured as $St_1 = 0.017$. The additional frequency peaks in figure $3(c)$ are all linear combinations of St_1 and St_2, corresponding to higher harmonics triggered by non-linear interactions between the two main frequencies.

Several additional time signals from other probes have been obtained and compared to the ones presented here, and in all of these the two frequencies St_1 and St_2 appear as the two dominant fundamental frequencies. In particular, in a probe upstream of the orifice close to the horseshoe vortex, a clearly dominating energy peak at St_1 is recorded. In probes located far downstream, a much broader spectrum is obtained, however, still being dominated by St_1 and St_2. This shows that due to non-linearity the region between the discrete frequencies is gradually filled up as the jet vortices decay into smaller eddies.

4. The separated region

There is some evidence (Hammond & Redekopp 1998) and numerous studies (Theofilis *et al.* 2000; Alam & Sandham 2000; Barkley *et al.* 2002; Marquillie & Ehrenstein 2002; Theofilis 2005; Giannetti & Luchini 2007; Åkervik *et al.* 2007) that connect self-sustained oscillations in fluid systems with large unsteady separated regions. The flow under investigation here has two regions of reversed flow: a smaller, essentially steady separated region upstream of the jet which coincides with the horseshoe vortex, and a larger unsteady region of reversed flow directly downstream of the emerging jet near the wall.

4.1. *Analysis of the steady near-field*

Figure 5(*a*) shows the two-dimensional steady flow in the center-plane $z = 0$ in the vicinity of the jet nozzle. Note that the mean flow essentially features the same qualitative properties as the steady flow described here. Upstream of the jet exit, a stagnation point and a small recirculation zone are observed. On the leeward side, a much larger region with backflow is located; however, interestingly a small region inside this recirculation zone has again positive u velocity. In this plane, the flow is dominated by the high, slightly deflected, wall-normal velocity due to the emerging jet, and a number of interesting stagnation/saddle points and vortex nodes. The wall-normal velocity component also changes sign from negative in the near-wall region to positive further away. The combination of the sign changes allows to identify three singular points of interest in the downstream part of the jet: Two locations (red dots in figure 5*a*) are characterized by positive divergence; and another constitutes a saddle point (green dot). From the streamlines plotted, it is clear that the jet is entraining crossflow fluid from the leeward side. The node located further downstream at $(x, y) \approx (15.7, 2.3)$ has already been described by Kelso *et al.* (1996) and, in the mean flow obtained from DNS, by Muppidi & Mahesh (2005). As opposed to these references, however, in the present study an additional node location could be identified at $(x, y) \approx (11.6, 0.63)$ inside the recirculation zone on the boundary of the above mentioned hole. In between these two nodes another saddle point can be found. The existence of two nodes in the steady flow further indicates the complex flow physics associated with the downstream region of the jet, and consequently, the various instabilities detected along the jet trajectory.

On the windward side, the dominant horseshoe vortex is located at $(x, y) \approx (7.21, 0.37)$ (black dot), and a second vortex centre, located much closer to the jet at $(x, y) = (8.13, 0.35)$, is commonly associated with the hovering vortex (Kelso *et al.* 1996). These two vortices have opposite directions of rotation. In addition, two saddle points can be identified; the upper one separating the crossflow fluid from being entrained in the jet or being recirculated.

A plan view of the streamlines in a (x, z)-plane close to the wall is shown in figure 5(*b*). Three foci are identified; one close to the axis of symmetry ($z = 0$), one on the downstream side of the jet boundary, and – most dominantly – in the wake of the jet at $(x, z) \approx (14.31, -1.19)$. In all these points, negative divergence is present indicating entrainment of fluid directed away from the wall. It is interesting to note that the steady flow features a slightly different layout of the various singular points as sketched by Kelso *et al.* (1996). In particular, the dominant focus is clearly downstream of the jet nozzle, and a secondary focus is present close to the axis of symmetry. This second focus is due to the region with positive streamwise velocity embedded in the larger region of backflow.
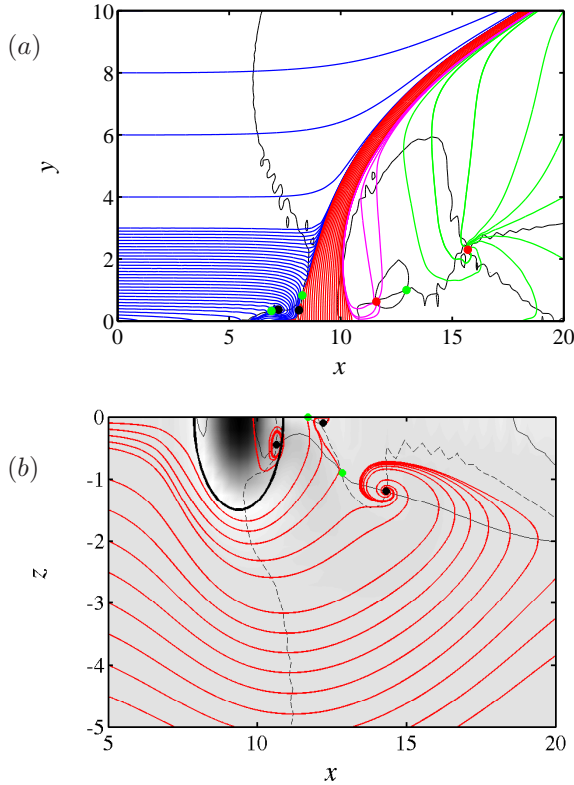
FIGURE 5. Two-dimensional cuts of the steady flow, (a) in a $z = 0$ plane and (b) in a wall-parallel plane close to the wall. The solid black lines correspond to zero streamwise velocity $u = 0$, the dashed black lines to $v = 0$. Saddle points are indicated by green dots; nodes with red dots and foci with black dots. Streamlines are plotted with colored lines. In (b) the background gray shade corresponds to the amplitude of the total velocity $(u^2 + v^2)^{(1/2)}$.

4.2. *Movement of the separation region*

The two recirculation regions described above are also detectable in the instantaneous visualization shown in figure 6. The animation of the DNS data shows that the separation region downstream of the jet orifice is highly unsteady. In the upper part of this region, patches of negative u are periodically released with the fundamental frequency $St_2 = 0.14$. This happens at a streamwise position close to the jet exit, at which the shear-layer vortices are not yet developed.
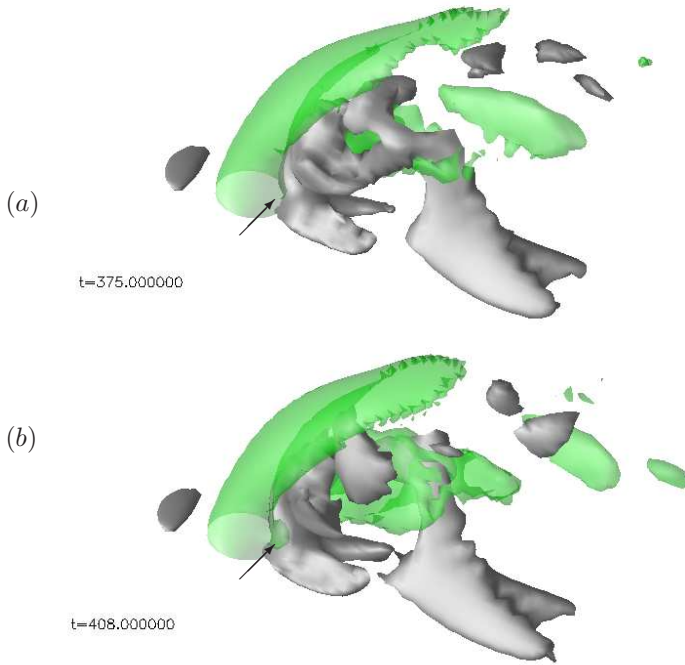
(a)

t=375.000000

(b)

t=408.000000

FIGURE 6. Instantaneous visualization of the region close to the jet orifice at $t = 375$ and $t = 408$. Green isocontours correspond to $v = 0.1$ and grey contours to $u = -0.1$. The arrows indicate the location of the low-frequency spanwise oscillation of the separation region.

In the animations, also the lower frequency St_1 characteristic of the present setup can be observed. The two snapshots shown in figure 6 are separated by $\Delta t = 32$ time units, which is approximately half the period of that lower frequency $St_1 = 0.017$. The visualizations show that the whole recirculation zone downstream of the jet is periodically moving back and forth in the spanwise direction. The respective positions are indicated in the figure by the arrows. As the probe signals in figure 3 show, the low frequency peak is most dominant just downstream of the jet. The oscillation of the separation region is subsequently felt by the whole jet body and the wake vortex system further downstream. One possible explanation for this motion is given by the comparison of the respective Strouhal number to that of a solid cylinder (see also the corresponding discussion by Fric & Roshko 1994; Ziefle 2008, on that topic). For a cylinder wake, the relevant Strouhal number is defined as $St_c = fD/U$ with U being the uniform flow velocity in the far field. Adapting the present definition of the frequency based on the jet velocity gives $St_c = St_1(V_{\text{jet}}/U_\infty)(U_\infty/U)$. Assuming $U/U_\infty \approx 1/3$ due to the reduced streamwise velocity in the proximity

of the wall gives $St_c \approx 9St_1 = 0.153$, which is on the same order of magnitude as expected for a solid cylinder. Note that this oscillation is not related to the upright vortices which are associated with the higher frequency St_2 as discussed above.

On the other hand, a careful analysis of the separation region upstream of the jet did not reveal any significant oscillation. In particular, the saddle point upstream of the jet trajectory did not move, which is in contrast to the prediction by Kelso *et al.* (1996). However, as mentioned earlier, the effect of the chosen inhomogeneous boundary conditions without modeling the inflow pipe might be a factor to explain this apparent difference.

We can thus conclude from observation in our DNS data that the separation region downstream of the jet is in fact oscillating in two directions with two distinct frequencies: A high frequency oscillation in the vertical direction, characterized by periodic shedding with the same frequency as the shear-layer vortices and the upright vortices in the wake, and a lower frequency oscillation, inducing a slow spanwise wiggling of the whole jet and its associated vortex systems.

5. Global modes

The objective of this section is to analyze global modes of the jet in crossflow, in order to gain further insight into the flow dynamics. A global mode is defined as a coherent flow structure (e.g. wavepacket) that exists within the full three-dimensional flow domain. In particular, we focus our attention on two different types of global modes, namely global eigenmodes and POD modes.

First, we consider the linear subspace spanned by the leading global eigenmodes of the Navier–Stokes equations linearized about the steady-state solution. In this subspace, the behavior of small-amplitude disturbances near the steady solution is captured. More specifically, the eigenmode of the linearized system with the largest growth rate determines whether the steady solution is unstable or stable. As established by Huerre & Monkewitz (1990) – although this analysis is constrained only to a neighborhood of the steady-state solution – if the baseflow is rendered unstable, the global (nonlinear) flow may self-sustain global oscillation (e.g. vortex shedding).

Second, we consider the linear subspace spanned by a number of POD modes – the eigenmodes of the spatial correlation matrix. This subspace identifies those parts of the phase space which contains the most kinetic energy, typically attractors in phase space (Holmes *et al.* 1996). For the jet in crossflow we observe as discussed in the previous section 3.2, two fundamental frequencies associated with two self-sustained global oscillations, indicating a quasi-periodic type of attractor.

5.1. *Linear global eigenmodes*

The evolution of infinitesimal perturbations $\boldsymbol{u}'(x,y,z,t)$ to a steady solution (e.g. baseflow) $\mathbf{U}(x,y,z)$ is found by inserting $\boldsymbol{u} = \mathbf{U} + \epsilon \boldsymbol{u}'$ and $p = P + \epsilon p'$,
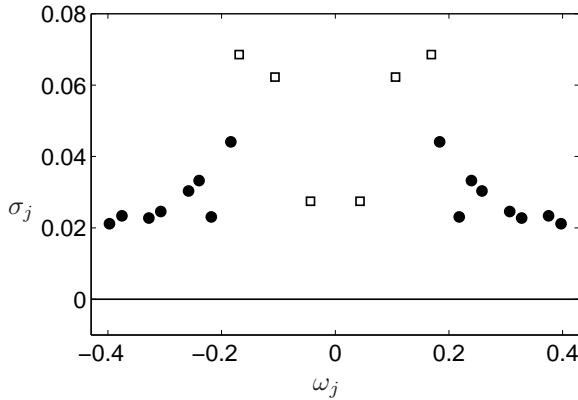
FIGURE 7. The linear spectrum of the jet in crossflow at $R = 3$. The eigenvalues marked with squares correspond to anti-symmetric eigenmodes, whereas black circles correspond to symmetric eigenmodes.

where p' is the pressure perturbation, into (1) and neglecting terms of order ϵ^2. These equations are solved subject to the same boundary conditions in x, y and z as eq. (1), however for the perturbation dynamics, the jet boundary condition is not imposed. By enforcing the incompressibility condition and incorporating the boundary conditions, the resulting linearized Navier–Stokes equations (LNS) can be written as initial value problem,

$$\frac{\partial \boldsymbol{u}}{\partial t} = A\boldsymbol{u}, \qquad \boldsymbol{u}(t=0) = \boldsymbol{u}_0 \ . \tag{7}$$

In a discretized setting A is the $n \times n$ Jabobian matrix, where $n = 3n_x n_y n_z$ is the total number of degrees of freedom. If the baseflow is a steady solution, equation (7) is autonomous and the eigenmodes of A are of the form

$$\boldsymbol{u}(x, y, z, t)' = e^{\lambda_j t}\boldsymbol{\phi}_j(x, y, z) \ , \quad j = 1, \ldots, n \tag{8}$$

where both the eigenvalues λ_j and eigenmodes $\boldsymbol{\phi}_j$ are complex functions. The eigenmode $\boldsymbol{\phi}_j$ grows or decays in time with a rate given by of $\sigma_j = \mathrm{Re}(\lambda_j)$ and oscillates with temporal frequency given by the $\omega_j = \mathrm{Im}(\lambda_j)$.

If the eigenmodes depend on two or three spatial coordinates they are called global eigenmodes to differentiate them from local stability analysis. In our fully three-dimensional case, $n \approx 10^7$, and therefore the eigenmodes of A have to be computed using an iterative algorithm (e.g. Arnoldi method) in combination with matrix-free methods. This time-stepper technique is described in Bagheri *et al.* (2009*a,b*). Linear global stability analysis of two-dimensional steady base flows has only recently become standard in field of hydrodynamics stability (see e.g. Theofilis 2005; Åkervik *et al.* 2007, 2008; Barkley *et al.* 2002; Giannetti & Luchini 2007, among others).

Mode	Growth-rate (σ)	Frequency (St)	Residual	Symmetry	Vortex type
1	0.0685	0.169	10^{-13}	A	Shear/Upright
2	0.0622	0.106	10^{-13}	A	Shear/Upright
3	0.0441	0.183	10^{-9}	S	Shear
4	0.0333	0.23	10^{-9}	S	Shear
5	0.0303	0.25	10^{-9}	S	Shear
6	0.0274	0.043	10^{-8}	A	Wall
7	0.0246	0.30	10^{-13}	S	Shear
8	0.0233	0.32	10^{-13}	S	Shear
9	0.0230	0.218	10^{-7}	S	Shear
10	0.0227	0.375	10^{-13}	S	Shear
11	0.0211	0.40	10^{-13}	S	Shear

TABLE 1. The properties of each linear global eigenmode. 'A' refers to anti-symmetric modes and 'S' to symmetric modes.

In figure 7 the linear spectrum is shown. The spectrum was computed using 1800 snapshots in order to obtain 22 eigenmodes with smaller residual error than 10^{-7}; see also Bagheri *et al.* (2009*b*). The eigenvalues, the properties of the corresponding eigenmodes and their residuals are listed in Table 5.1. All the computed modes are unstable and each mode ϕ_j is associated with an instability, evolving near to the steady-state baseflow.

5.1.1. *Anti-symmetric modes*

The most unstable mode (ϕ_1) is an anti-symmetric mode (symmetry refers to the u and v component with respect to the z-axis) as shown with red λ_2 contours in figure 8(*a*). In the figure the base flow is shown in blue (λ_2) and gray (u). This mode oscillates with $St = 0.169$. Although the most dominant feature of this instability is a wavepacket located on and around the CVP, it is also associated with the upright vortices; we could observe (see figure 5*b* in Bagheri *et al.* 2009*b*, where the same mode from a different angle is shown) a significant spatial structure on the leeward side of the CVP, extending towards the wall in a nearly normal direction to the CVP. The connection of these two vortex systems was also observed in the nonlinear DNS simulation. The amplitude of the mode very close to the wall is significantly smaller compared to the amplitude on the jet as shown in figure 8(*b*), where isocontours of the spanwise velocity component are plotted. The alternating positive and negative spanwise velocity in the streamwise direction contributes mainly to the wall-normal vorticity which constitute the upright vortices. In a linear approximation, the structures of the global mode in the jet region, wake region and wall region grow with the same rate and oscillate with the same frequency. The various vortex systems are thus coupled, which illustrates the global character of the flow. The second most unstable mode (ϕ_2) is also anti-symmetric, with a very similar spatial structure as the first mode as shown in figures 8(*c, d*). However, this mode
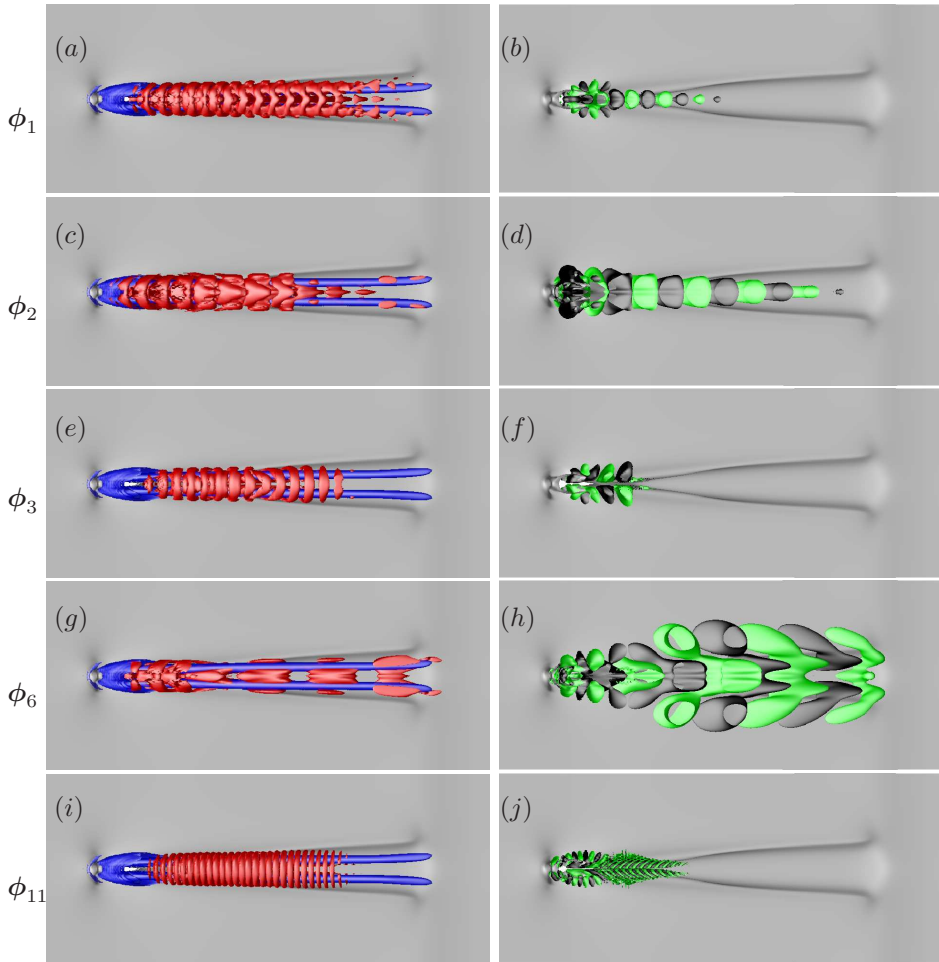
FIGURE 8. Top view of 5 eigenmodes. Left column: contour levels of the λ_2 criterion, whereas the baseflow is shown in blue (λ_2) and gray (u). Right column: the structure of the modes near the wall with positive (black) and negative (green) contours of the w component. The growth rate of the modes decrease from top to bottom. Modes shown on row 1,2 and 4 are anti-symmetric whereas row 3 and 5 show high-frequency symmetric modes.

oscillates with a lower frequency ($St = 0.1$) and is characterized by a somewhat larger spatial wavelength than ϕ_1. The global eigenmode (ϕ_6) with the lowest frequency $St = 0.043$ (anti-symmetric) is shown in figures 8(g, h). Its structure is mostly concentrated close to the wall, and has a rather small amplitude along
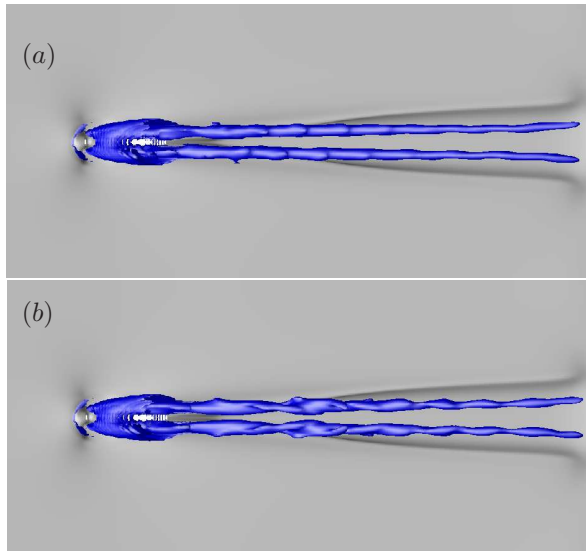
FIGURE 9. Top view of the superposition of the base flow and (*a*) the most unstable global mode (*b*) the most unstable symmetric mode.

the CVP. In particular, the structure near the wall is considerably different compared to the other modes. This mode is associated with the shedding of vortices from the spanwise oscillation of the separated region discussed earlier – reminiscent of the global mode of the cylinder wake (Giannetti & Luchini 2007).

To gain a better insight into how the instability affects the flow, we superimpose on the steady solution the most unstable anti-symmetric mode with a chosen amplitude such the modulation caused by the instability becomes clear. As shown in figure 9(*a*), the most unstable mode modifies mainly the CVP; a sinuous in-phase oscillation of the two vortex tubes is observed in top view whereas a side view (not shown) reveals out of phase oscillations of the tubes. Moreover, the wavelength of the modulation due to the instability seems of the same order as the vortex cores of the CVP. These can be interpreted as being the traits of a short-wavelength instability of a vortex pair as observed by numerical simulation of Laporte & Corjon (2000) and the experiments of Leweke & Williamson (1998). Such an instability is due to a resonance between two waves of one vortex and straining field induced by the other vortex. In figure 10 the streamwise vorticity component in a cross plane (yz-plane) far downstream is shown for the base flow and the most unstable global mode. The CVP centered around $y = 14$ can clearly be seen in figure 10(*a*). The global mode, figure 10(*b*), shows a characteristic two-lobe structure in each CVP vortex. This is remarkably similar to the vorticity computed analytically
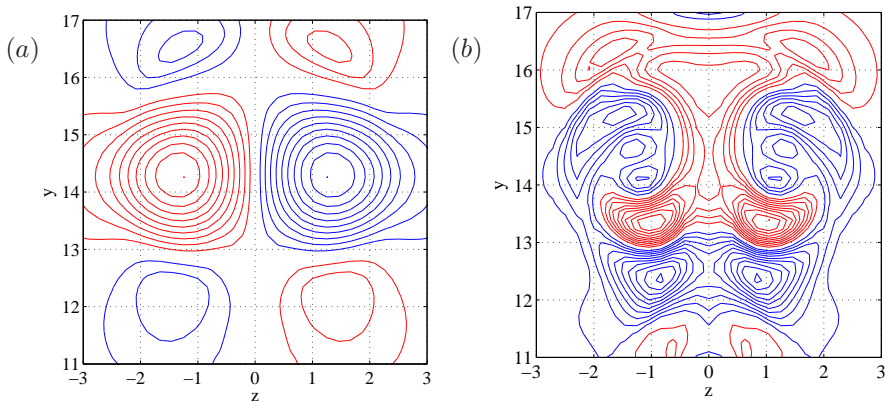
FIGURE 10. Streamwise vorticity at $x = 40$ for the steady base flow (a) and the most unstable mode (b). Contour levels are 0.1, 0.2, ..., $1.0 \cdot \omega_{z,\mathrm{max}}$, red is positive, blue negative.

for the elliptic instability (Waleffe 1990, figure 2) and the short-wave instability (Leweke & Williamson 1998, figure 10).

These observations suggest (see also Blanchard *et al.* 1999) that part of the globally unstable mode is an instability of elliptic type due to a strained vortex. However, to fully confirm an elliptic instability the CVP tubes have to analyzed locally similar to analysis of Fabre *et al.* (2000), which is not within the scope of the present paper. Previous investigations (Leweke & Williamson 1998; Laporte & Corjon 2000) show that at the nonlinear phase – when the amplitude of the short-wave instability has reached sufficiently large amplitude – transverse vortical structures are created between and around the vortex pair. The late stage of these vortical structures (see e.g. Laporte & Corjon 2000, figure 10) are somewhat similar to the structures shown in figure 1(b).

5.1.2. *Symmetric modes*

A number of the computed global modes (modes $\phi_3 - \phi_5, \phi_7 - \phi_{11}$ in Table 5.1 and marked with black circles in figure 7) represent symmetric shear-layer modes with a rather high temporal frequency. The most unstable symmetric mode is shown in figures 8(e, f) and the symmetric mode with the highest frequency is shown in figures 8(i, j). The common feature of the symmetric modes is that they have very small spatial support near the wall (see figures 8f and 8j). The global mode consists of a symmetric spanwise oriented row of vortex loop that wrap around the upper part of the CVP and are gradually stretched, and develop "legs" that align with the direction of CVP tubes; the direction of rotation in the loop at $z = 0$ is clockwise viewed in negative z direction. Figure

9(b) shows the superposition of the baseflow and the most unstable symmetric global mode. The CVP are modulated in varicose fashion viewed from top. Note that the wavelength of the symmetric instability is rather small compared to the wavelengths commonly observed in the Crow instability (Crow 1970) of a vortex pair. From a nonlinear simulation of the disturbance (not shown here) we could observe, that as the disturbance grows in amplitude "arches" are created, i.e. the vortex loops coil up around the upper side of the CVP and their bases join with the CVP. This type of symmetric structures have been observed in many studies (see e.g. Kelso *et al.* 1996; Cortelezzi & Karagozian 2001; Lim *et al.* 2001), and have been associated with the roll-up of the cylindrical vortex sheet (shear layer) emerging from the jet nozzle. The symmetric vortex arches observed in the unstable symmetric global modes could thus be partly a result of the Kelvin-Helmholtz roll-up at the upstream side of the jet column. The cylindrical vortex sheet undergoes various stretching and folding processes at the same time as the roll-up, resulting in significantly more complicated structures on the lee side (rear) of the shear layer.

5.1.3. *Connection to separated region*

Global instabilities are commonly associated with a region in the flow where there is a separation which induces vortex shedding (Theofilis *et al.* 2000; Barkley *et al.* 2002). In section 4 two separation regions were identified near the wall; one small steady separation region upstream of the jet orifice and one separation region just downstream of the jet orifice, oscillating in two directions, slowly in the spanwise direction with $St_1 = 0.017$ and rapidly along the jet trajectory with $St_2 = 0.14$. The Strouhal numbers of the unstable modes are in the range $[0.04, 0.17]$, and do not exactly match the two fundamental shedding frequencies observed in the DNS. However, the stability analysis merely accounts for the linear dynamics in the neighborhood of the steady-solution, where the Strouhal numbers can be considerably different from the saturated three-dimensional dynamics near the attractor.

It is well-known that when the reversed flow in an isolated free shear layer exceeds roughly 15% of the main stream, the flow is absolutely unstable (Huerre & Monkewitz 1985). Although the fully three-dimensional jet in crossflow is considerably more complex, it was shown by Hammond & Redekopp (1998) that typical backflow velocities in "realistic" separation bubbles are sufficiently large to induce absolute instability. Absolute instability is a local concept for weakly non-parallel flows and is not straight-forward to conduct such an analysis for the jet in crossflow. However, due to the fact that globally unstable flows have a region or pocket of local absolute instability somewhere in the flow (Chomaz *et al.* 1991) and that this pocket is connected to a region of significant backflow (Hammond & Redekopp 1998), it is likely that the separated region downstream acts as an oscillator in the flow. It periodically sheds patches of vorticity, which are convected into the jet, wake and wall region and amplified due to different *local* mechanisms (such as Kelvin-Helmholtz or short-wave elliptic instability).
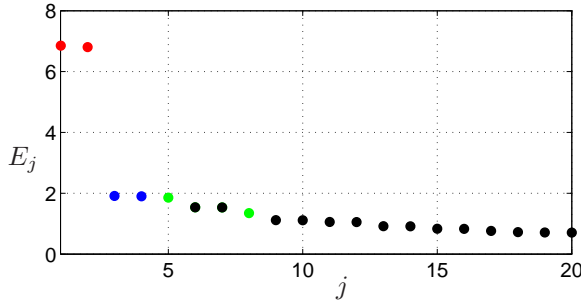
FIGURE 11. The energy $E_j = \gamma_j / \sum_i \gamma_i \times 100$ of the POD modes with $j = 1, \ldots, 20$. The POD modes and coefficients corresponding to the eigenvalues depicted in color are shown in figures 12 and 13, respectively. Red: antisymmetric high-frequency mode, blue: symmetric high-frequency mode, green: low-frequency mode.

Finally, it should be mentioned that a general feature of absolutely unstable spatially developing flows is that further downstream a convectively unstable region follows and finally a stable region. In such flows, the unstable global modes are located far downstream of the absolutely unstable region (Huerre & Monkewitz 1990); the maximum amplitude of the global mode being located in the convectively unstable region. In our setting, the shear layer and CVP could merely act as a noise amplifiers. Although the present analysis suggests such a scenario, additional local investigation of the current steady solution should be undertaken to fully ascertain our conjectures.

5.2. *POD decomposition*

Given a set of flow-field snapshots at discrete times $\{\boldsymbol{u}(t_1), \ldots, \boldsymbol{u}(t_m)\}$, the optimal finite-dimensional representation (in the L^2 Hilbert space) of size k of this data set is given by expansion into the first k POD modes (Holmes *et al.* 1996). This optimal basis is given by the eigenfunctions $\boldsymbol{\psi}_j$ of the autocorrelation function

$$\left(\int_0^t \boldsymbol{u}(t) \boldsymbol{u}(t)^T \mathrm{d}t \right) \boldsymbol{\psi}_j = \gamma_j \boldsymbol{\psi}_j \ . \tag{9}$$

The eigenfunctions are mutually orthogonal and the eigenvalues are positive valued, ordered by $\gamma_j \geq \gamma_{j+1}$. Moreover, the eigenvalues γ_j represent twice the kinetic energy in each mode $\boldsymbol{\psi}_j$. The subspace spanned the k POD modes corresponding to the largest k eigenvalues, contains the most energetic flow structures in the field. The POD modes can be computed using the method of snapshot (Sirovich 1987).

The POD modes of the jet in crossflow were computed using 550 snapshots equidistantly distributed in time from $t = 150$ to $t = 700$. The transient flow
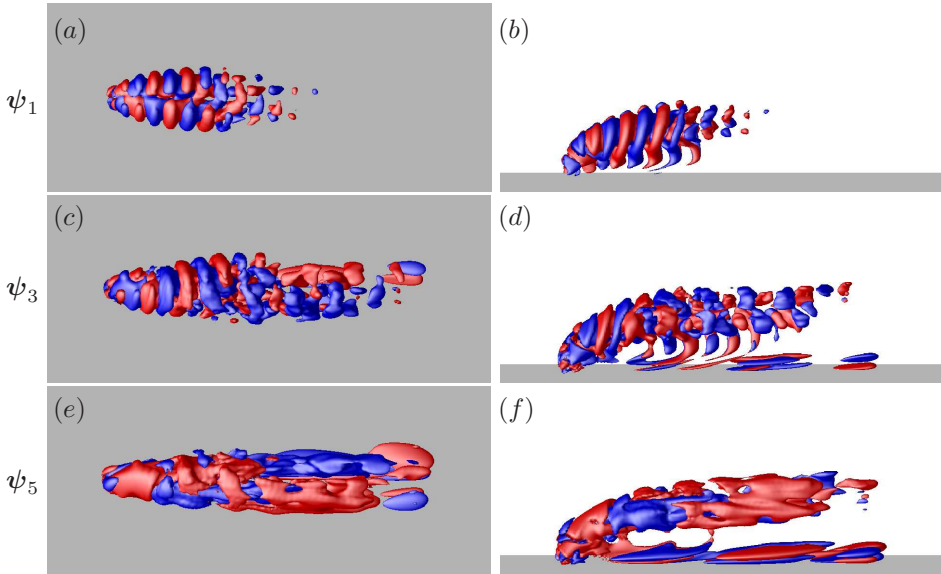
FIGURE 12. Positive (red) and negative (blue) isocontours of the u-velocity of 3 POD modes from top view and side view. The first row corresponds to the modes marked with red circles; the second row to blue circles and the third row to green circles in figure 11.

evolution was hence not included in the data set. All computed modes satisfy the orthogonality condition down to 10^{-10}. The zeroth mode (ψ_0) corresponds to the time-averaged mean flow (shown in figure 2) which has been discussed thoroughly earlier.

The energies of the modes $\psi_1 - \psi_{20}$ are shown in figure 11, were we clearly notice the pairing of modes, which is typically observed in flows containing traveling structures. Each pair describes the phase and amplitude of one traveling dynamical structure in the flow. The first pair of modes (ψ_1, ψ_2) contains 68% of the total energy (red circles in figure 11). The positive (red) and negative (blue) streamwise velocity component of one mode is shown in figures 12(a, b) from two angles. It clearly displays shear-layer vortices and to some extent the upright vortices. The temporal behavior of this mode is characterized by computing the POD coefficients via a Galerkin projection of the flow-field snapshots onto the mode. The POD coefficient of this pair and its corresponding power spectrum are shown with red lines in figures 13(a) and 13(d), respectively. There is one peak frequency at $St = 0.138$ which matches the Strouhal number of the shedding of the shear-layer vortices observed from DNS ($St_2 = 0.14$). The mode is anti-symmetric and is located mainly near the location where the shedding of the shear-layer vortices takes place. This

indicates that the flow mechanism that contributes the most to the total flow energy is the shedding of shear-layer vortices.

The second pair of modes $(\boldsymbol{\psi}_3, \boldsymbol{\psi}_4)$ contains 1.9% of the total flow energy, with one mode $(\boldsymbol{\psi}_3)$ shown in figures 12(c, d). In contrast to the first pair, this pair has a distinct spatial structure further downstream along the jet trajectory and more pronounced upright vortices on the leeward side. Moreover, anti-symmetric flow structures very close to the wall and far downstream along the flat plate corresponding to wall vortices are also detected. The POD coefficients and the corresponding power spectrum of this pair are shown in figures 13(b) and 13(d), respectively. The signal contains three frequency peaks, were the largest peak is obtained for $St_1 + St_2 = 0.158$ and the second largest is $-St_1 + St_2 = 0.121$, due to the interaction of the two fundamental shedding frequencies.

Finally, we pair up two modes with similar energy levels consisiting of modes $\boldsymbol{\psi}_5$ and $\boldsymbol{\psi}_8$, with the energy 1.8% and 1.3% respectively. Although these modes do not have exactly the same energy they form a pair as shown by the POD coefficients in figure 13(c). The corresponding power spectrum of the time signal, figure 13(d), clearly shows a low-frequency peak with $St = 0.0188$ which nearly matches the shedding frequency $St_1 = 0.017$ (associated with the separation region downstream of the jet orifice and close to the wall). Indeed, as shown in figure 12(f), this mode has a significant anti-symmetric and large-scale structure near the wall. However, this mode also has structures along the jet trajectory further away from the wall. This indicates that the shedding of wall vortices is coupled to the jet body, i.e. the low frequency can be detected nearly anywhere in the vicinity of the jet since the whole jet is oscillating with that frequency.

6. Discussion and conclusions

We have performed numerical simulations of a jet in crossflow and analyzed two steady and three unsteady vortex systems by means of the time-averaged mean flow and its associated POD modes and the steady solution to Navier–Stokes equations and its associated linear global eigenmodes.

The result can be summarized as follows.

(i) A steady-state solution of the jet has been analyzed, featuring a dominant counter-rotating vortex pair (CVP), horseshoe and wake vortices. The CVP is a true steady vortex system and the associated roll-up of shear-layer vortices is not the origin of the CVP. The steady-state solution also shows that the CVP is composed of an outer shell (shear layer), shielding the inner CVP from the crossflow fluid. The downstream deflection of the outer vortex sheet leads to the formation of a secondary (lower) CVP, composed of swirling fluid of the crossflow. This secondary CVP can be observed for long distances downstream, however, it is weaker than the main (upper) CVP.

(ii) Shear-layer vortices were observed in the non-linear DNS to be continuously shed with a frequency of $St_2 = 0.14$, initiated by a separation region
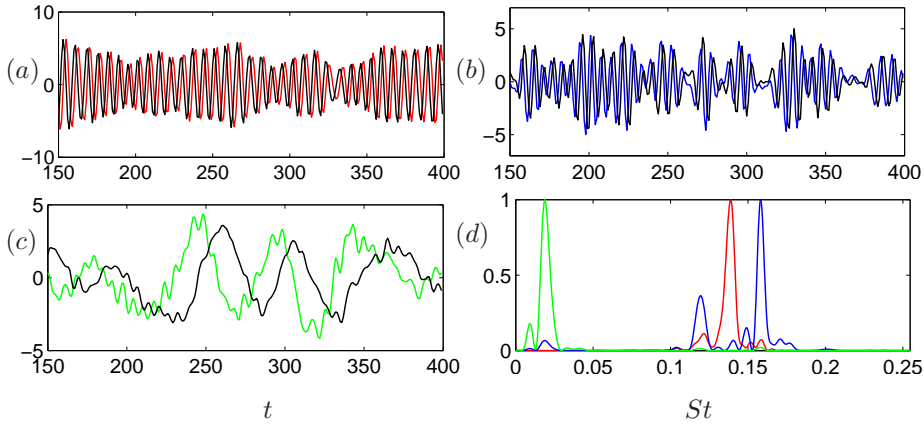
FIGURE 13. The temporal behavior of POD modes are show in terms of the POD coefficients. (*a*) POD coefficients of the first pair, (*b*) second pair and (*c*) third pair of modes. The power spectrum of the signals in (a,b,c) is shown with the same color.

about one jet diameter along the jet trajectory. This frequency is one of two fundamental frequencies in the flow, as all other frequencies in the flow were found to be higher harmonics of these two. The frequency $St_2 = 0.14$ matches the frequency obtained from the POD analysis $St = 0.138$ for the most energetic mode pair, whereas it is smaller than the Strouhal number 0.169 obtained from the linear global analysis for the most unstable global mode. The leading POD mode and most unstable linear global eigenmodes are both anti-symmetric coherent structures associated with the shear-layer vortices. In particular, we could identify "two-lobe" structures in the most unstable global mode that are strikingly similar to previous experimental, numerical and analytical studies of elliptic short-wave instability of a vortex pair. The symmetric unstable modes have "arch-like" structures of vortex loops that are similar to previous studies of the Kelvin-Helmholtz shear-layer roll-up on the upper side of the cylindrical vortex sheet. It remains to be shown if near the separated region a pocket of absolute instability exists that sheds vortices which then grow as they propagate along the CVP. However, we are investigating this issues further using both global and local techniques.

(iii) Upright vortices were observed in the DNS which connect the shear-layer vortices to the wall vortices. The upright vortices are also shed with the shear-layer frequency St_2. The connection of the vortex systems was also confirmed by both the linear and POD analysis, since the shear-layer global modes display significant connected structures on the leeward side of the CVP, oriented in the vertical direction towards the flat plate.

(iv) The second fundamental frequency is the shedding of wall vortices with $St_1 = 0.017$ from a separation region just downstream of the jet nozzle.

The spanwise oscillation of the separated region is similar to the von-Kármán vortex street observed behind bluff bodies. The global coherent structures also capture this dynamics. The physical insight gained by an unstable linear global eigenmode showed remarkable similarities with global modes of the wake behind circular cylinder. The POD mode associated with the wall vortices, on the other hand, indicates that the whole jet is oscillating with the low frequency as the coherent mode has non-zero amplitude along the jet trajectory. Similarly to high frequency St_2, the shedding frequency in the wall region $St_1 = 0.017$ is very close to $St = 0.0188$ obtained from the POD analysis, but significantly smaller than $St = 0.043$ obtained from the linear global analysis.

References

ÅKERVIK, E., BRANDT, L., HENNINGSON, D. S., HŒPFFNER, J., MARXEN, O. & SCHLATTER, P. 2006 Steady solutions of the Navier-Stokes equations by selective frequency damping. *Phys. Fluids* **18** (068102), 1–4.

ÅKERVIK, E., EHRENSTEIN, U., GALLAIRE, F. & HENNINGSON, D. S. 2008 Global two-dimensional stability measures of the flat plate boundary-layer flow. *Eur. J. Mech. B* **27**, 501–513.

ÅKERVIK, E., HŒPFFNER, J., EHRENSTEIN, U. & HENNINGSON, D. S. 2007 Optimal growth, model reduction and control in a separated boundary-layer flow using global eigenmodes. *J. Fluid. Mech.* **579**, 305–314.

ALAM, M. & SANDHAM, N. D. 2000 Direct numerical simulation of laminar separation bubbles with turbulent reattachment. *J. Fluid Mech.* **403**, 223–250.

BAGHERI, S., ÅKERVIK, E., BRANDT, L. & HENNINGSON, D. S. 2009*a* Matrix-free methods for the stability and control of boundary layers. *AIAA J.* **47**, 1057–1068.

BAGHERI, S., SCHLATTER, P., SCHMID, P. J. & HENNINGSON, D. S. 2009*b* Global stability of a jet in crossflow. *J. Fluid Mech.* **624**, 33–44.

BARKLEY, D., GOMES, M. G. & HENDERSON, R. D. 2002 Three-dimensional instability in flow over a backward-facing step. *J. Fluid Mech.* **473**, 167–190.

BERTOLOTTI, F. P., HERBERT, T. & SPALART, P. R. 1992 Linear and nonlinear stability of the Blasius boundary layer. *J. Fluid Mech.* **242**, 441–474.

BLANCHARD, J. N., BRUNET, Y. & MERLEN, A. 1999 Influence of a counter rotating vortex pair on the stability of a jet in a cross flow: An experimental study by flow visualizations. *Exp. Fluids* **26** (1), 63–74.

CHEVALIER, M., SCHLATTER, P., LUNDBLADH, A. & HENNINGSON, D. S. 2007 SIMSON - A Pseudo-Spectral Solver for Incompressible Boundary Layer Flows. *Tech. Rep.* TRITA-MEK 2007:07. KTH Mechanics, Stockholm, Sweden.

CHOMAZ, J., HUERRE, P. & REDEKOPP, L. 1991 A frequency selection criterion in spatially developing flows. *Stud. Appl. Math.* **84**, 119-114.

CORTELEZZI, L. & KARAGOZIAN, A. R. 2001 On the formation of the counter-rotating vortex pair in transverse jets. *J. Fluid Mech.* **446**, 347–373.

CROW, S. C. 1970 Stability theory for a pair of trailing vortices. *AIAA J.* **8**, 2172.

FABRE, D., COSSU, C. & JACQUIN, L. 2000 Spatio-temporal development of the long and short-wave vortex-pair instabilities. *Phys. Fluids* **12** (5), 1247–1250.

FRIC, T. F. & ROSHKO, A. 1994 Vortical structure in the wake of a transverse jet. *J. Fluid Mech.* **279**, 1–47.

GIANNETTI, F. & LUCHINI, P. 2007 Structural sensitivity of the first instability of the cylinder wake. *J. Fluid Mech.* **581**, 167–197.

HAMMOND, D. A. & REDEKOPP, L. G. 1998 Local and global instability properties of separation bubbles. *Euro. J. Mech. B/Fluids* **17** (2), 145 – 164.

HOLMES, P., LUMLEY, J. & G., B. 1996 *Turbulence Coherent Structuresm Dynamical Systems and Symmetry*. Cambridge University Press, Cambridge, U.K.

HUERRE, P. & MONKEWITZ, P. 1990 Local and global instabilities in spatially developing flows. *Ann. Rev. Fluid Mech.* **22**, 473–537.

HUERRE, P. & MONKEWITZ, P. A. 1985 Absolute and convective instabilities in free shear layers. *J. Fluid Mech.* **159**, 151–168.

Jeong, J. & Hussain, F. 1995 On the identification of a vortex. *J. Fluid Mech.* **285**, 69–94.

Kelso, R. M., Lim, T. T. & Perry, A. E. 1996 An experimental study of round jets in cross-flow. *J. Fluid Mech.* **306**, 111–144.

Laporte, F. & Corjon, A. 2000 Direct numerical simulations of the elliptic instability of a vortex pair. *Phys. Fluids* **12** (5), 1016–1031.

Leweke, T. & Williamson, C. H. K. 1998 Cooperative elliptic instability of a vortex pair. *J. Fluid Mech.* **360**, 85–119.

Lim, T. T., New, T. H. & Luo, S. C. 2001 On the development of large-scale structures of a jet normal to a cross flow. *Phys. Fluids* **13** (3), 770–775.

Marquillie, M. & Ehrenstein, U. 2002 On the onset of nonlinear oscillations in a separating boundary-layer flow. *J. Fluid Mech.* **458**, 407–417.

Megerian, S., Davitian, L., Alves, L. & Karagozian, A. 2007 Transverse-jet shear-layer instabilities. Part 1. Experimental studies. *J. Fluid Mech.* **593**, 93–129.

Muppidi, S. & Mahesh, K. 2005 Study of trajectories of jets in crossflow using direct numerical simulation. *J. Fluid Mech.* **530**, 81–100.

Muppidi, S. & Mahesh, K. 2006 Two-dimensional model problem to explain counter-rotating vortex pair formation in a transverse jet. *Phys. Fluids* **18** (085103), 1–9.

Muppidi, S. & Mahesh, K. 2007 Direct numerical simulation of round turbulent jets in crossflow. *J. Fluid Mech.* **574**, 59–84.

Nordström, J., Nordin, N. & Henningson, D. S. 1999 The fringe region technique and the Fourier method used in the direct numerical simulation of spatially evolving viscous flows. *SIAM J. Sci. Comput.* **20** (4), 1365–1393.

Sirovich, L. 1987 Turbulence and the dynamics of coherent structures i-iii. *Quart. Appl. Math.* **45**, 561–590.

Smith, S. H. & Mungal, M. G. 1998 Mixing, structure and scaling of the jet in crossflow. *J. Fluid Mech.* **357**, 83–122.

Theofilis, V. 2005 Advances in global linear instability analysis of nonparallel and three-dimensional flows. *Progr. Aerosp. Sci.* **39**, 249–315.

Theofilis, V., Hein, S. & Dallmann, U. 2000 On the origins of unsteadiness and three-dimensionality in a laminar separation bubble. *Philos. Trans. R. Soc. Lond. A* **358**, 3229–3246.

Waleffe, F. 1990 On the three-dimensional instability of strained vortices. *Phys. Fluids A* **2** (1), 76–80.

Yuan, L. L., Street, R. L. & Ferziger, J. H. 1999 Large-eddy simulation of a round jet in crossflow. *J. Fluid Mech.* **379**, 71–104.

Ziefle, J. 2008 Large-eddy simulation of complex massively-separated turbulent flows. PhD thesis, ETH Zürich, Switzerland, Diss. ETH No. 17846.

Paper 7

7

Spectral analysis of nonlinear flows

Clarence W. Rowley[1], Igor Mezić[2], Shervin Bagheri, Philipp Schlatter and Dan S. Henningson

We present a technique for describing the global behavior of complex, nonlinear flows, by decomposing the flow into modes determined from spectral analysis of the Koopman operator, an infinite-dimensional linear operator associated with the full nonlinear system. These modes, referred to as Koopman modes, are associated with a particular observable, and may be determined directly from data (either numerical or experimental) using a variant of a standard Arnoldi method. They have an associated temporal frequency and growth rate and may be viewed as a nonlinear generalization of global eigenmodes of a linearized system. They provide an alternative to Proper Orthogonal Decomposition, and in the case of periodic data the Koopman modes reduce to a discrete temporal Fourier transform. The Arnoldi method used for computations is identical to the Dynamic Mode Decomposition recently proposed by Schmid & Sesterhenn (2008), so Dynamic Mode Decomposition can be thought of as an algorithm for finding Koopman modes. We illustrate the method on an example of a jet in crossflow, and show that the method captures the dominant frequencies and elucidates the associated spatial structures.

1. Introduction

Many fluid flows exhibit complex phenomena that occur on a wide range of scales in both space and time. Even with large amounts of information available from simulations, and comprehensive experimental measurements such as time-resolved Particle Image Velocimetry (PIV), analysis of complex flow phenomena directly from raw time histories of the dynamics is usually not fruitful. In practice, one often analyzes flow structures by decomposing them into *modes.* Common techniques include global eigenmodes for linearized dynamics (see, *e.g.*, Bagheri *et al.* 2009), discrete Fourier transforms, Proper Orthogonal Decomposition (POD) for nonlinear flows (Holmes *et al.* 1996), balancing modes for linear systems (Rowley 2005), and many variants of these techniques, such as using shift modes (Noack *et al.* 2003) in conjunction with POD modes.

[1]Dept. of Mechanical and Aerospace Engineering, Princeton University, NJ 08544
[2]Dept. of Mechanical Engineering, University of California, Santa Barbara, CA 93106-5070

Here, we present a modal decomposition for nonlinear flows based on spectral analysis of a linear operator, called the *Koopman operator*, that is defined for any nonlinear system. Even if the governing dynamics are finite dimensional, the Koopman operator is infinite dimensional, and does not rely on linearization of the dynamics: indeed, it captures the full information of the nonlinear system. This operator has been used to analyze nonlinear dynamical systems, for instance in Mezić & Banaszuk (2004) and Mezić (2005), and in these works it was shown that for nonlinear systems evolving on an attractor, modes corresponding to eigenvalues of the Koopman operator may be computed using *harmonic averages*, or discrete Fourier transforms.

The paper is organized as follows. In section 2, we define the Koopman operator and its modes associated with a particular observable. In section 3, we show that one may compute approximations to these eigenvalues and their associated modes using a version of the familiar Arnoldi algorithm that does not require knowledge of an underlying linear operator. This algorithm is the same as that referred to as Dynamic Mode Decomposition by Schmid & Sesterhenn (2008). Finally, in section 4, we illustrate the method on an example of a jet in crossflow.

2. Koopman operator and Koopman modes

Consider a dynamical system evolving on a manifold M such that, for $\mathbf{x}_k \in M$,

$$\mathbf{x}_{k+1} = \mathbf{f}(\mathbf{x}_k), \tag{1}$$

where $\mathbf{f}$ is a map from M to itself, and k is an integer index. Note that one could equivalently study continuous-time systems of the form $\dot{\mathbf{x}}(t) = \mathbf{f}(\mathbf{x}(t))$, but here we adopt the discrete-time setting, as we are ultimately interested in analyzing discrete-time data. The *Koopman operator* is a linear operator U that acts on scalar-valued functions on M in the following manner: for any scalar-valued function $g : M \to \mathbb{R}$, U maps g into a new function Ug given by

$$Ug(\mathbf{x}) = g(\mathbf{f}(\mathbf{x})). \tag{2}$$

Note that U is a linear operator, since $U(\alpha g_1 + \beta g_2)(\mathbf{x}) = \alpha Ug_1(\mathbf{x}) + \beta Ug_2(\mathbf{x})$ for any functions g_1, g_2, and scalars α, β. Although the dynamical system is nonlinear and evolves on a finite-dimensional manifold M, the Koopman operator U is linear, but infinite-dimensional.

The idea is to analyze the flow dynamics governed by (1) only from available data—collected either numerically or experimentally—using the eigenfunctions and eigenvalues of U. To this end, let $\varphi_j : M \to \mathbb{R}$ denote eigenfunctions and $\lambda_j \in \mathbb{C}$ denote eigenvalues of the Koopman operator,

$$U\varphi_j(\mathbf{x}) = \lambda_j \varphi_j(\mathbf{x}), \qquad j = 1, 2, \ldots \tag{3}$$

and consider a vector-valued *observable* $\mathbf{g} : M \to \mathbb{R}^p$. For instance, if $\mathbf{x} \in M$ contains the full information about a flow field at a particular time, $\mathbf{g}(\mathbf{x})$ is a vector of any quantities of interest, such as a velocity measurements at various points in the flow. If each of the p components of $\mathbf{g}$ lies within the span of the

eigenfunctions φ_j, then as in Mezić (2005), we may expand[3] the vector-valued $\mathbf{g}$ in terms of these eigenfunctions, as

$$\mathbf{g}(\mathbf{x}) = \sum_{j=1}^{\infty} \varphi_j(\mathbf{x})\mathbf{v}_j. \tag{4}$$

We typically think of this expression as expanding $\mathbf{g}(\mathbf{x})$ as a linear combination of the vectors $\mathbf{v}_j$, but we may alternatively think of this expression as expanding the function $\mathbf{g}(\mathbf{x})$ as a linear combination of the eigenfunctions φ_j of U, where now $\mathbf{v}_j$ are the (vector) coefficients in the expansion. In this paper, we will refer to the eigenfunctions φ_j as *Koopman eigenfunctions*, and the corresponding vectors $\mathbf{v}_j$ in (4) the *Koopman modes* of the map $\mathbf{f}$, corresponding to the observable $\mathbf{g}$. Note that iterates of $\mathbf{x}_0$ are then given by

$$\mathbf{g}(\mathbf{x}_k) = \sum_{j=1}^{\infty} U^k \varphi_j(\mathbf{x}_0)\mathbf{v}_j = \sum_{j=1}^{\infty} \lambda_j^k \varphi_j(\mathbf{x}_0)\mathbf{v}_j. \tag{5}$$

The *Koopman eigenvalues*, $\lambda_j \in \mathbb{C}$, therefore characterize the temporal behavior of the corresponding Koopman mode $\mathbf{v}_j$: the phase of λ_j determines its frequency, and the magnitude determines the growth rate. Note that, as described in Mezić (2005), for a system evolving on an attractor, the Koopman eigenvalues always lie on the unit circle.

The following examples illustrate that eigenvalues and eigenfunctions of the Koopman operator are related to objects we routinely use in fluid mechanics, such as global eigenmodes (for linear systems) and the discrete Fourier transform (for periodic solutions of 1).

2.1. *Example: Koopman modes for linear systems*

Suppose M is an n-dimensional linear space, and suppose the map $\mathbf{f}$ is linear, given by

$$\mathbf{f}(\mathbf{x}) = \mathbf{A}\mathbf{x}. \tag{6}$$

It turns out that eigenvalues of $\mathbf{A}$ are also eigenvalues of U, and the eigenvectors of $\mathbf{A}$ are related to eigenfunctions of U as well.

Let $\mathbf{v}_j$ and λ_j denote eigenvectors and eigenvalues of $\mathbf{A}$:

$$\mathbf{A}\mathbf{v}_j = \lambda_j \mathbf{v}_j, \qquad j = 1, \dots, n, \tag{7}$$

and let $\mathbf{w}_j$ be corresponding eigenfunctions of the adjoint $\mathbf{A}^*$ (that is, $\mathbf{A}^*\mathbf{w}_j = \bar{\lambda}_j \mathbf{w}_j$), normalized so that $\langle \mathbf{v}_j, \mathbf{w}_k \rangle = \delta_{jk}$, where $\langle \cdot, \cdot \rangle$ denotes an inner product on M. Next, define scalar-valued functions

$$\varphi_j(\mathbf{x}) = \langle \mathbf{x}, \mathbf{w}_j \rangle, \qquad j = 1, \dots, n. \tag{8}$$

---

[3]Here, we assume that components of $\mathbf{g}$ lie within the span of the eigenfunctions of U. If this is not the case, then to proceed rigorously, one may split U into regular and singular components, and project components of $\mathbf{g}$ onto the span of the eigenfunctions, as done in Mezić (2005).

Then φ_j are eigenfunctions of U, with eigenvalues $\lambda_j{}^4$, since

$$U\varphi_j(\mathbf{x}) = \varphi_j(\mathbf{A}\mathbf{x}) = \langle \mathbf{A}\mathbf{x}, \mathbf{w}_j \rangle = \langle \mathbf{x}, \mathbf{A}^*\mathbf{w}_j \rangle = \lambda_j \langle \mathbf{x}, \mathbf{w}_j \rangle = \lambda_j \varphi_j(\mathbf{x}). \quad (9)$$

Now, for any $\mathbf{x} \in M$, as long as $\mathbf{A}$ has a full set of eigenvectors, we may write

$$\mathbf{x} = \sum_{j=1}^{n} \langle \mathbf{x}, \mathbf{w}_j \rangle \mathbf{v}_j = \sum_{j=1}^{n} \varphi_j(\mathbf{x})\mathbf{v}_j. \quad (10)$$

For linear systems, then, the Koopman modes coincide with the eigenvectors of $\mathbf{A}$.

2.2. *Example: Koopman modes for periodic solutions*

Returning to the nonlinear setting, suppose we have a set of distinct vectors $S = \{\mathbf{x}_0, \ldots, \mathbf{x}_{m-1}\}$ that form a periodic solution of (1), such that $\mathbf{x}_{k+m} = \mathbf{x}_k$ for all k. A common way to analyze such a solution is to take its discrete Fourier transform, which defines a new set of vectors $\{\hat{\mathbf{x}}_0, \ldots, \hat{\mathbf{x}}_{m-1}\}$ that satisfy

$$\mathbf{x}_k = \sum_{j=0}^{m-1} e^{2\pi i j k/m}\hat{\mathbf{x}}_j, \qquad k = 0, \ldots, m-1. \quad (11)$$

Now, define a set of functions $\varphi_j : S \to \mathbb{C}$ by

$$\varphi_j(\mathbf{x}_k) = e^{2\pi i j k/m}, \qquad j, k = 0, \ldots, m-1. \quad (12)$$

Then φ_j are eigenfunctions of the Koopman operator U, with eigenvalues $e^{2\pi i j/m}$, since

$$U\varphi_j(\mathbf{x}_k) = \varphi_j(\mathbf{f}(\mathbf{x}_k)) = \varphi_j(\mathbf{x}_{k+1}) = e^{2\pi i j(k+1)/m} = e^{2\pi i j/m}\varphi_j(\mathbf{x}_k). \quad (13)$$

Therefore, we may write the expansion (11) as

$$\mathbf{x}_k = \sum_{j=0}^{m-1} \varphi_j(\mathbf{x}_k)\hat{\mathbf{x}}_j. \quad (14)$$

Note the similarity with (10). Thus, if we restrict our phase space to the periodic orbit S, the Koopman modes defined as in the previous subsection are the vectors $\hat{\mathbf{x}}_j$ given by the discrete Fourier transform, and the phases of the corresponding eigenvalues are the frequencies $2\pi j/m$. This result in fact applies more generally to non-periodic systems, as discussed in Mezić & Banaszuk (2004) and Mezić (2005): when the dynamics are restricted to any attractor, the Koopman modes may be calculated by harmonic averages, which for finite-time datasets reduce to discrete Fourier transforms.

---

[4]Note that, unlike $\mathbf{A}$, the operator U has a countably infinite number of eigenvalues, since λ_j^k is also an eigenvalue, with eigenfunction $\varphi_j(\mathbf{x})^k$, for any integer k.

3. Computation of Koopman modes from snapshots

Here, we present an algorithm for computing the Koopman modes defined in the previous section, given only values of a particular observable (snapshots), sampled at regular times. As before, we will assume that the dynamics are governed by (1), and that for any state $\mathbf{x}$, we can measure a vector-valued observable $\mathbf{g}(\mathbf{x}) \in \mathbb{R}^p$. For instance, if we have access to a grid of velocity vectors in a limited region of space (e.g. obtained via PIV), then p is the number of grid points times velocity components.

In particular, below we show that the commonly-used Arnoldi algorithm, when applied to a nonlinear system, actually produces approximations to eigenvalues of the Koopman operator, and their corresponding modes as defined in the previous section. We first consider linear systems, and present a version of the Arnoldi algorithm that does not require explicit knowledge of the underlying operator $\mathbf{A}$. This variant of the algorithm is described on p. 287 of Saad (1980), and is the same as that referred to as Dynamic Mode Decomposition by Schmid & Sesterhenn (2008). We then provide an alternative interpretation of the algorithm that applies to nonlinear systems, and connects with the Koopman modes.

3.1. *Arnoldi algorithm for linear systems*

Assume one has a linear dynamical system

$$\mathbf{x}_{k+1} = \mathbf{A}\mathbf{x}_k \tag{15}$$

where $\mathbf{x}_k \in \mathbb{R}^n$, and n is so large that we cannot compute eigenvalues of $\mathbf{A}$ directly. A standard method for computing estimates of these eigenvalues is a *Krylov method*, in which one starts with an initial vector $\mathbf{x}_0$ (often chosen to be a random vector), and computes iterates of $\mathbf{x}_0$. After $m-1$ iterations, one has a collection of m vectors that span a *Krylov subspace*, given by

$$\text{span}\{\mathbf{x}_0, \mathbf{A}\mathbf{x}_0, \ldots, \mathbf{A}^{m-1}\mathbf{x}_0\}.$$

One then finds approximate eigenvalues and eigenvectors by projecting $\mathbf{A}$ onto this m-dimensional subspace, and computing eigenvectors and eigenvalues of the resulting low-rank operator. If we stack the data vectors into an $n \times m$ matrix

$$\mathbf{K} = \begin{bmatrix} \mathbf{x}_0 & \mathbf{A}\mathbf{x}_0 & \mathbf{A}^2\mathbf{x}_0 & \cdots & \mathbf{A}^{m-1}\mathbf{x}_0 \end{bmatrix} \tag{16}$$

$$= \begin{bmatrix} \mathbf{x}_0 & \mathbf{x}_1 & \mathbf{x}_2 & \cdots & \mathbf{x}_{m-1} \end{bmatrix}, \tag{17}$$

then we wish to find approximate eigenvectors of $\mathbf{A}$ as linear combinations of the columns of $\mathbf{K}$. The *Arnoldi algorithm* is a type of Krylov method in which one orthonormalizes the iterates at each step, and it therefore involves computing the action of $\mathbf{A}$ on arbitrary vectors. A variant of this algorithm that does not require explicit knowledge of $\mathbf{A}$ is given below.

First, consider the special case where the m-th iterate $\mathbf{x}_m$ is a linear combination of the previous iterates. Following section 2 of Ruhe (1984), we may

write

$$\mathbf{x}_m = \mathbf{A}\mathbf{x}_{m-1} = c_0\mathbf{x}_0 + \cdots + c_{m-1}\mathbf{x}_{m-1} = \mathbf{K}\mathbf{c} \tag{18}$$

where $\mathbf{c} = (c_0, \ldots, c_{m-1})$. Thus, we have

$$\mathbf{A}\mathbf{K} = \mathbf{K}\mathbf{C} \tag{19}$$

where $\mathbf{C}$ is a *companion matrix* given by

$$\mathbf{C} = \begin{bmatrix} 0 & 0 & \cdots & 0 & c_0 \\ 1 & 0 & & 0 & c_1 \\ 0 & 1 & & 0 & c_2 \\ \vdots & & \ddots & & \vdots \\ 0 & 0 & \cdots & 1 & c_{m-1} \end{bmatrix}. \tag{20}$$

The eigenvalues of $\mathbf{C}$ are then a subset of the eigenvalues of $\mathbf{A}$: if

$$\mathbf{C}\mathbf{a} = \lambda\mathbf{a},$$

then using (19), one verifies that $\mathbf{v} = \mathbf{K}\mathbf{a}$ is an eigenvector of $\mathbf{A}$, with eigenvalue λ.

More generally, if the m-th iterate is not a linear combination of the previous iterates, then instead of the equality (18), we have a residual

$$\mathbf{r} = \mathbf{x}_m - \mathbf{K}\mathbf{c},$$

which is minimized when $\mathbf{c}$ is chosen such that $\mathbf{r}$ is orthogonal to

$$\text{span}\{\mathbf{x}_0, \ldots, \mathbf{x}_{m-1}\}$$

. In this case, the relation (19) becomes

$$\mathbf{A}\mathbf{K} = \mathbf{K}\mathbf{C} + \mathbf{r}\mathbf{e}^T,$$

where $\mathbf{e} = (0, \ldots, 1) \in \mathbb{R}^m$. The eigenvalues of $\mathbf{C}$ are then approximations to the eigenvalues of $\mathbf{A}$, called *Ritz values*, and the corresponding approximate eigenvectors are given by $\mathbf{v} = \mathbf{K}\mathbf{a}$, called *Ritz vectors*. Note that the full Arnoldi method is more numerically stable than this method, and reduces $\mathbf{A}$ to an upper Hessenberg matrix, rather than a companion matrix.

Algorithm

An important feature of the above algorithm is that it does not require explicit knowledge of the matrix $\mathbf{A}$: all it requires is a sequence of vectors, as summarized below.

Consider a sequence $\{\mathbf{x}_0, \ldots, \mathbf{x}_m\}$ where $\mathbf{x}_j \subset \mathbb{R}^n$. Define the *empirical Ritz values* λ_j and *empirical Ritz vectors* $\mathbf{v}_j$ of this sequence by the following algorithm:

- Define $\mathbf{K}$ by (17) and find constants c_j such that

$$\mathbf{r} = \mathbf{x}_m - \sum_{j=0}^{m-1} c_j\mathbf{x}_j = \mathbf{x}_m - \mathbf{K}\mathbf{c}, \qquad \mathbf{r} \perp \text{span}\{\mathbf{x}_0, \ldots, \mathbf{x}_{m-1}\}. \tag{21}$$

- Define the companion matrix $\mathbf{C}$ by (20) and find its eigenvalues and eigenvectors

$$\mathbf{C} = \mathbf{T}^{-1}\mathbf{\Lambda}\mathbf{T}, \qquad \mathbf{\Lambda} = \mathrm{diag}(\lambda_1, \ldots, \lambda_m), \qquad (22)$$

  where eigenvectors are columns of $\mathbf{T}^{-1}$.
- Define $\mathbf{v}_j$ to be the columns of $\mathbf{V} = \mathbf{K}\mathbf{T}^{-1}$.

If $\mathbf{x}_j = \mathbf{A}^j \mathbf{x}_0$, then the empirical Ritz values λ_j are the usual Ritz values of $\mathbf{A}$ after m steps of the Arnoldi method, and $\mathbf{v}_j$ are the corresponding Ritz vectors. These, then, are (usually) good approximations of the eigenvalues and eigenvectors of $\mathbf{A}$. However, if we do not have $\mathbf{x}_j = \mathbf{A}^j \mathbf{x}_0$ (for instance, if the sequence is generated by a nonlinear map), then at this point, it is not clear what the above algorithm produces. We show below that for a nonlinear system, the algorithm produces approximations of the Koopman modes and associated eigenvalues.

3.2. *Modal decomposition for nonlinear systems*

A more general interpretation of the above algorithm is provided by the following theorem, which will be used below.

Theorem 1. *Consider a set of data $\{\mathbf{x}_0, \ldots, \mathbf{x}_m\}$, and let λ_j, $\mathbf{v}_j$ be the empirical Ritz values and vectors of this sequence. Assume the λ_j are distinct. Then*

$$\mathbf{x}_k = \sum_{j=1}^{m} \lambda_j^k \mathbf{v}_j, \qquad k = 0, \ldots, m-1 \qquad (23)$$

$$\mathbf{x}_m = \sum_{j=1}^{m} \lambda_j^m \mathbf{v}_j + \mathbf{r}, \qquad \mathbf{r} \perp \mathrm{span}\{\mathbf{x}_0, \ldots, \mathbf{x}_{m-1}\}. \qquad (24)$$

Proof. Note that (23) may be written in matrix form as

$$\mathbf{K} := \begin{bmatrix} \mathbf{x}_0 & \mathbf{x}_1 & \cdots & \mathbf{x}_{m-1} \end{bmatrix} = \begin{bmatrix} \mathbf{v}_1 & \cdots & \mathbf{v}_m \end{bmatrix} \begin{bmatrix} 1 & \lambda_1 & \lambda_1^2 & \cdots & \lambda_1^{m-1} \\ 1 & \lambda_2 & \lambda_2^2 & \cdots & \lambda_2^{m-1} \\ \vdots & \vdots & \vdots & \ddots & \vdots \\ 1 & \lambda_m & \lambda_m^2 & \cdots & \lambda_m^{m-1} \end{bmatrix}. \qquad (25)$$

The rightmost matrix above is a *Vandermonde matrix*, which we will denote $\tilde{\mathbf{T}}$. Note that Vandermonde matrices and companion matrices are closely related, in that $\tilde{\mathbf{T}}$ diagonalizes the companion matrix $\mathbf{C}$ defined in (20), as long as the eigenvalues $\lambda_1, \ldots, \lambda_m$ are distinct. That is, $\tilde{\mathbf{T}}$ is precisely the matrix $\mathbf{T}$ in (22), and so $\mathbf{K} = \mathbf{V}\tilde{\mathbf{T}}$, which verifies (25), and therefore (23). Equation (24) then follows from the last column of the equality

$$\begin{bmatrix} \mathbf{x}_1 & \mathbf{x}_2 & \cdots & \mathbf{x}_m \end{bmatrix} = \mathbf{K}\mathbf{C} + \mathbf{r}\mathbf{e}^T = \mathbf{K}\tilde{\mathbf{T}}^{-1}\mathbf{\Lambda}\tilde{\mathbf{T}} + \mathbf{r}\mathbf{e}^T = \mathbf{V}\mathbf{\Lambda}\tilde{\mathbf{T}} + \mathbf{r}\mathbf{e}^T. \qquad (26)$$

$\square$

To illustrate how this theorem provides a connection with Koopman modes, consider a vector-valued observable $\mathbf{g} : M \to \mathbb{R}^p$ for the dynamical system (1) and its expansion (4) in the Koopman modes. Suppose we have a sequence of observations $\mathbf{g}(\mathbf{x}_k)$, for $k = 0, \ldots, m$, and let $\tilde{\lambda}_j$ and $\tilde{\mathbf{v}}_j$ be the empirical Ritz values and vectors for this sequence. Then, by Theorem 1, we have

$$\mathbf{g}(\mathbf{x}_k) = \sum_{j=1}^m \tilde{\lambda}_j^k \tilde{\mathbf{v}}_j, \qquad k = 0, \ldots, m-1 \tag{27}$$

$$\mathbf{g}(\mathbf{x}_m) = \sum_{j=1}^m \tilde{\lambda}_j^m \tilde{\mathbf{v}}_j + \mathbf{r}, \tag{28}$$

with $\mathbf{r} \perp \mathrm{span}\{\mathbf{g}(\mathbf{x}_0), \ldots, \mathbf{g}(\mathbf{x}_{m-1})\}$. Comparing with the expansion (5), the empirical Ritz values $\tilde{\lambda}_j$ and vectors $\tilde{\mathbf{v}}_j$ behave in precisely the same manner as the eigenvalues λ_j and modes $\mathbf{v}_j$ of U, but for the finite sum in (27) instead of the infinite sum (5).

If $\mathbf{r} = \mathbf{0}$ in (28), then as far as the data is concerned, the approximate modes are indistinguishable from "true" eigenvalues and spectral modes of U, with the expansion (4) consisting only of a finite number of terms.

If $\mathbf{r} \neq \mathbf{0}$, then there is some error, but this is in a sense the best one can do, since the $m + 1$ observations cannot in general be spanned by m modes. In fact, by the projection theorem, the error $\mathbf{r}$ in (28) is the same as the smallest possible error in projecting $\mathbf{g}(\mathbf{x}_m)$ onto any modes $\tilde{\mathbf{v}}_j$ formed from linear combinations of the first m data vectors. In this sense, the values $\tilde{\lambda}_j$ are then approximations of true eigenvalues λ_j of U, and the vectors $\tilde{\mathbf{v}}_j$ are approximations of the spectral modes $\mathbf{v}_j$, scaled by the constant values $\varphi_j(\mathbf{x}_0)$.[5]

4. Example: Jet in crossflow

The jet-in-crossflow configuration appears in a variety of applications and is a common way of mixing a jet fluid—injected through an orifice—with a uniform crossflow. Recently, Bagheri *et al.* (2009) showed that the jet in crossflow exhibits self-sustained global oscillations that can be associated with vortex shedding in different spatial regions. Using time traces, we extract and quantify here the oscillatory behavior of the flow from fully nonlinear direct numerical simulations (DNS) and show that the computed Koopman modes identify the relevant frequencies and the corresponding three-dimensional flow structures automatically.

The parameters and the numerical code are the same as in the DNS performed in Bagheri *et al.* (2009); the jet inflow ratio is $R \equiv V_{\mathrm{jet}}/U_\infty = 3$, the Reynolds number is $Re_{\delta_0^*} \equiv U_\infty \delta_0^* / \nu = 165$ and the ratio between the crossflow

---

[5]An interesting situation occurs if $\mathbf{g}(\mathbf{x}_0) = \mathbf{g}(\mathbf{x}_m)$. Then in (21), $c_0 = 1$ and $c_j = 0$ for all other values of j. The empirical Ritz values are then the m-th roots of unity, $\lambda_j = e^{2\pi i j/m}$, and the Vandermonde matrix $\mathbf{T}$ is the discrete Fourier transform matrix. Thus, in this case, the empirical Ritz vectors are given by the discrete Fourier transform of the data, at frequencies $2\pi j/m$, as illustrated by the example in section 2.2.
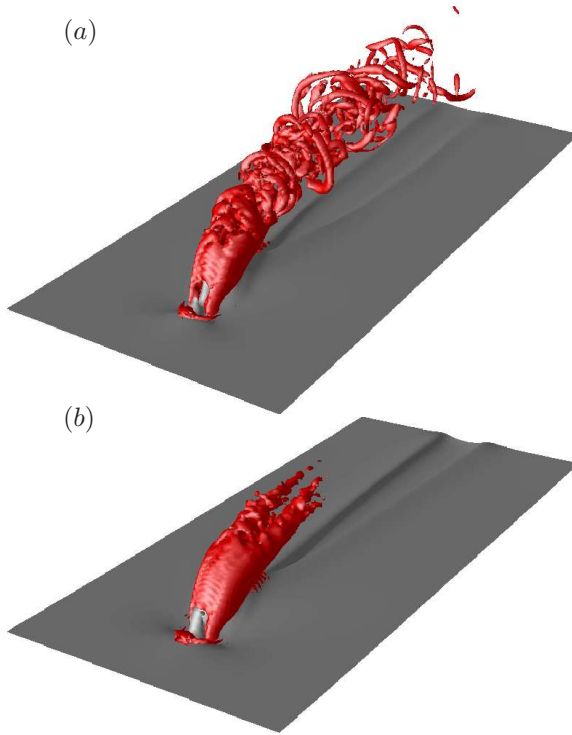
FIGURE 1. (*a*) Snapshot of the flow field at $t = 400$. Red and gray isocontours represent $\lambda_2 = -0.1$ and $u = 0.2$ (near the wall) respectively. (*b*) The same quantities for the time-averaged flow which also is the first Koopman mode.

displacement thickness and the jet diameter is $\delta_0^*/D = 1/3$. The incompressible Navier–Stokes equations over a flat-plate are solved using a Fourier-Chebyshev spectral method (Chevalier *et al.* 2007) and the jet with an initially parabolic velocity profile is introduced as an inhomogeneous boundary condition for the wall-normal velocity component at the wall ($y = 0$). The grid resolution is $256 \times 201 \times 144$ grid points in a computational box $(L_x, L_y, L_z) = (75, 20, 30)\delta_0^*$. The three-dimensional flow behavior is triggered by an asymmetric localized perturbation imposed at $t = 0$. For the exact form of the jet-profile and further numerical details see Bagheri *et al.* (2009).

The flow physics of the jet in crossflow has been studied extensively (see, *e.g.*, Fric & Roshko 1994; Kelso *et al.* 1996; Muppidi & Mahesh 2007) and it is shown that it is mainly characterized by four to five vortical structures depending on R and Re. In the present study, we could identify two steady, two unsteady and one quasi-steady vortex systems. Four of these can be seen in figure 1(a, b) where isocontours of the λ_2-criterion (red) (Jeong & Hussain
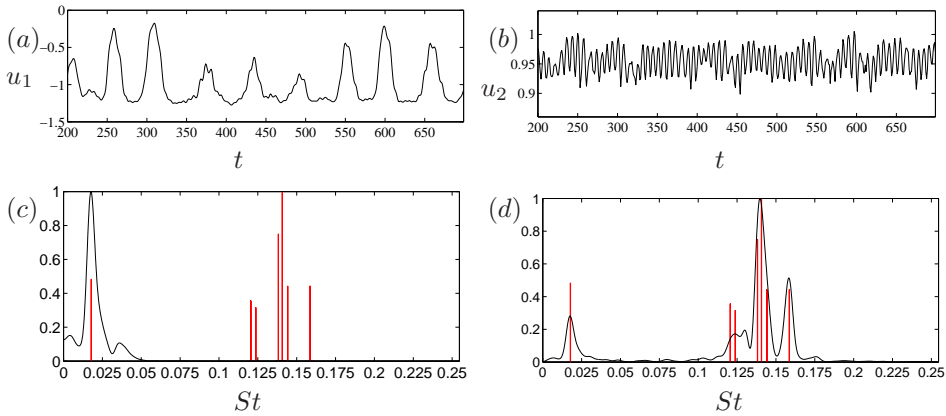
FIGURE 2. (a,b) Time signal probes located near the wall and on the jet shear layer respectively (see the text). (c,d) The spectral content of the corresponding time signals in (a,b) are shown in black and the magnitudes of the first seven pairs of spectral modes at each frequency are shown in red. The amplitudes are normalized with their maximum values.

1995) and the streamwise velocity (gray) are displayed. The most significant unsteady feature of the jet is the highly unsteady shear-layer vortices, see figure 1(*a*): These half-ringed shaped vortices grow along the jet trajectory, lead to a breakdown of the ordered flow and, eventually, dissipate due to viscous effects. Connected to the shear layer are the vertically oriented "upright vortices", which are periodically appearing vortices connecting the jet body and the wall layer in the wake of the jet. These structures are easily identified from the vorticity field, but are not visible here. On the other hand, the steady counter-rotating vortex pair (CVP), characteristic of the jet trajectory, is visible in the time-averaged mean flow, figure 1(*b*). Similarly visible in the mean, the horse-shoe vortices wrap around the column of jet very close to the wall and, further downstream, lead to the appearance of the quasi-steady wall-vortex system as shown by the distortion of the velocity isocontour in 1(*a, b*). These essentially streamwise-oriented vortices are subject to low-frequency oscillations of the wall-vortex system originating in a shedding of the separation zone just downstream of the jet orifice, and induce a movement of the whole jet body. The steady structures were also identified in the steady nonlinear Navier-Stokes solution computed numerically by Bagheri *et al.* (2009).

As found in Bagheri *et al.* (2009), two distinct self-sustained oscillations could be detected from the DNS. A high-frequency shedding of the shear-layer vortices and a very low frequency shedding of the wall vortices. Figure 2(*a*) shows the time signal of the streamwise velocity $u^1(\mathbf{x}_P^1, t)$ from a probe located just downstream of the jet orifice and close the wall, $\mathbf{x}_P^1 = (x, y, z) = (10.7, 1, 0)$. In figure 2(*c*) its corresponding power spectrum shows the frequency content
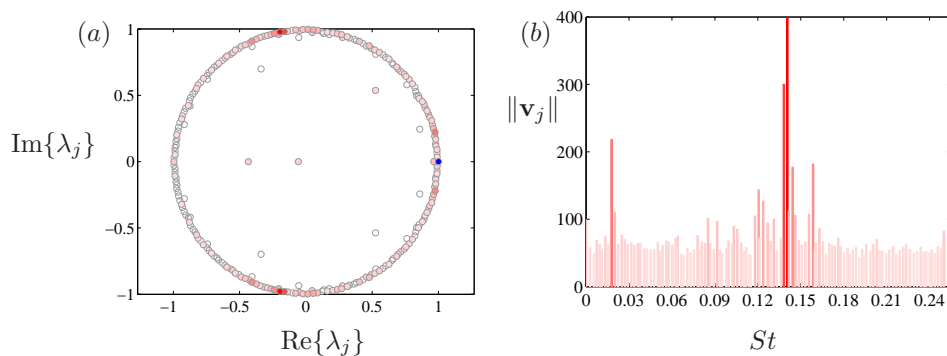
FIGURE 3. (*a*) The empirical Ritz values λ_j. The value corresponding to the first Koopman mode is shown with the blue symbol. (*b*) The magnitudes of the Koopman modes (except the first one) at each frequency. In both figures, the colors vary smoothly from red to white, depending on the magnitude of the corresponding mode.

$\hat{u}^1(\omega)$ of $u^1(t)$. The peak frequency corresponds to a vortex shedding of wake vortices with the Strouhal number $St \equiv fD/V_{jet} = 0.0174$.

In figure 2(b, d), a second probe located a few jet diameters along the jet trajectory $\mathbf{x}_P^2 = (12, 6, 2)$, shows a second oscillation that can be identified with the shedding of the shear-layer vortices. The peak frequency oscillates with $St = 0.141$ which is nearly one order of magnitude larger than the low-frequency mode. Note that the peak frequencies of the power spectra vary slightly depending on the location of the probe.

4.1. *Koopman modes and frequencies*

In this section we compute the Koopman modes and show that they directly allow an identification of the various shedding frequencies. The empirical Ritz values λ_j and the empirical vectors $\mathbf{v}_j$ of a sequence of flow-fields

$$\{\mathbf{u}_0, \mathbf{u}_1, \ldots, \mathbf{u}_{m-1}\} = \{\mathbf{u}(t = 200), \mathbf{u}(t = 202), \ldots, \mathbf{u}(t = 700)\}$$

with $m = 251$ are computed using the algorithm described earlier. Thus, the transient time ($t < 200$) is not sampled and only the asymptotic motion in phase space is considered.

Figure 3(a) shows that nearly all the Ritz values are on the unit circle $|\lambda_j| = 1$ indicating that the sample points $\mathbf{u}_i$ lie on or near an attracting set. The Koopman eigenvalue corresponding to the first Koopman mode is the time-averaged flow and is depicted with blue symbol in figure 3(a). This mode, shown in figure 1(b), captures the steady flow structures as discussed previously. In figure 3(a), the other (unsteady) Ritz values vary smoothly in color from red to white, depending on the magnitude of the corresponding Koopman mode.
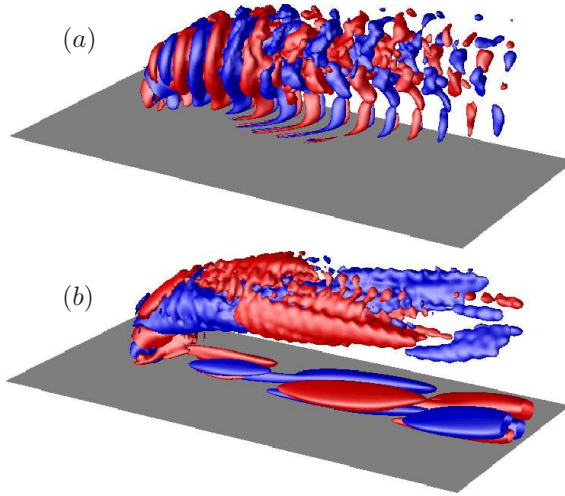
(*a*)

(*b*)

FIGURE 4. Positive (red) and negative (blue) contour levels of the streamwise velocity components of two Koopman modes. The wall is shown in gray. (*a*) Mode 2, with $\|\mathbf{v}_2\| = 400$ and $St_2 = 0.141$. (*b*) Mode 6, with $\|\mathbf{v}_6\| = 218$ and $St_6 = 0.0175$.

The magnitudes defined by the global energy norm $\|\mathbf{v}_j\|$, and are shown in figure 3(*b*) with the same coloring as the spectrum. In figure 3(*b*) each mode is displayed with a vertical line scaled with its magnitude at its corresponding frequency $\omega_j = \text{Im}\{\log(\lambda_j)\}/\Delta t$ (with $\Delta t = 2$ in our case). Only the $\omega_j \geq 0$ are shown, since the eigenvalues come in complex conjugate pairs. Ordering the modes with respect to their magnitude, the first (2-3) and second (4-5) pair of modes oscillate with $St_2 = 0.141$ and $St_4 = 0.136$ respectively, whereas the third pair of modes (6-7) oscillate with $St_6 = 0.017$. All linear combinations of the frequencies excite higher modes, for instance, the nonlinear interaction of the first and third pair results in the fourth pair, i.e. $St_8 = 0.157$ and so on.

In figures 2(*c*) and (*d*) the power spectra of the two DNS time signals (black lines) are compared to the frequencies obtained directly from the Ritz eigenvalues (red vertical lines). The shedding frequencies and a number of higher harmonics are in very good agreement with the frequencies of the Koopman modes. In particular, the dominant Koopman eigenvalues match the frequencies for the wall mode ($St = 0.017$) and the shear-layer mode ($St = 0.14$). Note that the probe signals are local measures of the frequencies at one spatial point, whereas the Koopman eigenvalues correspond to global modes in the flow with time-periodic motion.

The streamwise velocity component u of Koopman modes 2 and 6 are shown in figure 4. Each mode represents a flow structure that oscillates with one single frequency, and the superposition of several of these modes results in the quasiperiodic global system. The high-frequency mode 2 (figure 4*a*) can

Mode	DNS	Global	POD	Koopman
Shear layer	0.141	0.169	$0.138, 0.158, 0.121$	0.141
Wall	0.017	0.043	$0.0188, 0.0094, 0.158, 0.121$	0.017

TABLE 1. Comparison of the frequencies ($St = fD/V_{\text{jet}}$) obtained from DNS probes (shown in figure 2); the global eigenmodes of the linearized Navier-Stokes; POD modes 1 and 6, corresponding to mainly shear-layer and wall oscillations, respectively; and Koopman modes.

be associated with the shear layer vortices; along the jet trajectory there is first a formation of ring-like vortices that eventually dissolve into smaller scales due to viscous dissipation. Also visible are upright vortices: on the leeward side of the jet, there is a significant structure extending towards the wall. This indicates that the shear-layer vortices and the upright vortices are coupled and oscillate with the same frequency. The spatial structures of modes 4 and 8 are very similar to those of mode 2, as one expects, since the frequencies are very close.

On the other hand, the low-frequency mode 6 shown in figure 4(*b*) features large-scale positive and negative streamwise velocity near the wall, which can be associated with shedding of the wall vortices. However, this mode also has structures along the jet trajectory further away from the wall. This indicates that the shedding of wall vortices is coupled to the jet body, *i.e.* the low frequency can be detected nearly anywhere in the vicinity of the jet since the whole jet is oscillating with that frequency.

4.2. *Comparison with linear global modes and POD modes*

The linear global eigenmodes of the Navier-Stokes equations linearized about an unstable steady state solution were computed by Bagheri *et al.* (2009) for the same flow parameters as the current study. They computed 22 complex-conjugate unstable modes using the Arnoldi method combined with a time-stepper approach. The frequency of the most unstable (anti-symmetric) mode associated with the shear-layer instability was $St = 0.169$, not far from the value $St = 0.14$ observed for the DNS. However, the mode with the lowest frequency associated with the wall vortices was $St = 0.043$, far from the observed frequency of $St = 0.017$. These frequencies are summarized in table 1. The global eigenmodes capture the dynamics only in a neighborhood of the unstable fixed point, while the Koopman modes correctly capture the behavior on the attractor.

We also compared the Koopman modes with modes determined by Proper Orthogonal Decomposition (POD) of the same dataset. The POD modes themselves are shown in Schlatter *et al.* (2009), and capture similar spatial structures to the Koopman modes shown in figure 4. The most striking distinction is in
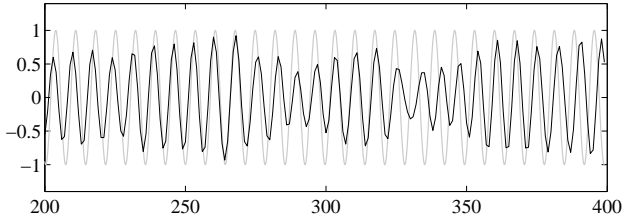
FIGURE 5. Comparison of time coefficients: the projection of the flow field onto the most energetic POD mode (black), and the coefficient of the most energetic Koopman mode (gray).

the time coefficients, an example of which is shown in figure 5: while a single Koopman mode contains, by construction, only a single frequency component, the POD modes capture the most energetic structures, resulting in modes that contains several frequencies. The coefficient of the first POD mode oscillates mainly with frequency $St = 0.138$, which is close to the shear-layer oscillation frequency $St = 0.141$ observed in DNS. However, the signal contains other frequencies as well, resulting from the interaction of the two fundamental oscillations (shear-layer and wall), $St = 0.138 \pm 0.017$, which cause the beating shown in figure 5. The frequencies present in this most energetic POD mode are also summarized in table 1. Higher POD modes (in this case the sixth) capture the wall oscillations, but the signal is polluted with other frequencies as well. For situations such as the jet in crossflow where one is interested in studying the dynamics of low-frequency oscillations (such as wall modes) separate from high-frequency oscillations (such as shear-layer modes), the Koopman modes are thus more effective at decoupling and isolating these dynamics.

5. Conclusions

We have presented a method for studying the dynamical behavior of nonlinear systems, and illustrated the method on a jet in crossflow. The method involves spectral analysis of the Koopman operator, an infinite-dimensional linear operator defined for any nonlinear dynamical system. In particular, given a particular observable (e.g. available measurements from an experiment or simulation), we have defined a set of *Koopman modes* associated with this observable, related to eigenfunctions of the Koopman operator. For the special case of linear systems where the observable is the full flow state, these modes reduce to the global eigenmodes, and for periodic systems, the modes can be determined by the discrete temporal Fourier transform. For more general systems, we have shown that these modes may be computed using a familiar Arnoldi algorithm, applied to samples of the nonlinear system.

We have used these modes to study the dynamical behavior of a jet in crossflow. The resulting modes illustrate the different spatial structures associated with the shear layer and the near-wall region. For this example, the Koopman

modes capture the relevant frequencies more accurately than global eigenmodes of the linearized dynamics, and decouple the different frequency components more effectively than modes determined by Proper Orthogonal Decomposition.

References

BAGHERI, S., SCHLATTER, P., SCHMID, P. & HENNINGSON, D. S. 2009*b* Global stability of a jet in crossflow. *J. Fluid Mech.* **624**, 33–44.

CHEVALIER, M., SCHLATTER, P., LUNDBLADH, A. & HENNINGSON, D. S. 2007 A pseudo spectral solver for incompressible boundary layer flows. *Tech Rep, Trita-Mek* **7**, KTH Mechanics, Stockholm.

FRIC, T. F. & ROSHKO, A. 1994 Vortical structure in the wake of a transverse jet. *J. Fluid Mech.* **279**, 1–47.

HOLMES, P., LUMLEY, J. L. & BERKOOZ, G. 1996 *Turbulence, Coherent Structures, Dynamical Systems and Symmetry*. Cambridge University Press.

JEONG, J. & HUSSAIN, F. 1995 On the identification of a vortex. *J. Fluid Mech.* **285**, 69–94.

KELSO, R., LIM, T. & PERRY, A. 1996 An experimental study of round jets in cross-flow. *J. Fluid Mech.* **306**, 111–144.

MEZIĆ, I. 2005 Spectral properties of dynamical systems, model reduction and decompositions. *Nonlin. Dyn.* **41**, 309–325.

MEZIĆ, I. & BANASZUK, A. 2004 Comparison of systems with complex behavior. *Phys. D* **197**, 101–133.

MUPPIDI, S. & MAHESH, K. 2007 Direct numerical simulation of round turbulent jets in crossflow. *J. Fluid Mech.* **574**, 59–84.

NOACK, B., AFANASIEV, K., MORZYŃSKI, M., TADMOR, G. & THIELE, F. 2003 A hierarchy of low-dimensional models for the transient and post-transient cylinder wake. *J. Fluid Mech.* **497**, 335–363.

ROWLEY, C. W. 2005 Model reduction for fluids using balanced proper orthogonal decomposition. *Int. J. Bifurcation Chaos* **15** (3), 997–1013.

RUHE, A. 1984 Rational Krylov sequence methods for eigenvalue computation. *Linear Algebra Appl.* **58**, 391–405.

SAAD, Y. 1980 Variations on Arnoldi's method for computing eigenelements of large unsymmetric matrices. *Linear Algebra Appl.* **34**, 269–295.

SCHMID, P. & SESTERHENN, J. 2008 Dynamic mode decomposition of numerical and experimental data. 61st Annual Meeting of the APS Division of Fluid Dynamics.

SCHLATTER, P., BAGHERI, S. & HENNINGSON, D. S. 2009*a* Self-sustained global oscillations in a jet in crossflow. *Theor. Comput. Fluid Dyn.* (submitted).

Paper 8

8

The stabilizing effect of streaks on Tollmien–Schlichting and oblique waves: A parametric study

Shervin Bagheri and Ardeshir Hanifi[1]

The stabilizing effect of finite amplitude streaks on the linear growth of un-stable perturbations (TS and oblique waves) is numerically investigated by means of the nonlinear Parabolized Stability Equations. We have found that for stabilization of a TS-wave, there exists an "optimal" spanwise spacing of the streaks. These streaks reach their maximum amplitudes close to the first neutral point of the TS-wave and induce the largest distortion of the mean flow in the unstable region of the TS-wave. For a such distribution, the required streak amplitude for complete stabilization of a given TS-wave is considerably lower than for $\beta = 0.45$, which is the optimal for streak growth and used in previous studies. We have also observed a damping effect of streaks on the growth rate of oblique waves in Blasius boundary layer and for TS-waves in Falkner-Skan boundary layers.

1. Introduction

In boundary-layer flows, the transition from a laminar state to a turbulent one is usually caused by growth and breakdown of small amplitude perturbations. For a long time the common understanding has been that any kind of flow perturbation inside the boundary layer has a promoting effect on transition. However, a number of recent studies (Saric *et al.* 1998; Cossu & Brandt 2002; Fransson *et al.* 2005, 2006) has indicated that certain types of perturbations inside the boundary layer can postpone the laminar-turbulent transition. General feature of these perturbations seems to be a modification of mean velocity profile to a more stable one. In two-dimensional mean flows, these are streaky structures which create regions of alternating negative and positive streamwise velocity perturbations. Streaks are usually found inside boundary layers subjected to high free-stream turbulence. A damping effect of moder-ate amplitude free-stream turbulence on Tollmien-Schlichting (TS) waves have been observed in some experiments (Boiko *et al.* 1994). Numerical investi-gations of Cossu & Brandt (2002) showed a clear stabilizing effect of streaks

---

[1]Also at Swedish Defence Research Agency, SE-164 90 Stockholm, Sweden

on growth of TS waves in Blasius flow. They reported an increasing damping effect with increasing streak amplitude. These results were later verified by experimental works of Fransson *et al.* (2005) who, generated the streaks by means of small roughness elements. Recently Fransson *et al.* (2006) also showed that these streaks can truly delay the transition. Here, the transition was triggered by means of high amplitude two-dimensional disturbances generated through random suction and blowing at the wall. These new results have received great attention, *e.g.* Choi (2006). However, in all these studies, both experimental and numerical, a single spanwise spacing ($\beta = 0.45$) of streaks has been used, which corresponds to the most growing streaks. Therefore, we aim to investigate whether other distributions of streaks are more efficient for stabilizing TS-waves, so that a lower streak amplitude would be required for transition delay. This is important because the amplitude of the streaks should not exceed the threshold for secondary instability and instead promoting the transition to turbulence. The present work is based on a parametric study of the streak spacing. The feasibility of such a study, requires a relative fast computational method, such as the nonlinear Parabolized Stability Equations (PSE)(Bertolotti *et al.* 1992).

2. Numerical procedure

We consider flow disturbances which are periodic in time t and spanwise direction z. These disturbances are decomposed in Fourier modes as

$$\mathbf{q}(\mathbf{x}, t) = \sum_{m=-M}^{M} \sum_{n=-N}^{N} \tilde{\mathbf{q}}_{mn}(x, y) \exp(in\beta_0 z - im\omega_0 t).$$

Here,

$$\tilde{\mathbf{q}}_{mn} = \hat{\mathbf{q}}_{mn}(x, y) \exp(i \int \alpha_{mn} \mathrm{d}x) \tag{1}$$

is the amplitude function of the mode $(m\omega_0, n\beta_0)$ (referred to as (m, n)), where β_0 denotes the fundamental spanwise wavenumber, ω_0 the fundamental frequency and α is the complex-valued streamwise wavenumber. Further, x and y are the streamwise and wall-normal coordinates, respectively. The evolution of each mode is described by the nonlinear PSE as given *e.g.* Bertolotti *et al.* (1992). In addition, we use a scaling proposed by Levin & Henningson (2003) to modify the PSE to correctly describe the evolution of streaks. These equations are then discretized using a fourth-order compact scheme for the wall-normal derivatives and first- or second-order backward Euler for the streamwise derivatives. It is well known that original PSE suffer from numerical instability for small streamwise step-size. Here, we use the technique proposed by Andersson *et al.* (1998) to stabilize the numerical integration. As initial condition for the streak, we use optimal disturbances (Andersson *et al.* 1999) at the leading edge, which in a linear framework lead to the maximum perturbation energy at a certain downstream position. These are computed with a spectral code
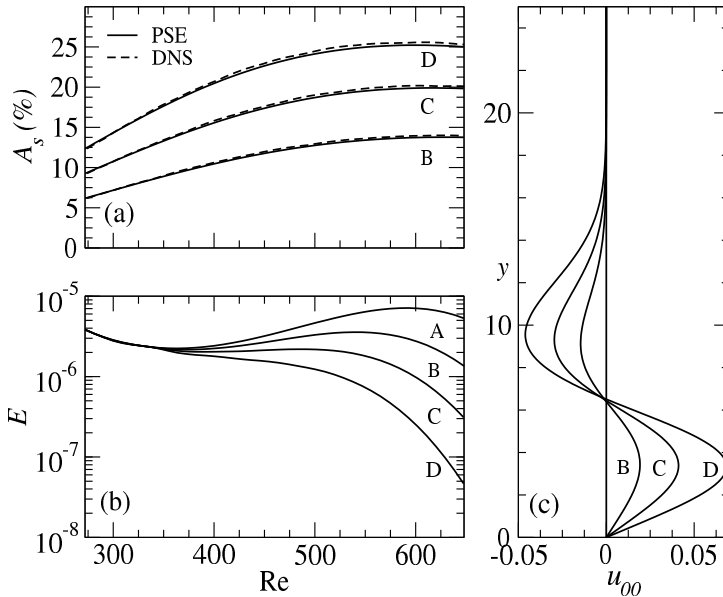
FIGURE 1.   (*a*) Comparison of DNS and PSE simulations of the non-linear downstream development of three streaks with increasing amplitudes. (*b*) The evolution of the TS-wave in presence of streaks. (*c*) The mean-flow distortion at $Re = 640$ caused by streaks.

used in Levin & Henningson (2003) based on an adjoint optimization technique described in Andersson *et al.* (1999).

The procedure of the simulations is as follows. An optimal disturbance is initiated close to the leading edge. Its linear downstream development is followed up to a specified streamwise position, where the nonlinear calculations begin by the assignment of an initial amplitude, defined as

$$A_s = \frac{1}{2} \left(\max_{y,z} \{u_s\} - \min_{y,z} \{u_s\} \right).$$

Here, u_s is the sum of the streamwise velocity component of all $(0, n)$-modes. At this location, a single exponential disturbance is initialized, (m, n)-mode, with an amplitude sufficiently low to insure its linear behavior. Unless otherwise stated, this location is upstream of the first neutral point of the exponential disturbances at $Re_0 = \sqrt{x_0 U_e/\nu} = 250$, where U_e is the streamwise velocity at the edge of the boundary layer and ν the kinematic viscosity. The length scale used here is $\sqrt{\nu x_0/U_e}$. Usually, $20 - 30$ modes were sufficient to correctly describe the evolution of the disturbances.

3. Results

3.1. *Validation*

The results obtained using the procedure described above, is verified against the direct numerical simulations of Cossu & Brandt (2002). As in Cossu & Brandt (2002), we consider the instability of a TS-wave of frequency $F = (\omega_0/Re) \times 10^6 = 131.6$ in the presence of a set of streaks $(\beta_0/Re = 6.36E - 4)$ with different amplitudes (figure 1a). The initial profiles of the streaks are optimized for maximum growth at $Re = 707$ and the nonlinear calculations begin at $Re_0 = 272$. As reported in Cossu & Brandt (2002) and shown in figure 1(b), the stabilizing effect on the TS-wave is observed for all streak amplitudes. Here, the following norm of the disturbance

$$E = \left(\int_0^\infty \mathbf{u} \cdot \mathbf{u}^* \, dy \right)^{1/2} ,$$

is used as a measure of the TS-wave size. In figure 1(b), case A corresponds to zero streak amplitude. For moderate streak amplitudes (B,C) a damping of the growth of the TS-wave is observed, whereas for a sufficiently large streak amplitude (D) the TS-wave is completely stabilized. In figure 1(c), the mean-flow distortion u_{00}, *i.e.* streamwise velocity component of the $(0,0)$-mode, is shown. This is induced by streaks and it modifies the velocity profile into a "fuller" shape close to the wall. This seems to be the main mechanism behind the stabilization effect of the streaks (Cossu & Brandt 2002).

3.2. *Effects of the spanwise wavenumber of the streak*

Previous studies (Cossu & Brandt 2002; Fransson *et al.* 2005, 2006) have solely been focusing on the effects of the streak amplitude. As the development of streaks also depends on its spanwise wavelength, it is of interest to investigate its effects on TS-wave instability. Therefore, we vary the spanwise wavenumber of streaks in the range $[0.1, 1]$. The initial profiles of these streaks are optimized for maximum growth at $Re = 400$. Assigning the same initial amplitude for each of them results in streaks with different maximum amplitudes. Since the stabilizing effect depends strongly on the streak amplitude, it is difficult to draw a definite conclusion about the significance of different values of β. Therefore, it seems reasonable to compare streaks with different β but same maximum amplitude. Here, for each streak we choose an appropriate initial amplitude such that the *maximum* amplitudes, A_s^*, of each of them is 10% of the free-stream velocity. To illustrate the effect of streak parameter β, we begin by investigating the stability of a two-dimensional TS-wave with frequency $F = 131.6$ in the presence of the two streaks shown in figure 2(a). The streaks, A and B, have the spanwise wavenumbers, $\beta_A = 0.45$ and $\beta_B = 0.65$ respectively and fixed maximum amplitude, $A_s^* = 10\%$. In figure 2(b), we show that in the absence of streaks the TS-wave (dotted line) grows exponentially (with a rate predicted by the linear theory) as it enters the unstable domain at branch I, the shaded domain, and decays as it is propagated downstream away from
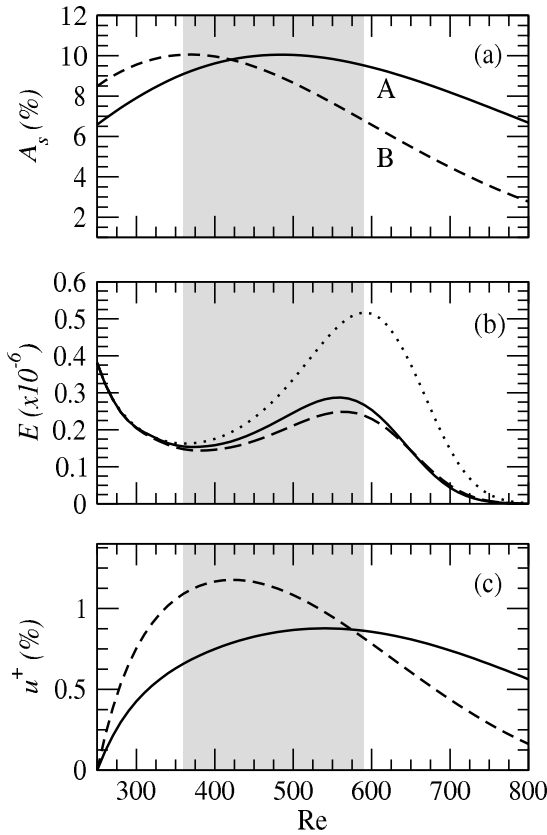
FIGURE 2.   (a) Evolution of amplitudes of two streaks with $\beta = 0.45$ (solid) and $\beta = 0.65$ (dashed). (b) TS wave with $F = 131.6$ in absence (dotted) and presence (dashed,solid) of streaks. (c) The maximum value of the mean flow distortion caused by the streaks.

the domain. In the presence of streaks a damping effect is observed, which is larger for streak B (dashed line) than for streak A (solid line), despite the fact that streak A maintains a *larger* amplitude in the most part of the unstable domain of the TS-wave. Streak B, on the other hand, attains its maximum amplitude close to the location of branch I of the TS-wave, and then rapidly decays downstream. This can be explained if the distortion of the mean flow, $(0,0)$-mode, induced by these two streaks are compared. In figure 2(c), the development of the maximum mean-flow distortion, *i.e.* $u^+ = \max_y\{u_{00}\}$, for streaks A and B is shown. It is apparent that streak B modifies the flow considerably more than streak A, between branch I and II, due to larger values of u^+. This is caused by the larger amplitude of streak B upstream of branch I.
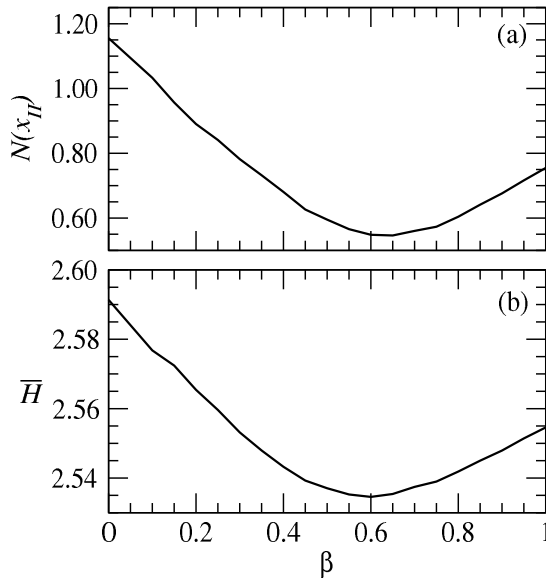
FIGURE 3.   (*a*) The N-factor at branch II of the TS-wave ($F = 131.6$) as a function of the spanwise wavenumber of streaks. The maximum amplitudes of the streaks have been fixed at $A_s^* = 10\%$. (*b*) The averaged shape factor $\bar{H}$ as a function of the same set of streaks as in (*a*).

As a measure of the amplification of the TS-waves, we compute the N-factor, defined as

$$N(x) = \ln(E(x)/E(x_I)).$$

In figure 3(*a*), $N(x_{II})$ for the TS-wave with $F = 131.6$ is plotted as a function of the spanwise wavenumber of the streaks, β. Here the maximum streak amplitudes are kept constant, $A_s^* = 10\%$. As shown in figure 3(*a*), $N(x_{II})$ attains a minimum value for $\beta \approx 0.65$. This indicates that there exists an optimal streaky boundary layer, when the objective is to minimize the amplification of the TS-wave. It should be mentioned that, due to nonlinear effects, there is a slight upstream shift of the location of the A_s^* with increasing initial streak amplitude (see figure 1*a*). Therefore, the "optimal" β depends weakly on the streak amplitude. In order to relate the total modification of the mean flow caused by streaks, to their stabilization effects we compare the N-factor with the averaged shape factor $\bar{H}$. Here, $\bar{H}$ is averaged in the streamwise direction between branch I and II of the TS-wave. In figure 3(*b*), $\bar{H}$ is plotted as a function of β. In the absence of streaks, the shape factor of a Blasuis profile is $\bar{H} = 2.59$, whereas in the presence of streaks $\bar{H}$ is smaller, indicating a fuller velocity profile. Furthermore, $\bar{H}$ attains a minimum value in the presence of streaks with $\beta = 0.6$, *i.e.* close to the β which minimizes the N-factor of the TS-wave (shown in figure 3*a*). This indicates that the commonly used streak with
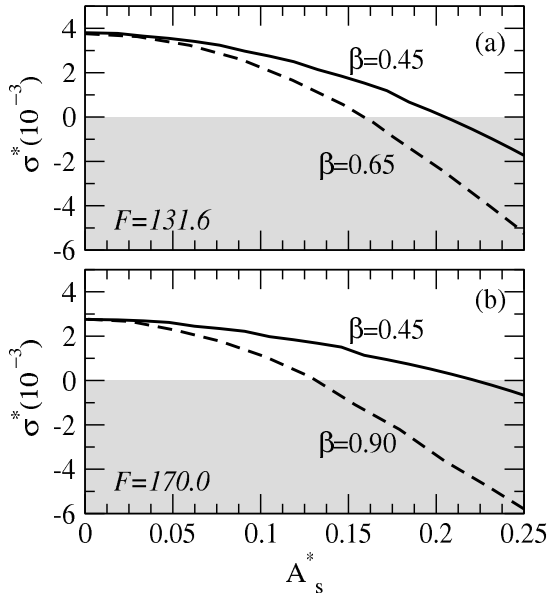
FIGURE 4.   The maximum growth rate σ^* of TS-waves, $F = 131.6$ in (a) and $F = 170$ in (b), in the presence of streaks.

$\beta = 0.45$ is not the most efficient stabilizing streak. This value of β corresponds to the vortices generated at the leading edge which experience the largest linear growth (Andersson *et al.* 1999). We have performed the same parametric study of β for two other frequencies, $F = 170$ and 90. For both frequencies the N-factor, $N(x_{II})$, attains a minimum at approximately the spanwise wavenumber (0.9 and 0.45 respectively), for which the streamwise averaged shape-factor is the smallest. Again, the streak which is the most efficient for stabilizing a TS-wave attains its maximum amplitude close to branch I of that TS-wave.

Now we aim at finding the minimum streak amplitude necessary for the complete stabilization of a TS-wave. We consider two different streaks: the optimal growing streak ($\beta = 0.45$) and a streak with $\beta = 0.65$, chosen such that the maximum streak amplitudes are close to branch I of the given TS wave. The maximum amplitudes are varied between $0 - 25\%$ and the maximum growth rates $\sigma^* = \max_x\{\sigma\}$ of the TS-wave are computed for each streak. The physical growth rates are calculated from the relation (Bertolotti *et al.* 1992) $\sigma = -\alpha_i + \frac{\partial}{\partial x} \ln(E)$. When $\sigma^* < 0$ the TS-wave is completely stabilized. For complete stabilization of a TS-wave with $F = 131.6$, the necessary amplitude of the streak with $\beta = 0.65$ is $A_s = 15\%$, whereas for $\beta = 0.45$ the corresponding amplitude is $A_s = 20\%$, see figure 4(a). For $F = 170$, the necessary amplitude is reduced from $A_s = 22\%$ to $A_s = 0.12\%$, when β is increased from 0.45 to 0.9, see figure 4(b). As the TS-wave frequency is decreased, the location of
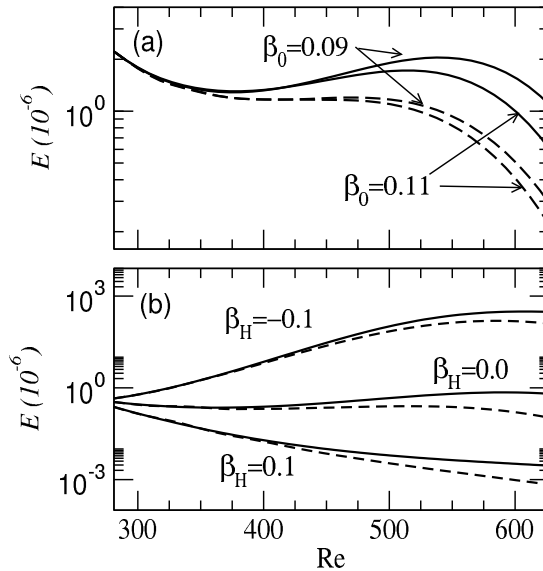
FIGURE 5.   (*a*) The downstream development of oblique waves ($F = 131.6$) in the absence (solid) and the presence (dashed) of streaks. (*b*) The downstream development of a TS-wave ($F = 131.6$) in the absence (solid) and the presence (dashed) of streaks in boundary layer with adverse, zero and favorable pressure gradient.

the branch I moves downstream and consequently streaks with smaller β are required to stabilize the flow.

3.3. *Stabilization of oblique waves*

The focus of previous investigations (Cossu & Brandt 2002; Fransson *et al.* 2005) has been on reducing the linear growth of two-dimensional TS-waves, as these disturbances are the first to become unstable in a Blasius boundary-layer. However, certain transition scenarios (Bertolotti *et al.* 1992), require the existence of oblique waves. Here, we choose two unstable oblique waves with frequency $F = 131.6$ and spanwise wavenumbers $\beta_0 = 0.09$ and 0.1123, respectively. For these values of β_0, a streak with a spanwise wavenumber $\beta = 0.45$ is initiated at $Re_0 = 272$ as modes $(0, 5\beta_0)$ and $(0, 4\beta_0)$, respectively. The oblique disturbances are initiated as a pair of modes $(1, \pm 1)$ with sufficiently small amplitude to insure a linear behavior. The results are shown in figure 5(*a*), where we compare the norm E of the oblique waves in the presence (dashed line) and the absence (solid line) of a streak with the maximum amplitude $A_s^* = 10\%$. Similar to TS-waves, the linear growth of the oblique waves is found to be damped when streaks are present.

3.4. *Effects of pressure gradient*

We have also investigated the effects of streaks on the linear growth of exponential disturbances in boundary-layer flows with pressure gradients. In particular, boundary layers with the free-stream velocities given as $U_e = U_\infty x^m$, $m = \beta_H/(2 - \beta_H)$, where β_H is the Hartree parameter. In figure 5(b), the evolution of a TS-wave with frequency $F = 131.6$ in boundary layers with favorable ($\beta_H = 0.1$), zero ($\beta_H = 0$) and adverse pressure ($\beta_H = -0.1$) gradients are shown by the solid lines. By introducing a streak at $Re_0 = 278$ with spanwise wavenumber $\beta = 0.45$ and amplitudes $A_s \approx 13 - 16\%$, the growth of TS-waves is damped (shown by dashed lines).

4. Conclusions

We have found that the stabilization effect of streaks on the linear growth of TS-waves in Blasius boundary layer, observed in previous studies, to also apply to three dimensional disturbances and Falkner-Skan boundary-layer flows. We have also found that by distributing the streaks "optimally" in the spanwise direction, it is possible to completely stabilize a TS-wave, with considerably lower streak amplitudes. For the TS-waves with high frequencies a reduction of the maximum streak amplitude of almost a factor two can be achieved. The streaks which most efficiently reduce the growth rate of a given disturbance attain their maximum amplitudes close to the branch I of that disturbance. These streaks generate a "fuller" velocity profile in the unstable domain of the TS-waves. By computing the streamwise averaged shape factor of the modified boundary layer, one can estimate the stabilization effect of streaks without actually calculating the interaction with the targeted TS (or oblique) waves. It should also be mentioned that the optimal growing streak, often associated with the spanwise wavenumber $\beta = 0.45$, is not the most efficient one to suppress TS-waves of all frequencies.

References

ANDERSSON, P., BERGGREN, M., & HENNINGSON, D.S. 1999 Optimal disturbances and bypass transition in boundary layers. *Phys. Fluids* **11**, 134–150.

ANDERSSON, P., HENNINGSON, D.S. & HANIFI, A. 1998 On a stabilization procedure for the parabolic stability equations. *J. Eng. Math.* **33**, 311–332.

BERTOLOTTI, F.P., HERBERT, TH., & SPALART, P.R. 1992 Linear and nonlinear stability of the Blasius boundary layer. *J. Fluid Mech.* **242**, 441–474.

BOIKO, A.V., WESTIN, K.J.A., KLINGMANN, B.G.B., KOZLOV, V.V. & ALFREDSSON, P.H. 1994 Experiments in a boundary layer subjected to free stream turbulence. Part 2. The role of TS-waves in the transition process. *J. Fluid Mech.* **281**, 219–245.

CHOI, K. 2006 The rough with the smooth. *Nature* **440**, 754.

COSSU C. & BRANDT L. 2002 Stabilization of Tollmien-Schlichting waves by finite amplitude optimal streaks in the Blasius boundary layer. *Phys. Fluids* **14**, L57.

FRANSSON J.H.M., BRANDT, L., TALAMELLI, A. & COSSU, C. 2005 Experimental study of the stabilization of Tollmien-Schlichting waves by finite amplitude streaks. *Phys. Fluids* **17**, 054110.

FRANSSON, J.H.M, TALAMELLI, A., BRANDT, L. & COSSU, C. 2006 Delaying transition to turbulence by a passive mechanism. *Phys. Rev. Lett.* **96**, 064501.

LEVIN, O. & HENNINGSON, D.S. 2003 Exponential vs algebraic growth and transition prediction in boundary layer flow. *Flow, Turbulence Combust* **70**, 183-210a.

SARIC, W.S., CARILLO R.B. JR. & REIBERT, M.S. 1998 Leading-edge roughness as a transition control mechanism. *AIAA Paper* **98**, 0781.